



**HEINRICH HEINE**  
**UNIVERSITÄT DÜSSELDORF**

**Metall-organische Koordinationsnetzwerke als  
Metallogele und in Membranen**

Inaugural-Dissertation

zur Erlangung des Doktorgrades  
der Mathematisch-Naturwissenschaftlichen Fakultät  
der Heinrich-Heine-Universität Düsseldorf

vorgelegt von

**Dennis Dietrich**

aus El Paso

Düsseldorf, April 2019

aus dem Institut für Bioanorganische und Strukturchemie  
der Heinrich-Heine-Universität Düsseldorf

Gedruckt mit der Genehmigung der Mathematisch-Naturwissenschaftlichen Fakultät  
der Heinrich-Heine-Universität Düsseldorf

Berichterstatter:

1. Herr Professor Doktor Christoph Janiak

2. Herr Professor Doktor Christian Ganter

Tag der mündlichen Prüfung:

17. 05. 2019

*„Wer uns vor nutzlosen Wegen warnt, leistet uns einen ebenso guten Dienst, wie  
derjenige, der uns den rechten Weg anzeigt.“*

Zur Geschichte der Religion und Philosophie in Deutschland

Heinrich Heine, 1835.

# EIDESSTATTLICHE ERKLÄRUNG

---

Ich versichere an Eides statt, dass die Dissertation von mir selbstständig und ohne unzulässige fremde Hilfe unter der Beachtung der „Grundsätze zur Sicherung guter wissenschaftlicher Praxis“ an der Heinrich-Heine-Universität Düsseldorf erstellt worden ist. Die aus fremden Quellen direkt oder indirekt übernommenen Gedanken sind als solche kenntlich gemacht. Die Arbeit wurde bisher weder im Inland noch im Ausland in gleicher oder ähnlicher Form einer anderen Prüfungsbehörde vorgelegt. Es wurden keine früheren erfolglosen Promotionsversuche unternommen.

.....

Ort, Datum

.....

Unterschrift

# DANKSAGUNG

---

Ich danke Herrn Prof. Dr. Christoph Janiak für die Möglichkeit, meine Dissertation in seinem Arbeitskreis anzufertigen. Außerdem danke ich ihm für die konstruktiven Diskussionen, die Beiträge zu meinen Arbeiten und die Freiräume beim Anfertigen eben dieser.

Herrn Prof. Dr. Christian Ganter danke ich für die Übernahme des Koreferates und zahlreiche Anregungen in meinen Seminarvorträgen.

Allen festangestellten Mitarbeitern möchte ich für ihre Kooperation danken, ganz besonders Annette Ricken, Birgit Tommes, Dietmar Frunzke und Marcell Demandt, für schnelle Messungen und Hilfestellung beim Basteln. Auch danke ich der NMR-Abteilung, besonders Frau Maria Beuer, sowie der Massenspektrometrie, besonders Herrn Ralf Bürgel und Herrn Dr. Peter Tommes.

Auch danke ich allen meinen Kooperationspartnern und Koautoren, welche am Gelingen der Veröffentlichungen mitgewirkt haben.

Meinen Bachelorstudenten Philipp Schmidt und Saskia Menzel danke ich für die eingesendeten Übungen in Zeichensetzung und Stoffmengenberechnung, welche sie als ihre „Bachelorarbeiten“ bezeichneten, sowie meinem Forschungspraktikanten Alexander Strzelczyk, für den Beitrag zu meiner Arbeit.

Meinem Masterstudenten Alexander Nuhnen danke ich für die hervorragende Kooperation und die wenige Arbeit, die er mir gemacht hat, sowie für niveauvolle Beiträge in wichtigen Diskussionen.

Dem Arbeitskreis danke ich für jegliche Unterstützung, sei es in Form von Ideen und Anregungen, gemeinsamen Feiern oder Ausflügen an verschiedenste Ziele.

Ich danke meinen Kollegen aus beiden Büros und dem Labor für viele anregende Gespräche über chemisch relevante und weniger relevante Themen, mit viel Gelächter und Getränken internationaler Braukunst. Namentlich zu erwähnen sind dabei in unbestimmter Reihenfolge: Janina Dechnik, für die Einführung in das Thema der

Membranen; Subarna Dey, für das Mitbringen leckerer Speisen; Martin Wickenheisser, für die Einführung in die Welt der Sorption, Seçil Öztürk, für die netten Gespräche und das leckere Essen sowie die moralische Unterstützung im Allgemeinen; Stefanie Bügel, für den gescheiterten Versuch, das Niveau zu heben; Yangyang Sun, für diverse Dinge, aber besonders den leckeren Chilis aus dem Garten ihrer Mutter; und Sandra Nießing, für jedes hilfreiche „tja“ als Antwort auf meine Probleme.

Ein besonderer Dank geht raus an Sebastian Glomb, welchen ich am Anfang des Studiums getroffen habe, da wir uns seitdem gegenseitig ertragen haben, gemeinsam erfolgreiche Vorträge und Übungen abgeliefert haben und viel Hopfenblütentee und Gerstenkaltschalen konsumiert haben.

Es gibt natürlich noch viel mehr Leute, denen ich danken möchte, darunter jeden einzelnen aus dem Arbeitskreis, der mich in irgendeiner Weise unterstützt hat, allerdings ließe sich allein mit der Auflistung der Namen schon ein Buch füllen. Ich hoffe, dass alle Leute, denen ich hier nicht namentlich gedankt habe und denen trotzdem mein Dank gebührt, wissen, dass ich sie nicht vergessen habe, sondern auch ihnen für alles danke.

Zuletzt danke ich noch meiner Familie und meinen Freunden, für bedingungslose Unterstützung bei Problemen aller Art, für finanzielle und seelische Unterstützung und für alles, was ich sonst noch so vergessen habe, aber dringend brauchte.

# KURZE ZUSAMMENFASSUNG

---

Die vorliegende Arbeit befasst sich mit metall-organischen Koordinationsverbindungen, einer Stoffklasse, bei welcher durch Koordination eines Liganden an ein Metallion polymere Strukturen aufgebaut werden. Dazu zählen die kristallinen Gerüstverbindungen, bei welchen hochgeordnete Strukturen mit potenzieller Porosität entstehen, sowie die Metallogele, bei welchen durch gestörte Koordination unregelmäßige Verbindungen entstehen, in denen ein Lösungsmittel immobilisiert ist. Durch überkritisches Trocknen dieser Gele lassen sich poröse Materialien erhalten. Beide Arten von porösen Materialien lassen sich zur Gasspeicherung und -trennung einsetzen.

In dieser Arbeit wurden dabei insgesamt acht neue Carbonsäuren und Carbonsäureester synthetisiert, welche teilweise für die Darstellung neuer metall-organischer Koordinationsverbindungen genutzt wurden. Dabei wurden entweder die kristallinen Gerüstverbindungen oder auf Koordinationschemie basierende Metallogele erhalten. Die kristallinen Verbindungen wurden in einkristalliner Form erhalten, in nicht ausreichender Größe für Einkristallstrukturanalysen, die Metallogele in ihren entweder überkritisch oder konventionell getrockneten Formen, welche dann mittels Pulver-Röntgendiffraktometrie, Infrarotspektroskopie, energiedispersiver Röntgenanalyse und Elementaranalyse untersucht wurden.

Auf die Stoffklasse der Metallogele wurde dabei besonderen Wert gelegt. Es konnten insgesamt sechs neue Metallogele mit einem Liganden synthetisiert werden, und drei dieser Verbindungen ließen sich in ihre Aero- oder Xerogele überführen (drei Aerogele, ein Xerogel). Die Aero- und Xerogele zeigten hohe BET-Oberflächen (bis zu  $600 \text{ m}^2 \text{ g}^{-1}$ ) sowie die zu diesem Zeitpunkt höchsten Aufnahmen des giftigen Gases Schwefeldioxid für die Stoffklasse der Aerogele.

Mit mehreren Liganden konnten außerdem kristalline Gerüstverbindungen erhalten werden, welche sich in ihrer Struktur nicht weiter aufklären ließen.

Es wurde außerdem noch das Themengebiet der Mixed-Matrix-Membranen bearbeitet, welches die kristallinen metall-organischen Gerüstverbindungen in einer Polymerschicht einbettet, um diese für die Gaspermeation zu nutzen. Dabei wurden die ersten unter inerten Bedingungen synthetisierten lumineszenten Mixed-Matrix-Membranen erhalten und untersucht.

Die Ergebnisse wurden aufgearbeitet und, wenn möglich, zur Veröffentlichung in wissenschaftlichen Journalen eingereicht.



## SHORT SUMMARY

---

This work deals with the topic of metal-organic coordination polymers, a group of materials in which structures are created by the coordination of a ligand to a metal center. This includes metal-organic frameworks, crystalline compounds with potential porosity, and metallogels, in which the coordination between ligand and metal is perturbed and results in disordered structures capable of immobilizing a solvent. By the way of supercritical drying the gels can be converted into porous compounds. Both types of porous materials can be used for gas separation and storage.

Eight new carboxylic acids or esters have been synthesized, which were supposed to be used for the synthesis of new metal-organic coordination polymers. Both the metal-organic frameworks as well as the metallogels were supposed to be obtained. The metal-organic frameworks were to undergo single crystal x-ray structure analysis, while the metallogels were subjected to either supercritical or conventional drying and underwent powder x-ray diffraction, infrared spectroscopy, energy dispersive x-ray and elemental analysis.

Special focus has been put on the metallogel compounds, of which six new metallogels could be obtained with a single ligand. Three of these compounds have been converted to their respective aero- or xerogels (three aerogels, one xerogel). These aero- and xerogels exhibited high BET surface areas (up to  $600 \text{ m}^2 \text{ g}^{-1}$ ) as well as the highest uptake capacity at that point in time for sulfur dioxide in any known aerogel.

Multiple ligands yielded crystalline coordination compounds, which could not be structurally solved.

Furthermore, the topic of mixed matrix membranes has been researched. Mixed matrix membranes in this case are crystalline metal-organic frameworks embedded within polymer film, used for gas permeation. The first luminescent mixed matrix membranes, which have been synthesized under inert conditions, were obtained and analyzed.

The results have been verified and, if possible, published in scientific journals.

# ABKÜRZUNGSVERZEICHNIS

---

$^1\text{H-NMR}$	$^1\text{H}$ -Kernspinresonanz („ <i>nuclear magnetic resonance</i> “)
4MCB	4-(Methoxycarbonyl)benzoesäure
At.%	Atomprozent
Boc	tert.-Butyloxycarbonyl (Schutzgruppe)
Bzw.	beziehungsweise
$\text{CDCl}_3$	Chloroform, deuteriert
d. h.	das heißt
DABCO	1,4-Diazabicyclo[2.2.2]octan
DC	Dünnschichtchromatographie
DCC	<i>N,N'</i> -Dicyclohexylcarbodiimid
DCM	Dichlormethan
DMAc	<i>N,N</i> -Dimethylacetamid
DMAP	4-Dimethylaminopyridin
DMF	<i>N,N'</i> -Dimethylformamid
DMSO	Dimethylsulfoxid
$\text{DMSO-}d_6$	Dimethylsulfoxid, deuteriert
DMT	Dimethylterephthalat
EDX	„ <i>energy-dispersive x-ray spectroscopy</i> “, energie-dispersive Röntgenspektroskopie

EE	Ethylacetat, Essigsäureethylester
EI	Elektronenionisation
ESI	Elektronensprayionisation
Et <sub>2</sub> O	Diethylether
Ggf.	Gegebenenfalls
LM	Lösemittel
M4CCB	Methyl-4-(chlorocarbonyl)benzoat
MeOH	Methanol
MHz	Megahertz
MS	Massenspektrometrie
<i>N,N'</i> -3,5-DiCPTAm	<i>N,N'</i> -(3,5-Dicarboxyphenyl)terephthalamid
<i>N,N'</i> -3Br-4CPTAm	<i>N,N'</i> -(3-Bromo,4-carboxyphenyl)terephthalamid
<i>N,N'</i> -3CPTAm	<i>N,N'</i> -(3-Carboxyphenyl)terephthalamid
<i>N,N'</i> -4CMOPTAm	<i>N,N'</i> -(4-Carboxy,2-methoxyphenyl)terephthalamid
<i>N,N'</i> -4CMPTAm	<i>N,N'</i> -(4-Carboxy,2-methylphenyl)terephthalamid
<i>N,N'</i> -4CPTAm	4-(Carboxyphenyl)terephthalamid
NEt <sub>3</sub>	Triethylamin
NMP	<i>N</i> -Methyl-2-pyrrolidon

ppm	„ <i>parts per million</i> “
p-Ts	para-Terephthalaldehydsäure
REM	Rasterelektronenmikroskopie
RT	Raumtemperatur
TFA	„ <i>trifluoroacetic acid</i> “, Trifluoressigsäure
THF	Tetrahydrofuran
TMAOH	Tetramethylammoniumhydroxid
U. ä.	und ähnliche
Uvm.	und viele mehr
V. l. n. r.	von links nach rechts
Z. B.	zum Beispiel

# INHALT

---

Eidesstattliche Erklärung.....	IV
Danksagung .....	V
Kurze Zusammenfassung.....	VII
Short summary .....	IX
Abkürzungsverzeichnis .....	X
1 Einleitung .....	1
1.1 Metall-organische Gerüstverbindungen und Porosität .....	1
1.2 Gele, Metallogele und metall-organische Aerogele .....	7
1.3 Membrantrennprozesse und Mixed-Matrix-Membranen.....	13
2 Aufgabenstellung .....	20
3 Kumulativer Teil .....	21
3.1 Metal-Organic Gels Based on a Bisamide Tetracarboxyl Ligand for Carbon Dioxide, Sulfur Dioxide and Selective Dye Uptake.....	22
3.1.1 Appendix.....	103
3.2 Luminescent Metal-Organic Framework Mixed-Matrix Membranes from Lanthanide Metal-Organic Frameworks in Polysulfone and Matrimid.....	114
3.3 Luminescent MOF polymer mixed matrix membranes for humidity sensing in real status analysis .....	124
3.4 Role of Filler Porosity and Filler/Polymer Interface Volume in Metal-Organic Framework/Polymer Mixed-Matrix Membranes for Gas Separation.....	135
3.5 Palladium Nanoparticle-immobilized Porous Polyurethane Material for Quick and Efficient Heterogeneous Catalysis of Suzuki-Miyaura Cross-Coupling Reaction at Room Temperature.....	148

3.6	Novel high throughput mixed matrix membranes embracing poly ionic liquid-grafted biopolymer: Fabrication, characterization, permeation and antifouling performance .....	155
4	Ergebnisse und Diskussion .....	167
4.1	Baylis-Hillman-Reaktion zur Synthese eines neuen Liganden .....	167
4.1.1	Veresterung von para-Terephthalaldehydsäure .....	167
4.1.2	Synthese von Methyl-4-(1-hydroxy-2-(methoxycarbonyl)allyl)benzoat. ....	168
4.2	Synthese eines neuen Liganden basierend auf Melamin .....	170
4.2.1	Synthese von $N,N',N''$ -(1,3,5-triazin-2,4,6-triyl)tris(4-methylbenzamid) ... ..	170
4.2.2	Synthese von 4,4',4''-(((1,3,5-triazin-2,4,6-triyl)tris(azanediyl))-tris(carbonyl))tribenzoesäure .....	171
4.2.3	Synthese von 4,4',4''-(((1,3,5-triazin-2,4,6-triyl)tris(azanediyl))tris(carbonyl))tribenzoesäure .....	174
4.2.4	Synthese von Dimethyl-5-(chlorocarbonyl)isophthalat .....	175
4.2.5	Syntheseversuche zu Hexamethyl-5,5',5''-(((1,3,5-Triazin-2,4,6-triyl)tris(azanediyl))tris(carbonyl))triisophthalat.....	176
4.2.6	Syntheseversuche zu 5,5',5''-(((1,3,5-Triazin-2,4,6-triyl)tris(azanediyl))tris(carbonyl))triisophthalsäure.....	177
4.2.7	Synthese von 2,2',2''-(((1,3,5-Triazin-2,4,6-triyl)tris(piperazin-4,1-diyl))triessigsäure ausgehend von Cyanurchlorid .....	178
4.3	Synthese neuer Amidliganden ausgehend von Terephthaloylchlorid .....	180
4.3.1	Synthese von $N,N'$ -(4-Carboxyphenyl)terephthalamid .....	180
4.3.2	Synthese von $N,N'$ -(3-Carboxyphenyl)terephthalamid .....	182
4.3.3	Synthese dreier weiterer Derivate von $N,N'$ -(4-Carboxyphenyl)-terephthalamid. ....	184

4.3.4	Synthese von <i>N,N'</i> -(3,5-Dicarboxyphenyl)terephthalamid.....	188
4.4	Synthese neuer Amidliganden ausgehend von Phenylendiamin.....	191
4.4.1	Synthese von Dimethyl-4,4'-((1,4-phenylenbis(azanediyl))-bis(carbonyl))dibenzoat .....	191
4.4.2	Synthese von Tetramethyl-5,5'-((1,4-phenylenbis(azanediyl))-bis(carbonyl))diisophthalat.....	192
4.4.3	Synthese von 5,5'-((1,4-Phenylenbis(azanediyl))bis(carbonyl))-diisophthalsäure.....	193
4.5	Sonstige Syntheseversuche neuer Amidliganden.....	194
4.5.1	Syntheseversuch von 5,5'-(Fumarylbis(azanediyl))diisophthalsäure .....	194
4.5.2	Syntheseversuche von 3,3'-(Oxalylbis(azanediyl))dibenzoesäure und 4,4'-(Oxalylbis(azanediyl))dibenzoesäure.....	196
4.6	Synthese neuer metall-organischer Gerüstverbindungen und Koordinationspolymere.....	198
4.6.1	Koordinationspolymere basierend auf 2,2',2''-((1,3,5-Triazin-2,4,6-triyl)tris(piperazin-4,1-diyl))triessigsäure.....	198
4.6.2	Koordinationspolymere basierend auf <i>N,N'</i> -(4-Carboxyphenyl)terephthalamid .....	200
4.6.3	Koordinationspolymere basierend auf <i>N,N'</i> -(3-Carboxyphenyl)terephthalamid .....	206
5	Zusammenfassung und Ausblick .....	211
6	Experimenteller Teil .....	218
6.1	Veresterung von para-Terephthalaldehydsäure.....	218
6.2	Synthese von Methyl-4-(1-hydroxy-2-(methoxycarbonyl)-allyl)benzoat .....	218
6.3	Syntheseversuche zu <i>N,N',N''</i> -(1,3,5-triazin-2,4,6-triyl)-tris(4-methylbenzamid).....	219

6.4	Synthese von Dimethyl-1,4-benzoldicarboxylat (DMT) .....	220
6.5	Synthese von 4-(Methoxycarbonyl)benzoesäure (4-MCB).....	220
6.6	Synthese von Methyl-4-(chlorocarbonyl)benzoat (M4CCB).....	221
6.7	Synthese von Trimethyl-4,4',4''-((benzol-1,3,5-triyltris (azanediyl))tris(carbonyl))tribenzoat.....	221
6.8	Synthese von 4,4',4''-(((1,3,5-triazin-2,4,6-triyl)tris (azanediyl))tris(carbonyl))tribenzoesäure .....	223
6.9	Synthese von Trimethylbenzol-1,3,5-tricarboxylat .....	224
6.10	Synthese von 3,5-Bis(methoxycarbonyl)benzoesäure .....	224
6.11	Synthese von Dimethyl-5-(chlorocarbonyl)isophthalat .....	225
6.12	Syntheseversuche zu Hexamethylen-5,5',5''-(((1,3,5-triazin-2,4,6- triyl)tris(azanediyl))tris(carbonyl))isophthalat .....	225
6.13	Synthese von Tri-tert.-butyl-4,4',4''-(1,3,5-triazin-2,4,6-triyl)tris(piperazin- 1-carboxylat) .....	226
6.14	Synthese von 2,4,6-Tri(piperazin-1-yl)-1,3,5-triazin.....	227
6.15	Synthese von 2,2',2''-((1,3,5-Triazin-2,4,6-triyl)-tris(piperazin-4,1- diyl))triessigsäure .....	228
6.16	Synthese von <i>N,N'</i> -(4-Carboxyphenyl)terephthalamid .....	229
6.17	Synthese von 3,3'-(Terephthaloylbis(azanediyl))dibenzoe-säure .....	230
6.18	Synthese von <i>N,N'</i> -(4-Carboxy,2-methylphenyl)terephthal-amid .....	230
6.19	Synthese von <i>N,N'</i> -(4-Carboxy,3-methoxyphenyl)-terephthalamid.....	231
6.20	Versuchte Synthese von <i>N,N'</i> -(3-Bromo,4-carboxyphenyl)-terephthalamid .. .....	231
6.21	Synthese von <i>N,N'</i> -(3,5-Dicarboxyphenyl)terephthalamid. ....	232
6.22	Synthese von Dimethyl-4,4'-((1,4-phenylenbis(azanediyl))- bis(carbonyl))dibenzoat .....	233



6.23	Synthese von Tetramethyl-5,5'-((1,4-phenylenbis(azanediyl))bis(carbonyl))diisophthalat .....	233
6.24	Syntheseversuch von 5,5'-(Fumarylbis(azanediyl))-diisophthalsäure .....	234
6.25	Syntheseversuch von 3,3'-(Oxalylbis(azanediyl))-dibenzoessäure .....	234
6.26	Syntheseversuch von 4,4'-(Oxalylbis(azanediyl))-dibenzoessäure .....	235
6.27	Syntheseversuch neuer Koordinationspolymere basierend auf 2,2',2''-((1,3,5-Triazin-2,4,6-triyl)tris(piperazin-4,1-diyl))triessigsäure .....	235
6.28	Syntheseversuche neuer Koordinationspolymere basierend auf <i>N,N'</i> -(4-Carboxyphenyl)terephthalamid .....	237
6.29	Syntheseversuche neuer Koordinationspolymere basierend auf <i>N,N'</i> -(3-Carboxyphenyl)terephthalamid .....	239
6.30	Reaktionen aus dem Appendix zu „Metal-Organic Framework Gels Based on a Bisamide Tetracarboxyl Ligand for Carbon Dioxide, Sulfur Dioxide and Selective Dye Uptake“ .....	241
6.30.1	Synthesen mit Co-Liganden .....	241
6.30.2	Synthesen entsprechend Cr-L1, Al-L1 und AlCr-L1 .....	242
6.30.3	Synthesen entsprechend Co-L1 .....	242
6.30.4	Raumtemperatursynthesen der Metallogele Cr-L1 und Al-L1 .....	242

# 1 EINLEITUNG

## 1.1 Metall-organische Gerüstverbindungen und Porosität

Metall-organische Gerüstverbindungen (*metal-organic frameworks*, MOFs) sind potentiell poröse Verbindungen aus der Stoffklasse der Koordinationspolymere. Sie bestehen aus Metallknotenpunkten, welche über organische Liganden miteinander verbrückt sind (Abbildung 1).

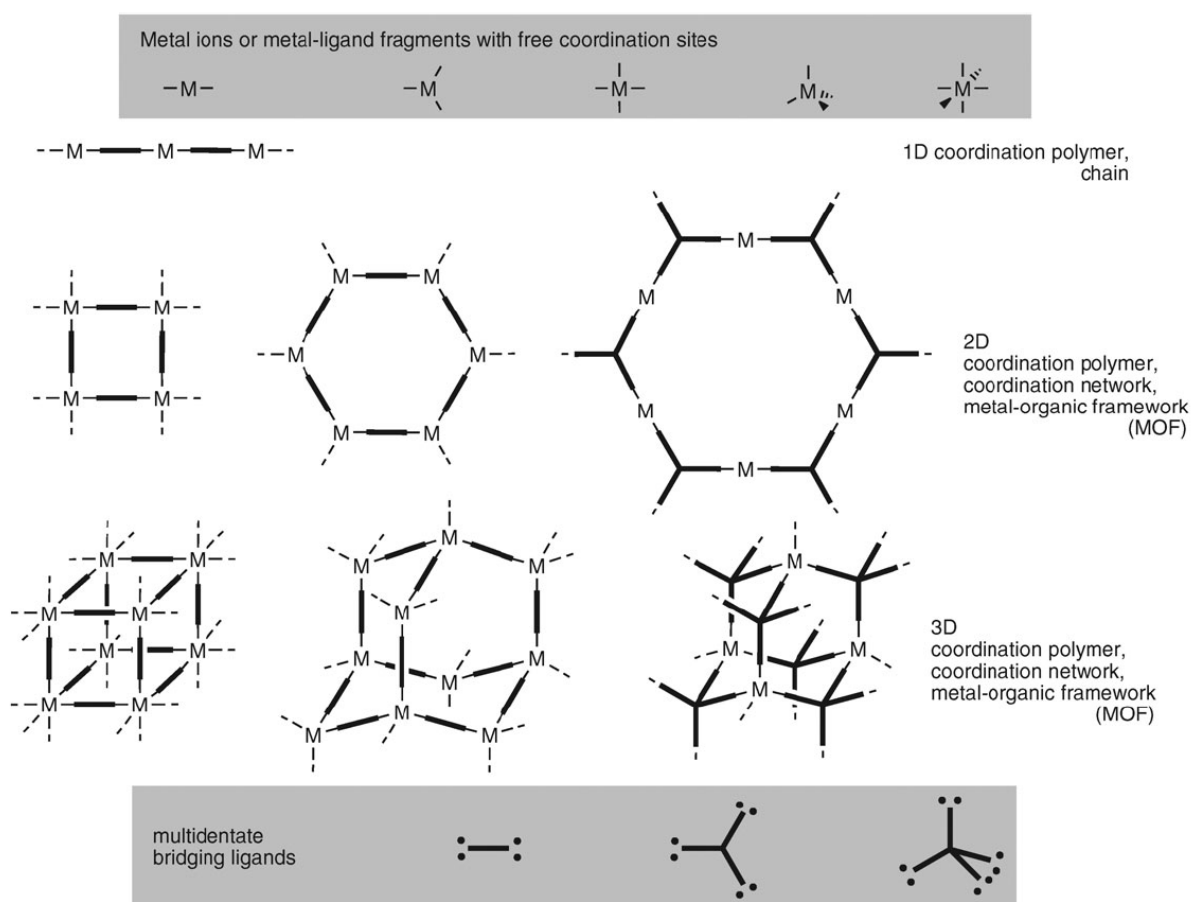


Abbildung 1. Schematische Darstellung über den Aufbau von Koordinationspolymeren. Oben sind mögliche Knotenpunkte gezeigt, unten mögliche Liganden. Nachdruck von Ref. 1 mit Genehmigung des Centre National de la Recherche Scientifique (CNRS) und der Royal Society of Chemistry.

Ein Gerüst oder Netzwerk wird dabei nur aufgespannt, wenn ein (Metall)knotenpunkt zu einer oder mehreren Maschen des Netzwerks gehört. Eine Masche besteht dabei aus einem geschlossenen Zug aus Knotenpunkten und verbrückenden Liganden. Per

Definition sind eindimensionale Koordinationspolymere demnach keine Netzwerke und können nicht als MOFs bezeichnet werden.

Hoskins und Robson hatten einen wichtigen Einfluss auf die Entwicklung der Koordinationspolymerchemie und seit ihren Artikeln in den frühen 90er Jahren hat sich das Interesse an dieser Stoffklasse stark erhöht.<sup>2,3</sup> Der Begriff des *metal-organic frameworks* wurde zuerst von Yaghi im Jahre 1995 verwendet.<sup>4,5</sup> Heutzutage sind MOFs großtechnisch hergestellte, kommerziell erhältliche Produkte.

Die Anwendungsbereiche für MOFs sind vielfältig. Abbildung 2 zeigt interessante, aktuelle Forschungsgebiete. Die oben bereits genannte Porosität bietet dabei den Zugang zum Bereich der Katalyse, da sie einen größen- oder formselektiven Zugang zu den möglicherweise katalytisch aktiven Übergangsmetallzentren liefern kann. Die zugrunde liegende Idee orientiert sich dabei an den Zeolithen und mikroporösen Aluminiumphosphaten, welche bereits auf ähnliche Weise angewendet wurden.<sup>6,7,8</sup>

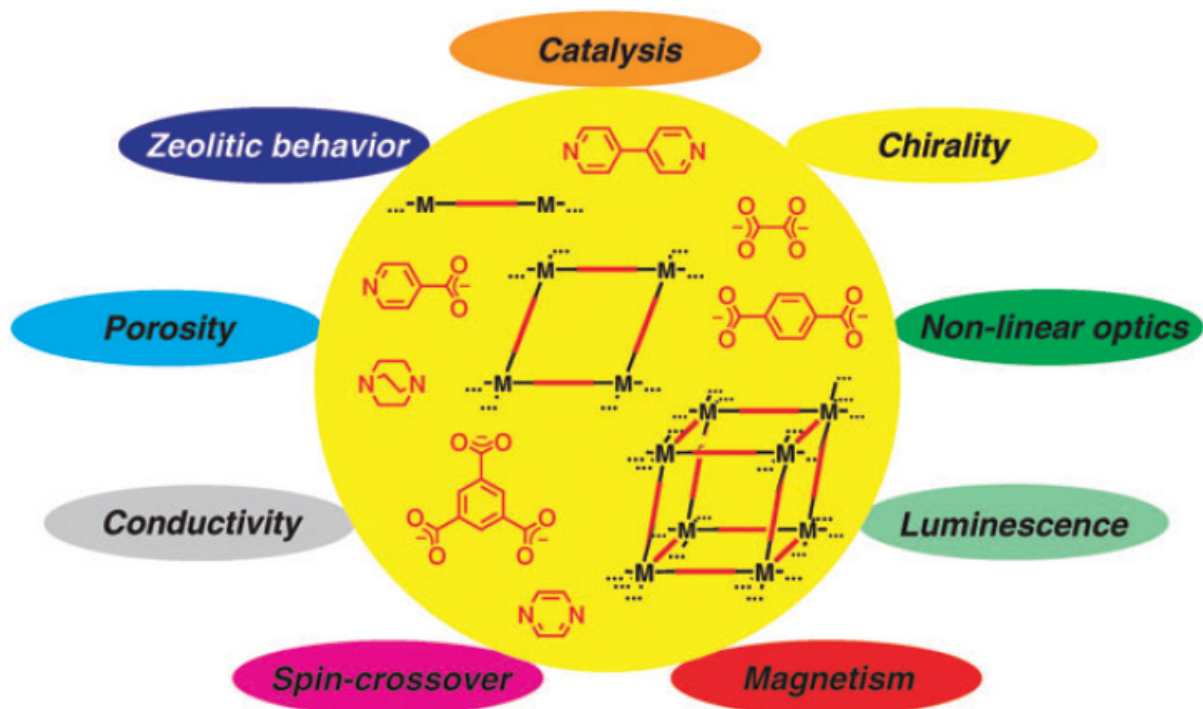


Abbildung 2. Potentielle Anwendungsbereiche für MOFs außen; prototypische Liganden und schematische Darstellung von MOFs in der Mitte. Nachdruck von Ref. 1 mit Genehmigung des Centre National de la Recherche Scientifique (CNRS) und der Royal Society of Chemistry.

Im Bereich der Lumineszenz zeichnen sich MOFs durch ihre höhere thermische Stabilität gegenüber den reinen Liganden aus, sowie durch die Möglichkeit, die Emissionswellenlänge durch Metallkoordination zu beeinflussen. Die potentiellen Anwendungen liegen unter anderem im Bereich der lichtemittierenden Dioden.<sup>9</sup>

Die Porositäts- und Oberflächenanalyse von MOFs wird für gewöhnlich über Gasadsorptionmethoden durchgeführt. Bei der Gasadsorption reichert sich das Analysegas, auch Adsorptiv genannt, an der Oberfläche des zu untersuchenden Materials, auch Adsorbens genannt, an. Das vom adsorbierten Gas eingenommene Volumen wird Adsorbat genannt. Bei der Gasadsorption geht es vorrangig um die Physisorption, das heißt um die schwache Wechselwirkung des Adsorptivs mit dem Adsorbens. Weitere Wechselwirkungen, z. B. durch Dipol- oder Quadrupolmomente des Adsorptivs, sollen wenn möglich unterdrückt werden. Als Resultat ist die Physisorption reversibel, da sich die Wechselwirkungen zwischen Adsorbat und Adsorbens durch Änderung der Bedingungen aufheben lassen und das Adsorptiv wieder freigesetzt wird. Dies steht im Kontrast zur Chemisorption, bei welcher eine chemische Reaktion zwischen Adsorbens und Adsorptiv stattfindet, sowie zur Absorption, bei welcher das Adsorptiv in das Adsorbens eindringt und damit nicht nur ein Adsorbat an der Oberfläche ausbildet.

Die Analysen der Porosität und Oberflächen mittels Physisorption werden unter isothermen Bedingungen durchgeführt. Die daraus resultierenden Isothermen weisen materialspezifische Eigenheiten auf. Die Einteilung der Isothermen basiert dabei auf der Empfehlung der IUPAC, welche wiederum auf Arbeiten von Irving Langmuir basiert (Abbildung 3).<sup>10,11</sup> Bei Isothermen vom Typ I handelt es sich um mikroporöse Feststoffe, bei welchen die Adsorption eher durch das zugängliche Porenvolumen als durch die Oberfläche limitiert ist. Typ I(a)-Isothermen stammen meist von Materialien mit Poren kleiner als 1 nm, während Typ I(b)-Isothermen Porenweiten bis zu 2,5 nm besitzen. Typ II-Isothermen stammen von nicht-porösen oder makroporösen Adsorbentien, bei welchen zuerst eine monoatomare Lage an Adsorbat entsteht, welche bei höheren Partialdrücken in eine multiatomare Schicht übergeht. Die Kondensation

in den Poren findet bei hohen Partialdrücken ungehindert statt. Typ III-Isothermen stammen ebenfalls von nicht-porösen und makroporösen Adsorbentien und zeigen noch schwächere Wechselwirkungen zwischen Adsorptiv und Adsorbens an. Das Adsorptiv bildet dabei keine Monolage aus und lagert sich an bevorzugten Adsorptionstellen an, an welchen es auch die multiatomare Lage ausbilden kann. Die adsorbierte Menge bleibt allerdings endlich, anders als bei Typ II-Isothermen.

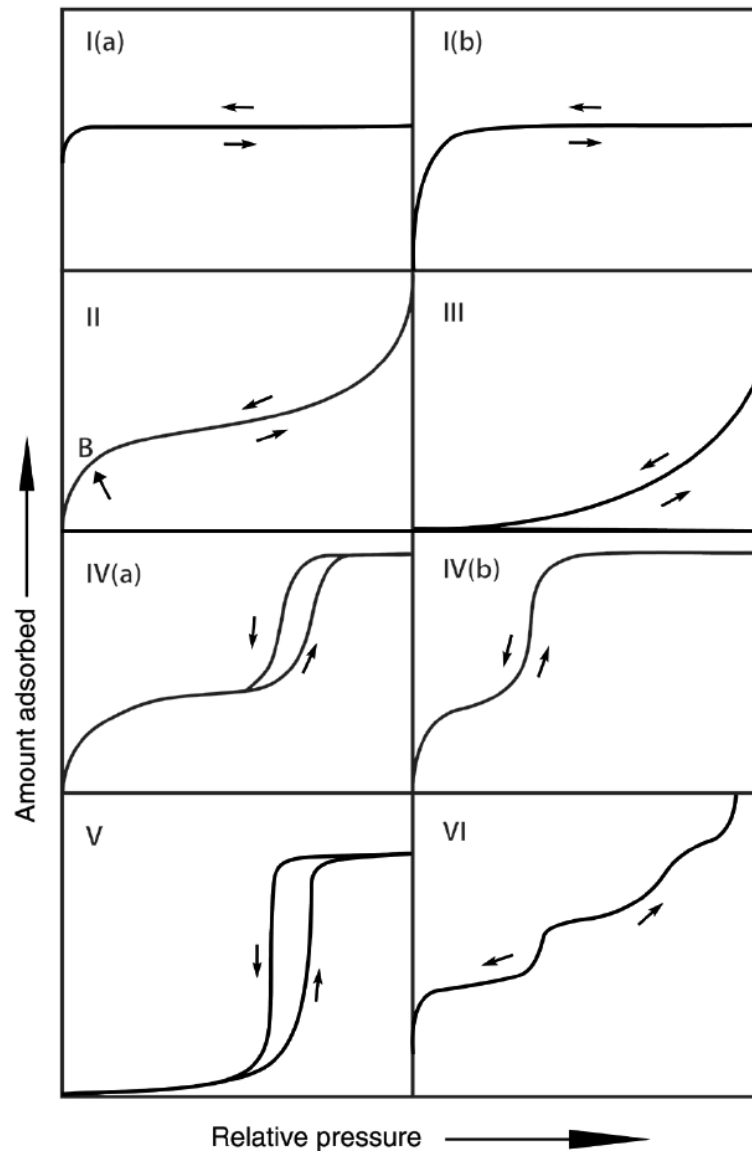


Abbildung 3. Isothermentypen nach IUPAC-Klassifizierung. Nachdruck aus Ref. 10 mit Genehmigung von De Gruyter, IUPAC, ©2015.

Typ IV-Isothermen stammen von mesoporösen Materialien, welche ähnlich zu Typ II-Isothermen zuerst eine monoatomare Lage an Adsorbat bilden, welche anschließend bei

höheren Partialdrücken durch Kondensation in eine multiatomare Lage übergeht. Anders als bei Typ (II)-Isothermen schließt die Isotherme bei Sättigung der Poren mit Adsorbat mit einem Plateau ab. Typ V-Isothermen zeigen ähnlich wie Typ III-Isothermen sehr schwache Wechselwirkungen zwischen Adsorptiv und Adsorbens an. Anders als bei Typ III-Isothermen beendet das verfügbare Porenvolumen die Adsorption. Typ VI-Isothermen sind das Resultat von schichtweiser Adsorption an nicht-porösen Adsorbentien.

Wird neben der Adsorption auch noch die Desorption gemessen, so entstehen vollständige Isothermen, welche sich neben der Einteilung nach ihrer Isothermenform auch noch über ihre Hysterese, d. h. der Abweichung der Desorptions- zur Adsorptionsisotherme, einteilen lassen. Dies tritt vorrangig bei Isothermen auf, bei denen Kapillarkondensation in den Poren einen wesentlichen Beitrag zur Isothermenform liefert (Typ II, Typ IV, Typ V). Die Einteilung richtet sich auch hier wieder nach den Empfehlungen der IUPAC (Abbildung 4).<sup>10</sup>

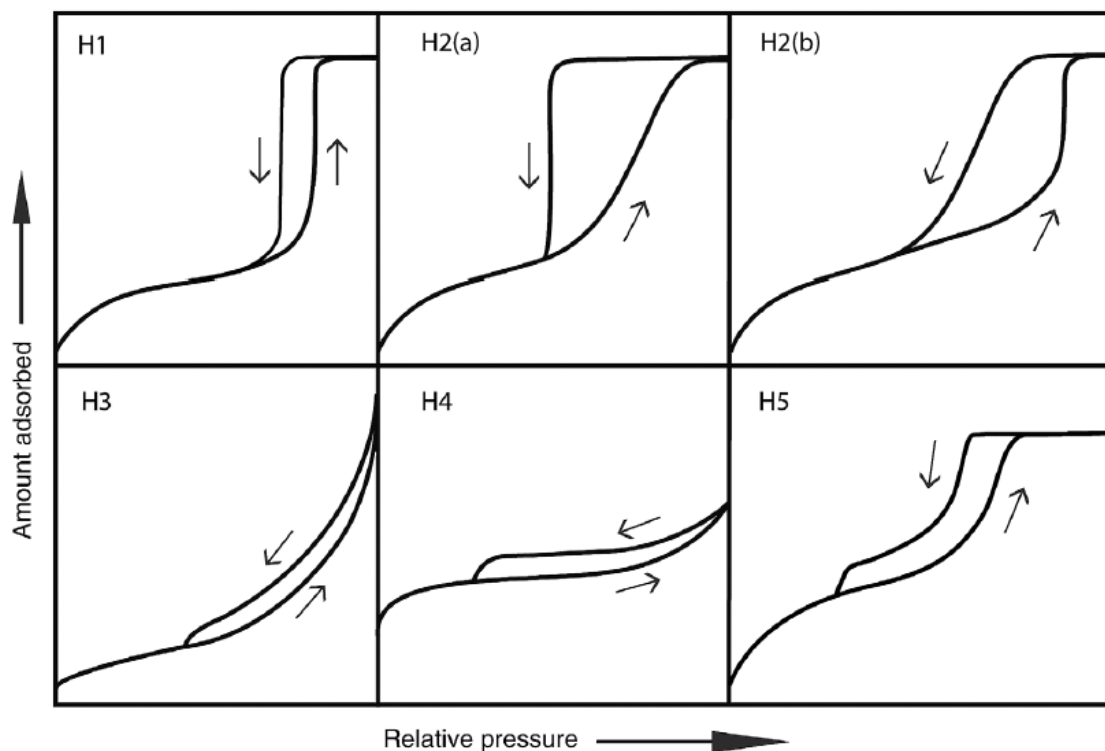


Abbildung 4. Hysteresetypen nach IUPAC-Empfehlung. Nachdruck aus Ref. 10 mit Genehmigung von De Gruyter, IUPAC, ©2015.

Typ H1-Hysteresen stammen von Materialien mit sehr einheitlichen Mesoporen. Die Evaporation des Adsorbats findet hier, ähnlich wie während der Kondensation, in einem kleinen Partialdruckbereich statt. Typ H2-Hysteresen sind das Resultat blockierter Poren oder Kavitation des Adsorbats während der Desorption. Der Unterschied zwischen H2(a)- und H2(b)-Hysteresen liegt dabei in der Porenweitenverteilung, welche bei H2(b)-Hysteresen größer ist. Typ H3-Hysteresen erfordern eine Adsorptionsisothermenform des Typs II und haben ihr Ende normalerweise im Bereich des für die Kavitation erforderlichen Partialdrucks. Sie treten bei nicht-porösen plättchenähnlichen Aggregaten sowie bei nicht vollständig gefüllten Makroporen auf. Typ H4-Hysteresen sind ähnlich zu Typ H3-Hysteresen, die Adsorption ist allerdings eine Mischung aus Typ I- und Typ II-Isothermen, hervorgerufen durch einen mikroporösen Anteil des Adsorbens. Typ H5-Hysteresen können in mesoporösen Materialien durch eine Mischung an blockierten sowie offenen Poren hervorgerufen werden.

Für nicht-poröse, meso- und makroporöse Materialien wird die BET-Theorie zur Berechnung der Oberfläche des Materials aus Typ II- und Typ IV(a)-Isothermen herangezogen. Die BET-Theorie macht ähnliche Annahmen wie das Langmuir-Adsorptionmodell, allerdings unter der Berücksichtigung von Multischichtenkondensation.<sup>12</sup> Es wird zunächst von der Ausbildung einer monoatomaren Lage an Adsorbat ausgegangen, welche an freien Adsorptionsstellen ohne Bevorzugung adsorbiert wird. Ausgehend vom Adsorbens finden die einzigen Wechselwirkungen nur mit der nächsten Lage an Adsorbat statt, und die oberste Lage befindet sich im Gleichgewicht mit der Gasphase. Die Sorptionswärme unterscheidet sich nur für die erste Lage an Adsorbat, für alle weiteren Lagen entspricht sie der Kondensationswärme für die Adsorption bzw. der Verdampfungswärme für die Desorption. Zur Berechnung wird zunächst die BET-Gleichung herangezogen, welche einen linearen Zusammenhang zwischen spezifischer Aufnahmekapazität  $n$ , bei Partialdruck  $p/p_0$ , dem Partialdruck  $p/p_0$  und der spezifischen Monolagekapazität  $n_m$  herstellt.

$$\frac{p/p_0}{n(1-p/p_0)} = \frac{1}{n_m C} + \frac{C-1}{n_m - C} (p/p_0)$$

Der Parameter  $C$  verhält sich exponentiell zur Energie der Monolagenadsorption und muss positiv sein, idealerweise liegt er ca. mittig zwischen 2 und 150.<sup>10</sup> Trägt man  $(p/p_0)/(n(1-p/p_0))$  gegen den Partialdruck  $p/p_0$  auf, den sogenannten BET-Plot, so lässt sich im linearen Bereich der Auftragung der Parameter der spezifischen Monolagekapazität  $n_m$  entnehmen. Der Partialdruckbereich, in welchem der BET-Plot linear verläuft, liegt für gewöhnlich bei 0,05 – 0,30. Aus der spezifischen Monolagekapazität  $n_m$ , der Querschnittsfläche  $\sigma_m$  der Adsorbatmoleküle, der Avogadrokonstante  $N_A$  und der Adsorbensmasse  $m$  lässt sich so die BET-Oberfläche  $a_s(\text{BET})$  berechnen.

$$a_s(\text{BET}) = \frac{n_m N_A \sigma_m}{m}$$

## 1.2 Gele, Metallogele und metall-organische Aerogele

Im Alltag sind Gele Gegenstände, welche einem vielfach begegnen: Als Stylingprodukte in Form von Haargel, als Nahrungsmittel in Form von z. B. Wackelpudding oder Pektinen, oder auch als Körperausscheidung wie dem Nasensekret, umgangssprachlich auch Schnodder genannt. Um als Gel zu gelten, muss ein Stoff in erster Linie den Inversionstest bestehen. Dazu wird ein Behälter, welcher das zu analysierende Material enthält, auf den Kopf gestellt. Ergießt sich der Inhalt des Behälters nicht über den Boden, wird bereits von einem Gel gesprochen.<sup>13</sup> Dies verleitete Dorothy Jordon Lloyd im Jahre 1926 zu der Aussage, dass Gele „leichter zu erkennen als zu definieren“ sind.<sup>14</sup> Im Allgemeinen wird häufig die Definition von Flory anerkannt, welche besagt, dass ein Gel eine kontinuierliche Struktur aufweisen muss, welche auf der analytischen Zeitskala beständig und in ihrem rheologischen Verhalten feststoffartig ist.<sup>15</sup> Flory unterscheidet Gele dabei in 4 Kategorien:



1. Geordnete, lamellare Strukturen, inklusive Gelmessphasen (z. B. Phospholipide).
2. Ungeordnete, kovalente Polymernetzwerke (z. B. Phenolharze).
3. Durch Aggregation gebildete Polymernetzwerke (z. B. Gelatine).
4. Partikuläre, ungeordnete Strukturen (z. B. durch Proteinaggregation).

Zu den Gelen unter Punkt 4 zählen dabei auch die Gele, welche aus nicht-kovalent vernetzten Aggregaten von Gelatoren niedrigem molekularen Gewichts entstanden sind. Die Komplexbildung mit oder die Koordination an Metallionen ist dabei der entscheidende Faktor, wenn es darum geht, sogenannte *Metallogele* zu bilden. Dabei handelt es sich um Gele, welche ein Metallion und einen Gelator enthalten, und ein aktuell stark wachsendes Forschungsfeld.<sup>16</sup> In ihrer Namensgebung sind Metallogele leichter einzuordnen als andere Gele. Gängige Bezeichnungen für Gele sind unter anderem *Hydrogele*, wenn die Hauptkomponente des Gels Wasser ist, *Alcogele*, bei welchen die Hauptkomponente ein Alkohol ist, oder *Organogele*, welches Gele mit beliebiger organischer Hauptkomponente beschreibt. Bei allen drei Varianten wird dabei nicht das gelbildende feststoffartige Netzwerk beschrieben, sondern das darin immobilisierte Lösungsmittel bzw. die flüssige Phase. Gele, welche die flüssige Phase noch enthalten werden als *Lyogele* zusammengefasst. Die Beschreibung der Hauptkomponente ist dann überflüssig, sobald das Gel in ein sogenanntes *Aerogel* umgewandelt wird, bei welchem das feststoffartige Netzwerk in seiner Struktur erhalten bleibt und die immobilisierte flüssige Phase entfernt wird. Die Hauptkomponente, Luft, ist dabei nicht notwendig für den Fortbestand des Gels und kann beliebig durch andere Gase oder ein Vakuum ersetzt werden. Ganz ähnlich verhält sich das *Xerogel*, bei welchem die flüssige Phase unter starkem Schrumpfen entfernt wird. Die griechische Vorsilbe „xero“ bedeutet dabei in etwa so viel wie „trocken“ oder auch „dürr“.

Metallogele umgehen dieses Problem, indem sie das fortbestehende Netzwerk beschreiben. Ein Metallogel kann daher ein Lyogel, Hydrogel, Alcogel, Organogel, Xerogel oder auch Aerogel sein. In der Literatur finden sich zahlreiche Nennungen der Stoffklasse Metallogele.<sup>17,18,19,20,21,22,uvv.</sup> Die auf diese Art und Weise entstehende

Methodik der Gelbeschreibung ist präziser und vereinfacht damit erheblich die Literaturrecherche. Als weiteres Beispiel einer Stoffklasse, bei der diese Art von Nomenklatur angewandt wird und welche den fortbestehenden, feststoffartigen Bestandteil der Gele beschreibt, sind die Silicagele zu nennen. Diese bestehen aus einer porösen Form von Siliziumdioxid, auch *Silica* genannt.

Allgemein werden Gele über den Sol-Gel-Prozess geformt. Dabei wird eine Lösung, das Sol, verarbeitet, bis das gewünschte Gel entsteht. Wie schon beschrieben, entsteht dabei ein Material, in welchem ein feststoffartiges Netzwerk eine flüssige Phase immobilisiert (für gewöhnlich das im Sol enthaltene Lösungsmittel). Neben Kapillarkräften treten verschiedene Wechselwirkungen zwischen Lösungsmittel und Gelator auf.<sup>23</sup>

Aerogele entstehen durch Entfernen des Lösungsmittels aus dem Gel bei gleichzeitiger Unterdrückung auftretender Kapillarkräfte, welche das Netzwerk stark schrumpfen lassen würden. Sie wurden das erste Mal in 1931 durch Samuel Kistler beschrieben, der im Rahmen einer Wette mit Charles Learned einen Weg finden musste, als Erster die Flüssigkeit in einem Gel durch ein Gas zu ersetzen.<sup>24,25</sup> Die gewählte Methode war dabei die Entfernung des Lösungsmittels unter überkritischen Bedingungen in einem Autoklaven. Auf diese Weise entstanden Silica-, Alumina-, Nickeltartrat-, Zinnoxid-, Gelatine-, Agar-, Nitrocellulose-, Cellulose-, und Albuminaerogele. Die überkritische Methode ist dabei meist die einfachste, um einen Zugang zu Aerogelen zu bekommen. Die Literatur beschreibt allerdings auch noch andere Methoden. So lassen sich unter anderem auch das Netzwerk verstärken oder der Gelator polymerisieren, um anschließend den bei der regulären Trocknung auftretenden Kapillarkräften zu widerstehen (Abbildung 5, Abbildung 6, Abbildung 7).<sup>26,27</sup> In den hier gezeigten Beispielen werden dabei metall-organische Netzwerke verwendet, um das Templat für das spätere Gel zu bilden.

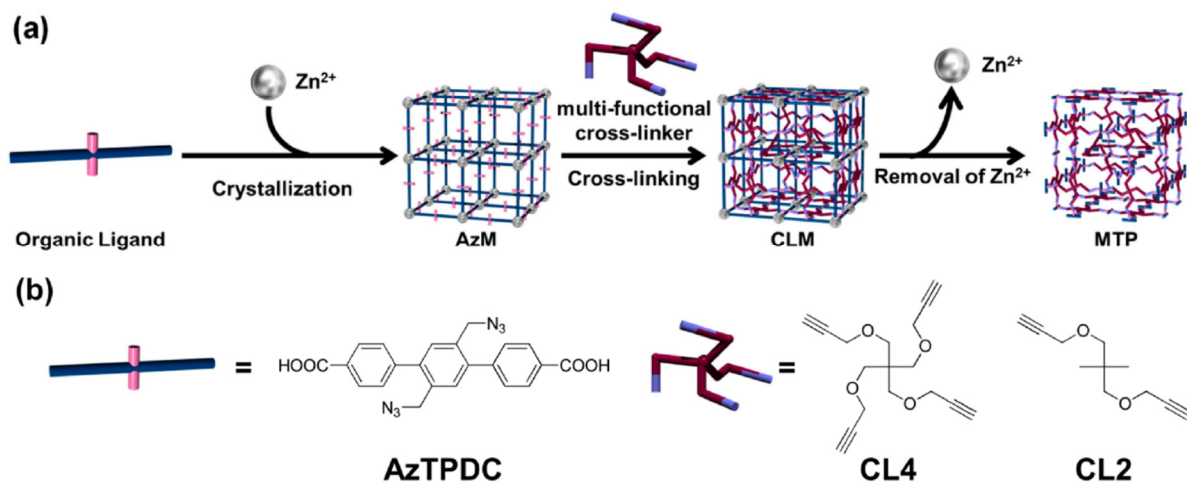


Abbildung 5. (a) Schematische Darstellung des Quervernetzens des organischen Liganden in einem MOF (AzM) und anschließende Zerstörung des MOF-Netzwerkes, um ein polymeres Gel zu erhalten. (b) Molekülstrukturen des Liganden (AzTPDC) und der Quervernetzer. Nachdruck mit Genehmigung von Ref. 28. Copyright 2013 American Chemical Society.

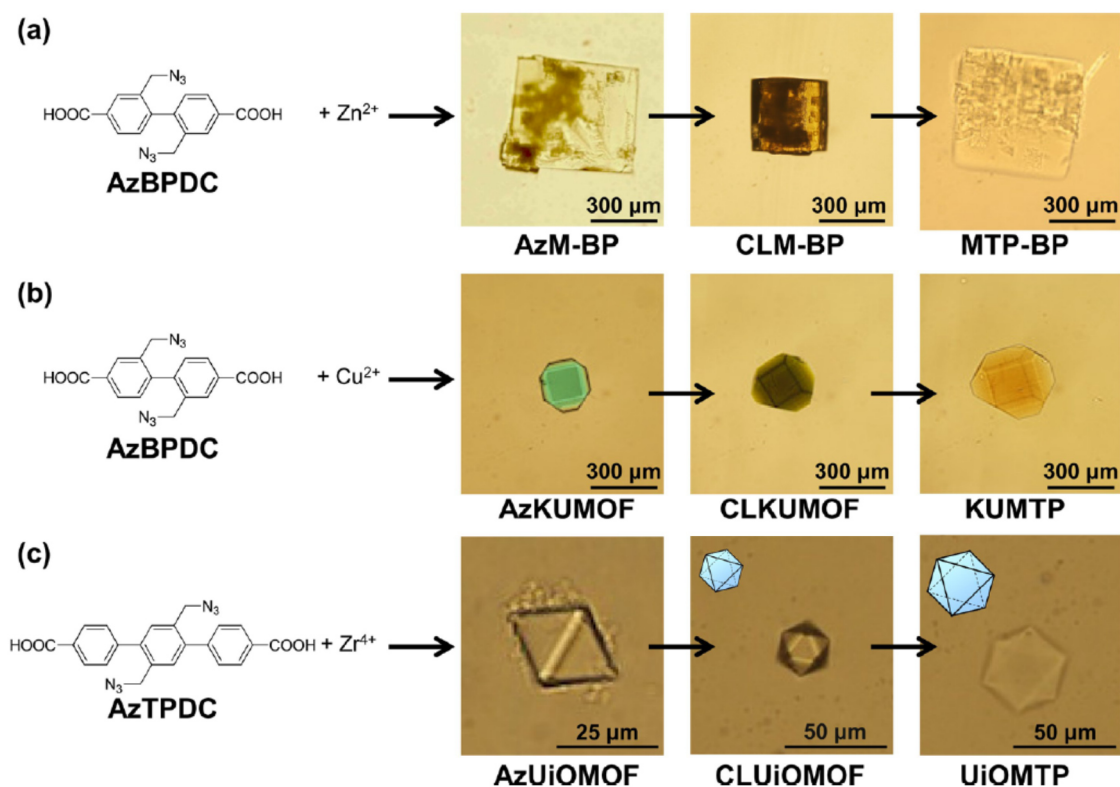


Abbildung 6. Mikroskopische Aufnahmen der MOFs (a) AzM-BP, (b) AzKUMOF, (c) AzUiOMOF, ihrer quervernetzten Zwischenprodukte und den daraus resultierenden polymeren Gelen. Nachdruck mit Genehmigung von Ref. 28. Copyright 2013 American Chemical Society.

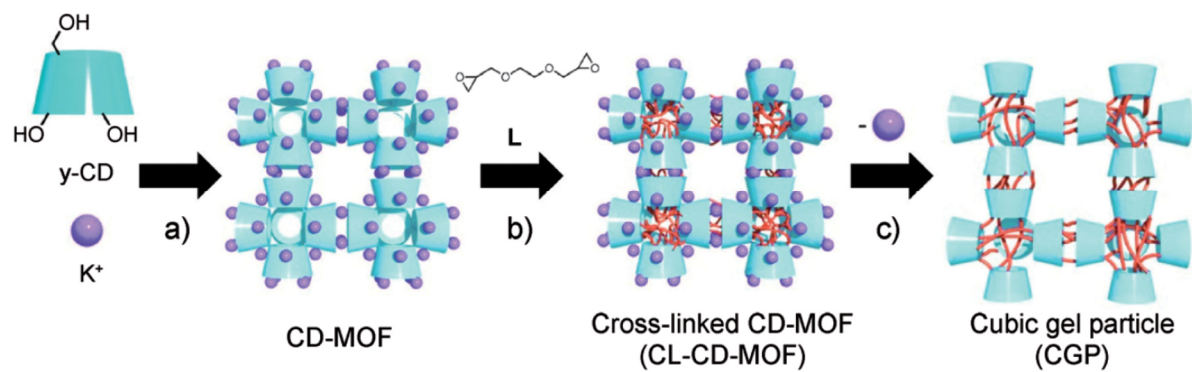


Abbildung 7. Schematische Darstellung der Synthese von kubischen Gelpartikeln. (a) Kristallisation, (b) Quervernetzungsreaktion, (c) Entfernen der koordinierten Metallionen. Nachdruck mit Genehmigung von Ref. 29. Copyright 2012 John Wiley and Sons.

Neben den größten Klassen an Aerogelen, den Silica-, Carbon-, Polymer- und Metalloxidaerogelen, gibt es noch weitere, aufstrebende Klassen. Als relativ neu angesehen werden dabei die metall-organischen Aerogele (MOAGs). Erstmals in 2009 von Kaskel et al. synthetisiert, basieren diese Materialien auf der Koordinationschemie, welche auch den Zugang zu metall-organischen Netzwerken ermöglicht.<sup>30</sup> Eine Suche nach Stichworten in der Datenbank SciFinder zeigt dabei, dass die Anzahl der Publikationen auf dem Gebiet noch gering ist, das Interesse aber rapide ansteigt (Abbildung 8).<sup>31</sup>

Der Mechanismus der Synthese von metall-organischen Gelen und den daraus resultierenden Aerogelen ist dabei noch nicht vollständig verstanden. In der Literatur wird davon ausgegangen, dass bereits gebildete Cluster bei weiterer Nukleation auf Grund von hoher Anzahl an Fehlstellen oder gestörter Koordination weniger symmetrisch wachsen, oder dass die Liganden durch Flexibilität ungeordnete Netzwerke bilden (Abbildung 9).

Die Anwendungen der entstehenden metall-organischen Aerogele sind dabei ähnlich derer von metall-organischen Netzwerken. So wurden MOAGs bereits für Sorptionsanwendungen, Festphasenmikroextraktion oder auch elektrokatalytische Reduktion verwendet.<sup>36,32,33</sup>

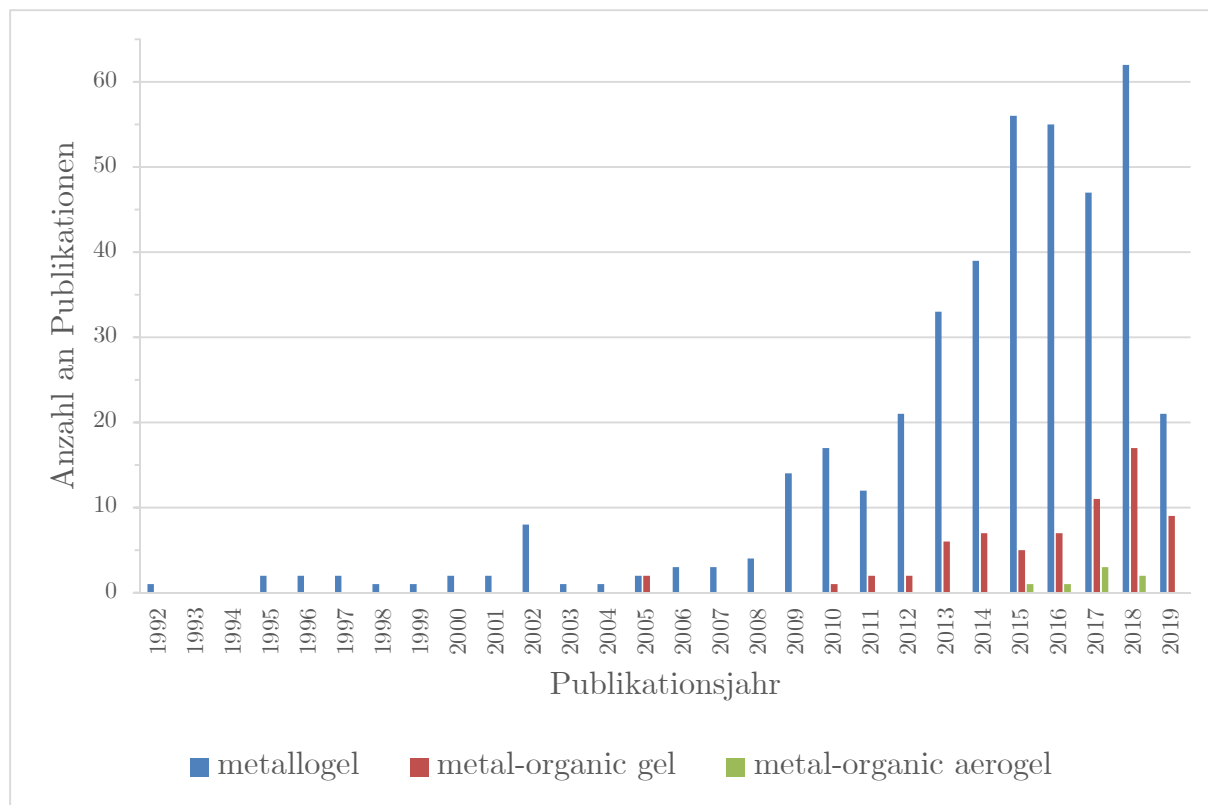


Abbildung 8. Ergebnisse der Suche nach Publikationen bei SciFinder, nach Stichworten und Jahr sortiert.

Der enorme Vorteil der MOAGs besteht darin, dass ihre Gelvorstufe in bestimmte Formen gebracht werden kann, während MOFs als Pulver vorliegen und für Anwendungen als Komposite mit Polymeren oder anderen Materialien gemischt werden müssen, was zu einem teilweisen Verlust der Eigenschaften führen kann.<sup>34</sup> Die für die Synthese benötigte überkritische Trocknung ist dabei ein Arbeitsmittel, welches bereits häufig in etablierten MOF-Arbeitsgruppen anzutreffen ist, da die überkritische Trocknung auch Vorteile in der MOF-Chemie bringt.<sup>35</sup> Bei der überkritischen Trocknung mit CO<sub>2</sub> wird das zu trocknende Material entweder mit einem mit flüssigem CO<sub>2</sub> mischbaren Lösungsmittel, gewöhnlich Aceton oder Ethanol, gewaschen oder das vorhandene Lösungsmittel ausgetauscht. Ersetzt man das Lösungsmittel nun durch flüssiges CO<sub>2</sub> und bringt dieses anschließend in den überkritischen Zustand, so lassen sich die Kapillarkräfte, welche die Poren bei der konventiellen Trocknung teilweise kollabieren lassen, unterdrücken.

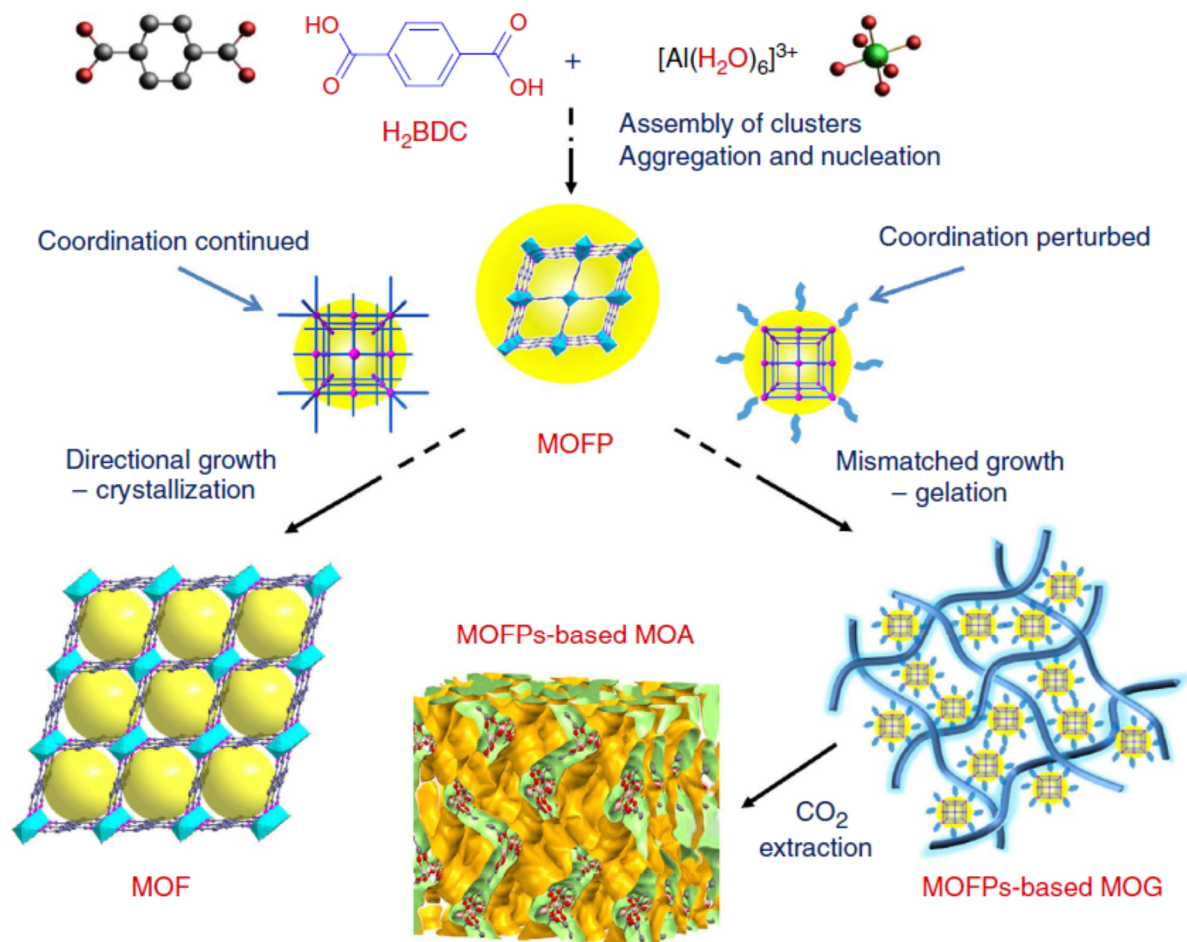


Abbildung 9. Bildung von metall-organischen Gelen über den Weg des gestörten Wachstums. Es bilden sich nano-MOF-Cluster, welche dann unregelmäßig miteinander vernetzen (rechte Hälfte der Abbildung). Nachdruck mit Genehmigung von Ref. 36. Copyright 2013 Springer Nature.

### 1.3 Membrantrennprozesse und Mixed-Matrix-Membranen

Bei Membranen handelt es sich um Filme oder dünne Schichten, bei welchen die Ausdehnung in der Ebene deutlich größer ist als in der Dicke. Diese Art von Material ist in der Industrie bereits weit verbreitet. Die Anwendung bestimmt dabei, welcher Membrantyp verwendet werden kann. Zu den verschiedenen Arten der Membranen gehören unter anderem die dichten Membranen und die porösen Membranen.<sup>37</sup>

Bei den dichten Membranen findet die Trennung über das Lösungs-Diffusions-Modell statt (Abbildung 10).

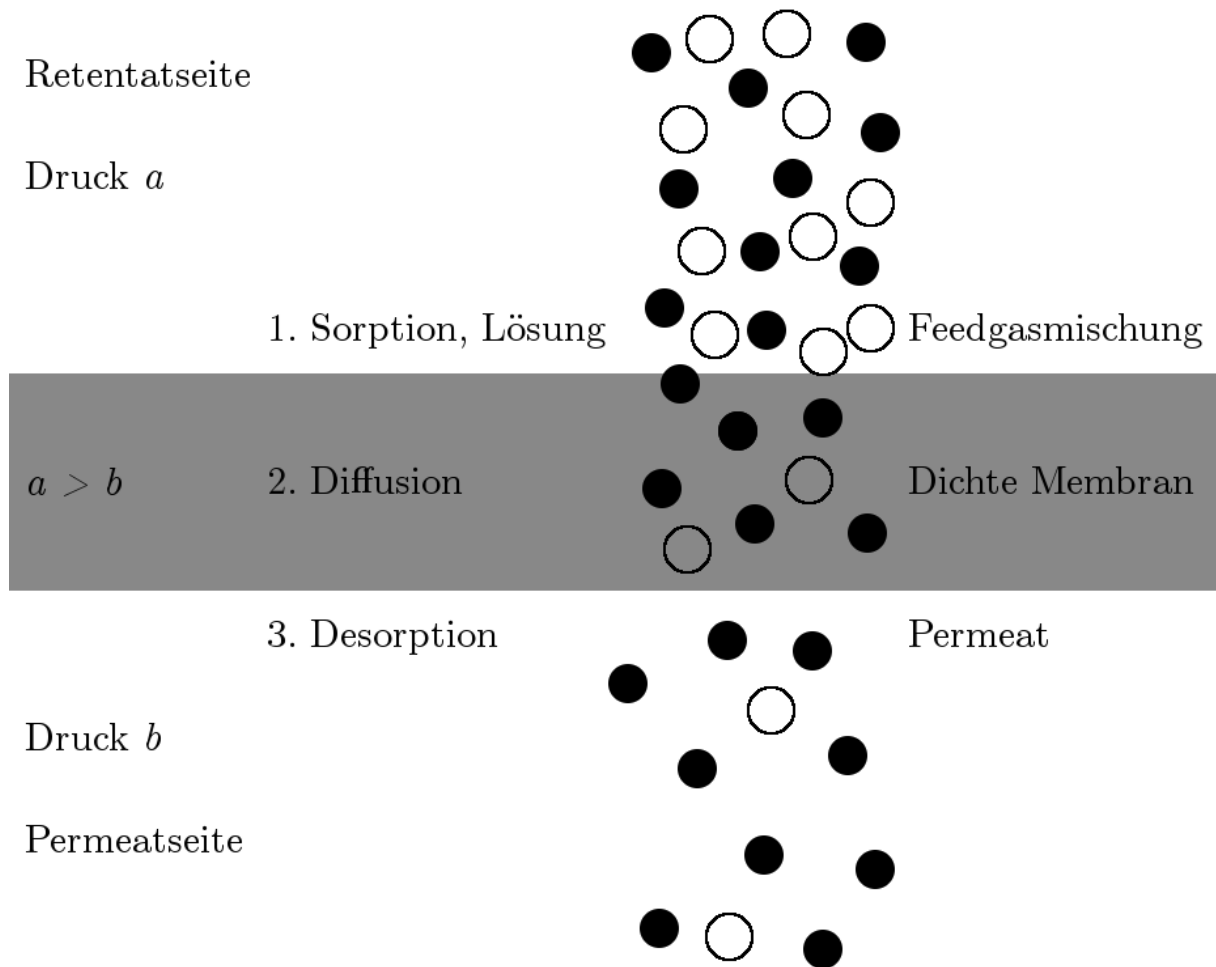


Abbildung 10. Schematische Darstellung der Permeation eines Gasgemisches durch eine dichte Membran.

Die beeinflussenden Faktoren sind hierbei Löslichkeit des Gases im Membranmaterial sowie die Diffusionsgeschwindigkeit des Gases im Material, welche durch die brownische Molekularbewegung des Membranmaterials beeinflusst wird. Auf der Seite, auf der sich die zu trennende Mischung befindet, auch Retentatseite genannt, herrscht dabei ein höherer Druck als auf der Seite des Permeats, welches das Gas ist, was durch die Membran permeiert ist.

Bei den porösen Membranen gibt es verschiedene Arten der Auftrennung. Bei der durch die Knudsen-Diffusion getriebenen Gastrennung wird das Gemisch nach unterschiedlicher Größe oder Gewicht getrennt (Abbildung 11).

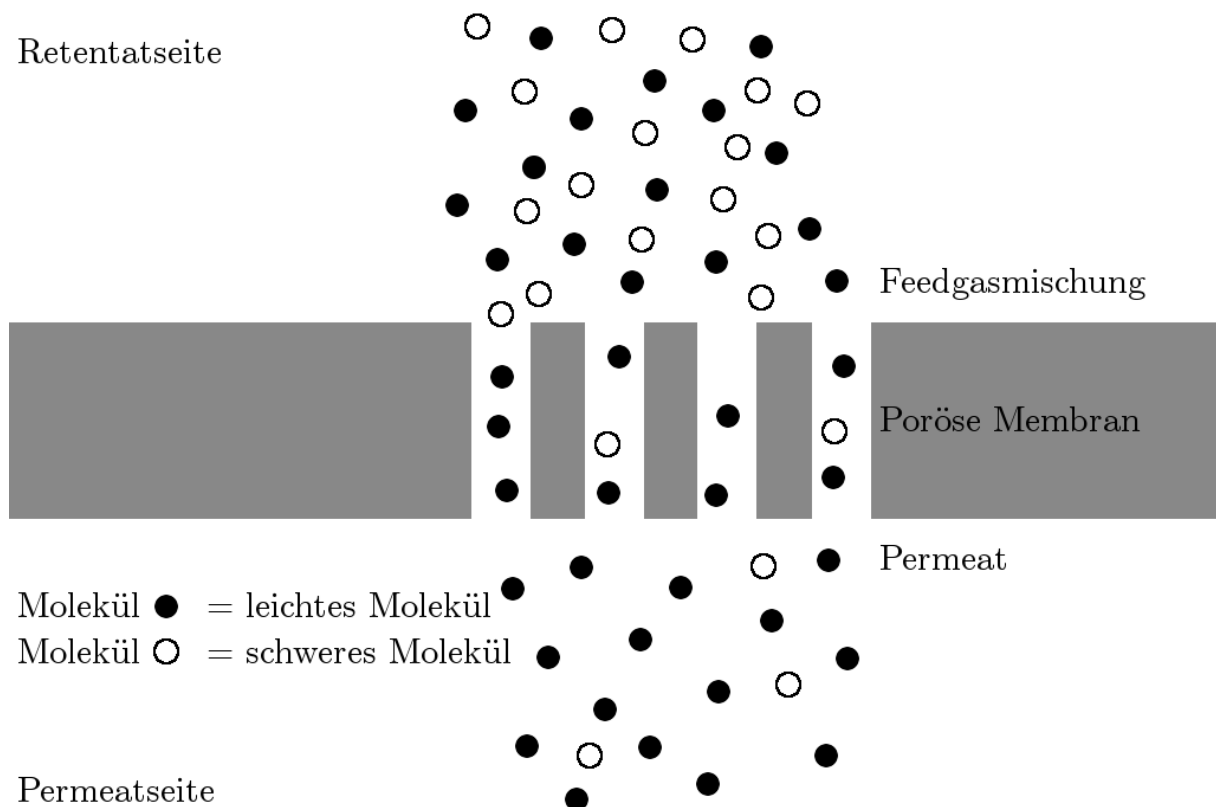


Abbildung 11. Schematische Darstellung der Gastrennung an einer porösen Membran durch Knudsen-Diffusion.

Entscheidend ist hierbei der Unterschied in der Wechselwirkungsenergie, wenn die Gasmoleküle mit der Porenwand kollidieren. Durch andere Wechselwirkungsenergien haben leichtere bzw. kleinere Gasmoleküle dabei eine höhere Transportrate durch die Membran als größere bzw. schwerere Gasmoleküle.

Bei den durch Oberflächendiffusion trennenden porösen Membranen reichert sich eines der Gase durch bevorzugte Adsorption an den Porenwänden in den Poren an. Das sich anreichernde Gas besitzt dadurch den höheren Fluss durch die Membran (Abbildung 12).



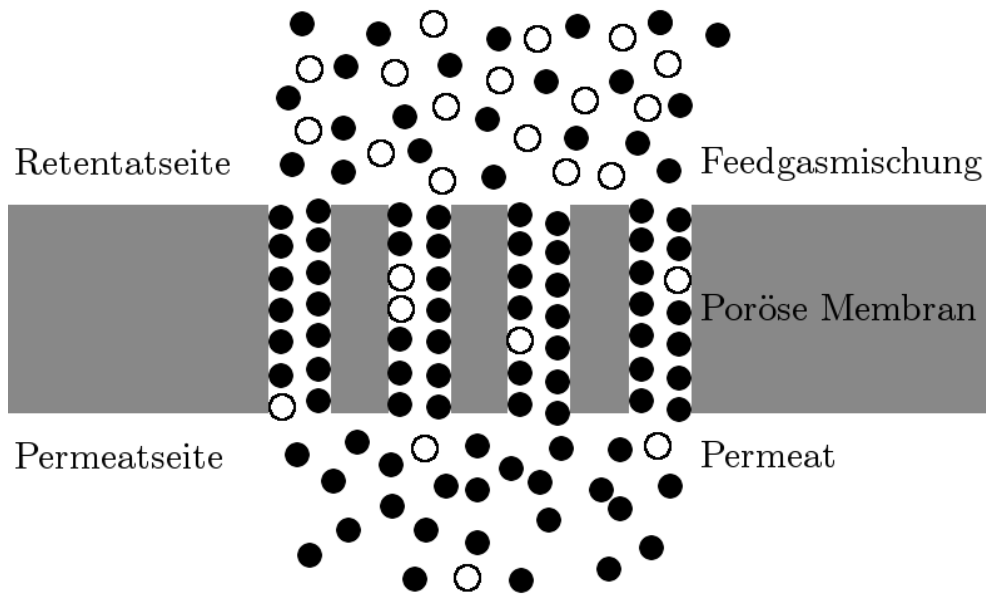


Abbildung 12. Schematische Darstellung der Gastrennung an einer porösen Membran durch Oberflächendiffusion.

In den porösen Molsiebmembranen existieren sehr schmale Poren. Diese Poren können Gasmoleküle unter anderem nach Größe auftrennen, aber auch über bevorzugte Adsorption in den Poren oder Kapillarkondensation, welche die Poren für das andere Gas unzugänglich macht (Abbildung 13). Mit Molsiebmembranen lassen sich – genau wie mit Oberflächendifusionsmembranen auch – Gase nach anderen Parametern als der Größe auftrennen, da auch die Adsorptionseffekte des größeren oder schwereren Gases überwiegen können.

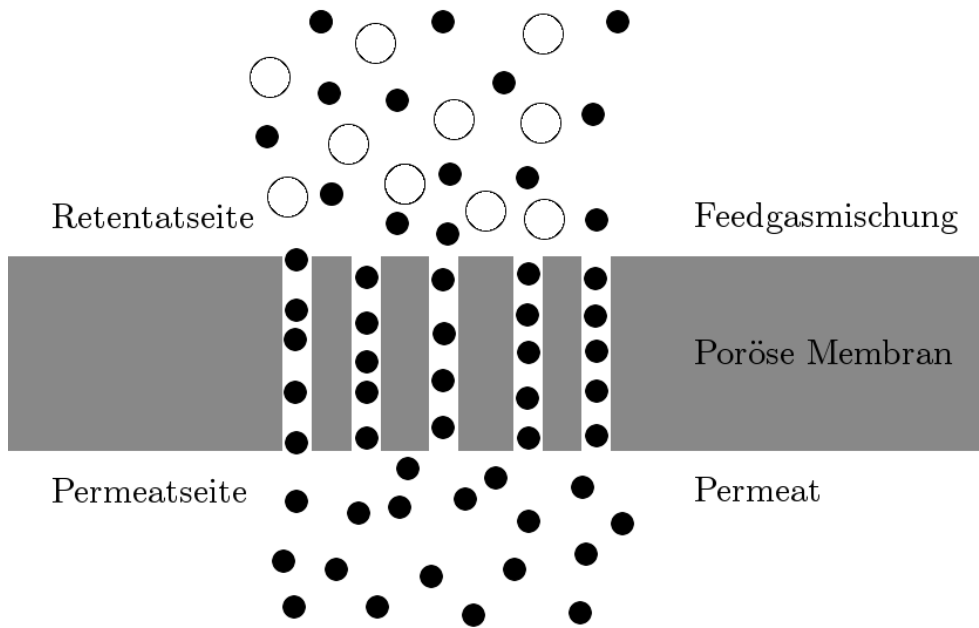


Abbildung 13. Schematische Darstellung der Gastrennung an einer porösen Molekularsiebmembran.

Membrantrennungprozesse sind in der Anwendung interessant, da ihre Eigenschaften gut an die zu trennenden Stoffe anpassbar sind. Gegenüber herkömmlichen Trennungprozessen, wie z. B. der Destillation, Kristallisation oder Adsorption, besitzen Membranen deutliche Vorteile. Die Trennung mit Membranen spart Energiekosten ein und die Bedingungen, unter welchen ein Membrantrennungsprozess betrieben werden kann, sind deutlich moderater. Aus diesem Grund haben sich Membranen als die bevorzugte Technologie für Trennungsprozesse hervorgetan.<sup>37</sup> Membranen werden bereits in der Industrie eingesetzt, unter anderem für die Trennung von CO<sub>2</sub> aus Erdgas, die Wasserstoffrückgewinnung im Crackingverfahren, Sauerstoff- und Stickstoffanreicherung von Luft für medizinische Zwecke, Dampfrückgewinnung und Lösungsmittelaufreinigung.<sup>38,39,40,41</sup>

Die Fähigkeit von Membranen, Stoffe aufzutrennen, wird dabei über zwei Größen ausgewertet, der Permeabilität und der Selektivität. Die Permeabilität  $P_i$  ist dabei definiert als der Fluss des Stoffes  $i$  durch die Membran, unter Berücksichtigung der Differenz der Partialdrücke des Gases auf beiden Seiten der Membran sowie der

Schichtdicke der Membran. Der Fluss entspricht dabei der Flussrate pro Einheit an Membranfläche. Die Einheit der Permeabilität ist Barrer:

$$1 \text{ Barrer} = 1 \times 10^{-10} \frac{\text{cm}_{\text{STP}}^3 \text{ cm}}{\text{cm}^2 \text{ s cmHg}} = 3,35 \times 10^{-16} \frac{\text{mol m}}{\text{m}^2 \text{ s Pa}}$$

Die Selektivität ist der Trennungsfaktor für eine Komponente der Mischung. Für Gasmischungen der Gase m und k wird die Selektivität wie folgt berechnet:

$$\alpha_{m,k} = \frac{X_m/X_k}{Y_m/Y_k}$$

Dabei entsprechen  $X_m$  und  $X_k$  dem Molenbruch der Komponenten auf der Permeatseite, während  $Y_m$  und  $Y_k$  dem Molenbruch der Komponenten auf der Retentatseite entsprechen.

Selektivität und Permeabilität sind für gewöhnlich invers miteinander korreliert. Steigende Selektivität bedeutet demnach geringere Permeabilität und umgekehrt. Dieser Zusammenhang wurde von Robeson in einer Kurve zusammengetragen. Das Mittel dieser Kurven, auch *Robeson upper bounds* genannt, stellt dabei einen Schnitt durch die aktuellen Trennleistungen der Membranen dar (Abbildung 14).<sup>42,43</sup>

Kommerziell interessant sind dabei die Membranen, welche sich im Bereich der *upper bounds* befinden oder diese übertreffen. Die Entwicklung neuer Polymere und anorganischer Membranen soll dabei helfen.<sup>44, 45, 46</sup> Als weitere zukunftssträchtige Materialien haben sich Membranen erwiesen, welche Polymere mit anorganischen Komponenten vereinen. Diese sogenannten Mixed-Matrix-Membranen bestehen dabei aus einem Polymer, in welchem ein für gewöhnlich poröser und anorganischer Füllstoff dispergiert und immobilisiert ist (Abbildung 15). Als besonders vorteilhaft haben sich dabei MOFs erwiesen, da diese noch interessantere Eigenschaften besitzen als Zeolithe (siehe Kapitel 1.1).

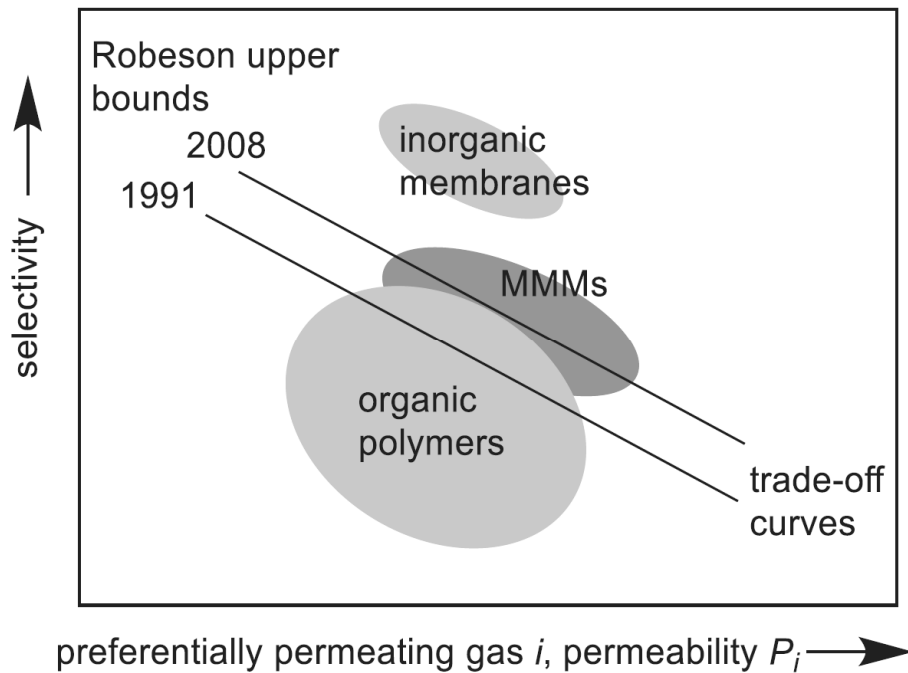


Abbildung 14. Schematische Darstellung der umgekehrten Korrelation zwischen Permeabilität und Selektivität, genannt *Robeson upper bounds*. Kommerziell relevante Materialien bewegen sich im Bereich dieser *upper bounds* oder übertreffen sie. Nachdruck von Ref. 47 mit Genehmigung der Royal Society of Chemistry.

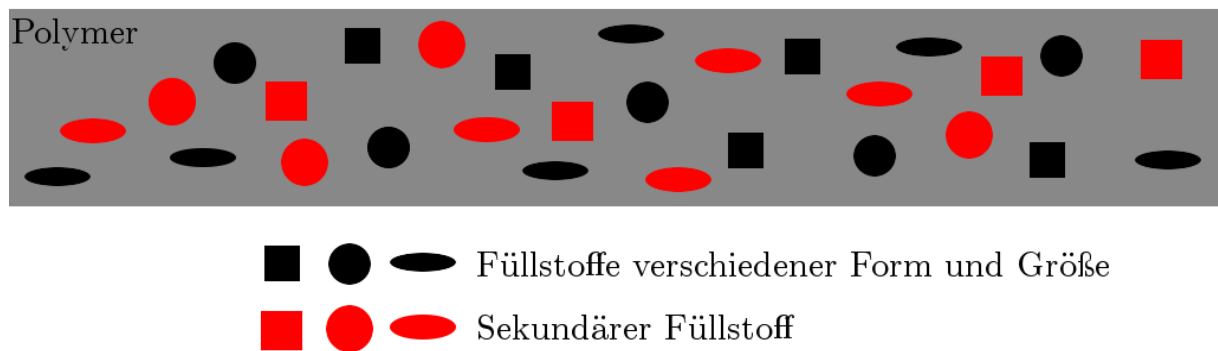


Abbildung 15. Schematische Darstellung einer Mixed-Matrix-Membran mit Füllstoffen verschiedener Größe und Form.

In dieser synergistischen Kombination wird die einfache Verarbeitung der Polymere mit den überlegenen Trennleistungen der anorganischen Komponente vereint. Zuerst in 1980 synthetisiert, ist das Interesse an diesen neuen Materialien in letzter Zeit stark gewachsen.<sup>40</sup> Das Hauptaugenmerk liegt dabei auf der Chance, die *Robeson upper bounds* deutlich zu übertreffen.<sup>48</sup>

## 2 AUFGABENSTELLUNG

---

Im Rahmen dieser Arbeit sollten neue Liganden zur Herstellung von metall-organischen Koordinationsverbindungen synthetisiert und charakterisiert werden. Diese neuen Liganden sollten im Anschluss zur Synthese neuer metall-organischer Koordinationsverbindungen und Hybridmaterialien dienen. Die Koordinationsverbindungen und Hybridmaterialien sollten Untersuchungen unterlaufen, bei welchen abhängig vom Material die Porosität und Viskosität untersucht wurde, um die für die selektive Aufnahme von Gasen und gegebenenfalls Kationen und Anionen einzusetzen. Bei den Koordinationsverbindungen sollte das Hauptaugenmerk auf den Metallo-, Aero- und Xerogelen liegen.

Des Weiteren sollte die Synthese neuer Mixed-Matrix-Membranen durchgeführt werden, welche für die Gaspermeation genutzt werden sollten.

Die relevanten Ergebnisse sollten aufgearbeitet und wenn möglich in wissenschaftlichen Journalen publiziert werden.

### **3 KUMULATIVER TEIL**

---

In diesem Kapitel sind die Ergebnisse dieser Dissertation dargestellt, welche in Form von Veröffentlichungen in internationalen Journalen publiziert wurden. Die Publikationen werden so präsentiert, wie sie im jeweiligen Journal erschienen sind. Sie sind mit eigenen Nummerierungen, Abbildungen, Referenzlisten und Tabellen versehen, welche nicht den Reihenfolgen im restlichen Teil dieser Dissertation entsprechen. Zu jeder Publikation gibt es eine kurze Zusammenfassung, welche die Relevanz der Arbeit im Rahmen dieser Dissertation einordnet und den eigenen Beitrag zur Veröffentlichung darstellt. Die Publikationen werden teilweise um einen Appendix erweitert, welcher relevante, nicht veröffentlichte Ergebnisse enthält, sowie ein Kapitel über unveröffentlichte Ergebnisse, welche im Rahmen der Dissertation entstanden sind.

### 3.1 Metal-Organic Gels Based on a Bisamide Tetracarboxyl Ligand for Carbon Dioxide, Sulfur Dioxide and Selective Dye Uptake

Dennis Dietrich, Christopher Licht, Alexander Nuhnen, Simon-Patrick Höfert, Laura De Laporte, Christoph Janiak

DOI: 10.1021/acsami.9b04659

Der neue Ligand „H<sub>4</sub>L1“, *N*<sup>1</sup>,*N*<sup>4</sup>-(Diterephthalsäure)terephthalamid wurde in Verbindung mit Chrom- und Aluminiumsalzen in ein Metallogel überführt. Die entstandenen Metallogele zeigten mehrere interessante Eigenschaften. Die Metallogele mit Cr(III) ließen sich in bestimmte Formen bringen und zeigten auch gute rheologische Eigenschaften, welche zusammen mit der Fähigkeit, Lösemittelaustausch und überkritische Trocknung mit CO<sub>2</sub> zu überstehen, neue poröse Materialien für die Gassorption erzeugten. Ähnlich verfahren wurde mit zwei weiteren Metallogelen basierend auf Al(III) und einer Mischung von Cr(III) und Al(III), sowie mit einem konventionell getrockneten Xerogel basierend auf H<sub>4</sub>L1 und Cr(III). Anschließend wurden diese neuen porösen Materialien mehreren Sorptionsmessungen unterzogen und die entstandenen Daten für die Evaluation der Trennleistung bei Einsatz dieser Materialien z. B. als Filter genutzt.

Anteile an der Veröffentlichung:

- Idee, Konzept, experimentelle Arbeiten und Analytik (bis auf unten gelistete Ausnahmen).
- Aufarbeiten der Ergebnisse und Verfassen des Manuskripts. Korrekturen durch Herrn Prof. Dr. Christoph Janiak.
- Einkristallmessung und Strukturlösung durch Herrn Simon-Patrick Höfert.
- Rheologische Messungen und Verfassen des Absatzes über die dazugehörigen Ergebnisse durch Herrn Christopher Licht.
- Sorptionsmessungen von Argon und Schwefeldioxid durch Herrn Alexander Nuhnen.

# Metal-Organic Gels Based on a Bisamide Tetracarboxyl Ligand for Carbon Dioxide, Sulfur Dioxide and Selective Dye Uptake

*Dennis Dietrich,<sup>†</sup> Christopher Licht,<sup>‡</sup> Alexander Nuhnen,<sup>†</sup> Simon-Patrick Höfert,<sup>†</sup> Laura De Laporte,<sup>‡</sup> Christoph Janiak.<sup>†\*</sup>*

<sup>†</sup> Institut für Anorganische Chemie und Strukturchemie, Heinrich-Heine-Universität  
Düsseldorf, Universitätsstraße 1, 40225 Düsseldorf.

<sup>‡</sup> DWI – Leibniz Institute for Interactive Materials, Forckenbeckstraße 50, 52056 Aachen.

KEYWORDS. metallogel; metal-organic aerogel; xerogel; amide-functionalized linker; sulfur dioxide sorption; gas sorption; dye sorption

## **Abstract**

A metal-organic gel (metallogel) based on the new tetracarboxyl ligand N<sup>1</sup>,N<sup>4</sup>-(diterephthalic acid)terephthalamide in combination with chromium(III) has been converted into its xero- and aerogel and demonstrated to have excellent specific sorption properties for dyes in its metallogel state, where fuchsine is adsorbed faster than two other dyes, calcein and disulfine blue, and for water, sulfur dioxide and carbon dioxide in its xero- and aerogel state. The metallogel showed very good shape retention and could be extruded from molds in designed shapes. In a rheology experiment, the storage modulus was determined to be 1440 Pa, and the metallogel is elastic up to 3 Hz, breaking at strains higher than 0.3 %. Additional metallogels



utilizing the same ligand with a wide range of metal ions (Al(III), Fe(III), Co(III), In(III), Hg(II)) have also been synthesized, and the aluminum and mixed aluminum-chromium derivative has also been converted into its aerogel. The highly porous Cr, Al and AlCr metal-organic aerogels proved stable against water vapor in a physisorption experiment and were used to model breakthrough curves for SO<sub>2</sub>/CO<sub>2</sub> gas mixtures with the idealized adsorbed solution theory (IAST) from their physisorption isotherms. The breakthrough simulation utilized SO<sub>2</sub>/CO<sub>2</sub> equivalencies from a real world application and showed effective retention of SO<sub>2</sub> from the gas mixture. Furthermore, the materials in this work exhibit the highest SO<sub>2</sub> uptake values for metal-organic aerogels so far (up to 116.8 cm<sup>3</sup> g<sup>-1</sup>, or 23.4 wt %).

## Introduction

Porous metal-organic frameworks (MOFs) with high surface areas and potential applications in gas storage and purification, catalysis, drug delivery and pollutant sequestration<sup>1</sup> are a current field of high interest.<sup>2,3,4,5,6,7</sup> The properties of MOFs can be tuned towards their respective applications, through various modifications of the organic linker or the metal nodes.<sup>8,9,10</sup> As MOFs are most commonly available as crystalline powders, shaping with retention of porosity is a critical issue. By embedding MOFs into different types of polymers to yield xerogels and aerogels, it is possible to tailor these composite systems into shapes suitable to the application without losing much of the physisorption properties.<sup>11,12,13,14</sup>

Aerogels are amorphous solids with low density, which, when properly dried, can possess high accessible surface areas. On their way to becoming an aerogel, the material usually starts out as a solution, or sol, which is then processed to form a gel. Within the gel, a solid-like network immobilizes the liquid-like phase, typically the solvent, through capillary forces and solvent-gelator interactions.<sup>15</sup> Removal of all swelling agents without suppressing the capillary

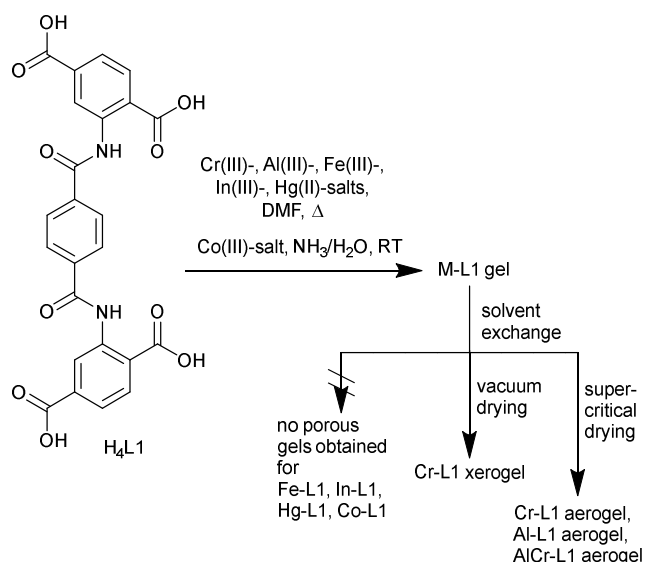
forces within the gel produces a xerogel, often accompanied by a collapse of the micropores in the solid-like network. The xerogels may sometimes retain their mesopores, and surface areas can even be comparable to those of the subsequent aerogels.<sup>16</sup> If the swelling agent is removed under supercritical conditions, the capillary forces are suppressed, preventing pore collapse and leading to a highly porous solid with low density and high surface area called aerogel. Aerogels can also be formed if the network in the gel is strengthened enough to withstand evaporation of the solvent.<sup>17,18</sup> Common types of aerogels are of organic nature, either as polymers or as pure carbon aerogels, with the precursor to the carbon aerogels often being an organic aerogel, or of metal-oxide nature, including silica and metal oxide aerogels.<sup>19</sup> Their applications also include gas storage and separation as well as catalysis, but also thermal or acoustic insulation.<sup>20,21,22</sup>

In 2009, Kaskel et al. bridged the gap between MOFs and aerogels by synthesizing a metal-organic aerogel (MOAG) based on Fe-1,3,5-benzene tricarboxylate with a surface area above  $1600 \text{ m}^2 \text{ g}^{-1}$ .<sup>23</sup> As a first step, a metallogel based on coordination chemistry is formed. These metallogels readily exhibit interesting properties in applications, and have been shown to respond to a variety of thermal and chemical stimuli.<sup>24</sup> The easy processability of these gels allows them to be used in many industrial fields, including drug delivery, gas storage and optoelectronics, omitting the embedding often required for metal-organic frameworks.<sup>25</sup> Afterwards, the aerogel is formed by supercritical drying of the metallogel, and the coordination bonds between the linker and the metal nodes can be observed by IR spectra. In recent times the interest in metal-organic aerogels has grown. MOAGs have been used for dye uptake, microcystin removal from water, solid-phase microextraction and electrocatalytic reduction.<sup>26,27,28,29</sup> The use of porous metal-organic compounds for flue-gas desulfurization is currently investigated and discussed as a highly interesting class of materials.<sup>30,31</sup> As a minor constituent of flue gas, up to 95 % of sulfur dioxide can be removed using limestone as chemical absorbent.<sup>32,33</sup> The remaining 5 % of  $\text{SO}_2$  is the major contributor to the 80 Mt of worldwide

SO<sub>2</sub> emissions from energy related sources in 2015, which represents a significant effect on the health of humans and on the environment.<sup>34,35,36</sup>

In this work, we present a bisamide tetracarboxyl ligand (Scheme 1) which readily forms metallogels with a variety of metal ions. The resulting metallogels have been converted to xero- and aerogels, by exchanging the solvent, and vacuum drying for the xerogels or supercritical removal of the solvent for the aerogels, and have been characterized in terms of their porosity using N<sub>2</sub>, CO<sub>2</sub> and Ar physisorption and gas uptake capacity. The analyzed gases include CO<sub>2</sub>, H<sub>2</sub>O and SO<sub>2</sub>, as they should show enhanced interaction with the functional amide groups present in the linker of the MOAGs. Furthermore, the metallogel based on chromium showed selective uptake of dyes from aqueous solution. To the best of our knowledge there were, so far, no reports on chromium- or aluminum-based MOAGs for SO<sub>2</sub> sorption.

### Scheme 1. Bisamide Tetracarboxyl Linker Used in Metal-Organic Gel Synthesis and Overview on the Syntheses and Gel Products.



## Results and Discussion

### Ligand and Gel Synthesis

The ligand  $N^1,N^4$ -(diterephthalic acid)terephthalamide,  $H_4L1$ , was synthesized from 2-aminoterephthalic acid and terephthaloyl chloride in water with the addition of excess potassium carbonate in good yields. A single crystal X-ray structure analysis of  $H_4L1$  after recrystallization from DMF confirmed the ligand configuration (Figure 1).

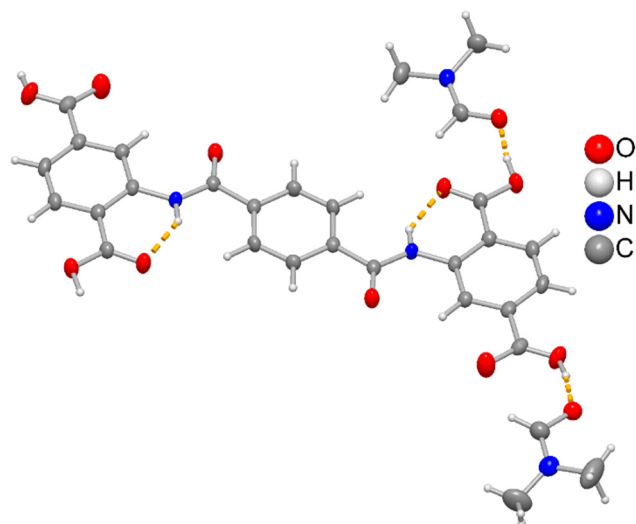


**Figure 1.** Molecular structure of  $H_4L1$  with two of the four hydrogen-bonded DMF molecules in  $H_4L1 \cdot 4DMF$  (70 % thermal ellipsoids, H atoms with arbitrary radii). The resolved DMF disorder is not shown for clarity. For further crystallographic details and information on hydrogen-bonding see Table S1, S2 and Figure S1, Supp. Info. The structural data has been deposited with the Cambridge Crystallographic Data Center (CCDC No. 1889949).

The chromium(III), aluminum(III), iron(III), mercury(II) and indium(III) metallogels were synthesized from their nitrate salts, with the exception of mercury, where the acetate salt was used, and  $H_4L1$  in a solvothermal reaction in DMF. Due to poor solubility of the ligand, the reaction mixture had to be heated to 80 °C to dissolve the ligand. An attempt was made to dissolve the ligand in DMF at 80 °C first, but the ligand stayed mostly insoluble without the addition of a metal salt. Adding various bases or acids to help dissolve the ligand in DMF usually prevented the metallogels from forming. The red iron and white indium metallogels were not homogeneous, as the gels already started to form while the ligand had not completely dissolved yet. Processing of **Fe-L1** and **In-L1** proved to be impossible, and these irregular

metallogels were not investigated further. The white metallogel of mercury was formed by separately heating suspensions of H<sub>4</sub>L1 in DMF and solutions of mercury acetate in DMF to 80 °C and mixing the two. The mercury metallogel formed instantly and stays stable for a while before turning back into a liquid. Reheating the liquid did not reform the mercury metallogel. The same mixing procedure was also unsuccessfully tried on the iron and indium gel. The mercury metallogel has not been processed further due to the potential toxicity. The cobalt(III) metallogel was synthesized by dissolving H<sub>4</sub>L1 and hexaamminecobalt chloride in 25 % ammonia water before mixing the two solutions and letting the ammonia evaporate (see Supp. Info. and Table S4 for synthetic details). The orange metallogel of cobalt could not be handled outside of its reaction vessel, as it did not prove to be stable enough to withstand the transfer to another vessel. This was most likely due to the inert nature and stability of the [Co(NH<sub>3</sub>)<sub>6</sub>]<sup>3+</sup> ion (as indicated by the retention of its original orange color) which prevents formation of Co-L1 carboxylate linkages but instead gives a supramolecular [Co(NH<sub>3</sub>)<sub>6</sub>]<sup>3+</sup>-H<sub>4-n</sub>L1<sup>n-</sup> hydrogen-bonded gel structure. Altogether this left only the handleable chromium and aluminum metallogels and a mixed AlCr metallogel for further investigations. The different metallogels were repeatedly synthesized to ensure reproducibility. The gel constitution was qualitatively shown by the inversion test (Figure 2).

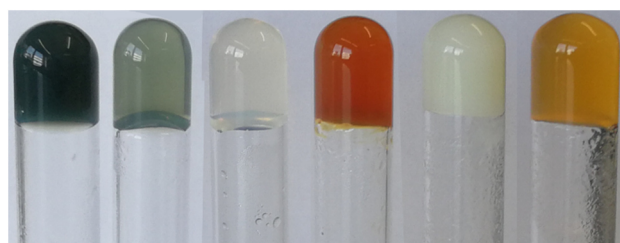


**Figure 2.** From left to right: Metallogel **Cr-L1**, **AlCr-L1**, **Al-L1**, **Fe-L1**, **In-L1**, **Co-L1**. All vessels are presented in an upturned state. A picture of **Hg-L1** can be found in the supporting information (Figure S2, SI).

The dark-green chromium metallogel showed excellent stability and were easily removed from their reaction vessels while retaining their shape (Figure 9). The white aluminum metallogels remained stable enough for further processing, however handling them outside of moving them to the next reaction vessel usually resulted in the destruction of the metallogel.

From the metallogels the xerogels of chromium and aluminum were formed by removing the solvent *in vacuo* after exchanging DMF with ethanol while the aerogels were formed by first exchanging the DMF with ethanol followed by supercritical drying with CO<sub>2</sub>. The mixed chromium-aluminum metallogel **AICr-L1** was processed in the same way (see exp. section for details on solvent exchange and supercritical drying procedure). The successful DMF-to-ethanol solvent exchange was followed using infrared techniques (Figure 3).

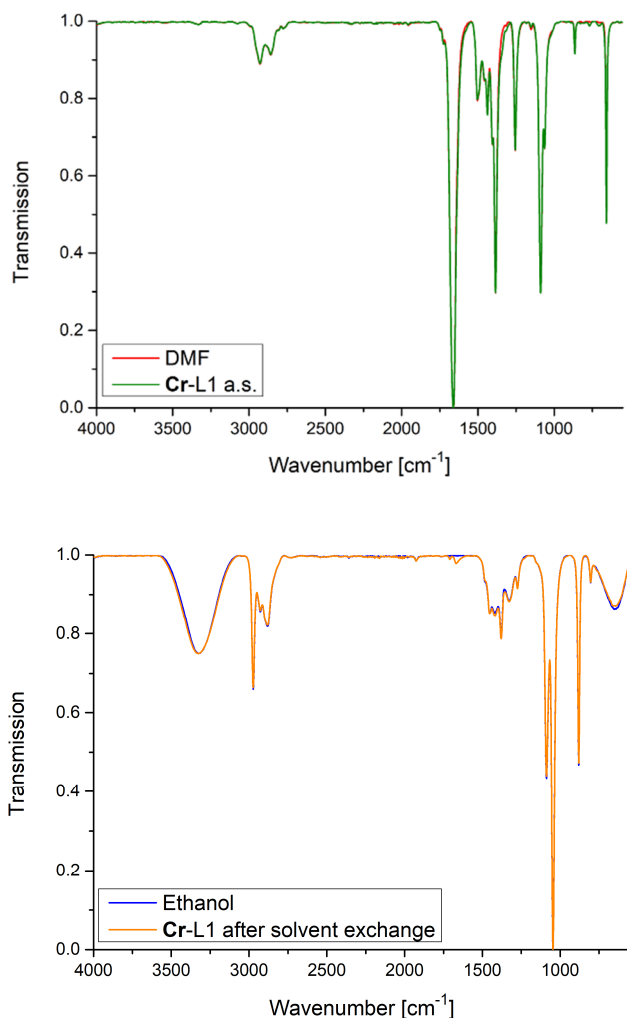


**Figure 3.** Exemplary infrared spectra of the metallogel **Cr-L1**. The solvent spectra dominate, as even the gels with the lowest amount of solvent are still made up of over 96 wt % solvent (for **Cr-L1** as synthesized, a.s.). Top: Spectrum of **Cr-L1** as synthesized superimposed with the spectrum of pure DMF. Bottom: Spectrum of **Cr-L1** after solvent exchange with ethanol superimposed with the spectrum of neat ethanol.

The infrared spectra of the aerogels of **Cr-L1**, **AlCr-L1** and **Al-L1** exhibited the disappearance of the major peaks caused by the carboxylic acid group at around  $1650\text{--}1700\text{ cm}^{-1}$  and  $1190\text{ cm}^{-1}$ . The appearance of new peaks at around  $1425$  and  $1567\text{ cm}^{-1}$  indicate successful formation of the carboxylate (Figure 4). The characteristic absorption bands for the coordinated ligand at  $1567\text{ cm}^{-1}$  correspond to the asymmetric stretching vibration ( $\nu_{\text{as}}$ ) and the band at  $1425\text{ cm}^{-1}$  to the symmetric stretching vibration ( $\nu_{\text{s}}$ ) of the carboxylate group. The frequency

gap ( $\Delta\nu$ ) between these bands  $\Delta\nu = \nu_{\text{as}}(\text{COO}^-) - \nu_{\text{s}}(\text{COO}^-)$  of  $142 \text{ cm}^{-1}$  reveals that the carboxylate ligation is in the bidentate bridging mode ( $\mu_{1,3}$ - or  $\eta^1:\eta^1:\mu_2\text{-M-O-C-O-M}$ ).<sup>37,38</sup>

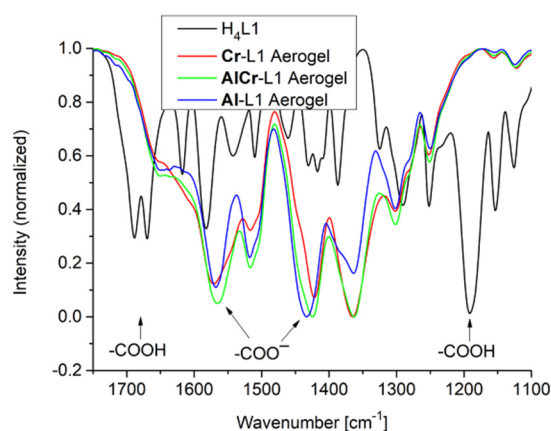


**Figure 4.** IR spectra from L1 and the respective aerogels. The carboxylic acid bands at 1650-1700  $\text{cm}^{-1}$  and at 1191  $\text{cm}^{-1}$  in the spectrum of L1 vanish in the aerogel spectra, and new bands, which can be attributed to carboxylate vibrations, appear instead.

In common aerogel literature, the XRD patterns of gels derived from their respective metal-organic frameworks often show similar peaks. The reason given for this occurrence is due to formation of metal-organic framework nanoparticles, where further coordination is perturbed, which then results in the formation of a gel.<sup>26</sup> In the materials of this work, no discrete peaks were visible in the XRD patterns, suggesting that there might have been no such formation of nanostructures (Figure 5).



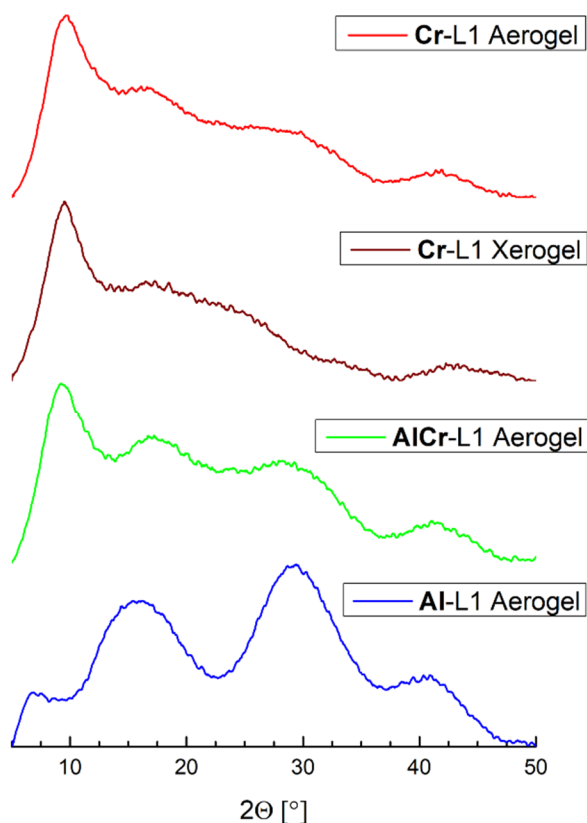


**Figure 5.** XRD patterns of the Cr- and Al-based aero- and xerogels.

The similar powder X-ray diffractograms (PXRDs) for the Cr-based aerogel and xerogel exhibit only very broad ill-defined bands, as does the **Al-L1** aerogel. Remarkably, the PXRD pattern of the **AlCr-L1** aerogel appears to be a combination of the patterns of the respective monometallic aerogels, with the broad maxima of the **Cr-L1** and **Al-L1** aerogel being superimposed. This suggests that the **AlCr-L1** aerogel may be a physical mixture of the **Cr-L1** and **Al-L1** aerogel, instead of a mixed-metal aerogel. In general, the metal-organic materials can be considered amorphous. Thus, we exclude the formation of nano-MOF clusters which are interconnected to a gel phase. The observed peaks are too broad as to stem from distinct nanoparticles.

The IR spectra showed a bidentate bridging of the ligand and the PXRD patterns lacked discrete peaks, and only suggested a certain long-range order through the broad bands. In the

metal-organic gel literature one-dimensional infinite metallogelators are often reported.<sup>39,40,41</sup> Here the ligand H<sub>4</sub>L1 allows for coordination of four metal ions.

For the microstructure of the Cr- and Al-organic gels we assume the metal atoms with their typical octahedral coordination environment. Irrespective if the metal building units are monometallic or form a polynuclear hydroxido-bridged metals chains as in MIL-53(Cr, Al)<sup>42,43</sup> and most Al-MOFs (CAU-10-H,<sup>44</sup> Al-fumarate<sup>45</sup>) the tetratopic flexible ligand can then link these metal units to an up to three-dimensional structure. The metal and linker groups can readily incorporate solvent molecules in a second-sphere coordination through coordination and hydrogen bonding. Further solvent molecules then fill the voids. Because of the flexible nature of the linker, the metal-ligand structure is unlikely to be crystalline but forms an amorphous metal-organic gel (Figure 6). In the current metal-organic gel literature, the microstructures are often based on “educated guesses”, especially when the structure is not derived from a known metal-organic framework.<sup>46,47</sup>

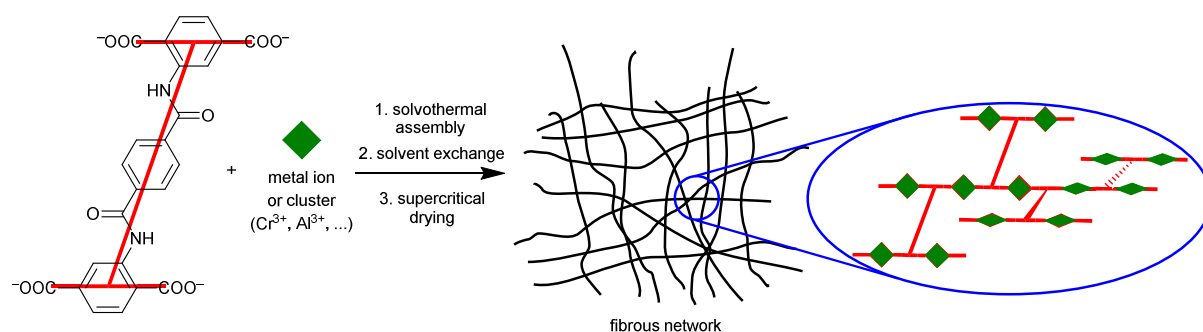


**Figure 6.** Schematic synthesis procedure of metal-organic gel formation. For the metal unit (green) an octahedral coordination sphere is assumed where at least two carboxylate groups of the tetratopic linker (red) are cis- or trans-coordinated. The resulting coordination polymer chains can be interlinked in three dimensions and are randomly oriented. The gel is formed through supramolecular interactions of the solvent with the coordination polymer chains. The resulting fibrous network randomly propagates in multiple directions.

Where possible, the morphology of the xero- and aerogels has been analyzed by scanning electron microscopy (SEM). Fibrous networks with pore-like voids could be observed for the aerogels of **Cr-L1**, **Al-L1** and **AlCr-L1**. The xerogel of **Cr-L1** showed a rough surface with potential porosity (Figure 7). The xerogel of **Fe-L1** appeared as smooth and without distinctive surface features at all magnifications. The xerogels of **Co-L1** and **In-L1** had no directly visible pores and appeared to be consisting of unconnected fibers (Figure S10). Scanning electron microscopy – energy dispersive X-ray spectroscopy (SEM-EDX) analyses reveal through the metal element mapping a homogenous distribution of metal atoms throughout the metal-organic gel materials (Figure S5-S8, SI).

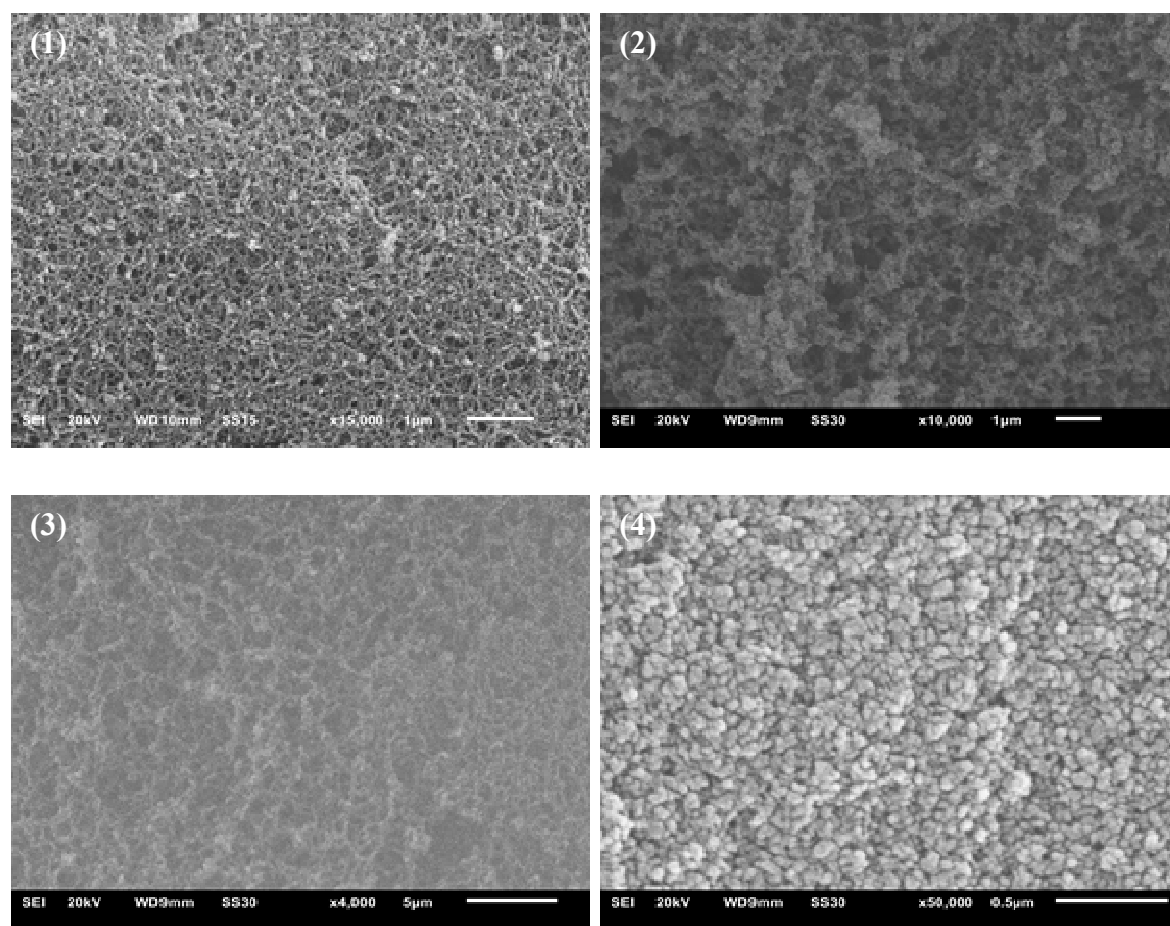


**Figure 7.** SEM micrographs of the aerogels of **Cr-L1** (1), **Al-L1** (2), and **AlCr-L1** (3), and the xerogel of **Cr-L1** (4).

### Rheological experiments.

Rheological measurements have been performed in order to investigate the mechanical properties of Cr-L1. The metallogels are pre-formed in a round-shaped mold of stainless steel by heating at 100 °C for 24 hrs (Figure 8a). After gelation, the metallogels are carefully moved to the rheometer plate (Figure 8b). In the case of Al-L1 and AlCr-L1, the metallogels were too fragile for transfer to the rheometer. Both amplitude and frequency sweeps were performed, revealing a storage modulus of  $1440 \pm 139$  Pa for the Cr-L1 gel. The metallogel is elastic up to 3 Hz and starts to break at strains higher than 0.3 % (Figure 8c, d).

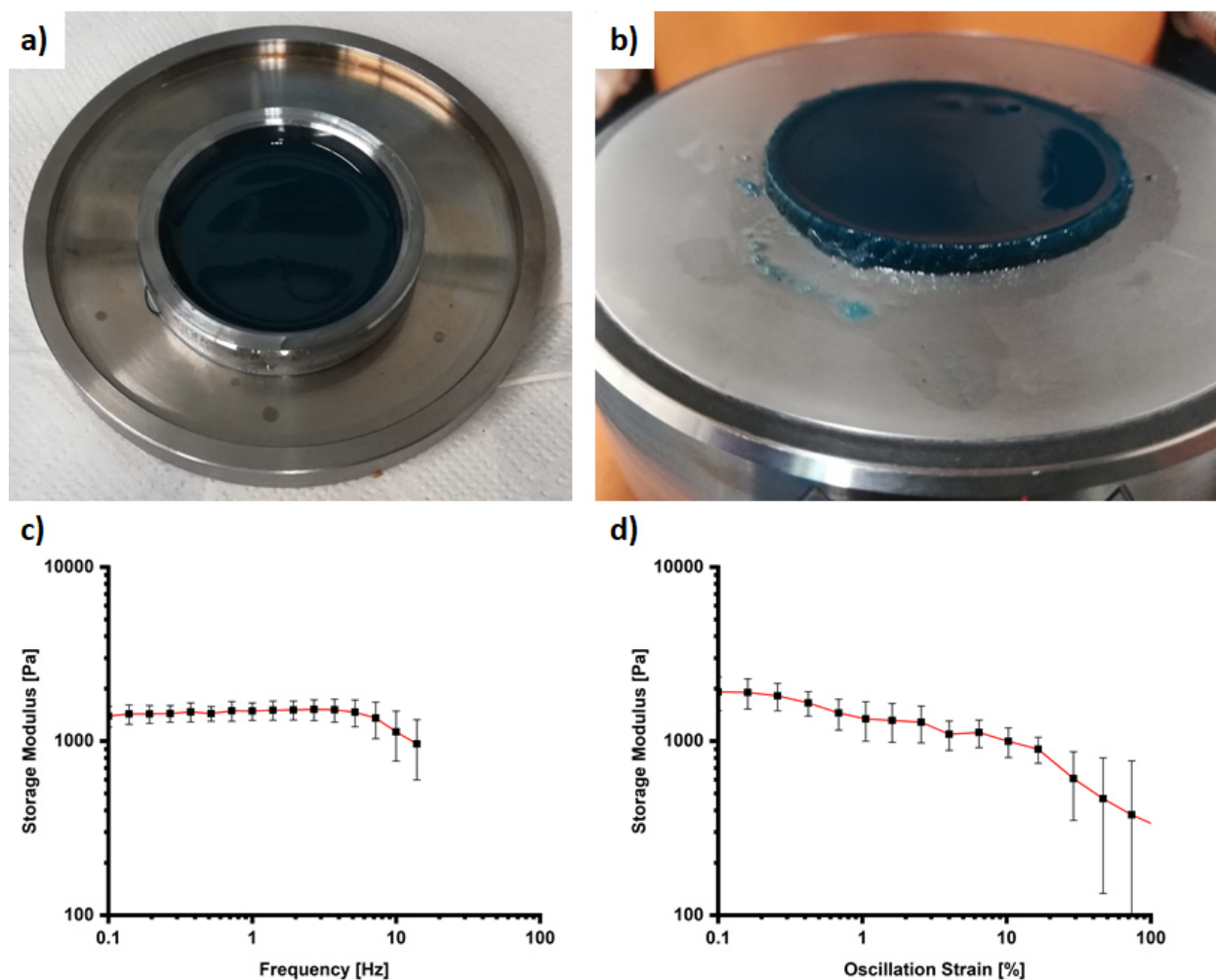


**Figure 8.** A Cr-L1 metallogel in a ring of stainless steel after 24 h at 100°C (a) and subsequent placing onto the rheometer plate (b). (c, d): Axial force controlled rheology measurements show the average storage modulus during a frequency (strain set at 0.3 %) and amplitude (frequency set at 0.5 Hz) sweep, respectively.

### Shaping.

The rheological behavior of the metallogels influenced also their shapeability. The metallogels can be casted into various forms, but without additional support only the Cr-L1 metallogel was able to maintain its shape outside of its reaction vessel (Figure 9). It was possible to cast Cr-L1 into complex shapes, which were stable as long as solvent evaporation was prevented.



**Figure 9.** The metallogels of Cr-L1, AlCr-L1 and Al-L1 in “wet” and dry states. Left: Cr-L1 (dark green), AlCr-L1 (light green) and Al-L1 (colorless) as poured directly from a cylindrical vessel. Shape retention for the mixed metal AlCr-L1 metallogel is poor, while the Al-L1 metallogel does not maintain its shape at all. Middle: Aerogel and xerogel pieces of Cr-L1, AlCr-L1 and Al-L1. Right: Cr-L1 cast into a shape with a total volume of 32 mL. Tin foil can be seen on top which was added to alleviate a suction problem when removing the metallogel from its cast.

### Dye uptake.

The stable metallogels of Cr-L1 and AlCr-L1 show potential applications in wastewater treatment. Dye uptake studies from aqueous solution have been carried out with fuchsine, a red cationic dye which is listed as an IARC Group 2B carcinogen (“possibly carcinogenic to humans”), calcein, a yellow and fluorescent neutral dye, and disulfine blue VN 150 (or Acid

Blue 1), a blue anionic dye.<sup>48</sup> The **Cr-L1** metallogel shows high uptakes for all three dyes. Upon reaching adsorption equilibrium, 1 mL of the **Cr-L1** metallogel is capable of completely removing fuchsine from 2 mL of a dye solution with a concentration of 100 mg L<sup>-1</sup>. Furthermore, the equilibrium for calcein sorption is reached within 24 h (Figure 10, 11). The **AlCr-L1** metallogel is also capable of taking up fuchsine and disulfine blue VN 150, although not as thoroughly as the **Cr-L1** metallogel (Figure 10). For calcein, the measurements with gels containing Al are unreliable, as the dye is known to form inter alia with Al<sup>3+</sup> soluble Al-calcein complexes which lead to quenching or shifts in the absorption spectrum.<sup>49</sup> Determinations of dye uptake were not possible with the **Al-L1** metallogel in general, as the gel breaks apart upon adding the dye solutions.

Dyes are frequently used in the biosciences for labelling reactions. Removing excess dye after a labeling reaction is often difficult and time-consuming but is essential for accurate determination of dye-to-protein ratios. We point to a kit sold by Thermo Scientific as “Pierce Dye Removal Columns” to effectively bind to unconjugated fluorescent dye molecules, such as calcein, from protein solutions to rapidly purify fluorescent conjugated antibodies and other proteins after labeling reactions. These fluorescent dye removal columns enable fast and efficient removal of non-reacted fluorescent dyes from protein labeling reactions.<sup>50</sup>

Further, the dyes are a model system to show selective uptake of large molecules with different charges. In general the removal of dyes from wastewater is of industrial interest, to mitigate the potential effects on the aquatic environment.<sup>51,52</sup> The only problematic among the three dyes tested here, which is to be removed from wastewater is the carcinogenic fuchsine.

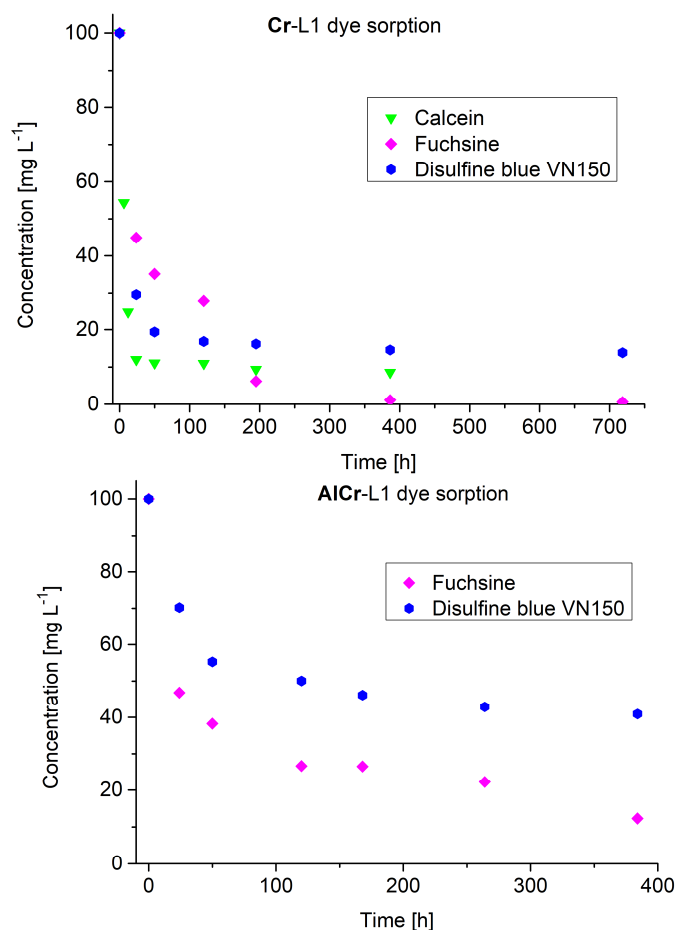


**Figure 10.** Sorption performance of 1 mL Cr-L1 and AICr-L1 metallogel for 2 mL of different dye solutions with a concentration of 100 mg L<sup>-1</sup> each.



**Figure 11.** Metallogels with dye solutions as prepared and used for UV experiments. The upturned vessels shows the retained gel state of the samples. Top: Dye uptake after 7 days.

Bottom: Dye uptake after one month. The fuchsine dye has been almost completely absorbed, while calcein and disulfine blue VN150 partially remain in solution.

The specific fuchsine uptake in the **Cr-L1** metallogel is greater than  $200 \text{ mg g}^{-1}$ , as the density of the metallogel approaches  $1 \text{ g cm}^{-3}$  and 1 mL of metallogel was capable of removing 0.2 mg fuchsine from 2 mL of water. The specific uptake capacity of the **AlCr-L1** metallogel is  $176 \text{ mg g}^{-1}$ . Comparison with materials in the literature suggest acceptable uptakes of basic fuchsine to the point that the metal-organic gel materials are outperforming the reported fuchsine sorbents in the literature (Table 1).

**Table 1.** Basic Fuchsine uptake of different materials in the literature.

Material	Uptake capacity [ $\text{mg g}^{-1}$ ]	Ref.
<b>Cr-L1</b> metallogel	>200	This work
<b>AlCr-L1</b> metallogel	176	This work
Calcined mussel shell	141.65	53
Epichlorohydrin crosslinked peanut husk	116.28	54
Mesoporous carbon C-KS	10.66	55
Ceramic microsphere gangue	24.16	56
Bottom ash	91.56	57
Deoiled Soya	134.81	57

We have also tested the leaching or metal ion release from the gels through atomic absorption spectroscopy. 2 mL of the **Cr-L1** and **AlCr-L1** gel were covered with 1 mL of water and left standing for five days. The accumulated amount of released Cr ions for the **Cr-L1** metallogel was  $0.47 \text{ mg L}^{-1}$ , while the accumulated amount of released Al and Cr ions for the **AlCr-L1** metallogel were below the detection limit ( $<0.01 \text{ mg L}^{-1}$ ).



## Surface area and pore constitution analysis of the aerogels and xerogel.

Aerogels are commonly associated with high accessible surface areas and the xerogels based on the same gel may sometimes retain the surface area while undergoing changes in pore constitution, as discussed in the introduction. To determine the surface area and porosity, gas adsorption isotherms of CO<sub>2</sub> at 195 and 273 K, Ar at 87 K and N<sub>2</sub> at 77 K have been measured (Figure 12, Figure S12-S14).

The Cr-L1 aerogel showed the highest BET surface area in the Ar physisorption experiments with a value of 609 m<sup>2</sup> g<sup>-1</sup>, followed by the Cr-L1 xerogel (604 m<sup>2</sup> g<sup>-1</sup>) and the aerogels of AlCr-L1 and Al-L1, (441 and 479 m<sup>2</sup> g<sup>-1</sup>, respectively) (Table 2). Both Ar and N<sub>2</sub> physisorption experiments reveal Type II isotherms with H3 hysteresis loops for the aerogels, which suggests that, in combination with the high surface areas, the materials are macroporous. This assumption is in line with the results from the SEM micrographs. The xerogel exhibits a Type IV isotherms with an H2b hysteresis loop, easily observed in both the N<sub>2</sub> and Ar physisorption isotherms, suggesting that the material is mainly mesoporous.

**Table 2.** Surface area and porosity analysis of aero- and xerogels from Ar, N<sub>2</sub> and CO<sub>2</sub> sorption data.

Compound	S <sub>BET</sub> , Ar at 87 K [m <sup>2</sup> g <sup>-1</sup> ] <sup>a</sup>	S <sub>BET</sub> , N <sub>2</sub> at 77 K [m <sup>2</sup> g <sup>-1</sup> ] <sup>b</sup>	V <sub>tot.</sub> (Ar) [cm <sup>3</sup> g <sup>-1</sup> ] <sup>c</sup>	V <sub>tot.</sub> (N <sub>2</sub> ) [cm <sup>3</sup> g <sup>-1</sup> ] <sup>d</sup>	V <sub>micro.</sub> (CO <sub>2</sub> ) [cm <sup>3</sup> g <sup>-1</sup> ] <sup>e</sup>
Cr-L1 Aerogel	609	860	1.90	1.58	0.049
Cr-L1 Xerogel	604	503	1.20	1.44	0.030
AlCr-L1 Aerogel	441	480	0.69	1.21	0.036
Al-L1 Aerogel	479	523	1.01	1.82	0.044

<sup>a</sup> Surface area was derived from the BET plot mostly in the  $p/p_0$  range 0.08-0.25. <sup>b</sup> Surface area was derived from the BET plot in the  $p/p_0$  range of mostly 0.10-0.20. <sup>c</sup> Total pore volume at  $p/p_0 = 0.95$  for pores  $\leq 20$  nm. <sup>d</sup> Total pore volume at  $p/p_0 = 0.95$  for pores  $\leq 20$  nm. <sup>e</sup> Pore

volume for pores with  $d \leq 1$  nm (10 Å) from the NLDFT calculations with a “CO<sub>2</sub> on carbon, slit pores” model at 273 K.

The different BET surface areas derived from Ar and N<sub>2</sub> sorption are due to the better micropore filling with the former. Argon as adsorptive at the boiling point temperature of liquid argon (87 K) fills micropores of dimensions 0.5–1 nm at higher relative pressures  $p/p_0$  of  $10^{-5}$  to  $10^{-3}$  compared to nitrogen at 77 K ( $p/p_0 = 10^{-7}$  to  $10^{-5}$ ), which leads to accelerated diffusion and equilibration processes for argon. Further, argon does not have a quadrupole moment, unlike N<sub>2</sub> (4.7 cm<sup>2</sup>). Due to its quadrupole moment, the orientation of an N<sub>2</sub> molecule depends on the chemical surface structure of the adsorbent, so that specific quadrupole interactions of N<sub>2</sub> to the adsorbent can falsify the measurement by about 20 %. In summary, the adsorptive argon is seen as less sensitive to artefact differences in the structure of the adsorbent surface than nitrogen and is now recommended as an alternative adsorptive for surface area determination.<sup>58</sup>

As a downside, kinetic restrictions do not allow Ar to be used for the determination of very narrow micropores.<sup>58</sup> CO<sub>2</sub> physisorption at 273 K offers the benefits of accelerated diffusion of the analysis gas, and therefore allows for determination of even the narrowest micropores with  $d \leq 1$  nm (10 Å). The transition from metallo- to xerogel is often accompanied by a collapse of the micropores in the resulting xerogel network.<sup>16</sup> Thus, it is remarkable that the micropores of the xerogel of Cr-L1 did not completely collapse by the capillary forces acting upon the material during the vacuum drying process. Still, the micropore volume is lower than in the aerogels, which were obtained under supercritical drying conditions suppressing the capillary forces to prevent pore collapse.

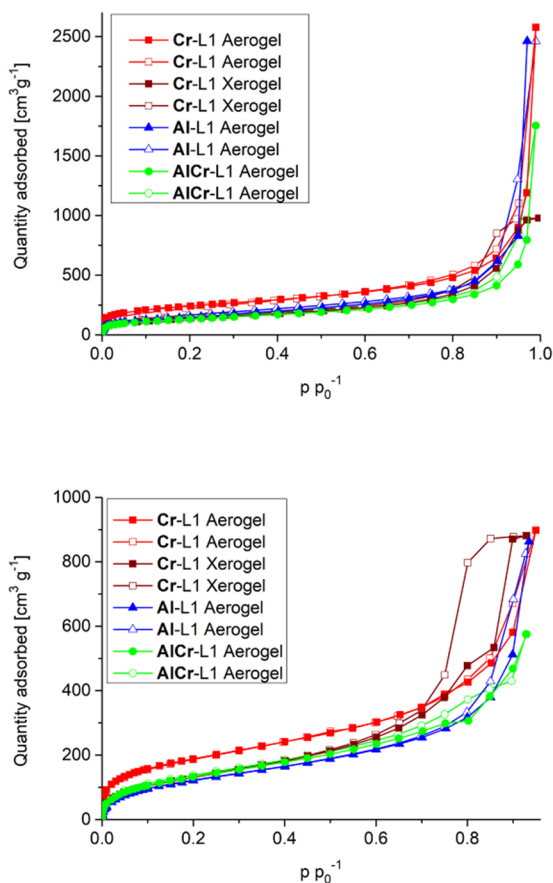


**Figure 12.** Adsorption (filled symbols) and desorption (empty symbols) for N<sub>2</sub> at 77 K (top) and Ar at 87 K (bottom) for the aerogels of compounds **Cr-L1** aerogel (red squares), **Cr-L1** xerogel (brown squares), **Al-L1** (blue triangles), **AlCr-L1** (green circles). Full range Ar isotherms can be found in the SI (Figure S14).

All aerogels show the expected wide pore size distribution, while the xerogel of **Cr-L1** shows a narrower pore size distribution (Figure 13). We note that the BET method based on Ar and N<sub>2</sub> adsorption addresses micropores (pores < 20 Å) and mesopores smaller than ~200 Å (at  $p/p_0 = 0.95$ ) out of the full mesopore range up to 500 Å. The similarity in porosity between the aerogels of **Cr-L1** and **Al-L1** is quite obvious, and their main difference is the lower total pore volume for the **Al-L1** aerogel (Table 2, Figure S16). The major contribution to the pore volume is found in the range above 140 Å of pore width for these two aerogels (Figure S16). As a result, the metal ion does not seem to influence the general pore constitution other than changing the

total volume. For the xerogel of Cr-L1, porosity was retained, as was already shown by the above physisorption experiments. The pore size distribution is different to the aerogels, with more than 80 % of the total pore volume in the relevant range stemming from pores in the range of 50 to 100 Å (Figure 13).

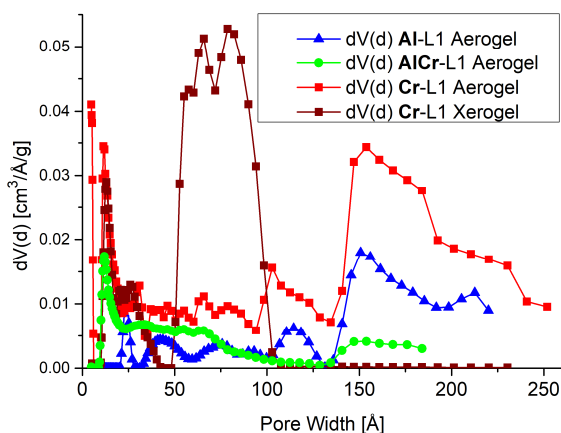


**Figure 13.** QSDFT pore size distribution curves of the aerogel materials and the xerogel, obtained from Ar physisorption at 87 K, which addresses pores sizes up to  $\sim 200$  Å. The pore widths of the aerogels are distributed over the whole range, while the xerogel does not exhibit pores wider than 100 Å in the accessible range.

It is evident that stable aerogels of Cr-L1, Al-L1 and AlCr-L1 and a xerogel of Cr-L1 could be obtained with permanent micro- and mesoporosity. Pore volumes for metal-organic aerogels containing Cr or Al extend over a wide range of  $0.067\text{--}4.5\text{ cm g}^{-1}$ . (Table S9).<sup>26,27,46,47,59</sup> The literature suggests that a majority of those aerogels exhibit pore volumes between  $1$  and  $2\text{ cm g}^{-1}$ , and thus the pore volumes of the Cr- and Al aerogels from this work compare well to the pore volumes of typical aero- and xerogels in the literature.

### Uptake of H<sub>2</sub>O vapor and gases CO<sub>2</sub> and SO<sub>2</sub>.

Cr- and Al-MOFs have been shown to be hydrothermally among the most stable MOFs.<sup>60,61</sup> Hence, the porous Cr- and Al-gels have been tested for their H<sub>2</sub>O uptake at 20 °C (Figure 14) and their CO<sub>2</sub> and SO<sub>2</sub> uptakes at different temperatures (Figure 15). The water sorption isotherms show no special behavior and pore condensation is visible at larger partial pressures. A large desorption hysteresis for all materials and the adsorptives H<sub>2</sub>O and SO<sub>2</sub> is indicative of their strong interactions with the network. The H<sub>2</sub>O desorption isotherm only closes at very low pressure. The SO<sub>2</sub> sorption isotherms exhibit pore condensation at all three measured temperatures. For SO<sub>2</sub> especially strong interactions are observed through the large hysteresis for materials containing Al, while the hystereses for the Cr materials are generally smaller. This behavior transfers to the CO<sub>2</sub> sorption isotherms. When comparing uptake performance, the **Al-L1** aerogel has the highest uptake of SO<sub>2</sub> and H<sub>2</sub>O (before onset of pore condensation) and the lowest uptake of CO<sub>2</sub>, suggesting that this material preferably forms strong bonds with highly polar gases. The presence of Cr in the networks of the other materials seemingly disturbs this preference, as the mixed-metal material **AlCr-L1** falls more in line with the **Cr-L1** aero- and xerogel in terms of uptake performance, although larger hystereses are still observed when Al is present.

For MOFs a variety of interactions with sulfur dioxide have been elucidated, which act together to enhance its adsorption. Modeling calculations, *in situ* powder X-ray diffraction, inelastic neutron scattering and infrared studies on SO<sub>2</sub> in MOFs have revealed interactions of sulfur dioxide by hydrogen bonding to hydroxyl groups, formation of hydrogen bonds between aromatic H atoms of the ligand and oxygen of sulfur dioxide (H<sup>δ+</sup>⋯O<sup>δ-</sup> interactions), interactions between open metal sites and oxygen of sulfur dioxide (M<sup>δ+</sup>⋯O<sup>δ-</sup> interactions) as well as interactions between sulfur and the carboxylate oxygen atoms of the ligand (S<sup>δ+</sup>⋯O<sup>δ-</sup> interactions).<sup>31,62,63,64,65</sup>

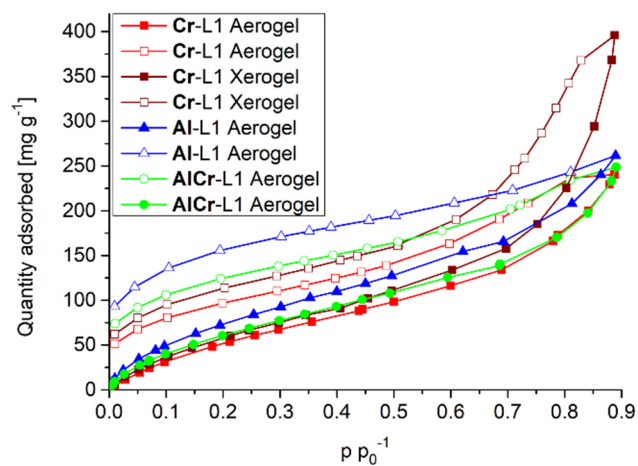


**Figure 14.** Water sorption isotherms of the xero- and aerogels. The isotherms show an onset of pore condensation effects at high  $p/p_0$  and a large hysteresis, the latter suggesting prominent interactions between  $H_2O$  and the framework.

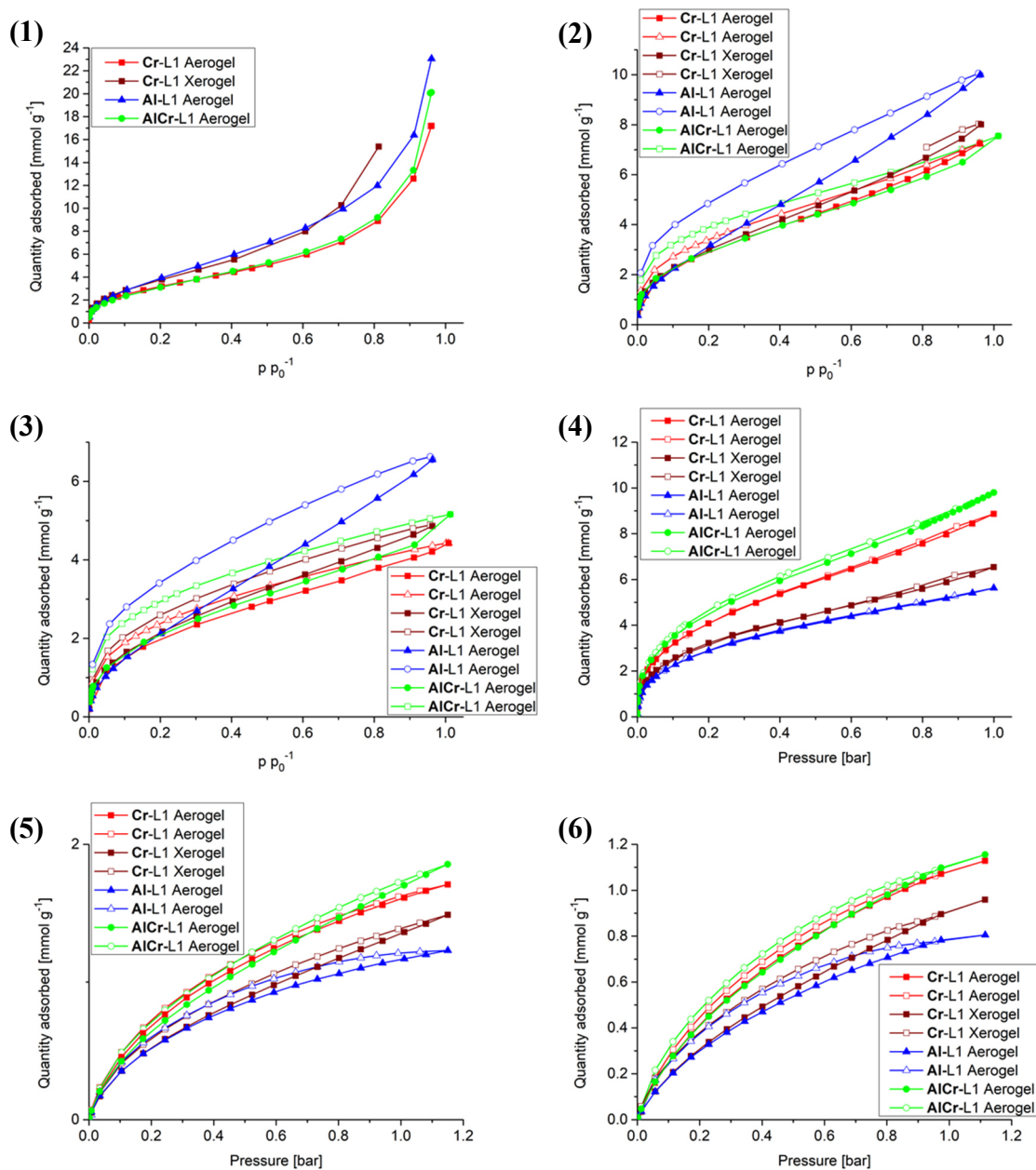


**Figure 15.** Adsorption (filled symbols) and desorption (empty symbols) isotherms for SO<sub>2</sub> and CO<sub>2</sub> on the synthesized materials at different temperatures. (1): SO<sub>2</sub> at 263 K, (2) SO<sub>2</sub> at 273 K, (3) SO<sub>2</sub> at 293 K, (4) CO<sub>2</sub> at 195 K, (5) CO<sub>2</sub> at 273 K, (6) CO<sub>2</sub> at 293 K.

### Uptake at elevated temperature and breakthrough curve simulations.

Existing applications for sorbent materials may not necessarily be at room temperature. In order to evaluate the materials for their uptake capacity at any temperature, the data obtained

from the dual-site Langmuir isotherm fits recorded at different temperatures can be linearized against the measurement temperature. This circumvents possible device limitations, as many sorption devices do not allow measurements at elevated temperatures. For CO<sub>2</sub> sorption, the data often already exists, as measurements performed at 195 K are used for surface area determination, at 273 K for micropore evaluation and at 293 K for maximum uptake capacity at NTP. For SO<sub>2</sub> sorption, the temperature selection becomes a bit troublesome. SO<sub>2</sub> readily liquefies at 263 K, which in returns means that isotherms recorded at 293 K are just 30K above the boiling point. These isotherms still show pore condensation effects at higher partial pressures, as it can be seen in Figure 15. In order to fit these isotherms to the dual-site Langmuir model, data obtained above 0.5 p p<sub>0</sub><sup>-1</sup> has been neglected.

As expected, the isotherm fits of CO<sub>2</sub> are in good accordance with each other, making it possible to calculate isotherms at various temperatures (see Figure S18, Table S12).

For the SO<sub>2</sub> isotherms, the quality of fit was rather low. Possible reasons are, as stated above, condensation effects, which affect the dual-site Langmuir fit, or a possible degradation of the material by condensing SO<sub>2</sub>. Only the materials containing Cr seem to have suffered from SO<sub>2</sub> exposure, as the quality of fit for the aerogel of Al-L1 stayed high throughout all measurements (Figure S19, Table S11). Table 3 contains the maximum uptake for CO<sub>2</sub> and SO<sub>2</sub> at 293 K as measured and 353 K as calculated and Table 4 shows a comparison to the maximum uptakes of some other aero- and xerogels, as well as MOFs.

**Table 3.** Maximum uptakes of CO<sub>2</sub> and SO<sub>2</sub> at 293 K and 353 K for the synthesized materials.

Compound	Max. uptake CO <sub>2</sub> at 293 K [cm <sup>3</sup> g <sup>-1</sup> , mmol g <sup>-1</sup> ], exp.	Max. uptake CO <sub>2</sub> at 353 K [cm <sup>3</sup> g <sup>-1</sup> , mmol g <sup>-1</sup> ], calc.	Max. uptake SO <sub>2</sub> at 293 K [cm <sup>3</sup> g <sup>-1</sup> , mmol g <sup>-1</sup> ], exp.	Max. uptake SO <sub>2</sub> at 353 K [cm <sup>3</sup> g <sup>-1</sup> , mmol g <sup>-1</sup> ], calc.
Cr-L1 Aerogel	24.0, 1.0	7.9, 0.3	116.8, 4.8	18.8, 0.8
Cr-L1 Xerogel	21.5, 1.0	6.3, 0.3	109.5, 4.5	15.7, 0.6



AlCr-L1 Aerogel	28.1, 1.2	7.3, 0.3	115.6, 4.7	27.0, 1.1
Al-L1 Aerogel	19.8, 0.8	6.1 ,0.3	146.8, 6.6	36.9, 1.5

**Table 4.** Comparison of SO<sub>2</sub> uptake of different materials.

Compound	SO <sub>2</sub> uptake [mmol g <sup>-1</sup> ]	SO <sub>2</sub> uptake [wt. %]	Pressure [bar]	Temperature [K]	Reference
Cr-L1 Aerogel	4.8	23.4	1	293	this work
Cr-L1 Xerogel	4.5	22.3	1	293	this work
AlCr-L1 Aerogel	4.7	23.2	1	293	this work
Al-L1 Aerogel	6.6	29.7	1	293	this work
NOTT-300 (MOF)	8.1	34.1	1	273	62
Mg-MOF-74	8.6	35.5	1.02	298	63
Ni(bdc)(ted) <sub>0.5</sub> (MOF)	9.97	39.0	1.13	298	63
Zn <sub>2</sub> (oxo-di-hbac) <sub>2</sub> (bipy)	10.9	41.2	1	293	66
Na-MnOx Xerogel	1	6.0	1		16
Na-MnOx Aerogel	0.6	3.7	1		16
SiN-rGO Aerogel	2.19	12.3	1	298	67

While the metal-organic framework aerogels synthesized in this work are unable to compete with the best metal-organic frameworks when it comes to maximum SO<sub>2</sub> uptake, e.g., 6.6 mmol g<sup>-1</sup> for the aerogel of Al-L1, compared to 10.9 mmol g<sup>-1</sup> for Zn<sub>2</sub>(oxo-di-hbac)<sub>2</sub>(bipy), the MOF aerogels perform better than any known silica or metal oxide aerogel, with uptakes of 2.19 mmol g<sup>-1</sup> for a silica aerogel and 1 mmol g<sup>-1</sup> for a metal oxide aerogel.

Breakthrough curves have been calculated using the software 3P sim version 1.1.07, employing the “ideal adsorbed solution theory“ (IAST) with data from fitted dual-site Langmuir isotherms.<sup>68</sup> The formula for the dual-site Langmuir isotherm is

$$m_{\text{eq}} = m_1 \frac{K_1 * P}{1 + K_1 * P} + m_2 \frac{K_2 * P}{1 + K_2 * P}$$

where  $m_{\text{eq}}$  is the loading at equilibrium,  $P$  the pressure,  $K_n$  the affinity constant and  $m_n$  the maximal loading. The additional parameters used in the dual-site Langmuir isotherms compared to the Langmuir model allow for a greater degree of heterogeneity of adsorption sites in the material.<sup>69</sup> The breakthrough curves were simulated at 20 °C under isothermal conditions. The percentage of CO<sub>2</sub> to SO<sub>2</sub> was taken from an article in which the exhaust gas composition of berthed marine vessels has been measured.<sup>70</sup> The results for CO<sub>2</sub> and SO<sub>2</sub> were given in g kWh<sup>-1</sup>, and the engine/fuel combination with the highest amount of SO<sub>2</sub> emission was chosen (9.6 g kWh<sup>-1</sup> SO<sub>2</sub>, 697 g kWh<sup>-1</sup> CO<sub>2</sub>, 5.57 vol. % CO<sub>2</sub>, SO<sub>2</sub>:CO<sub>2</sub> ratio: 0.0138). The simulation for the exhaust gas constitution therefore ran at the percentages of 5.57 % CO<sub>2</sub> and 0.076 % SO<sub>2</sub>. Water has been neglected as a possible exhaust component, as other literature suggests that humidity only increases SO<sub>2</sub> uptake performance, but the large affinity for the materials to water would result in incorrect simulations.<sup>16,71</sup> In recent literature, gas separation studies based on single-gas isotherms have been shown to be a convenient way to preselect an adsorbent materials for further evaluation, as they give a good indication of separation performance. For this interpretation, a prediction of mixture equilibrium data based on pure component isotherms is required. It has been shown that the quality of the simulations, which were performed with a similar software, approaches the experimental breakthrough studies, as long as the separation is based on thermodynamic effects and not on kinetic-steric effects.<sup>72</sup>

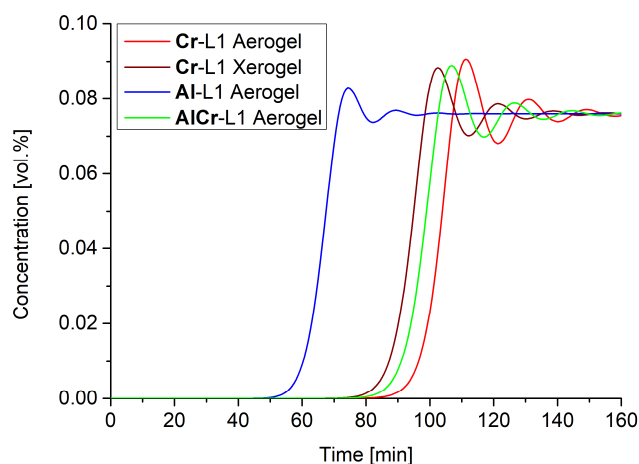


**Figure 16.** Simulated SO<sub>2</sub> breakthrough curves for the aero- and xerogels from a 1:73 v:v (0.076/5.57 vol. %) SO<sub>2</sub>/CO<sub>2</sub> gas mixture in an ideal inert gas. The CO<sub>2</sub> breakthrough curve is shown in Figure S20, SI. The retention time for **Al-L1** is severely lacking, despite its high total uptake.

The simulation suggests that SO<sub>2</sub> is retained reasonably well for all materials except for the aerogel of **Al-L1**, which can of course be expected when considering the low affinity constant for SO<sub>2</sub> (Figure 16). To elaborate on that, the high total uptake for the **Al-L1** aerogel is irrelevant for gas separation, as the uptake at low partial pressures is more decisive for the selectivity and therefore separation performance (Figure 17). Table 5 lists the retention times for SO<sub>2</sub> and CO<sub>2</sub>, as calculated by the software for the breakthrough simulations (cf. breakthrough curve simulation parameters and results in SI).

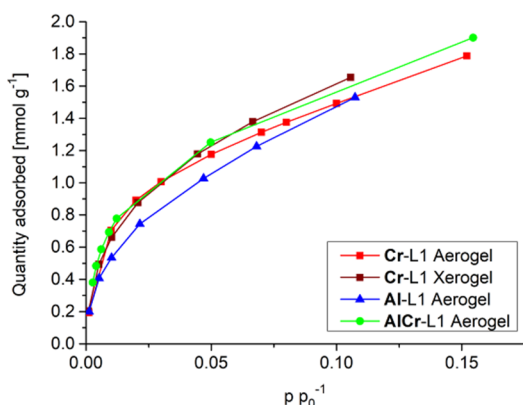


**Figure 17.** SO<sub>2</sub> isotherms at lower partial pressures. Despite the high maximum uptake of SO<sub>2</sub> on the aerogel of Al-L1, the uptake at lower partial pressures the least of the materials investigated here.

**Table 5.** Retention times of the synthesized materials for the breakthrough simulations.<sup>a</sup>

Compound	Retention time [min]	
	SO <sub>2</sub>	CO <sub>2</sub>
Cr-L1 Aerogel	102	2
Cr-L1 Xerogel	93	1
AlCr-L1 Aerogel	97	2
Al-L1 Aerogel	66	1

<sup>a</sup> For details of the simulation see breakthrough curve simulation parameters and results in SI.

## CONCLUSIONS

We were able to synthesize the new ligand N<sup>1</sup>,N<sup>4</sup>-(diterephthalic acid)terephthalamide, (H<sub>4</sub>L1) and have successfully implemented it into new materials based on gel chemistry. The material based on Cr and H<sub>4</sub>L1 exhibited excellent stability in its gel state and retained the shape even after conversion into its xero- and aerogel. Furthermore, in its metallogel state it could successfully be utilized to selectively adsorb a dye from solution, which served as a model

system for potential uptake of large molecules and pollutants from water. The Cr based xero- and aerogel, combined with two additional aerogels based on Al and a mixture of Al and Cr, retain their porosity during the drying process, with large accessible surface areas. By putting the materials through a variety of physisorption experiments, the data derived from those experiments could be used to simulate breakthrough curves as well as the maximum uptake at elevated temperatures. The results show that the xero- and aerogels are able to filter a harmful gas, SO<sub>2</sub>, from a gas mixture and that their maximum uptakes for this gas are the highest recorded for aerogels, rivalling uptakes of MOFs. In combination with their shapeability, these materials could be used as monolithic filter materials, unlike MOFs, which often have to be composited with a secondary material. The topic of metal-organic aerogels is often overlooked, although gels are sometimes an unwanted by-product of different synthesis strategies for new MOFs. This work demonstrates that there might be potential applications for gels based on metal-organic coordination chemistry. With supercritical drying becoming more prevalent in MOF workgroups as a way to dry porous materials without straining the framework, it should become more attractive to not discard metallogels, and instead convert them into their xero- and aerogels and determine their usefulness in selective sorption applications.

## EXPERIMENTAL SECTION

**Materials and methods.** The chemicals used were of analytical grade obtained from commercial sources and used without further purification (see Table S3 in the SI for possible suppliers).

FT-IR spectra were measured in ATR-mode (Platinum ATR-QL, Diamond) on a Bruker TENSOR 37 IR spectrometer in the range of 4000–600 cm<sup>-1</sup>.

CHNS analysis was performed on a Perkin Elmer CHN 2400.

Rheological characterization was performed with a DHR 3 Rheometer using a 40 mm plate geometry from TA Instruments to determine the mechanical properties. All measurements were

performed at a constant axial force of 0.2 N at 25 °C. A frequency sweep (0.1-100 Hz) was performed at a constant strain of 0.3 %, while an amplitude sweep was carried out at a constant frequency of 0.5 Hz and a strain of 0.1-100 %.

Thermogravimetric analysis (TGA) was performed on a Netzsch TG 209 F3 Tarsus in the range of 20 to 600 °C, equipped with Al-crucibles and applying a heat rate of 5 K min<sup>-1</sup> under nitrogen.

The powder X-ray diffraction patterns were obtained using a Bruker D2 Phaser powder diffractometer at 30 kV, 10 mA for Cu-K $\alpha$  radiation ( $\lambda = 1.51418 \text{ \AA}$ ).

Sorption measurements: All sorption isotherms were determined on monolithic pieces of the materials. CO<sub>2</sub> sorption isotherms were measured with a Micromeritics ASAP 2020 gas sorption analyzer. The heat of adsorption values and BET surface areas were calculated using the ASAP 2020 v3.05 software. N<sub>2</sub> sorption isotherms were measured with Quantachrome Nova 4000e at 77 K. N<sub>2</sub> BET surface areas were calculated from the nitrogen adsorption isotherms using the NovaWin 11.03 software. Ar and SO<sub>2</sub> sorption isotherms were measured on a Quantachrome Autosorb IQ MP. Each SO<sub>2</sub> sorption run had to be completed within 6.5 h. This time limit was specified by the company Quantachrome to prevent damage to the gaskets. After this time the system had to be regenerated by flushing with nitrogen. At the temperature of 263 K, the condensation point of SO<sub>2</sub> the sorption kinetics were so slow that only the adsorption isotherms could be completed in the given time limit. Ar BET surface area and DFT calculations were performed using the ASiQwin 4.01 software. The pore size distributions were obtained using QSDFT calculations with an “Ar on carbon, slit pores” model, with the exception of the AI-L1 aerogel, where an “Ar on carbon, cylindrical pores” model has been used and no satisfying calculations could be performed with any other model. QSDFT calculations assume a greater degree of heterogeneity between adsorption sites compared to more standard NLDFT calculations, where each adsorption site is assumed to be equal. Water sorption isotherms have been measured on a Quantachrome VSTAR and have been evaluated using the VStarWin 1.1.15

software. All gases for the sorption measurements were of ultrapure grades (99.999 %, 5.0), except for SO<sub>2</sub> (99.98 %, 3.8), and the NTP volumes are given according to the NIST standards (293.15 K, 101.325 kPa). Helium gas was used for the determination of the cold and warm free space of the sample tubes. All samples have been degassed at 150 °C for at least 3 hours prior to measurement. The fits of adsorption isotherms and the breakthrough curves have been calculated using the 3Psim 1.1.0.7 software by 3P Instruments GmbH & Co. KG.

Supercritical drying with CO<sub>2</sub> was performed on a Leica EM CPD300 using porous pots of pore sizes 120-200 µm. The solvent exchange has been performed at 10 °C for 99 cycles before heating to 50 °C and release of CO<sub>2</sub>.

Scanning electron microscopy images have been recorded with a Jeol JSM-6510LV QSEM advanced electron microscope equipped with a LaB<sub>6</sub> cathode. The microscope was equipped with a Bruker Xflash 410 silicon drift detector and Bruker ESPRIT software for energy-dispersive X-ray spectroscopic (EDX) analysis. The samples were prepared for SEM microscopy by coating them with gold using a Jeol JFC 1200 fine-coater.

<sup>1</sup>H NMR spectra were recorded with a Bruker Avance III 300 MHz and 600 MHz.

Flame atomic absorption spectroscopy was performed with PerkinElmer PinAAcle 900T and evaluated using the Syngistix Software AA Version 3.0.

*Synthesis of N<sup>1</sup>,N<sup>4</sup>-(diterephthalic acid)terephthalamide (H<sub>4</sub>Ditatam, H<sub>4</sub>L1).* In a 500 mL round bottom flask, a mixture of 2.5 g (13.8 mmol) 2-aminoterephthalic acid and 8 g (57.88 mmol) potassium carbonate in 200 mL water was vigorously stirred until the 2-aminoterephthalic acid had dissolved. 1.39 g (6.83 mmol) terephthaloyl chloride were added, a cap was loosely put on the flask and it was stirred in a dark place for 5 days. The resulting mixture was carefully poured into 300 mL 2M hydrochloric acid (being wary of foaming from excess potassium carbonate). The resulting suspension was filtered through a Büchner funnel and the funnel content was washed with water until the water ran off neutral. The resulting

yellow-ish residue was suspended in 300 mL dimethylformamide and, under stirring, heated to 140 °C for 5 minutes. After letting the mixture cool down, the white solid was centrifuged off and the DMF was decanted. The white solid was suspended in cold DMF and centrifuged off again. Afterwards, this step was repeated three times with acetone instead of DMF. *In vacuo* dried at 80 °C, 1.00 g (2.03 mmol, 30 %) were obtained. Elemental analysis calc.: C 58.54, H 3.28, N 5.69; found: C 57.99, H 3.50, N 5.66. <sup>1</sup>H NMR (300 MHz, DMSO-*d*<sub>6</sub>): δ = 13.41 (s, 2 -COOH), 12.19 (s, 2 -NHCO-), 9.23 (s, 2 =CH-), 8.16 (s, 4 =CH-), 8.15 (d, *J* = 8.4 Hz, 2 =CH-), 7.77 (dd, *J* = 1.70, 8.33, 2 =CH-).

Suitable single crystals placed in viscous oil were carefully selected under a polarizing microscope and mounted in air onto a nylon loop. Crystallographic data and refinement details for the structure of H<sub>4</sub>L1 are given in Table S1, SI. The structural data has been deposited with the Cambridge Crystallographic Data Center (CCDC No. 1889949).

*Synthesis of Cr-L1 (Cr-Ditatom).* 60.0 mg (0.121 mmol) of H<sub>4</sub>L1 and 97.5 mg (0.242 mmol) of Cr(NO<sub>3</sub>)<sub>3</sub>·9H<sub>2</sub>O (0.242 mmol) were added to a reaction vessel containing 5 mL dimethylformamide, sealed and placed in an ultrasonic bath at 80 °C until the ligand had dissolved. The reaction vessel was transferred to an isothermal oven preheated to 80 °C. After 24 h, the gel was removed from the oven and left to cool. Elemental analysis calc. for aerogel of Cr<sub>2</sub>-Ditatom·6H<sub>2</sub>O·1DMF: C 41.92, H 4.04, N 5.43; found: C 41.92, H 4.03, N 5.84. Karl Fischer titration calc. from EA: 16.2 % H<sub>2</sub>O, found 10.8 % H<sub>2</sub>O.

*Synthesis of Al-L1 (Al-Ditatom).* 10.0 mg (0.020 mmol) of H<sub>4</sub>L1 and 15.2 mg (0.041 mmol) Al(NO<sub>3</sub>)<sub>3</sub>·9H<sub>2</sub>O, were added to a reaction vessel containing 5 mL dimethylformamide, sealed and placed in an ultrasonic bath at 80 °C until the ligand had dissolved. The reaction vessel was transferred to an isothermal oven preheated to 100 °C. After 24 h, the gel was removed from the oven and left to cool. Elemental analysis calc. for the aerogel of Al<sub>2</sub>-Ditatom·7H<sub>2</sub>O·0.5DMF: C 43.45, H 4.22, N 4.57; found: C 43.28, H 4.13, N 4.66. Karl Fischer titration calc. from EA: 21.8 % H<sub>2</sub>O, found 16.1 %.



*Synthesis of **AlCr-L1** (AlCr-Ditatom).* 20.0 mg (0.041 mmol) of H<sub>4</sub>L1, 15.2 mg (0.041 mmol) Al(NO<sub>3</sub>)<sub>3</sub>·9 H<sub>2</sub>O and 16.25 (0.041 mmol) Cr(NO<sub>3</sub>)<sub>3</sub>·9 H<sub>2</sub>O were added to a reaction vessel containing 5 mL dimethylformamide, sealed and placed in an ultrasonic bath at 80 °C until the ligand had dissolved. The reaction vessel was transferred to an isothermal oven preheated to 100 °C. After 24 h, the gel was removed from the oven and left to cool. Elemental analysis calc. for the aerogel of AlCr-Ditatom·6.5H<sub>2</sub>O·0.5DMF: C 42.48, H 3.98, N 4.86; found: C 41.88, H 3.78, N 4.98. Karl Fischer titration calc. from EA: 19.4 % H<sub>2</sub>O, found 13.6 %.

*Synthesis of the **Cr-L1**, **AlCr-L1** and **Al-L1** aerogels.* Pieces of the synthesized aerogels were directly transferred to macroporous specimen capsules with pore sizes of 120-200 μm. The capsules were put into a solvent exchange apparatus (Figure S22), in which they were kept for 5 days while continuously running the solvent exchange. Afterwards, the capsules were removed from the apparatus and placed in a supercritical drying apparatus. After supercritical drying with CO<sub>2</sub>, the aerogels were removed from the capsules.

*Synthesis of the **Cr-L1** xerogel.* The samples were prepared like the aerogels (solvent exchange), but underwent conventional vacuum drying at elevated temperature (80 °C at 50 mbar) instead of supercritical drying.

*Synthesis of **In-L1** (In-Ditatom) and **Fe-L1** (Fe-Ditatom).* The synthesis of **In-L1** and **Fe-L1** was carried out analogous to the synthesis of **Al-L1**, using In(NO<sub>3</sub>)<sub>3</sub>·xH<sub>2</sub>O and Fe(NO<sub>3</sub>)<sub>3</sub>·9H<sub>2</sub>O instead as the metal salts. In(NO<sub>3</sub>)<sub>3</sub>·xH<sub>2</sub>O was not previously dried, as drying the salt resulted in lower gel stability, and x = 6 was assumed for the stoichiometric calculations, as it provided the best results for the metallogel.

*Synthesis of **Hg-L1** (Hg-Ditatom).* 10.0 mg (0.02 mmol) of H<sub>4</sub>L1 were suspended in 4 mL of DMF and heated to 80 °C in a sonification bath. 13.1 mg (0.041 mmol) of mercury acetate, Hg(CH<sub>3</sub>COO)<sub>2</sub>, were dissolved in 1 mL of DMF in a separate vessel and also heated to 80 °C. After one hour, the contents of both vessels were combined to instantly form the metallogel of **Hg-L1**.

*Synthesis of Co-L1 (Co-Ditatam).* 10.0 mg (0.02 mmol) of H<sub>4</sub>L1 were dissolved in 4 mL 25 % ammonia solution. 11.0 mg (0.041 mmol) of hexamminecobalt chloride, [Co(NH<sub>3</sub>)<sub>6</sub>]Cl<sub>3</sub>, were dissolved in 1 mL 25 % ammonia solution. The solutions were combined and the vessel was left open to let the ammonia evaporate. After ammonia evaporation, determined by olfactory analysis, the metallogel of Co-L1 had formed.

*Dye uptake experiments.* 1 mL of Cr-L1 metallogel was synthesized in a 5 mL vial, and 2 mL of aqueous dye solution with a concentration of 100 mg L<sup>-1</sup> were added to the vial. The vials were placed on a plate shaker at 250 rpm. The adsorption of the dyes was supposed to mainly happen at the interface between the gel and the dye solution, but in some cases the metallogel separated from the vial and therefore increased the solution-gel interface surface area. There was no measurable difference in equilibration time for those damaged gels.

## ASSOCIATED CONTENT

### **Supporting Information.**

The Supporting Information is available free of charge on the ACS Publications website at DOI: 10.1021/acsami.XXXXX

The following files are available free of charge.

Crystal data, reaction data, elemental and EDX analysis, IR spectra, SEM images, sorption data, Dual-Site Langmuir fitting data, breakthrough simulation parameters, H<sub>4</sub>L1 NMR spectrum, compound densities (PDF)

X-ray crystallographic data for compound H<sub>4</sub>L1 (CIF). The structural data has also been deposited with the Cambridge Crystallographic Data Center (CCDC No. 1889949).

## AUTHOR INFORMATION

## Corresponding Author

\*Tel.: +49 211 81 12286. Fax: +49 211 81 12287. E-mail: janiak@uni-duesseldorf.de

## ORCID

Christoph Janiak: 0000-0002-6288-9605

## Notes

The authors declare no competing financial interest.

## ACKNOWLEDGMENT

The research was funded in part by the German Science Foundation (DFG) through grant Ja466/29-1 and by the Federal German Ministry of Education and Research (BMBF) in the project Optimat under grant no. 03SF0492C.

## ABBREVIATIONS

BET = Brunauer-Emmett-Teller

DMF = Dimethylformamide

IAST = Idealized Adsorbed Solution Theory

MOAG = Metal-organic Aerogel

MOF = Metal-organic Framework

NLDFT = Non-linear Density Functional Theory

PXRD = Powder X-ray diffractometry

SEM-EDX = Scanning-Electron Microscopy – Energy-Dispersive X-ray Spectroscopy

QSDFT = Quenched Solid State Density Functional Theory

## REFERENCES

- (1) Bobbitt, N. S.; Mendonca, M. L.; Howarth, A. J.; Islamoglu, T.; Hupp, J. T.; Farha, O. K.; Snurr, R. Q. Metal–Organic Frameworks for the Removal of Toxic Industrial Chemicals and Chemical Warfare Agents. *Chem. Soc. Rev.* **2017**, *46*, 3357-3385.

(2) Maurin, G.; Serre, C.; Cooper, A.; Férey, G. The New Age of MOFs and of their Porous-Related Solids. *Chem. Soc. Rev.* **2017**, *46*, 3104–3107.

(3) Adil, K.; Belmabkhout, Y.; Pillai, R. S.; Cadiau, A.; Bhatt, P. M.; Assen, A. H.; Maurin, G.; Eddaoudi, M. Gas/Vapour Separation Using Ultra-Microporous Metal–Organic Frameworks: Insights into the Structure/Separation Relationship. *Chem. Soc. Rev.* **2017**, *46*, 3402–3430.

(4) Zhang, T.; Hu, Y. Q.; Han, T.; Zhai, Y. Q.; Zheng, Y. Z., Redox-Active Cobalt(II/III) Metal-Organic Framework for Selective Oxidation of Cyclohexene. *ACS Appl. Mater. Interfaces* **2018**, *10*, 15786-15792.

(5) Li, J. R.; Sculley, J.; Zhou, H. C., Metal-Organic Frameworks for Separations. *Chem. Rev.* **2012**, *112*, 869-932.

(6) Lei, B.; Wang, M.; Jiang, Z.; Qi, W.; Su, R.; He, Z., Constructing Redox-Responsive Metal-Organic Framework Nanocarriers for Anticancer Drug Delivery. *ACS Appl. Mater. Interfaces* **2018**, *10*, 16698-16706.

(7) Pankajakshan, A.; Sinha, M.; Ojha, A. A.; Mandal, S., Water-Stable Nanoscale Zirconium-Based Metal–Organic Frameworks for the Effective Removal of Glyphosate from Aqueous Media. *ACS Omega* **2018**, *3*, 7832-7839.

(8) Su, X.; Bromberg, L.; Martis, V.; Simeon, F.; Huq, A.; Hatton, T. A. Postsynthetic Functionalization of Mg-MOF-74 with Tetraethylenepentamine: Structural Characterization and Enhanced CO<sub>2</sub> Adsorption. *ACS Appl. Mater. Interfaces* **2017**, *9*, 11299–11306.

(9) Bonnefoy, J.; Legrand, A.; Quadrelli, E. A.; Canivet, J.; Farrusseng, D. Enantiopure Peptide-Functionalized Metal-Organic Frameworks. *J. Am. Chem. Soc.* **2015**, *137*, 9409-9416.

- (10) El-Kaderi, H. M.; Hunt, J. R.; Mendoza-Cortes, J. L.; Cote, A. P.; Taylor, R. E.; O'Keeffe, M.; Yaghi, O. M., Designed Synthesis of 3D Covalent Organic Frameworks. *Science* **2007**, *316*, 268-72.
- (11) Kitao, T.; Zhang, Y.; Kitagawa, S.; Wang, B.; Uemura, T. Hybridization of MOFs and Polymers. *Chem. Soc. Rev.* **2017**, *46*, 3108-3133.
- (12) Wickenheisser, M.; Herbst, A.; Tannert, R.; Milow, B.; Janiak, C. Hierarchical MOF-xerogel Monolith Composites from Embedding MIL-100(Fe,Cr) and MIL-101(Cr) in Resorcinol-Formaldehyde Xerogels for Water Adsorption Applications. *Micropor. Mesopor. Mater.* **2015**, *215*, 143-153.
- (13) Wickenheisser, M.; Paul, T.; Janiak, C. Prospects of Monolithic MIL-MOF@poly(NIPAM)HIPE Composites as Water Sorption Materials. *Micropor. Mesopor. Mater.* **2016**, *220*, 258-269.
- (14) Maldonado-Hódar, F. J.; Ferro-García, M. A.; Rivera-Utrilla, J.; Moreno-Castilla, C. Synthesis and Textural Characteristics of Organic Aerogels, Transition-Metal-Containing Organic Aerogels and their Carbonized Derivatives. *Carbon* **1999**, *37*, 1199-1205.
- (15) Hirst, A. R.; Escuder, B.; Miravet, J. F.; Smith, D. K. High-Tech Applications of Self-Assembling Supramolecular Nanostructured Gel-Phase Materials: From Regenerative Medicine to Electronic Devices. *Angew. Chem. Int. Ed.* **2008**, *47*, 8002-8018.
- (16) Long, J. W.; Wallace, J. M.; Peterson, G. W.; Huynh, K. Manganese Oxide Nanoarchitectures as Broad-Spectrum Sorbents for Toxic Gases. *ACS Appl. Mater. Interfaces* **2016**, *8*, 1184-1193.
- (17) Kistler, S. Coherent Expanded Aerogels and Jellies. *Nature* **1931**, *127*, 741.

- (18) Maleki, H.; Durães, L.; Portugal, A.; An Overview on Silica Aerogels Synthesis and Different Mechanical Reinforcing Strategies. *J. Non-Cryst. Solids* **2014**, *385*, 55-74.
- (19) Kumar, A.; Rana, A.; Sharma, G.; Sharma, S.; Naushad, M.; Mola, G. T.; Dhiman, P.; Stadler, F. J. Aerogels and Metal-Organic Frameworks for Environmental Remediation and Energy Production. *Environ. Chem. Lett.* **2018**.
- (20) Pierre, A. C.; Pajonk, G. M. Chemistry of Aerogels and their Applications. *Chem. Rev.* **2002**, *102*, 4243-4265.
- (21) Hüsing, N.; Schubert, U. Aerogels – Airy Materials: Chemistry, Structure, and Properties. *Angew. Chem. Int. Ed.* **1998**, *37*, 22-45.
- (22) Soleimani Dorcheh, A.; Abbasi, M. H. Silica Aerogel; Synthesis, Properties and Characterization. *J. Mater. Process. Technol.* **2008**, *199*, 10-26.
- (23) Lohe, M. R.; Rose, M.; Kaskel, S. Metal-Organic Framework (MOF) Aerogels with High Micro- and Macroporosity. *Chem. Commun.* **2009**, 6056-6058.
- (24) Tam, A. Y.; Yam, V. W., Recent Advances in Metallogels. *Chem. Soc. Rev.* **2013**, *42*, 1540-67.
- (25) Sutar, P.; Maji, T. K., Coordination Polymer Gels: Soft Metal-Organic Supramolecular Materials and Versatile Applications. *Chem. Commun. (Camb)*. **2016**, *52*, 8055-74.
- (26) Li, L.; Xiang, S.; Cao, S.; Zhang, J.; Ouyang, G.; Chen, L.; Su, C.-Y. A Synthetic Route to Ultralight Hierarchically Micro/Mesoporous Al(III)-Carboxylate Metal-Organic Aerogels. *Nat. Commun.* **2013**.

- (27) Xia, W.; Zhang, X.; Xu, L.; Wang, Y.; Lin, J.; Zou, R. Facile and Economical Synthesis of Metal-Organic Framework MIL-100(Al) Gels for High Efficiency Removal of Microcystin-LR. *RSC Adv.* **2013**, *3*, 11007-11013.
- (28) Saraji, M.; Shahvar, A. Metal-organic aerogel as a coating for solid-phase microextraction. *Anal. Chim. Acta* **2017**, *973*, 51-58.
- (29) Albo, J.; Vallejo, D.; Beobide, G.; Castillo, O.; Castaño, P.; Irabien, A. Copper-Based Metal-Organic Porous Materials for CO<sub>2</sub> Electrocatalytic Reduction to Alcohols. *ChemSusChem* **2017**, *10*, 1100-1109.
- (30) Han, X.; Yang, S.; Schröder, M. Porous metal-organic frameworks as emerging sorbents for clean air. *Nat. Rev. Chem.* **2019**, *3*, 108-118.
- (31) Zhang, Y.; Zhang, P.; Yu, W.; Zhang, J.; Huang, J.; Wang, J.; Xu, M.; Deng, Q.; Zeng, Z.; Deng, S. Highly Selective and Reversible Sulfur Dioxide Adsorption on a Microporous Metal-Organic Framework via Polar Sites. *ACS Appl. Mater. Interfaces* **2019**.
- (32) Lee, J.-Y.; Keener, T. C.; Yang, Y. J. J. Potential Flue Gas Impurities in Carbon Dioxide Streams Separated from Coal-Fired Power Plants. *Air Waste Manage. Assoc.* **2012**, *59*, 725–732.
- (33) Srivastava, R. K.; Jozewicz, W. J. Flue Gas Desulfurization: The State of the Art. *Air Waste Manage. Assoc.* **2011**, *51*, 1676–1688.
- (34) Rall, D. P. Review of the Health Effects of Sulfur Oxides. *Environ. Health Perspect.* **1974**, *8*, 97-121.
- (35) Gregory, K.; Webster, C.; Durk, S. Estimates of Damage to Forests in Europe due to Emissions of Acidifying Pollutants. *Energy Pollution* **1996**, *24*, 655-664.

(36) Likens, G. E.; Driscoll, C. T.; Buso, D. C. Long-Term Effects of Acid Rain: Response and Recovery of a Forest Ecosystem. *Science* **1996**, *272*, 244-246.

(37) Nakamoto, K. Infrared and Raman Spectra of Inorganic and Coordination Compounds, 3rd ed., **1978**, Wiley-Interscience, New York.

(38) Deacon, G. B.; Phillips, R. J. Relationships Between the Carbon-Oxygen Stretching Frequencies of Carboxylato Complexes and the Type of Carboxylate Coordination. *Coord. Chem. Rev.* **1980**, *33*, 227-250.

(39) Dastidar, P.; Ganguly, S.; Sarkar, K. Metallogels from Coordination Complexes, Organometallic, and Coordination Polymers. *Chem. Asian. J.* **2016**, *11*, 2484-98.

(40) Piepenbrock, M. O.; Lloyd, G. O.; Clarke, N.; Steed, J. W. Metal- and anion-binding supramolecular gels. *Chem. Rev.* **2010**, *110*, 1960-2004.

(41) Vallejo-Sánchez, D.; Amo-Ochoa, P.; Beobide, G.; Castillo, O.; Fröba, M.; Hoffmann, F.; Luque, A.; Ocón, P.; Pérez-Yáñez, S. Chemically Resistant, Shapeable, and Conducting Metal-Organic Gels and Aerogels Built from Dithiooxamidato Ligand. *Adv. Funct. Mater.* **2017**, *27*, 1605448.

(42) Serre, C.; Millange, F.; Thouvenot, C.; Noguès, M.; Marsolier, G.; Louër, D.; Férey, G. Very Large Breathing Effect in the First Nanoporous Chromium(III)-Based Solids: MIL-53 or  $\text{CrIII}(\text{OH}) \cdot \{\text{O}_2\text{C}-\text{C}_6\text{H}_4-\text{CO}_2\} \cdot \{\text{HO}_2\text{C}-\text{C}_6\text{H}_4-\text{CO}_2\text{H}\}_x \cdot \text{H}_2\text{O}_y$ . *J. Am. Chem. Soc.* **2002**, *124* (45), 13519-13526.

(43) Loiseau, T.; Serre, C.; Huguenard, C.; Fink, G.; Taulelle, F.; Henry, M.; Bataille, T.; Férey, G. A Rationale for the Large Breathing of the Porous Aluminum Terephthalate (MIL-53) Upon Hydration. *Chemistry* **2004**, *10*, 1373-82.



(44) Reinsch, H.; van der Veen, M. A.; Gil, B.; Marszalek, B.; Verbiest, T.; de Vos, D.; Stock, N. Structures, Sorption Characteristics, and Nonlinear Optical Properties of a New Series of Highly Stable Aluminum MOFs. *Chem. Mater.* **2012**, *25*, 17-26.

(45) Alvarez, E.; Guillou, N.; Martineau, C.; Bueken, B.; Van de Voorde, B.; Le Guillouzer, C.; Fabry, P.; Nouar, F.; Taulelle, F.; de Vos, D.; Chang, J. S.; Cho, K. H.; Ramsahye, N.; Devic, T.; Daturi, M.; Maurin, G.; Serre, C. The Structure of the Aluminum Fumarate Metal-Organic Framework A520. *Angew. Chem. Int. Ed. Engl.* **2015**, *54*, 3664-3668.

(46) Zhao, X.; Yuan, L.; Zhang, Z. Q.; Wang, Y. S.; Yu, Q.; Li, J. Synthetic Methodology for the Fabrication of Porous Porphyrin Materials with Metal-Organic-Polymer Aerogels. *Inorg. Chem.* **2016**, *55*, 5287-96.

(47) Xiang, S.; Li, L.; Zhang, J.; Tan, X.; Cui, H.; Shi, J.; Hu, Y.; Chen, L.; Su, C.-Y.; James, S. L. Porous Organic–Inorganic Hybrid Aerogels Based on Cr<sup>3+</sup>/Fe<sup>3+</sup> and Rigid Bridging Carboxylates. *J. Mater. Chem.* **2012**, *22*, 1862-1867.

(48) International Agency for Research on Cancer. IARC Monographs on the Evaluation of Carcinogenic Risks to Humans. List of Classifications, Volumes 1-123. <https://monographs.iarc.fr/list-of-classifications-volumes/>

(49) Furry, J. W. Preparation, properties and applications of Calcein in a highly pure form. *Retrospective Theses and Dissertations*, **1985**, 12062.

(50) <https://www.thermofisher.com/order/catalog/product/22858>

(51) Brown, D. Effects of colorants in the aquatic environment. *Ecotoxicol. Environ. Saf.* **1987**, *13*, 139-147.

(52) Farré, M. I.; Pérez, S.; Kantiani, L.; Barceló, D. Fate and toxicity of emerging pollutants, their metabolites and transformation products in the aquatic environment. *Trends Anal. Chem.* **2008**, *27*, 991-1007.

(53) El Haddad, M. Removal of Basic Fuchsin Dye from Water Using Mussel Shell Biomass Waste as an Adsorbent: Equilibrium, Kinetics, and Thermodynamics. *J. Taibah Univ. Sci.* **2018**, *10*, 664-674.

(54) Song, Y. H.; Chen, S. M.; Ren, J. M.; Gao, Y.; Xu, H. Fuchsine Adsorption from Aqueous Solution by Epichlorohydrin Crosslinked Peanut Husk. *Adv. Mater. Res.* **2012**, *549*, 362-365.

(55) Jedynak, K.; Repelewicz, M. Adsorption of Acid Red 114 and Basic Fuchsin from Aqueous Solutions on Mesoporous Carbon Materials. *Environ. Prot. Eng.* **2016**, *19*, 227-239.

(56) Yan, S.; Pan, Y.; Wang, L.; Liu, J.; Zhang, Z.; Huo, W.; Yang, J.; Huang, Y. Synthesis of Low-Cost Porous Ceramic Microspheres from Waste Gangue for Dye Adsorption. *J. Adv. Ceram.* **2017**, *7*, 30-40.

(57) Gupta, V. K.; Mittal, A.; Gajbe, V.; Mittal, J. Adsorption of Basic Fuchsin Using Waste Materials--Bottom Ash and Deoiled Soya--as Adsorbents. *J. Colloid Interface Sci.* **2008**, *319*, 30-9.

(58) Thommes, M.; Kaneko, K.; Neimark, A. V.; Olivier, J. P.; Rodriguez-Reinoso, F.; Rouquerol, J.; Sing, K. S. W. Physisorption of Gases, with Special Reference to the Evaluation of Surface Area and Pore Size Distribution (IUPAC Technical Report). *Pure and Applied Chemistry* **2015**, *87*, 1051-1069.

(59) Yang, Q.; Tan, X.; Wang, S.; Zhang, J.; Chen, L.; Zhang, J.-P.; Su, C.-Y. Porous Organic–Inorganic Hybrid Aerogels Based on Bridging Acetylacetonate. *Micropor. Mesopor. Mater.* **2014**, *187*, 108-113.

(60) Low, J. J.; Benin, A. I.; Jakubczak, P.; Abrahamian, J. F.; Faheem, S. A.; Willis, R. R. Virtual High Throughput Screening Confirmed Experimentally: Porous Coordination Polymer Hydration. *J. Am. Chem. Soc.* **2009**, *131*, 15834-42.

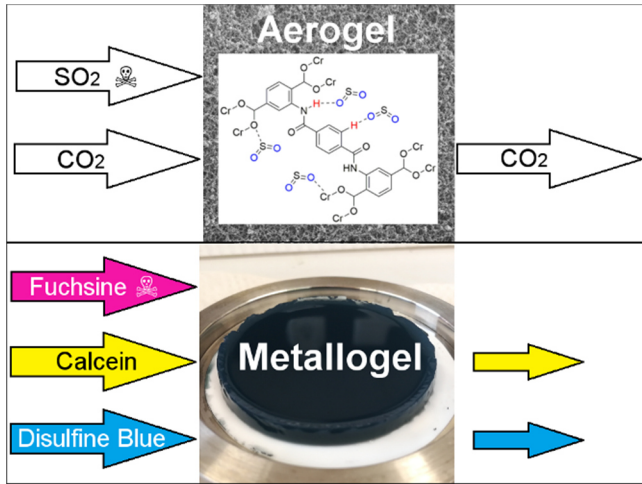
(61) Leus, K.; Bogaerts, T.; De Decker, J.; Depauw, H.; Hendrickx, K.; Vrielinck, H.; Van Speybroeck, V.; Van Der Voort, P. Systematic Study of the Chemical and Hydrothermal Stability of Selected “Stable” Metal Organic Frameworks. *Micropor. Mesopor. Mater.* **2016**, *226*, 110-116.

(62) Yang, S.; Sun, J.; Ramirez-Cuesta, A. J.; Callear, S. K.; David, W. I. F.; Anderson, D. P.; Newby, R.; Blake, A. J.; Parker, J. E.; Tang, C. C.; Schröder, M. Selectivity and Direct Visualization of Carbon Dioxide and Sulfur Dioxide in a Decorated Porous Host. *Nat. Chem.* **2012**, *4*, 887-894.

(63) Tan, K.; Canepa, P.; Gong, Q.; Liu, J.; Johnson, D. H.; Dyevoich, A.; Thallapally, P. K.; Thonhauser, T.; Li, J.; Chabal, Y. J. Mechanism of Preferential Adsorption of SO<sub>2</sub> into Two Microporous Paddle Wheel Frameworks M(bdc)(ted)<sub>0.5</sub>. *Chem. Mater.* **2013**, *25*, 4653-4662.

(64) Li, L.; da Silva, I.; Kolokolov, D. I.; Han, X.; Li, J.; Smith, G.; Cheng, Y.; Daemen, L. L.; Morris, C. G.; Godfrey, H. G. W.; Jacques, N. M.; Zhang, X.; Manuel, P.; Frogley, M. D.; Murray, C. A.; Ramirez-Cuesta, A. J.; Cinque, G.; Tang, C. C.; Stepanov, A. G.; Yang, S.; Schroder, M. Post-Synthetic Modulation of the Charge Distribution in a Metal-Organic Framework for Optimal Binding of Carbon Dioxide and Sulfur Dioxide. *Chem. Sci.* **2019**, *10*, 1472-1482.

- (65) Tan, K.; Zuluaga, S.; Wang, H.; Canepa, P.; Soliman, K.; Cure, J.; Li, J.; Thonhauser, T.; Chabal, Y. J. Interaction of Acid Gases SO<sub>2</sub> and NO<sub>2</sub> with Coordinatively Unsaturated Metal Organic Frameworks: M-MOF-74 (M = Zn, Mg, Ni, Co). *Chem. Mater.* **2017**, *29*, 4227-4235.
- (66) Glomb, S.; Woschko, D.; Makhloufi, G.; Janiak, C. Metal-Organic Frameworks with Internal Urea-Functionalized Dicarboxylate Linkers for SO<sub>2</sub> and NH<sub>3</sub> Adsorption. *ACS Appl. Mater. Interfaces* **2017**, *9*, 37419-37434.
- (67) Yun, S.; Kim, H.; Lee, H.; Park, H. S. Three-Dimensionally Macroporous, Si and N-Incorporated Graphene Aerogels for Gas Adsorbents. *Mater. Express*, **2015**, *5*, 463-469.
- (68) Myers, A.L.; Prausnitz, J. M. Thermodynamics of Mixed-Gas Adsorption. *AIChE* **1965**, *11*, 121-127.
- (69) Mathias, P. M.; Kumar, R.; Moyer Jr., J. D.; Schork, J. M.; Srinivasan, S. R.; Auvil, S. R.; Talu, O. Correlation of Multicomponent Gas Adsorption by the Dual-Site Langmuir Model. Application to Nitrogen/Oxygen Adsorption on 5A-Zeolite. *Ind. Eng. Chem. Res.* **1996**, *35*, 2477-2483.
- (70) Cooper, D. Exhaust Emissions From Ships at Berth. *Atmospheric Environment* **2003**, *37*, 3817-3830.
- (71) Peterson, W. P.; Karwacki, C. J.; Feaver, W. B.; Rossin, J. A. Zirconium Hydroxide as a Reactive Substrate for the Removal of Sulfur Dioxide. *Ind. Eng. Chem. Res.* **2009**, *48*, 1694-1698.
- (72) Möller, A.; Eschrich, R.; Reichenbach, C.; Guderian, J.; Lange, M.; Möllmer, J. Dynamic and Equilibrium-Based Investigations of CO<sub>2</sub>-Removal from CH<sub>4</sub>-Rich Gas Mixtures on Microporous Adsorbents. *Adsorption* **2016**, *23*, 197-209.



## Supporting Information

### Metal-Organic Framework Gels Based on a Bisamide Tetracarboxyl Ligand for Carbon Dioxide, Sulfur Dioxide and Selective Dye Uptake

Dennis Dietrich,<sup>†</sup> Christopher Licht,<sup>‡</sup> Alexander Nuhnen,<sup>†</sup> Simon-Patrick Höfert,<sup>†</sup> Laura De Laporte,<sup>‡</sup> Christoph Janiak.<sup>†\*</sup>

<sup>†</sup> Institut für Anorganische Chemie und Strukturchemie, Heinrich-Heine-Universität Düsseldorf, Universitätsstraße 1, 40225 Düsseldorf.

<sup>‡</sup> DWI – Leibniz Institute for Interactive Materials, Forckenbeckstraße 50, 52056 Aachen.

\* Corresponding author:

C. Janiak Tel.: +49 211 81 12286; fax: +49 211 81 12287. E-mail address: [janiak@hhu.de](mailto:janiak@hhu.de)

**E-mail addresses:** [dennis.dietrich@hhu.de](mailto:dennis.dietrich@hhu.de), [licht@dwirwth-aachen.de](mailto:licht@dwirwth-aachen.de),  
[alexander.nuhnen@uni-duesseldorf.de](mailto:alexander.nuhnen@uni-duesseldorf.de), [simon-patrick.hoefert@uni-duesseldorf.de](mailto:simon-patrick.hoefert@uni-duesseldorf.de),  
[delaporte@dwirwth-aachen.de](mailto:delaporte@dwirwth-aachen.de), [janiak@hhu.de](mailto:janiak@hhu.de)

#### Content

<b>Crystallographic Data</b>	<b>75</b>
<b>Gel synthesis data summary</b>	<b>77</b>
<b>Metallogel images</b>	<b>79</b>
<b>Elemental and EDX analysis results of the metal-organic framework aerogels and xerogels</b>	<b>81</b>
<b>IR spectra of the metal-organic framework aerogels and xerogels</b>	<b>87</b>
<b>Scanning electron microscopy (SEM) images of the metal-organic framework aerogels and xerogels</b>	<b>88</b>
<b>Dye sorption data</b>	<b>93</b>
<b>Nitrogen and argon physisorption data</b>	<b>94</b>
<b>CO<sub>2</sub>, SO<sub>2</sub> and H<sub>2</sub>O physisorption data</b>	<b>100</b>
<b>Dual-Site Langmuir fitting data</b>	<b>102</b>
<b>Breakthrough curve simulation parameters and results</b>	<b>104</b>
<b>NMR spectrum of H4L1</b>	<b>106</b>
<b>Solvent exchange apparatus</b>	<b>107</b>
<b>Aerogel densities</b>	<b>107</b>

## Crystallographic Data

**Table S1.** Crystallographic data and refinement details for N<sup>1</sup>,N<sup>4</sup>-(diterephthalic acid)terephthalamide, H<sub>4</sub>L1.

### Crystal data

C <sub>24</sub> H <sub>16</sub> N <sub>2</sub> O <sub>10</sub> ·4(C <sub>3</sub> H <sub>7</sub> NO)	Z = 1
M <sub>r</sub> = 784.77	F(000) = 414
Triclinic, P <sup>-</sup> 1	D <sub>x</sub> = 1.354 Mg m <sup>-3</sup>
a = 6.3468 (4) Å	Mo Kα radiation, λ = 0.71073 Å
b = 12.4679 (8) Å	Cell parameters from 9926 reflections
c = 13.0046 (9) Å	θ = 3.2–27.6°
α = 70.524 (3)°	μ = 0.11 mm <sup>-1</sup>
β = 85.858 (3)°	T = 110 K
γ = 82.850 (3)°	Needle, clear colorless
V = 962.12 (11) Å <sup>3</sup>	0.13 × 0.08 × 0.05 mm

### Data collection

Bruker Kappa APEX-II CCD area detector diffractometer	3835 independent reflections
Radiation source: microfocus sealed tube	3537 reflections with I > 2σ(I)
Multilayer mirror monochromator	R <sub>int</sub> = 0.021
ω scans, φ scans	θ <sub>max</sub> = 26.2°, θ <sub>min</sub> = 1.7°
Absorption correction: multi-scan (SADABS; Sheldrick, 1996)	h = -7→7
T <sub>min</sub> = 0.945, T <sub>max</sub> = 1.000	k = -15→15
24165 measured reflections	l = -16→16

### Refinement

Refinement on F <sup>2</sup>	Primary atom site location: structure-invariant direct methods
Least-squares matrix: full	Secondary atom site location: difference Fourier map
R[F <sup>2</sup> > 2σ(F <sup>2</sup> )] = 0.036	Hydrogen site location: mixed
wR(F <sup>2</sup> ) = 0.100	H atoms treated by a mixture of independent and constrained refinement
S = 1.03	w = 1/[σ <sup>2</sup> (F <sub>o</sub> <sup>2</sup> ) + (0.0509P) <sup>2</sup> + 0.4028P] where P = (F <sub>o</sub> <sup>2</sup> + 2F <sub>c</sub> <sup>2</sup> )/3
3835 reflections	(Δ/σ) <sub>max</sub> < 0.001
285 parameters	Δ <sub>max</sub> = 0.37 e Å <sup>-3</sup>
4 restraints	Δ <sub>min</sub> = -0.28 e Å <sup>-3</sup>

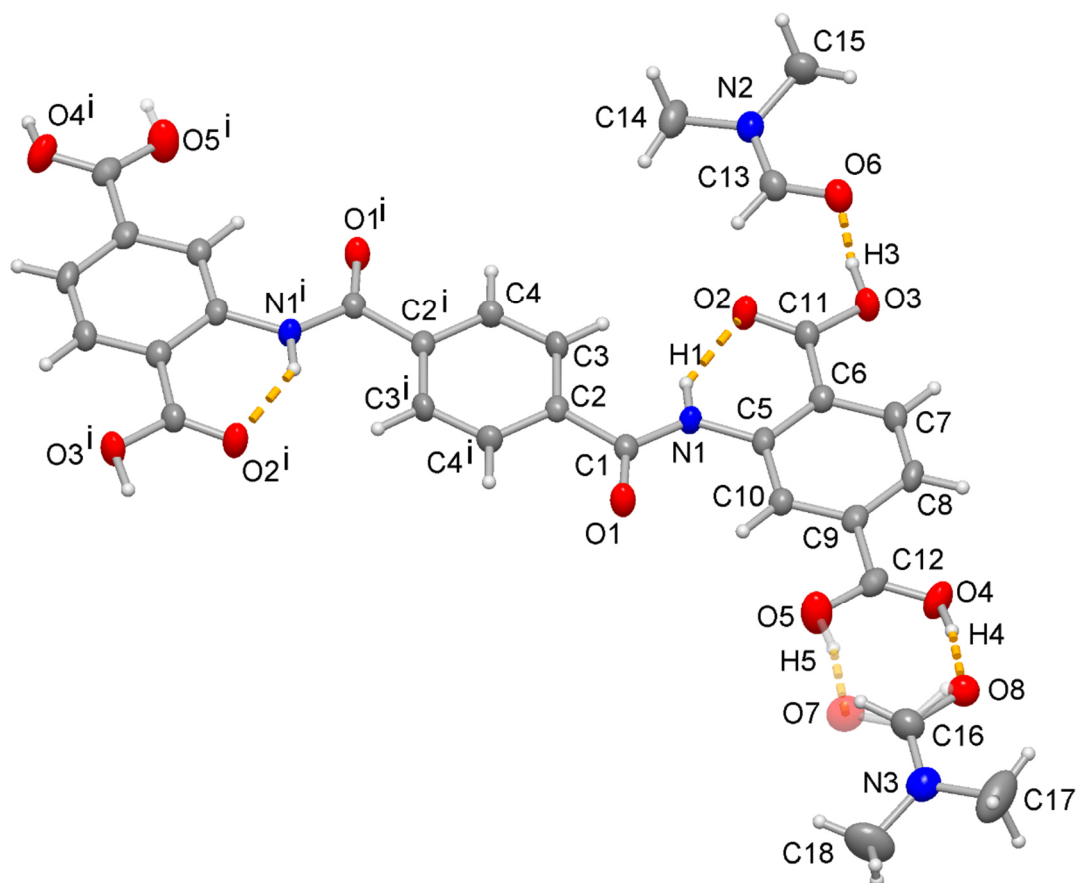


**Figure S1.** Molecular structure of H<sub>4</sub>L1·4DMF with atom numbering and two of the four hydrogen-bonded DMF molecules; hydrogen bonds as dashed orange lines (70% thermal ellipsoids, H atoms with arbitrary radii). The minor components (O7, about 40% occupation) one fully resolved disordered DMF molecule and concomitant carboxyl hydrogen atom H5 on H<sub>4</sub>L1 are shown semi-transparent. Symmetry transformation  $i = -x+1, -y+1, -z$ . The structural data has been deposited with the Cambridge Crystallographic Data Center (CCDC No. 1889949).

**Table S2.** Hydrogen-bond geometry (Å, °) for H<sub>4</sub>L1·4DMF

$D-H\cdots A$	$D-H$	$H\cdots A$	$D\cdots A$	$D-H\cdots A$
O3—H3 $\cdots$ O6	0.959 (18)	1.592 (18)	2.5451 (12)	172 (2)
O4—H4 $\cdots$ O8	1.00 (11)	1.60 (11)	2.595 (5)	171 (9)
O5—H5 $\cdots$ O7	0.91 (3)	1.64 (3)	2.5425 (15)	169 (2)
N1—H1 $\cdots$ O2	0.858 (16)	1.920 (16)	2.6459 (13)	142 (2)

**Gel synthesis data summary**



**Table S3.** Possible commercial sources of the used chemicals for the synthesis of the metal-organic gels.

Terephthaloyl chloride	Sigma-Aldrich	1 kg	87.20 €
2-Aminoterephthalic acid	Alfa Aesar	100 g	149.00 €
Potassium carbonate	Fischer Scientific	25 kg	436.28 \$
Chromium(III) nitrate nonahydrate	Acros Organics	5 kg	772.29 \$
Aluminum(III) nitrate nonahydrate	Fischer Chemical	10 kg	1582 \$
N,N'-Dimethylformamide	Fischer Scientific	25 L	660.53 \$
Acetone	Fischer Scientific	200 L	2063.00 \$

**Table S4.** Reaction data for the synthesized metallo-, aero- and xerogels. The aero- and xerogels are formed from the metallogels by removal of the solvent, otherwise they are equal in concentration, reaction time and temperature and therefore not listed as unique compounds.

Compound name	Amount of L1 [mmol]	Metal salt	Amount of metal salt [mmol]	Solvent	Amount of solvent [ml]	Reaction temp. [°C]	Time [h]
Cr-L1	0.121	Cr(NO <sub>3</sub> ) <sub>3</sub> • 9 H <sub>2</sub> O	0.242	DMF	5	100	48
AlCr-L1	0.041	Al(NO <sub>3</sub> ) <sub>3</sub> • 9 H <sub>2</sub> O; Cr(NO <sub>3</sub> ) <sub>3</sub> • 9 H <sub>2</sub> O	0.041; 0.041	DMF	5	100	48
Al-L1	0.020	Al(NO <sub>3</sub> ) <sub>3</sub> • 9 H <sub>2</sub> O	0.041	DMF	5	100	48
Fe-L1	0.020	Fe(NO <sub>3</sub> ) <sub>3</sub> • 9 H <sub>2</sub> O	0.041	DMF	5	100	24
In-L1	0.020	In(NO <sub>3</sub> ) <sub>3</sub>	0.041	DMF	5	100	24
Co-L1	0.020	(NH <sub>3</sub> ) <sub>6</sub> CoCl <sub>3</sub>	0.041	NH <sub>3</sub> 25%	5	RT	instant
Hg-L1	0.020	Hg(CH <sub>3</sub> COO) <sub>2</sub>	0.041	DMF	5	80	instant

## Metallogel images



**Figure S2.** Metallogels of **Fe-L1**, **Hg-L1** and **Cr-L1** in an upturned state. The irregularity of the iron and mercury gels can be seen by their slight separation at the capped end of the tube. The chromium metallogel is semi-transparent, very homogenous and stable.



**Figure S3.** Original image for the metallogels. From left to right: Half ligand/metal salt concentration of **Cr-L1**, **Cr-L1**, **AlCr-L1**, doubled Cr concentration and stoichiometric ligand concentration increased **AlCr-L1**, doubled Al concentration and stoichiometric ligand concentration increased **AlCr-L1**, doubled ligand/metal salt concentration of **AlCr-L1**, **Al-L1**, **Fe-L1**, doubled ligand/metal salt concentration of **Fe-L1**, **In-L1**, **Co-L1**. Metallogels not evaluated in the article did not show increased performance compared to those in the article.

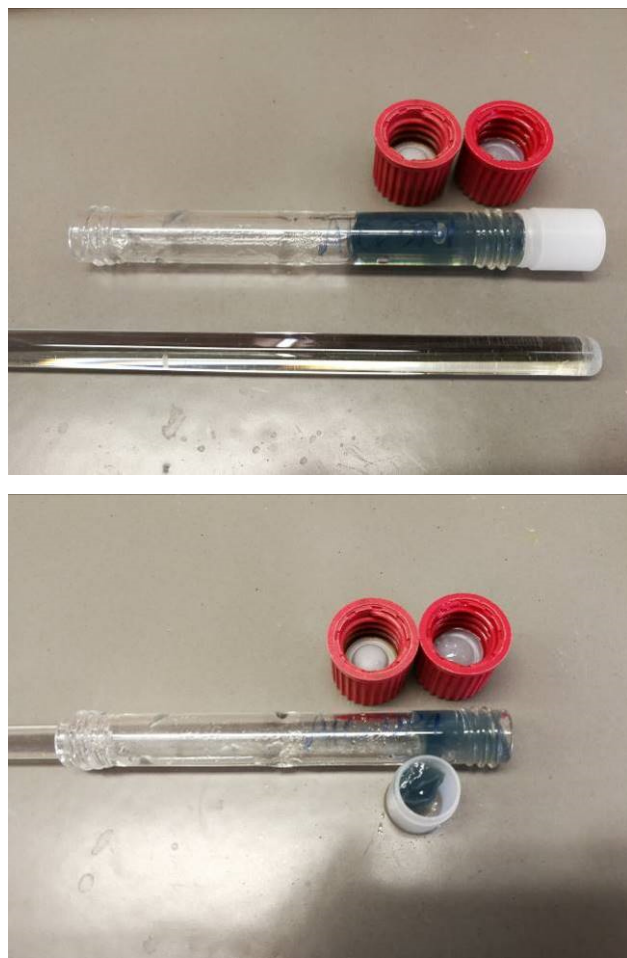


**Figure S4.** Exemplary transfer of AICr-L1 gel to a macroporous specimen chamber. The gel was synthesized in a cylindrical vessel with openings on both ends. The macroporous chamber was placed next to one opening, while a glass rod was used to push the gel into the chamber from the other opening.

The composition of the gels was further determined using energy-dispersive x-ray spectroscopy (EDX) and elemental analysis. Aerogels of Cr and Al with L1 have been examined, as well as xerogels of Cr, Fe, Co and In. The EDX analysis shows good correlation of the measured compounds with the theoretical values. The elemental analysis shows that considerable amounts of water and low amounts of DMF remain in the compounds.

#### **Elemental and EDX analysis results of the metal-organic framework aerogels and xerogels**

**Table S5.** Elemental analysis data of the aero- and xerogels.

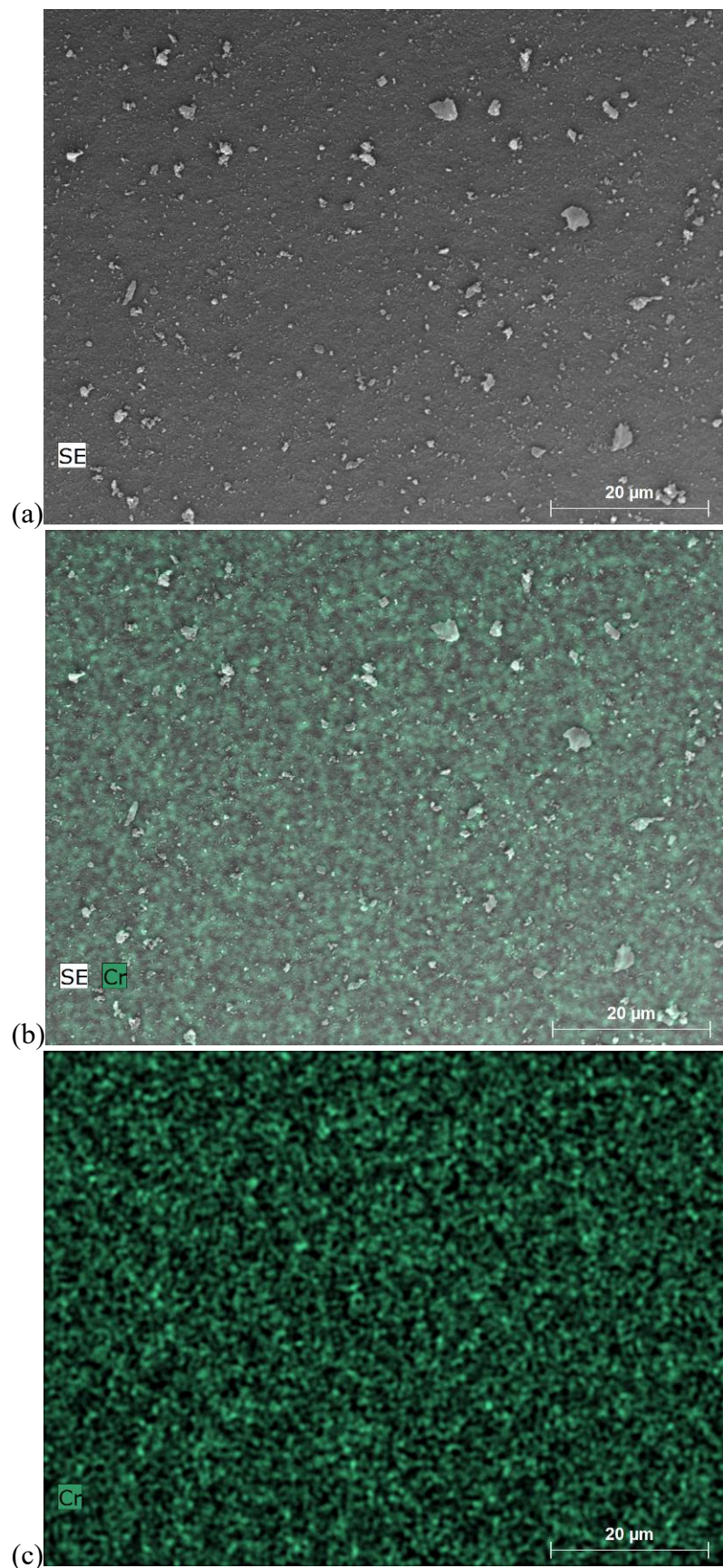
Compound	C exp.	C calc.	H exp.	H calc.	N exp.	N calc.
Cr-L1 Aerogel	41.65	48.5	4.03	2.37	5.84	4.71
Cr-L1 Xerogel	39.69	48.5	4.09	2.37	4.39	4.71

<b>Al-L1 Aerogel</b>	43.28	52.96	4.13	2.59	4.66	5.15
<b>AlCr-L1 Aerogel</b>	41.88	50.63	3.78	2.48	4.98	4.92
<b>Fe-L1 Xerogel</b>	48.4	48.04	2.29	2.02	5.48	4.67
<b>Co-L1 Xerogel</b>	59.12	28.06	5.82	5.10	24.51	19.09
<b>In-L1 Xerogel</b>	42.82	40.15	1.79	1.68	2.25	3.90

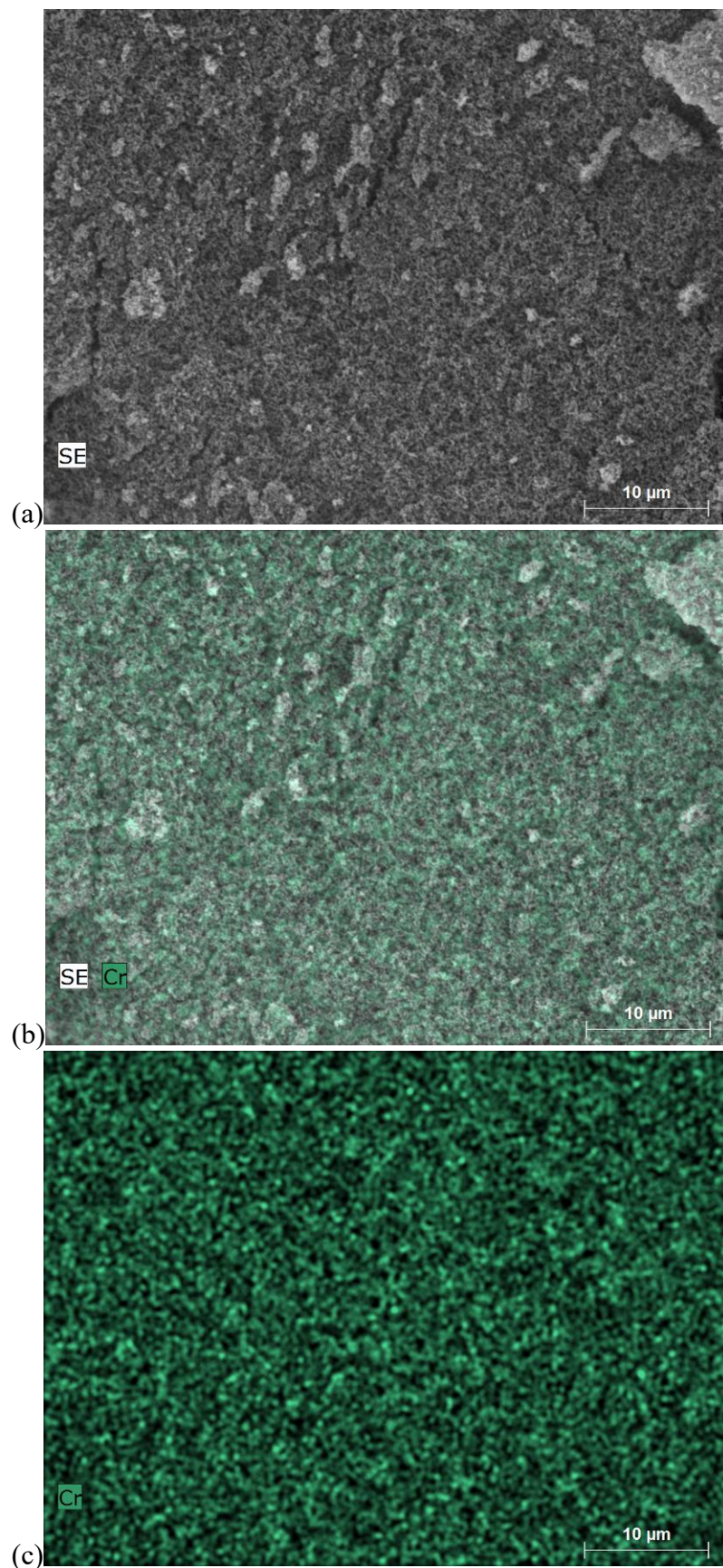
**Table S6.** EDX analysis data of the aero- and xerogels.

Compound	C exp.	C calc.	N exp.	N calc.	O exp.	O calc.	M exp.	M calc.
<b>Cr-L1 Aerogel</b>	69.28	63.16	5.44	5.26	20.64	26.32	4.63	5.26
<b>Cr-L1 Xerogel</b>	69.81	63.16	6.95	5.26	18.71	26.32	4.31	5.26
<b>Al-L1 Aerogel</b>	68.8	63.16	6.95	5.26	23.71	26.32	2.72	5.26
<b>AlCr-L1 Aerogel</b>	69.40	63.16	5.13	5.26	21.84	26.32	3.78	5.26
<b>Fe-L1 Xerogel</b>	64.6	63.16	5.13	5.26	18.33	26.32	11.97	5.26
<b>Co-L1 Xerogel<sup>a</sup></b>	45.28	22.22	19.99	12.96	8.69	9.25	7.87	1.85
<b>In-L1 Xerogel</b>	68.61	63.16	2.50	5.26	24.25	26.32	4.64	5.26

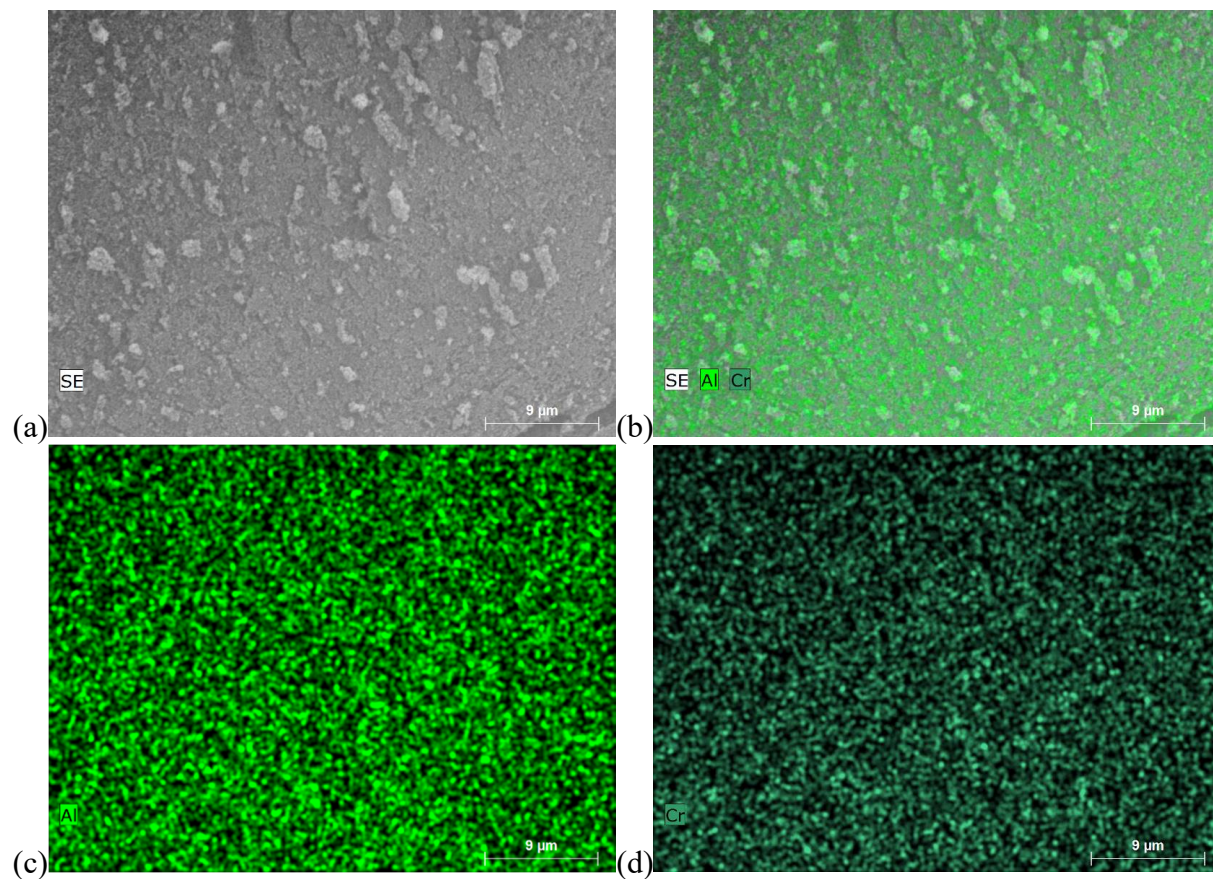
<sup>a</sup> Assuming 1 mol of L1 with 2 mol of  $(\text{NH}_3)_6\text{CoCl}_3$  for the calculated values.



**Figure S5.** (a) SEM image, (b) SEM with superimposed EDX Cr mapping and (c) EDX Cr mappings alone of Cr-L1 xerogel.

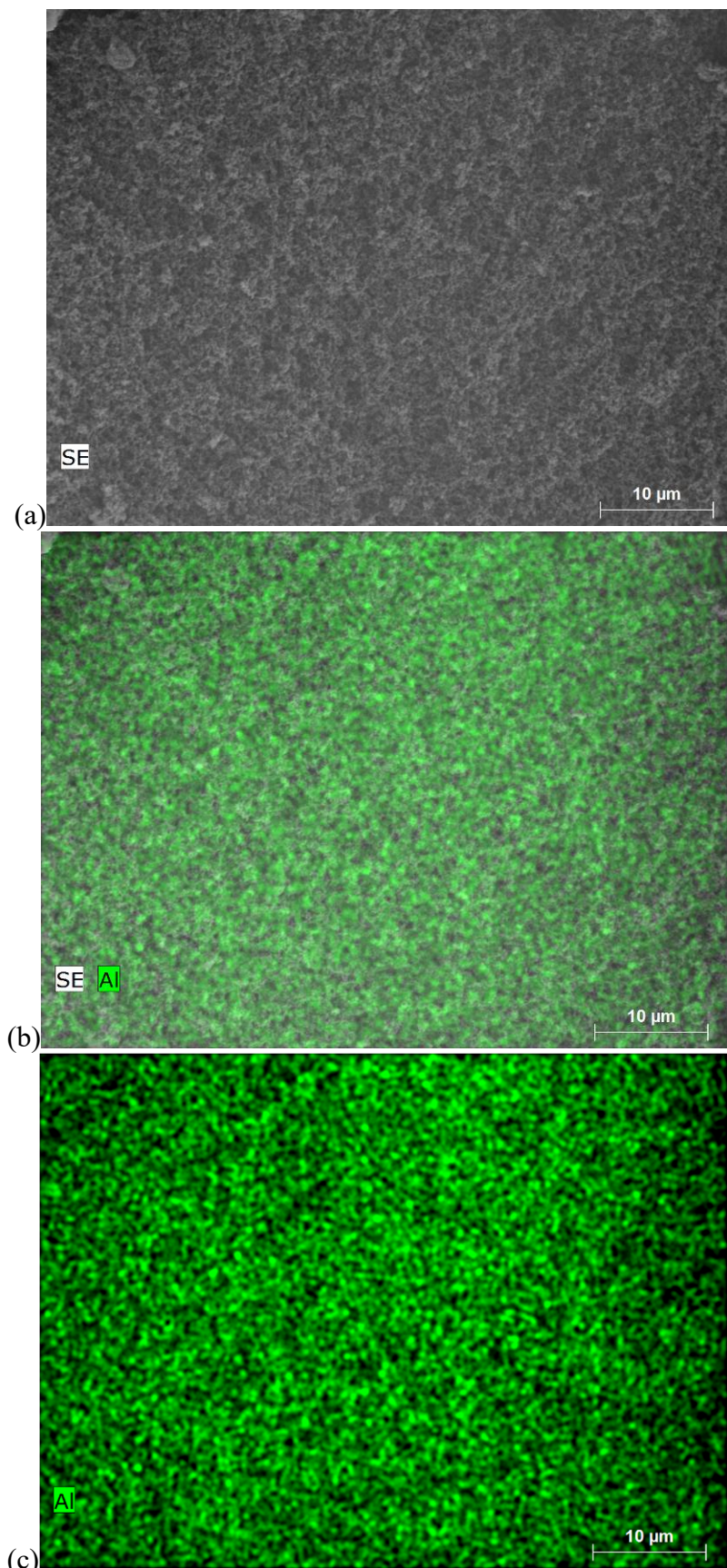


**Figure S6.** (a) SEM image, (b) SEM with superimposed EDX Cr mapping and (c) EDX Cr mappings alone of Cr-L1 aerogel.



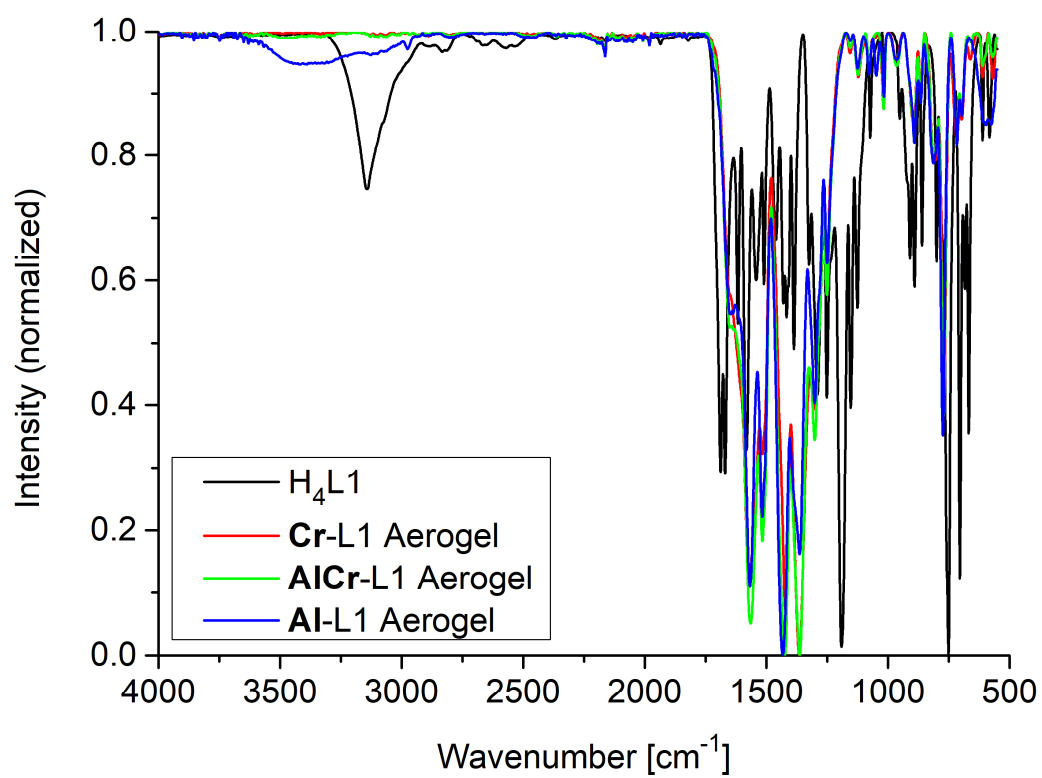
**Figure S7.** (a) SEM image, (b) SEM with superimposed EDX Cr mapping and (c, d) EDX Al and Cr mappings alone of AlCr-L1 aerogel.





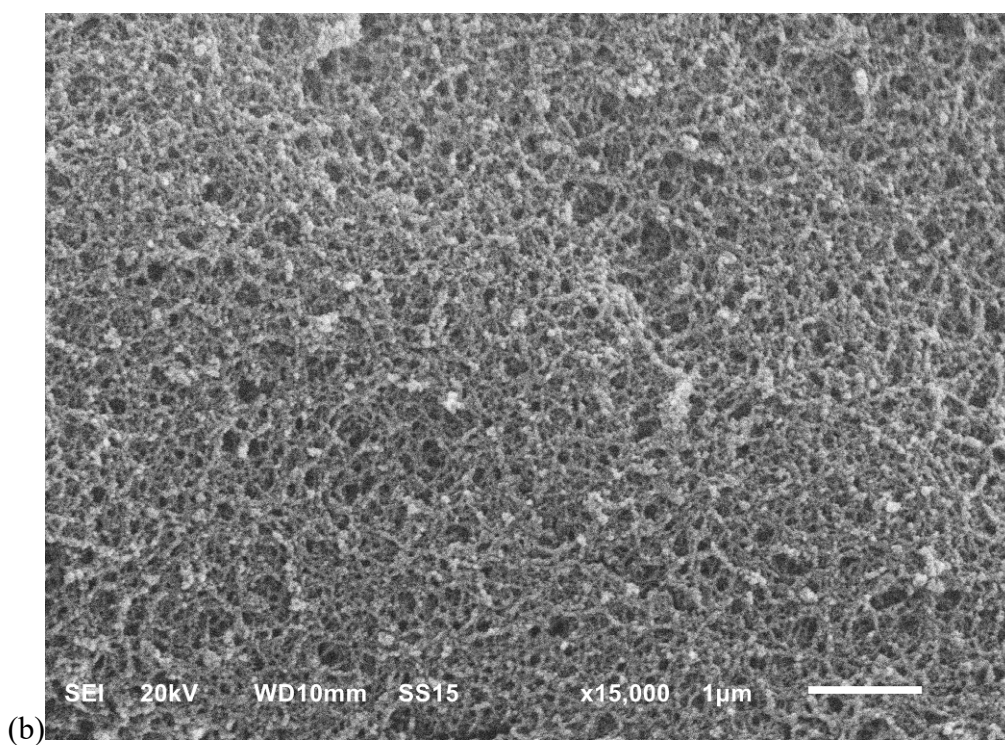
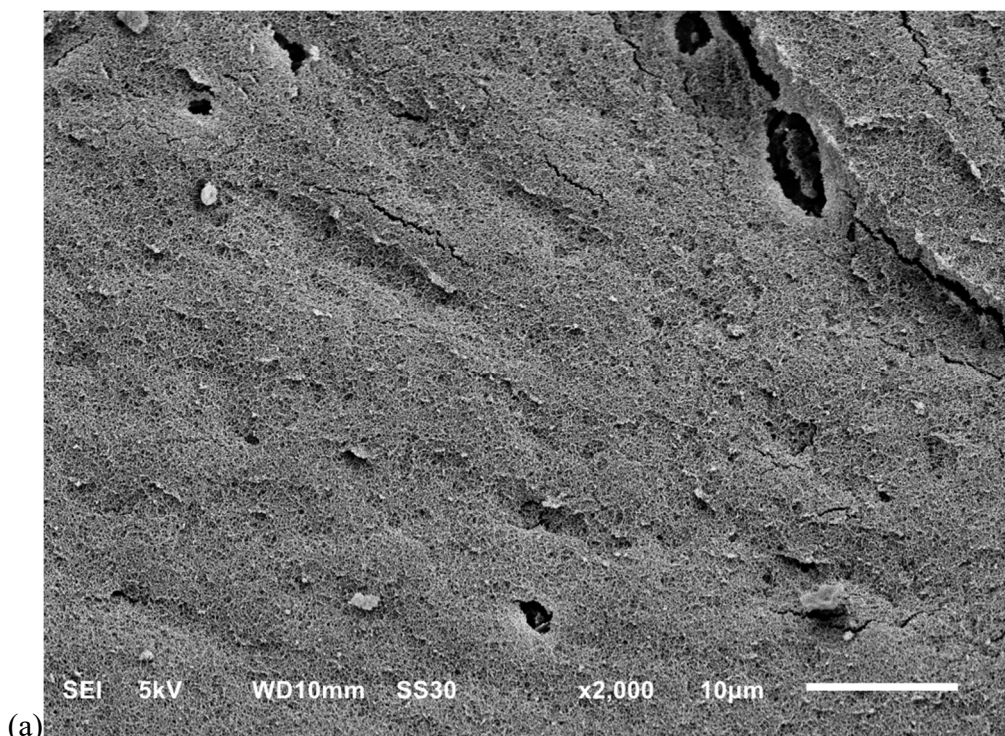
**Figure S8.** (a) SEM image, (b) SEM with superimposed EDX Al mapping and (c) EDX Al mapping alone of Al-L1 aerogel.

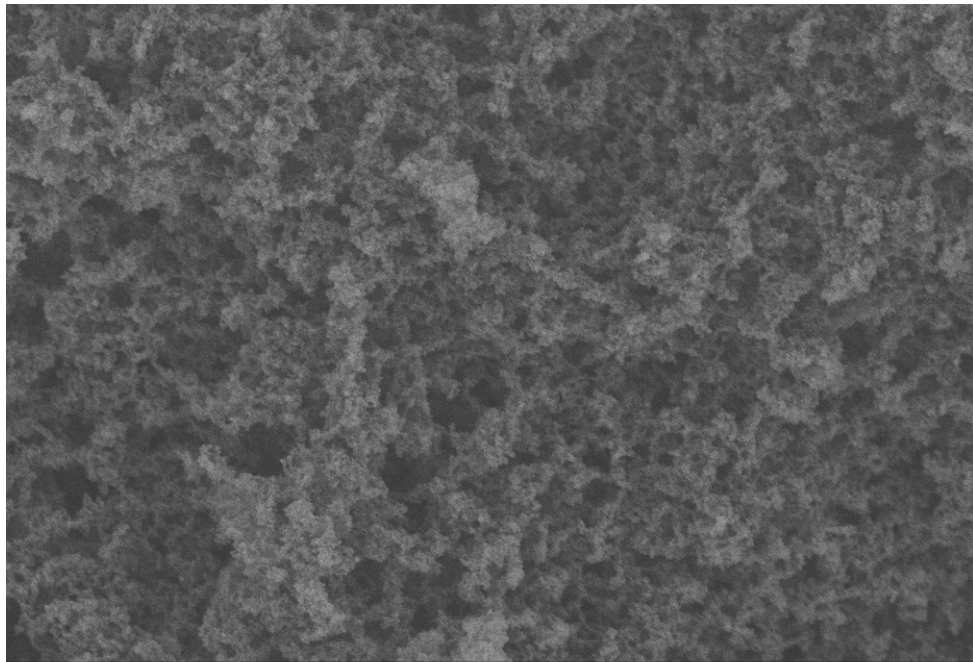
**IR spectra of the metal-organic framework aerogels and xerogels**



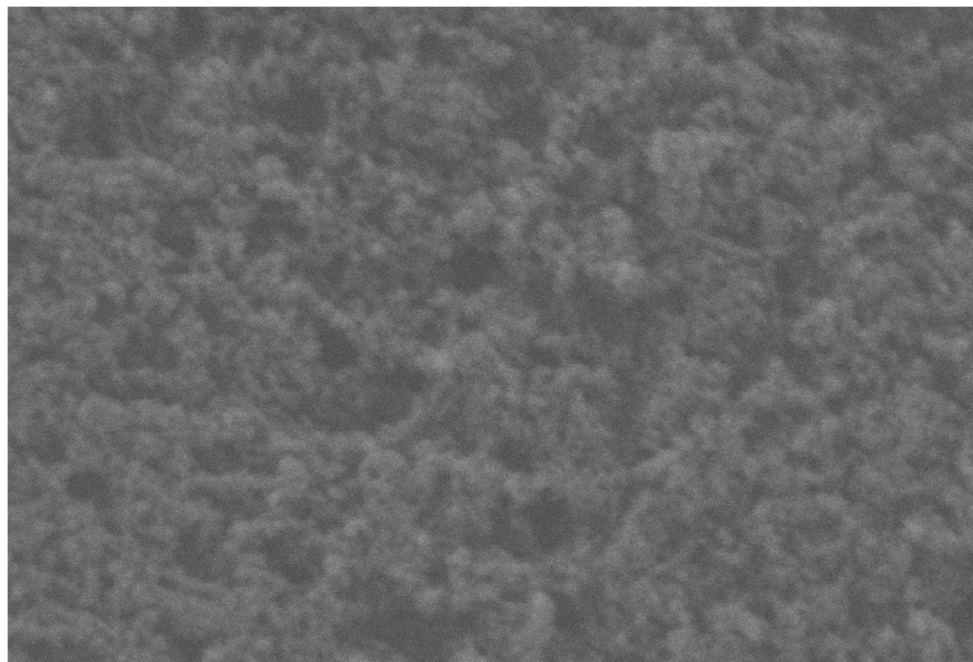
**Figure S9.** IR spectra of the aerogels and L1.

Scanning electron microscopy (SEM) images of the metal-organic framework aerogels and xerogels

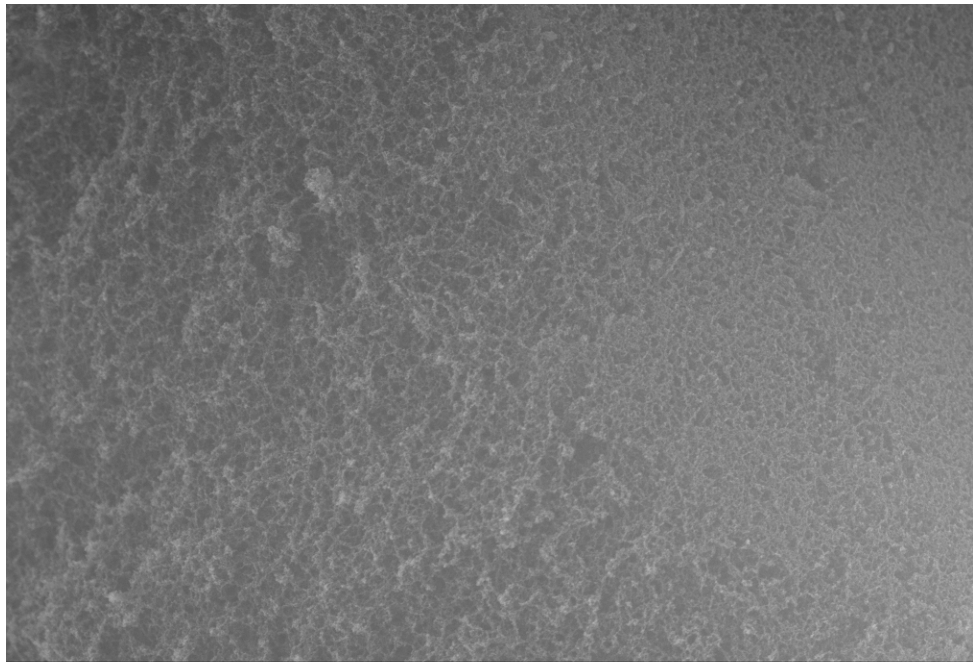




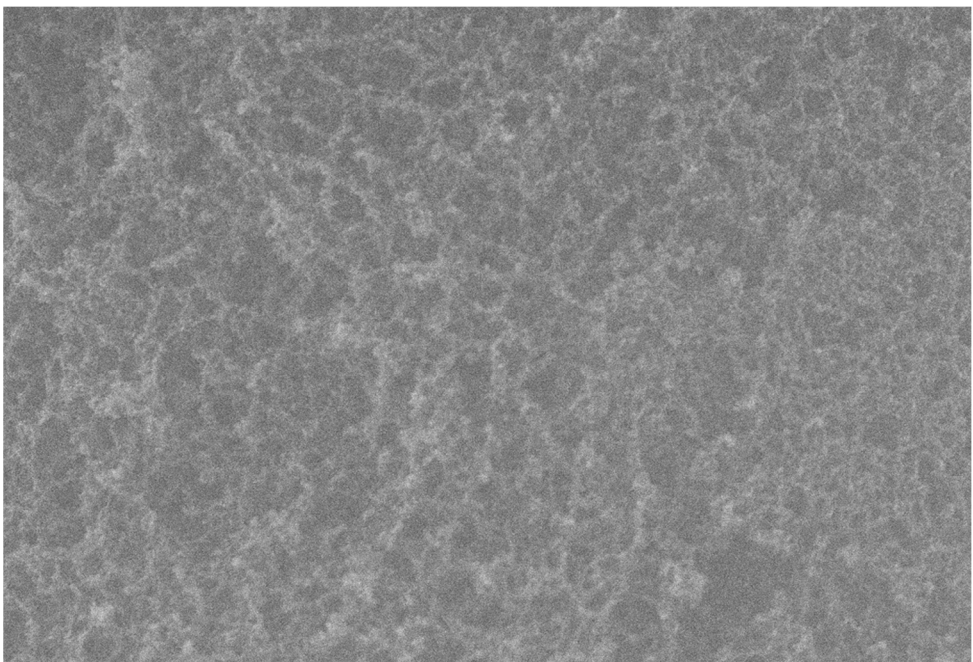
(c)



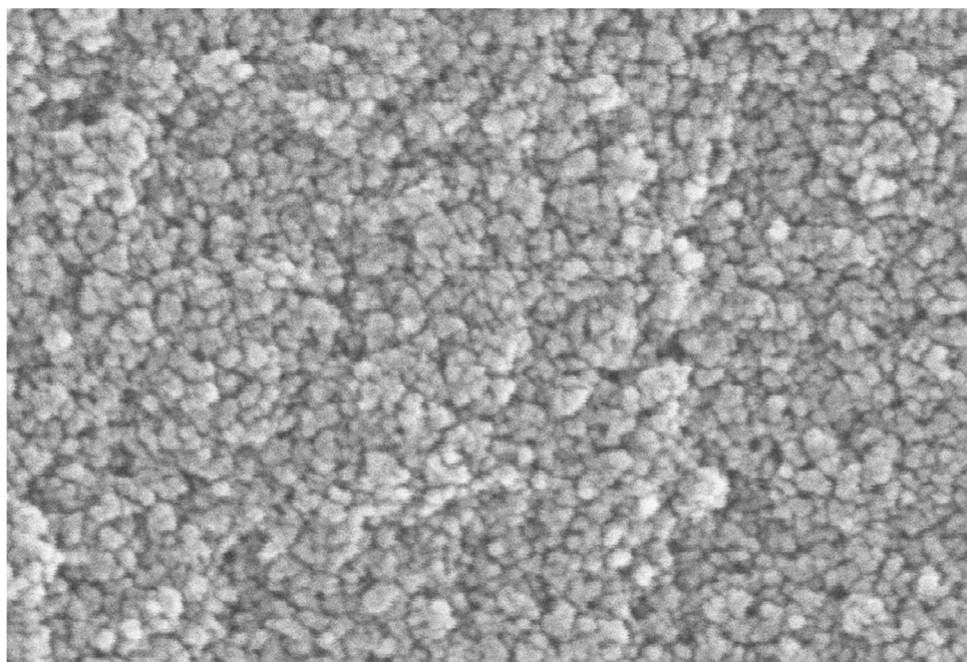
(d)



(e)

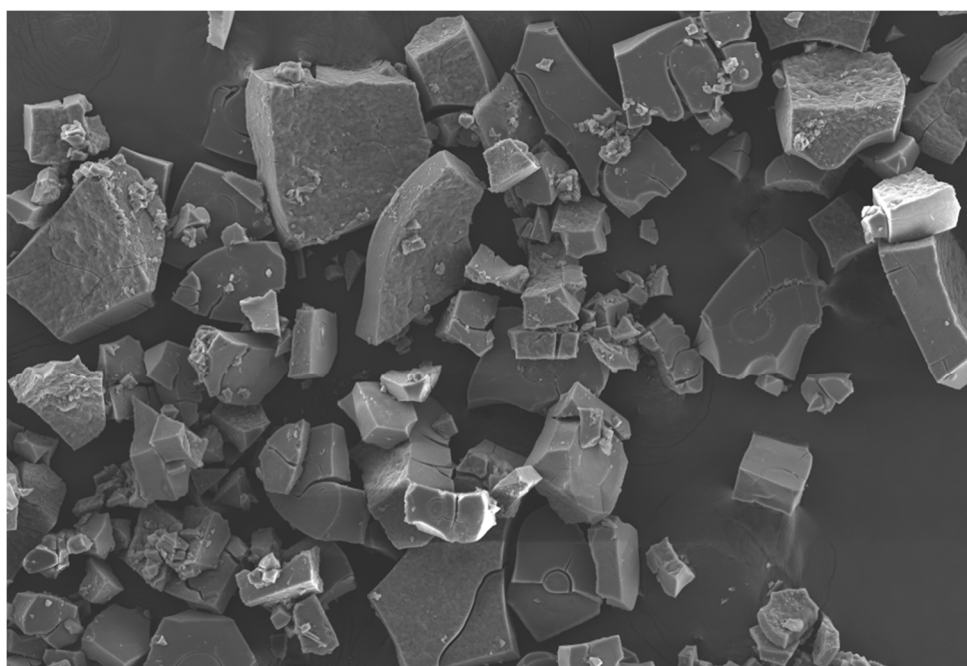


(f)



SEI 20kV WD9mm SS30 x50,000 0.5 $\mu$ m

(g)



SEI 20kV WD9mm SS60 x100 100 $\mu$ m

(h)

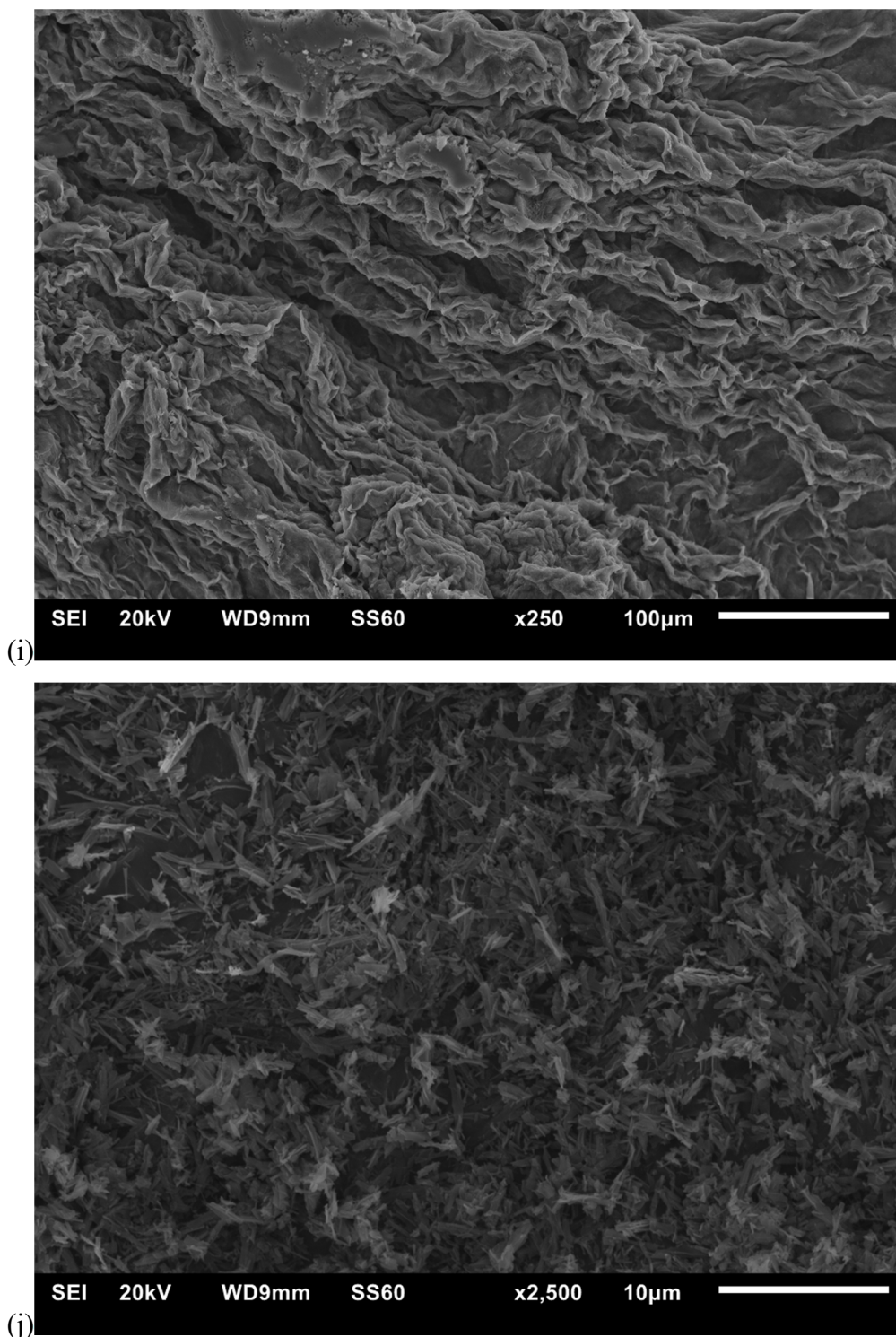


**Figure S10.** SEM images of the xero- and aerogels. (a-f) Aerogels of **Cr-L1** (a/b), **Al-L1** (c/d) and **AlCr-L1** (e/f) at different magnifications. (g) Xerogel of **Cr-L1** at high magnification. (h): Xerogel of **Fe-L1** at low magnification. The surface of the xerogel appears smooth at all magnifications and shows no porosity. (i): Xerogel of **Co-L1**. (j): Xerogel of **In-L1**.

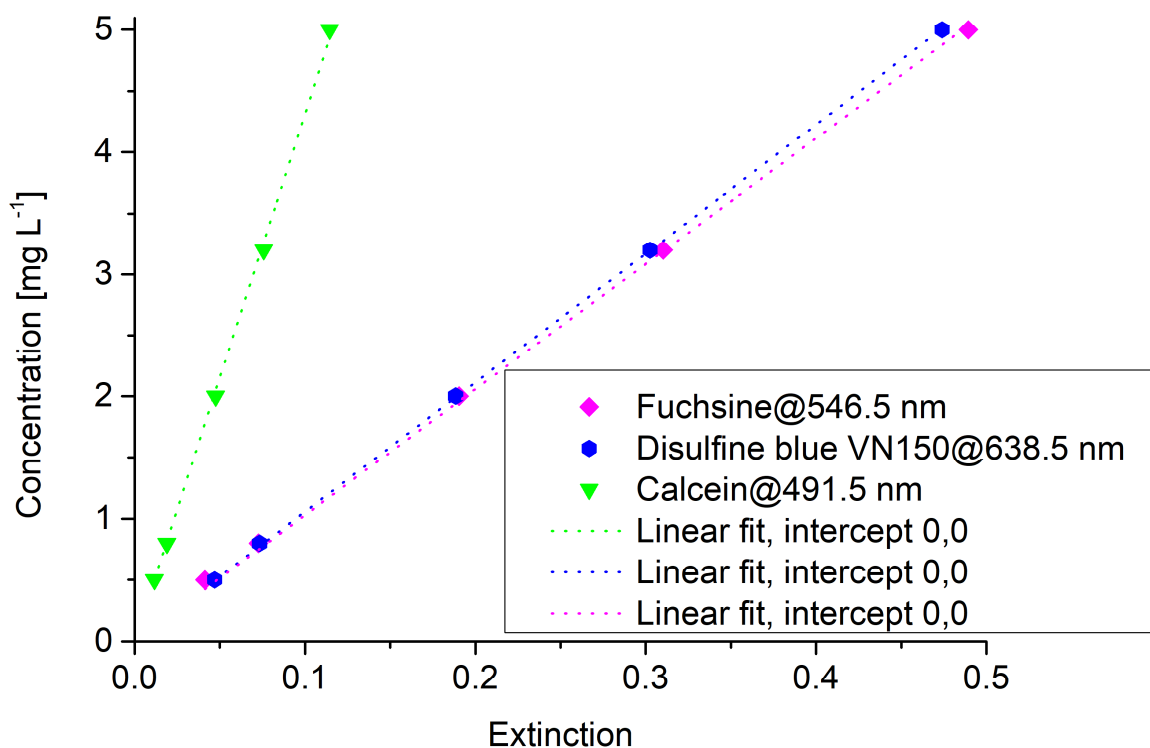


**Figure S11.** Dye sorption calibration curves used for concentration determinations.

**Table S7.** Calibration curve formulas for each dye.

Dye	Calibration curve formula	R <sup>2</sup> value
Fuchsine	$y = 10.29x$	0.9996
Calcein	$y = 43.10x$	0.9996
Disulfine blue VN150	$y = 10.57x$	0.9999



## Nitrogen and argon physisorption data

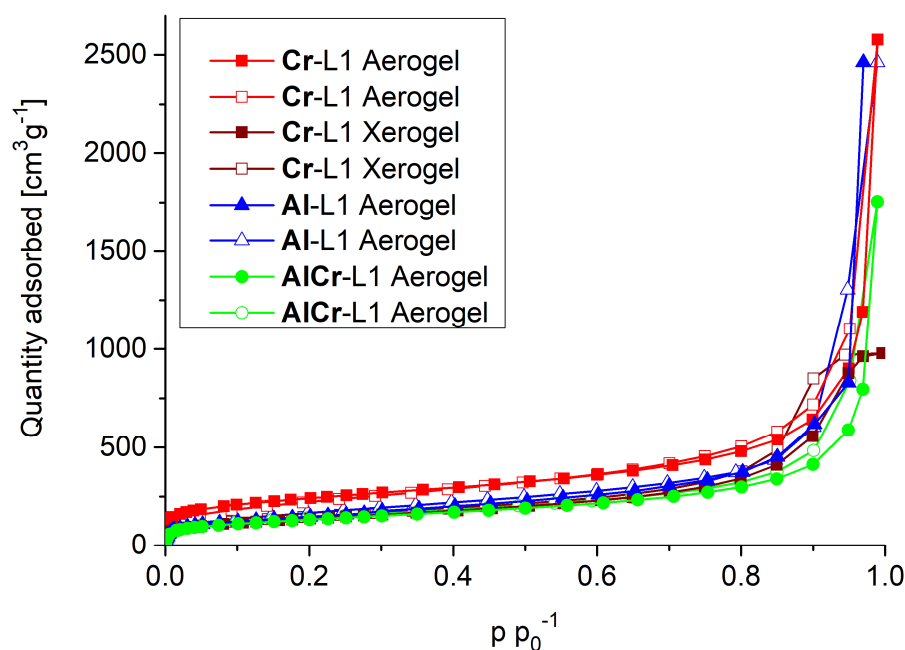


**Figure S12.** Full range  $\text{N}_2$  sorption isotherms of the aerogels and the Cr xerogel. All aerogels show Type II isotherms with pore condensation at high  $p/p_0$ . The xerogel (brown curve) displays a Type IV isotherm with finite pore condensation.

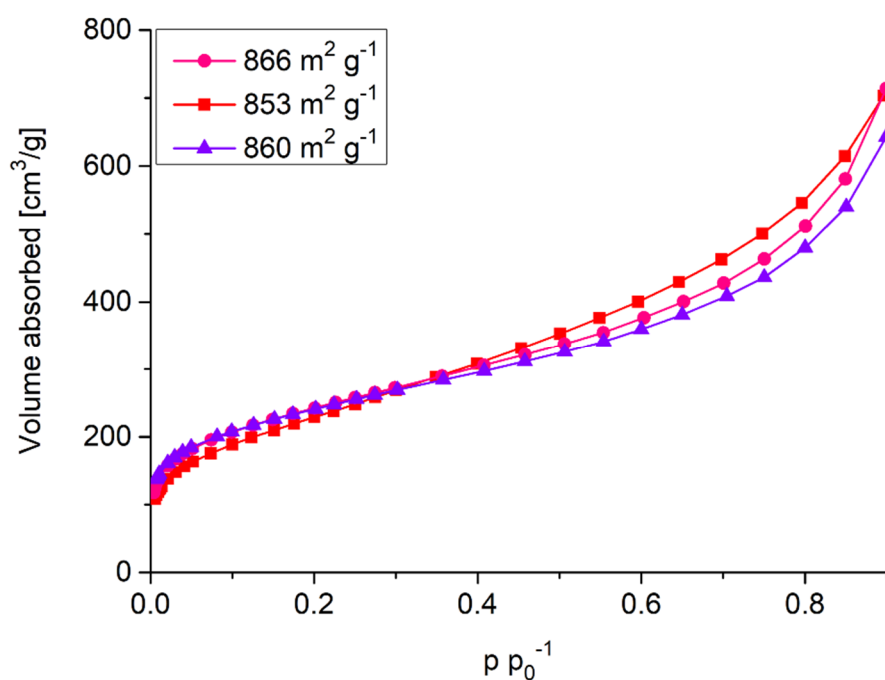


**Figure S13.** Nitrogen physisorption isotherms of Cr-L1 aerogels of different batches. The specific surface area was successfully reproduced, despite lower specific surface areas determined by  $\text{CO}_2$  and Ar sorption.

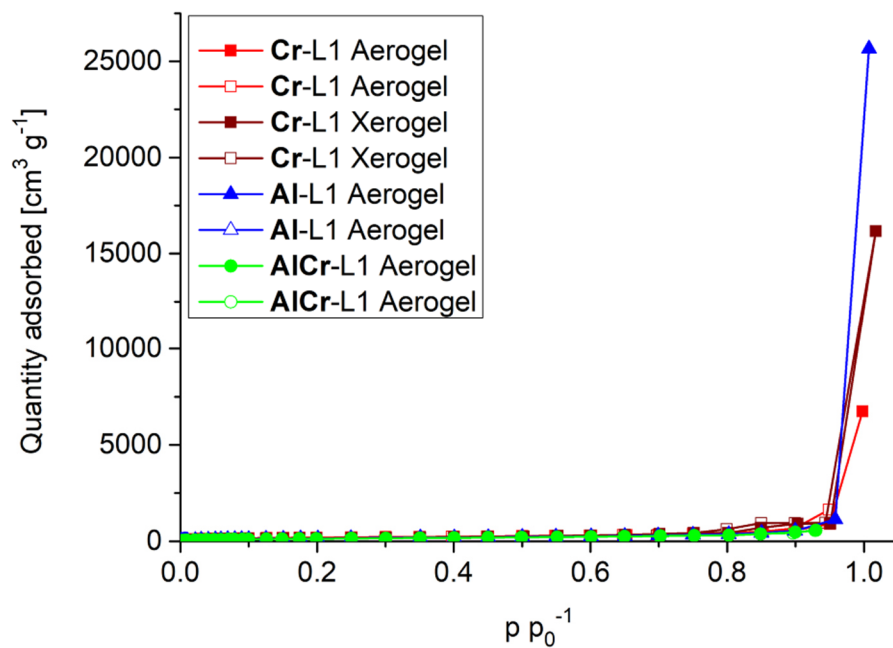


**Figure S14.** Full range Ar physisorption isotherms at 87 K.

**Table S8.** Summary of Ar physisorption DFT calculations.

Compound	DFT surface area [m <sup>2</sup> g <sup>-1</sup> ]	Pore volume [cm <sup>3</sup> g <sup>-1</sup> ]	DFT fitting error	Lower confidence limit [Å]
Cr-L1 Aerogel	624	1.90	1.06%	2.42
Cr-L1 Xerogel	533	1.20	1.21%	2.62
AlCr-L1 Aerogel	385	0.69	0.69%	4.84
Al-L1 Aerogel	462	1.35	1.50%	8.97

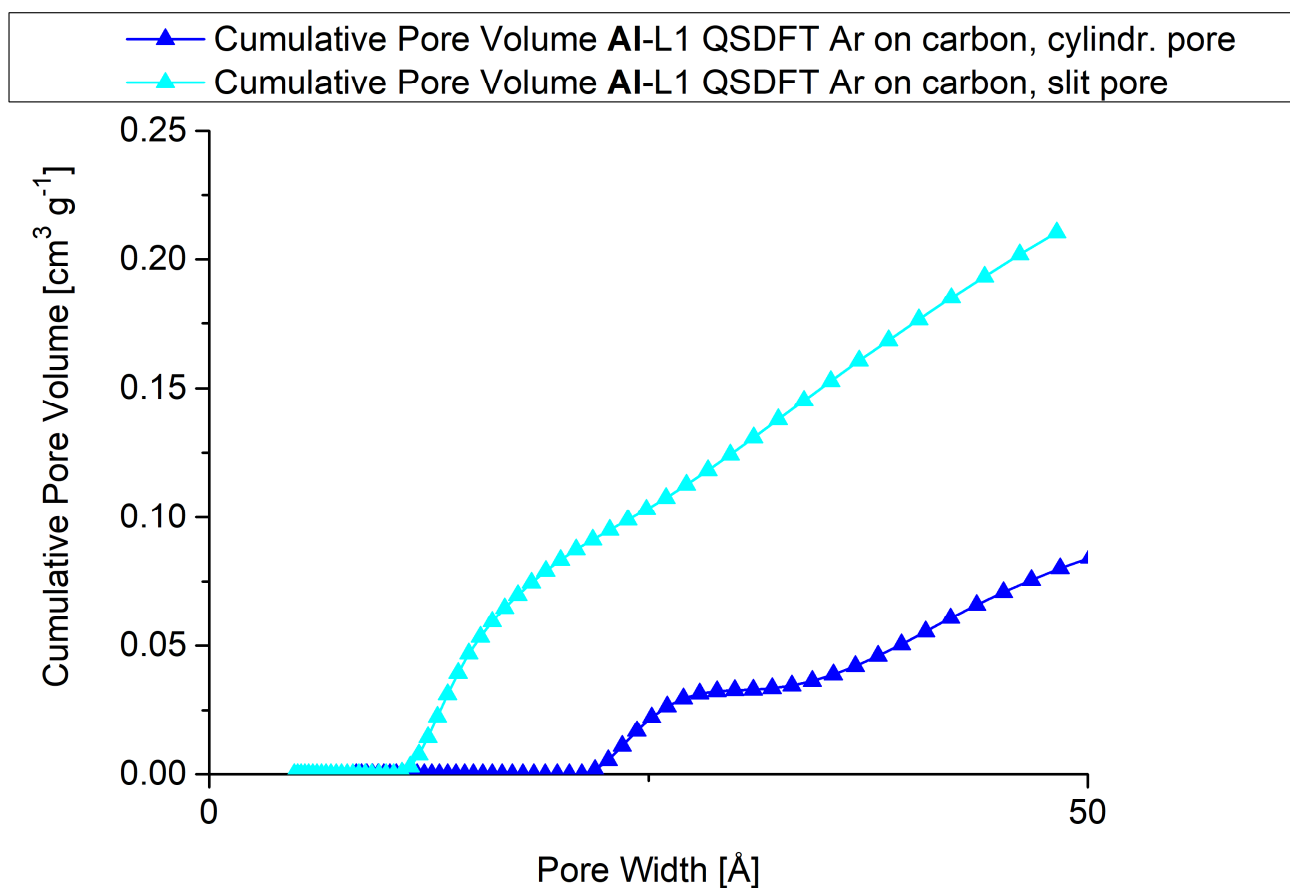


**Figure S15.** Cumulative pore volume for the AI-L1 aerogel, simulated using a QSDFT calculation with an "Ar on carbon, cylindrical pore" model (dark blue) and an "Ar on carbon, slit pore" model (cyan blue). The simulation using the slit pore model did not determine pore volume values past 50 Å of pore width, therefore a cylindrical pore model has been utilized to reveal the pore size distribution.

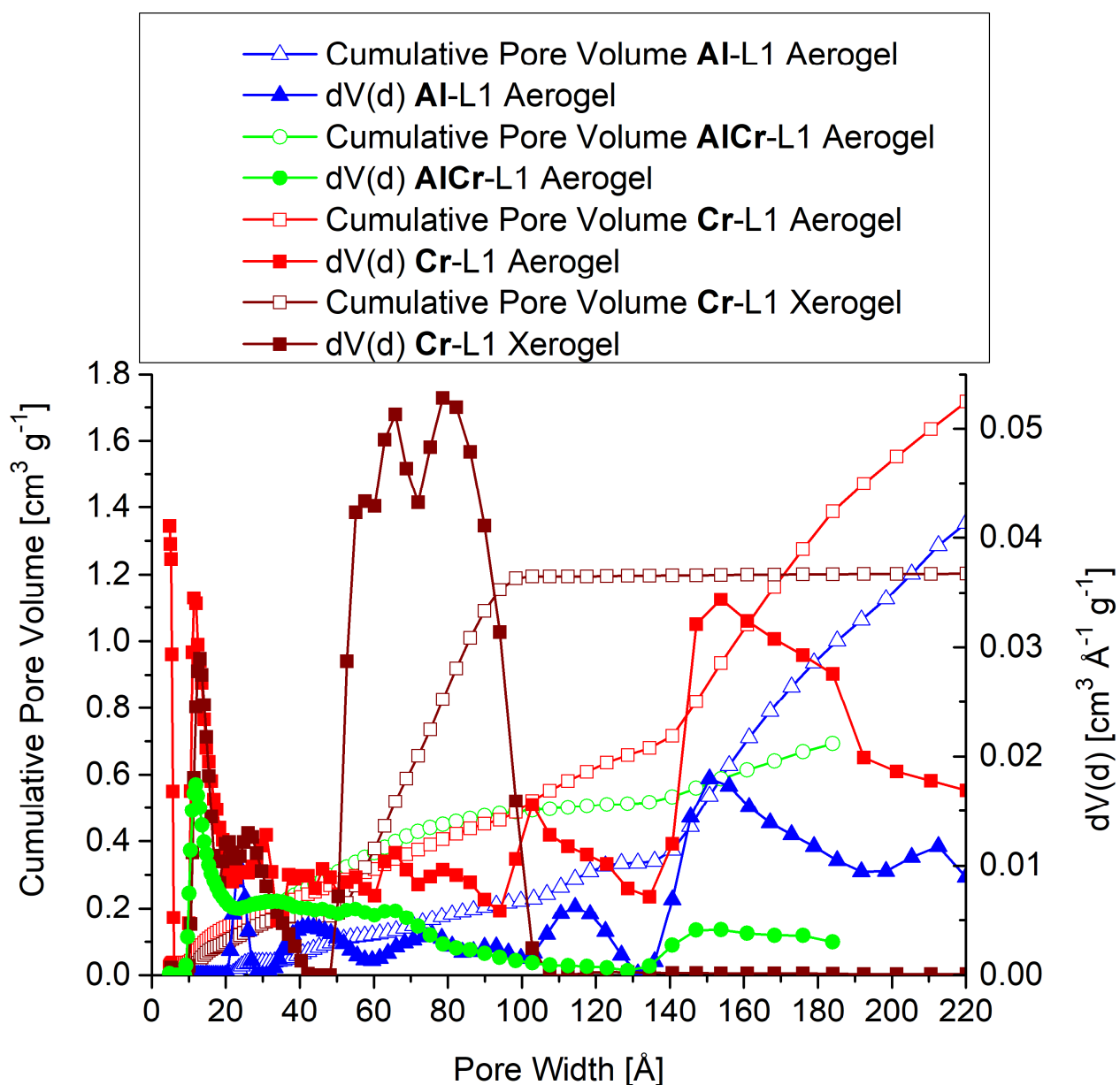


**Figure S16.** Cumulative pore volume (dashed line) and derivate of the pore volume change (full line) plotted against the pore width, obtained from Ar physisorption at 87 K. The pore widths of the aerogels are distributed over the whole range (addressed up to 220 Å), while the xerogel does not exhibit pores wider than 100 Å.

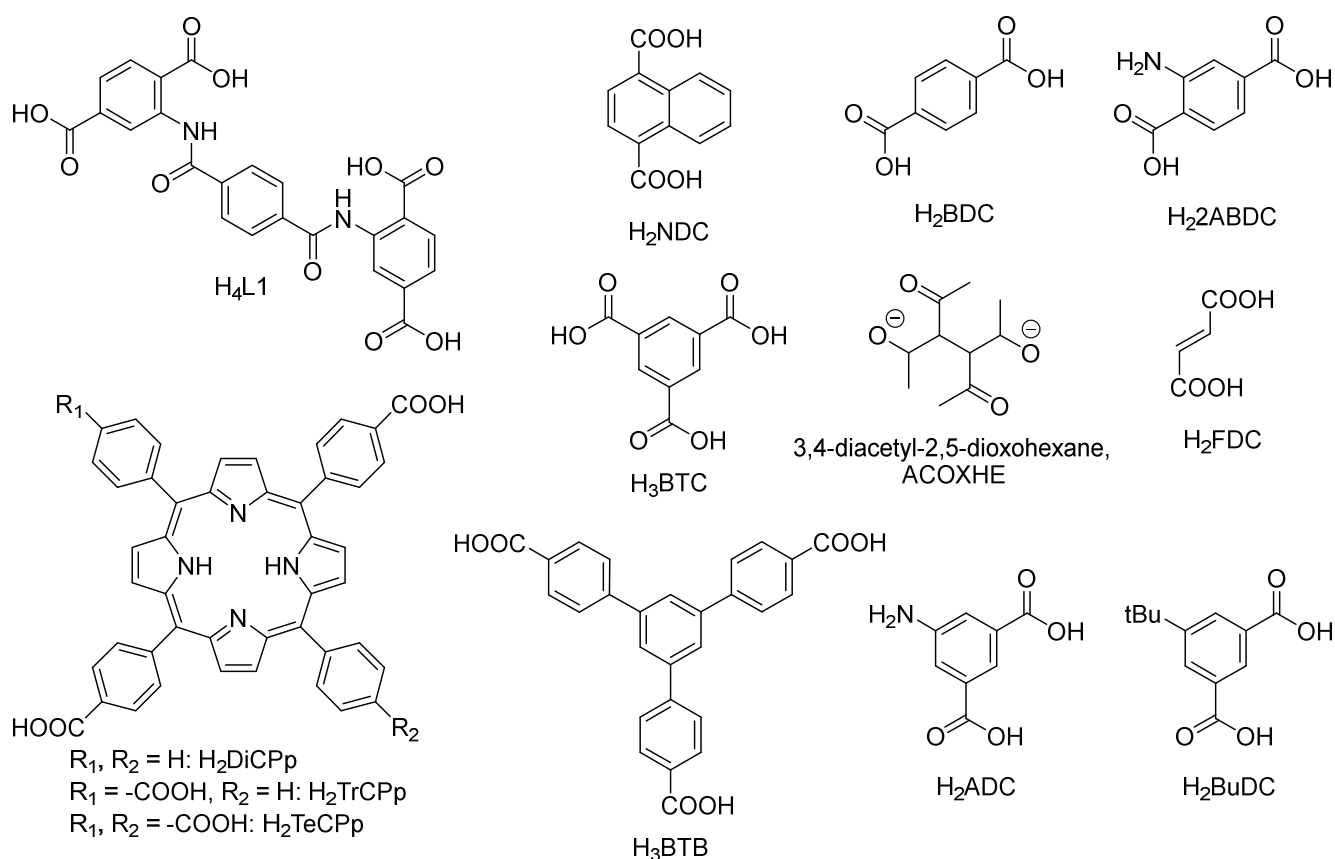


**Figure S17.** Ligands discussed in pore volume comparison of their related aero- and xerogels.

**Table S9.** Selected pore volumes for known Cr and Al metal-organic framework aerogels.

Compound	V <sub>tot.</sub> [cm <sup>3</sup> g <sup>-1</sup> ]	Analysis gas, temperature	Ref.
Cr-L1 Aerogel	1.90	Ar, 87 K	this work
Cr-L1 Xerogel	1.20	Ar, 87 K	this work
AlCr-L1 Aerogel	0.69	Ar, 87 K	this work
Al-L1 Aerogel	1.01	Ar, 87 K	this work
AlBDC aerogel	1.10-6.27	N <sub>2</sub> , 77 K	1
AlBTC aerogel	0.82-7.16	N <sub>2</sub> , 77 K	1
AlBTC xerogel	1.31	N <sub>2</sub> , 77 K	2
AlBTC aerogel	4.5	N <sub>2</sub> , 77 K	2
CrBTC	0.233-0.695	N <sub>2</sub> , 77 K	3
CrBDC	1.527	N <sub>2</sub> , 77 K	3
CrNDC	1.489	N <sub>2</sub> , 77 K	3

CrADC	0.912	N <sub>2</sub> , 77 K	3
CrFDC	0.401	N <sub>2</sub> , 77 K	3
CrBuBDC	0.085	N <sub>2</sub> , 77 K	3
CrBTB	0.067	N <sub>2</sub> , 77 K	3
MOPA1 (CrTeCPp)	1.72	N <sub>2</sub> , 77 K	4
MOPA2 (AlTeCPp)	1.32	N <sub>2</sub> , 77 K	4
MOPA4 (CrTrCPp)	1.62	N <sub>2</sub> , 77 K	4
MOPA5 (AlTrCPp)	2.86	N <sub>2</sub> , 77 K	4
MOPA6 (CrDiCPp)	1.93	N <sub>2</sub> , 77 K	4
AlACOXHE	0.78	N <sub>2</sub> , 77 K	5
CrACOXHE	2.65	N <sub>2</sub> , 77 K	5

## CO<sub>2</sub>, SO<sub>2</sub> and H<sub>2</sub>O physisorption data

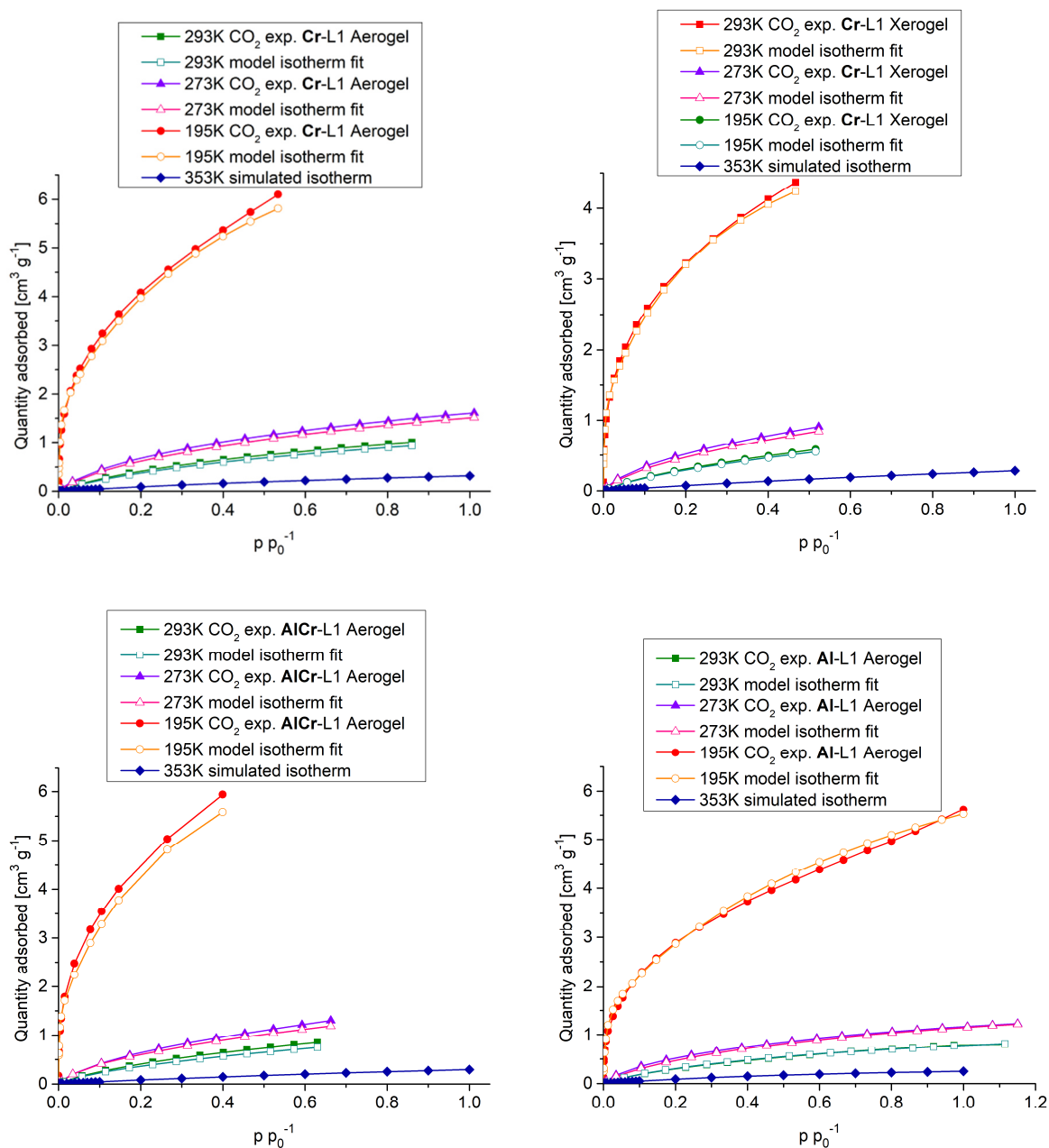


**Figure S18.** CO<sub>2</sub> physisorption isotherms of the porous gels recorded at different temperatures. The measured isotherms were linearized against the measurement temperatures, and isotherms at 80 °C have been calculated.

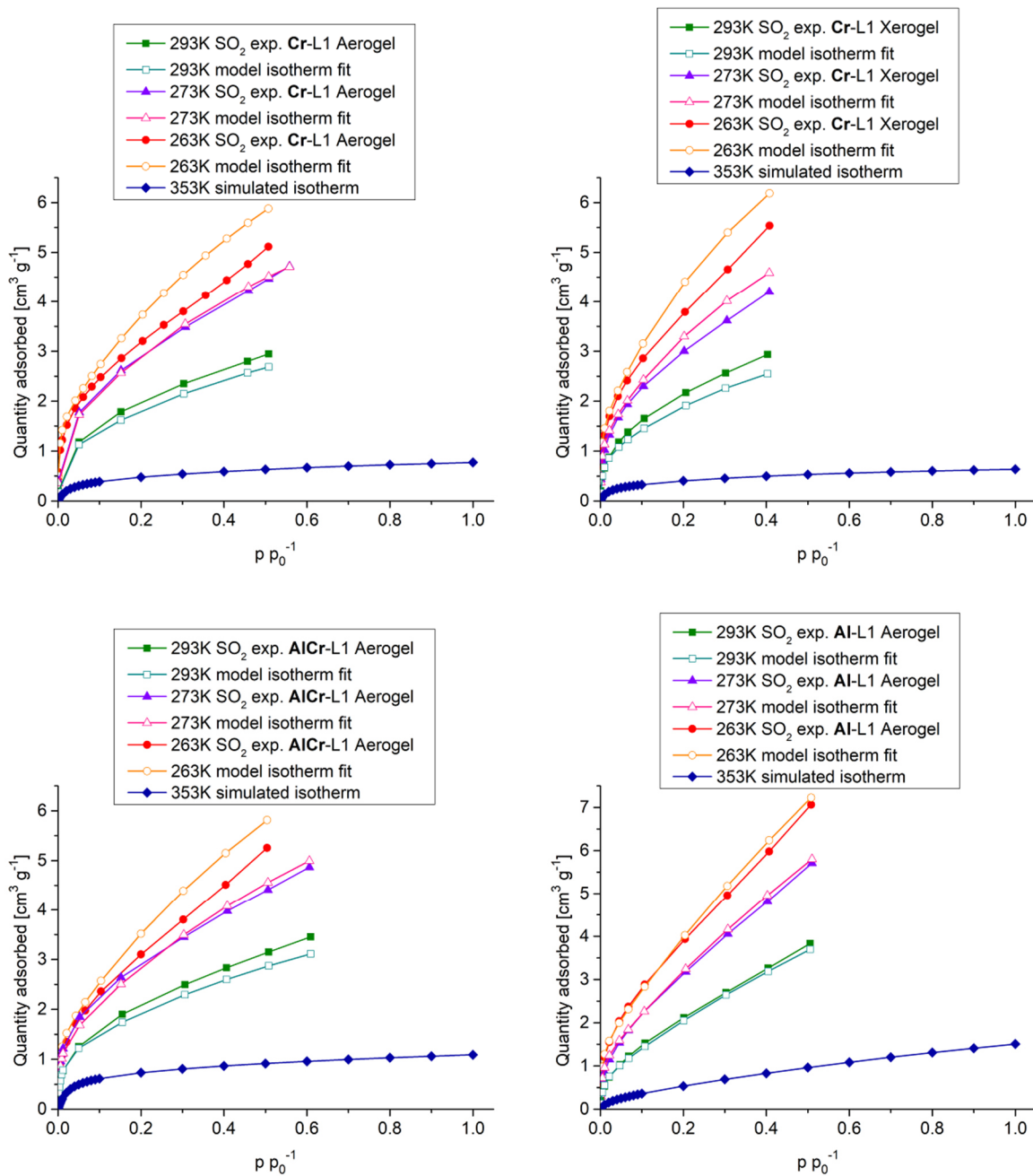


**Figure S19.** SO<sub>2</sub> physisorption isotherms of the porous gels recorded at different temperatures. The measured isotherms were linearized against the measurement temperatures, and isotherms at 80 °C have been calculated. Measurement points after onset of pore condensation have been disregarded (usually past 0.5-0.6 p p<sub>0</sub><sup>-1</sup>).



**Table S10.** Maximum water uptake of the synthesized compounds.

Compound	Water uptake at 0.9 p p <sub>0</sub> <sup>-1</sup> (mg g <sup>-1</sup> ), 293K
Cr-L1 Aerogel	240
Cr-L1 Xerogel	396
AlCr-L1 Aerogel	249
Al-L1 Aerogel	261

**Dual-Site Langmuir fitting data****Table S11.** Dual-Site Langmuir fitting parameters for SO<sub>2</sub> physisorption curves at 20 °C.

Compound	K <sub>1</sub> SO <sub>2</sub> [bar <sup>-1</sup> ]	m <sub>1</sub> SO <sub>2</sub> [mmol g <sup>-1</sup> ]	K <sub>2</sub> SO <sub>2</sub> [bar <sup>-1</sup> ]	m <sub>2</sub> SO <sub>2</sub> [mmol g <sup>-1</sup> ]	R <sup>2</sup>
Cr-L1 Aerogel	210.90	0.94	1.44	4.73	0.9998
Cr-L1 Xerogel	195.64	0.90	1.86	4.74	0.9993
AlCr-L1 Aerogel	173.96	1.07	0.94	6.50	0.9996
Al-L1 Aerogel	157.53	0.80	0.39	18.69	0.9994

**Table S12.** Dual-Site Langmuir fitting parameters for CO<sub>2</sub> physisorption curves at 20 °C.

Compound	K <sub>1</sub> CO <sub>2</sub> [bar <sup>-1</sup> ]	m <sub>1</sub> CO <sub>2</sub> [mmol g <sup>-1</sup> ]	K <sub>2</sub> CO <sub>2</sub> [bar <sup>-1</sup> ]	m <sub>2</sub> CO <sub>2</sub> [mmol g <sup>-1</sup> ]	R <sup>2</sup>
Cr-L1 Aerogel	9.08	0.24	0.71	2.10	0.9999
Cr-L1 Xerogel	12.18	0.15	0.51	2.17	0.9999
AlCr-L1 Aerogel	9.23	0.27	0.49	2.60	0.9999
Al-L1 Aerogel	27.39	0.07	0.98	1.44	0.9995

**Table S13.** Dual-Site Langmuir fitting parameters for H<sub>2</sub>O physisorption curves at 20 °C.

Compound	K <sub>1</sub> H <sub>2</sub> O [bar <sup>-1</sup> ]	m <sub>1</sub> H <sub>2</sub> O [mmol g <sup>-1</sup> ]	K <sub>2</sub> H <sub>2</sub> O [bar <sup>-1</sup> ]	m <sub>2</sub> H <sub>2</sub> O [mmol g <sup>-1</sup> ]	R <sup>2</sup>
Cr-L1 Aerogel	2368.89	0.32	66.43	10.92	0.9998
Cr-L1 Xerogel	1675.36	0.74	47.64	13.85	0.9998
AlCr-L1 Aerogel	3043.87	1.01	43.29	14.29	0.9998
Al-L1 Aerogel	3594.40	1.27	51.17	14.81	0.9996

**Table S14.** Quality of fit of the model isotherms to the experimental isotherms at different temperatures.

Compound	CO <sub>2</sub> quality of model fit (R <sup>2</sup> ) at 195K, 273K, 293K	SO <sub>2</sub> quality of model fit (R <sup>2</sup> ) at 263K, 273K, 293K
Cr-L1 Aerogel	0.99, 0.98, 0.98	0.93, 0.99, 0.96
Cr-L1 Xerogel	0.99, 0.98, 0.99	0.95, 0.97, 0.93
AlCr-L1 Aerogel	0.99, 0.98, 0.94	0.96, 0.99, 0.97
Al-L1 Aerogel	0.99, 0.99, 0.99	0.99, 0.99, 0.99

**Table S15.** Temperature dependency of the maximal loadings and heat of adsorptions for CO<sub>2</sub>, as calculated by the 3P sim software.

Compound	CO <sub>2</sub> temperature dependency of max. loading 1	CO <sub>2</sub> temperature dependency of max. loading 2	Heat of adsorption 1 [kJ mol <sup>-1</sup> ]	Heat of adsorption 2 [kJ mol <sup>-1</sup> ]
Cr-L1 Aerogel	6.74	4.72	19.21	5.98
Cr-L1 Xerogel	7.20	2.85	19.24	9.88
AlCr-L1 Aerogel	6.31	3.46	20.71	10.32
Al-L1 Aerogel	10.08	9.31	11.2	0

**Table S16.** Temperature dependency of the maximal loadings and heat of adsorptions for SO<sub>2</sub>, as calculated by the 3P sim software.

Compound	SO <sub>2</sub> temperature dependency of max. loading 1	SO <sub>2</sub> temperature dependency of max. loading 2	Heat of adsorption 1 [kJ mol <sup>-1</sup> ]	Heat of adsorption 2 [kJ mol <sup>-1</sup> ]
Cr-L1 Aerogel	5.59	10.85	19.17	0
Cr-L1 Xerogel	6.63	11.91	15.51	0
AlCr-L1 Aerogel	3.09	10.72	17.38	0
Al-L1 Aerogel	7.48	7.94	14.56	0

As expected, the isotherm fits of CO<sub>2</sub> are in good accordance with each other, making it possible to calculate isotherms at various temperatures (shown here: 80 °C). The isotherms have been cross-checked, which means that after obtaining the linearized fits of the dual-site Langmuir parameters against the temperature, the isotherms at their respective temperatures have been calculated and the quality of fit has been determined. The quality of fit values are listed in

### Breakthrough curve simulation parameters and results

**Table S17.** Breakthrough curve simulation cell parameters.

Adsorber height	20 cm
Adsorber diameter	3 cm
Environmental temperature	20 °C
Gas flow (STP)	1000 cm <sup>3</sup> min <sup>-1</sup>
Pressure	1 bar
Adsorbent mass	30 g
Bed porosity	0.3
Particle porosity	0.3
Apparent particle density	0.303 g cm <sup>-3</sup>
Skeleton density	0.433 g cm <sup>-3</sup>
Particle diameter	3 mm
Axial dispersion	50 cm <sup>2</sup> min <sup>-1</sup>
Molecular weight of carrier gas	30 g mol <sup>-1</sup>

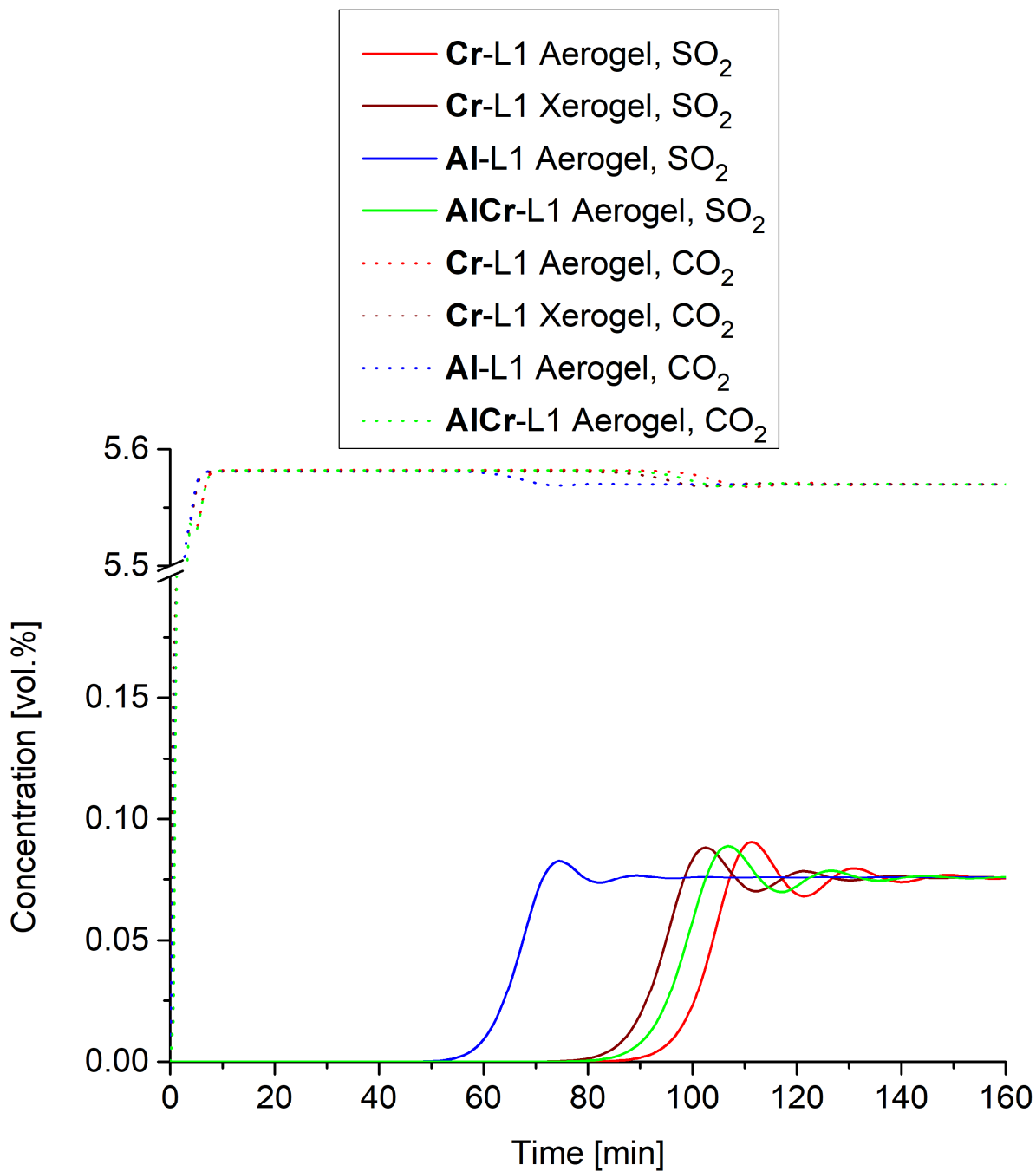


**Figure S20.** Simulated SO<sub>2</sub> and CO<sub>2</sub> breakthrough curves for the aero- and xerogels from a 1:73 (0.076:5.57) SO<sub>2</sub>/CO<sub>2</sub> gas mixture.

## NMR spectrum of H<sub>4</sub>L1

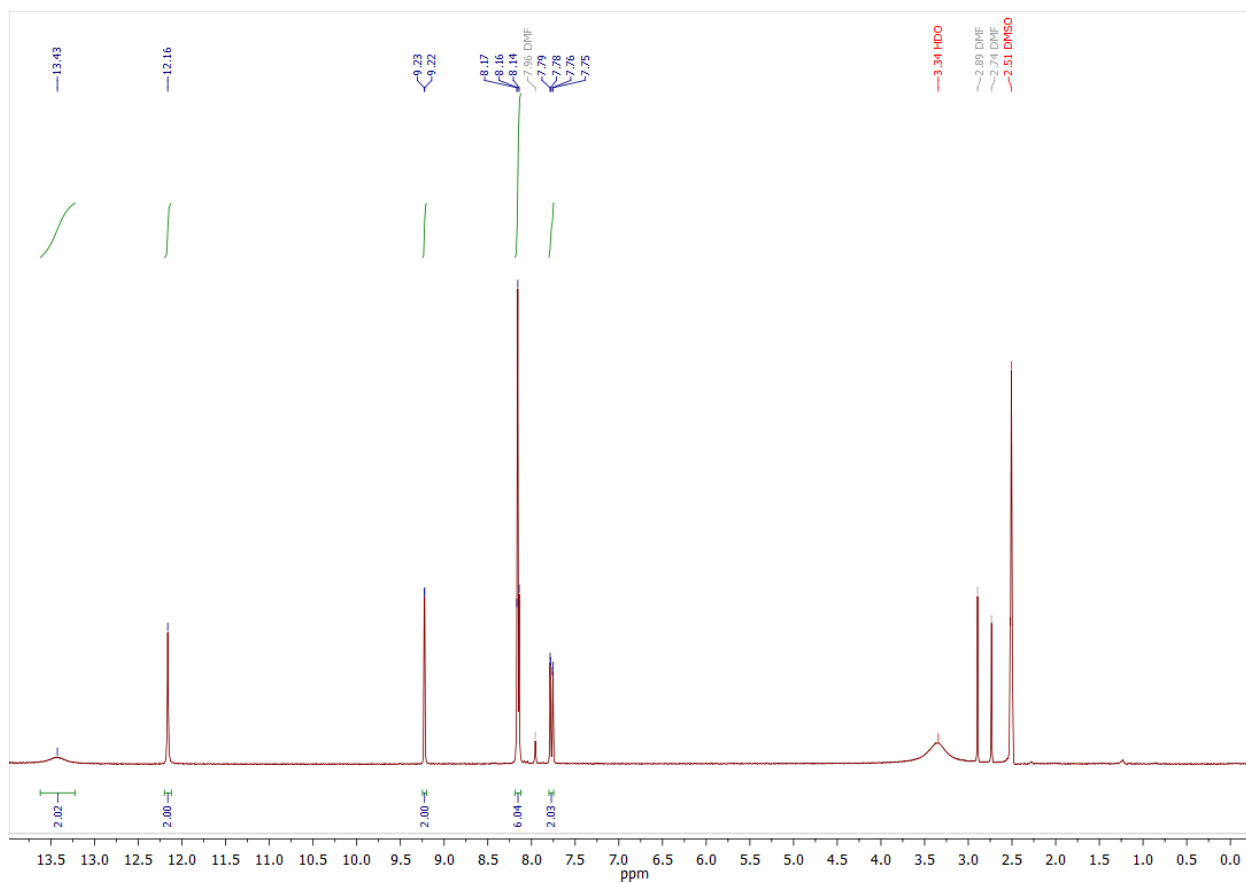


**Figure S21.** <sup>1</sup>H NMR spectrum of H<sub>4</sub>L1. Due to water impurities in the solvent DMSO-*d*<sub>6</sub>, two of the carboxylic acid protons are not visible (13.43 ppm). DMF impurities are a direct result of boiling H<sub>4</sub>L1 in DMF, as it apparently partly dissolves and recrystallizes, which incorporates DMF in the structure. Further proof of this is seen in the crystal structure of H<sub>4</sub>L1.

## Solvent exchange apparatus

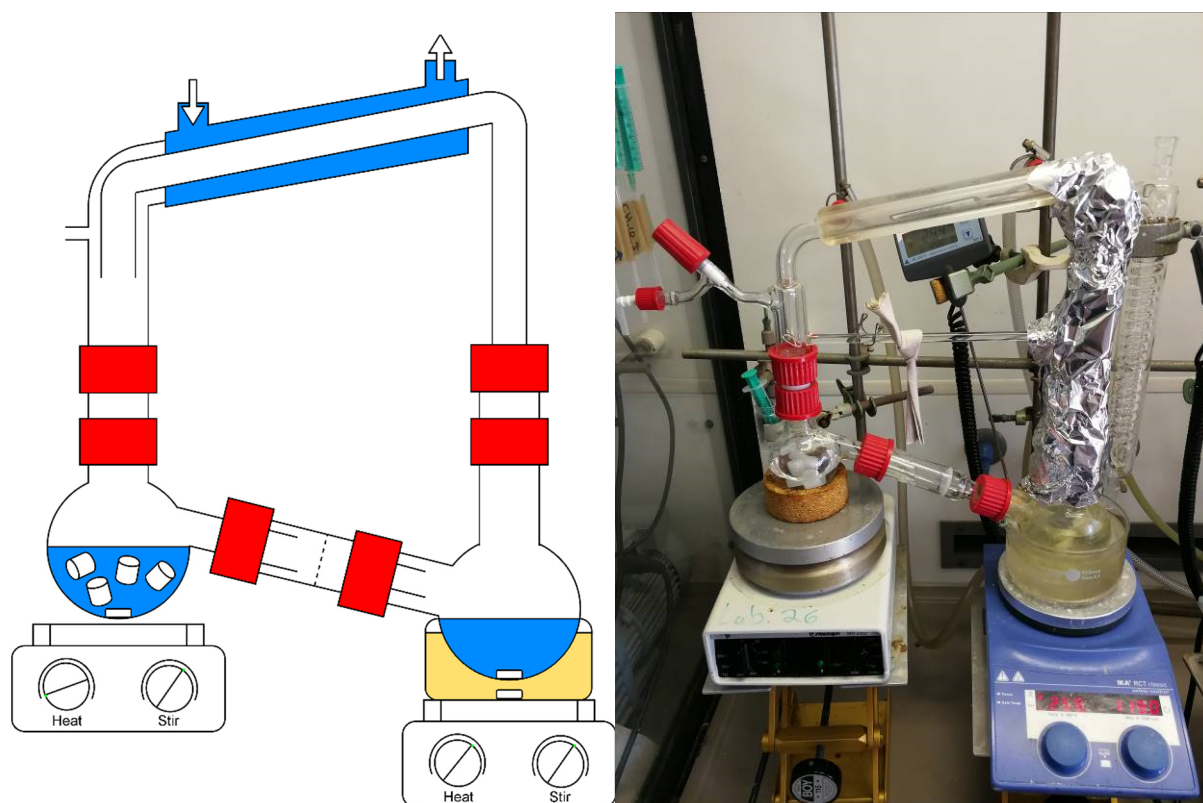


**Figure S22.** Schematic and picture of the apparatus used for continuous solvent exchange.

## Aerogel densities

**Table S18.** Measured density of the xero- and aerogels. The physical dimensions of a cylindrical piece of gel have been measured, and the piece of gel has been weighed in order to determine the density.

Compound	Density [g cm <sup>3</sup> ]
Cr-L1 Aerogel	0.127
Cr-L1 Xerogel	0.368
AlCr-L1 Aerogel	0.101
Al-L1 Aerogel	0.082

(1) Li, L.; Xiang, S.; Cao, S.; Zhang, J.; Ouyang, G.; Chen, L.; Su, C.-Y.; A Synthetic Route to Ultralight Hierarchically Micro/Mesoporous Al(III)-Carboxylate Metal-Organic Aerogels. *Nat. Commun.* **2013**, *4*, article number 1774.

(2) Xia, W.; Zhang, X.; Xu, L.; Wang, Y.; Lin, J.; Zou, R.; Facile and Economical Synthesis of Metal-Organic Framework MIL-100(Al) Gels for High Efficiency Removal of Microcystin-LR. *RSC Adv.* **2013**, *3*, 11007-11013.

(3) Xiang, S.; Li, L.; Zhang, J.; Tan, X.; Cui, H.; Shi, J.; Hu, Y.; Chen, L.; Su, C.-Y.; James, S. L., Porous Organic–Inorganic Hybrid Aerogels Based on Cr<sup>3+</sup>/Fe<sup>3+</sup> and Rigid Bridging Carboxylates. *J. Mater. Chem.* **2012**, *22*, 1862-1867.

(4) Zhao, X.; Yuan, L.; Zhang, Z. Q.; Wang, Y. S.; Yu, Q.; Li, J., Synthetic Methodology for the Fabrication of Porous Porphyrin Materials with Metal-Organic-Polymer Aerogels. *Inorg. Chem.* **2016**, *55*, 5287-96.

(5) Yang, Q.; Tan, X.; Wang, S.; Zhang, J.; Chen, L.; Zhang, J.-P.; Su, C.-Y., Porous Organic–Inorganic Hybrid Aerogels Based on Bridging Acetylacetonate. *Micropor. Mesopor. Mater.* **2014**, *187*, 108-113.

### 3.1.1 Appendix

Neben den Ergebnissen, welche in der obigen Publikation veröffentlicht wurden, wurde noch eine Reihe weiterer Experimente mit dem neuen Liganden  $H_4L1$  ( $H_4$ Ditatom) durchgeführt.

Berücksichtigt man bei der Synthese neuer MOFs nur geometrische Aufbauprinzipien, so kann man sich der Einfachheit halber Liganden als Brücken zwischen Metallzentren vorstellen und auf diese Weise neue MOFs „designen“. <sup>49</sup> Der Ligand  $H_4L1$  kann dabei als eine Brücke dargestellt werden, wie sie in Abbildung 16 dargestellt ist.

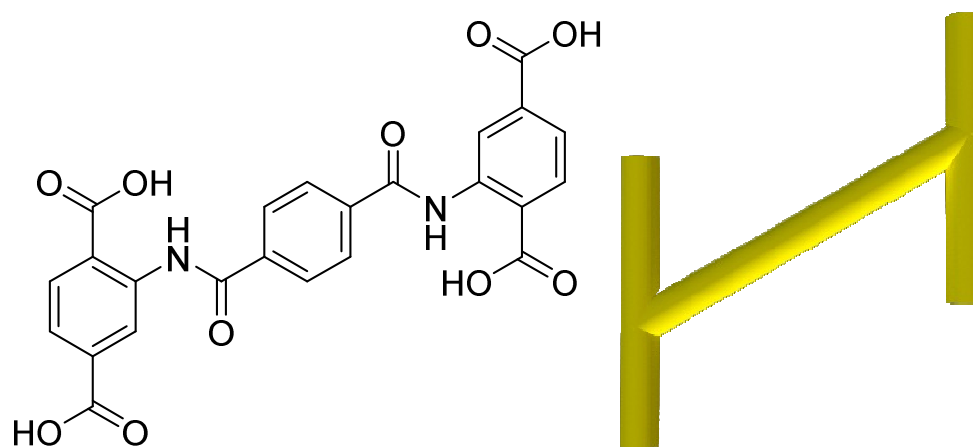


Abbildung 16. Ligand  $H_4L1$  und seine schematische Darstellung als „Brücke“.

Mit den Metallzentren als verbindende Knotenpunkte lassen sich eindimensionale Strukturen darstellen (Abbildung 17a). Verknüpft man diese jetzt über einen neutralen, linearen Co-Liganden, z. B. DABCO, 4,4'-Bipyridin oder Pyrazin, lassen sich in der Theorie zwei- und dreidimensionale Strukturen verwirklichen (Abbildung 17b/c).

In der Praxis ließen sich bei allen Versuchen mit einem Co-Liganden jedoch keine kristallinen Koordinationsnetzwerke ausbilden. Es existiert höchstwahrscheinlich nur ein ungeordnetes Netzwerk, welches zu den in der Publikation veröffentlichten Metallo- und Aerogelen sowie dem dort vorhandenen Mikrostrukturvorschlag führt und die flüssige Phase immobilisiert.



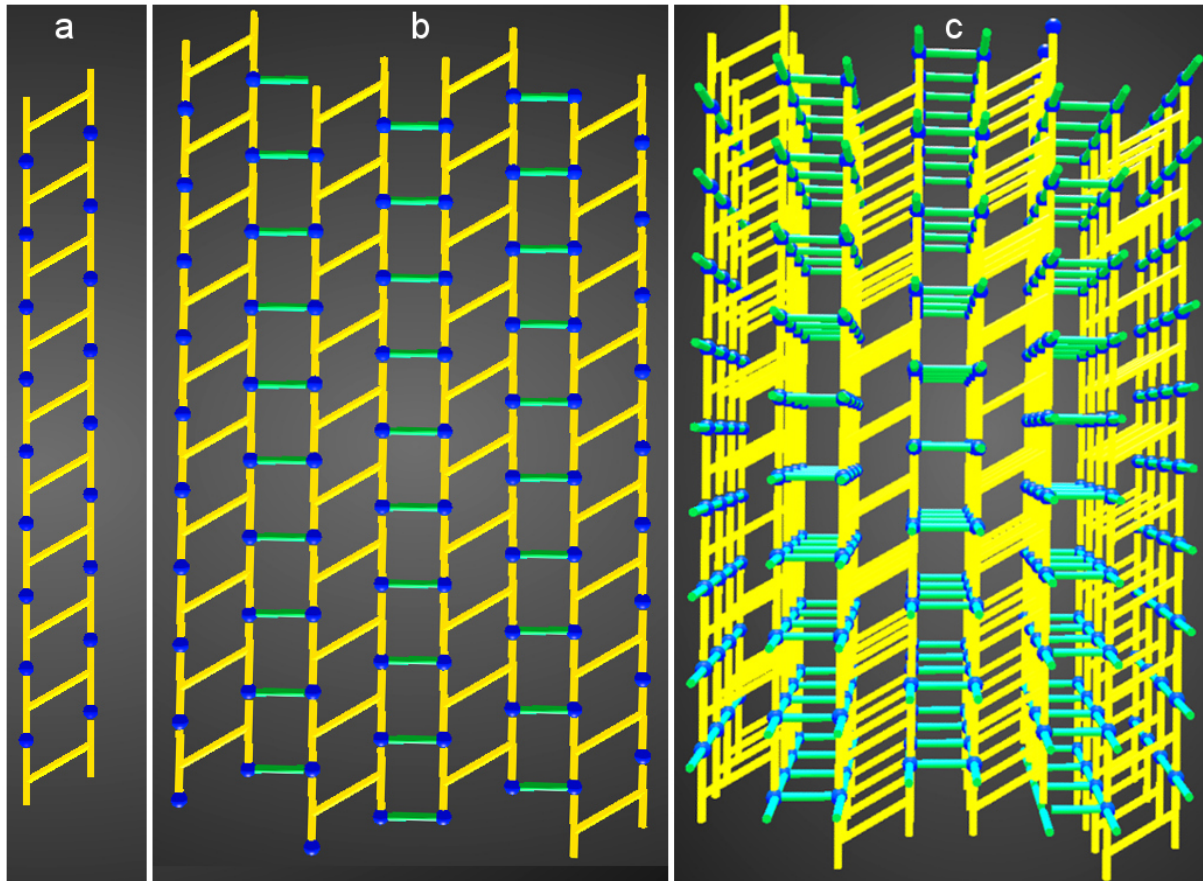
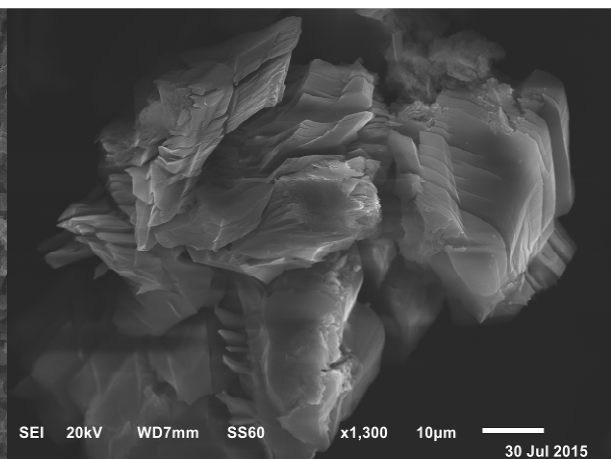
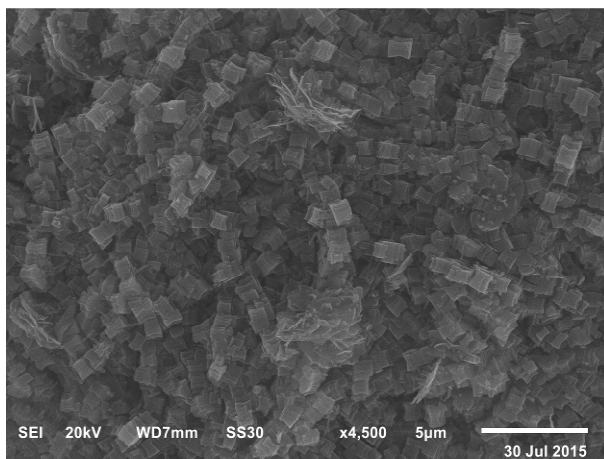
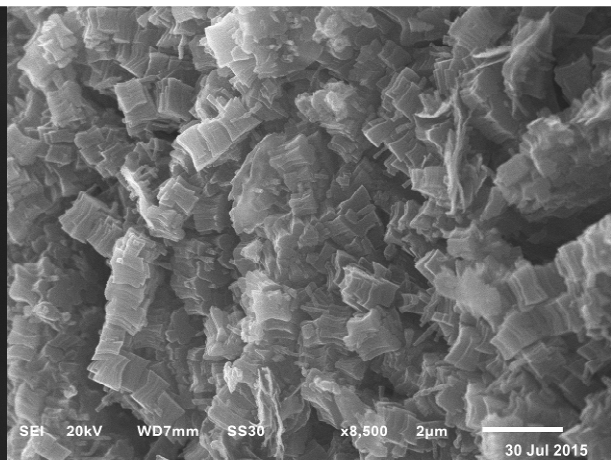
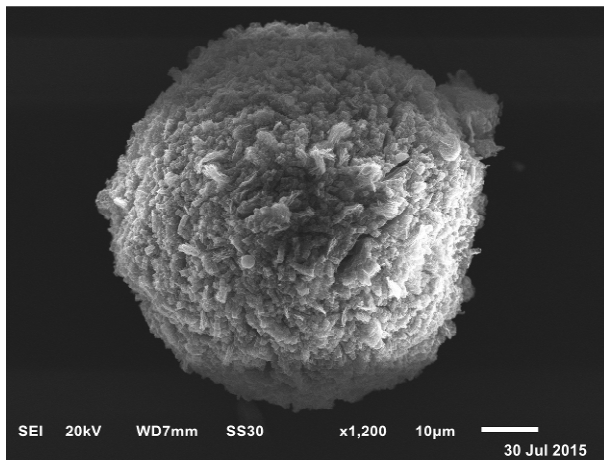
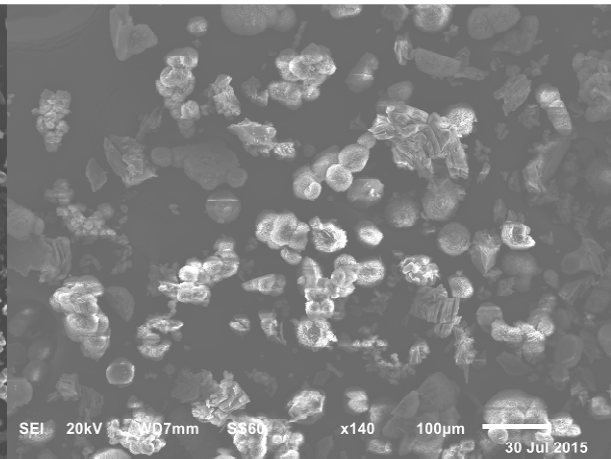
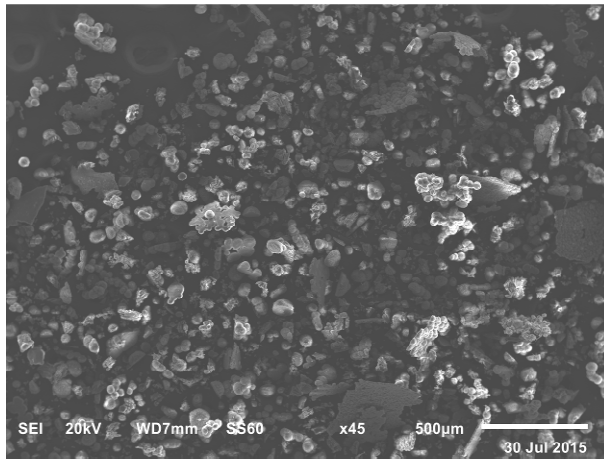


Abbildung 17.  $H_4L1$  in verschiedenen geometrischen Aufbauten. Der Ligand ist gelb gefärbt, das Metallzentrum blau, neutrale Co-Liganden hellgrün. (a)  $H_4L1$  in einer „eindimensionalen“ Kettenstruktur. (b) Über einen neutralen Co-Liganden zweidimensional verknüpfte Ketten. (c) Dreidimensionales Koordinationsnetzwerk basierend auf  $H_4L1$  und einem neutralen Co-Liganden.

Co(III), welches in der Publikation im wässrigen basischen Medium ein Gel bildete (Co-L1), wurde selbstverständlich auch in Synthesen verwendet, welche ähnlich zu denen der dimethylformamidhaltigen Gele waren. Es bildete sich hierbei allerdings kein gelartiges Material, sondern ein Feststoff. In der EDX-Analyse zeigte sich, dass Co(III) ungefähr im erwarteten Verhältnis eingebaut wurde (Tabelle 1). In den Rasterelektronenmikroskopaufnahmen war ein Material zu sehen, welches eine gewisse Regelmäßigkeit aufwies (Abbildung 18). Die dazugehörigen Röntgenpulverdiffraktogramme wurden allerdings unsorgfältig aufgenommen, weshalb nicht sicher von Kristallinität ausgegangen werden kann.



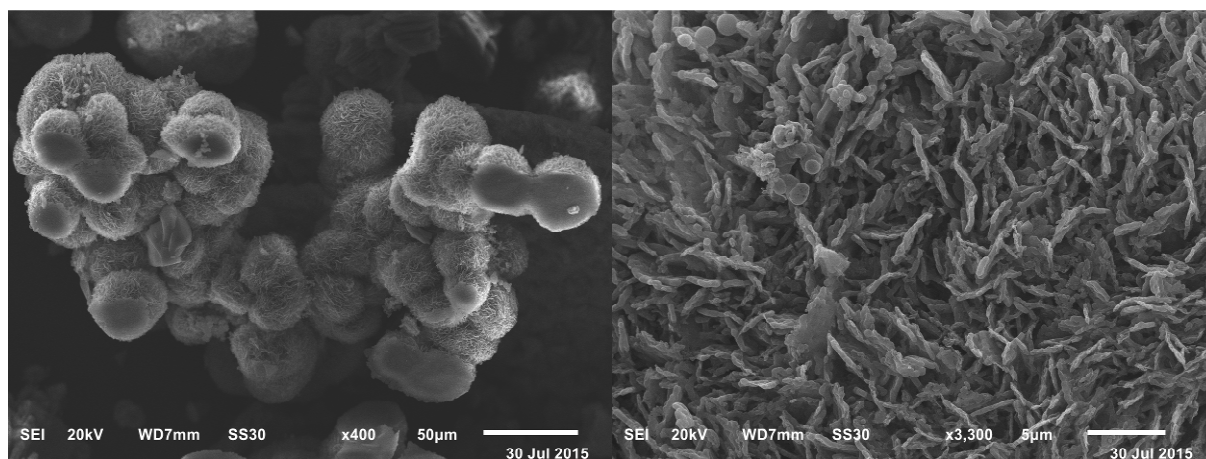


Abbildung 18. Rasterelektronenmikroskopaufnahmen von **Co-L1**, welches in Dimethylformamid synthetisiert wurde.

Tabelle 1. EDX-Analyseergebnisse von **Co-L1**.

Element	Normierte At.% aus EDX-Analyse	Berechnete At.% <sup>a</sup>
C	61,7	64,3
O	25,3	26,8
N	5,9	5,4
Co	7,1	3,6

<sup>a</sup> Bei einem molaren Metall:Ligand-Verhältnis von 4:3.

In weiteren Synthesen wurden die Metalle Mn(II), Fe(III), Ni(II), Cu(II) und Zn(II) eingesetzt. Die EDX-Analysen lassen darauf schließen, dass nur bei der Synthese mit Zn(II) die erwarteten Mengen an Metall eingebaut werden (Tabelle 2). Abbildung 19 zeigt Aufnahmen der Materialien mit Mn(II), Fe(II), Ni(II) und Cu(II).

Röntgenpulverdiffraktogramme des synthetisierten Materials mit Zn(II) zeigen, dass es sich dabei nicht um den Liganden oder um literaturbekannte Verbindungen handelt (Abbildung 21). In den Rasterelektronenmikroskopaufnahmen der Verbindungen lässt sich eine schichtartige Struktur erkennen (Abbildung 20).

Tabelle 2. EDX-Analyseergebnisse der verschiedenen Synthesen mit H<sub>4</sub>L1 und diversen Metallionen in Dimethylformamid.

Element	At.% exp. Mn(II)	At.% exp. Fe(II)	At.% exp. Ni(II)	At.% exp. Cu(II)	At.% exp. Zn(II)	Berechnete At.% <sup>a</sup>
C	63,5	57,7	63,3	78,5	68,8	64,3
O	21,3	23,6	11,8	11,9	17,4	26,8
N	5,9	4,4	3,3	8,7	8,2	5,4
M	9,3	14,3	21,6	0,9	5,6	3,6

<sup>a</sup> Bei einem Metall:Ligand-Verhältnis von 2:1.

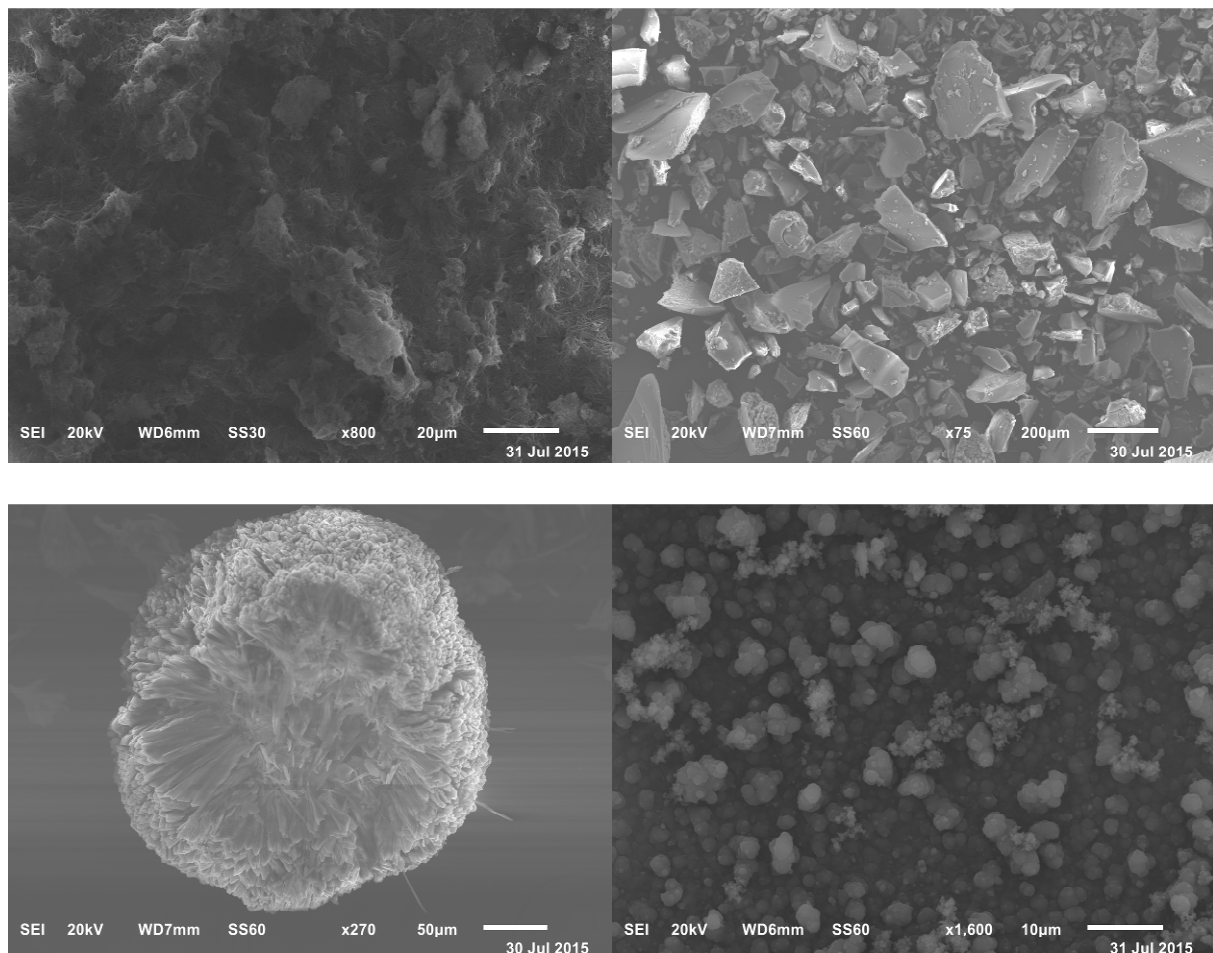


Abbildung 19. Rasterelektronenmikroskopaufnahmen von **Cu-L1** (oben links), **Fe-L1** (oben rechts), **Mn-L1** (unten links) und **Ni-L1** (unten rechts).

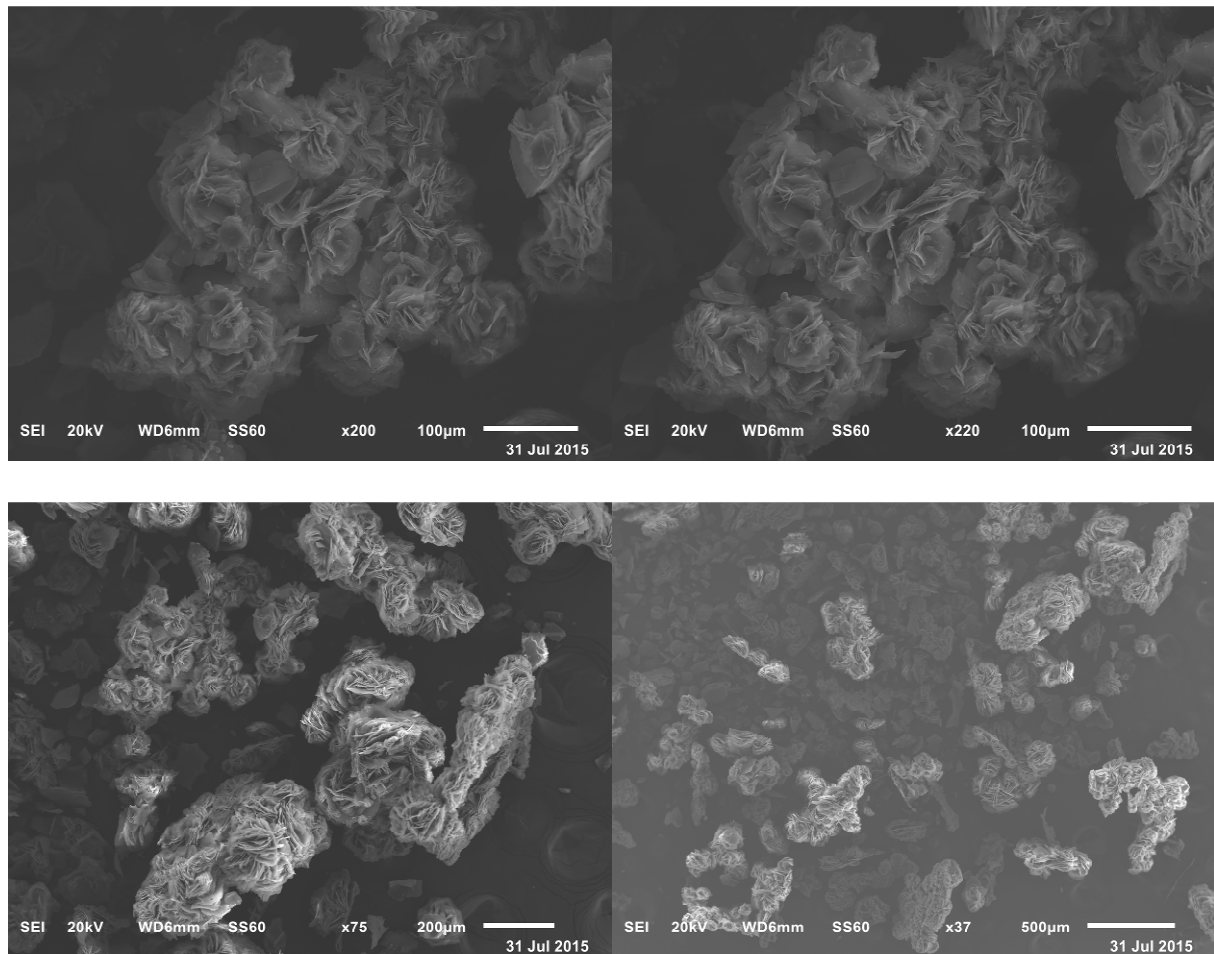


Abbildung 20. Rasterelektronenmikroskopaufnahmen von **Zn-L1** bei verschiedenen Vergrößerungen.

Alle Versuche, die Kristalle deutlich zu vergrößern und für die Einkristallstrukturanalyse zu verwenden waren jedoch erfolglos.

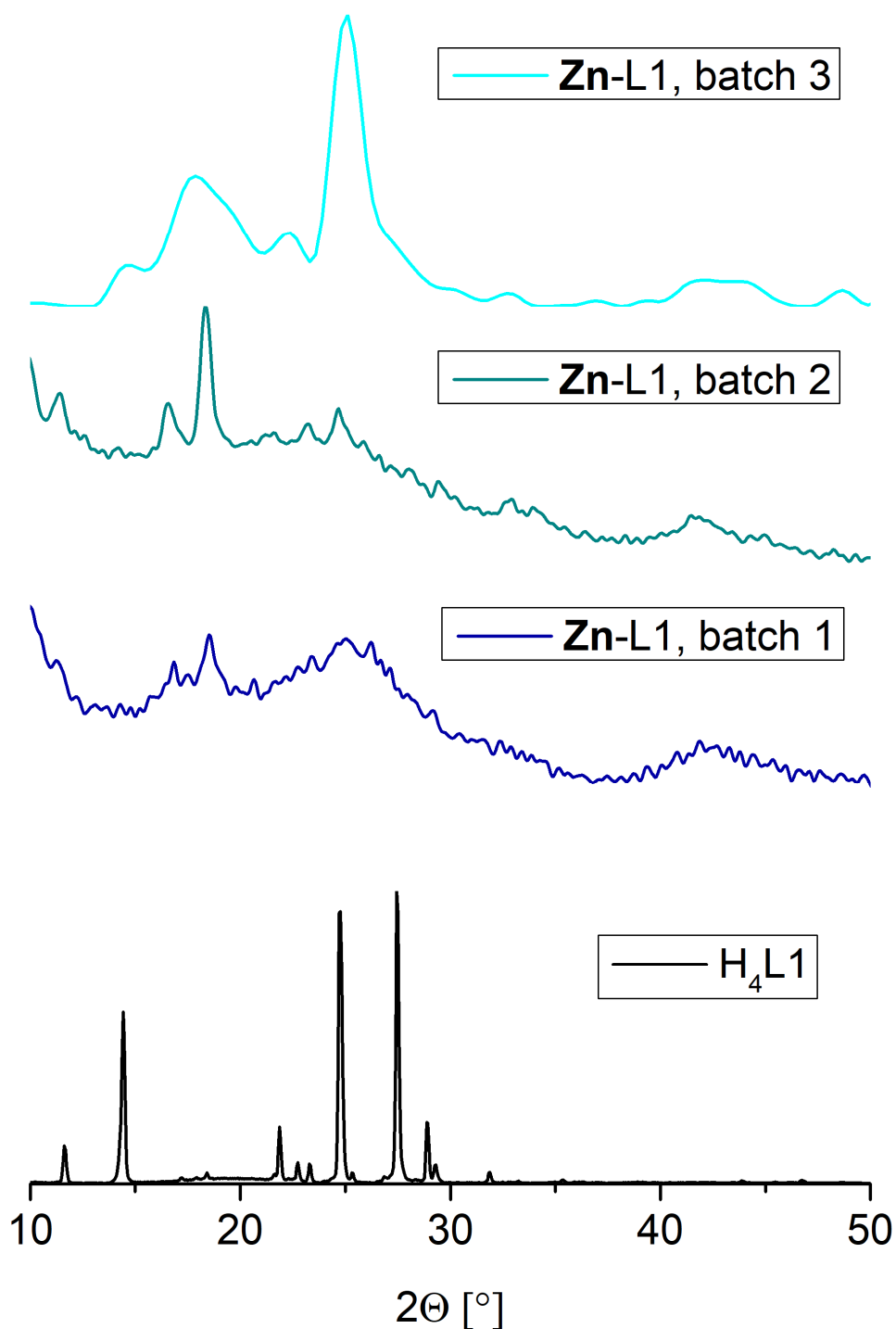


Abbildung 21. Röntgenpulverdiffraktogramme von  $H_4L1$  und der Verbindungen mit Zn(II).

Entsprechend der Synthese von **Co-L1** in der Publikation wurden ähnliche Experimente auch noch mit anderen Metallsalzen getestet. Dazu wurde in der Ligand

zusammen mit einem Metallsalz in 25%-igem Ammoniumhydroxid gelöst und anschließend das Gefäß zum langsamen Abdampfen des Ammoniaks offen stehen gelassen.

Bei den Ansätzen mit den Metallen Zn(II), Cu(II), Cu(I), Co(II) und Ni(II) wurden Niederschläge erhalten. Diese Niederschläge zeigten eine dem Metallion entsprechende Färbung. Bei Cr(III) lagen Metallsalz und ein weißer Niederschlag nebeneinander vor, da sich das Chromnitrat nicht in der Ammoniumhydroxidlösung auflösen ließ (Abbildung 22).

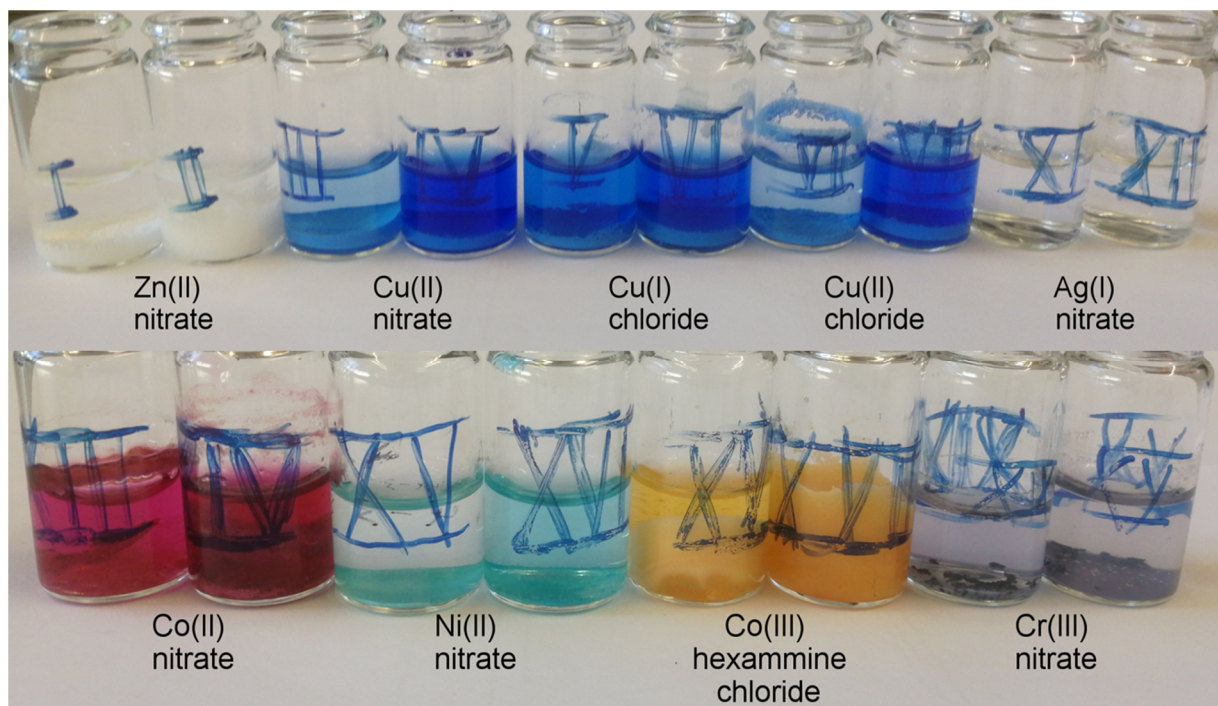


Abbildung 22. **Co-L1** nachempfundene Ansätze mit verschiedenen Metallsalzen nach Abdampfen des Ammoniaks. Der Ansatz **Co-L1** ist hier ebenfalls zu sehen, über der Bildbeschriftung „Co(III) hexammine chloride“. Be den Ansätzen mit Ag(I) und Cr(III) konnten als einzige keine Niederschläge erhalten werden.  $\text{Cr}(\text{NO}_3)_3 \cdot 9\text{H}_2\text{O}$  erwies sich als unlöslich.

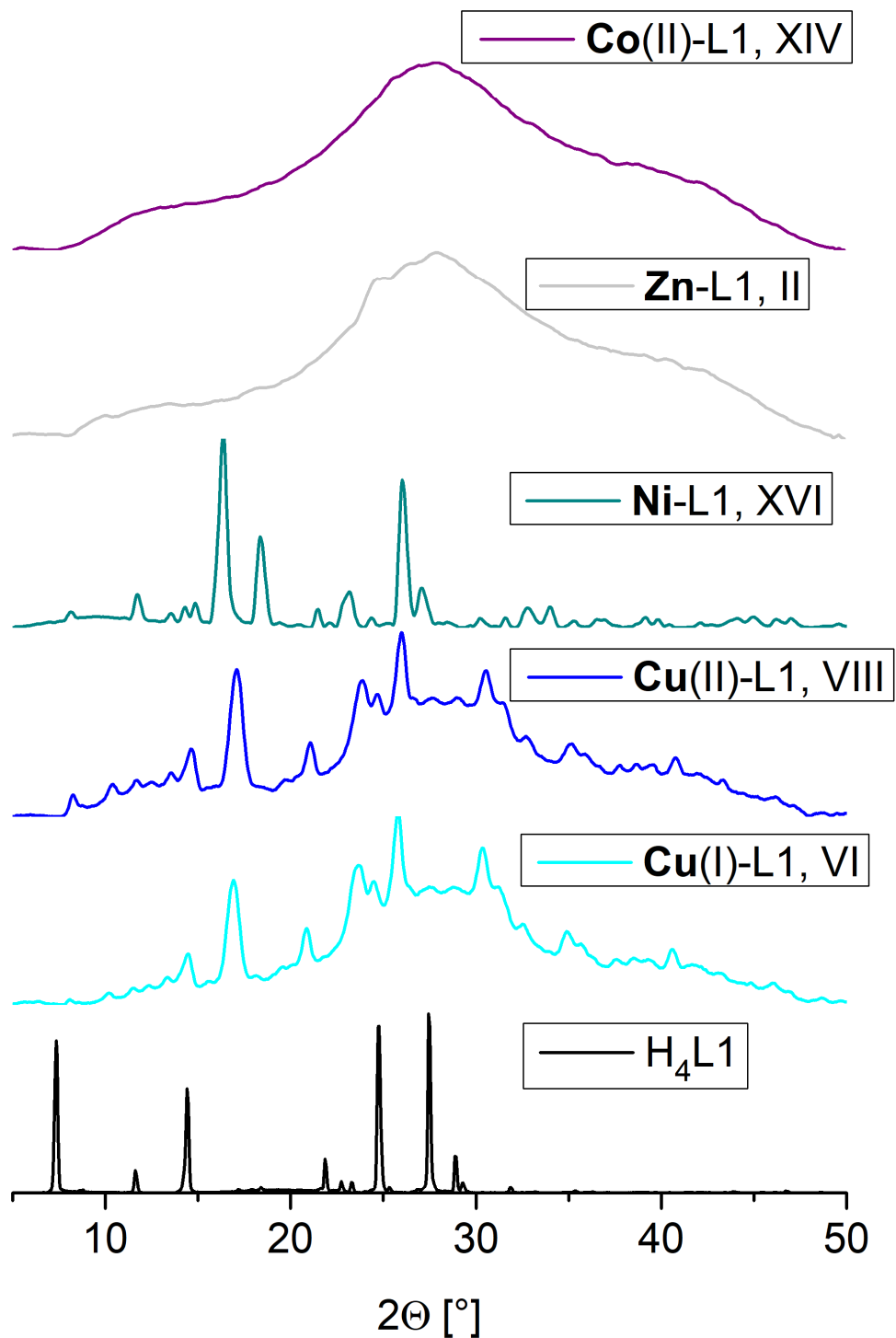


Abbildung 23. Röntgenpulverdiffraktogramme der Co-L1 nachempfundenen Ansätze mit verschiedenen anderen Metallionen.

Röntgenpulverdiffraktogramme der Niederschläge zeigen für Cu(I), Cu(II) und Ni(II), dass diese Verbindungen kristallin sind und ihr Diffraktogramm nicht dem des freien



Liganden entspricht. Die Niederschläge mit Co(II) und Zn(II) zeigen keinerlei Reflexe. Ähnlich wie auch mit Co(III) ist der Niederschlag mit Co(II) leicht gelartig, allerdings sehr unregelmäßig. Die Niederschläge mit den Cu-Ionen sind deutlich voluminöser als die mit Ni(II), in beiden Fällen ergibt sich ein Diffraktogramm, welches nicht mit literaturbekannten Diffraktogrammen übereinstimmt. Da keine Analysen über den tatsächlichen Metallgehalt durchgeführt und keine Kristalle einer entsprechenden Größe erhalten wurden, welche für die Einkristallröntgenstrukturanalyse verwendet werden können, lässt sich allerdings nicht bestimmen, ob es sich hierbei tatsächlich um Koordinationspolymere oder einfache Einschlussverbindungen handelt. Die Metallsalze wurden für gewöhnlich im Überschuss eingesetzt, jedoch wurden die Lösungen mit Cu(I), Cu(II) und Ni(II) deutlich entfärbt.

In weiteren Tests mit dem Liganden wurden Variationen in der Synthese der Cr- und Al-Metallogele durchgeführt. Durch Beimengen eines zweiten Lösemittels sollte unter anderem die Gelbildung unter Bevorzugung von Kristallbildung unterdrückt werden. Da dies bei erhöhter Temperatur nicht gelang, wurde eine Methode gewählt, bei welcher die vorbereiteten Mischungen in einem Exsikkator einer triethylaminhaltigen Atmosphäre ausgesetzt wurden. Wie in Abbildung 24 zu sehen ist, hat das Beimengen von Ethanol keinen Einfluss auf die Gelbildung. Mit *N*-Methylpyrrolidon (NMP) verfärbt sich das Cr-Metallogel, die Stabilität scheint jedoch nicht beeinflusst zu sein. Die Lösemittel DMA, DMSO und Wasser stören die Cr-Gelbildung deutlich. Bei den Al-Gelen sieht es ähnlich aus, die Gelbildung wird allerdings durch NMP stärker gestört, durch DMA und DMSO weniger. In keinem der Ansätze waren kristalline Niederschläge zu beobachten.

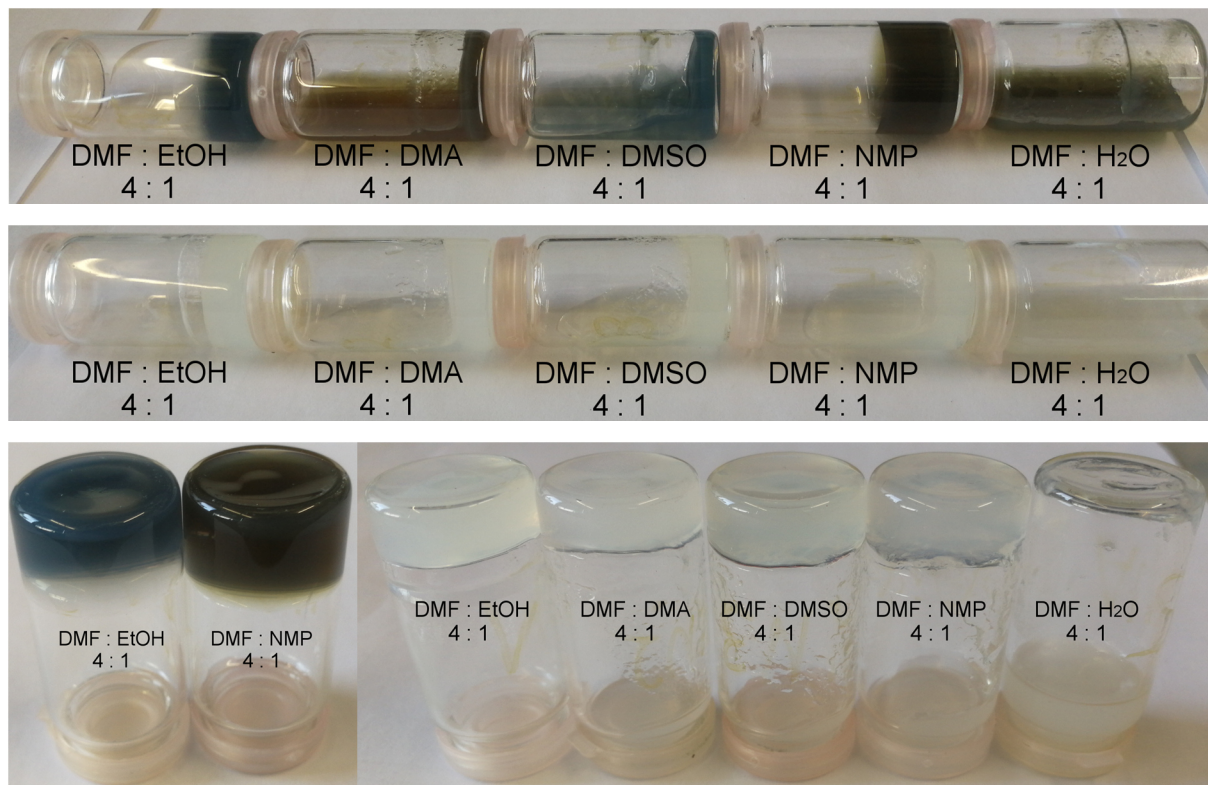


Abbildung 24. In einer triethylaminhaltigen Atmosphäre und bei Raumtemperatur synthetisierte Cr- und Al-Metallogele unter Beimengung eines zweiten Lösemittels. Die grünen und braungrünen Gele enthalten Cr(III), die farblosen Gele Al(III).

### **3.2 Luminescent Metal-Organic Framework Mixed-Matrix Membranes from Lanthanide Metal-Organic Frameworks in Polysulfone and Matrimid**

Janina Dechnik, Friedrich Mühlbach, Dennis Dietrich, Tobias Wehner, Marcus Gutmann, Tessa Lühmann, Lorenz Meinel, Christoph Janiak, Klaus Müller-Buschbaum

Zwei lumineszente, feuchtigkeitsempfindliche Lanthanoid-MOFs wurden unter inerten Bedingungen in die Polymere Polysulfon und Matrimid eingelagert und als Mixed-Matrix-Membranen auf ihre lumineszenten und fluoreszenten Eigenschaften untersucht. Die zerstörungsfreie sowie homogene Einbettung wurde mittels Röntgenpulverdiffraktogrammen sowie Rasterelektronenmikroskopie nachgewiesen und die Zusammensetzung der Membranen über energiedispersive Röntgenanalyse bestimmt. Die Defektfreiheit der Membranen wurde anschließend über Sauerstoffpermeationsmessungen bewiesen. Diese Arbeit stellt die erste erfolgreiche zerstörungsfreie Einbettung von lumineszenten, feuchtigkeitsempfindlichen MOFs in Polymeren dar.

Anteile an der Veröffentlichung:

- Entwicklung einer Kammer zum inerten Herstellen von MMMs, welche die Publikation überhaupt erst ermöglicht hat.
- Digitalisierung der Einzelgaspermeationsanlage für hochpräzise Messungen.
- Experimentelle Arbeiten und Analytik in der Rasterelektronenmikroskopie und anteilig an der Membranherstellung und Gaspermeation, Fotos der Membranen unter UV-Licht.
- Aufarbeiten der Ergebnisse und Verfassen des Abschnitts über Rasterelektronenmikroskopie und energiedispersive Röntgenanalyse. Korrekturen durch Herrn Prof. Dr. Christoph Janiak.
- Gaspermeations-, Röntgenpulverdiffraktogrammmessungen und -auswertungen sowie Membranherstellung anteilig durch Frau Janina Dechnik.

- Lumineszenzspektroskopie und Fluoreszenzmikroskopie sowie Verfassen des restlichen Manuskripts durch die übrigen Kooperationspartner.



## MOF Polymer Membranes

## Luminescent Metal–Organic Framework Mixed-Matrix Membranes from Lanthanide Metal–Organic Frameworks in Polysulfone and Matrimid

Janina Dechnik,<sup>[a]</sup> Friedrich Mühlbach,<sup>[b]</sup> Dennis Dietrich,<sup>[a]</sup> Tobias Wehner,<sup>[b]</sup> Marcus Gutmann,<sup>[c]</sup> Tessa Lühmann,<sup>[c]</sup> Lorenz Meinel,<sup>[c]</sup> Christoph Janiak,<sup>\*,[a]</sup> and Klaus Müller-Buschbaum<sup>\*,[b]</sup>

**Abstract:** Metal–organic framework/polymer (MOF–polymer) mixed-matrix membranes (MMMs) have been prepared by embedding the luminescent lanthanide (Ln) MOFs  $^3_{\infty}[\text{Sr}_{0.9}\text{Eu}_{0.1}\text{Im}_2]$  and  $^2_{\infty}[\text{Tb}_2\text{Cl}_6(\text{bipy})_3]\cdot 2\text{bipy}$  ( $\text{Im}^- = \text{imidazolate}$ ,  $\text{bipy} = 4,4'$ -bipyridine) into polysulfone (PSF, Ultrason® S) and Matrimid® polymer films. The successful embedding of the Sr and Eu MOFs has been achieved for both matrixes, and the original MOF luminescence is maintained. The defect-free nature of the membranes was proven by the slightly lower gas permeation of the MMMs with the dense filler particles. For the Tb–bipy MOF, successful embedding is possible for polysulfone only. For the preparation of the MOF polymer membranes, the influence of

different mass fractions of the luminescent MOFs ranging from 8–16 wt.-% and preparation from suspensions with and without ultrasonic radiation were studied. The influence of the MOF fraction is different for both membrane materials. For the polysulfone, lower amounts of MOF are preferable and lead to an increase of the overall luminescence intensity, whereas the opposite was observed for Matrimid. Altogether, the parity-allowed emission of the  $\text{Eu}^{2+}$  ions is apparently stronger than the  $\text{Tb}^{3+}$  emission and leads to membranes with strong emission that is visible to the naked eye under normal daylight. Thereby, the Ln MOF polymer membranes open new options for the handling of luminescent MOFs.

## Introduction

Coordination polymers and metal–organic frameworks (MOFs) are a high research priority in coordination chemistry.<sup>[1]</sup> These hybrid materials exhibit a broad variety of physical properties,<sup>[2]</sup> and photoluminescence<sup>[3]</sup> and sensing are current focusses.<sup>[4]</sup> For the application of MOFs, as well as the availability of pure bulk materials, stability and processability play important roles. For technical applications, MOFs have to be formulated,<sup>[5]</sup> for example, as layers,<sup>[6]</sup> pressed into tablets,<sup>[7]</sup> fabricated into monolithic structures<sup>[8]</sup> or used as composite materials.<sup>[9]</sup> MOFs can also be luminescent as nanoparticles<sup>[10]</sup> or in thin films.<sup>[11]</sup>

MOF–polymer mixed-matrix membranes (MMMs) are established composites and have been investigated widely for gas separations.<sup>[12–15]</sup>

Among luminescent MOFs and coordination polymers, lanthanide-containing (Ln containing) compounds<sup>[16]</sup> are of

special interest for photoluminescence owing to their beneficial photophysical properties through suitable metal–ligand combinations.<sup>[17]</sup> Effective  $\text{Ln}^{3+}$  luminescence is achieved by circumventing the low light-absorption coefficients of the  $4f-4f$  transitions through the combination of the  $\text{Ln}^{3+}$  ions with suitable organic light-harvesting ligands that work as sensitizers for the metal emission (the so-called “antenna effect”)<sup>[18]</sup> by transferring excitation energy from the ligand to the metal centers. MOFs with N-donor ligands, such as the series  $^2_{\infty}[\text{Ln}_2\text{Cl}_6(\text{bipy})_3]\cdot 2\text{bipy}$ <sup>[19]</sup> ( $\text{bipy} = 4,4'$ -bipyridine), show effective antenna effects, as the energetic position of the singlet and triplet states<sup>[20]</sup> of the ligand in the coordination polymer matches with suitable excited metal states.<sup>[21]</sup> For example, the linker 1,2-di(4-pyridyl)ethylene exhibits both structural and electronic properties for the formation of coordination polymers with effective photoluminescence. In principle, the energetic positions of the involved excited ligand states<sup>[22]</sup> are exactly in the range for the possible sensitization of the lanthanide ions for visible or near-infrared emission.<sup>[23]</sup> Another option, although much less frequent for MOFs, is the use of the divalent  $\text{Eu}^{2+}$  ion, which utilizes  $5d-4f$  transitions. These transitions are parity-allowed and strong; therefore, they do not require ligand sensitization, as the series  $^3_{\infty}[\text{Sr}_{1-x}\text{Eu}_x\text{Im}_2]$  shows ( $\text{Im}^- = \text{imidazolate}$ ).<sup>[24]</sup>

As a proof-of-principle, we show here that it is possible to embed luminescent MOFs into organic polysulfone (PSF) Ultrason® S 6010 and Matrimid® 5218 polymers and generate, to the best of our knowledge, the first luminescent MOF mixed-matrix

[a] Institut für Anorganische Chemie und Strukturchemie, Universität Düsseldorf, Universitätsstraße 1, 40225 Düsseldorf, Germany  
E-mail: Christoph.Janiak@uni-duesseldorf.de  
<http://www.janiak.hhu.de/>

[b] Institut für Anorganische Chemie, Universität Würzburg, Am Hubland, 97074 Würzburg, Germany  
E-mail: k.mueller-buschbaum@uni-wuerzburg.de

[c] Institut für Pharmazie und Lebensmittelchemie, Universität Würzburg, Am Hubland, 97074 Würzburg, Germany

Supporting information and ORCID(s) from the author(s) for this article are available on the WWW under <http://dx.doi.org/10.1002/ejic.201600235>.

membranes (see Figure 1). The LnMOF@MMMs have been characterized by photoluminescence spectroscopy, X-ray powder diffraction, electron microscopy, energy-dispersive X-ray (EDX) analysis, gas permeation, and fluorescence microscopy.

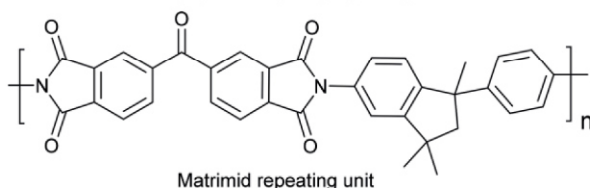
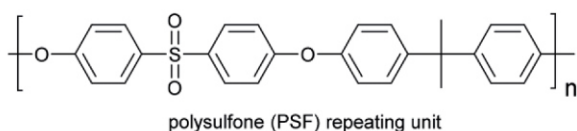
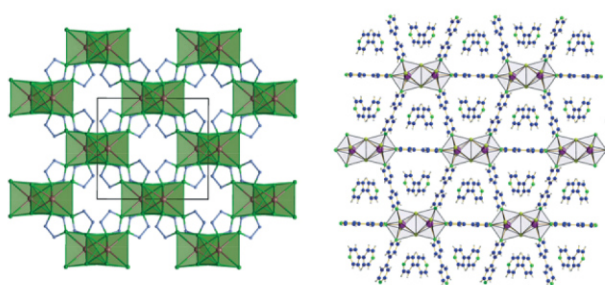
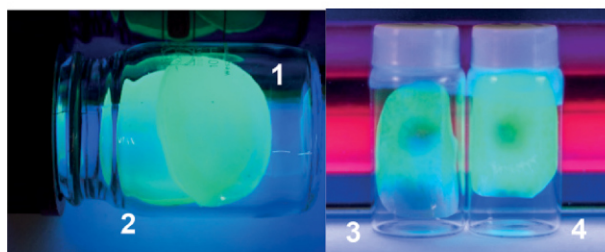


Figure 1. Top: The luminescent MOF MMMs  $^3_{\infty}[\text{Sr}_{0.9}\text{Eu}_{0.1}\text{Im}_2]@\text{PSF}$  (**1**: 8 wt.-% MOF; **2**: 16 wt.-% MOF) and  $^3_{\infty}[\text{Sr}_{0.9}\text{Eu}_{0.1}\text{Im}_2]@\text{Matrimid}$  (**3**: 8 wt.-% MOF; **4**: 16 wt.-% MOF). Center: The structures of the MOFs  $^3_{\infty}[\text{Sr}_{0.9}\text{Eu}_{0.1}\text{Im}_2]$  (left) and  $^2_{\infty}[\text{Ln}_2\text{Cl}_6(\text{bipy})_3]\cdot 2\text{bipy}$  (right), adapted from ref.<sup>[3f]</sup> with permission of the Royal Society of Chemistry, 2013. Bottom: PSF Ultrason® 5 and Matrimid®.

PSF<sup>[25]</sup> and Matrimid<sup>[26]</sup> are low-flux glassy polymers for gas-separation applications. Both polymers were chosen because of their good mechanical properties and availability. They are well-known to have good film-formation properties and are suitable matrixes for MMMs with MOFs as filler materials.<sup>[13]</sup>

The fillers are sensitive to hydrolysis and oxidation, which results in the loss of luminescence. To expand their processability for practical applications through embedding in or coating with a convenient polymer, the moisture stability of these compounds is expected to be enhanced.<sup>[27]</sup>

## Results and Discussion

### Preparation of LnMOF@polysulfone and LnMOF@Matrimid MMMs

For membrane preparation, the chosen amounts of MOF and polymer were combined under nitrogen in dichloromethane (DCM) and treated (by stirring or ultrasound) to form homogeneous dispersions (see Exp. Sect. for details). The dispersion was

cast into metal rings on a flat glass surface in a desiccator filled with nitrogen gas and a desiccant. The conditions for film formation were chosen in terms of polymer concentration to influence the viscosity of the casting solution and time of stirring to form a homogeneous dispersion of the fillers in the casting solution. These factors are essential in the formation of defect-free MMMs with good filler dispersion. The solvent was evaporated overnight with a slight stream of predried nitrogen gas. The membrane was finally dried at 25 °C under reduced pressure. Eight different membranes of 5 cm diameter with 8 and 16 wt.-% MOF in ca. 200 mg of polymer were prepared this way (Table 1; see also Figure 1).

Table 1. Overview of prepared membranes.<sup>[a]</sup>

MOF@polymer	8 wt.-%	16 wt.-%
$^3_{\infty}[\text{Sr}_{0.9}\text{Eu}_{0.1}\text{Im}_2]@\text{PSF}$	<b>1</b>	<b>2</b>
$^3_{\infty}[\text{Sr}_{0.9}\text{Eu}_{0.1}\text{Im}_2]@\text{Matrimid}$	<b>3</b>	<b>4</b>
$^3_{\infty}[\text{Sr}_{0.9}\text{Eu}_{0.1}\text{Im}_2]@\text{Matrimid}$ with ultrasound	<b>5</b> <sup>[b]</sup>	–
$^2_{\infty}[\text{Tb}_2\text{Cl}_6(\text{bipy})_3]\cdot 2\text{bipy}$ @PSF	<b>6</b>	<b>7</b>
$^2_{\infty}[\text{Tb}_2\text{Cl}_6(\text{bipy})_3]\cdot 2\text{bipy}$ @Matrimid	gel formation	gel formation
$^2_{\infty}[\text{Tb}_2\text{Cl}_6(\text{bipy})_3]\cdot 2\text{bipy}$ @PSF with ultrasound	<b>8</b> <sup>[b]</sup>	–

[a] Approximately 200 mg of polymer casted into 5 cm diameter membranes from 4 mL of  $\text{CH}_2\text{Cl}_2$  dispersion. [b] 200 mg of polymer casted from 2 mL of  $\text{CH}_2\text{Cl}_2$  dispersion.

### Characterization of LnMOF@polysulfone and LnMOF@Matrimid MMMs

#### Photoluminescence Spectroscopy

For all prepared MOF MMMs, excitation and emission spectra were recorded at room temperature. Both  $^3_{\infty}[\text{Sr}_{0.9}\text{Eu}_{0.1}\text{Im}_2]@\text{PSF}$  (**1** and **2**) and  $^3_{\infty}[\text{Sr}_{0.9}\text{Eu}_{0.1}\text{Im}_2]@\text{Matrimid}$  (**3** and **4**) show the typical excitation and emission spectra of their respective frameworks.<sup>[19,24]</sup> The membrane polymers were selected to allow MOF luminescence without interference with the polymer. For PSF, a weak fluorescence in the blue region is observed, whereas Matrimid does not show any significant luminescence. The combination of  $^3_{\infty}[\text{Sr}_{0.9}\text{Eu}_{0.1}\text{Im}_2]$  with PSF shifts the excitation away from the polymer to the lower energies of the allowed  $\text{Eu}^{2+}$  excitation (see Figures 2, 3, and S5).

Therefore, the spectra exhibit transitions between the 4f ground state and excited 5d states of the  $\text{Eu}^{2+}$  ions. The luminescence is turquoise-green and strong, and no participation of the membrane polymer is detected (see Figure 2). Owing to the geometric differences between the ground and excited states, the peaks are broad with half-widths of ca. 75 nm and maxima at  $\lambda = 498$  nm for **1** and **2** and  $\lambda = 500$  nm for **3** and **4**.

For Matrimid®, a slight shift is observed for the  $5d \leftarrow 4f$   $\text{Eu}^{2+}$  excitation maximum from  $\lambda = 315$  nm for the pure MOF to  $\lambda = 328$  nm for the MMMs. This may hint towards an impact of the organic polymer on the  $\text{Eu}$  5d states. However, the emission maxima and band profiles are similar within 2 nm. Moreover, the lifetimes of the luminescence processes give  $\text{Eu}^{2+}$  decay times  $\tau_{\text{obs}} = 609(4)$  and  $584(2)$  ns for the PSF membranes **1** and **2**, respectively, and  $\tau_{\text{obs}} = 620(2)$  and  $605(3)$  ns for the Matrimid membranes **3** and **4**, respectively. The similarities to the proper-

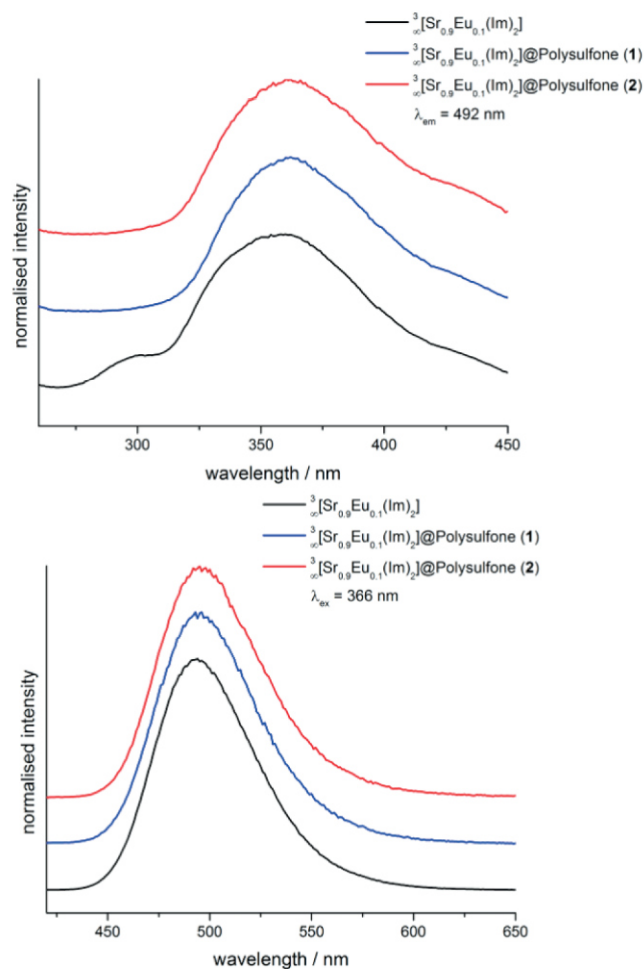


Figure 2. Normalized excitation (top) and emission spectra (bottom) of the framework  $^3\text{Sr}_{0.9}\text{Eu}_{0.1}(\text{Im})_2$  (black) in comparison with those of  $^3\text{Sr}_{0.9}\text{Eu}_{0.1}(\text{Im})_2$ @PSF (blue: **1**, red: **2**); the MOF luminescence is maintained after the MOF is embedded in the polysulfone membrane.

ties of the MOF itself are prominent; therefore, it is clear that the embedded framework is unaltered. This similarity was also present when the membranes were prepared from suspensions with [MMM **5**:  $\tau = 601(3)$  ns] or without ultrasonic radiation (MMMs **1–4**).

It is intriguing that the intensity of the MOF luminescence depends on the amount of MOF and the membrane matrix material. For polysulfone, an inversely proportional behavior is observed, and higher emission intensities are observed for the lower MOF fraction; therefore, the higher amount of 16 wt.-% leads to concentration quenching, whereas the lower MOF fraction of only 8 wt.-% gives a significantly higher luminescence intensity (see also Figure S1). For Matrimid<sup>®</sup>, the opposite behavior is observed, and the intensity increases as the MOF fraction increases (see Figure S2). Therefore, polysulfone and Matrimid differ in their concentration quenching, which is not reached for 16 wt.-% MOF in Matrimid. A comparison of the absolute intensities is possible on the basis of the otherwise identical sample and instrumentation parameters.

For the MOF  $^2\text{[Tb}_2\text{Cl}_6(\text{bipy})_3\text{]}\cdot 2\text{bipy}$ , the photoluminescence properties were determined for polysulfone membranes only, because of the gel formation of the MOF with Matrimid. For  $^2\text{[Tb}_2\text{Cl}_6(\text{bipy})_3\text{]}\cdot 2\text{bipy}$ @PSF (**6** and **7**), the typical luminescence

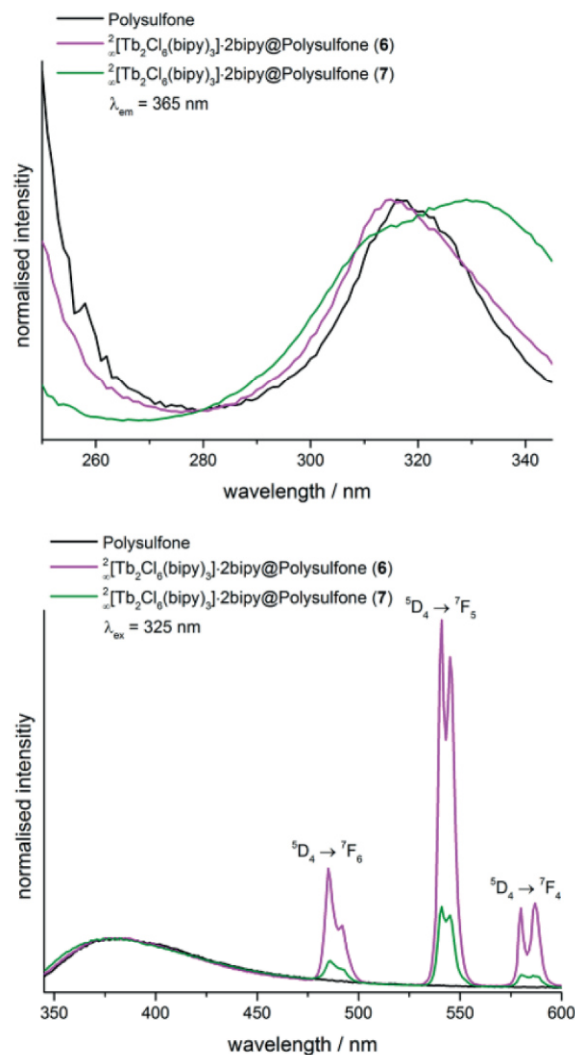


Figure 3. Excitation (top) and emission spectra (bottom) of the MMMs  $^2\text{[Tb}_2\text{Cl}_6(\text{bipy})_3\text{]}\cdot 2\text{bipy}$ @PSF (**6**: purple, **7**: green) normalized for polysulfone and in comparison with those of polysulfone without MOF (black). The emission indicates the dependence of the luminescence intensity on the amount of MOF.

of the MOF can again be observed.<sup>[24]</sup> It is attributed to the 4f–4f transitions of the  $\text{Tb}^{3+}$  ions ( $^5\text{D}_4 \rightarrow ^7\text{F}_J$ ,  $J = 6-0$ ) and leads to a green emission of the MOF. In addition, a broad emission of the PSF matrix is also visible in the blue region with a maximum at  $\lambda = 380$  nm. This is possible as the  $\text{Tb}^{3+}$  emission is less intense than the  $\text{Eu}^{2+}$  emission (see also Figures 3, S3, and S4).

The excitation spectra are again similar to that of the MOF and exhibit light absorption mainly by the 4,4'-bipyridine ligand together with weak excitation of the PSF matrix. A comparison of the excitation and emission spectra of the MMMs **6** and **7** with that of the pure MOF is shown in Figure 3. Again, the lower MOF weight fraction results in higher emission intensity, in agreement with the findings for the polysulfone MMMs **1** and **2**. The lifetimes of the luminescence process reflect the typical long decay times of  $\text{Tb}^{3+}$  ions; we observed biexponential decay times of 747(37) and 1253(32)  $\mu\text{s}$  for **5** and 763(22) and 1650(56)  $\mu\text{s}$  for **6**, and these values are again an excellent match with the behavior of the MOF itself.

### Powder X-ray Diffraction

The MOF-polymer membranes  $^3\text{[Sr}_{0.9}\text{Eu}_{0.1}\text{Im}_2]\text{@PSF}$  (**1**: 8 wt.-% MOF; **2**: 16 wt.-% MOF),  $^3\text{[Sr}_{0.9}\text{Eu}_{0.1}\text{Im}_2]\text{@Matrimid}$  (**3-5**), and  $^2\text{[Tb}_2\text{Cl}_6(\text{bipy})_3]\cdot 2\text{bipy}\text{@PSF}$  (**6-8**) were investigated by X-ray powder diffraction. The powder pattern for a successfully embedded MOF is expected to show the reflections of the crystalline MOFs together with a slight amorphous background from the polymer matrix.

As Figure 4 shows, the MOFs were indeed embedded successfully and without decomposition, whereas ultrasonication gave an ideal pattern only for  $^3\text{[Sr}_{0.9}\text{Eu}_{0.1}\text{Im}_2]\text{@Matrimid}$  (**5**) and induced decomposition for the Tb MMM **8** (see also Figure S13).

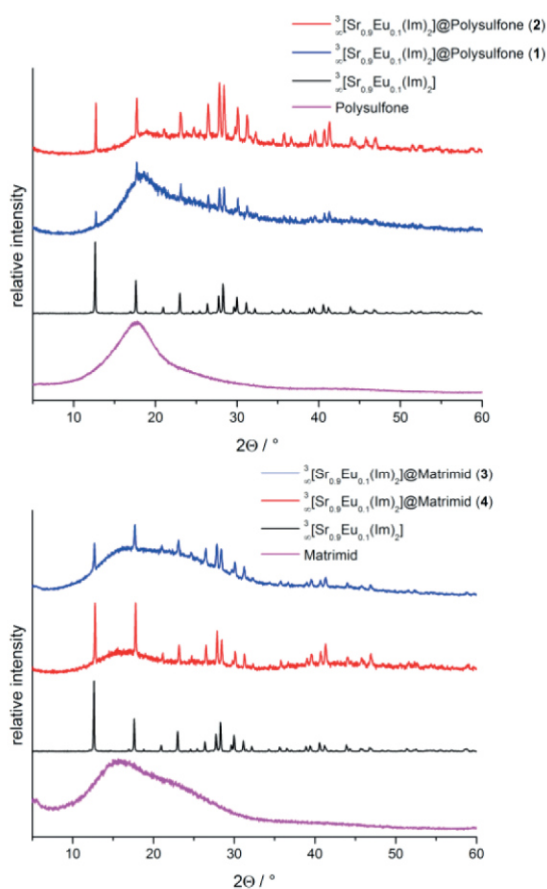


Figure 4. Comparison of the observed powder X-ray diffraction patterns of the mixed MOF membranes **1-4** at room temp. with the diffraction patterns of the pure MOF  $^3\text{[Sr}_{0.9}\text{Eu}_{0.1}\text{Im}_2]$ . The reflections of the MOF and the amorphous background of the polymer matrix can be observed.

Hence, the embedding of the MOF without ultrasonic treatment is mild enough to generate luminescent membranes with unaltered MOFs. Although both MOFs have exceptional thermal stabilities,<sup>[24,28]</sup> ultrasonic treatment provokes decomposition of the MOFs with the exception of the membrane **5**. Altogether, the suspension method without ultrasonication is preferable for stability reasons.

### Fluorescence Microscopy, SEM, and EDX

A combination of fluorescence microscopy, scanning electron microscopy (SEM), and element mapping by spatially resolved energy-dispersive X-ray spectroscopy (EDX) was applied for the

mixed-matrix membranes **1-7** to get information on the distribution of the MOF particles in the membranes. The complimentary character of these methods gives insights into the MOF distribution through their photophysical properties as well as imaging and elemental analysis.

High-resolution fluorescence microscopy was applied to the complete membranes **1-8** and the membranes without the MOFs (Figure 5). In addition to the overview, detailed point investigations at a high zoom level were also applied.

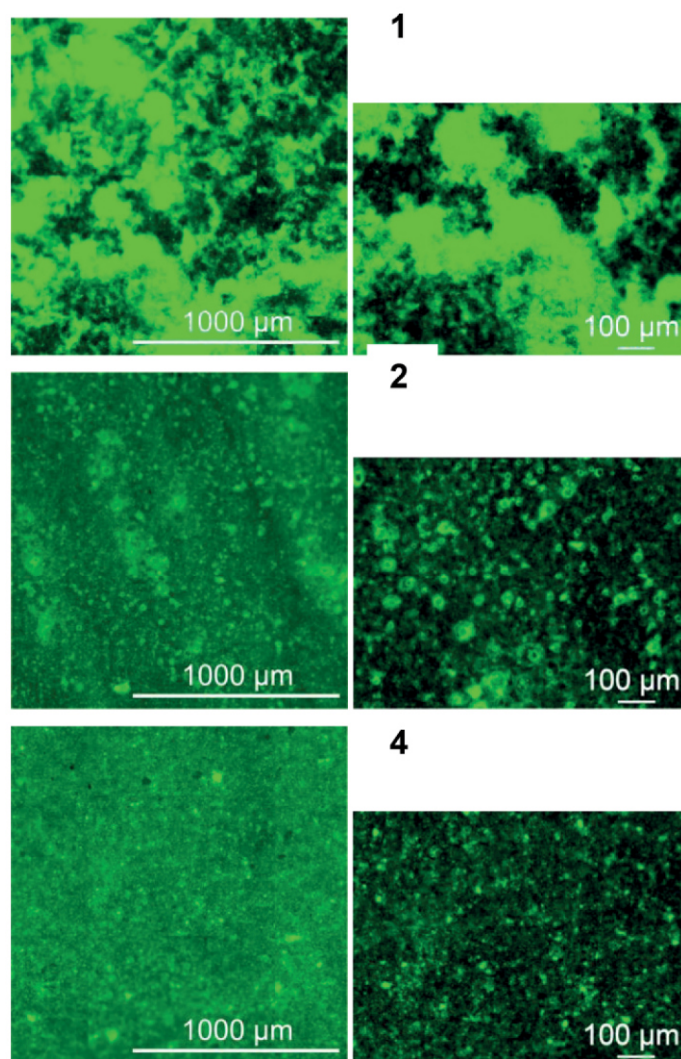


Figure 5. Fluorescence microscopy images of  $^3\text{[Sr}_{0.9}\text{Eu}_{0.1}\text{Im}_2]\text{@PSF}$  (**1**, top; **2**, center) and  $^3\text{[Sr}_{0.9}\text{Eu}_{0.1}\text{Im}_2]\text{@Matrimid}$  (**4**, bottom) showing the MOF distribution as an overview (left) and microscopic excerpt (right) of the fluorescence intensity (22 ms exposure each; views on membrane top). The images of membrane **1** do not reflect particle aggregation but extraordinarily high luminescence intensity; the particle size is the same as those of the other films. The emission is so bright that even the shortest recording times of 22 ms show an overflow.

Most prominent are the MMMs  $^3\text{[Sr}_{0.9}\text{Eu}_{0.1}\text{Im}_2]\text{@PSF}$  (**1** and **2**) as they show the highest fluorescence intensities of all membranes. The intensity reaches the detection maximum of the instrumentation for MMM **1** after an ultrashort exposure time of only 22 ms. In agreement with the photoluminescence spectroscopy observations, a concentration dependence applies



(see also Figures S5–S9 for fluorescence microscopy). The MOF particles are quite evenly distributed within the membrane.

The single MOF crystallites have an average size of 2–20  $\mu\text{m}$  in addition to aggregates of particles larger than 100  $\mu\text{m}$  if no ultrasonic radiation is applied during preparation. The particle size was estimated from a combination of SEM (Figures S11 and S12) and fluorescence microscopy (Figure 5 and S7–9). The impression of further aggregation for membrane **1** can be attributed to the high emission intensity, which reaches the detection limit; it is not a result of real aggregation.

To investigate the effect of the ultrasonic treatment, membrane **5** and the partly decomposed membrane **8** were studied (Figure S8–9). The membranes treated with ultrasound are weaker in luminescence intensity and also show less preferable MOF distribution; therefore, these results stress the importance of mild embedding conditions. The ultrasound-treated membranes show significant MOF degradation and gas inclusion. We are currently investigating the degradation reaction, and we could identify the formation of the hydrate  $\text{LnCl}_3 \cdot 6\text{H}_2\text{O}$  from the membranes and  $\text{LnO}(\text{OH})$  for the bulk MOFs. A further problem could be gel formation, as observed for the Tb–bipy MOF together with Matrimid.

The cross-section SEM images of membranes **1–4**, **6**, and **7** show good particle distribution and adhesion on a scale of 10–20  $\mu\text{m}$  for the MOFs with both polysulfone and Matrimid (Figure 6). At higher magnification, slight MOF particle aggregation was detected for membrane **3** (see Figure S10). The good MOF distribution is supported by element mapping through spatially resolved EDX analysis of the MMMs (Figure 7). A slight MOF sedimentation at the “bottom” of the casted membranes is revealed by the locally increased intensity of the mapped metals. Membrane **2** also showed a slight aggregation of MOF particles. Overall, the MOFs were well-distributed along the cross-section in the Eu and Tb MOF MMMs, and the EDX results confirmed the observations from the SEM images.

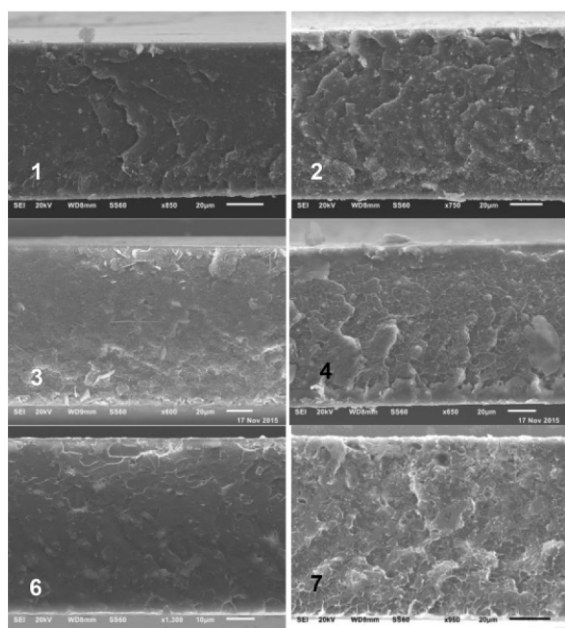


Figure 6. Cross-section SEM images of membranes **1–4**, **6**, and **7**.

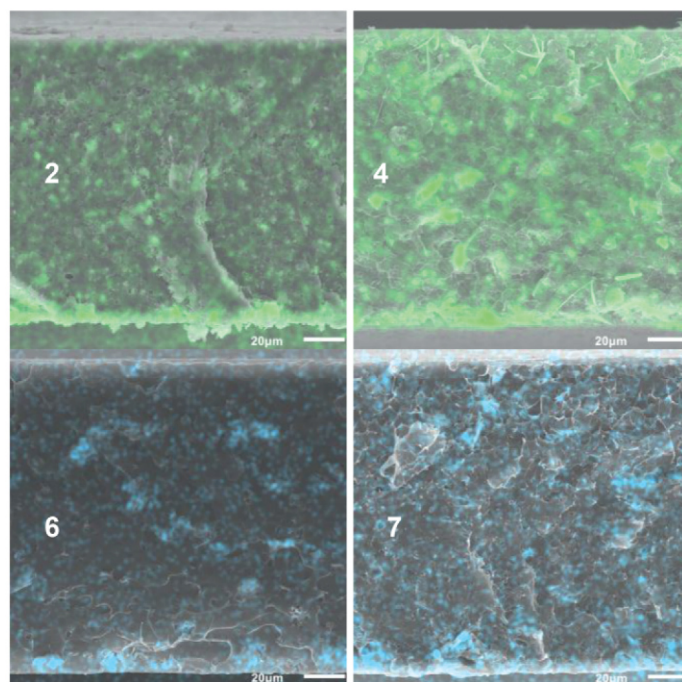


Figure 7. EDX element mapping of membranes **2**, **4**, **6**, and **7** showing the distribution of strontium (green) from  ${}^3\text{Sr}_{0.9}\text{Eu}_{0.1}\text{Im}_2$  and terbium (blue) from  ${}^2\text{Tb}_2\text{Cl}_6(\text{bipy})_3 \cdot 2\text{bipy}$ . The bottom of the images corresponds to the bottom of the casted membrane.

### Gas Permeation

Dioxygen gas-permeation experiments were performed to confirm that the membranes were defect-free and that the morphology at the polymer/particle interface was not defective, as defects would result in much higher gas fluxes compared with those of the pure polymers.<sup>[14c]</sup> These defects would result in a decrease of the stabilizing properties of the polymer film towards the MOFs. The gas-permeation measurements (Table 2) indicate that the MOF MMMs  ${}^3\text{Sr}_{0.9}\text{Eu}_{0.1}\text{Im}_2$ @PSF and  ${}^3\text{Sr}_{0.9}\text{Eu}_{0.1}\text{Im}_2$ @Matrimid are defect-free and even have slightly lower permeabilities than those of the pure polymer membranes, as could be expected in view of the dense character of the MOF fillers.<sup>[12–14]</sup>

Table 2. Gas-permeation results.<sup>[a]</sup>

Membrane	$P(\text{O}_2)$ [Barrer] <sup>[b]</sup>
Pure PSF	1.4
Pure Matrimid	2.1
<b>2</b>	1.0
<b>4</b>	1.4

[a] Permeation experiments performed at 30  $^\circ\text{C}$  and 3 bar total feed pressure. [b] 1 Barrer =  $1 \times 10^{-10} \text{ cm}^3(\text{STP}) \text{ cm}/(\text{cm}^2 \text{ s cmHg})$  or  $7.5005 \times 10^{-18} \text{ m}^2 \text{ s}^{-1} \text{ Pa}^{-1}$  in SI units.

### Conclusions

Luminescent MOF–polymer mixed-matrix membranes have been prepared from the MOFs  ${}^3\text{Sr}_{0.9}\text{Eu}_{0.1}\text{Im}_2$  and  ${}^2\text{Tb}_2\text{Cl}_6(\text{bipy})_3 \cdot 2\text{bipy}$  together with the polysulfone Ultrason<sup>®</sup> S and Matrimid<sup>®</sup>. For the MMMs  ${}^3\text{Sr}_{0.9}\text{Eu}_{0.1}\text{Im}_2$ @PSF (**1** and **2**),  ${}^3\text{Sr}_{0.9}\text{Eu}_{0.1}\text{Im}_2$ @Matrimid (**3–5**), and  ${}^2\text{Tb}_2\text{Cl}_6(\text{bipy})_3$ ·

2bipy@PSF (**6** and **7**), the luminescence of the MOF could be maintained. The luminescence is especially strong for **1** and **2**. The membrane polymers influence the luminescence intensity: in the polysulfone membranes, both MOFs show higher emission intensity for lower MOF concentrations, whereas Matrimid® shows the opposite behavior. This indicates a different concentration quenching depending on the membrane polymer. The distribution of the MOFs in the membranes has been investigated by SEM, EDX, and fluorescence microscopy. Except for some sedimentation, the MOFs were distributed evenly within the membranes without significant aggregation. The use of ultrasonication proved less beneficial, as the resulting membranes showed inferior luminescence properties. Gas-permeation measurements proved that the MOF MMMs  $^3_{\infty}[\text{Sr}_{0.9}\text{Eu}_{0.1}\text{Im}_2]@\text{PSF}$  and  $^3_{\infty}[\text{Sr}_{0.9}\text{Eu}_{0.1}\text{Im}_2]@\text{Matrimid}$  were defect-free, as they exhibit slightly lower permeabilities than those of the pure polymer membranes. To the best of our knowledge, these are the first examples of luminescent MMMs. Altogether, these examples show that the concept of MOF mixed-matrix membranes can be expanded from gas permeation to new applications. The fabrication of membranes can be an option to increase the stabilities and processabilities of the bulk MOFs.

## Experimental Section

**General:** All experiments were performed under inert conditions (argon or nitrogen atmosphere) through vacuum-line, Schlenk, and glovebox (MBraun, LabMaster SP and Innovative technology, Pure Lab) techniques with DURAN™ ampoules. The MOFs were prepared in heating furnaces with  $\text{Al}_2\text{O}_3$  tubes, a Kanthal resistance heating wire, and NiCr/Ni temperature elements controlled by Eurotherm 2416 control units together with sealed glass ampoules. Anhydrous terbium chloride was synthesized by the ammonium halide route<sup>[29,30]</sup> from  $\text{Tb}_4\text{O}_7$  (99.9 %, Auer-Remy), HCl solution (10 mol L<sup>-1</sup>, reagent grade) and  $\text{NH}_4\text{Cl}$  (99.9 %, Fluka). The intermediate trivalent terbium ammonium chloride was decomposed and further purified by sublimation under vacuum. Strontium and europium metal (Smart Elements, 99.99 %), bipy (Sigma–Aldrich 98 %), and 1*H*-imidazole (Hlm, Sigma–Aldrich 99.5 %) were applied as purchased. The solvent DCM (>99.9 %) was purchased from Fisher Chemicals and dried with an MBraun solvent purification system.  $\text{O}_2$  gas for the gas-permeation experiments was supplied by Air Liquide (Germany) and used as received (purity 99.998 %).

$^3_{\infty}[\text{Sr}_{0.9}\text{Eu}_{0.1}(\text{Im})_2]$  and  $^2_{\infty}[\text{Tb}_2\text{Cl}_6(\text{bipy})_3]\cdot 2\text{bipy}$ :  $^3_{\infty}[\text{Sr}_{0.9}\text{Eu}_{0.1}(\text{Im})_2]$  was synthesized by a modification of the method reported in ref.<sup>[24]</sup> Freshly filed europium metal (0.1 mmol, 15.2 mg), small pieces of strontium metal (0.9 mmol, 78.9 mg), and 1*H*-imidazole (3.0 mmol, 204.3 mg) were sealed in an evacuated DURAN™ glass ampoule. The ampoule was heated to 186 °C in a tube oven over 2 h. The temperature was kept constant for 48 h. The ampoule was cooled to 66 °C over 6 h and then to room temperature over 1 h. The excess 1*H*-imidazole was removed by sublimation (140 °C, 24 h). The remaining reaction product was a fine yellow powder.

$^2_{\infty}[\text{Tb}_2\text{Cl}_6(\text{bipy})_3]\cdot 2(\text{bipy})$  was synthesized by a modified solvent-free melt reaction according to refs.<sup>[19,25]</sup> Anhydrous  $\text{TbCl}_3$  (0.76 mmol, 201.6 mg) and 4,4'-bipyridine (2.28 mmol, 356.1 mg) were homogenized by grinding. The reaction mixture was then sealed in an evacuated DURAN™ glass ampoule, which was heated to 140 °C in a tube oven at a rate of 20 °C h<sup>-1</sup>. The temperature was kept constant for 168 h, and then the ampoule was cooled to room temperature

over 1 h. The excess 4,4'-bipyridine was removed by sublimation (120 °C, 48 h). The collected product was a fine grey powder.

**Membrane Preparation (1–4, 6–7) without Ultrasonication:** The embedding of MOFs without sonication was achieved with solutions of 3.6 wt.-% polymer in DCM. Portions (200 mg) of the dry polymer, the MOF material (18 or 39 mg), and dry DCM (4 mL) were combined in a 10 mL Schlenk flask to produce MMMs with 8 and 16 wt.-% of MOF. The dispersions were stirred for 2 d in order to achieve homogeneous mixtures. The dispersions were cast into metal rings, 5 cm in diameter, which were placed on a flat glass surface in a desiccator filled with nitrogen gas and a desiccant. The solvent was evaporated overnight by a slight stream of predried nitrogen gas to achieve some control over the evaporation rate. As soon as all of the solvent was evaporated, the membrane was removed from the metal ring and the glass surface. The membrane was finally dried at 25 °C under reduced pressure.

**Membrane Preparation (5 and 8) with Ultrasonication:** The embedding of MOFs with ultrasonication was achieved as described above with minor alterations. The amount of polymer in DCM was 8.0 wt.-% (200 mg of polymer in 2 mL of DCM), and the dispersion of the MOF in polymer solution was sonicated for 60 min in an ultrasonic bath (ELMA Transsonic 310, 35 Hz) to try to achieve good dispersion of the MOF particles before membrane casting.

**Powder X-ray Diffraction:** Samples for powder X-ray diffraction were prepared in open-stage sample holders with a poly(methyl methacrylate) (PMMA) cupola and a Si-wafer platform. The diffraction data were collected with a Bruker AXS D8 Discover powder X-ray diffractometer equipped with Lynx-Eye detector in reflection geometry. The X-ray radiation ( $\text{Cu-K}_{\alpha 1}$ ;  $\lambda = 154.06$  pm) was focused with a Goebel mirror, and  $\text{Cu-K}_{\alpha 2}$  radiation was eliminated by the application of a Ni absorber. The diffraction patterns were recorded and analyzed with the Bruker AXS Diffac-Suite.<sup>[31]</sup>

**Photoluminescence Spectroscopy:** The excitation and emission spectra were recorded with a HORIBA Jobin Yvon Spex Fluorolog 3 spectrometer equipped with a 450-W Xe lamp, double-grated excitation and emission monochromators, and a photomultiplier tube (R928P) at room temp. with the FluorEssence software. The excitation spectra were corrected for the spectral distribution of the lamp intensity by using a photodiode reference detector. Additionally, the excitation and emission spectra were corrected for the spectral responses of the monochromators and the detector by using the correction spectra provided by the manufacturer. All samples were investigated as solids in spectroscopically pure quartz cuvettes in front-face mode at room temperature. Edge filters were applied when appropriate.

The fluorescence lifetimes were obtained with a Horiba Fluoromax FL3-22 spectrophotometer. The samples were prepared in quartz glass cuvettes under an inert-gas atmosphere. The decay times were recorded by time-correlated single-photon counting (TCSPC) with a 375 nm pulsed laser diode or a microsecond flash lamp with an excitation wavelength of 330 nm. The fluorescence emission was collected at right angles to the excitation source, and the emission wavelength was selected with a monochromator and detected by a single-photon avalanche diode (SPAD). The resulting intensity decays were calculated through tail fits.

**SEM/EDX:** The SEM images were recorded with a Jeol JSM-6510LV QSEM Advanced electron microscope with a LAB-6 cathode at 5–20 keV. The microscope was equipped with a Bruker Xflash 410 silicon drift detector and the Bruker ESPRIT software for EDX analysis. The membrane cross-sections were prepared through freeze-fracturing after immersion in liquid nitrogen and then coated with

gold by a Jeol JFC 1200 fine-coater (at an approximate current of 20 mA for 20–30 s).

**Fluorescence Microscopy:** The fluorescence microscopy of oxygen-free sealed MOF–membrane preparations was performed with an Axio Observer.Z1 microscope equipped with an A-Plan 10×/0.25 Ph1 objective and an Optovar 1×/1.6× tube lens (Zeiss). The images were recorded with a phase-contrast channel and a 49 DAPI or 38 HE Green Fluorescent Protein Reflector (Zeiss) with excitation wavelength of 450–490 nm and an emission wavelength of 500–550 nm after 22 ms exposure time with a mercury vapor short-arc lamp.

**Gas Permeation:** The O<sub>2</sub> permeabilities were evaluated with a permeation cell described elsewhere.<sup>[32]</sup> The membrane thickness was measured as the average over ten different spots with a micrometer screw. The gas-permeation measurements were performed by the pressure-rise method under steady-state conditions at 30 °C. The membrane was placed into the sample cell, the permeate side was evacuated, and then the feed side was evacuated. The feed side was filled with O<sub>2</sub> gas to a pressure of 3.0 bar. The linear pressure increase upon permeation from the feed to the permeate side was recorded and used to calculate the permeability *P* in Barrer units [1 Barrer = 1 × 10<sup>-10</sup> cm<sup>3</sup>(STP) cm/(cm<sup>2</sup> s cmHg) or 7.5005 × 10<sup>-18</sup> m<sup>2</sup> s<sup>-1</sup> Pa<sup>-1</sup> in SI units]. The Permeability *P* is defined as the gas flow rate *J* multiplied by the thickness *d* of the membrane, divided by the area *A* and by the pressure difference Δ*p* across the material [Equation (1)].

$$P = (Jd)/\Delta pA \quad (1)$$

## Acknowledgments

The work was partly supported by the Bundesministerium für Bildung und Forschung (BMBF), Germany (project “Robust Porous Coordination Polymers for Mixed-Matrix Membranes”, grant number 01DK13026).

**Keywords:** Metal–organic frameworks · Polymers · Mixed-matrix membranes · Luminescence · Lanthanides

- [1] a) H.-C. J. Zhou, S. Kitagawa, *Chem. Soc. Rev.* **2014**, *43*, 5415–5418; b) Z.-J. Lin, J. Lü, M. Hong, R. Cao, *Chem. Soc. Rev.* **2014**, *43*, 5867–5895; c) J. R. Long, O. M. Yaghi, *Chem. Soc. Rev.* **2009**, *38*, 1213–1214; d) N. Stock, S. Biswas, *Chem. Rev.* **2012**, *112*, 933–969; e) C. Janiak, J. K. Vieth, *New J. Chem.* **2010**, *34*, 2366–2388.
- [2] a) O. K. Farha, J. T. Hupp, *Acc. Chem. Res.* **2010**, *43*, 1166–1175; b) C. Janiak, S. K. Henninger, *Chimia* **2013**, *67*, 419–424; c) S. K. Henninger, F. Jeremias, H. Kummer, C. Janiak, *Eur. J. Inorg. Chem.* **2012**, 2625–2634.
- [3] a) M. D. Allendorf, C. A. Bauer, R. K. Bhakta, R. J. T. Houk, *Chem. Soc. Rev.* **2009**, *38*, 1330–1352; b) M. D. Allendorf, C. A. Bauer, R. K. Bhakta, R. J. T. Houk, *Chem. Soc. Rev.* **2009**, *38*, 1330–1352; c) K. Binnemans, *Chem. Rev.* **2009**, *109*, 4283–4374; d) J. Rocha, L. D. Carlos, F. A. A. Paz, D. Ananias, *Chem. Soc. Rev.* **2011**, *40*, 926–940; e) Y. Chen, S. Ma, *Rev. Inorg. Chem.* **2012**, *32*, 81–100; f) J. Heine, K. Müller-Buschbaum, *Chem. Soc. Rev.* **2013**, *42*, 9232–9242.
- [4] a) D. Liu, K. Lu, C. Poon, W. Lin, *Inorg. Chem.* **2014**, *53*, 1916–1924; b) Z. Hu, B. J. Deibert, J. Li, *Chem. Soc. Rev.* **2014**, *43*, 5815–5840; c) J. Lei, R. Qian, P. Ling, L. Cui, H. Ju, *TrAC Trends Anal. Chem.* **2014**, *58*, 71–78; d) K. Müller-Buschbaum, F. Beuerle, C. Feldmann, *Microporous Mesoporous Mater.* **2015**, *216*, 171–199.
- [5] B. Böhlinger, R. Fischer, M. R. Lohe, M. Rose, S. Kaskel, P. Küsgens, *Metal–Organic Frameworks: Applications from Catalysis to Gas Storage* (Ed.: D. Farrusseng), 1st ed., Wiley-VCH, Weinheim, Germany, **2011**, chapter 15, p. 353–381.
- [6] a) F. Jeremias, S. K. Henninger, C. Janiak, *Chem. Commun.* **2012**, *48*, 9708–9710; b) F. Jeremias, D. Fröhlich, C. Janiak, S. K. Henninger, *RSC Adv.* **2014**, *4*, 24073–24082.
- [7] V. Finsy, L. Ma, L. Alaerts, D. E. De Vos, G. V. Baron, J. F. M. Denayer, *Microporous Mesoporous Mater.* **2009**, *120*, 221–227.
- [8] a) R. Zacharia, D. Cossement, L. Lafi, R. Chahine, *J. Mater. Chem.* **2010**, *20*, 2145–2151; b) M. R. Lohe, M. Rose, S. Kaskel, *Chem. Commun.* **2009**, 6056–6058.
- [9] a) M. Wickenheisser, T. Paul, C. Janiak, *Microporous Mesoporous Mater.* **2016**, *220*, 258–269; b) M. Wickenheisser, A. Herbst, R. Tannert, B. Milow, C. Janiak, *Microporous Mesoporous Mater.* **2015**, *215*, 143–153; c) M. Wickenheisser, C. Janiak, *Microporous Mesoporous Mater.* **2015**, *204*, 242–250; d) A. Sachse, R. Ameloot, B. Coq, F. Fajula, B. Coasne, D. De Vos, A. Galarneau, *Chem. Commun.* **2012**, *48*, 4749–4751; e) P. Küsgens, A. Zgaverdea, H. Fritz, S. Siegle, S. Kaskel, *J. Am. Ceram. Soc.* **2010**, *93*, 2476–2479; f) M. G. Schwab, I. Senkowska, M. Rose, M. Koch, J. Pahnke, G. Jonschker, S. Kaskel, *Adv. Eng. Mater.* **2008**, *10*, 1151–1155.
- [10] A. M. Spokoiny, D. Kim, A. Sumrein, C. A. Mirkin, *Chem. Soc. Rev.* **2009**, *38*, 1218–1227.
- [11] a) D. Zacher, O. Shekhah, C. Wöll, R. A. Fischer, *Chem. Soc. Rev.* **2009**, *38*, 1418–1429; b) O. Shekhah, J. Liu, R. A. Fischer, C. Wöll, *Chem. Soc. Rev.* **2011**, *40*, 1081–1106.
- [12] a) H. B. Tanh Jeazet, C. Staudt, C. Janiak, *Dalton Trans.* **2012**, *41*, 14003–14027; b) K. Hunger, N. Schmeling, H. B. Tanh Jeazet, C. Janiak, C. Staudt, K. Kleinermanns, *Membranes* **2012**, *2*, 727–763; c) H. B. Tanh Jeazet, C. Janiak, *Metal–Organic Frameworks*, in: *Mixed-Matrix Membranes*, in: *Metal–Organic Framework Materials* (Eds.: L. R. MacGillivray, C. Lukehart), John Wiley & Sons, Chichester, UK, **2014**, p. 403–417.
- [13] a) B. Seoane, J. Coronas, I. Gascon, M. Etxebarria Benavides, O. Karvan, J. Caro, F. Kapteijn, J. Gascon, *Chem. Soc. Rev.* **2015**, *44*, 2421–2454; b) B. Zornoza, C. Tellez, J. Coronas, J. Gascon, F. Kapteijn, *Microporous Mesoporous Mater.* **2013**, *166*, 67–78.
- [14] a) S. R. Venna, M. A. Carreon, *Chem. Eng. Sci.* **2015**, *124*, 3–19; b) W. Li, Y. Zhang, Q. Li, G. Zhang, *Chem. Eng. Sci.* **2015**, *135*, 232–257; c) G. Dong, H. Li, V. Chen, *J. Mater. Chem. A* **2013**, *1*, 4610–4630.
- [15] H. B. Tanh Jeazet, T. Koschine, C. Staudt, K. Raetzke, C. Janiak, *Membranes* **2013**, *3*, 331–353; H. B. Tanh Jeazet, C. Staudt, C. Janiak, *Chem. Commun.* **2012**, *48*, 2140–2142.
- [16] a) S. Roy, A. Chakraborty, T. K. Maji, *Coord. Chem. Rev.* **2014**, *273*, 139–164; b) L. V. Meyer, F. Schönfeld, K. Müller-Buschbaum, *Chem. Commun.* **2014**, *50*, 8093–8108; c) Y. Cui, B. Chen, G. Qian, *Coord. Chem. Rev.* **2014**, *273*, 76–86; d) L. Ma, O. R. Evans, B. M. Foxman, W. Lin, *Inorg. Chem.* **1999**, *38*, 5837–5840; e) T. M. Reinecke, M. Eddaoudi, M. Fehr, D. Kelly, O. M. Yaghi, *J. Am. Chem. Soc.* **1999**, *121*, 1651–1657; f) Z.-S. Bai, J. Xu, T. Okamura, M.-S. Chen, W.-Y. Sun, N. Ueyama, *Dalton Trans.* **2009**, *14*, 2528–2539.
- [17] a) S. V. Eliseeva, J.-C. G. Bünzli, *New J. Chem.* **2011**, *35*, 1165–1176; b) K. Binnemans, *Chem. Rev.* **2009**, *109*, 4283–4374; c) L. Sorace, C. Benelli, D. Gatteschi, *Chem. Soc. Rev.* **2011**, *40*, 3092–3104.
- [18] S. I. Weissman, *J. Chem. Phys.* **1942**, *10*, 214–217.
- [19] a) C. J. Höller, M. Mai, C. Feldmann, K. Müller-Buschbaum, *Dalton Trans.* **2010**, *39*, 461–468; b) P. R. Matthes, C. J. Höller, M. Mai, J. Heck, S. J. Sedlmaier, S. Schmichen, C. Feldmann, W. Schnick, K. Müller-Buschbaum, *J. Mater. Chem.* **2012**, *22*, 10179–10187.
- [20] G. A. Crosby, R. E. Whan, R. M. Alire, *J. Chem. Phys.* **1961**, *34*, 743–748.
- [21] a) L. Armelao, S. Quici, F. Barigelli, G. Accorsi, G. Bottaro, M. Cavazzini, E. Tondello, *Coord. Chem. Rev.* **2010**, *254*, 487–505; b) P. A. Tanner, C.-K. Duan, *Coord. Chem. Rev.* **2010**, *254*, 3026–3029; c) D. Parker, J. A. G. Williams, *J. Chem. Soc., Dalton Trans.* **1996**, 3613–3628; d) P. Gawryszewska, J. Sokolnicki, J. Legendziewicz, *Coord. Chem. Rev.* **2005**, *249*, 2489–2509.
- [22] M. Noda, K. Matsushima, K. Seki, M. Yagi, *Chem. Phys. Lett.* **1998**, *296*, 599–604.
- [23] P. Hänninen, H. Härma (Eds.), *Springer Series on Fluorescence Vol 7: Lanthanide Luminescence*, Springer-Verlag, Berlin, **2011**.
- [24] a) A. Zurawski, M. Mai, D. Baumann, C. Feldmann, K. Müller-Buschbaum, *Chem. Commun.* **2011**, *47*, 496–498; b) L. V. Meyer, J. Vogt, H. Schäfer, M. Steinhart, R. Böttcher, A. Pöpl, M. Mai, C. Feldmann, K. Müller-Buschbaum, *Inorg. Chem. Front.* **2015**, *2*, 237–245.
- [25] a) J. Won, J. S. Seo, J. H. Kim, H. S. Kim, Y. S. Kang, S. J. Kim, Y. Kim, J. Jegal, *Adv. Mater.* **2005**, *17*, 80–84; b) A. Car, C. Stropnik, K.-V. Peinemann,

- Desalination* **2006**, *200*, 424–426; c) B. Seoane, J. M. Zamaro, C. Téllez, J. Coronas, *RSC Adv.* **2011**, *1*, 917–922; d) B. Zornoza, B. Seoane, J. M. Zamaro, C. Téllez, J. Coronas, *ChemPhysChem* **2011**, *12*, 2781–2785.
- [26] a) S. Basu, M. Maes, A. Cano-Odena, L. Alaerts, D. E. De Vos, I. F. J. Vankelecom, *J. Membr. Sci.* **2009**, *344*, 190–198; b) M. J. C. Ordoñez, K. J. Balkus Jr., J. P. Ferraris, I. H. Musselman, *J. Membr. Sci.* **2010**, *361*, 28–37; c) E. V. Perez, K. J. Balkus Jr., J. P. Ferraris, I. H. Musselman, *J. Membr. Sci.* **2009**, *328*, 165–173; d) Y. Zhang, I. H. Musselman, J. P. Ferraris, K. J. Balkus Jr., *J. Membr. Sci.* **2008**, *313*, 170–181.
- [27] W. Zhang, Y. Hu, J. Ge, H.-L. Jiang, S.-H. Yu, *J. Am. Chem. Soc.* **2014**, *136*, 16978–16981.
- [28] P. R. Matthes, F. Schönfeld, S. H. Zottnick, K. Müller-Buschbaum, *Molecules* **2015**, *20*, 12125–12153.
- [29] G. Jantsch, H. Jawurek, N. Skalla, H. Gawalonski, *Z. Anorg. Allg. Chem.* **1932**, *207*, 353–367.
- [30] G. Meyer, *Inorg. Synth.* **1989**, *25*, 146.
- [31] Bruker, *SMART Apex Suite 2001*, Bruker AXS Inc., Madison, WI.
- [32] J. U. Wieneke, C. Staudt, *Polym. Degrad. Stab.* **2010**, *95*, 684–693.

---

Received: March 3, 2016

Published Online: May 30, 2016

### 3.3 Luminescent MOF polymer mixed matrix membranes for humidity sensing in real status analysis

Johannes M. Stangl, Dennis Dietrich, Alexander E. Sedykh, Christoph Janiak, Klaus Müller-Buschbaum



Drei lumineszente, feuchtigkeitsempfindliche Lanthanoid-MOFs wurden unter inerten Bedingungen in Polysulfon eingelagert und als Mixed-Matrix-Membranen auf ihre lumineszenten und fluoreszenten Eigenschaften untersucht. Die zerstörungsfreie sowie homogene Einbettung wurde mittels Röntgenpulverdiffraktogrammen sowie Rasterelektronenmikroskopie nachgewiesen. Die Defektfreiheit der Membranen wurde anschließend unter Zuhilfenahme des Maxwell-Modells bewiesen. Kinetische Untersuchungen zum Lumineszenzverfall in der Membran unter Feuchtigkeitseinfluss im Vergleich zum losen MOF zeigten eine Erhöhung der Lumineszenzhalbwertszeit. Die Polymermembran stabilisiert somit das MOF gegen Hydrolyse.

Anteile an der Veröffentlichung:

- Entwicklung einer Kammer zum inerten Herstellen von MMMs, welche die Publikation überhaupt erst ermöglicht hat.
- Digitalisierung der Einzelgaspermeationsanlage für hochpräzise Messungen.
- Experimentelle Arbeiten und Analytik in der Rasterelektronenmikroskopie und der Membranherstellung und Gaspermeation.
- Aufarbeiten der Ergebnisse und Verfassen des Abschnitts über Rasterelektronenmikroskopie, energiedispersive Röntgenanalyse und Maxwell-Modell-Rechnungen. Korrekturen durch Herrn Prof. Dr. Christoph Janiak.
- Lumineszenzspektroskopie und Fluoreszenzmikroskopie, Verfassen des restlichen Manuskripts sowie kinetische Berechnungen zum Lumineszenzverfall durch die übrigen Kooperationspartner



# Luminescent MOF polymer mixed matrix membranes for humidity sensing in real status analysis†

Johannes M. Stangl,<sup>a</sup> Dennis Dietrich,<sup>b</sup> Alexander E. Sedykh,<sup>a</sup> <sup>a</sup>  
Christoph Janiak <sup>b</sup> and Klaus Müller-Buschbaum <sup>\*a</sup>

Humidity sensing properties of luminescent metal–organic framework (MOF) polymer mixed-matrix membranes (MMMs)  $\frac{3}{\infty}[\text{Ba}_{0.98}\text{Eu}_{0.02}(\text{Im})_2]@\text{PSF}$  (Im = imidazolate, PSF = polysulfone Ultrason<sup>®</sup> S),  $\frac{3}{\infty}[\text{Sr}_{0.90}\text{Eu}_{0.10}(\text{Im})_2]@\text{PSF}$ , and  $\frac{3}{\infty}[\text{Ce}(\text{Im})_3\text{ImH}]\cdot\text{ImH}@\text{PSF}$  were investigated. MMMs show superior properties compared to bulk MOFs especially in stability, handling and long-term monitoring. In order to evaluate these films for such real status analyses, both their sensitivity and stability were determined and compared to bulk MOFs. Therefore, the progress of the humidity induced luminescence intensity quenching of the MMMs and the corresponding bulk substances was investigated for several pre-set relative humidities at room temperature. The MMMs show distinct and diverse luminescence loss and sensitivity rendering the monitoring of a very low relative humidity of only 2% accessible.

Cite this: *J. Mater. Chem. C*, 2018, **6**, 9248

Received 28th March 2018,  
Accepted 30th July 2018

DOI: 10.1039/c8tc01454j

rsc.li/materials-c

## Introduction

Many processes in technical fabrications and chemical reactions have to be observed and monitored appropriately. Subsequent to production chains, storage conditions and transport challenges also apply to packaged materials. The translation of such processes, such as changes in the status of a system or in environmental parameters, to an observable value can be achieved with sensors and detectors.<sup>1–6</sup> The detected parameters can be based on different processes such as suitable optical processes, for instance, changes in the intensity of luminescence such as “turn-on”<sup>7</sup> or “turn-off” sensing<sup>8</sup> or in energy and therefore chromaticity shifts of luminescence.<sup>9</sup> Besides optical detection, several other physical processes, such as conductivity changes,<sup>10</sup> magnetism<sup>11</sup> or chemical processes, such as changes in pH-values<sup>12</sup> or in ion concentrations,<sup>13</sup> are used for sensing. The requirements for possible sensors are typically high sensitivity, defined threshold values, specificity, steadiness, fast reaction times and low costs. In order to avoid erroneous detection, sensing devices should be designed according to their respective application.<sup>14</sup> Humidity, and thus water vapour, has a strong impact on packaged materials in face of world-wide transportation and day-to-day storage related

to the relative humidity of at least several percent, especially, if the materials have certain sensitivity to water. Here, sensing is possible chemically, *e.g.* based on classic cobalt salts<sup>15,16</sup> but also on MOFs<sup>17</sup> and lanthanide containing compounds.<sup>18</sup> Physical humidity sensing is also possible based on optic behaviour (refractive index)<sup>19</sup> or coulometric with *e.g.* the well-known Keidel cell.<sup>20</sup>

The material groups of coordination polymers and especially metal–organic frameworks (MOFs) are known for their versatility, not only in structures<sup>21</sup> but also in physical and chemical properties,<sup>22</sup> including options for processing.<sup>23</sup> For two decades, MOFs are a research topic with a high priority now.<sup>24</sup> For luminescent MOFs and sensors, lanthanide-containing compounds (lanthanide-containing MOFs are called LnMOFs in the following) have mainly been investigated due to the possibility of an Ln<sup>3+</sup>-based intrinsic luminescence.<sup>25–27</sup> As luminescence is a parameter that can be monitored “on-the-fly”, it is highly attractive for status analysis. By suitable combination of lanthanide ions and organic linkers, characteristic luminescence properties can be achieved,<sup>28</sup> including sensitization by light-harvesting organic ligands and metal-based emission.<sup>29</sup> In addition to typical 4f-Ln<sup>3+</sup>-systems, a few MOFs have been shown to utilize parity allowed, strong 5d–4f transitions for Eu<sup>2+</sup> and Ce<sup>3+</sup>.<sup>30</sup> With the possibility of doping various amounts of lanthanides in different host lattices, different specific luminescence properties can be achieved in addition to the porosity of MOFs, which provides increased access for analyte molecules due to their additional inner surface. Both options make the material class of LnMOFs superior to *e.g.* Ln-complexes. Recently, particles of the MOF  $\frac{3}{\infty}[\text{Sr}_{0.90}\text{Eu}_{0.10}(\text{Im})_2]$  (**2**) have been embedded<sup>31</sup> into a polysulfone

<sup>a</sup> Institut für Anorganische Chemie, Universität Würzburg, Am Hubland, 97074 Würzburg, Germany. E-mail: k.mueller-buschbaum@uni-wuerzburg.de

<sup>b</sup> Institut für Anorganische Chemie und Strukturchemie, Universität Düsseldorf, Universitätsstraße 1, 40225 Düsseldorf, Germany

† Electronic supplementary information (ESI) available: 13 figures and 3 tables on PL spectroscopy, PXRD, IR spectroscopy, elemental analysis, gas permeation, particle volume distribution, and SEM. See DOI: 10.1039/c8tc01454j

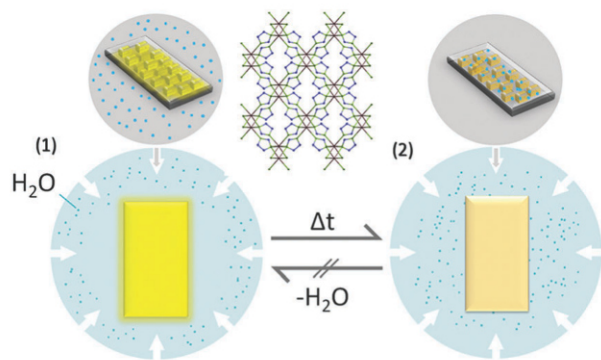


Fig. 1 Schematic presentation of the MMM sensing properties from the microscopic (upper part) to macroscopic (lower part) scale. Left: Luminescent MMM prior to the detection of humidity, right: quenched MMM-luminescence after sensing of humidity.

(PSF)<sup>32</sup> matrix to create the first luminescent LnMOF mixed-matrix membranes (LnMOF@MMMs). Such embedding has also just been shown for luminescent Eu<sup>3+</sup>/Tb<sup>3+</sup> complexes in poly(methylmethacrylate).<sup>33</sup>

In this work, we have investigated the humidity sensitivity of different LnMOF@MMMs and their possible application as humidity sensors (Fig. 1). For applications such as transport or long-term storage, in which real status analysis is not based on 24 hour monitoring, irreversible detection is strongly preferable, as it prevents erroneous analysis based on non-continuous reversible sensing, which would result from several changes in humidity over time. Therefore, an experimental setup was created in which the loss of luminescence could be detected under defined and reproducible conditions for the MMMs described here which show irreversible luminescence changes upon contact with humidity. For a better understanding of the physical and chemical processes kinetic calculations were made and the accumulated recesses were analysed. The results were then compared to the properties of the bulk MOFs in order to analyse the influence of the polymer matrix and its gas permeation properties.

## Results and discussion

### Preparation and characterization of LnMOF@PSF MMMs and bulk MOFs

Successful membrane preparation of lanthanide imidazolate MOFs has been achieved for polysulfone (PSF) as an organic polymer material for  ${}^3_{\infty}[\text{Ba}_{0.98}\text{Eu}_{0.02}(\text{Im})_2]$  and  ${}^3_{\infty}[\text{Sr}_{0.90}\text{Eu}_{0.10}(\text{Im})_2]$ , retaining the strong MOF luminescence. Relatively low loadings with the MOF as filler particles are preferable, as reported previously,<sup>31</sup> and 8 wt% proved to be some kind of optimum regarding the properties of the MOF (luminescence intensity, distribution of particles) and the mechanical film stability and flexibility. Therefore, the embedding in this work was carried out with 8 wt% particles of the MOFs  ${}^3_{\infty}[\text{Ba}_{0.98}\text{Eu}_{0.02}(\text{Im})_2]$  (**1**),<sup>34</sup>  ${}^3_{\infty}[\text{Sr}_{0.90}\text{Eu}_{0.10}(\text{Im})_2]$  (**2**),<sup>35</sup> and  ${}^3_{\infty}[\text{Ce}(\text{Im})_3\text{ImH}]\cdot\text{ImH}$  (**3**)<sup>36</sup> in PSF. The corresponding bulk substances were ball milled to equalize the particle size. Embedding resulted in the formation of membranes of the constitution  ${}^3_{\infty}[\text{Ba}_{0.98}\text{Eu}_{0.02}(\text{Im})_2]\text{@PSF}$  (**1@PSF**) and  ${}^3_{\infty}[\text{Sr}_{0.90}\text{Eu}_{0.10}(\text{Im})_2]\text{@PSF}$  (**2@PSF**). The generation of a

luminescent MMM of the constitution  ${}^3_{\infty}[\text{Ce}(\text{Im})_3\text{ImH}]\cdot\text{ImH}\text{@PSF}$  (**3@PSF**) could not be achieved; as for the resulting films, no Ce-based luminescence could be detected and also no MOF reflections could be found by PXRD, leading to the conclusion that embedding of **3** was not successful but resulted in decomposition of the MOF.

The generated MMM films were investigated by a combination of photoluminescence spectroscopy, powder X-ray diffraction, SEM/EDX and *in situ* investigations of property changes upon interaction with pre-set relative humidities for sensing. The results were then compared to the properties of the bulk MOFs including potential sensing properties.

### Photoluminescence spectroscopy

Both the co-doped MOFs of the formula  ${}^3_{\infty}[\text{Ba}_{0.98}\text{Eu}_{0.02}(\text{Im})_2]$  (**1**) and  ${}^3_{\infty}[\text{Sr}_{0.90}\text{Eu}_{0.10}(\text{Im})_2]$  (**2**) keep their luminescence properties unchanged upon embedding into the polysulfone matrix (PSF) as  ${}^3_{\infty}[\text{Ba}_{0.98}\text{Eu}_{0.02}(\text{Im})_2]\text{@PSF}$  (**1@PSF**) and  ${}^3_{\infty}[\text{Sr}_{0.90}\text{Eu}_{0.10}(\text{Im})_2]\text{@PSF}$  (**2@PSF**).<sup>31</sup> It is worth mentioning that both archetype structures of  ${}^3_{\infty}[\text{Ba}(\text{Im})_2]$ ,  ${}^3_{\infty}[\text{Sr}(\text{Im})_2]$  and  ${}^3_{\infty}[\text{Eu}(\text{Im})_2]$  are closely related, with the Ba-MOF being a distorted structure variant of the isotypic Sr- and Eu-MOFs.<sup>35</sup> Emission and excitation spectra were recorded at room temperature and compared to pure bulk MOFs. For both **1@PSF** and **2@PSF**, no deviation was observed between the emission of the bulk MOFs and the respective MMMs (Fig. 2).

This is an interesting feature, because different from typical Ln<sup>3+</sup>-intra-4f-based luminescence, the participation of 5d–4f transitions in the luminescence of Eu<sup>2+</sup>-ions should show energetic shifts if changes in the chemical surrounding apply. As this can be excluded, the fingerprint character of the photoluminescence (PL) already hints at embedding of chemically unchanged MOF particles that have little electronic interaction with the organic polymer. For **1**, **2** and **1@PSF**, **2@PSF**, both excitation and emission are dominated by 5d–4f-transitions of Eu<sup>2+</sup>. However, in the excitation spectra, a certain bathochromic shift is caused by embedding into PSF.

Excitation at 365 nm leads to a strong yellow emission with a maximum at  $\lambda = 555$  nm and a half width of about  $\lambda = 105$  nm for **1** and **1@PSF**. Also, data on the lifetimes of the Eu<sup>2+</sup>-emission for **1** and **1@PSF** were collected and compared. Both cases can be described with a biexponential decay, which is also almost identical for the bulk MOF and the MMM ( $\tau_1 = 215(3)$  ns and  $\tau_2 = 450(8)$  ns, ( $\lambda_{\text{exc.}} = 375$ ) for MOF **1** and  $\tau_1 = 213(7)$  ns and  $\tau_2 = 472(1)$  ns, ( $\lambda_{\text{exc.}} = 375$  nm) for **1@PSF**). Again, the strong similarities are a proof that the embedded MOF is unaltered. An according behaviour is observed for the photoluminescence properties of **2** and **2@PSF**, which have been described recently,<sup>31</sup> with identical photoluminescence properties for bulk MOF and MMM and a turquoise-green emission due to 5d–4f-transitions of Eu<sup>2+</sup>. Generation of an MMM of the constitution  ${}^3_{\infty}[\text{Ce}(\text{Im})_3\text{ImH}]\cdot\text{ImH}\text{@PSF}$  (**3@PSF**) could not be proven, and the resulting films showed no Ce-based luminescence at all.

### Powder X-ray diffraction, fluorescence microscopy, SEM and EDX

Subsequent to embedding, MMMs **1@PSF**, **2@PSF** and **3@PSF** were further characterized *via* powder X-ray diffraction (PXRD),

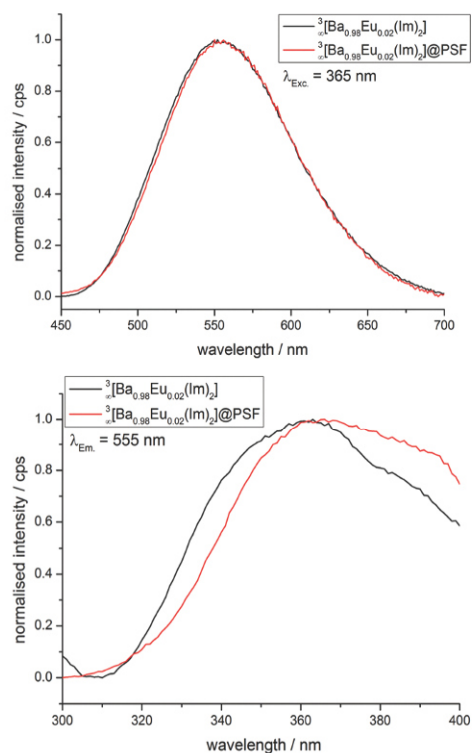


Fig. 2 Comparison of the emission (above) and excitation (below) spectra of bulk MOF **1** and MMM **1**@PSF with no difference being detected in emission.

fluorescence microscopy, scanning electron microscopy (SEM) and energy-dispersive X-ray spectroscopy (EDX). Unaltered MOF reflections could be detected in addition to the amorphous background of the organic polymer *via* PXRD for **1**@PSF and **2**@PSF (Fig. 3). However, no MOF reflections could be found for MMM **3**@PSF, leading to the conclusion that the embedding of **3** resulted in decomposition of the Ce-MOF instead. The decomposition can be recognized by a visible change in colour of the suspension, from grey to yellow as well as steady loss of the MOF luminescence, and starts upon stirring of the dispersion of the components. Removal of the solvent accelerates the decomposition (see also Fig. S11–S13, ESI†).

SEM together with EDX was applied to investigate the distribution of the MOF particles in the polymer membrane. The analysis shows a reasonably homogenous distribution of **1** in the matrix of the MMM **1**@PSF (Fig. 4), as can be seen by the distribution of the Ba<sup>2+</sup> and Eu<sup>2+</sup> ions over the complete area of the investigated MMM. An equally homogeneous distribution of **2** in **2**@PSF has been shown recently.<sup>31</sup> Altogether, a homogenous luminescence on the macroscopic level can be seen by the eye if the MMMs are excited by UV-light ( $\lambda_{exc.} = 365$  nm, Fig. S1, ESI†). Sedimentation and aggregation are the result of decomposition of **3** in PSF.

### Gas permeation

Gas permeation experiments have been conducted in order to determine whether the cast composite membranes were free of defects and without disturbances at the polymer–particle interface. Since the MOF filler is dense and does not exhibit

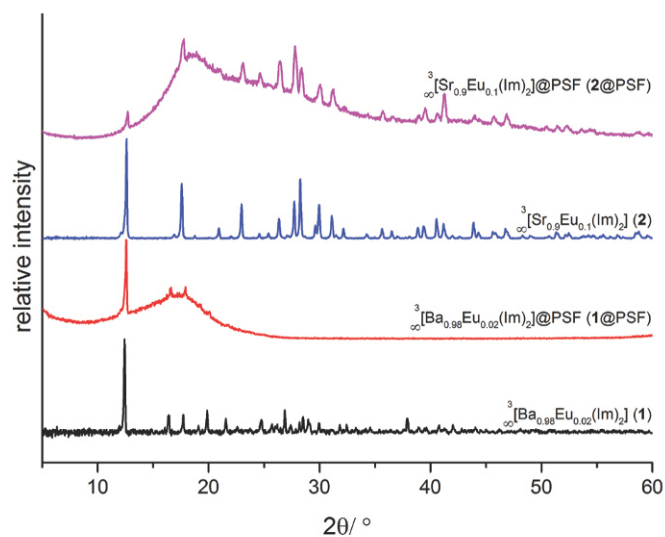


Fig. 3 Comparison of the observed powder X-ray diffraction patterns of MMMs **1**@PSF and **2**@PSF in comparison to the patterns of bulk MOFs **1** and **2**. The reflections of the MOFs and the amorphous background of the polymer matrix can be observed.

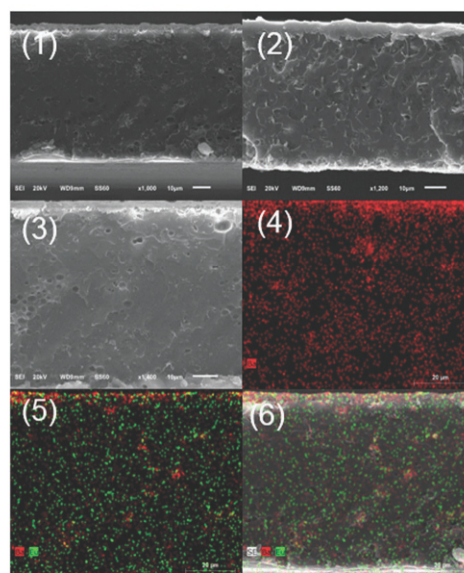


Fig. 4 (1–3) Cross-sectional SEM images of MMM **1**@PSF. (4–6) EDX elemental mapping for MMM showing the distribution of barium (red in 4–6) and europium (green in 5 and 6) in polysulfone. Image (6) includes image (1) together with EDX mapping.

porosity, its effect on the change in permeability of the membrane can be predicted using the Maxwell equation

$$P_c = P_m \cdot \frac{n \cdot P_f + (1 - n) \cdot P_m + (1 - n) \cdot (P_f - P_m) \cdot \phi_f}{n \cdot P_f + (1 - n) \cdot P_m - n \cdot (P_f - P_m) \cdot \phi_f}$$

wherein  $P_c$ ,  $P_m$  and  $P_f$  are the permeabilities of the composite, pure polymer and filler, respectively,  $\phi_f$  the volume fraction of the filler and  $n$ , a shape factor for the filler, in this case  $n = 1/3$  for spherical particles.<sup>39</sup> Solving the equation for a non-porous filler, where  $P_f = 0$ , shows that the theoretical permeability through the MMM should be lower compared to the permeability of the pure polymer membrane. Dioxygen permeation experiments suggest that this is indeed the case for **1**@PSF and



Table 1 Gas permeation results<sup>a</sup>

Membrane type	$\phi_f$	$P_{O_2}(\text{exp.})$ [Barrer]	$P_c(\text{exp.})$ [Barrer]	$P_c(\text{calc.})$ [Barrer]	Relative deviation <sup>b</sup>
PSF	—	1.05	—	—	—
(1)@PSF	0.05	0.95	0.91	0.93	0.03
(2)@PSF	0.05	0.98	0.93	0.93	0.01

<sup>a</sup> Individual values for different membranes for each MOF are given in Table S3 (ESI). <sup>b</sup> Relative deviation:  $|(P_c(\text{exp.}) - P_c(\text{calc.})) / P_c(\text{calc.})|$ .

for 2@PSF (Table 1). This confirms the assumption that the membranes are free of defects, as defects would have increased the permeability by allowing unhindered gas flux through the membrane.

### Sensing properties of LnMOF@PSF MMMs in comparison to the bulk MOFs

For the detection of the quantitative luminescence decay during the sensing process, an experimental setup including a sample cell was built (Fig. 5). The sample cell consists of an inner and outer chamber, so that the outer chamber can only interact with the inner chamber, in which the MOF sample is placed, over the atmosphere in the hermetically sealed glass pipe. Humidity and temperature sensors were applied from the top. The outer chamber was filled with different cold saturated salt solutions to set a specific humidity value in the sample cell. Several salts were selected to reach the subsequent humidity levels of: LiCl for 12% rel. humidity, K(OOCH<sub>3</sub>) for 22%, K<sub>2</sub>CO<sub>3</sub> for 42% and Mg(NO<sub>3</sub>)<sub>2</sub> for 50% relative humidity. To avoid variation in the humidity values and the drying of the environment by the luminescent sample, the solutions were applied in excess so that *via* the evaporation equilibrium at constant humidity can be provided throughout all experiments at all time periods.

To keep the temperature constant, the chamber was placed in a temperature isolating box. After the humidity value reached equilibrium, the sample was exposed to this defined atmosphere, and the photoluminescence recording was started. Subsequently, the remaining samples were extracted and examined *via* X-ray powder diffraction and IR spectroscopy. Elemental analysis was carried out for the bulk substances.

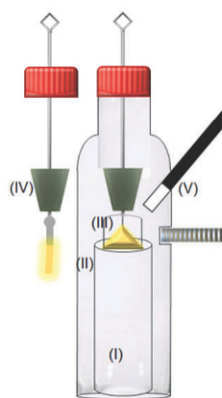


Fig. 5 Scheme of the sample cell for the sensing of humidity: the inner and outer chamber (I & II), the sample carrier (bulk MOF (III) or MMM (IV)) and attachment for the humidity and temperature sensor (V).

### Sensing investigation of humidity on the bulk MOFs

If MOFs **1**, **2** and **3**<sup>39</sup> are exposed to humidity, a luminescence decay can be detected over time. This process can easily be visualised, if the collected emission spectra are plotted in a three dimensional arrangement with time as the z-axis, which is shown here for MOFs **1** and **2**, which were successfully embedded into PSF matrices 1@PSF and 2@PSF (Fig. 6). It is possible to describe these decay plots with the following exponential functions:

$$y = a \cdot \exp\left(\frac{-x}{t}\right) + y_0$$

$$y = A_1 \cdot \exp\left(\frac{-x}{t}\right) + A_2 \cdot \exp\left(\frac{-x}{t}\right) + y_0$$

$y_0$  = starting intensity, (MOFs),  $t$  = time (s), and  $y$  = intensity at the moment  $t$  (MOFs).

Due to the reservoir of saturated salt solution, a constant humidity can be provided leading to a decay which can kinetically be described as pseudo first order<sup>37</sup> behaviour. As anticipated, low humidity levels lead to a slower decay, which speeds up towards higher humidities. For all measurements, the reaction rate constant and half-life were calculated based on the fitted maxima of the 5d–4f transitions (555 nm (**1**) and 495 nm (**2**), (Table 2)). The calculated  $k'$  values were plotted against the concentration, which leads to a linear connection. The reaction rate constant for the overall humidity spectra can be anticipated from the slope of that line.

Although the two MOF systems appear to behave rather similar on the first glance, the luminescence decays vary in two points. First, the rate of the decay differs and based on it also the half-life, and second, the linear trend of the plotted  $k'$  values: for low humidity levels (12 or 22% rh), both MOFs show similar properties, and neither  $k'$  nor  $t_{1/2}$  differ a lot between both systems. Above this point the decay of the luminescence of **2** is nearly six times faster than for **1**, which leads to a much shorter relative half-life (Fig. 7).

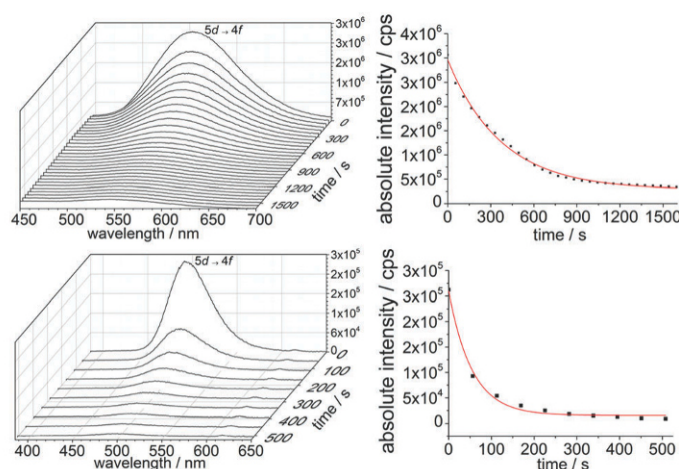


Fig. 6 3D-photoluminescence emission spectra of the collected time-intensity related data for  ${}^3_{}[Ba_{0.98}Eu_{0.02}(Im)_2]$  (**1**, top) and  ${}^3_{}[Sr_{0.90}Eu_{0.10}(Im)_2]$  (**2**, bottom), their corresponding courses of emission (left, excited at 365 and 366 nm, respectively) and the respective exponential fits (right) for 50% relative humidity (rh).

Table 2 Parameters of luminescence decay of MOFs for **1** and **2**<sup>a</sup>

${}^3\text{Ba}_{0.98}\text{Eu}_{0.02}(\text{Im})_2$ , <b>1</b>	Kinetic ( $k'$ ) ( $\text{s}^{-1}$ )	Half-life ( $t_{1/2}$ ) (s)
12% rh	$2.0 \times 10^{-4} \pm 0.4 \times 10^{-4}$	$2360 \pm 643$
22% rh	$3.1 \times 10^{-4} \pm 0.2 \times 10^{-4}$	$1540 \pm 158$
50% rh	$30.0 \times 10^{-4} \pm 2.0 \times 10^{-4}$	$286 \pm 10$
${}^3\text{Sr}_{0.90}\text{Eu}_{0.10}(\text{Im})_2$ , <b>2</b>	Kinetic ( $k'$ ) ( $\text{s}^{-1}$ )	Half-life ( $t_{1/2}$ ) (s)
12% rh	$1.4 \times 10^{-4} \pm 0.4 \times 10^{-4}$	$3055 \pm 132$
22% rh	$43.0 \times 10^{-4} \pm 0.1 \times 10^{-4}$	$1193 \pm 200$
50% rh	$170 \times 10^{-4} \pm 1 \times 10^{-4}$	$39 \pm 3$

<sup>a</sup> Deviation was calculated based on the experimental variance of the determined parameter for  $k'$ .

Based on these experimental results, it was possible to calculate the rate constant for the whole humidity range at 25 °C (Fig. 8). Both MOFs do not show the ideal behaviour, in which the plotted  $k'$  values should be located on a line crossing the origin. In the ideal case, the decay should start at atmospheric water concentrations close to zero. The actual linear fits ( $y = ax + b$ ) cross the  $x$ -axis at water concentrations, which were calculated based on humidity and temperature, of 0.3 mmol L<sup>-1</sup> for **1** and 0.14 mmol L<sup>-1</sup> for **2**. Those intersections define the threshold values of the MOF systems, at which it can be reasonably used as sensors. An unusual observation was made for **1**: no intersection with the  $x$ -axis could be observed but a convergence below 17% rh. As a result, it is possible to identify two threshold values based on the different behaviour of the luminescence decay. For rather short

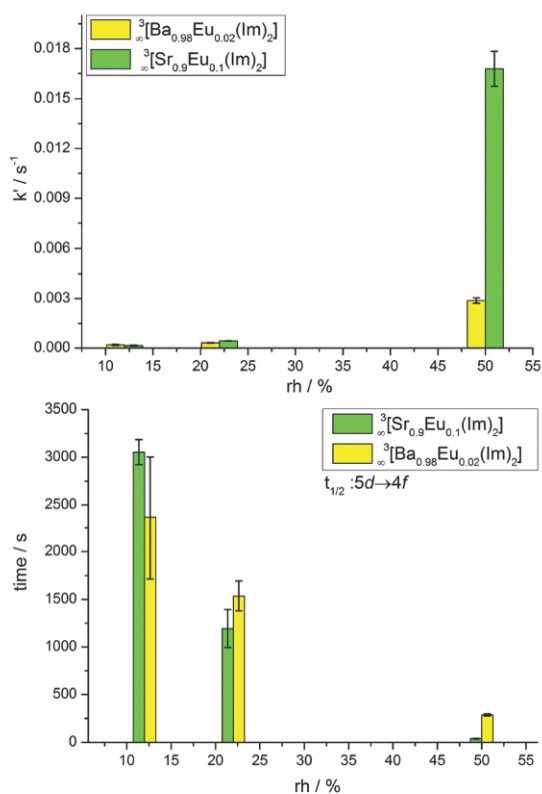


Fig. 7 Comparison of the  $k'$  values (above) and the half-life (below) of the bulk MOFs **1** (yellow bars) and **2** (green bars) at different relative humidity (rh) levels.

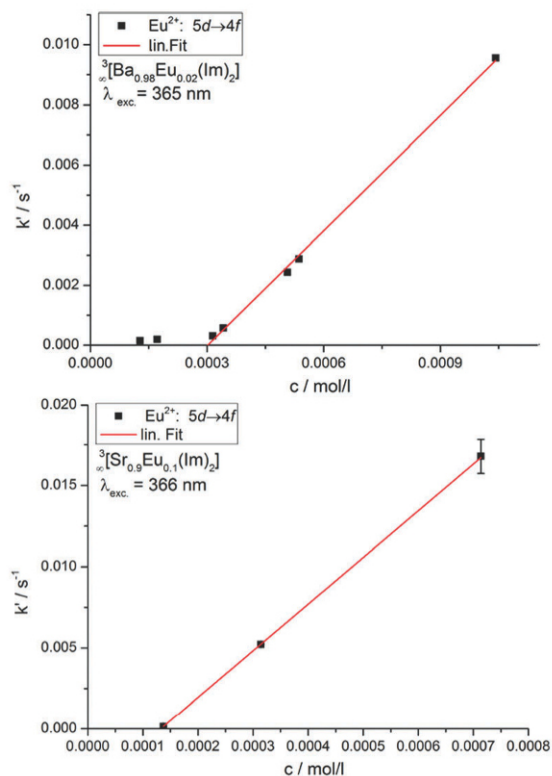


Fig. 8 Plot of the  $k'$  values of the luminescence decay of **1** (above) and **2** (below). In contrast to **2**, the  $k'$  values of **1** do not follow one linear function, but also a second almost linear function below 17% rh with a smaller slope.

periods of observation times, a threshold after the intersection of the linear fit with the  $x$ -axis applies, for which the rate of the decay rises and shortens the detection time to a few minutes (ideal for “on-the-fly”-real status determination) resulting in a threshold value of 10% rh for **2** and 25% rh for **1**.

However, it is possible to detect a lower limit of relative humidity from 2% rh (extrapolation) for **2** by the very slow decay over a long time (hours to days, ideal for storage), resulting in a significant difference of the MOFs **1** and **2** (Fig. 8).

### Sensing investigations of humidity for MMMs of LnMOF@PSF

The corresponding MMMs  ${}^3\text{Ba}_{0.98}\text{Eu}_{0.02}(\text{Im})_2$ @PSF (**1**@PSF) and  ${}^3\text{Sr}_{0.90}\text{Eu}_{0.10}(\text{Im})_2$ @PSF (**2**@PSF) were investigated in the same way as the bulk MOFs in order to allow a direct comparison of the sensing properties. An investigation of **3**@PSF was omitted due to the lack of significant luminescence. The respective 3D-photoluminescence spectra and plots of the kinetics of decay are depicted in Fig. 9. As expected, the MMMs show a different behaviour than the bulk MOFs (see Table 3).

A closer look on the data reveals expected and unexpected results. The embedding of **1** in the PSF membrane leads to an overall higher stability of the MOF particles in **1**@PSF. As expected, the luminescence decay is slowed down, overall,  $t_{1/2}$  values are getting higher for the MMMs and the decay cannot be described with a single function, anymore, but consists of two different kinetic processes (Fig. 10). This reflects that the permeation and the water interaction of the bulk particles have a different reaction rate. Consequently, this results in an

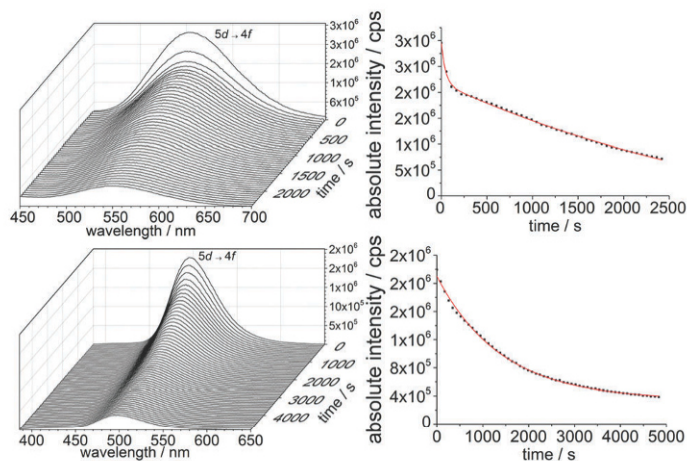


Fig. 9 3D-photoluminescence emission spectra of the collected time-intensity related data for  ${}^3\text{Ba}_{0.98}\text{Eu}_{0.02}(\text{Im})_2$ @PSF (1@PSF, top) and  ${}^3\text{Sr}_{0.90}\text{Eu}_{0.10}(\text{Im})_2$ @PSF (2@PSF, bottom), their corresponding courses of emission (left, excited at 365 and 366 nm, respectively) and the respective exponential fits (right) for 50% relative humidity (rh).

Table 3 Parameters for luminescence decay of 1@PSF and 2@PSF<sup>a</sup>

${}^3\text{Ba}_{0.98}\text{Eu}_{0.02}(\text{Im})_2$ @PSF, 1@PSF	Kinetic ( $k_1'$ ) ( $\text{s}^{-1}$ )	Half-life ( $t_{1/2}$ ) (s)
12% rh	$33 \times 10^{-4} \pm 8 \times 10^{-4}$	$222 \pm 52$
42% rh	$66 \times 10^{-4} \pm 2 \times 10^{-4}$	$106 \pm 2$
50% rh	$225 \times 10^{-4} \pm 2 \times 10^{-4}$	$31 \pm 3$
	Kinetic ( $k_2'$ ) ( $\text{s}^{-1}$ )	Half-life ( $t_{1/2}$ ) (s)
12% rh	$3.0 \times 10^{-4} + 0.7 \times 10^{-4}$	$2454 \pm 571$
42% rh	$4.9 \times 10^{-4} + 0.3 \times 10^{-4}$	$1433 \pm 85$
50% rh	$2.7 \times 10^{-4} + 0.3 \times 10^{-4}$	$2642 \pm 285$
${}^3\text{Sr}_{0.90}\text{Eu}_{0.10}(\text{Im})_2$ @PSF, 2@PSF	Kinetic ( $k_1'$ ) ( $\text{s}^{-1}$ )	Half-life ( $t_{1/2}$ ) (s)
12% rh	$1.5 \times 10^{-4} \pm 0.1 \times 10^{-4}$	$4616 \pm 406$
22% rh	$4.5 \times 10^{-4} \pm 0.1 \times 10^{-4}$	$1529 \pm 21$
50% rh	$7.1 \times 10^{-4} \pm 0.1 \times 10^{-4}$	$973 \pm 17$

<sup>a</sup> Deviation was calculated based on the experimental variance of the determined parameter for  $k'$ .

increase of the stability of the MOFs in the MMMs and thereby also better processability of the films in potential applications compared to the bulk MOFs. The gas molecules can now no longer directly affect the MOF but are influenced by the permeation properties of the films, as they need to permeate through the organic polymer matrix in order to reach the MOF.

However, this also implies that a possible sensing process is influenced by the permeation of the analyte through the film, which requires additional time. This extends the time scale for MOF-luminescence intensity changes from minutes to hours, although the recording of spectra itself remains equally fast. In principle, this increase on the detection time scale is not a problem for the monitoring of long-term storage, as the latter is based on many hours rather than minutes. Also, the threshold value for the MOF hydrolysis is shifted to lower concentrations (intersection with  $x$ -axis at  $0.1 \text{ mmol L}^{-1}$ , Fig. 11), as a certain hydrophilic nature of the membrane together with constant

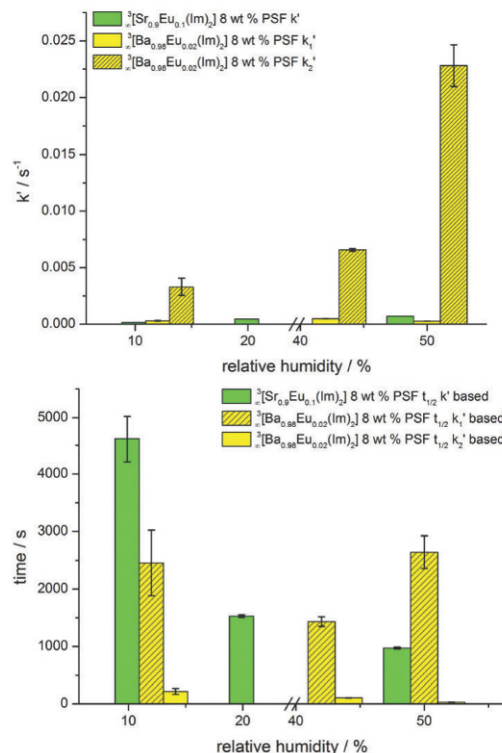


Fig. 10 Comparison of the  $k'$  values (above) and the half-life (below) of 1@PSF (yellow bars) and 2@PSF (green bars) at different relative humidity (rh) levels.

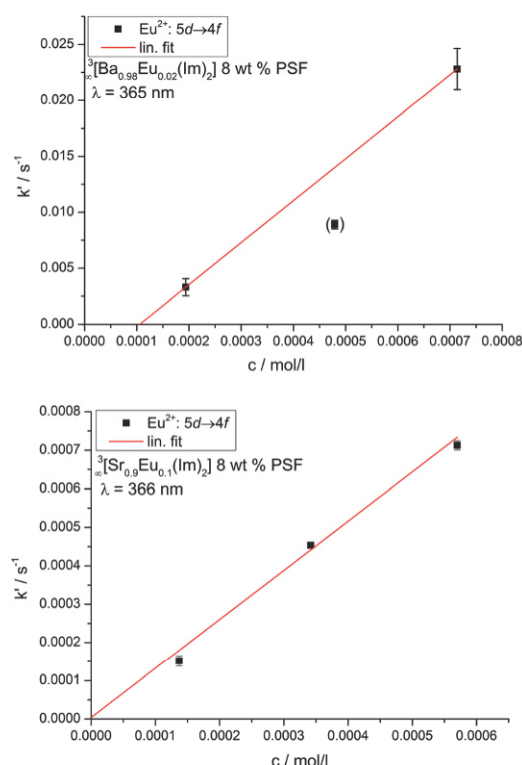


Fig. 11 The plotted  $k'$  values of 1@PSF (above) and 2@PSF (below), and the latter showing ideal behaviour by crossing the origin.

supply of humidity allows for a preconcentration effect influencing the detection over a long time and influencing the sensitivity. Deviation in MMM permeation may also result from different thicknesses of the MMM sensor membrane.

The properties of MMMs of type 2@PSF differ from MMM 1@PSF. In contrast to 1@PSF, the luminescence decay of 2@PSF can be described with one function leading to the assumption that the two processes (gas permeation and hydrolysis) have approximately equal rates. The overall stability of the embedded MOF particles is 1.5 times higher for 12% rh and nearly 4 times higher for 50% rh, leading to a half-life of 4616(405) s for 12% rh. The main difference of 2@PSF to 1@PSF but also to the bulk experiments is that the threshold value extrapolated from the linear fit shows ideal behaviour by crossing the origin.

### PXRD, infrared spectroscopy and elemental analysis

Prior to and subsequent to the sensing experiments, samples of the MOFs and the respective MMMs were investigated by several analytic methods. Each sample was investigated by PXRD and IR spectroscopy; MOF bulk samples were also analysed *via* elemental analysis for their CHN content. Furthermore, a comparison of powder X-ray diffraction of the MMMs and the respective bulk MOFs was carried out (Fig. S6, ESI<sup>†</sup>).

For bulk MOF 1, even for low humidity levels ( $\geq 12\%$  rh), reflections of imidazole can be found pointing towards protonation of the anionic ligands. As a trend, these intensities increase at higher humidity ( $\geq 22\%$  rh). At high humidity levels ( $\geq 50\%$  rh), the powder pattern consists of imidazole, Ba(OH)<sub>2</sub> and small reflection intensities of bulk MOF, indicating the hydrolysis of the MOF. In contrast to these findings,  ${}^3_{\infty}[\text{Ba}_{0.98}\text{Eu}_{0.02}(\text{Im})_2]@\text{PSF}$  membranes 1@PSF only show the MOF reflections for 12% rh. It is possible that due to the rigid structure of the organic polymer matrix, released imidazole cannot crystallize inside the polymer film, so that none of its reflections appear. For high humidities ( $> 42\%$  rh), reflections of Ba(OH)<sub>2</sub> can be detected, corroborating the interpretation of the hydrolysis process, as found for the bulk MOF at 50% rh.

MOF  ${}^3_{\infty}[\text{Sr}_{0.90}\text{Eu}_{0.10}(\text{Im})_2]$  (2) and its MMM 2@PSF were also investigated according to a previous description (Fig. S7, ESI<sup>†</sup>). For low humidity levels ( $\leq 12\%$  rh), both MMM and bulk material show no differences to the corresponding starting material, indicating that changes are too limited to be observable by PXRD. Raising the humidity level to 22% rh leads to slight changes in the pattern of both 2 and 2@PSF, showing additional reflections that can be found in addition to the reflections of 2 and imidazole. Hence, the anionic ligand is protonated, released and an additional unknown crystalline phase is formed during sensing, corroborating the assumption of an irreversible detection process. The main reflection of this phase can be seen in the MMM pattern 2@PSF for 50% rh. Due to the character of the surrounding organic film, no large crystalline growth inside the MMM is possible, leading to weaker intensities of the reflections compared to the bulk MOF. For the highest humidity level tested (50% rh), the powder pattern of 2@PSF exhibits no MOF reflections of 2 but reflections of Sr(OH)<sub>2</sub> and the already mentioned unknown phase, again indicating hydrolysis as the base of the irreversible detection.

IR-spectroscopy is another useful method to detect vibrational groups including OH, water, N–H of imidazole or potential species that may not be found by PXRD, as they may be non-crystalline or too low in amount. For 1 and 2 (Fig. S7 and S9, ESI<sup>†</sup>) at low

humidity levels (12–22% rh), very weak bands of the N–H stretching vibration between 3500 and 3300 cm<sup>-1</sup> are found. For 50% rh free imidazole dominates the spectrum in addition to two OH related bands at 3305 cm<sup>-1</sup> and 3608 cm<sup>-1</sup>. For membranes 1@PSF and 2@PSF, no changes in the IR spectra can be detected at 12% rh, and only slight changes appear at 22% rh (weak bands at 2918 and 2850 cm<sup>-1</sup> belonging to imidazole). A significant change in the pattern of the IR spectra of 1@PSF can be observed at 50% rh, and at this humidity level the fingerprint region is dominated by broad and diffuse bands. For membrane 2@PSF at 50% rh, only the bands of imidazole can be detected. Typical N–H vibrations appear, and the bathochromic shift of bonded imidazolate vanishes, both prove that during the hydrolysis process imidazole is released.

To check the amount of water that was taken up by the MOFs during the sensing process, the bulk MOFs were also checked *via* elemental analysis and based on the changes in the amount of carbon the amount of water was calculated (0–2 equivalents for 1 and 0–5.5 equivalents for 2) (Table S1, ESI<sup>†</sup>). It can be seen that for both 1 and 2, the amount of water increases for higher humidity levels. Unfortunately, the high and not specifically defined organic content and therefore the elemental composition of MMMs prohibit suitable CHN analysis of the MMMs.

## Conclusion

Mixed matrix membranes were generated from luminescent co-doped alkaline earth/lanthanide imidazolate MOFs and poly-sulfone. Sensitive sensor MMMs were generated that exceed bulk MOFs in stability, handling and long-term monitoring, which can be especially interesting for overseas transport or long-term storage under atmospheric conditions (rh of several percent) whilst retaining the general sensitivity of the sensing process. Three highly luminescent Ln-imidazolate MOFs  ${}^3_{\infty}[\text{Sr}_{0.90}\text{Eu}_{0.10}(\text{Im})_2]$ ,  ${}^3_{\infty}[\text{Ba}_{0.98}\text{Eu}_{0.02}(\text{Im})_2]$  and  ${}^3_{\infty}[\text{Ce}(\text{Im})_3\text{ImH}]\cdot\text{ImH}$  were investigated, of which the Sr/Eu and Ba/Eu combinations gave luminescent membranes by embedding of the unchanged MOFs. The product MMMs were investigated for potential humidity sensing and the results were compared to the sensing properties of the bulk MOFs for several pre-set humidity values including a study of the kinetics of the sensing processes. To the best of our knowledge, these are the first luminescence sensing investigations with MOF containing membrane systems. The bulk MOFs and especially the membranes exhibit sensing of humidity starting at 2% rel. humidity, observable by quenching of the MOF luminescence as a function of the water concentration. Due to the gas permeation through the organic polymer, the membranes show slower detection compared to the bulk MOFs but also improved stability towards air and therefore better processability in potential applications, as they can be handled in a normal atmosphere – different to the MOFs themselves. As the delay in monitoring caused by the permeation processes is no issue for real status analysis of long-term processes, the stability increase is strongly favourable, and the error free character of

irreversible detection if preferable over reversible sensing in all cases that do not allow for 24/7 monitoring.

The detection process was monitored *in situ* to the interaction of the sensor system and the analyte and was characterized as ongoing hydrolysis. Permeation experiments have verified that the membranes are free of defects. The calculated theoretical permeabilities for the mixed matrix membranes show little deviation from the measured permeabilities.

Altogether, it was possible to show that MMMs can be used as sensors or detectors for different levels of humidity and time scales, and the occurring luminescence decay can also be kinetically and mathematically described. It can be shown that embedding of MOF particles influences the detection sensitivity to lower reaction rate constants and can change the threshold value for the selected MOF, creating design space for selective adaption of LnMOF based sensors for highly specific applications. Overall, the presented results can open a pathway to long term sensing *via* luminescence in mixed matrix membrane systems.

## Experimental section

For general experimental considerations, please see the ESI.†

### Synthesis of ${}^3_{\infty}[\text{Ba}_{0.98}\text{Eu}_{0.02}(\text{Im})_2]$ (1)

The MOF was synthesised according to the literature.<sup>34</sup> The gained product was a yellow fine powder of **1**. Yield: 350.66 mg = 87%. Anal. calcd for  $\text{C}_6\text{H}_6\text{N}_4\text{Ba}_{0.98}\text{Eu}_{0.02}$  ( $M_r = 205.70 \text{ g mol}^{-1}$ ): C, 26.52%; N, 20.61%; H, 2.95%. Found: C, 26.89%; N, 19.78%; H, 2.23%.

### Synthesis of ${}^3_{\infty}[\text{Sr}_{0.90}\text{Eu}_{0.10}(\text{Im})_2]$ (2)

Substance **2** was synthesised according to the literature.<sup>35</sup> The product was gained as a yellow crystalline powder. Yield: 203.02 mg = 89%; anal. calcd for  $\text{C}_6\text{H}_6\text{N}_4\text{Sr}_{0.9}\text{Eu}_{0.10}$  ( $M_r = 228.21 \text{ g mol}^{-1}$ ): C, 31.58%; N, 24.55%; H, 2.65%. Found: C, 32.26%; N, 24.24%; H, 2.84%.

### Synthesis of ${}^3_{\infty}[\text{Ce}(\text{Im})_3\text{ImH}]\cdot\text{ImH}$ (3)

Substance **3** was synthesised according to the literature.<sup>39</sup> The gained product was a greyish fine powder of **3**. Yield: 368.4 mg = 90% anal. calcd for  $\text{CeC}_{15}\text{H}_{17}\text{N}_{10}$  ( $M_r = 477.48 \text{ g mol}^{-1}$ ): C, 37.73%; N, 29.33%; H, 3.59%. Found: C, 36.95%; N 28.22%; H 3.68%.

### Membrane preparation (1@PSF–3@PSF)

Before embedding into the polymer, the MOFs were ground in a ball mill under argon to adjust the particle size to about 50  $\mu\text{m}$  for (**1**) (Fig. S11, ESI†) (150 s at 15 Hz). Portions (200 mg) of the dry polymer, the MOF material (18 mg), and dry dichloromethane (4 mL) were combined in a 10 mL Schlenk flask to produce MMMs with 8 wt% of the respective MOFs **1–3**. The dispersions were stirred for 2 d in order to achieve homogeneous mixtures and were cast into metal rings, 5 cm in diameter, which were placed on a flat glass surface in a desiccator filled with nitrogen gas and a desiccant. The solvent was evaporated

overnight by a slight stream of pre-dried nitrogen gas to ensure a sufficient evaporation rate. As soon as all of the solvent was evaporated, the membrane was removed from the metal ring and the glass surface. The membrane was finally dried at 25 °C under reduced pressure.

For details on the powder X-ray diffraction (PXRD) analyses, please check the ESI.†

For details on the SEM/EDX analyses, please see the ESI.†

### Photoluminescence spectroscopy

Excitation and emission spectra were recorded with a Horiba Jobin Yvon Fluorolog 3 photoluminescence spectrometer with a 450 W Xe lamp, Czerny–Turner double grating (1200 grooves per mm) excitation and emission monochromators and an R928P detector. Emission spectra range from 400 to 680 nm and were corrected for the spherical response of the monochromators and the detector using typical correction spectra. Excitation spectra were recorded from 300 to 400 nm and corrected for the spectral distribution of the lamp intensity using a photodiode reference detector.

The overall luminescence process lifetimes of the MMM 2@PSF and of the films 1@PSF and 2@PSF subsequent to sensing were obtained by determination of the luminescence decay with a Horiba Fluoromax FL3-22 spectrophotometer. Samples were prepared in quartz glass cuvettes under an inert-gas atmosphere, and the decay times were recorded by time-correlated single-photon counting (TCSPC) with a 375 nm pulsed laser diode or a microsecond flash lamp with an excitation wavelength of 330 nm. The fluorescence emission was collected at right angles to the excitation source, and the emission wavelength was selected with a monochromator and detected using a single-photon avalanche diode (SPAD). The resulting intensity decays were calculated through tail fits.

### Gas permeation

The  $\text{O}_2$  permeabilities were evaluated with a permeation cell described elsewhere.<sup>38</sup> The membrane thickness was measured as the average over ten different spots with a micrometer screw. The gas permeation measurements were performed using the pressure-rise method under steady-state conditions at 30 °C. The membrane was placed into the sample cell; permeate and feed sides were evacuated. The feed side was filled with  $\text{O}_2$  gas to a pressure of 3.0 bar. The linear pressure increase upon permeation from the feed to the permeate side was recorded and used to calculate the permeability  $P$  in Barrer units [1 Barrer =  $1 \times 10^{-10} \text{ cm}^3$  (STP) cm (cm s cmHg) $^{-1}$  or  $7.5005 \times 10^{-18} \text{ m}^2 \text{ s}^{-1} \text{ Pa}^{-1}$  in SI units]. Permeability  $P$  is defined as gas flow rate  $J$  multiplied by thickness  $d$  of the membrane, divided by area  $A$  and by pressure difference  $\Delta p$  across the material:

$$P = (J \cdot d) / \Delta p \cdot A$$

For the Maxwell equation, assumed shape factor  $n$  was 1/3, as it is commonly used for spherical particles. The density of the polymer was taken from the material data sheet, the density of the fillers were calculated from the crystal structures, permeability  $P_f$  of the filler was assumed to be 0 for a non-porous

material and permeability  $P_m$  of the pure polymer was measured under the same conditions in the same permeation cell as those in the MMMs.<sup>35,40,41</sup>

### Sensing/detection investigations

For the sensing experiments of the bulk MOFs, 7.0 mg (0.034 mmol) of  ${}^3\text{Ba}_{0.98}\text{Eu}_{0.02}(\text{Im})_2$  (1) or 7.0 mg (0.030 mmol) of  ${}^3\text{Sr}_{0.90}\text{Eu}_{0.10}(\text{Im})_2$  (2), respectively, were placed in a sample cell consisting of a reservoir for different saturated salt solutions, a hygrometer and the hermetically closed sample carrier. The cell was filled under inert conditions to avoid premature hydrolysis. After the sample carrier was capped, the reservoir was filled with 80 mL of saturated salt solutions adjusting different, constant humidity values, which were equilibrated ( $\text{LiCl} \approx 12\%$ ,  $\text{K}(\text{CH}_3\text{COO}) \approx 22\%$ ,  $\text{K}_2\text{CO}_3 \approx 42\%$  and  $\text{Mg}(\text{NO}_3)_2 \approx 50\%$ ). Humidity and temperature in the sample cell were monitored with a humidity and temperature sensor. The sample was exposed to a defined humidity-containing atmosphere and simultaneously the recording of the emission spectra was started. For the measurement of the MMMs, the films were fixed with a clip in the hermetically closed sample carrier. In both cases, emission spectra were recorded every 30 s. The measuring cell was coupled with a Horiba Fluorolog-3 photoluminescence spectrometer *via* a fibre-optic cable.

### Humidity detection

For the *in situ* humidity detection a Testo 645 humidity and temperature measuring device was used with a temperature and humidity detector capped with a PTFE cap. The device is able to detect humidity and temperature in the range of 0–100(2)% rh from –20 to 70(2) °C.

### Elemental analysis

The bulk materials of 1–3 were investigated using elemental analysis for C, H and N, before and after the hydrolysis process, performed with an ELEMENTAR Vario El CHN analyser.

### Vibrational spectroscopy

FTIR spectra were recorded using a Thermo Nicolet FTIR-380 spectrometer.

## Conflicts of interest

There are no conflicts to declare.

## Acknowledgements

We gratefully acknowledge support from the Volkswagen Stiftung within the project “Multifunctional Molecular Materials”.

## References

- L. G. Qiu, Z. Q. Li, Y. Wu, W. Wang, T. Xu and X. Jiang, *Chem. Commun.*, 2008, 3642–3644.
- Z. Xie, L. Ma, K. E. de Krafft, A. Jin and W. J. Lin, *J. Am. Chem. Soc.*, 2009, **132**, 922–923.
- Q. Tan, J. Liu and Z. Liu, *Dalton Trans.*, 2016, **45**, 18450–18454.
- Z. Chen, J. Chen and D. Pan, *Anal. Bioanal. Chem.*, 2017, **409**, 2429–2435.
- C. Zhi and C. Lu, *Sens. Lett.*, 2005, **4**, 274–295.
- L. E. Kreno, K. Leong, O. K. Farha, M. Allendorf, R. P. Van Duyne and J. T. Hupp, *Chem. Rev.*, 2012, **112**, 1105–1125.
- D. K. Singha and P. Mahata, *Inorg. Chem.*, 2015, **54**, 6373–6379.
- S. Bhattacharyya, A. Chakraborty, K. Jayaramulu, A. Hazra and T. K. Maji, *Chem. Commun.*, 2014, **50**, 13567–13570.
- H. Lee, S. H. Jung, W. S. Han, J. H. Moon, S. Kang, J. Y. Lee, J. H. Jung and S. Shinkai, *Chem. – Eur. J.*, 2011, **17**, 2823–2827.
- G. Lu, O. K. Farha, L. E. Kreno, P. M. Schoenecker, K. S. Walton, R. P. Van Duyne and J. T. Hupp, *Adv. Mater.*, 2011, **23**, 4449–4452.
- E. Coronado and G. Minguez Espallargas, *Chem. Soc. Rev.*, 2013, **42**, 1525–1539.
- H. Y. Li, Y. L. Wei, X. Y. Dong, S. Q. Zang and T. C. W. Mak, *Chem. Mater.*, 2015, **27**, 1327–1331.
- B. Chen, L. Wang, Y. Xiao, F. R. Fronczek, M. Xue, Y. Cui and G. Qian, *Angew. Chem.*, 2009, **121**, 508–511 (*Angew. Chem., Int. Ed.*, 2009, **48**, 500–503).
- X. S. Wang, L. Li, D. Q. Yuan, Y. B. Huang and R. Cao, *J. Hazard. Mater.*, 2017, **16**(344), 283–290.
- F. Boltinghouse and K. Abel, *Anal. Chem.*, 1989, **61**, 1863–1866.
- A. Tsigara, G. Mountrichas, K. Gatsouli, A. Nichelatti, S. Pispas, N. Madamopoulos, N. A. Vainos, H. L. Du and F. Roubani-Kalantzopoulou, *Sens. Actuators, B*, 2007, **120**, 481–486.
- (a) A. Weiss, N. Reimer, N. Stock, M. Tiemann and T. Wagner, *Microporous Mesoporous Mater.*, 2016, **220**, 39–43; (b) Y. Yu, X. Zhang, J. Ma, Q. Liu, P. Wang and Y. Dong, *Chem. Commun.*, 2014, **50**, 1444–1446; (c) J. Wu and B. Yan, *Dalton Trans.*, 2017, **46**, 7098–7105; (d) D. Wang, Q. Tan, J. Liu and Z. Liu, *Dalton Trans.*, 2016, **45**, 18450–18454; (e) L. V. Meyer, F. Schönfeld, A. Zurawski, M. Mai, C. Feldmann and K. Müller-Buschbaum, *Dalton Trans.*, 2015, **44**, 4070–4079; (f) F. Wang, Y.-T. Wang, H. Yu, J.-X. Chen, B.-B. Gao and J.-P. Lang, *Inorg. Chem.*, 2016, **55**, 9417–9423.
- F. Y. Yi, D. Chen, M. K. Wu, L. Han and H. L. Jiang, *ChemPlusChem*, 2016, **81**, 675–690.
- D. Gomez, S. P. Morgan, B. R. Hayes-Gill, R. G. Correia and S. Korposh, *Sens. Actuators, B*, 2018, **254**, 887–895.
- F. A. Keidel, *Anal. Chem.*, 1959, **31**, 2043–2048.
- O. M. Yaghi, *Acc. Chem. Res.*, 2010, **43**, 58–67.
- (a) O. K. Farha and J. T. Hupp, *Acc. Chem. Res.*, 2010, **43**, 1166–1175; (b) C. Janiak and S. K. Henninger, *Chimia*, 2013, **67**, 419–424; (c) S. K. Henninger, F. Jeremias, H. Kummer and C. Janiak, *Eur. J. Inorg. Chem.*, 2012, 2625–2634; (d) F. P. Doty, C. A. Bauer, A. J. Skulan, P. G. Grant and M. D. Allendorf, *Adv. Mater.*, 2009, **21**, 95–101; (e) H. Lee, S. H. Jung, W. S. Han, J. H. Moon, S. Kang, J. Y. Lee, J. H. Jung and S. Shinkai, *Chem. – Eur. J.*, 2011, **17**, 2823–2827.
- P. Falcaro, R. Ricco, C. M. Doherty, K. Liang, J. A. Hill and M. J. Styles, *Chem. Soc. Rev.*, 2014, **43**, 5513–5560.

- 24 H. C. Zhou, J. R. Long and O. M. Yaghi, *Chem. Rev.*, 2012, **112**, 673–674.
- 25 (a) S. Roy, A. Chakraborty and T. K. Maji, *Coord. Chem. Rev.*, 2014, **273**, 139–164; (b) L. V. Meyer, F. Schönfeld and K. Müller-Buschbaum, *Chem. Commun.*, 2014, **50**, 8093–8108; (c) Y. Cui, B. Chen and G. Qian, *Chem. Rev.*, 2014, **273**, 76–86; (d) L. Ma, O. R. Evans, B. M. Foxman and W. Lin, *Inorg. Chem.*, 1999, **38**, 5837–5840; (e) T. M. Reinecke, M. Eddaoudi, M. Fehr, D. Kelly and O. M. Yaghi, *J. Am. Chem. Soc.*, 1999, **121**, 1651–1657; (f) Z. S. Bai, J. Xu, T. Okamura, M. S. Chen, W. Y. Sun and N. Ueyama, *Dalton Trans.*, 2009, 2528–2539.
- 26 (a) Y. Xiao, Y. Cui, Q. Zheng, S. Xiang, G. Qian and B. Chen, *Chem. Commun.*, 2010, **46**, 5503–5505; (b) Z. Guo, H. Xu, S. Su, J. Cai, S. Dang, S. Xiang, G. Qian, H. Zhang, M. O’Keeffe and B. Chen, *Chem. Commun.*, 2011, **47**, 5551–5553.
- 27 T. Wehner, M. T. Seuffert, J. R. Sorg, M. Schneider, K. Mandel, G. Sxltl and K. Müller-Buschbaum, *J. Mater. Chem. C*, 2017, **5**, 10133–10142.
- 28 K. Müller-Buschbaum, F. Beuerle and C. Feldmann, *Micro-porous Mesoporous Mater.*, 2015, **216**, 171–199.
- 29 K. Binnemans, *Chem. Rev.*, 2009, **109**, 4283–4374.
- 30 L. V. Meyer, F. Schönfeld, A. Zurawski, M. Mai, C. Feldmann and K. Müller-Buschbaum, *Dalton Trans.*, 2015, **44**, 4070.
- 31 J. Dechnik, F. Mühlbach, D. Dietrich, T. Wehner, M. Gutmann, T. Lühmann, L. Meinel, C. Janiak and K. Müller-Buschbaum, *Eur. J. Inorg. Chem.*, 2016, 4408.
- 32 (a) J. Won, J. S. Seo, J. H. Kim, H. S. Kim, Y. S. Kang, S. J. Kim, Y. Kim and J. Jegal, *Adv. Mater.*, 2005, **17**, 80–84; (b) A. Car, C. Stropnik and K. V. Peinemann, *Desalination*, 2006, **200**, 424–426; (c) B. Seoane, J. M. Zamaro, C. Tellez and J. Coronas, *RSC Adv.*, 2011, **1**, 917–922; (d) B. Zornoza, B. Seoane, J. M. Zamaro, C. Tellez and J. Coronas, *Chem-PhysChem*, 2011, **12**, 2781–2785.
- 33 D. Yang, D. Liu, C. Tian, S. Wang and H. Li, *J. Colloid Interface Sci.*, 2018, **519**, 11–17.
- 34 J. C. Rybak, M. Hailmann, P. R. Matthes, A. Zurawski, J. Nitsch, A. Steffen, J. G. Heck, C. Feldmann, S. Götzendörfer, J. Meinhardt, G. Sxltl, H. Kohlmann, S. J. Sedlmaier, W. Schnick and K. Müller-Buschbaum, *J. Am. Chem. Soc.*, 2013, **135**, 6896–6902.
- 35 (a) A. Zurawski, M. Mai, D. Baumann, C. Feldmann and K. Müller-Buschbaum, *Chem. Commun.*, 2011, **47**, 496–498; (b) L. V. Meyer, J. Vogt, H. Schafer, M. Steinhart, R. Bottcher, A. Poppl, M. Mai, C. Feldmann and K. Müller-Buschbaum, *Inorg. Chem. Front.*, 2015, **2**, 237–245.
- 36 L. V. Meyer, F. Schönfeld, A. Zurawski, M. Mai, C. Feldmann and K. Müller-Buschbaum, *Dalton Trans.*, 2015, **44**, 4070–4079.
- 37 J. I. Steinfeld, J. S. Francisco and W. L. Hase, *Chemical Kinetics and Dynamics*, Prentice Hall, 2nd edn, 1998.
- 38 J. U. Wieneke and C. Staudt, *Polym. Degrad. Stab.*, 2010, **95**, 684–693.
- 39 R. H. B. Bouma, A. Checchetti, G. Chidichimo and E. Drioli, *J. Membr. Sci.*, 1997, **128**, 141–149.
- 40 BASF Ultrason S 6060 ISO Data Sheet.
- 41 A. Zurawski, J. C. Rybak, L. V. Meyer, P. R. Matthes, V. Stepanenko, N. Dannenbauer, F. Würthner and K. Müller-Buschbaum, *Dalton Trans.*, 2012, **41**, 4067–4078.

### **3.4 Role of Filler Porosity and Filler/Polymer Interface Volume in Metal-Organic Framework/Polymer Mixed-Matrix Membranes for Gas Separation**

Alexander Nuhnen, Dennis Dietrich, Simon Millan, Christoph Janiak

Die Publikation beinhaltet Untersuchungen zum Einfluss von porösen und nicht-porösen Füllstoffen, welche sich von ihren sonstigen Eigenschaften (z. B. Oberflächenbeschaffenheit, Partikelgröße und -form, u. ä.) nicht weiter unterscheiden. Des Weiteren wurden Untersuchungen zur Defektfreiheit der Membranen sowie zur Einbettung der Partikel durchgeführt. Es konnte gezeigt werden, dass die Porosität dem Maxwell-Modell entsprechenden Einfluss hat, die Membranen defektfrei sind und es gute Wechselwirkungen zwischen dem Polymer und den Partikeln gibt, was wiederum für eine gute Einbettung ohne Leervolumen an den Grenzflächen sorgt.

Anteile an der Veröffentlichung:

- Rasterelektronenmikroskopische Strukturuntersuchungen der Membranquerschnitte.
- Ortsaufgelöste energiedispersive Röntgenanalyse zur Bestimmung der homogenen Einbettung des Füllmaterials in den Polymermembranen.
- Mitentwicklungen an Methoden zur Charakterisierung bestimmter Membraneigenschaften.
- Charakterisierung der Membranen, Permeationsmessungen, theoretische Rechnung zu den Modellen und Vergleichen mit den empirischen Daten sowie Verfassen des Manuskriptes durch Herrn Alexander Nuhnen. Korrekturen durch Herrn Prof. Dr. Christoph Janiak.
- Anteilige Arbeiten durch die übrigen Kooperationspartner.



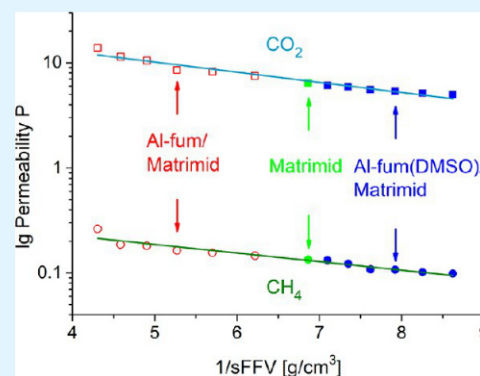
# Role of Filler Porosity and Filler/Polymer Interface Volume in Metal–Organic Framework/Polymer Mixed-Matrix Membranes for Gas Separation

Alexander Nuhnen, Dennis Dietrich, Simon Millan, and Christoph Janiak\*<sup>ib</sup>

Institut für Anorganische Chemie und Strukturchemie, Heinrich-Heine-Universität, Universitätsstraße 1, D-40225 Düsseldorf, Germany

## Supporting Information

**ABSTRACT:** Metal–organic frameworks (MOFs) and inorganic fillers are frequently incorporated into mixed-matrix membranes (MMMs) to overcome the traditional trade-off in permeability ( $P$ ) and selectivity for pure organic polymer membranes. Therefore, it is of great interest to examine the influence of porous and nonporous fillers in MMMs with respect to the possible role of the polymer–filler interface, that is, the void volume. In this work, we compare the same MOF filler in a porous and nonporous state, so that artifacts from a different polymer–filler interface are excluded. MMMs with the porous MOF aluminum fumarate (Al-fum) and with a nonporous dimethyl sulfoxide solvent-filled aluminum fumarate (Al-fum(DMSO)), both with Matrimid as polymer, were prepared. Filler contents ranged from 4 to 24 wt %. Gas separation performances of both MMMs were studied by mixed gas measurements using a binary mixture of CO<sub>2</sub>/CH<sub>4</sub> with gas permeation following the theoretical prediction by the Maxwell model for both porous and nonporous dispersed phase (filler). MMMs with the porous Al-fum filler showed increased CO<sub>2</sub> and CH<sub>4</sub> permeability with a moderate rise in selectivity upon increasing filler fraction. The MMMs with the nonporous Al-fum(DMSO) filler displayed a reduction in permeability while maintaining the selectivity of the neat polymer. A linear dependence of  $\log P$  versus the reciprocal specific free fractional volume (sFFV) rules out a significant contribution from a void volume. The sFFV includes the free volume of the polymer and the MOF, but not the polymer–filler interface volume (so-called void volume). The sFFV for the MMM was calculated between 0.23 cm<sup>3</sup>/g for a 24 wt % Al-fum/Matrimid MMM and 0.12 cm<sup>3</sup>/g for a 24 wt % Al-fum(DMSO)/Matrimid MMM. The negligible effect of an interface volume is supported by a good matching of theoretical and experimental density of the Al-fum and Al-fum/(DMSO) MMMs which gave a specific void volume below 0.02 cm<sup>3</sup>/g, often even below 0.01 cm<sup>3</sup>/g.



**KEYWORDS:** MOFs, metal–organic frameworks, Matrimid, mixed-matrix membrane, nonporous filler, free fractional volume, void volume, gas separation

## INTRODUCTION

Membrane science and technology has attracted continuous attention over the last few decades due to its superior separation properties in comparison to conventional methods, such as crystallization, distillation, or adsorption processes.<sup>1–3</sup> Since purification processes based on membranes feature high energy efficiency, low production costs, and simple process conditions, they are very attractive for industrial application.<sup>4,5</sup>

Gas separation efficiency through dense polymer membranes is generated through a unique separation process as no high energy phase transformation is needed, unlike in the conventional separation processes. Separation through membranes is dependent instead on size, shape, and interaction of the molecules with the membrane material.<sup>6</sup> Membranes therefore can be characterized by two main properties to determine their efficiency. The permeability describes the velocity in which the gases travel through the membrane, and

the selectivity exhibits the separation potential between two or more gases.<sup>7</sup>

At the current state low flux polymeric membranes are widely used in industrial processes because of their high flexibility, easy processing, low costs, and mechanical strength.<sup>8</sup> Yet, polymeric membranes display a major disadvantage since they exhibit an inverse relation, a trade-off between high gas permeation or good selectivity.<sup>9</sup> This inverse relation between permeation and selectivity is illustrated in the so-called Robeson upper bound.<sup>9,10</sup> A possible way to overcome this trade-off is realized by embedding inorganic or organic–inorganic hybrid materials as fillers into the polymer matrix to receive mixed-matrix membranes (MMMs).<sup>11–14</sup>

Received: July 30, 2018

Accepted: September 7, 2018

Published: September 7, 2018

The used fillers can generally be divided into two groups: porous and nonporous fillers. In the field of porous fillers zeolites and highly porous metal organic frameworks (MOFs) are the most studied materials in MMMs.<sup>15–17</sup> Because of their high tuneability and structural diversity MOFs can be customized for different polymer matrices to obtain micro-defect free MMMs or enhance their separation properties.<sup>18,19</sup> Usually it is found that the permeability of defect free MMMs increases with the loading of the MOF and the selectivity remains unaltered or raises only in a moderate way in comparison to the neat polymer.<sup>20</sup> The increase of permeability is either associated with the porous nature of the MOFs, which therefore increases the free fractional volume (FFV) of the MMMs, or to the presence of isolated voids in the interface between the MOF and the polymer.<sup>21,22</sup> Free fractional volume refers to the inherent porosity within the polymer and the porous filler, here the MOF. The FFV does not include any voids formed around the filler particles due to phase incompatibility. However, a consequence of voids, which become connected through a membrane because of high filler loading, will be that these MMMs show an increased permeability and a partial or complete loss of selectivity as such connected voids would be nonselective.<sup>23,24</sup>

Exemplary for this behavior Basu et al. studied the permeation properties of MIL-53(Al)/Matrimid, Cu-BTC/Matrimid, and ZIF-8/Matrimid MMMs for CO<sub>2</sub> and CH<sub>4</sub> and found a continuous increase in CO<sub>2</sub> and CH<sub>4</sub> permeation with growing amount of MOF. Thereby CO<sub>2</sub> permeation enhancement was slightly higher in relation to CH<sub>4</sub>, resulting in a moderate rise of their selectivity.<sup>25</sup> A way to enhance the selectivity in a significant manner was specified by Zornoza et al., using the amino modified NH<sub>2</sub>-MIL-53(Al) embedded in a polysulfone matrix.<sup>13</sup> The characterization of the MMMs showed a doubling in selectivity for the MMMs with 25 wt % MOF including a minor raise in CO<sub>2</sub> permeability, before losing their separation properties with higher loadings up to 40 wt % MOF.

Studies of nonporous fillers in MMMs mostly focus on nanoparticles based on fumed silica or other oxides.<sup>14,26</sup> As nonporous fillers are not permeable for gases, they should lower the permeability of the MMMs with increasing amount of the filler, as long as one obtains an ideal MMM. This behavior was shown by Sadeghi et al. when they incorporated silica nanoparticles into a polyether polymer matrix. The MMMs show a reduction of permeability for several gases with increasing amount of silica.<sup>27</sup> Nevertheless Merkel et al., Ahn et al., and Ahmadpour et al. experienced an increase of the permeability for their MMMs with nonporous nanoparticles in comparison to the neat polymer.<sup>14,26,28</sup> Ahn et al. explained the rise in permeability as a result of interfacial voids between nanoparticles and polymer. They quantified the resulting voids by comparing the actual density of the MMMs with the theoretically calculated density and could therefore determine the void volume of the MMMs.<sup>28</sup> The interfacial voids were associated with poor interactions of the inorganic nanoparticles with the polymer phase.<sup>29</sup> With porous fillers the determination of interfacial voids is rarely done. It was shown that there is a correlating increase between FFV and permeability, but no such correlation could be seen between void volume and permeability.<sup>21</sup>

With porous fillers an increase in permeability is seen as normal and viewed as an expected property. However, it cannot automatically be deduced that this increase is due to

the porosity of the filler. With the formation of interfacial voids, such an increase could also derive therefrom.<sup>23,24</sup>

To the best of our knowledge, the relative role of porosity in the filler and interfacial voids between filler and polymer have not been clearly elucidated. Understandably it is not straightforward to conceive how the chemically same filler material could be prepared in a porous and nonporous way. Therefore, we prepared for the first time (to the best of our knowledge) a porous and a nonporous filler based on the same MOF, with the same properties as particle size, structure, and interaction with the polymer, only differing in their porosity. By embedding both fillers in the polymer Matrimid one should see which influence porosity and interfacial voids have, respectively. If the void volume is responsible for a higher permeability in MMMs, compared to the neat polymer, then one would expect a rise in permeability for both kinds of filler. If, however, the porosity is responsible for an increase in permeability, then one would expect a rise in permeability only for the MMMs with the porous filler.

## RESULTS AND DISCUSSION

**Al-fum and Al-fum(DMSO) Characterization.** In this study the properties of porous and nonporous fillers in MMMs, based on the MOF aluminum fumarate as filler and Matrimid as polymer, is examined. Aluminum fumarate (Al-fum) was synthesized according to a recently described procedure which yields submicrometre particles of the MOF.<sup>30</sup> Particle size and morphology of fillers have great influence on the distribution of MOF particles in the polymer matrix. Thus, they affect phenomena such as sedimentation and agglomeration of the filler and ultimately reduce or increase microdefects in MMMs which affects permeation results.<sup>13,31,32</sup> Here, the obtained Al-fum particles had a size of about 250 nm, characterized by SEM (Figure S2 of the Supporting Information, SI), which is in good agreement with the literature.<sup>30</sup> Furthermore, the successful synthesis of aluminum fumarate was shown by a positive matching of the experimental PXRD to the simulated pattern (Figure 1). The synthesis of aluminum fumarate-(DMSO) (Al-fum(DMSO)), that is, pore filling of Al-fum by dimethyl sulfoxide, was achieved by stirring Al-fum in dimethyl sulfoxide at 180 °C overnight. DMSO-filling did neither alter the Al-fum particle size of about 250 nm (Figure S2) nor the crystallinity (Figure 1). The PXRD in Figure 1 shows slightly

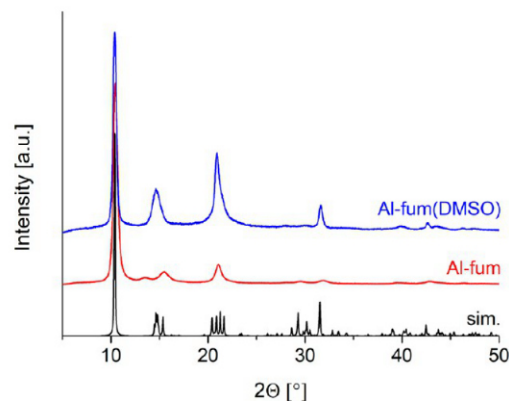


**Figure 1.** Powder X-ray diffractograms for Al-fum in red and Al-fum(DMSO) in blue in comparison with the simulated diffractogram (sim., based on the X-ray data refinement, CCDC number: 1051975)<sup>37</sup> in black.

higher intensities for reflections after  $11^\circ 2\theta$  for Al-fum(DMSO), in comparison to the activated Al-fum. The enhancement is induced by DMSO inside the pores of Al-fum(DMSO) which contributes to the scattering. This behavior was already observed by Thoma et al. for incorporated DMSO in  $\text{NH}_2\text{-MIL-53(Al)}$ .<sup>33,34</sup> The broadening of the reflections for both Al-fum and Al-fum(DMSO), in comparison to the simulated pattern, is due to the small crystallite size.<sup>35,36</sup> Following the Scherrer equation (eq 5) the crystallite size from the (0 1 1) reflection at  $2\theta = 10.45^\circ$  was calculated to 20 nm. Note that the crystallite size is not comparable to the particle size, as particles can be made up of several different crystallites or crystallite domains or consist of a crystalline and amorphous fraction.

Besides the morphology, other crucial characteristics for the synthesized MOF, used as a filler for MMMs, are sorption properties of the very compound. Recent studies of Kanehashi et al. showed a linear dependence between the gas permeability and the fractional free volume (FFV) of the MMMs.<sup>21</sup> Therefore, Brunauer, Emmett, Teller (BET) surface area and pore volume for Al-fum and Al-fum(DMSO) were determined from a nitrogen sorption isotherm at 77 K (Figure 2). Al-fum

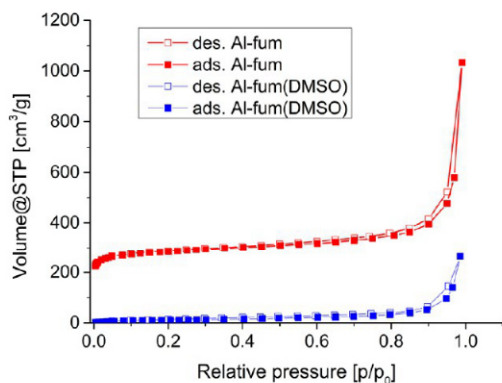


**Figure 2.** Nitrogen sorption isotherms of Al-fum (red) and Al-fum(DMSO) (blue) at 77 K.

shows as a first approximation a Type I nitrogen adsorption isotherm, typical for microporous materials,<sup>38</sup> yielding a BET surface area of  $1100 \text{ m}^2 \text{ g}^{-1}$  and a total pore volume of  $0.47 \text{ cm}^3 \text{ g}^{-1}$ . The micropore volume, given by the V-t-plot method according to DeBoer, is  $0.37 \text{ cm}^3 \text{ g}^{-1}$ . For comparison BET surface areas and pore volumes of several Al-fum literature reports are collected in Table S1.

In contrast Al-fum(DMSO) shows no nitrogen uptake upon low relative pressures, hence displays no micropore volume. The calculated BET surface area of Al-fum(DMSO) of  $40 \text{ m}^2 \text{ g}^{-1}$  represents primarily the external surface area due to the small particle size of the MOF. Both  $\text{N}_2$  sorption isotherms for Al-fum and Al-fum(DMSO) show a continuous slight increase in gas uptake above  $p/p_0 = 0.4$  with increasing relative pressure. A strong rise in gas uptake above  $p/p_0 = 0.9$  gives the isotherms a Type II or Type III isotherm appearance and high nitrogen uptake for both compounds toward the saturation pressure (i.e., at  $p/p_0 = 1$ ). This curvature can be explained by interparticle condensation in the macropores formed by the particle aggregates, which is showing here because of the intentionally prepared submicrometer particles.<sup>39,40</sup> Al-fum samples of larger particle size, porous or nonporous (DMSO-filled), do not show this continuous gas uptake with increasing relative pressure (Figure S3 in the SI). Hence, the MOF-pore

volume determination must be limited to the MOF-inherent micro- and mesoporosity. A comparison of Figures 2 and S3 in SI shows that at  $p/p_0 > 0.4$  the interparticle volume between submicrometer particles and concomitant pore condensation leads to a nitrogen uptake, which would then include this external volume. We decided to take the total pore volume at  $p/p_0 = 0.4$  in order not to overestimate the micro- and mesopore volume inside the framework.

IR spectra of Al-fum(DMSO) showed an additional peak which can be assigned to the stretching vibration of the sulfur–oxygen double bond ( $1040\text{--}1060 \text{ cm}^{-1}$ ) (Figure S4).

Thermogravimetric analysis (TGA) and elemental analysis were conducted to determine the exact amount and ratio of the loaded DMSO to the MOF.

From TGA (Figure 3), Al-fum exhibits its typical degradation at around  $400^\circ \text{C}$  with a mass loss of 59%

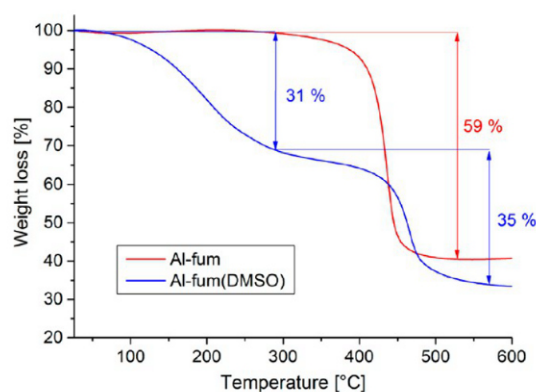


**Figure 3.** Thermogravimetric analysis (TGA) curves of Al-fum (red) and Al-fum(DMSO) (blue) under synthetic air at a heating flow of 2 K/min.

associated with the decay of the organic linker. In comparison Al-fum(DMSO) shows a continuous mass loss of 31% from  $100^\circ \text{C}$  to  $280^\circ \text{C}$ , where the Al-fum material starts to degrade, followed by the mass loss for the linker decay. The presence and loss of 0.31 g DMSO per g Al-fum(DMSO) with 0.69 g Al-fum sample correlates with a liquid DMSO density of  $1.1 \text{ g/cm}^3$ , hence the volume of  $0.28 \text{ cm}^3$  in the pore volume of  $0.47 \text{ cm}^3/\text{g} \times 0.69 \text{ g} = 0.32 \text{ cm}^3$ . Since the continuous mass loss occurs after thorough drying at  $1 \times 10^{-3}$  mbar at room temperature, it can be attributed to the desorption of DMSO from inside the pores other than just free solvent. The mass ratio of 0.31 g DMSO and 0.69 g Al-fum yields a molar ratio of approximately 0.8:1. Elemental analysis for Al-fum and Al-fum(DMSO) are represented in Table S2 and show a ratio of about 0.8:1 for DMSO to Al-fum. The slight difference in calculated and experimental elemental analysis can result from water retained in DMSO or in the MOF itself, which is in good agreement with the higher amount of hydrogen and the fewer amount of sulfur in comparison to the calculated value for both samples.

The porous filler material of MMMs is usually thought to contribute to the gas separation properties of the MMMs and could even enhance the selectivity of the MMMs compared to the neat polymer membrane.<sup>41,42</sup> Here the separation of  $\text{CO}_2$  and  $\text{CH}_4$  is used to test for this effect (Figure S5). The gas uptake in the porous Al-fum for  $\text{CO}_2$  and  $\text{CH}_4$  at 870 mmHg was  $3.8 \text{ mmol/g}$  and  $1.4 \text{ mmol/g}$ , respectively. The selectivity of 3.98 was obtained by the Henry plots of the adsorption isotherms (Figure S6) and is in good agreement with the

literature for gas adsorptions measurements with a neat microsized Al-fum powder.<sup>43</sup> Note that the value of the selectivity for single-gas adsorption has little to do with the selectivity for neat or mixed-matrix membranes made from this MOF.<sup>44,45</sup>

**Membrane Preparation and Gas Permeation Experiments.** For the MMMs Matrimid 5218 (Figure 4) was chosen

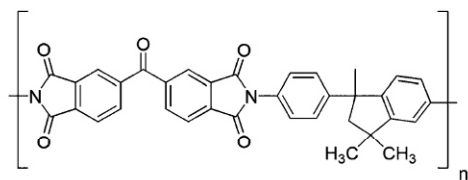


Figure 4. Structure of Matrimid.

as a polymer due to its high thermal and chemical stability as well as its widespread implementation in MMMs so far. Matrimid has shown good interaction capability with MOFs as filler materials caused by polar carbonyl and imide groups which can interact with the MOF crystallites.<sup>46,47</sup>

All MMMs were prepared in the same procedure using a priming protocol in combination with multiple ultrasonication steps to receive uniform dispersed MOF particles in the polymer matrix. To determine the MOF particle distribution and embedment in the MMMs, SEM images of the cross sections in combination with an energy-dispersive X-ray spectroscopic (EDX) mapping of aluminum and sulfur were realized.

Figure 5 shows typical SEM images of cross sections for MMMs of Al-fum/Matrimid MMMs with different MOF loadings, prepared by freeze fracturing. The SEM images together with EDX depict an excellent particle distribution throughout all membranes. Close-up images of the cross section endorse a good compatibility between MOF and polymer, marked by no significant interfacial void formation around the filler particles.

EDX mapping of aluminum confirms homogeneous distribution of the filler despite minor sedimentation for various MMMs with different MOF loadings, shown by locally increased intensity of the mapped aluminum (Figure 6). Most important is to point out that even with higher loadings of Al-fum, the sedimentation of the filler remains in a reasonable scope and therefore uniformly homogeneous, dense MMMs are formed.

In the same manner MMMs of Al-fum(DMSO)/Matrimid were analyzed. Overviews and close-ups of the cross section of MMMs loaded with 4 and 24 wt % Al-fum(DSMO) are shown in Figure 7. They show equally good particle distribution across the whole MMMs. Close-up images are rather similar to the MMMs of Al-fum/Matrimid MMMs and show no interfacial void formation around the filler particles and the polymer. Figure 8 displays EDX-mapping of aluminum in red and sulfur in blue of the same cross sections shown in Figure 7. Aluminum as well as sulfur are detected homogeneously throughout the MMMs and in a similar intensity, which indicates a uniform distribution and high loading of DMSO in the pores of Al-fum. Moreover, EDX-mapping reveals minimal sedimentation for MMMs with 24 wt % MOF.

Mixed gas permeation experiments were carried out from a 50:50 v:v CO<sub>2</sub>/CH<sub>4</sub> mixture at 25 °C and a transmembrane pressure of 3 bar. CO<sub>2</sub> and CH<sub>4</sub> gas permeabilities of the neat

polymer and Al-fum/Matrimid MMMs are presented in Table S5 and Figure 9.

In general gas permeability increases with the increase of Al-fum loading. The selectivity increases slightly up to a loading of 20 wt %. Only for a loading of 24 wt % the selectivity drops again due to emerging microdefects, like agglomeration of MOF particles, resulting in connected nonselective voids between polymer and MOF or MOF particles themselves.<sup>23</sup> The 24 wt % membrane is also mechanically sensitive and quite brittle. Al-fum/Matrimid MMMs with 20 wt % performed the best with an improvement of 63% in CO<sub>2</sub> permeation and 28% in selectivity compared to the neat polymer. The observed trend of higher MOF loading resulting in an increased permeability is intrinsic for porous fillers in MMMs and is frequently observed.<sup>48–50</sup> The gas permeability and selectivity enhancement can be traced back to improved gas diffusivity and adsorption of the MMMs. Diffusivity is either influenced by the free fractional volume (FFV) of the polymer and the MOF or by interfacial voids between polymer and MOF (void volume).<sup>21,28</sup> The influence of both FFV and void volume is discussed in a following section. Adsorption properties of Al-fum affect the selectivity of MMMs in a desired way. The adsorption properties of Al-fum with a near 4:1 selectivity of CO<sub>2</sub> over CH<sub>4</sub>, calculated from the initial Henry plot of the CO<sub>2</sub> and CH<sub>4</sub> adsorption isotherms (Figures S5 and S6), cause an improvement of selectivity with increasing MOF loading. Due to its quadrupole moment CO<sub>2</sub> is more likely to interact and adsorb on Al-fum causing its superior selectivity of CO<sub>2</sub> over CH<sub>4</sub>.

Likewise mixed gas permeation experiments with Al-fum(DMSO)/Matrimid MMMs were carried out. The results are presented in Table S6 and in Figure 10. An Al:S quantification of the Al-fum(DMSO)/Matrimid MMMs before and after the gas permeation studies gave the same molar ratio within experimental error (Tables S3 and S4 in the SI). This ensured that no DMSO was removed upon gas permeation, hence, the nonporous nature of Al-fum(DMSO) was retained.

For the membrane with the nonporous Al-fum(DMSO) filler both CO<sub>2</sub> and CH<sub>4</sub> permeabilities are reduced in similar proportion with increased loading of Al-fum(DMSO). Consequently, the selectivity stays largely constant for the different MMM loadings. CO<sub>2</sub> permeabilities decrease constantly from about 6.6 Barrer of the neat polymer to 5.0 Barrer in the MMMs with 24 wt % MOF loading (24% reduction). Equally CH<sub>4</sub> permeability reduces from 0.14 Barrer to 0.10 Barrer (28% reduction), respectively. As described in the Introduction, compared to the effect of porous fillers, nonporous fillers have shown diverse impacts in MMMs. Either nonporous fillers increase the permeability while mostly reducing the selectivity due to the formation of defects,<sup>25</sup> or to the contrary nonporous fillers lead to a decrease in permeability while retaining the selectivity of the polymer.<sup>28,51</sup> In this work the latter is observed, which emerges out of the nature of the used filler. Usually inorganic oxides were used as nonporous fillers, showing poor interactions with most polymers. MOFs on the other hand are known to develop favorable interactions with the polymer, which leads to fewer microdefects in the MMMs. Therefore, it is not surprising that MMMs consisting of nonporous Al-fum(DMSO) and Matrimid show a reduction in permeability with increasing filler loading, as the FFV of the MOF is essentially zero and the volume of the polymer is constantly reduced.

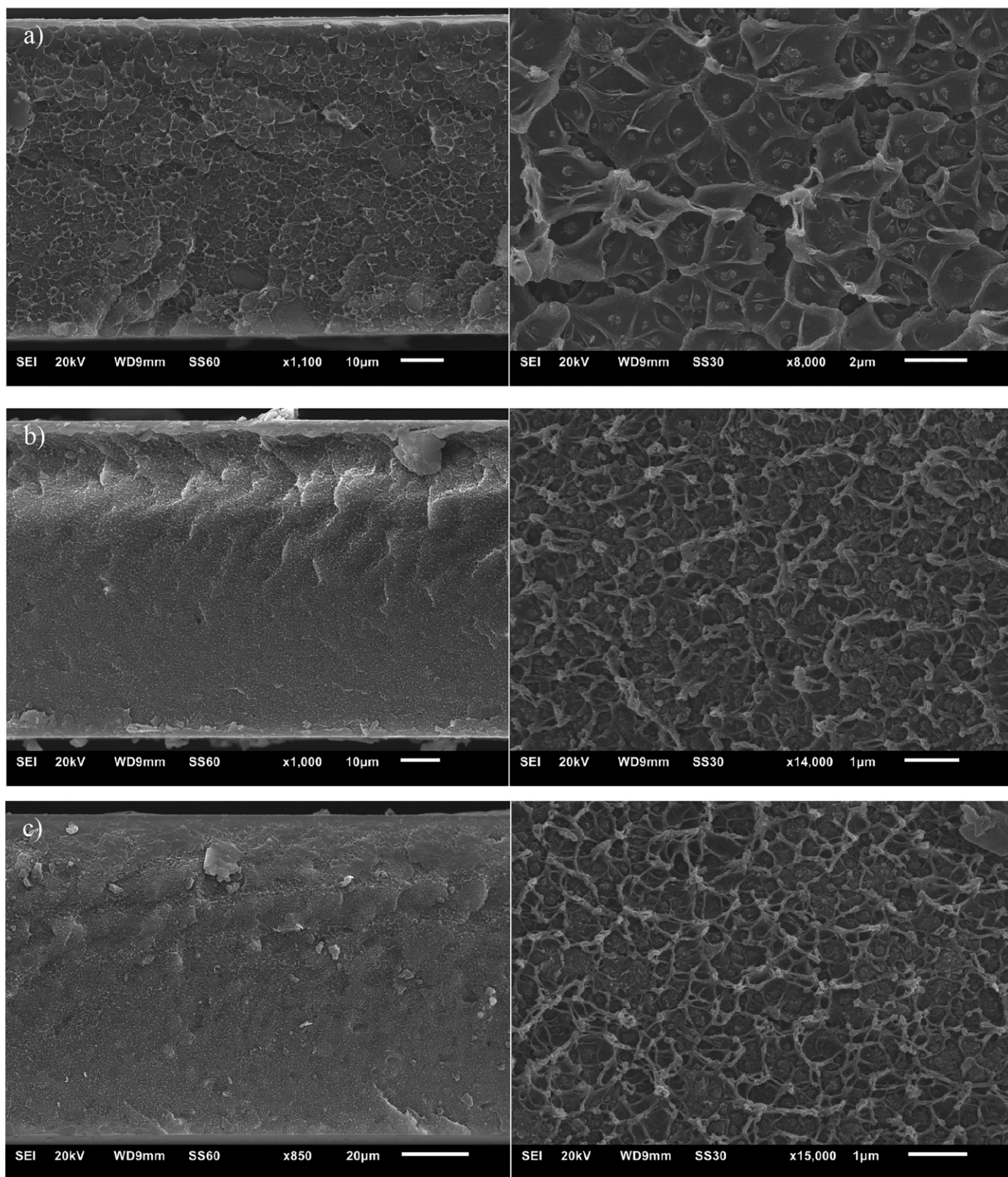
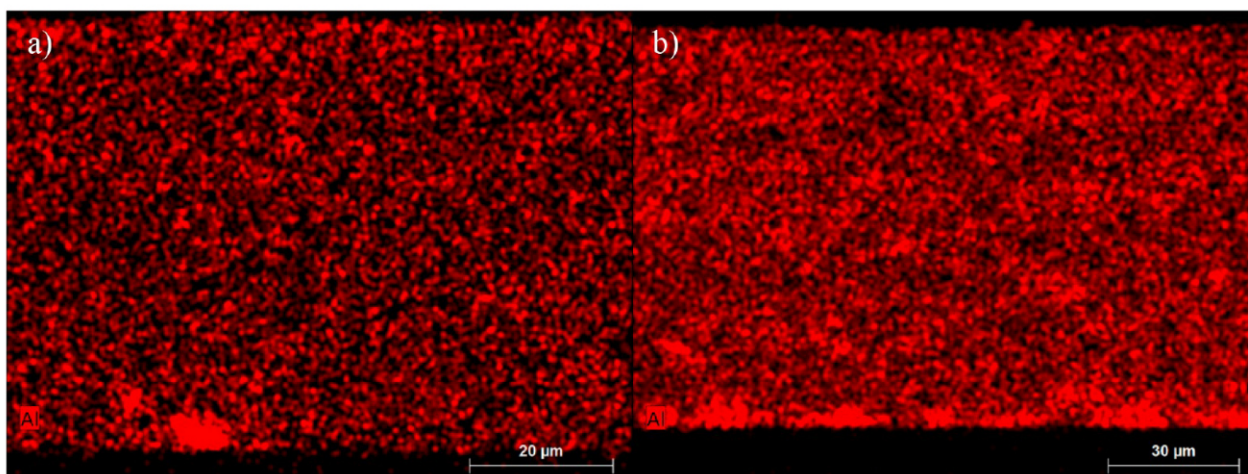


Figure 5. SEM images of cross section of Matrimid with different loadings of Al-fum as filler a) 8 wt %, b) 16 wt %, and c) 24 wt %.

**Modeling of Gas Permeation. Maxwell Model.** The Maxwell model can be applied to both porous and nonporous fillers in composite membranes to predict the permeability of the composite membrane. Prior works have shown poor or only qualitative trend agreements for porous and nonporous fillers compared to the predicted values of the Maxwell model.<sup>51–54</sup> The values for the observed permeability could

often not be reproduced with the model. The discrepancy between model and experiment can result from stronger deviations between assumptions and reality, for example, for particle geometry, dispersion, or maximum filler loading, which are essential for the model, or the unaccounted presence of microdefects due to poor interaction between filler and polymer. Figure 11 shows the comparison between predicted



**Figure 6.** EDX-mapping of aluminum (red) in MMM cross sections of a) 4 wt % Al-fum and b) 24 wt % Al-fum. The bottom of the images corresponds to the bottom of the membrane when casted.

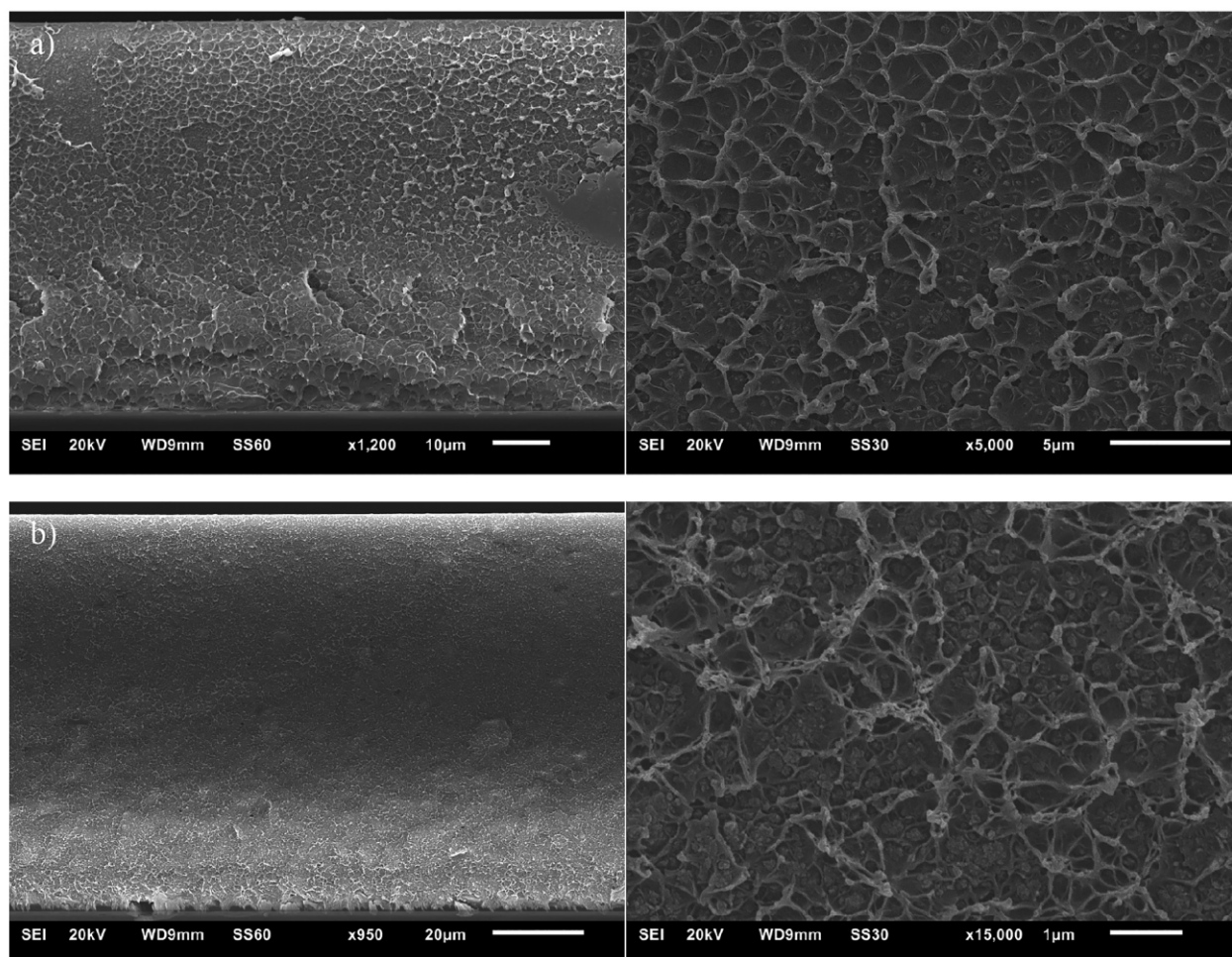


**Figure 7.** SEM images of cross-section of Matrimid with different loadings of Al-fum(DMSO) as filler a) 4 wt %, b) 24 wt %.

(Maxwell model) and experimental relative  $\text{CO}_2$  permeabilities for MOF–Matrimid composite membranes with porous Al-fum and nonporous Al-fum(DMSO) fillers.

Relative experimental  $\text{CO}_2$  permeabilities for Al-fum/Matrimid MMMs are in good agreement with the theoretical values from the Maxwell model for porous fillers ( $P_d \gg P_c$ ). The reduction of the relative experimental  $\text{CO}_2$  permeability for Al-fum(DMSO)/Matrimid MMMs is a good indicator for homogeneous dispersed filler particle and good interactions

between polymer and MOF. Otherwise interparticular, non-selective voids should result in increased permeabilities and reduced selectivity.

Similarly, the relative  $\text{CH}_4$  permeabilities were plotted against the filler volume in Figure S7. For  $\text{CH}_4$  the experimental permeabilities also follow the theoretical prediction albeit with a slightly larger deviation than for  $\text{CO}_2$ .

*Free Fractional Volume (FFV)*. In the literature, the (total) FFV was defined as the sum of the volume-weighted specific

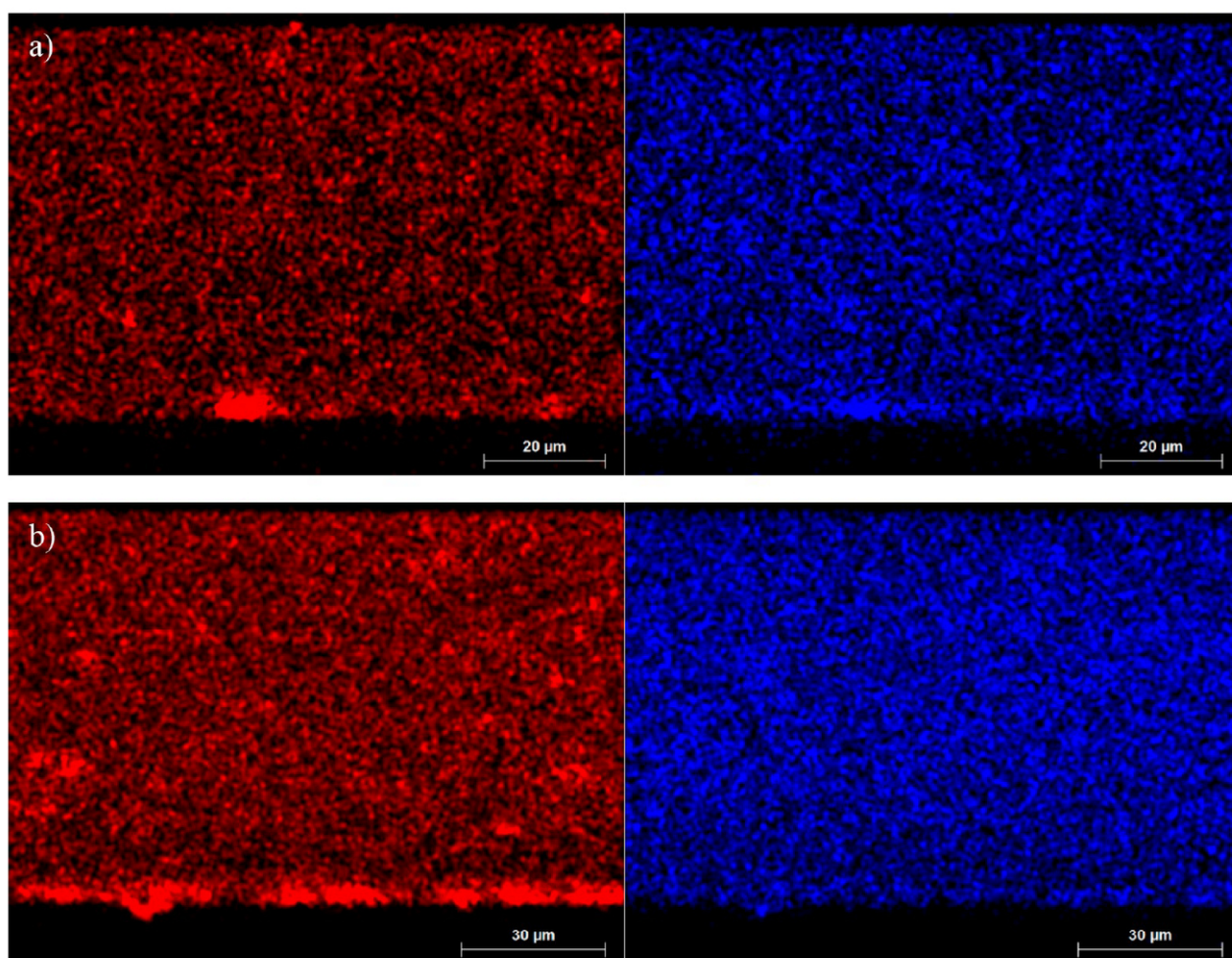


**Figure 8.** EDX-mapping of aluminum (red) and sulfur (blue) in MMM cross sections of a) 4 wt % Al-fum(DMSO) and b) 24 wt % Al-fum(DMSO). The molar Al:S quantification in Al-fum(DMSO) by EDX spectroscopy is given in Tables S3 and S4.

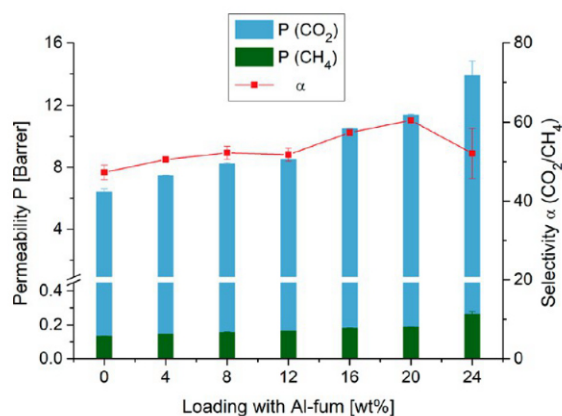


**Figure 9.** Performance of Al-fum/Matrimid MMMs with different Al-fum loadings in the separation of CO<sub>2</sub> and CH<sub>4</sub>. The 24 wt % membrane was prepared and measured four times to ensure reproducibility and significance of the selectivity drop.

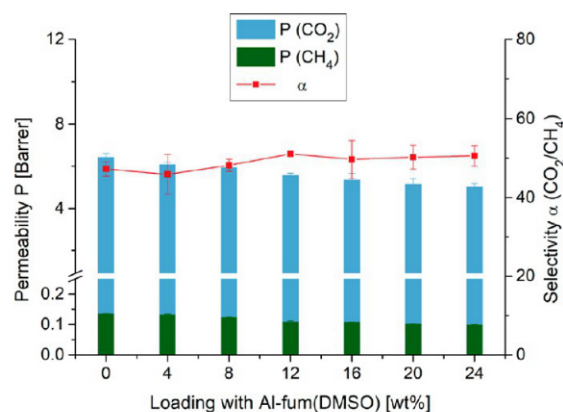


**Figure 10.** Performance of Al-fum(DMSO)/Matrimid MMMs with different Al-fum loadings in the separation of CO<sub>2</sub> and CH<sub>4</sub>.

pore volumes (in cm<sup>3</sup>/g) multiplied with the specific densities (in g/cm<sup>3</sup>) of the materials (polymer, filler) in the MMM. Thereby, the FFV became a dimensionless entity (see Section S10 in the SI). Multiplication of pore volume with density was done to allow for comparison of the correlated permeability for different fillers.<sup>21</sup>

Here we want to elucidate the possible relative role of the FFV of the polymer, the MOF, and the void volume of the

MOF–polymer interface. Therefore, we need to elucidate and compare actual specific free volumes (in units cm<sup>3</sup>/g).

Thus, we define here a (total) specific free fractional volume sFFV as the sum of the volume-weighted ( $\phi_v \phi_d$ ) specific free volumes (sFV) of the polymer and the filler (eq 1). The sFV of the neat polymer Matrimid (density 1.167 g/cm<sup>3</sup>) was reported to approximately 0.146 cm<sup>3</sup>/g.<sup>21,55</sup> The sFV of the MOF is usually taken as equal to the total specific pore volume  $V_p$  determined by nitrogen sorption (Table S1).<sup>21</sup>

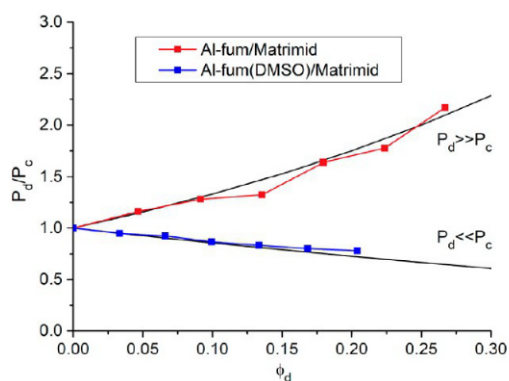


**Figure 11.** Relative experimental CO<sub>2</sub> permeabilities (referenced to the permeability  $P_c$  of the pure polymer membrane) for Al-fum/Matrimid (red curve) and Al-fum(DMSO)/MMMs (blue curve) with different filler volume fraction  $\phi_d$ . The black lines give the relative theoretical CO<sub>2</sub> permeabilities for porous (filler permeability  $P_d \gg P_c$ ) and nonporous ( $P_d \ll P_c$ ) fillers. Note that for the same wt % of MOF the higher density of nonporous Al-fum(DMSO) leads to a lower filler volume fraction.

$$(\text{total}) \text{ sFFV} = \text{sFFV}_{\text{polymer}} \times \phi_c + \text{sFFV}_{\text{MOF}} \times \phi_d \quad (1)$$

A listing of the sFFV values for the MMMs with different filler fractions is given in Table S7 and Table S8 in the SI. The sFFV ranges from 0.23 cm<sup>3</sup>/g for a 24 wt % Al-fum/Matrimid MMM to 0.12 cm<sup>3</sup>/g for a 24 wt % Al-fum(DMSO)/Matrimid MMM.

The FFV includes only the porosity in the polymer and filler and does not include any voids formed around the filler particles due to phase incompatibility. For the FFV the correlation with permeability  $P$  is given by the following:

$$P = A_p \times \exp^{(-B_p/\text{FFV})} \quad (2)$$

which is linearized to

$$\lg P = \lg A_p - \frac{B_p}{2.303\text{FFV}} \quad (3)$$

with  $A_p$  and  $B_p$  being gas- and temperature-dependent constants.<sup>56</sup>

Thus, if indeed the FFV determines the permeability a plot of  $\lg P$  versus  $1/\text{FFV}$  should give a straight line with slope  $-B_p/2.303$  and intercept  $\lg A_p$ .

A plot of  $\lg P$  versus the inverse of the specific free fractional volume sFFV, is given in Figure 12 for the two gases CO<sub>2</sub> and CH<sub>4</sub> which were tested with the porous and nonporous Al-fum/Matrimid MMMs.

The plot of  $\lg P$  versus  $1/\text{sFFV}$  shows for both gases a very good linear correlation over the Al-fum and Al-fum(DMSO)/Matrimid MMMs. As the sFFV rises with decreasing nonporous Al-fum(DMSO) filler and increasing filler volume of porous Al-fum, the inverse sFFV decreases.

This illustrates that the sFFV is not only applicable for composite membranes with porous fillers, but is also usable for composite membranes with nonporous fillers. The values for  $A_p$  and  $B_p$ , calculated from the linear regression of the  $\lg P$  versus  $1/\text{sFFV}$  ( $1/\text{FFV}$ ) plot (Figures 12 and S12), are presented in Table S9 (SI). Similar to previous studies the values for  $B_p$  are relatively similar for CO<sub>2</sub> and CH<sub>4</sub> for both FFV and sFFV.  $A_p$  values differ highly between CO<sub>2</sub> to CH<sub>4</sub> which is also in good agreement with the literature.<sup>56,57</sup> The difference in  $A_p$ , in unit Barrer, could be a result of the smaller

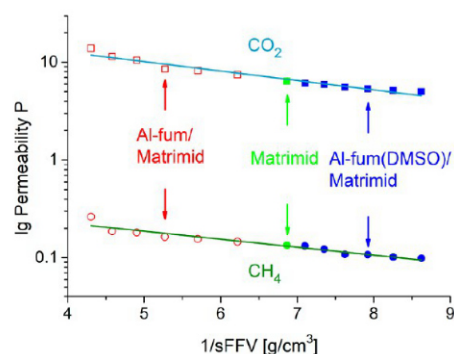


**Figure 12.** Combined experimental CO<sub>2</sub> and CH<sub>4</sub> permeabilities of porous and nonporous Al-fum and Al-fum(DMSO)/Matrimid MMMs as a function of the inverse (total) specific free fractional volume, sFFV. The neat polymer Matrimid has  $1/\text{sFFV} = 6.9$ , the 24 wt % Al-fum/MMM 4.3, and the 24 wt % Al-fum(DMSO)/MMM 8.6. The straight lines are only intended as a guide to the eye.

kinetic diameter of CO<sub>2</sub> (3.3 Å) compared to CH<sub>4</sub> (3.8 Å) which leads to a faster motion within the free volume of the polymer lamellar and MOF. Furthermore, CO<sub>2</sub> is more likely to get adsorbed in the MOF and therefore may travel faster through the fractional free volume introduced by the MOF.

**Void Volume (VV).** Besides the sFFV, which focuses on the free volume inside the polymer and the MOF, one can likewise determine the interface volume (void volume) between the polymer and the embedded MOF particles and its impact on the gas permeability. Takahashi and Paul showed that excess free volume between polymer and silica filler particles can lead to an increase in permeability, even for nonporous fillers due to poor interactions of the inorganic nanoparticles with the polymer phase and contrary to the Maxwell model. They obtained the excess void volume from a lower measured density than the theoretically determined one.<sup>28,29</sup> Further they described various possible morphologies of interparticle voids in composite membranes and acknowledged that the effect of the voids will be highly dependent on their distribution throughout the system.

In the literature, the void volume was derived from the difference between theoretical ( $D_{\text{theo}}$ ) and measured density ( $D_{\text{exp}}$ ) of the MMM according to  $([1 - D_{\text{exp}}/D_{\text{theo}}] \times 100\%)$ . Thereby, the void volume became a dimensionless entity.<sup>23,29</sup>

As we want to elucidate the relative role of the FFV of the polymer, the MOF and the void volume of the MOF–polymer interface, we need to elucidate and compare actual specific free and void volumes (in units cm<sup>3</sup>/g).

The possible specific void volume (sVV) between continuous and dispersed phase is determined according to eq 4:

$$\text{specific void volume, sVV} = \frac{1}{D_{\text{exp}}} - \frac{1}{D_{\text{theo}}} \quad (4)$$

The results for the specific void volume determination of Al-fum/Matrimid MMMs are depicted in Figure 13.

The deviation in theoretical and measured density is very small and mostly within the error bar. Thus, none of the MMMs show significant specific void volume formation. Overall there is no apparent trend for an increasing void volume formation with increasing filler volume observed. This is in contrast to the continuous rise of the permeability with increasing filler volume for the composite membranes. Hence,



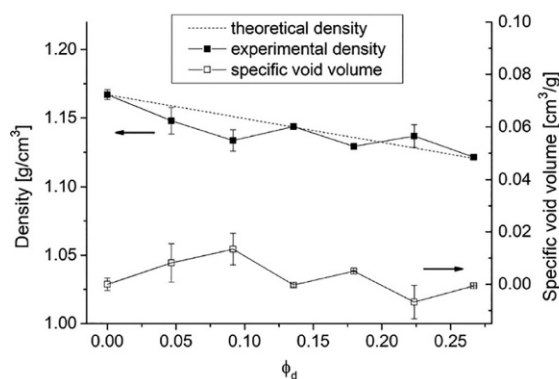


**Figure 13.** Specific void volume (eq 4) for Al-fum/Matrimid MMMs with different filler volumes. MMMs with 24 wt % MOF were not included in the presentation.

the void volume seems to have at most only a slight influence on the performance of the prepared MMMs.

Similar results for Al-fum(DMSO)/Matrimid MMMs are shown in Figure 14. The overall void volume is approximately

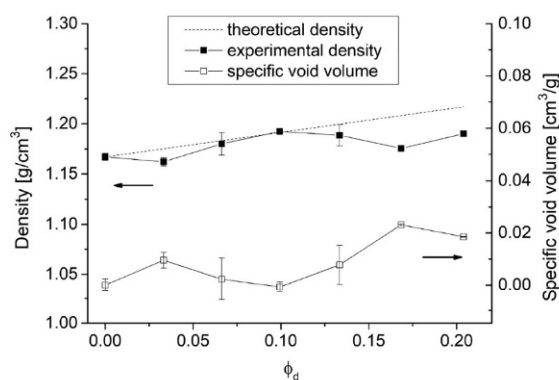


**Figure 14.** Specific void volume (eq 4) derived by the difference between theoretical and measured density for Al-fum(DMSO)/Matrimid MMMs with different filler volumes.

the same as for the MMMs with the porous filler, but this time there might be a trend to higher specific void volume formation for MMMs with higher filler volumes. But since the CO<sub>2</sub> and CH<sub>4</sub> permeability for Al-fum(DMSO)/Matrimid MMMs decreases with higher MOF loadings (Table S6) there clearly is no correlation between void volume formation and separation performance in this case.

## CONCLUSIONS

In this work porous, submicrometer sized Al-fum was synthesized according to the literature.<sup>30</sup> Nonporous Al-fum(DMSO) was obtained by heating Al-fum in DMSO and characterized with various methods. Both porous and nonporous aluminum fumarate fillers were embedded in a Matrimid matrix, thereby leading to the same polymer–filler interface. SEM images in combination with EDX-mapping revealed a mostly homogeneous filler distribution throughout all MMMs. CO<sub>2</sub>/CH<sub>4</sub> separation performances showed reverse effects for porous and nonporous fillers. MMMs with the porous filler showed a continuous increase in CO<sub>2</sub> and CH<sub>4</sub> permeability while MMMs with the nonporous filler displayed a decrease in CO<sub>2</sub> and CH<sub>4</sub> permeability with rising filler content. These results are in good agreement with the Maxwell model, which predicts an increase in gas permeability for

porous fillers and a decrease for nonporous fillers, respectively. The increase and decrease in gas permeability in general seems to be traceable to the difference in FFV, that is, the increased and decreased free volume of the polymer and filler. The interfacial void volume between filler and polymer contributes roughly only 10% to the available free volume in the MMM. This is most obvious regarding the gas permeation results of the MMMs with the nonporous filler compared to the measured void volume. Despite a constant to slightly growing void volume for higher nonporous filler loadings the gas permeabilities decrease. This clearly shows the negligible effect of an interfacial volume, both in absolute as in relative terms to the FFV. The organic/inorganic hybrid nature of the MOF filler certainly allowed for good compatibility with the polymer which is crucial to obtain defect free MMMs. As the free fractional volume, introduced by both the polymer and the MOF is decisive for the permeability both materials should be chosen accordingly. An increase in permeability requires high free volumes in both polymer and MOF. Thus, for MOFs a high pore volume is decisive for high permeable MMMs. In comparison to other porous fillers like zeolites MOFs should not only be advantageous because of their better compatibilities with organic polymers but also because of their higher pore volumes. Furthermore, a loss of linearity between FFV and permeability in MMMs would be a good indicator for an insufficient compatibility of the MOF and polymer which then probably results in void volume formation, with rise in permeability and partial loss of selectivity.

## EXPERIMENTAL SECTION

**Materials and Methods.** All starting materials and solvents were obtained from commercial sources and used without further purification unless otherwise mentioned in the experimental description. Sodium aluminate (calculated as Al<sub>2</sub>O<sub>3</sub> 50–56%) was received from VWR chemicals, fumaric acid (99%) was obtained from TCI, dichloromethane (99%), *N,N*-dimethylformamide (99.99%) and dimethyl sulfoxide (99%) were purchased from Fisher Chemicals. Ethanol (99.99%) was obtained from Sigma-Aldrich. The polymer Matrimid 5218 was kindly supplied by Huntsman Advanced Materials.

Aluminum fumarate was synthesized according to the literature with the aim to obtain particles around 250 nm in size.<sup>30</sup> In a 100 mL round-bottom flask 0.45 g (5.49 mmol) of sodium aluminate and 0.9 g (7.76 mmol) of fumaric acid were dissolved in 50 mL of water and heated in a 90 °C preheated water bath for 30 min. After cooling down to room temperature the precipitate was collected by filtration and washed with water and ethanol for 1 day each. The collected product was dried at 150 °C in vacuum (50 mbar) overnight (yield 0.81 g, 94% based on sodium aluminate). The product was positively characterized as the MOF aluminum fumarate by powder X-ray diffraction, thermogravimetric analysis, and nitrogen sorption measurements as is detailed in the Results and Discussion.

Aluminum fumarate(DMSO) was synthesized by suspending 0.8 g aluminum fumarate in 100 mL dimethyl sulfoxide and then refluxed at 180 °C bath temperature overnight. The product was collected by filtration and dried at room temperature in vacuum (1 × 10<sup>-3</sup> mbar) for 24 h. The pore filling and the amount of DMSO was determined by thermogravimetric analysis and elemental analysis as is detailed in the Results and Discussion.

Matrimid was dried at 80 °C for several days to remove the adsorbed moisture. All MMMs were prepared using a prime protocol to reduce agglomeration of the MOF particles and ensure a successful preparation. In the following the procedure for MMMs with 4 wt % MOF is described as an example of all prepared MMMs. The amount of 0.4 g of Matrimid was dissolved in 3.5 mL of dichloromethane and stirred for 24 h. At the same time 17 mg of the MOF was suspended

in 4.5 mL of dichloromethane and also stirred for 24 h. Then the MOF suspension was ultrasonicated three times for 15 min with an amplitude of 20% at an ultrasonic liquid processor (VCX 750 Sonics, Microtip 630–0419) to homogenize the suspension. Between the ultrasonication steps, the suspension was stirred for 30 min. Afterward 0.16 mL of the polymer solution were added to the MOF suspension to receive an equal polymer/MOF mass ratio. After another 24 h of stirring and the same homogenization procedure, the remaining polymer was added to the MOF/polymer mixture and stirred further for 1 h. Afterward this mixture was casted into a metal ring, which was placed on a flat glass plate. To ensure slow evaporation of the solvent and to protect the membranes from dust the metal rings were immediately covered with inverted funnels. The membranes were left to dry for 3 h at room temperature and then taken off the glass plate by immersing in water and afterward dried at 150 °C overnight in the vacuum oven (50 mbar). The MMMs with 8, 12, 16, 20, 24 wt % MOF were prepared in the same way with 35 mg, 54.5 mg, 76 mg, 100 mg, and 126.5 mg MOF, respectively. The added polymer solution was adapted as follows: 0.33 mL, 0.52 mL, 0.72 mL, 0.95 mL, and 1.20 mL, respectively.

Powder X-ray diffraction (PXRD) patterns were obtained on a Bruker D2 Phaser powder diffractometer equipped with a flat silicon, low background sample holder using Cu–K $\alpha$  radiation ( $\lambda = 1.5418 \text{ \AA}$ , 30 kV, 10 Ma, ambient temperature). With this sample holder at  $2\theta < \sim 10^\circ$  the beam spot is strongly broadened so that only a fraction of the reflected radiation reaches the detector; hence lower relative intensities are measured in this range. All samples were measured with a scan speed of 2s/step and a step size of  $0.028^\circ$  ( $2\theta$ ). Simulated patterns of aluminum fumarate were calculated with CCDC Mercury 3.9 program using the single crystal data of Basolite A520 obtained by Rietveld refinement (CCDC no. 1051975, Refcode DOYBEA).<sup>37</sup> The Bruker D2 Phaser had been calibrated with an LaB $_6$  NIST standard sample of known crystallite size (0.8  $\mu\text{m}$ ) for calculating the Al-fum crystallite size with the Scherrer equation (eq 5). The full width at half-maximum ( $\Delta(2\theta)$ ) of the reflexes depends inversely on the crystallite size ( $L$ ), which results in broadened reflexes for small crystallite sizes as seen in Figure 1.

$$\Delta(2\theta) = \frac{K \times \lambda}{L \times \cos(\theta_0)} \quad (5)$$

SEM images were recorded with a Jeol JSM-6510LV QSEM Advanced electron microscope with a LAB-6 cathode at 20 keV. The microscope was equipped with a Bruker Xflash 410 silicon drift detector and the Bruker ESPRIT software for EDX analysis. The membrane cross sections were prepared through freeze-fracturing after immersion in liquid nitrogen and then coated with gold by a Jeol JFC 1200 fine-coater at an approximate current of 20 mA for 20–30 s.

Thermogravimetric analysis (TGA) were carried out with a Netzsch TG 209 F3 Tarsus in the range of 25 °C to 600 °C with a heating rate of 2 K min<sup>-1</sup> under oxygen atmosphere.

Infrared (IR) spectra were obtained with a Bruker FT-IR Tensor 37 as attenuated total reflection. The scanning frequency range was 4000–500 cm<sup>-1</sup>.

Nitrogen sorption measurements at 77 K were carried out on a Quantachrome NOVA 4000e gas sorption analyzer and evaluated with the AsiQwin V3 software. For activation the sample was degassed in a vacuum of  $5 \times 10^{-2}$  mbar at 150 °C for 3 h. The Brunauer–Emmett–Teller (BET) surface areas were calculated in the  $p/p_0$ -range of 0.01–0.05. Total pore volumes were calculated from nitrogen adsorptions isotherms at  $p/p_0 = 0.4$ . Micropore analysis was done with DeBoer thickness method via V-t-Plot method in the pressure range of  $p/p_0$  0.25–0.5 of the adsorption isotherm. Adsorption isotherms for aluminum fumarate with CO $_2$  and CH $_4$  were recorded on a Micromeritics ASAP 2020 gas sorption analyzer equipped with oil-free vacuum pumps and valves, which guaranteed contamination free measurements. CO $_2$  and CH $_4$  isotherms were measured at 0 °C (ice/deionized water bath). All gases were of ultrapure grades (99.999%) supplied by Air Liquide Germany and used as-received.

Binary gas separation experiments were performed with a continuous flow permeation system (OSMO inspector, provided by Convergence Industry B.V., 7532 SM Enschede, The Netherlands) with helium as sweep gas and an Agilent 490  $\mu\text{GC}$  gas chromatograph to measure the gas concentration in the permeate. The membranes were cut in a round sheet, placed in the permeation module (4.5 cm diameter) and covered by a rubber mask to provide an effective inner diameter of 3.6 cm with an area of 11.3 cm $^2$ . All permeation experiments were conducted at 25 °C and with 3 bar transmembrane pressure. The feed gases were mixed in a 50/50 volume flow mixture of CO $_2$  and CH $_4$  by two Bronkhorst Coriolis-flow controllers as well as the helium gas stream with a total upstream flow of 160 mL min<sup>-1</sup>. The downstream is swept with helium at a rate of 1 mL min<sup>-1</sup> at ambient pressure. The gas concentration in the permeate stream was measured with an Agilent 490  $\mu$  gas chromatograph with thermal conductivity detector and a Pora PLOT Q column every 30 min until steady state (up to 8 h). Each membrane sample was produced twice to ensure reproducibility. Permeability of the membranes was calculated according to the following equation:

$$P_A = \frac{x_{1A} \times S_{Fl} \times d}{x_{He}^p \times A \times (p_2 \times x_{2A} - p_1 \times x_{1A})} \quad (6)$$

where  $P_A$  is the permeability of the gas A in Barrer (1 Barrer =  $10^{-10}$  cm $^3$ (STP)cm/(cm $^2$ ·s·cmHg)),  $x_{1A}$  the molar fraction of the gas A,  $S_{Fl}$  the flow of the sweep gas in cm $^3$  s<sup>-1</sup>,  $d$  the thickness of the membrane,  $x_{He}^p$  the molar fraction of the sweep gas in the permeate,  $A$  the membrane area in cm $^2$ ,  $x_{2A}$  the molar fraction of the gas A in the feed and  $p_1$  and  $p_2$  the permeate and feed pressure in cmHg, respectively. The error bars in the permselectivity diagrams mark the range of values obtained from the independent measurement of two membranes.

Density ( $\rho$ ) of the membranes was determined by measuring their volume and mass (eq 8). The membranes were measured 3 times on an analytical balance ( $d = 0.1$  mg) to receive the mean mass. The volume ( $V$ ) was derived with the formula of a cylindrical body (eq 7). Both diameter ( $2r$ ) and thickness ( $h$ ) were measured at 10 different sites to receive an average diameter and thickness.

$$V = \pi \times r^2 \times h \quad (7)$$

$$\rho = \frac{\text{mass}}{\text{volume}} \quad (8)$$

Equations for the gas transport in polymeric membranes and the Maxwell model are given Section S12 in the SI.

## ■ ASSOCIATED CONTENT

### 📄 Supporting Information

The Supporting Information is available free of charge on the ACS Publications website at DOI: 10.1021/acsami.8b12938.

Structure description of aluminum fumarate, SEM images of aluminum fumarate and aluminum fumarate-(DMSO); additional N $_2$  sorption isotherms of micrometer sized aluminum fumarate particles; IR spectra and elemental analysis of both compounds; Al:S quantification of various MMMs by EDX spectroscopy; CO $_2$  and CH $_4$  sorption of aluminum fumarate; gas separation performances of all MMMs; relative experimental CH $_4$  permeabilities compared to the Maxwell model; additional theoretical and experimental properties of all MMMs regarding the FFV, sFFV, and void volume; and equations for the gas transport in polymeric membranes and the Maxwell model (PDF)

## AUTHOR INFORMATION

### Corresponding Author

\*Tel.: +49 211 81 12286. Fax: +49 211 81 12287. E-mail: janiak@hhu.de (C.J.).

### ORCID

Christoph Janiak: 0000-0002-6288-9605

### Notes

The authors declare no competing financial interest.

## ACKNOWLEDGMENTS

The authors acknowledge the financial support of the Federal German Ministry of Education and Research (BMBF) in the project Optimat under grant no. 03SF0492C. We thank Mrs. Alexa Schmitz and Mr. Moritz Steinert for the thermogravimetric analyses.

## ABBREVIATIONS

- Al-fum = aluminum fumarate  
DMSO = dimethyl sulfoxide  
FVV = free fractional volume  
fum = fumarate  
MMM = mixed-matrix membrane  
MOF = metal-organic framework  
VV = void volume

## REFERENCES

- (1) Bernardo, P.; Drioli, E.; Golemme, G. Membrane Gas Separation: A review/State of the Art. *Ind. Eng. Chem. Res.* **2009**, *48*, 4638–4663.
- (2) Moulijn, J. A.; Makkee, M.; van Diepen, A. *Chemical Process Technology*; John Wiley & Sons: Chichester, England, 2001.
- (3) Tobin, J.; Shambaugh, P.; Mastrangelo, E. *Energy Information Administration, Office of Oil and Gas*, January 2006. [http://www.dnr.louisiana.gov/assets/docs/oilgas/naturalgas/ngprocess\\_20060131.pdf](http://www.dnr.louisiana.gov/assets/docs/oilgas/naturalgas/ngprocess_20060131.pdf) (assessed July 30, 2018).
- (4) Davis, J. C.; Valus, R. J.; Eshraghi, R.; Velikoff, A. E. Facilitated Transport Membrane Hybrid Systems for Olefin Purification. *Sep. Sci. Technol.* **1993**, *28*, 463–476.
- (5) Koros, W. J.; Mahajan, R. J. Pushing the limits on possibilities for large-scale gas separation: which strategies? *J. Membr. Sci.* **2000**, *175*, 181–196.
- (6) Coronas, J.; Santamaría, J. Separations Using Zeolite Membranes. *Sep. Purif. Methods* **1999**, *28*, 127–177.
- (7) Baker, R. W. Future Directions of Membrane Gas Separation Technology. *Ind. Eng. Chem. Res.* **2002**, *41*, 1393–1411.
- (8) Koros, W. J.; Fleming, G. K. Membran-based gas separation. *J. Membr. Sci.* **1993**, *83*, 1–80.
- (9) Robeson, L. M. Correlation of separation factor versus permeability for polymeric membranes. *J. Membr. Sci.* **1991**, *62*, 165–185.
- (10) Robeson, L. M. The upper bound revisited. *J. Membr. Sci.* **2008**, *320*, 390–400.
- (11) Zimmerman, C. M.; Singh, A.; Koros, W. J. Tailoring mixed matrix composite membranes for gas separations. *J. Membr. Sci.* **1997**, *137*, 145–154.
- (12) Tanh Jeazet, H. B.; Staudt, C.; Janiak, C. Metal-organic frameworks in mixed-matrix membranes for gas separation. *Dalton Trans* **2012**, *41*, 14003–14027.
- (13) Zornoza, B.; Martinez-Joaristi, A.; Serra-Crespo, P.; Tellez, C.; Coronas, J.; Gascon, J.; Kapteijn, F. Functionalized flexible MOFs as fillers in mixed matrix membranes for highly selective separation of CO<sub>2</sub> from CH<sub>4</sub> at elevated pressures. *Chem. Commun.* **2011**, *47*, 9522–9524.
- (14) Merkel, T. C.; Freeman, B. D.; Spontak, R. J.; He, Z.; Pinnau, I.; Meakin, P.; Hill, A. J. Ultraporous, reverse-selective nanocomposite membranes. *Science* **2002**, *296*, 519–522.
- (15) Caro, J.; Noack, M. Zeolite membranes – Recent developments and progress. *Microporous Mesoporous Mater.* **2008**, *115*, 215–233.
- (16) Zornoza, B.; Tellez, C.; Coronas, J.; Gascon, J.; Kapteijn, F. Metal organic framework based mixed matrix membranes: An increasingly important field of research with a large application potential. *Microporous Mesoporous Mater.* **2013**, *166*, 67–78.
- (17) Kosinov, N.; Gascon, J.; Kapteijn, F.; Hensen, E. J. M. Recent developments in zeolite membranes for gas separation. *J. Membr. Sci.* **2016**, *499*, 65–79.
- (18) Sorribas, S.; Zornoza, B.; Tellez, C.; Coronas, J. Mixed matrix membranes comprising silica-(ZIF-8) core-shell spheres with ordered meso-microporosity for natural- and bio-gas upgrading. *J. Membr. Sci.* **2014**, *452*, 184–192.
- (19) Furukawa, H.; Cordova, K. E.; O’Keeffe, M.; Yaghi, O. M. The chemistry and applications of metal-organic frameworks. *Science* **2013**, *341*, 1230444.
- (20) Dechnik, J.; Sumby, C. J.; Janiak, C. Enhancing Mixed-Matrix Membrane Performance with Metal-Organic Framework Additives. *Cryst. Growth Des.* **2017**, *17*, 4467–4488.
- (21) Kanehashi, S.; Chen, G. Q.; Scholes, C. A.; Ozcelik, B.; Hua, C.; Ciddor, L.; Southon, P. D.; D’Alessandro, D. M.; Kentish, S. E. Enhancing gas permeability in mixed matrix membranes through tuning the nanoparticle properties. *J. Membr. Sci.* **2015**, *482*, 49–55.
- (22) Dong, G.; Li, H.; Chen, V. Challenges and opportunities for mixed-matrix membranes for gas separation. *J. Mater. Chem. A* **2013**, *1*, 4610–4630.
- (23) Takahashi, S.; Paul, D. R. Gas permeation in poly(ether imide) nanocomposite membranes based on surface-treated silica. Part 1: Without chemical coupling to matrix. *Polymer* **2006**, *47*, 7519–7534.
- (24) Zhang, Y.; Feng, X.; Yuan, S.; Zhou, J.; Wang, B. Challenges and recent advances in MOF-polymer composite membranes for gas separation. *Inorg. Chem. Front.* **2016**, *3*, 896–909.
- (25) Basu, S.; Cano-Odena, A.; Vankelecom, I. F. J. MOF-containing mixed-matrix membranes for CO<sub>2</sub>/CH<sub>4</sub> and CO<sub>2</sub>/N<sub>2</sub> binary gas mixture separations. *Sep. Purif. Technol.* **2011**, *81*, 31–40.
- (26) Ahmadpour, E.; Sarfaraz, M. V.; Behbahani, R. M.; Shamsabadi, A. A.; Aghajani, M. Fabrication of mixed matrix membranes containing TiO<sub>2</sub> nanoparticles in Pebax 1657 as a copolymer on an ultra-porous PVC support. *J. Nat. Gas Sci. Eng.* **2016**, *35*, 33–41.
- (27) Sadeghi, M.; Semsarzadeh, M. A.; Barikani, M.; Pourafshari Chenar, M. Gas separation properties of polyether-based polyurethane-silica nanocomposite membranes. *J. Membr. Sci.* **2011**, *376*, 188–195.
- (28) Ahn, J.; Chung, W.-J.; Pinnau, I.; Guiver, M. D. Polysulfone/silica nanoparticle mixed-matrix membranes for gas separation. *J. Membr. Sci.* **2008**, *314*, 123–133.
- (29) Takahashi, S.; Paul, D. R. Gas permeation in poly(ether imide) nanocomposite membranes based on surface-treated silica. Part 2: With chemical coupling to matrix. *Polymer* **2006**, *47*, 7535–7547.
- (30) Zhou, L.; Zhang, X.; Chen, Y. Facile synthesis of Al-fumarate metal-organic framework nano-flakes and their highly selective adsorption of volatile organic compounds. *Mater. Lett.* **2017**, *197*, 224–227.
- (31) Dechnik, J.; Nuhnen, A.; Janiak, C. Mixed-Matrix Membranes of the Air-Stable MOF-5 Analogue [Co<sub>4</sub>(μ<sub>4</sub>-O)(Me<sub>2</sub>pzba)<sub>3</sub>] with a Mixed-Functional Pyrazolate-Carboxylate Linker for CO<sub>2</sub>/CH<sub>4</sub> Separation. *Cryst. Growth Des.* **2017**, *17*, 4090–4099.
- (32) Sabetghadam, A.; Seoane, B.; Keskin, D.; Duim, N.; Rodenas, T.; Shahid, S.; Sorribas, S.; Le Guillouzer, C.; Clet, G.; Tellez, C.; Daturi, M.; Coronas, J.; Kapteijn, F.; Gascon, J. Metal Organic Framework Crystals in Mixed-Matrix Membranes: Impact of the Filler Morphology on the Gas Separation Performance. *Adv. Funct. Mater.* **2016**, *26*, 3154–3163.
- (33) Thoma, R.; Kärger, J.; de Sousa Amadeu, N.; Niessing, S.; Janiak, C. Assessing Guest-Molecule Diffusion in Heterogeneous Powder Samples of Metal-Organic Frameworks through Pulsed-Field-

Gradient (PFG) NMR Spectroscopy. *Chem. - Eur. J.* **2017**, *23*, 13000–13005.

(34) Glomb, S.; Woschko, D.; Makhoulfi, G.; Janiak, C. Metal-Organic Frameworks with Internal Urea-Functionalized Dicarboxylate Linkers for SO<sub>2</sub> and NH<sub>3</sub> Adsorption. *ACS Appl. Mater. Interfaces* **2017**, *9*, 37419–37434.

(35) Loiseau, T.; Serre, C.; Huguenard, C.; Fink, G.; Taulelle, F.; Henry, M.; Bataille, T.; Ferey, G. A rationale for the large breathing of the porous aluminum terephthalate (MIL-53) upon hydration. *Chem. - Eur. J.* **2004**, *10*, 1373–1382.

(36) Gaab, M.; Trukhan, N.; Maurer, S.; Gummaraju, R.; Müller, U. The progression of Al-based metal-organic frameworks – From academic research to industrial production and applications. *Micro-porous Mesoporous Mater.* **2012**, *157*, 131–136.

(37) Alvarez, E.; Guillou, N.; Martineau, C.; Bueken, B.; Van de Voorde, B.; Le Guillouzer, C.; Fabry, P.; Nouar, F.; Taulelle, F.; de Vos, D.; Chang, J. S.; Cho, K. H.; Ramsahye, N.; Devic, T.; Daturi, M.; Maurin, G.; Serre, C. The structure of the aluminum fumarate metal-organic framework A520. *Angew. Chem., Int. Ed.* **2015**, *54*, 3664–3668.

(38) Thommes, M.; Kaneko, K.; Neimark, A. V.; Olivier, J. P.; Rodriguez-Reinoso, F.; Rouquerol, J.; Sing, K. S. W. Physisorption of gases, with special reference to the evaluation of surface area and pore size distribution (IUPAC Technical Report). *Pure Appl. Chem.* **2015**, *87*, 1051–1069.

(39) Jiang, D.; Burrows, A. D.; Edler, K. J. Size-controlled synthesis of MIL-101(Cr) nanoparticles with enhanced selectivity for CO<sub>2</sub> over N<sub>2</sub>. *CrystEngComm* **2011**, *13*, 6916–6919.

(40) Zamidi Ahmad, M.; Navarro, M.; Lhotka, M.; Zornoza, B.; Téllez, C.; Fila, V.; Coronas, J. Enhancement of CO<sub>2</sub>/CH<sub>4</sub> separation performances of 6FDA-based co-polyimides mixed matrix membranes embedded with UiO-66 nanoparticles. *Sep. Purif. Technol.* **2018**, *192*, 465–474.

(41) Yang, S.; Sun, J.; Ramirez-Cuesta, A. J.; Callear, S. K.; David, W. I.; Anderson, D. P.; Newby, R.; Blake, A. J.; Parker, J. E.; Tang, C. C.; Schroder, M. Selectivity and direct visualization of carbon dioxide and sulfur dioxide in a decorated porous host. *Nat. Chem.* **2012**, *4*, 887–894.

(42) Jacques, N. M.; Rought, P. R. E.; Fritsch, D.; Savage, M.; Godfrey, H. G. W.; Li, L.; Mitra, T.; Frogley, M. D.; Cinque, G.; Yang, S.; Schroder, M. Locating the binding domains in a highly selective mixed matrix membrane via synchrotron IR microspectroscopy. *Chem. Commun.* **2018**, *54*, 2866–2869.

(43) Rubio-Martinez, M.; Leong, T.; Juliano, P.; Hadley, T. D.; Batten, M. P.; Polyzos, A.; Lim, K.-S.; Hill, M. R. Scalable simultaneous activation and separation of metal-organic frameworks. *RSC Adv.* **2016**, *6*, 5523–5527.

(44) Bux, H.; Liang, F.; Li, Y.; Cravillon, J.; Wiebcke, M.; Caro, J. Zeolitic Imidazolate Framework Membrane with Molecular Sieving Properties by Microwave-Assisted Solvothermal Synthesis. *J. Am. Chem. Soc.* **2009**, *131*, 16000–16001.

(45) Guo, H.; Zhu, G.; Hewitt, I. J.; Qiu, S. Twin Copper Source Growth of Metal-Organic Framework Membrane: Cu<sub>3</sub>(BTC)<sub>2</sub> with High Permeability and Selectivity for Recycling H<sub>2</sub>. *J. Am. Chem. Soc.* **2009**, *131*, 1646–1647.

(46) Hwang, S.; Chi, W. S.; Lee, S. J.; Im, S. H.; Kim, J. H.; Kim, J. Hollow ZIF-8 nanoparticles improve the permeability of mixed matrix membranes for CO<sub>2</sub>/CH<sub>4</sub> gas separation. *J. Membr. Sci.* **2015**, *480*, 11–19.

(47) Venna, S. R.; Lartey, M.; Li, T.; Spore, A.; Kumar, S.; Nulwala, H. B.; Luebke, D. R.; Rosi, N. L.; Albenze, E. Fabrication of MMMs with improved gas separation properties using externally-functionalized MOF particles. *J. Mater. Chem. A* **2015**, *3*, 5014–5022.

(48) Ordoñez, M. J. C.; Balkus, K. J.; Ferraris, J. P.; Musselman, I. H. Molecular sieving realized with ZIF-8/Matrimid® mixed-matrix membranes. *J. Membr. Sci.* **2010**, *361*, 28–37.

(49) Zhang, Y.; Musselman, I. H.; Ferraris, J. P.; Balkus, K. J. Gas permeability properties of Matrimid® membranes containing the

metal-organic framework Cu–BPY–HFS. *J. Membr. Sci.* **2008**, *313*, 170–181.

(50) Etxeberria-Benavides, M.; David, O.; Johnson, T.; Łozińska, M. M.; Orsi, A.; Wright, P. A.; Mastel, S.; Hillenbrand, R.; Kapteijn, F.; Gascon, J. High performance mixed matrix membranes (MMMs) composed of ZIF-94 filler and 6FDA-DAM polymer. *J. Membr. Sci.* **2018**, *550*, 198–207.

(51) Shen, Y.; Lua, A. C. Theoretical and experimental studies on the gas transport properties of mixed matrix membranes based on polyvinylidene fluoride. *AIChE J.* **2013**, *59*, 4715–4726.

(52) Rafiq, S.; Maulud, A.; Man, Z.; Mutalib, M. I. A.; Ahmad, F.; Khan, A. U.; Khan, A. L.; Ghauri, M.; Muhammad, N. Modelling in mixed matrix membranes for gas separation. *Can. J. Chem. Eng.* **2015**, *93*, 88–95.

(53) Sadeghi, Z.; Omidkhan, M.; Masoumi, M. E.; Abedini, R. Modification of existing permeation models of mixed matrix membranes filled with porous particles for gas separation. *Can. J. Chem. Eng.* **2016**, *94*, 547–555.

(54) Jeazet, H. B.; Koschine, T.; Staudt, C.; Raetzke, K.; Janiak, C. Correlation of Gas Permeability in a Metal-Organic Framework MIL-101(Cr)-Polysulfone Mixed-Matrix Membrane with Free Volume Measurements by Positron Annihilation Lifetime Spectroscopy (PALS). *Membranes (Basel, Switz.)* **2013**, *3*, 331–353.

(55) Huang, Y.; Wang, X.; Paul, D. Physical aging of thin glassy polymer films: Free volume interpretation. *J. Membr. Sci.* **2006**, *277*, 219–229.

(56) Kanehashi, S.; Nagai, K. Analysis of dual-mode model parameters for gas sorption in glassy polymers. *J. Membr. Sci.* **2005**, *253*, 117–138.

(57) Park, J. Y.; Paul, D. R. Correlation and prediction of gas permeability in glassy polymer membrane materials via a modified free volume based group contribution method. *J. Membr. Sci.* **1997**, *125*, 23–39.

### **3.5 Palladium Nanoparticle-immobilized Porous Polyurethane Material for Quick and Efficient Heterogeneous Catalysis of Suzuki-Miyaura Cross-Coupling Reaction at Room Temperature**

Sandeep Kumar Dey, Dennis Dietrich, Susann Wegner, Beatriz Gil-Hernández, Sarvesh Shyam Harmalkar, Nader de Sousa Amadeu, Christoph Janiak

Die Publikation beinhaltet die erfolgreiche Synthese eines Pd<sup>0</sup>-basierten Katalysators für die Suzuki-Miyaura-Kreuzkupplung, welcher als Nanopartikel auf einem porösen, organischen Polymer immobilisiert wurde. Das Kompositmaterial wurde über Atomabsorptionsspektroskopie, Röntgenphotoelektronenspektroskopie und Elektronenmikroskopie charakterisiert. In katalytischen Tests zeigten sich exzellente Umsätze bei geringem Katalysatoreinsatz.

Anteile an der Veröffentlichung:

- Rasterelektronenmikroskopische Erstcharakterisierung aller Syntheseergebnisse, größtenteils nicht veröffentlicht.
- Ortsaufgelöste energiedispersive Röntgenanalyse zur Bestimmung des Palladiumanteils in den Kompositmaterialien.
- Synthese, Charakterisierung, katalytische Tests sowie Verfassen des Manuskripts durch Herrn Sandeep Kumar Dey. Korrekturen durch Herrn Prof. Dr. Christoph Janiak.
- Anteilige Arbeiten durch die übrigen Kooperationspartner.

## Catalysis

## Palladium Nanoparticle-Immobilized Porous Polyurethane Material for Quick and Efficient Heterogeneous Catalysis of Suzuki-Miyaura Cross-Coupling Reaction at Room Temperature

Sandeep Kumar Dey,<sup>[a, b]</sup> Dennis Dietrich,<sup>[a]</sup> Susann Wegner,<sup>[a]</sup> Beatriz Gil-Hernández,<sup>[a]</sup> Sarvesh Shyam Harmalkar,<sup>[b]</sup> Nader de Sousa Amadeu,<sup>[a]</sup> and Christoph Janiak<sup>\*[a]</sup>

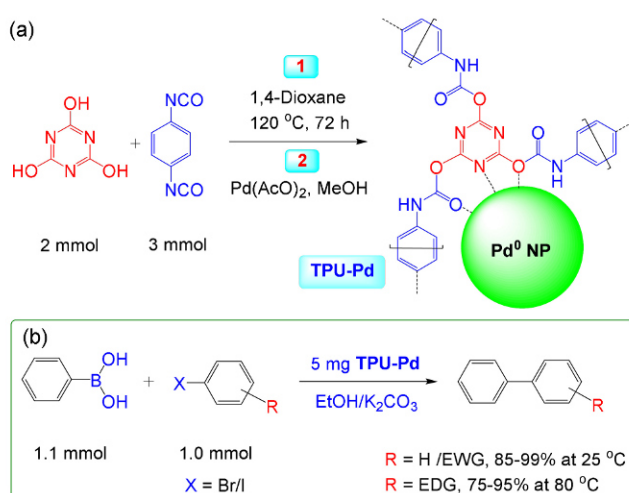
Here we report, room temperature heterogeneous catalysis of the Suzuki-Miyaura cross-coupling reaction by a Pd<sup>0</sup> nanoparticle-immobilized porous organic polymer (TPU-Pd), providing excellent yields (up to 99%) using low catalyst loading. High nitrogen- and oxygen-donor content of triazine-based porous polyurethane (TPU) makes it an efficient porous polymer for Pd-immobilization and subsequent heterogeneous catalysis of C–C cross-coupling reactions. X-ray photoelectron spectroscopy of TPU-Pd showed characteristic binding energy peaks of Pd<sup>0</sup>. Atomic absorption spectroscopy revealed

10.4 wt% of Pd<sup>0</sup> in TPU-Pd, and transmission electron microscopy images showed well-dispersed and faceted Pd<sup>0</sup> nanoparticles of size 5–20 nm. Catalysis of Suzuki-Miyaura reaction was observed to be completed in 3 h at 25 °C for a wide range of aryl halide substrates with phenylboronic acid, whereas increasing the reaction temperature to 80 °C largely allows decreasing the reaction time to 0.5–1 h. The porosity and surface area of the catalyst was not affected after catalysis, and the catalyst has been reused for five consecutive runs.

## Introduction

Over the last decade rapid development has been achieved on the rational design and synthesis of porous organic polymers (POPs) based on their applications in the field of gas storage and separation, water sorption, catalysis, and optoelectronics.<sup>[1]</sup> From catalysis point of view, nitrogen rich crystalline and amorphous POPs have been efficiently employed as heterogeneous organocatalysts for aldol-type C–C bond forming reactions and conjugate addition reactions.<sup>[2]</sup> Moreover, POPs having suitable chemical functionalities and permanent porosity can act as versatile and efficient supports for various catalytically active metals. Along this line, imine-based and triazine-based POPs have been established as suitable candidates for anchoring and immobilizing noble metal ions such as, palladium (Pd), platinum (Pt), ruthenium (Ru) and gold (Au) within the porous framework.<sup>[3]</sup> These hybrid metal-grafted POP materials have been used to carry out heterogeneous catalysis

of several important organic reactions, often with excellent catalytic activity and recyclability.<sup>[3]</sup> In recent years, both microporous and mesoporous Pd-immobilized (Pd<sup>2+</sup> ions or Pd<sup>0</sup> nanoparticles) POPs have been shown to catalyze some representative Pd-catalyzed reactions, such as the Suzuki-Miyaura (Scheme 1),<sup>[4]</sup> Heck/Sonogashira<sup>[4e,5]</sup> and Hiyama<sup>[6]</sup>



**Scheme 1.** (a) Solvothermal synthesis of triazine-based porous polyurethane (TPU), and its post-synthetic functionalization with palladium acetate to obtain Pd<sup>0</sup>-immobilized TPU (TPU-Pd), (b) TPU-Pd catalyzed Suzuki-Miyaura cross-coupling reaction of phenylboronic acid with various aryl halide substrates at 25 °C and 80 °C (EWG = electron withdrawing group, and EDG = electron donating group, see Table 1).

[a] Dr. S. K. Dey, D. Dietrich, S. Wegner, Dr. B. Gil-Hernández, Dr. N. de Sousa Amadeu, Prof. Dr. C. Janiak  
Institut für Anorganische Chemie und Strukturchemie  
Heinrich-Heine-Universität Düsseldorf  
40225 Düsseldorf, Germany  
Fax: +49-211-81-12287  
Tel: +49-211-81-12286  
E-mail: janiak@uni-duesseldorf.de

[b] Dr. S. K. Dey, S. S. Harmalkar  
Department of Chemistry  
Goa University  
Taleigao Plateau, Goa 403206, India

Supporting information for this article is available on the WWW under <https://doi.org/10.1002/slct.201702083>

cross-coupling reactions. The difficulty in separating and recycling the expensive  $\text{Pd}^{2+}$  salt catalysts applied in homogeneous reaction media eventually demands for an efficient and recyclable heterogeneous catalyst for the Pd-catalyzed reactions, preferably under ambient and sustainable conditions.

The Pd-catalyzed Suzuki-Miyaura (S–M) cross-coupling reaction of aryl halides with arylboronic acid is one of the most efficient methods for the synthesis of biaryls, triaryls or introduction of substituted aryl moieties in organic synthesis. Although, several Pd-grafted POPs have been used for S–M reaction,<sup>[4]</sup> a quick and efficient heterogeneous catalysis of this reaction by a Pd-POP catalyst at room temperature under environmentally benign conditions has not been reported. All reported S–M cross-coupling reactions catalyzed by Pd-grafted POPs have employed a temperature of 60 °C or above (up to 150 °C) using ethanol-water solvent mixture in most cases (Table S4 in the Supporting Information).<sup>[4]</sup> Several post-modified Pd-grafted MOFs and other Pd-grafted porous materials like porous carbon and silica have also been used for heterogeneous S–M catalysis (Table S4, in the Supporting Information).<sup>[7]</sup> To further add to this list, a couple of heterogeneous Pd-catalysts (nonporous) and metallodendritic grafted  $\text{Fe}_2\text{O}_3$  nanoparticles have shown good recyclability and efficiency of catalyst.<sup>[8]</sup>

However, quick and efficient heterogeneous catalysis of S–M cross-coupling reaction by a Pd-grafted POP at room temperature under ambient conditions is not known, to the best of our knowledge.

Because of their biocompatibility and biodegradability, several porous polyurethane (PU) materials have been used for soft tissue engineering applications and also in biosensor and magnetic resonance imaging (MRI) applications.<sup>[9]</sup> In our attempt to design a heterogeneous solid support for noble metal catalyst, we have synthesized a triazine-based porous polyurethane (TPU) material and functionalized the material with  $\text{Pd}^0$  nanoparticles (NPs) to obtain TPU-Pd, for the purpose of catalysis of the S–M cross-coupling reaction under ambient conditions (Scheme 1).<sup>[10]</sup> High nitrogen- and oxygen-donor content of TPU makes it an efficient porous polymer for Pd-immobilization and subsequent heterogeneous catalysis. Herein, we report the quick and efficient heterogeneous catalysis of the S–M cross-coupling reactions of aryl halides with phenylboronic acid by TPU-Pd at room temperature (25 °C) in ethanol, showing excellent conversions (up to 99%) for most of the bromobenzene and iodobenzene derivatives. The reactions of all aryl halide substrates with phenylboronic acid have also been carried out at 80 °C to examine the effect of temperature on the reaction rates, and to improve the performance of the few substrates giving poor yield at 25 °C.

## Results and Discussion

The triazine-based porous polyurethane (TPU) was synthesized by the condensation of cyanuric acid and 1,4-phenylenediisocyanate in 1,4-dioxane at 120 °C under solvothermal conditions (Scheme 1 and experimental section below). FT-IR spectrum of TPU showed presence of the carbonyl (C=O) and triazine

stretching bands at 1637 and 1559  $\text{cm}^{-1}$  respectively, (Figure S3 in the Supporting Information) indicating formation of the urethane-linked polymer. However, a low intensity isocyanate (N=C=O) stretching band was observed at 2270  $\text{cm}^{-1}$ , indicating the presence of a small percentage of unreacted N=C=O groups in TPU. Solid-state  $^{13}\text{C}$  CP/MAS NMR spectrum of TPU further confirmed the presence of carbonyl carbon of the urethane group at 159 ppm, whereas other peaks at 137 and 128 ppm were assigned to aryl rings (Figure S7 in the Supporting Information). The powder X-ray diffraction (PXRD) pattern of TPU displays several peaks over a broad background of the amorphous TPU (Figure 1a). The broad peaks at around 2-theta 21° and between 26–30° can be matched with the PXRD patterns of presumably nanocrystals of 1,4-phenylenediisocyanate and cyanuric acid (See Fig. S63 and S64 in Supporting Information) which may remain occluded in the pores of TPU. Scanning electron microscopy (SEM) images revealed that TPU forms as small proliferated flakes, which are aggregated into an overall sponge-like morphology (Figure 2a and S11 in the Supporting Information). CHN analysis showed 19.2 wt% of nitrogen in TPU which makes it an ideal material for metal-immobilization (Table S1 in the Supporting Information). Thermogravimetric analysis (TGA) showed that no solvent molecules were included within the pores of TPU, and the material was stable up to 280 °C (Figure S24 in the Supporting Information).

A nitrogen sorption measurement at 77 K showed permanent porosity in TPU with a BET surface area of 124  $\text{m}^2 \text{g}^{-1}$  (Table S3 in the Supporting Information) and a total pore volume of 0.26  $\text{cm}^3 \text{g}^{-1}$ , calculated by using the DFT method. The non-local density functional theory (NLDFT) pore size distribution curve indicated a significant fraction of mesopores (20–200 Å) in TPU, and only a small fraction of micropores centred at a diameter of 17 Å (Figure S19b in the Supporting Information; note that macropores are not accounted for in  $\text{N}_2$  sorption measurements). The nitrogen sorption isotherms of porous polymers with a broad pore size distribution are often difficult to analyze as they consist of micropores, mesopores and even macropores in some cases, and thereby, give complex adsorption-desorption curves which are generally difficult to assign to a particular type of isotherm. Low nitrogen uptake by TPU at low relative pressure ( $P/P_0 < 0.1$ ) is due to the lack of abundant micropores, and a sharp rise at high pressure regions ( $P/P_0 = 0.8$ –1.0) indicates the pore filling phenomena of mesopores (2–50 nm) by a multilayer adsorption process (Figure S19a, in the Supporting Information).<sup>[4d,12c]</sup> The nitrogen sorption isotherm of TPU can be considered as a composite of Type II and Type III (mostly observed with nonporous or macroporous adsorbents), with a H4 hysteresis loop.<sup>[11]</sup> Hysteresis appearing in the multilayer range of physisorption isotherms is usually associated with capillary condensation in mesopore structures. A H4 hysteresis is generally observed for adsorbent particles with internal voids of irregular size and having a broad particle size distribution.<sup>[11]</sup> Therefore, a H4 hysteresis loop is a possible indication towards the presence of both mesopores and also towards aggregation induced

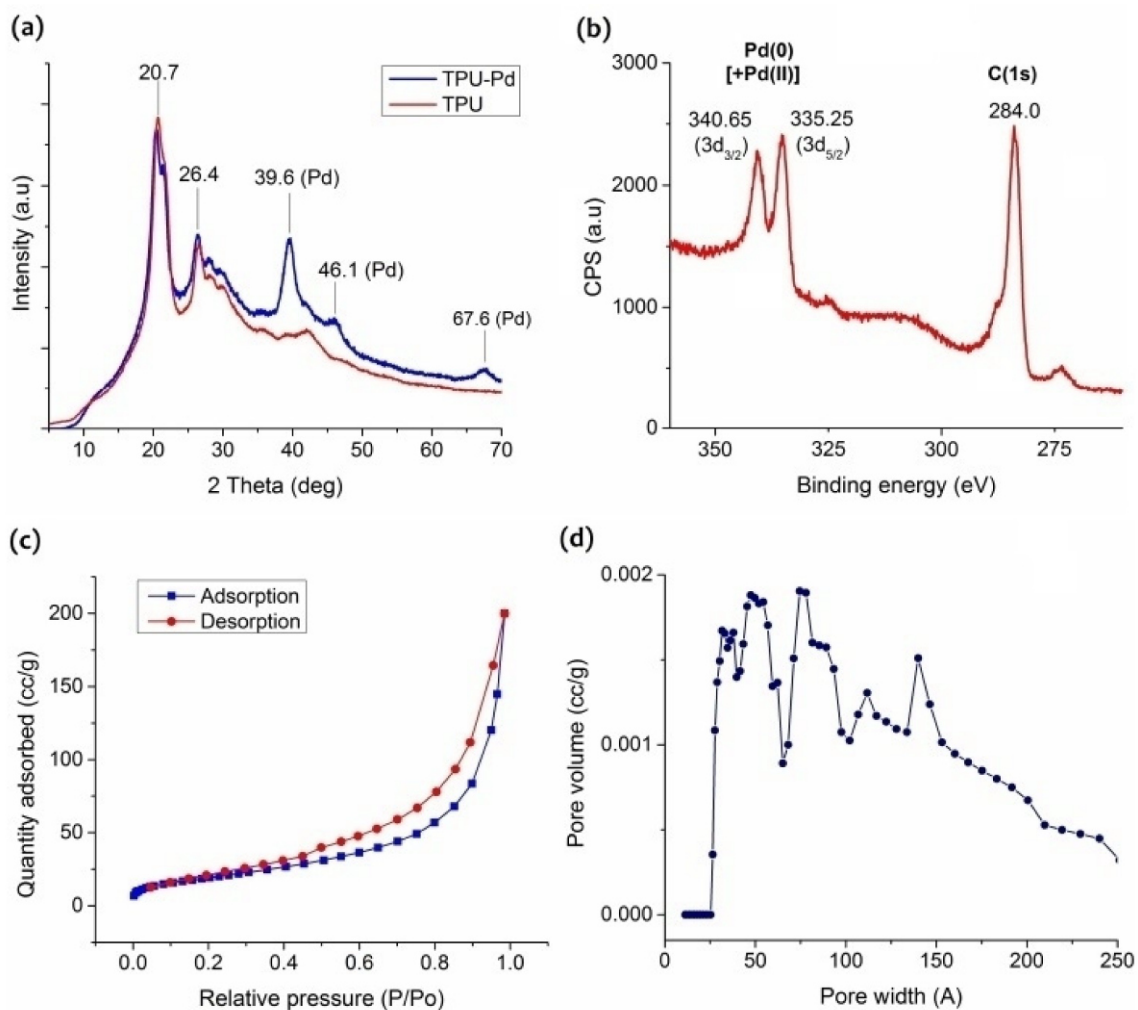


**Figure 1.** (a) PXRD patterns of TPU and TPU-Pd, (b) XP spectrum of TPU-Pd showing the presence of Pd(0); (c) Nitrogen sorption isotherm of TPU-Pd at 77 K, and (d) NLDFT pore size distribution curve of TPU-Pd using a slit pore model.

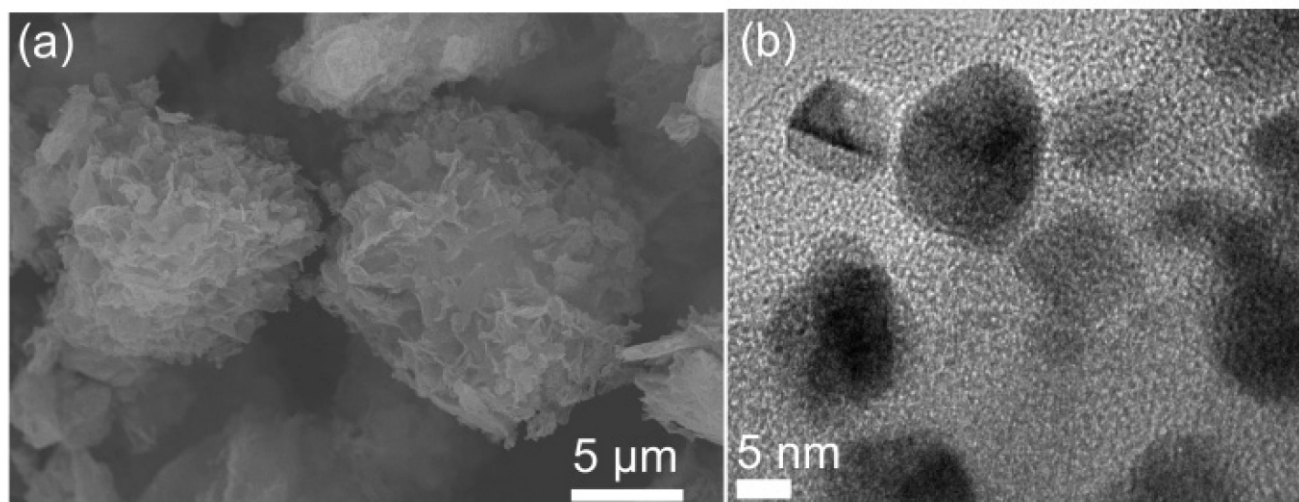


**Figure 2.** (a) SEM image of TPU, and (b) TEM image of TPU-Pd.



formation of slit like pores in the **TPU** material, as hinted in the SEM image (Figure 2a).

The unexpectedly low surface area of **TPU** results from the interpenetration in the polymeric network. The flexibility of the urethane groups and their tendency to form hydrogen bonds involving the carbonyl oxygen (C=O) and amide hydrogen (O=C-NH) is probably responsible for interpenetration during the framework formation. Framework interpenetration results in random orientation of the pores in the polymer giving a broad range of pore size distribution. Low BET surface area values have also been observed in related urea-based and amide-based porous organic polymers.<sup>[4f,12]</sup>

Simple post-treatment of **TPU** with palladium acetate, Pd(AcO)<sub>2</sub> in dichloromethane and then with methanol at room temperature afforded the Pd<sup>0</sup>-immobilized **TPU** material, **TPU-Pd** (see Supporting Information).<sup>[5c,13]</sup> A comparison of the PXRD patterns and SEM images of **TPU** and **TPU-Pd** revealed that the structure of the material was well preserved after Pd<sup>0</sup>-immobilization. The PXRD of **TPU-Pd** showed an additional intense peak at 39.6° and two broad peaks at 47.1° and 67.6° which can be assigned to (111), (200) and (220) crystal planes of Pd<sup>0</sup> nanoparticles (Figure 1a).<sup>[14]</sup> X-ray photoelectron spectroscopy (XPS) measurement of **TPU-Pd** confirmed that Pd<sup>2+</sup> has been largely reduced to the Pd<sup>0</sup> metallic state.<sup>[13]</sup> The high-resolution XPS analysis shows a Pd(0) (335.5 and 341.1 eV for the 3d<sub>5/2</sub> and 3d<sub>3/2</sub> states) and a Pd(II) species (337.3 and 343.4 eV) with contributions of about 75% and 25%, respectively (Figure 1b and Figure S26 in the Supporting Information).<sup>[4c,5a]</sup> The well-dispersed and faceted Pd<sup>0</sup> NPs (size 5–20 nm) with distinct interference patterns (lattice planes) could be clearly observed in the TEM images of **TPU-Pd** (Figure 2b and Figure S29 in the Supporting Information). Selected area electron diffraction (SAED) showed sharp rings with reflections of the Pd<sup>0</sup> NPs, which are in good comparison with the cubic phase (Fm-3 m) of pure Pd<sup>0</sup> NPs (COD reference 1534921) (Figure S30 in the Supporting Information). Atomic absorption spectroscopy (AAS) of the dissolved Pd-species obtained after digesting **TPU-Pd** in aqua regia showed 10.4 wt% of Pd in **TPU-Pd**. A nitrogen sorption measurement (77 K) of **TPU-Pd** showed a decreased BET surface area of 80 m<sup>2</sup> g<sup>-1</sup> (Figure 1c), however, without much affecting the total pore volume (0.25 cm<sup>3</sup> g<sup>-1</sup>) due to the predominantly mesoporous nature of the **TPU** material. A decrease in the BET surface area is consistent with the fact that Pd<sup>0</sup>-immobilization partially occupies the pores in **TPU**. NLDTF pore size distribution curve of **TPU-Pd** showed the presence of only mesopores (20–200 Å), while the 17 Å micropores in **TPU** are not been observed anymore in **TPU-Pd** (Figure 1d). While a macro/mesoporous structure can accelerate the mass transfer of reactants and products, micropores of suitable size are favorable for anchoring metal particles.

To evaluate the catalytic activity of **TPU-Pd** for the S–M cross-coupling reaction, we have initially examined the reactions of phenylboronic acid (1.1 mmol) with 4-haloacetophenone (1.0 mmol) in ethanol at room temperature (aerobic condition) using K<sub>2</sub>CO<sub>3</sub> as a base and 5 mg of **TPU-Pd** (0.5 mg, 4.7 μmol Pd). The reaction of 4-bromoacetophenone and 4-iodoacetophenone with phenylboronic acid was observed to

be completed in 3 h giving 99% yield of 4-phenylacetophenone, as monitored by <sup>1</sup>H NMR spectroscopy (Figure S61 in the Supporting Information). Both bromobenzene and iodobenzene also afforded 99% of biphenyl under the same reaction conditions (Table 1). In the context of room temperature

**Table 1.** Catalytic data of **TPU-Pd** catalysed Suzuki-Miyaura cross-coupling reactions.

Aryl halides	Catalysis at 25 °C <sup>[a]</sup>		Catalysis at 80 °C <sup>[b]</sup>	
	Time/h	Yield, % <sup>[c]</sup>	Time/h	Yield, % <sup>[c]</sup>
1-bromobenzene	3	99 <sup>[d]</sup>	0.5	99 <sup>[d]</sup>
4-bromoacetophenone	3	99 <sup>[d]</sup>	0.5	99 <sup>[d]</sup>
3-bromoacetophenone	3	93 <sup>[e]</sup>	0.5	95 <sup>[e]</sup>
2-bromoacetophenone	3	99 <sup>[d]</sup>	0.5	99 <sup>[d]</sup>
4-bromobenzonitrile	3	99 <sup>[d]</sup>	0.5	99 <sup>[d]</sup>
1-bromo-4-nitrobenzene	3	99 <sup>[d]</sup>	0.5	99 <sup>[d]</sup>
1-bromo-4-fluorobenzene	3	99 <sup>[d]</sup>	0.5	99 <sup>[d]</sup>
methyl-4-bromobenzoate	3	99 <sup>[d]</sup>	0.5	99 <sup>[d]</sup>
2-bromoanisole	3	94 <sup>[e]</sup>	1	95 <sup>[e]</sup>
4-bromoanisole	3	30 <sup>[e]</sup>	3	75 <sup>[e]</sup>
2-bromotoluene	3	65 <sup>[e]</sup>	2.5	93 <sup>[e]</sup>
4-bromotoluene	3	30 <sup>[e]</sup>	3	75 <sup>[e]</sup>
1,3-dibromobenzene	3	50 <sup>[e]</sup>	1.5	99 <sup>[d]</sup>
1,4-dibromobenzene	3	n.d. <sup>[f]</sup>	1.5	99 <sup>[d]</sup>
9-bromoanthracene	3	81 <sup>[e]</sup>	1	99 <sup>[d]</sup>
1-iodobenzene	3	99 <sup>[d]</sup>	0.5	99 <sup>[d]</sup>
4-iodoacetophenone	3	99 <sup>[d]</sup>	0.5	99 <sup>[d]</sup>
methyl-4-iodobenzoate	3	99 <sup>[d]</sup>	0.5	99 <sup>[d]</sup>
4-iodoacetanilide	3	85 <sup>[e]</sup>	1	99 <sup>[d]</sup>
4-iodoaniline	3	25 <sup>[e]</sup>	3	88 <sup>[e]</sup>

[a] General conditions: aryl halide (1.0 mmol), phenylboronic acid (135 mg, 1.1 mmol) in the presence of 5 mg **TPU-Pd** (0.5 mg, 4.7 μmol Pd) in ethanol at 25 °C, [b] general conditions: aryl halide (1.0 mmol), phenylboronic acid (135 mg, 1.1 mmol) in the presence of 5 mg **TPU-Pd** (0.5 mg, 4.7 μmol Pd) in ethanol at 80 °C, [c] yields reported are average of two independent runs under same conditions, [d] isolated yield, [e] yields corresponding to aryl halide conversion are based on <sup>1</sup>H NMR analysis of the isolated crude product (Figures S32–S62 in the Supporting Information), [f] yield could not be determined (n.d.) due to the complex nature of the <sup>1</sup>H-NMR spectrum.

heterogeneous catalysis of S–M cross coupling reaction, Pd-NP immobilized metal organic frameworks (MOFs) namely MIL-101-Cr and MIL-101-Cr-NH<sub>2</sub> were shown to be efficient catalysts for the coupling of aryl halides with arylboronic acid at room temperature.<sup>[7a–b]</sup> Further, Pd-NP immobilized carbon nanotube was also found to be effective in promoting the coupling of aryl halides with arylboronic acid, providing good yields (75–98%) at room temperature.<sup>[7h]</sup> Table S4 in the supporting information provides a detailed comparison of reaction conditions of the S–M cross-coupling reactions catalyzed by different Pd-grafted heterogeneous porous catalysts and **TPU-Pd**. From Table S4, it is clear that the amount of **TPU-Pd** (0.5 mg, 4.7 μmol Pd for 1.0 mmol of aryl halide) used is significantly less when compared to the Pd-loading used for most of the Pd-grafted porous catalysts in S–M cross-coupling reaction.

Solvents have remarkable influences on the catalytic activity of **TPU-Pd**, as no biphenyl product was observed to be formed in aprotic solvents such as, acetonitrile and tetrahydrofuran under the same conditions. When the reaction was carried out

in neat water, only trace amounts of the desired product (~5%) were formed. According to the Pfizer solvent selection guide, ethanol is considered as a preferable choice of environmentally benign solvent if a reaction cannot be carried out in water medium.<sup>[15]</sup> Although there is a report where the S–M coupling has been carried out in neat water providing good yields of the desired product,<sup>[4f]</sup> but in our case, **TPU-Pd** catalyst worked most efficiently only in ethanol. To study the effect of temperature on the reaction kinetics, 4-bromoacetophenone and phenylboronic acid were allowed to react at 50 °C and 80 °C keeping all other reaction parameters the same. Quantitative yield (99%) of 4-phenylacetophenone was obtained within 1 h at 50 °C and in 0.5 h at 80 °C, indicative of faster reaction rate with gradual increase in temperature. The reaction of 4-bromoacetophenone with phenylboronic acid has also been carried out in gram scale (10 mmol) using **TPU-Pd** (50 mg), which yielded 99% product at room temperature within the same time frame of 3 h.

In order to validate the heterogeneity of the reaction, the filtrate from the reaction between 4-bromoacetophenone and phenylboronic acid (at 25 °C in ethanol for 3 h) has been analyzed by AAS to detect any Pd-leaching from **TPU-Pd**. No Pd was found within the detectable limit of AAS (0.22 mg/L). Furthermore, 4-bromoacetophenone and phenylboronic acid were allowed to react at room temperature for 1 h under standardized conditions (45% product yield), and the reaction mixture was filtered to remove the **TPU-Pd** catalyst. The filtrate was then stirred for another 2 h at room temperature, and <sup>1</sup>H NMR analysis of the isolated crude product showed no significant increase in the conversion to the desired product (49% product yield). These experiments suggested a strong interaction of Pd<sup>0</sup> NPs with **TPU** in **TPU-Pd**, and prove that the active phase was neither dissolved nor that active Pd<sup>0</sup> species leached from the **TPU** support. Further, to assess the heterogeneous pathway of **TPU-Pd** catalyst, poison experiments were carried out using carbon disulfide (CS<sub>2</sub>), pyridine, and triphenyl phosphine (PPh<sub>3</sub>) as poisoning additives. In the poison experiments which were carried out at room temperature, no catalytic activity of **TPU-Pd** was detected when the reaction of 4-bromoacetophenone and phenylboronic acid was performed in the presence of 45 μL (0.74 mmol) of carbon disulfide. CS<sub>2</sub> as a known catalyst poison binds strongly to active metal sites and blocks access to the substrates.<sup>[4f]</sup> Also addition of one equivalent of pyridine (relative to 4-bromoacetophenone) in the reaction mixture resulted in complete quenching of the cross-coupling reaction, whereas addition of one equivalent of triphenyl phosphine (relative to 4-bromoacetophenone) showed 89% quenching under the ideal reaction conditions (see Supporting Information). The incomplete quenching of the cross-coupling reaction is likely due to the fact that PPh<sub>3</sub> being a bulky molecule could not efficiently enter into the smaller pores of the frameworks to poison the palladium active sites.

To explore the substrate scope and generality of the catalytic system, a series of substituted aryl bromides and aryl iodides with different steric and electronic characters were tested under the given optimal conditions at 25 °C and 80 °C. In general, the reactivity of aryl halides with electron-withdrawing

substituents (EWGs) was higher than that of electron-donating substituents (EDGs). The aryl halides with EWGs afforded the desired cross-coupling products in excellent yields (85–99%) at 25 °C (Table 1). Moderate to low yields (25–65%) were observed for the aryl halides with EDGs, except for 2-bromoanisole which yielded 94% of the desired product under the same conditions. However, the yield of the cross-coupling reactions between phenylboronic acid and aryl halides with EDGs can be significantly improved (75–95%) by increasing the reaction temperature to 80 °C (Table 1), which largely allows to decrease the reaction time to 0.5 or 1 h.

It is noted that the reactions of 2-bromoanisole and 2-bromotoluene with phenylboronic acid gave the desired products comparatively in much higher yield than 4-bromoanisole and 4-bromotoluene, suggesting that the electronic and steric nature of substituted aryl bromides have an effect on the cross-coupling reaction (Table 1). This was also reflected in the reactions of 2-, 3-, and 4-bromoacetophenone with phenylboronic acid where 2-bromoacetophenone and 4-bromoacetophenone gave 99% yield, and 3-bromoacetophenone yielded only 93% of the desired product (Table 1).

The catalyst was recycled and used for four consecutive runs with gradual loss in its activity for the cross-coupling reaction between 4-bromoacetophenone and phenylboronic acid at 25 °C (Figure S62 in the Supporting Information). No significant changes have been observed in the FT-IR, PXRD, TEM and XPS analysis data of the recycled **TPU-Pd** (see Supporting Information). Further, no significant decrease in the BET surface areas of recycled **TPU-Pd** samples have been observed from N<sub>2</sub> sorption measurements (Table S3 in the Supporting Information). However, SEM images showed that the flake like morphology of the aggregated crystals of **TPU-Pd** was slightly lost after the first catalysis run (Figure S12 in the Supporting Information), which perhaps affects the reaction yield in the consecutive runs. It is noted that, gradual decrease in the catalytic activity of Pd-grafted heterogeneous porous material is rather common and hence, the pursuit for a suitable Pd-grafted heterogeneous porous catalyst which would retain its catalytic activity for several cycles is utmost desirable.<sup>[4–7]</sup>

## Conclusions

Overall in this contribution, we have shown the first instance of utilizing a Pd-nanoparticle immobilized porous polyurethane material for heterogeneous catalysis of the S–M cross-coupling reaction at room temperature, with high yield and some catalyst recyclability. The heterogeneous mesoporous structure of **TPU-Pd** catalyst allowed facile diffusion of organic reactant and product molecules in and out the pores during the reaction and thereby, facilitating faster reaction rate under mild conditions. Ambient condition, environmentally benign solvent, facile synthesis approach, gram scale synthesis, less reaction time, high yield and low catalyst loading (10 wt%, 0.5 mg, 4.7 μmol Pd in 5 mg composite) establish **TPU-Pd** as an excellent heterogeneous porous catalyst for the Suzuki-Miyaura cross-coupling reactions, when compared to the other known Pd-

grafted porous materials (Table S4 in the Supporting Information).<sup>[4,7]</sup>

## Acknowledgements

Dr. Sandeep Kumar Dey gratefully acknowledges the Alexander von Humboldt foundation, Germany for awarding a postdoctoral research fellowship. We also acknowledge Dr. Raghavender Medishetty and Prof. Dr. Roland A. Fischer from Technical University of Munich for offering their help with thermogravimetric analysis of our samples. We thank Mrs. Laura Schmolke for measuring the high-resolution XPS.

## Conflict of Interest

The authors declare no conflict of interest.

**Keywords:** cross-coupling reaction · heterogeneous catalysis · nanoparticle · palladium · porous material

- [1] a) S.-Y. Ding, W. Wang, *Chem. Soc. Rev.* **2013**, *42*, 548–568; b) X. Feng, X. Ding, D. Jiang, *Chem. Soc. Rev.* **2012**, *41*, 6010–6022; c) Z. Xiang, D. Cao, L. Dai, *Polym. Chem.* **2015**, *6*, 1896–1911; d) J. L. Segura, M. J. Mancheno, F. Zamora, *Chem. Soc. Rev.* **2016**, *45*, 5635–5671.
- [2] a) Q. Fang, S. Gu, J. Zheng, Z. Zhuang, S. Qiu, Y. Yan, *Angew. Chem. Int. Ed.* **2014**, *53*, 2878–2882; *Angew. Chem.* **2014**, *126*, 2922–2926; b) P. Kaur, J. T. Hupp, S. T. Nguyen, *ACS Catal.* **2011**, *1*, 819–835; c) D. B. Shinde, S. Kandambeth, P. Pachfule, R. R. Kumar, R. Banerjee, *Chem. Commun.* **2015**, *51*, 310–313; d) S. K. Dey, N. de Sousa Amadeu, C. Janiak, *Chem. Commun.* **2016**, *52*, 7834–7837; e) H. Xu, X. Chen, J. Gao, J. Lin, M. Addicoat, S. Irleb, D. Jiang, *Chem. Commun.* **2014**, *50*, 1292–1294.
- [3] a) Y. Zhang, S. N. Riduan, *Chem. Soc. Rev.* **2012**, *41*, 2083–2094; b) P. Pachfule, S. Kandambeth, D. D. Diaz, R. Banerjee, *Chem. Commun.* **2014**, *50*, 3169–3172; c) S. Hug, M. E. Tauchert, S. Li, U. E. Pachmayr, B. V. Lotsch, *J. Mater. Chem.* **2012**, *22*, 13956–13964; d) R. Palkovits, M. Antonietti, P. Kuhn, A. Thomas, F. Schüth, *Angew. Chem. Int. Ed.* **2009**, *48*, 6909–6912; *Angew. Chem.* **2009**, *121*, 7042–7045; e) C. E. Chan-Thaw, A. Villa, L. Prati, A. Thomas, *Chem. Eur. J.* **2011**, *17*, 1052; f) J. Artz, R. Palkovits, *ChemSusChem* **2015**, *8*, 3832–3838.
- [4] a) M. K. Bhunia, S. K. Das, P. Pachfule, R. Banerjee, A. Bhaumik, *Dalton Trans.* **2012**, *41*, 1304–1311; b) C.-A. Wang, Y.-F. Han, Y.-W. Li, K. Nie, X.-L. Cheng, J.-P. Zhang, *RSC Adv.* **2016**, *6*, 34866–34871; c) S.-Y. Ding, J. Gao, Q. Wang, Y. Zhang, W.-G. Song, C.-Y. Su, W. Wang, *J. Am. Chem. Soc.* **2011**, *133*, 19816–19822; d) B. Li, Z. Guan, W. Wang, X. Yang, J. Hu, B. Tan, T. Li, *Adv. Mater.* **2012**, *24*, 3390–3395; e) A. Modak, J. Mondal, M. Sasidharan, A. Bhaumik, *Green Chem.* **2011**, *13*, 1317–1331; f) L. Li, Z. Chen, H. Zhong, R. Wang, *Chem. Eur. J.* **2014**, *20*, 3050–3060; g) C.-A. Wang, Y.-W. Li, X.-M. Hou, Y.-F. Han, K. Nie, J.-P. Zhang, *ChemistrySelect* **2016**, *1*, 1371–1376; h) V. Sadhasivam, R. Balasaravanan, C. Chithiraikumar, A. Siva, *ChemistrySelect* **2017**, *2*, 1063–1070.
- [5] a) P. Pachfule, M. K. Panda, S. Kandambeth, S. M. Shivaprasad, D. D. Diaz, R. Banerjee, *J. Mater. Chem. A* **2014**, *2*, 7944–7952; b) A. Modak, M. Pramanik, S. Inagaki, A. Bhaumik, *J. Mater. Chem. A* **2014**, *2*, 11642–11650; c) D. Mullangi, S. Nandi, S. Shalini, S. Sreedhala, C. P. Vinod, R. Vaidhyanathan, *Sci. Rep.* **2015**, *5*, 10876; d) A. V. Nakhate, G. D. Yadav, *ChemistrySelect* **2016**, *1*, 3954–3965.
- [6] a) S. Lin, Y. Hou, X. Deng, H. Wang, S. Suna, X. Zhang, *RSC Adv.* **2015**, *5*, 41017–41024; b) A. R. Hajipour, Z. Tavangar-Rizi, *ChemistrySelect* **2017**, *2*, 8990–8999.
- [7] a) N. Shang, S. Gao, X. Zhou, C. Feng, Z. Wang, C. Wang, *RSC Adv.* **2014**, *4*, 54487–54493; b) V. Pascanu, Q. Yao, A. B. Gómez, M. Gustafsson, Y. Yun, W. Wan, L. Samain, X. Zou, B. Martín-Matute, *Chem. Eur. J.* **2013**, *19*, 17483–17493; c) Y. Huang, Z. Zheng, T. Liu, J. Lü, Z. Lin, H. Li, R. Cao, *Catal. Commun.* **2011**, *14*, 27–31; d) D. Saha, R. Sen, T. Maity, S. Koner, *Langmuir* **2013**, *29*, 3140–3151; e) R. Sen, D. Saha, S. Koner, P. Brandão, Z. Lin, *Chem. Eur. J.* **2015**, *21*, 5962–5971; f) F. Xamena, A. Abad, A. Corma, H. Garcia, *J. Catal.* **2007**, *250*, 294–298; g) W. Dong, L. Zhang, C. Wang, C. Feng, N. Shang, S. Gao, C. Wang, *RSC Adv.* **2016**, *6*, 37118–37123; h) D. V. Jawale, E. Gravel, C. Boudet, N. Shah, V. Geertsen, H. Li, I. N. N. Namboothiri, E. Doris, *Catal. Sci. Technol.* **2015**, *5*, 2388–2392; i) S. Jana, S. Haldar, S. Koner, *Tetrahedron Lett.* **2009**, *50*, 4820–4823; j) M. Cai, Q. Xu, Y. Huang, *J. Mol. Catal. A: Chem.* **2007**, *271*, 93–97; k) J. C. Park, E. Heo, A. Kim, M. Kim, K. H. Park, H. Song, *J. Phys. Chem. C* **2011**, *115*, 15772–15777.
- [8] a) E. Hariprasad, T. P. Radhakrishnan, *ACS Catal.* **2012**, *2*, 1179–1186; b) Z. Wang, Y. Yu, Y. X. Zhang, S. Z. Li, H. Qian, Z. Y. Lin, *Green Chem.* **2015**, *17*, 413–420; c) D. Rosario-Amorin, M. Gaboyard, R. Clérac, L. Vellutini, S. Nlate, K. Heuzé, *Chem. Eur. J.* **2012**, *18*, 3305–3315.
- [9] a) J. Guan, K. L. Fujimoto, M. S. Sacks, W. R. Wagner, *Biomaterials* **2005**, *26*, 3961–3971; b) Y.-C. Wang, F. Fang, Y.-K. Wu, X.-L. Ai, T. Lan, R.-C. Liang, Y. Zhang, N. M. Trishul, M. He, C. You, C. Yu, H. Tan, *RSC Adv.* **2016**, *6*, 3840–3849; c) A. Koh, Y. Lu, M. H. Schoenfish, *Anal. Chem.* **2013**, *85*, 10488–10491; d) X. Zhang, Z. Du, W. Zou, H. Li, C. Zhang, S. Li, W. Guo, *RSC Adv.* **2015**, *5*, 65890–65896; e) S. Garmendia, D. Mantione, S. Alonso de Castro, C. Jehanno, L. Lezama, J. L. Hedrick, D. Mecerreyes, L. Salassa, H. Sardon, *Polym. Chem.* **2017**, *8*, 2693–2701.
- [10] a) M. Akkoc, F. Imik, S. Yasar, V. Dorcet, T. Roisnel, C. Bruneau, I. Özdemiir, *ChemistrySelect* **2017**, *2*, 5729–5734; b) X. Li, C. Liu, L. Wang, Q. Ye, Z. Jin, *ChemistrySelect* **2017**, *2*, 4016–4020.
- [11] a) K. S. W. Sing, D. H. Everett, R. A. W. Haul, L. Moscou, R. A. Pierotti, J. Rouquerol, T. Siemeniewska, *Pure Appl. Chem.* **1985**, *57*, 603–619; b) M. Thommes, K. Kaneko, A. V. Neimark, J. P. Olivier, F. Rodriguez-Reinoso, J. Rouquerol, K. S. W. Sing, *Pure Appl. Chem.* **2015**, *87*, 1051–1062.
- [12] a) V. M. Suresh, S. Bonakala, H. S. Atreya, S. Balasubramanian, T. K. Maji, *ACS Appl. Mater. Interfaces* **2014**, *6*, 4630–4637; b) S. Zulfiqar, M. I. Sarwar, C. T. Yavuz, *RSC Adv.* **2014**, *4*, 52263–52269; c) L. Rajput, R. Banerjee, *Cryst. Growth Des.* **2014**, *14*, 2729–2732; d) S. Zulfiqar, D. Mantione, O. E. Tall, M. I. Sarwar, F. Ruipérez, A. Rothenberger, D. Mecerreyes, *J. Mater. Chem. A* **2016**, *4*, 8190–8197.
- [13] T. A. Stephenson, S. M. Morehouse, A. R. Powell, J. P. Heffer, G. Wilkinson, *J. Chem. Soc.* **1965**, 3632–3640.
- [14] W. Dong, L. Zhang, C. Wang, C. Feng, N. Shang, S. Gao, C. Wang, *RSC Adv.* **2016**, *6*, 37118–37123.
- [15] K. Alfonsi, J. Colberg, P. J. Dunn, T. Fevig, S. Jennings, T. A. Johnson, H. P. Kleine, C. Knight, M. A. Nagy, D. A. Perry, M. Stefaniak, *Green Chem.* **2008**, *10*, 31–36.

Submitted: September 7, 2017

Revised: January 12, 2018

Accepted: January 15, 2017

### **3.6 Novel high throughput mixed matrix membranes embracing poly ionic liquid-grafted biopolymer: Fabrication, characterization, permeation and antifouling performance**

Reda F. M. Elshaarawy, Janina Dechnik, Hassan M. A. Hassan, Dennis Dietrich, Mohamed A. Betiha, Stephan Schmidt, Christoph Janiak

Die Publikation beinhaltet Untersuchungen einer Polysulfonmembran, welche mit Titanoxidnanopartikeln, regulärem Chitosan und Chitosan, welches mit einer poly-ionischen Flüssigkeit grafted wurde, modifiziert und in Anwesenheit eines Porenstabilisierungsreagenz zur Ultrafiltration eingesetzt wurde. Die Einflüsse auf die Ultrafiltrationsmembran bezüglich der Morphologie, Porosität, Antifoulingeneigenschaften und des Durchflusses wurden untersucht. Der Fluss durch die Membran konnte dabei deutlich gegenüber einer reinen Polysulfonmembran erhöht werden.

Anteile an der Veröffentlichung:

- Rasterelektronenmikroskopische Strukturuntersuchungen der Membranquerschnitte und Nanopartikel.
- Ortsaufgelöste energiedispersive Röntgenanalyse zur Bestimmung der homogenen Einbettung des Füllmaterials in den Polymermembranen.
- Mitentwicklung an Methoden zur Charakterisierung bestimmter Membraneigenschaften, u.a. Digitalisierung der Wasserpermeationsanlage.
- Charakterisierung der Membranen, Permeationsmessungen, und Verfassen des Manuskriptes durch Herrn Reda F. M. Elshaarawy. Korrekturen durch Herrn Prof. Dr. Christoph Janiak.
- Anteilige Arbeiten durch die übrigen Kooperationspartner.



# Novel high throughput mixed matrix membranes embracing poly ionic liquid-grafted biopolymer: Fabrication, characterization, permeation and antifouling performance

Reda F.M. Elshaarawy<sup>a,b,\*</sup>, Janina Dechnik<sup>a</sup>, Hassan M.A. Hassan<sup>b</sup>, Dennis Dietrich<sup>a</sup>, Mohamed A. Betiha<sup>c</sup>, Stephan Schmidt<sup>d</sup>, Christoph Janiak<sup>a,\*\*</sup>

<sup>a</sup> Anorganische Chemie und Strukturchemie Institut, Heinrich-Heine Universität Düsseldorf, 40204 Düsseldorf, Germany

<sup>b</sup> Faculty of Science, Suez University, Suez, Egypt

<sup>c</sup> Egyptian Petroleum Research Institute, Nasr City, Cairo 11727, Egypt

<sup>d</sup> Department of Colloidal Adhesion, Organic and Macromolecular Chemistry Institute, Heinrich-Heine Universität Düsseldorf, 40225 Düsseldorf, Germany

## ARTICLE INFO

### Article history:

Received 28 May 2018

Received in revised form 22 June 2018

Accepted 25 June 2018

Available online 26 June 2018

### Keywords:

Mixed matrix membranes

PIL-grafted biopolymer

Nanocomposite

Antibiofouling

Water flux

## ABSTRACT

We report a simple and effective protocol for preparation of a poly-ionic liquid (PIL)-grafted chitosan Schiff base (PILCSB) and titanium oxide nanoparticles (TNPs) for application as an antibiofouling nanocomposite in the fabrication of new polysulfone (PSU) ultrafiltration mixed matrix membranes (MMMs). The effect new additive (PILCSB@TNPs) on the porosity texture, pure water flux (PWF) and antibiofouling profile for modified MMMs was investigated. Interestingly, the surface hydrophilicity of these MMMs was remarkably enhanced in comparison to the neat PSU membrane (M0) as revealed from wettability and water contact-angle results (wettability/water contact angle = 29.18%/93.48° and 83.46%/57.35° for M0 and MMM6, respectively).

© 2018 Elsevier B.V. All rights reserved.

## 1. Introduction

During last few decades, the worldwide population has quadrupled while global water demands grown seven-fold [1]. Where by the end of 2030, 3.9 billion people will suffer strongly from water scarcity as predicted by the World Water Council [2]. Therefore, water scarcity along with poor water quality is a dormant crisis about to explode worldwide. One of the most promising efforts to stem the global water crisis is the domestic and industrial wastewater reclamation. Membrane technologies are favored over many other technologies for purification of water due to their unmatched features such as mild operating conditions, no chemical additives or thermal inputs requirements, efficient, selective, reliable separations and eco-friendliness [3].

Outstanding physicochemical features of polysulfone (PSU) including excellent thermal, chemical, oxidative and hydrolytic stability with preserving its constancy toward pH-fluctuation [4, 5], superior mechanical properties such as toughness, strength, rigidity and flexibility along with good film forming characteristic [5, 6] put it in the forefront of

attention of many researchers for manufacturing of diverse membranes [5, 7]. However, the wide-ranging applications of PSU in water treatment are often limited by its inherent hydrophobicity and non-wetting characteristics that facilitate the hydrophobic interaction, deposition and adsorption between the surface of PSU membranes and microorganisms or lipophilic foulants in the feed solution which in turn leads to serious membrane biofouling [8, 9] resulting in poor permeation and diminishing of permeate flux, increasing maintenance costs, alteration of membrane selectivity and durability. Therefore, there is growing demand for fabrication of antifouling UF membranes through an enhancement of the hydrophilicity of PSU surface *via* physical or chemical refinements. So far, surface grafting, surface coating and blending are the most common techniques employed for enhancing membrane surface hydrophilicity and antifouling efficacy, accordingly [10, 11]. Recently, surface modification by blending of the host membrane matrix with hydrophilic or amphiphilic macromolecular additives revealed it as a simple and an effective method for fabrication of hydrophilic antibiofouling membranes [12]. For instance, Poly-(ethylene glycol)-based and polyzwitterionic architectures of significant hydration capacity are effectively used as hydrophilicity fine-tuning additives [13].

Among natural biopolymers, chitosan (CS), a copolymer of glucosamine (GlcNH<sub>2</sub>) and *N*-acetylglucosamine (GlcNHAc) blocks, can offer a key starting material for fabrication of ideal promising eco-friendly

\* Corresponding author at: Faculty of Science, Suez University, Suez, Egypt.

\*\* Corresponding author.

E-mail addresses: [reda.elshaarawy@suezuniv.edu.eg](mailto:reda.elshaarawy@suezuniv.edu.eg), [reel-001@hhu.de](mailto:reel-001@hhu.de), (R.F.M. Elshaarawy), [janiak@hhu.de](mailto:janiak@hhu.de) (C. Janiak).

membrane antibiofouling modulators owing to its wide-spectrum anti-algal, antimicrobial efficacies [14], amazing antibiofouling properties [15], and superior film-forming ability. Furthermore, CS offers a green protocol to combat biofouling as it is produced by mining of marine wastes (e.g., shrimp- and crab-shells) [16]. However, application of neat CS for the blended membrane technology is restricted due to its limited solubility and lower thermo-mechanical stability [17]. Thus, surface-functionalization of CS was addressed to overcome the aforementioned challenges and construct surface-functionalized CS which may act as a key contributor for improving the hydrophilicity and antibiofouling behaviors of UF membranes [18, 19].

Notable, polymeric ionic liquids (PILs) have been used to fabricate diverse “smart” materials [20, 21] for various applications in gas separation, membranes technologies, electrochemical energy devices, antimicrobials, catalysis, stimuli-responsive materials, carbon materials, sensors [22] and wettability-switchable materials [23]. Recent works revealed that surface functionalization of membrane with PIL brushes can offer undeniable engineering and economic advantages over the native membrane including tunable charge, wettability and antifouling properties. For instance, Ye et al [24] and others [25, 26] reported that PIL brushes could be reversibly switched the surface wettability from hydrophilicity to hydrophobicity and synergistically enhanced the antimicrobial and antifouling properties of the surface as compared with traditionally polymer terminals. Moreover, the antimicrobial and antibiofouling efficacies of PIL brushes could be fine-tuned by exchanging their counter anions. Interestingly, the hexafluorophosphate-based poly(ionic liquid) coated Titania nanoparticles (TNPs) exhibited excellent antibacterial activity in comparison with pristine TiO<sub>2</sub> NPs. Moreover, TNPs-based membranes displayed superior antibacterial, photocatalytic effects [27] and enhanced antifouling performance [28].

Inspired by previous outstanding facts and in our endeavor toward the designing and fabrication of novel architectures for bioapplications [14a, 15a, 29] we aimed in this work to design a simple efficient protocol for preparing an eco-friendly anti-biofoulant (based on a poly-ionic liquids-grafted chitosan Schiff base, PILCSB) and TNPs as synergistic (anti-microbial and anti-biofouling) modulator for a PSU membrane (Fig. 1) which may significantly improve the anti-biofouling and filtration performance of new MMMs.

## 2. Materials and methods

Instrumentation, sources of materials, extraction of CS from shrimp shells and preparation details of TNPs and 4-methoxypyridinium ethoxysalicylaldehyde ionic liquid ((EtO)Sal-MeOPy<sup>+</sup>X<sup>-</sup>, 3a,b) are available in the electronic supplementary information (ESI†).

### 2.1. Synthesis of 5-(4-methoxypyridinium hexafluorophosphate)-ethoxysalicylidene chitosan (PILCSB)

CS (1 g) was dissolved in 100 mL of a mixture of ethanol and 1% aqueous acetic acid (1:1 v/v) by stirring at 50 °C for 30 min. (EtO)Sal-MeOPy<sup>+</sup>PF<sub>6</sub><sup>-</sup>, **3b** (equivalent to the NH<sub>2</sub>-content in CS) was dissolved in a hot ethanol (30 mL) and then the obtained solution was added portionwise to a stirring homogeneous solution of CS over a time of 30 min at the same temperature. Then, the reaction temperature was raised to 80 °C and the reaction mixture was further stirred at this temperature for 24 h. The desired product was isolated from the reaction media by adding an excessive amount of ethyl acetate (AcOEt) coupled with ultrasonication at r.t. for 5 h. The obtained product (**PILCSB**) was filtered and then washed with EtOH:AcOEt mixtures (30:70, 20:80, and 0:100 v/v) (3 × 10 mL). Finally, **PILCSB** was dried under vacuum at 40 °C for 24 h to obtain the desired PILCSB: It is obtained as a yellowish-orange powder, Yield (2.13 g, 97.9%). FTIR (KBr, cm<sup>-1</sup>): 3445 (vs, br), 3211 (m, br), 1658 (s, sh), 1636 (vs, sh), 1532 (m, sh), 1379 (m, sh), 1284 (m, sh), 1158 (s, sh), 1065 (m, sh), 896 (m, sh), 836 (s, sh) 767, 656 (m, sh). <sup>1</sup>H NMR (600 MHz, 1% CD<sub>3</sub>COOD/D<sub>2</sub>O)<sub>60</sub> °C δ (ppm): 11.23 (s, 1H), 10.89 (s, 1H), 8.92 (d, J = 7.1 Hz, 2H), 8.51 (d, J = 7.3 Hz, 4H), 8.28 (d, J = 7.2 Hz, 1H), 7.99 (d, J = 8.3 Hz, 4H), 7.80–7.67 (m, 4H), 5.95 (s, 4H), 5.23 (d, J = 7.6 Hz, 1H), 4.39 (q, 4H), 4.14 (br, s, 2H), 4.01 (s, 6H), 3.91–3.79 (m, 2H), 3.65 (t, J = 7.1 Hz, 2H), 3.53 (br, s, 2H), 3.32–3.19 (m, 4H), 2.78 (t, J = 8.1 Hz, 2H), 2.45 (dd, J = 13.8, 8.4 Hz, 3H), 1.39 (t, J = 7.6 Hz, 6H). <sup>13</sup>C NMR (151 MHz, 1% CD<sub>3</sub>COOD/D<sub>2</sub>O)<sub>60</sub> °C δ (ppm): 178.35, 178.10, 176.61, 164.55, 163.28, 153.48, 152.26, 151.18, 150.03, 148.49, 148.14, 147.26, 146.31, 134.85, 134.09, 127.86, 126.91, 118.99, 118.19, 110.77, 109.88, 109.11, 89.71, 85.42, 83.36, 81.51, 80.49, 79.13, 78.22, 76.26, 75.63, 75.21, 74.37, 73.45, 72.28, 71.31, 71.10, 68.34, 65.43, 65.18, 62.06, 58.38, 56.41, 19.89 and 18.63. <sup>31</sup>P NMR (202 MHz, DMSO-d<sub>6</sub>): −159.38 to −117.33 ppm (septet, <sup>2</sup>J<sub>PF</sub> = 711.18 Hz). <sup>19</sup>F NMR (470 MHz, DMSO-d<sub>6</sub>): −67.81 to −64.78 ppm (doublet, <sup>1</sup>J<sub>PF</sub> = 711.24 Hz).

### 2.2. Preparation of neat PSU membrane (M0)

All membranes have been fabricated via modified non-solvent induced phase inversion (NSIPI) and slow evaporation methods. To prepare the casting solution, a certain amount (3.8 g) of PSU was dissolved in NMP (15.2 g, 15.66 mL) under vigorous stirring at 60 °C to obtain a homogeneous PSU solution which was further stirred at 300 rpm for 8 h. Then, the casting solution was debubbled using vacuum for 15 min. Afterwards, the bubble-free solution was then casted on either a nonwoven polyester fabric (novatex2483) and immediately

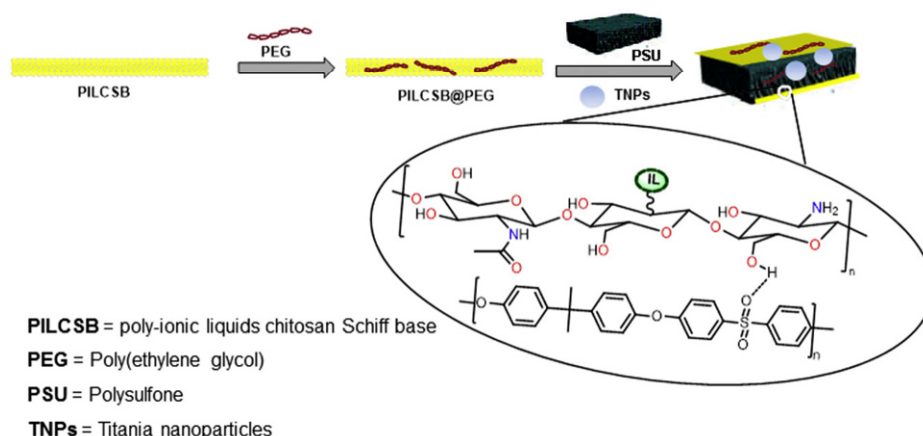


Fig. 1. Diagrammatic representation for the functionalization of the PSU surface with PILCSB, PEG and TNPs to fabricate the target MMMs, PSU@PILCSB@PEG@TNPs.

exposed to warmed water vapor for 15 min and then immersed into a milli-Q water as a non-solvent at r.t. for NSIPI, or onto 2.5 cm Petri dishes, for slow evaporation in vacuum oven at 50 °C/2 days. Noteworthy, the membranes obtained by NSIPI should be stored in a milli-Q water for 3 days for complete removal of a residual NMP.

### 2.3. Fabrication of UF MMMs (MMM1, MMM2, MMM4, MMM5)

General procedure to fabricate PSU@CS (**MMM1**) and PSU@PILCSB (**MMM4**) membranes (see Table 1 for the membrane composition) is described as follows: A 2% solution of CS is obtained by dissolving 1 g CS in 50 mL of 1% aqueous AcOH (solution of PILCSB obtained by dissolving 0.10 g in 5 mL NMP). PSU (3.8 g) was dissolved in (9.20 g, 9.50 mL) of NMP by stirring at 60 °C for 4 h to obtain a clear homogeneous solution. Then, 5.0 mL of the obtained CS or **PILCSB** solution was added dropwise to the PSU solution under vigorous stirring at 1100 rpm, maintaining the temperature at 60 °C. Thereafter, further 0.93 mL (0.90 g) of NMP was added. While CS was being added, it is re-precipitated resulting in a formation of turbid solution which was stirred vigorously, at 900 rpm, at 70 °C for 12 h to obtain clear viscous casting solution. Then, this casting solution was deaerated under vacuum to obtain bubbles-free casting solution. Afterwards, the bubble-free solution was then casted on either a nonwoven polyester fabric (novatex2483), for NSIPI, or onto 2.5 cm petri dishes, for slow evaporation, as described above. The fabricated MMMs were washed several times with distilled water and then milli-Q water before being dried at 30 °C. Similar procedures were employed for the preparation of the PSU@CS@PEG (**MMM2**) and PSU@PILCSB@PEG (**MMM5**) membranes by replacing definite amount of NMP with equivalent amount of PEG.

### 2.4. Fabrication of nanocomposite mixed matrix membranes (MMM3) and (MMM6)

Generally, 2 wt% solutions of CS (2 g/100 mL) and **PILCSB** were prepared by dissolving 0.1 g of CS and **PILCSB**, separately, in 5 mL of 1 wt% aqueous acetic acid and 5 mL of NMP, respectively. To these solutions, PEG was added with continuous stirring at 500 rpm to obtain CS@PEG and **PILCSB**@PEG. Then, two equal amounts (3.8 g) of PSU were dissolved separately in two quantities (9.20 g, 9.50 mL) of NMP by stirring at 60 °C/500 rpm for 4 h to obtain two homogenous solutions. Afterwards, previously prepared CS@PEG and **PILCSB**@PEG solutions were added separately to the PSU solutions under vigorous stirring, 1100 rpm, at 60 °C. Then, additional 0.93 mL (0.90 g) of NMP was added. The obtained turbid solution was vigorously stirred at 70 °C for 12 h to obtain clear highly viscous solutions. Thereafter, TNPs were added to these solutions under continuous stirring at 60 °C for 1 h followed by sonication for 1 h at the same temperature. Then, the casting solutions were deaerated under vacuum and casted on either a nonwoven polyester fabric (novatex2483), for NSIPI, or onto 2.5 cm petri dishes, for slow evaporation, as described above.

**Table 1**  
Composition (W %) of the prepared MMMs.<sup>†</sup>

Membrane ID	PSU	NMP	AcOH	PEG	CS	PILCSB	TNPs
M0	20.0	80.0	–	–	–	–	–
MMM1	20.0	53.2	26.3	–	0.5	–	–
MMM2	20.0	53.0	26.3	0.2	0.5	–	–
MMM3	20.0	52.9	26.3	0.2	0.5	–	0.1
MMM4	20.0	79.5	–	–	–	0.5	–
MMM5	20.0	79.3	–	0.2	–	0.5	–
MMM6	20.0	79.2	–	0.2	–	0.5	0.1

<sup>†</sup> PSU, polysulfone; MMM, mixed matrix membrane; NMP, N-methyl-2-pyrrolidone; AcOH, 1% acetic acid; CS, chitosan; PEG, polyethylene glycol; TNPs, TiO<sub>2</sub> nanoparticles.

## 2.5. Membranes structural and surface characterization

### 2.5.1. ATR-IR analysis

Attenuated Total Reflection-Fourier Transform Infrared Spectroscopy (ATR-FTIR) spectrometer (BRUKER Tensor-37) was used to examine the surface-functionalization of the new membranes in the range of 4000–400 cm<sup>-1</sup>. A diamond prism was used as the waveguide and membrane holder. The membrane samples were dried at 40 °C/overnight before analysis. The following abbreviations were used to specify the spectral bands: vs (very strong), s (strong), m (medium), w (weak), very weak (vw), sh (shoulder) and br (broad).

### 2.5.2. Morphological survey of the membranes

The cross-sectional and surface morphologies of the neat membrane and modified membranes were compared on the basis of scanning electron microscopy (SEM) micrographs. These SEM samples were prepared by breaking the membranes under liquid N<sub>2</sub> to produce a generally consistent and clean cut. Then, the membranes were spin-coated with thin film of gold. Thereafter, the membrane samples were mounted on brass plates. Cross-sectional micrographs for our membranes were picked-up by an ESEM Quanta 400 FEG SEM equipped with a secondary electron detector (SED) and operated at 20 keV.

### 2.5.3. Hydrophilicity, water swelling (uptake) and contact angles of the membrane surface

Hydrophilicity of our new membranes was estimated by measuring the water contact angle (CA) using a steady contact angle measuring equipment (HHU, Düsseldorf, Germany). A schematic diagram of the measurement of CA of our membranes is depicted in Fig. S1. Multiple CA values have been measured and the average value was calculated with standard deviation.

The pH dependent swelling or water uptake features of the MMMs were examined following the procedure reported earlier in the previous work [30]. Briefly, a pre-weighed and ultra-dry membrane sample of weight  $W_d$  and 1 cm<sup>2</sup> area was immersed in phosphate buffer solutions with different pH values of 3, 5, 7, 9 and 11 for 24 h. Afterwards, the wet membrane was removed from the solution and the excess water on the outer surface of membrane was discarded using a blotting paper. Thereafter, the MMM sample was re-weighed as ( $W_w$ ) and the percentage of swelling or water uptake was calculated using Eq. (1):

$$\% \text{Swelling (water uptake)} = \left( \frac{W_w - W_d}{W_d} \right) \times 100 \quad (1)$$

### 2.5.4. Membranes porosity

A QUANTACHROME POREMASTER 60-GT was used for pore analysis by means of mercury porosimetry. The basis of this method is the so-called Washburn equation, which used for a non-wettable liquid (mercury) represents the dependence of the pressure (to be filled) or empty (extrusion) pore diameter of the applied pressure. With the POREMASTER 60-GT, filling of the measuring cells before the actual measurement is done in a horizontal position: This prevents a static pressure of the heavy mercury (density approx. 13.5 g/cm<sup>3</sup>) on the sample and an undetected filling of large pores. Two strips of approximately 8 × 30 mm were used for the measurement per sample. The samples were not previously dried but measured in the initial state. The results of the measurements are shown as an intruded volume versus pressure or versus pore diameter.

## 2.6. Membrane performance characterization

### 2.6.1. Pure water permeation ultrafiltration experiments

The PWF of the MMM with an effective area of 5 cm<sup>2</sup> was carried out using a cross-flow ultrafiltration laboratory apparatus (Fig. 2). The

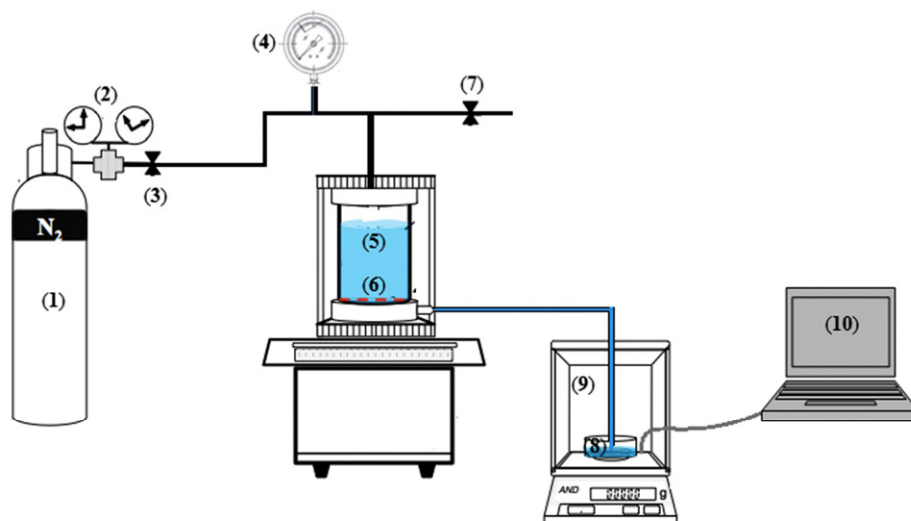


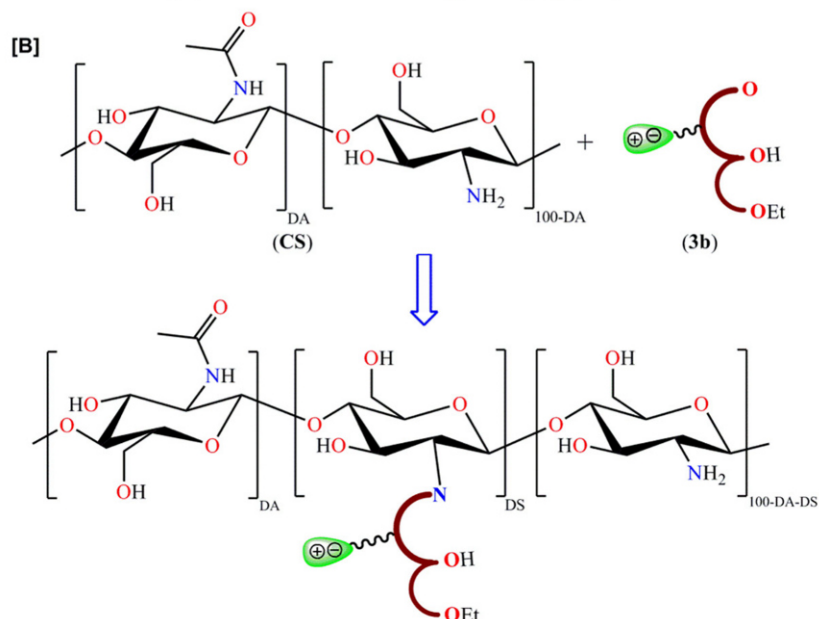
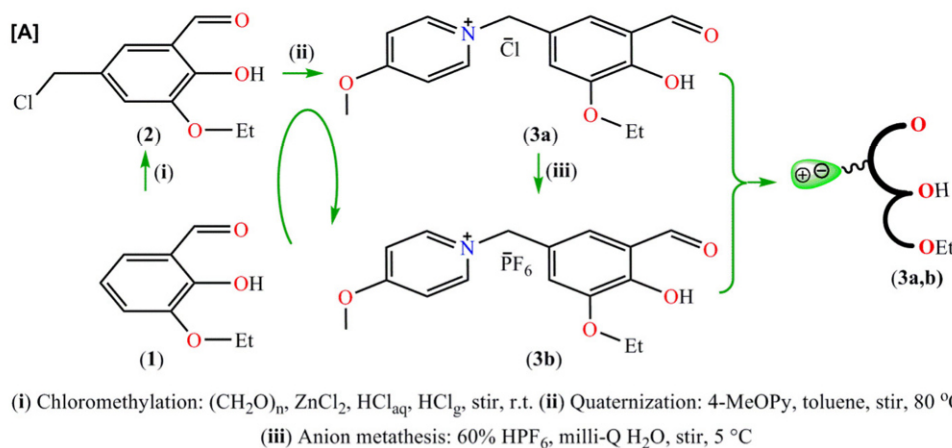
**Fig. 2.** Schematic diagram of the permeation experimental apparatus: (1)  $N_2$  gas; (2,4) pressure gauges; (3,7) valves; (5) feed tank; (6) membrane; (8) permeate reservoir; (9) electronic balance; (10) computer.

membrane was soaked in milli-Q water for 24 h before running the water permeation experiment.

Afterwards, membrane was compacted at a trans-membrane-pressure (TMP) of 0.10 MPa for 30 min. Then, the time dependent PWF was measured at 0.3 MPa. The permeate samples were collected after 15 min of exposure of a membrane to the target TMP at 26 °C

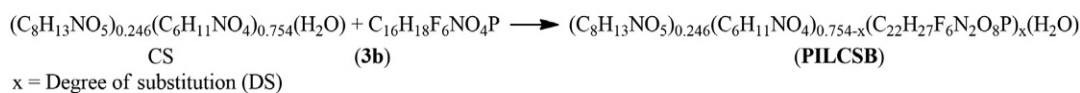
and the amount of water permeate was weighted every 10 min. Then the PWF ( $J_w$ ) was calculated using Eq. (2):

$$J_w = \left( \frac{Q}{A\Delta t} \right) \quad (2)$$



**Scheme 1.** Schematic diagram for different chemical strategies used in the synthesis of poly-methoxyppyridinium ethoxysalicylidene brushes-based CS (PILCSB).





**Scheme 2.** Schematic conversion of CS into the corresponding Schiff base (**PILCSB**), antifoulant.

where Q = volume of pure water collected during time  $\Delta t$  (h) using a MMM of area A ( $\text{m}^2$ ) and Jw is expressed in  $\text{L}/\text{m}^2\text{h}$ .

### 2.6.2. Antifouling assessment

Bovine serum albumin (BSA) has been chosen as a model fouling-induced protein to examine the antifouling efficacy of new modified MMMs [31].

**2.6.2.1. BSA ultrafiltration experiments.** The membrane fouling propensity was evaluated during the ultrafiltration of BSA aqueous solution. Initially, all MMMs were compacted at 0.1 MPa for 30 min. Then, the TMP was raised to 0.3 MPa. After 90 min of a water flow, the steady state water flux was calculated and assigned as  $J_{w1}$  ( $\text{L}/\text{m}^2\text{h}$ ). Afterwards, the pure water was replaced by a BSA aqueous solution (0.8 g/L). BSA flux at the end of the next 90 min was calculated and assigned as  $J_{BSA}$  ( $\text{L}/\text{m}^2\text{h}$ ). BSA rejection ( $R\%$ ) was estimated by UV–Vis spectroscopy at a wavelength of 280 nm and calculated using Eq. (3):

$$R\% = \left( 1 - \frac{C_{BSA}^{\text{Permeate}}}{C_{BSA}^{\text{Feed}}} \right) \times 100 \quad (3)$$

Here,  $C_{BSA}^{\text{Permeate}}$  (mg/mL) and  $C_{BSA}^{\text{Feed}}$  (mg/mL) represent the concentration of BSA solution in permeate and feed, respectively. After BSA UF experiment, the MMM was flushed with milli-Q water for 15 min before measuring the steady state PWF again a 90 min and assigned as  $J_{w2}$  ( $\text{L}/\text{m}^2\text{h}$ ). Finally, the membrane antifouling efficacy was calculated as a flux recovery ratio (FRR) using Eq. (4):

$$FRR\% = \left( \frac{J_{w2}}{J_{w1}} \right) \times 100 \quad (4)$$

Eventually, the antifouling capacities of these MMMs can be predicted from several ratios including FRR (%) and total fouling Rt ( $R_t = 1 - J_{BSA}/J_{w1}$ ), reversible fouling  $F_r$  ( $F_r = (J_{w2} - J_{BSA})/J_{w1}$ ) and irreversible fouling  $F_{ir}$  ( $F_{ir} = (J_{w1} - J_{w2})/J_{w1}$ ) [32].

## 3. Results and discussion

### 3.1. Chemistry

Multiple chemical strategies (chloromethylation, quaternization, anion metathesis and Schiff-base condensation, as well) (Scheme 1) were utilized for the surface modification of a natural biopolymer chitosan (CS). We have prepared a new hydrophilic antifouling agent, poly-methoxyppyridinium ethoxysalicylidene grafted-CS (**PILCSB**), from methoxyppyridinium-ethoxysalicylaldehyde hexafluorophosphate (**3b**), which was in turn obtained from 3-ethoxysalicylaldehyde (**1**) according

to Scheme 1. Chloromethylation of **1** was carried out with hydrochloric acid and polyoxymethylene (POM) as a formaldehyde precursor in a catalytic zinc chloride environment under aqueous biphasic conditions. The obtained chloromethylaldehyde (**2**) was then effectively aminated with 4-methoxyppyridine (4-MeOPy) to yield methoxyppyridinium-based salicylaldehyde chloride (**3a**). Subsequent chloride-hexafluorophosphate anion metathesis of **3a** using hexafluorophosphoric acid yielded the corresponding hexafluorophosphate salt (**3b**).

Eventually, the desired poly-methoxyppyridinium ethoxysalicylidene brushes-based CS (**PILCSB**), was obtained by a simple efficient Schiff base condensation of ionic salicylaldehyde hexafluorophosphate (**3b**) with the natural biopolymer, CS. This new antifoulant was isolated in excellent overall yield of 97.9%, structurally characterized based upon elemental analysis, ATR-FTIR, NMR ( $^1\text{H}$ ,  $^{13}\text{C}$ ,  $^{19}\text{F}$ ,  $^{31}\text{P}$ ) and morphologically examined by SEM micrographs.

### 3.2. Structural characterizations of CS and PILCSB

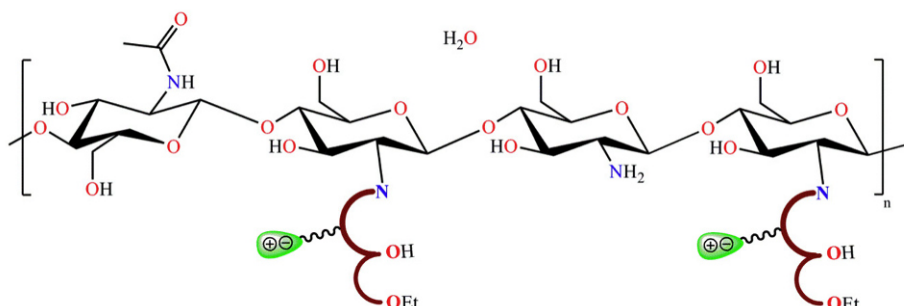
#### 3.2.1. Structural characterizations of CS

Based on the elemental and spectral data for CS, the degree of deacetylation (DDA) was found to be ~75.4% (see ESI†). Thus the plausible building unit of CS is a copolymer from GlcNHAc and GlcNH<sub>2</sub> kept at ca. 1:3 M ratio, i.e.  $(\text{GlcNHAc})_{0.246}(\text{GlcNH}_2)_{0.754}$  or  $(\text{C}_8\text{H}_{13}\text{NO}_5)_{0.246}(\text{C}_6\text{H}_{11}\text{NO}_4)_{0.754} \cdot \text{H}_2\text{O}$ .

#### 3.2.2. Structural characterizations of PILCSB

**3.2.2.1. Microanalytical data and degree of substitution DS (Iminization) for PILCSB.** During the synthesis protocol of PILCSB, the experimental conditions were optimized for achieving almost complete conversion of CS into the corresponding PILCSB. Thus, the experimental yield of **PILCSB** may be plausibly used for calculation of its degree of substitution (DS) (iminization) according to the reaction depicted in Scheme 2;

Here, Schiff base condensation of (1.00 g) CS with **3b** yielded 2.13 g of **PILCSB** which means a 113% massive increase in the weight of CS and the MW of the building block of **PILCSB**, accordingly. Thus, the MW of the resulting **PILCSB** is higher than that of CS ( $\text{MW}_{CS} = 189.51 \text{ g/mol}$ ) by 113%, i.e.  $\text{MW}_{4b} = 403.84 \text{ g/mol}$  which represents the MW of the monomeric building block suggested for **PILCSB** in Scheme 2,  $(\text{C}_8\text{H}_{13}\text{NO}_5)_{0.246}(\text{C}_6\text{H}_{11}\text{NO}_4)_{0.754-x}(\text{C}_{22}\text{H}_{27}\text{F}_6\text{N}_2\text{O}_8\text{P})_x(\text{H}_2\text{O})$ . Solving this formula gives the value of DS as 49.7% which is in good agreement with the results obtained from CHN analysis for **PILCSB**. Anal. Calcd for  $(\text{C}_8\text{H}_{13}\text{NO}_5)_{0.246}(\text{C}_6\text{H}_{11}\text{NO}_4)_{0.257}(\text{C}_{22}\text{H}_{27}\text{F}_6\text{N}_2\text{O}_8\text{P})_{0.497}(\text{H}_2\text{O})$  ( $\text{MW} = 403.85 \text{ g/mol}$ ): C, 42.85; H, 5.42; N, 5.03. Found for **PILCSB** (DS = 49.7%) C, 42.85; H, 5.42; N, 5.03. So, on the basis of elemental analyses, the suggested structure for the desired antifoulant, poly-methoxyppyridinium



**Scheme 3.** Suggested structural formula for **PILCSB**.

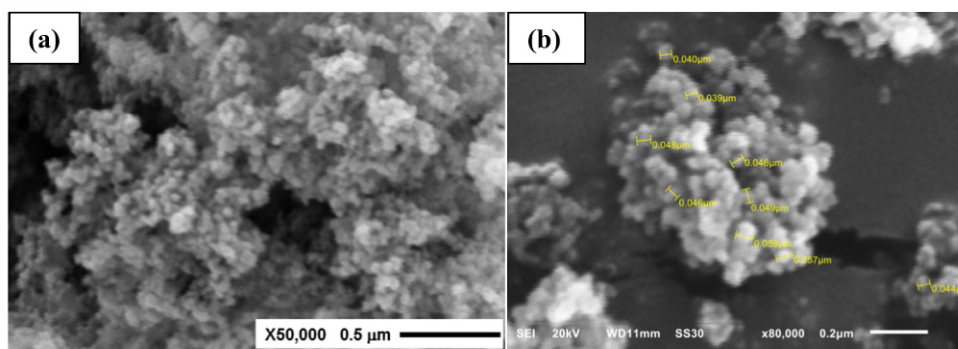


Fig. 3. SEM micrograph of TNPs; (a) general view, (b) an approximate grain-size range (in  $\mu\text{m}$ ) of TNPs.

ethoxy-salicylidene brushes-based CS (**PILCSB**), is depicted in Scheme 3.

**3.2.2.2. FTIR.** Changes in the ATR-FTIR signatures of **PILCSB** in comparison to the parent CS (Fig. S2, ESI) demonstrate the successful covalent grafting of the hydrophilic poly-methoxypyridinium ethoxysalicylidene brushes on the surface of CS fibers. Where, the absorption at  $ca. 3438\text{ cm}^{-1}$  along with two maxima at  $1644\text{ cm}^{-1}$ , characteristic for superimposed C=O (amide I) and azomethine (H—C=N) stretching vibrations, and  $1277\text{ cm}^{-1}$ , characteristic for aryl—O vibration, can be attributed to the overlapping of phenolic O—H and amide N—H stretching modes. Pertinacity of  $\nu_{\text{NH}_2}$  peak to participate in the spectrum of **PILCSB**, however, with a very feeble extent compared to that of CS, confirms the predominance poly-methoxypyridinium ethoxysalicylidene brushes on the CS surface, *via* partial Schiff base condensation, with minor contribution of neat glucosamine (GlcNH<sub>2</sub>) units. Three predominant peaks (C=N stretching:  $1526\text{ cm}^{-1}$ ; PF<sub>6</sub><sup>−</sup> stretching:  $840\text{ cm}^{-1}$  and bending:  $740\text{ cm}^{-1}$ ) are assignable to the methoxypyridinium terminals.

**3.2.2.3. NMR spectroscopy.** Consistent with a successful surface modification of CS with poly-methoxypyridinium ethoxysalicylidene brushes is the appearance of novel signals in the <sup>1</sup>H NMR spectrum of **PILCSB** compared to the one of CS such as the highly deshielded peaks at  $\delta = 12.28$  and  $8.91\text{ ppm}$  arising from phenolic OH involved in an intramolecularly H-bonded environment [33] and aldimine protons, respectively. A set of multiplets in the range of  $8.36\text{--}7.24\text{ ppm}$  is due to the resonance of aromatic protons. The <sup>13</sup>C NMR spectrum for **PILCSB** offers further evidence for the successful chemical anchoring of poly-methoxypyridinium ethoxy-salicylidene compartments to the chitosan

skeleton as revealed from the observation of two low-field resonance signals at 166 and 158 ppm attributed to phenolic and azomethinic carbons, respectively. The hexafluorophosphate ion was authenticated by a septet signal centered at *ca.*  $-138\text{ ppm}$  with  $^2J_{\text{PF}} = 711.18\text{ Hz}$  coupled with a doublet signal centered at *ca.*  $-65.5\text{ ppm}$  with  $^1J_{\text{PF}} = 711.24\text{ Hz}$  in their <sup>31</sup>P/<sup>19</sup>F NMR spectra which are characteristic for PF<sub>6</sub><sup>−</sup> counter anions.

### 3.2.3. Morphological and topographical characterizations of **PILCSB**

The morphology of the texture for the **PILCSB** was investigated from SEM micrographs (see Fig. S3, ESI), which revealed a significant difference between the surface morphology of **PILCSB** and CS. Where CS exhibits a flat surface with a smooth and dense texture while **PILCSB** has a rough sponge-like texture. This could be attributed to the expected interactions between CS matrix and **PILCSB** through H-bonding and imine linkages leading to the formation of many hydrophilic sites at the surface with cross-sectional pores and micro voids network.

### 3.3. Morphological and textural properties of TNPs

The morphology of TNPs prepared starting from TiCl<sub>4</sub> by a solution-based method was probed using SEM analysis (Fig. 3, Fig. S4). SEM image revealed that most of the TNPs were spherical with a regular diameter ranging from 39 nm to 57 nm.

The phase purity of TNPs was estimated from the XRD diffractogram (Fig. 4a). All observed major peaks are well recorded to the TNPs in an anatase phase as indicated by the standard (JCPDS card No. 21-1272).

The specific surface areas and pore size distributions of the as-synthesized TNPs were established using nitrogen adsorption-desorption isotherm (Fig. 4b) which reflect a type IV isotherm with

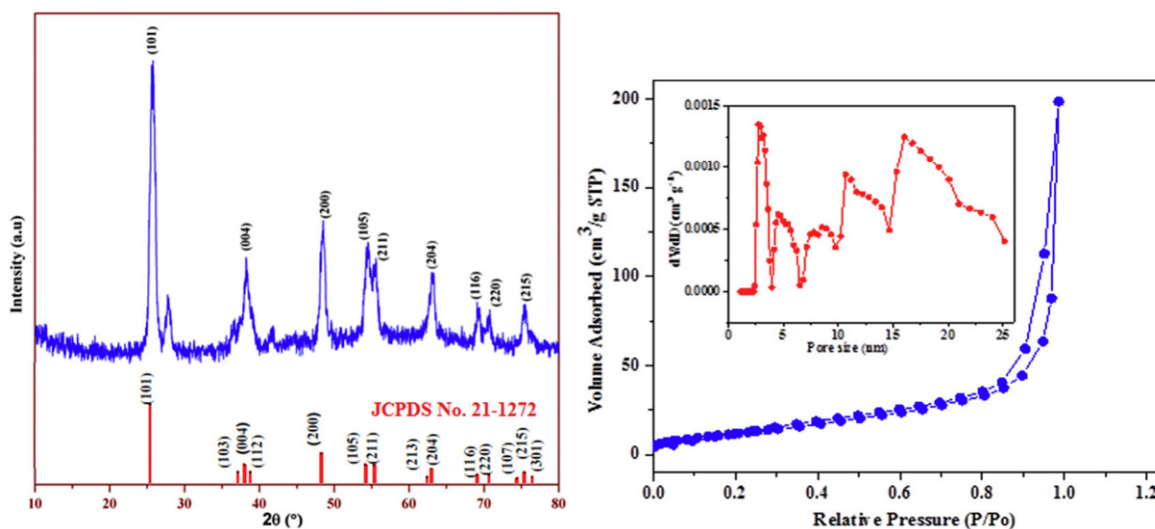


Fig. 4. (a) X-ray diffraction patterns (Cu-K $\alpha$  radiation) of TNPs. (b) N<sub>2</sub> adsorption-desorption isotherms along with the corresponding pore size distributions (inset) of the TNPs at 77 K.

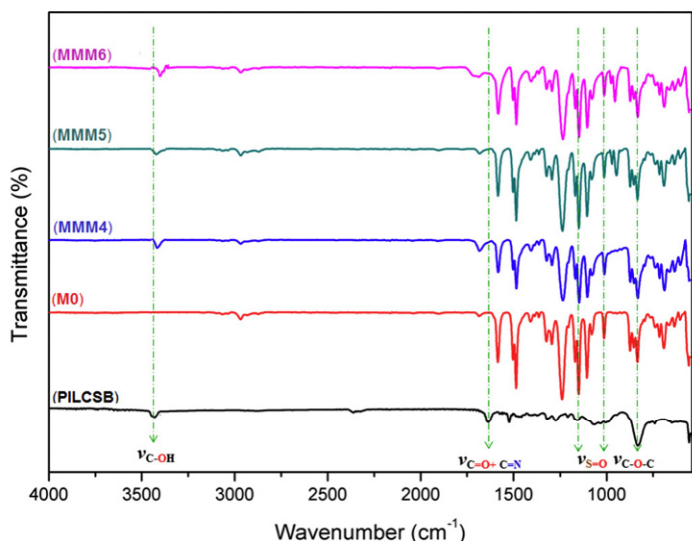


Fig. 5. ATR-FTIR patterns for comparison of the FTIR signatures of MMMs with parents **PILCSB** and PSU.

H2 hysteresis loop according to Brunauer–Deming–Deming–Teller (BDDT) classification [34]. This hysteresis loop implies that the TNPs have mesoporous structure, with specific surface area of  $94 \text{ m}^2 \text{ g}^{-1}$  and the pore size distribution curve (inset in Fig. 4b) shows a wide range of pore size from 3.3 to 25 nm with a maximum population of  $\sim 3.3 \text{ nm}$ .

### 3.4. Membranes characterization

#### 3.4.1. ATR-FTIR

ATR-FTIR spectroscopy can provide information about the surface and near-surface composition of the membranes. Where the presence of CS or new antifoulant (**PILCSB**) onto the outer surface of PSU was evident by ATR-FTIR spectroscopy. In comparison to the FTIR spectra of pure PSU and **PILCSB**, PSU@**PILCSB**@(PEG)@(TNPs) (MMM4, MMM5, MMM6) membranes exhibit collective infrared spectral signatures of their woven components, confirming successful fabrication of MMMs.

The ATR-FTIR spectra of the new membranes (Fig. 5) revealed common features represented by the characteristic peaks around  $3420 \text{ cm}^{-1}$  corresponding to the amide N–H and alcoholic/phenolic OH stretches of **PILCSB**. The amide N–H peaks is in line with the characteristic for amide C=O peak around  $1670 \text{ cm}^{-1}$ . The OH peak is in line with the Ar–O vibration mode around  $1275 \text{ cm}^{-1}$ . The vibration peaks characteristic for PSU are seen around  $1294$  and  $1150 \text{ cm}^{-1}$ , assignable to asymmetric and symmetric stretching vibrations, respectively, of the O=S=O group, along with a peak observed around  $1240 \text{ cm}^{-1}$  attributable for the C–O–C vibration.

#### 3.4.2. Morphology of the membranes

The overall thicknesses of the newly fabricated MMMs were in the range of  $80$ – $110 \mu\text{m}$ . The surface and cross-section morphologies of these new MMMs were inspected by SEM. The cross-sectional SEM micrographs (Fig. 6) revealed that all membranes exhibited asymmetric porous structure of a dense skin layer and a highly porous sub-layer containing sponge-like structure (for CS-based MMMs) or macrovoid-type structure (in case of **PILCSB**-based MMMs). These changes in membrane morphologies could be ascribed to the replacement of CS with a poly-methoxyppyridinium ethoxysalicylidene brush-based CS, a violent hydrophilic antifouling additive, which enhances the hydrophilicity and subsequently the affinity of the PSU@**PILCSB**@PEG@(TNPs) (MMM6) casting composite which already dissolved in NMP to the non-solvent (water) coagulation bath compared to PSU@CS@PEG@(TNPs) (MMM3) which reduce the mutual diffusivity between casting solvent (NMP) and non-solvent (water). This prolonged mutual diffusion allowed longer phase inversion time along with lower segregation rate of **PILCSB** from the bulk casting solution up to the NMP-water interface and self-induced pore growth, as well. Moreover, the hydrophilic nature of the TNPs facilitated the mass transfer between the NMP and the water during phase inversion resulting in the development of longer macrovoids and subsequently the enhancement of overall membrane porosity [35].

The successful formulation of TNPs into the membrane matrix was proved by EDX results (mapping and spectra) as depicted in Fig. S6 (ESI†). All new MMMs are typical UF membranes with micrometer-scale pores upon the surface layer and micron-sized macrovoids embedded across the membrane network.

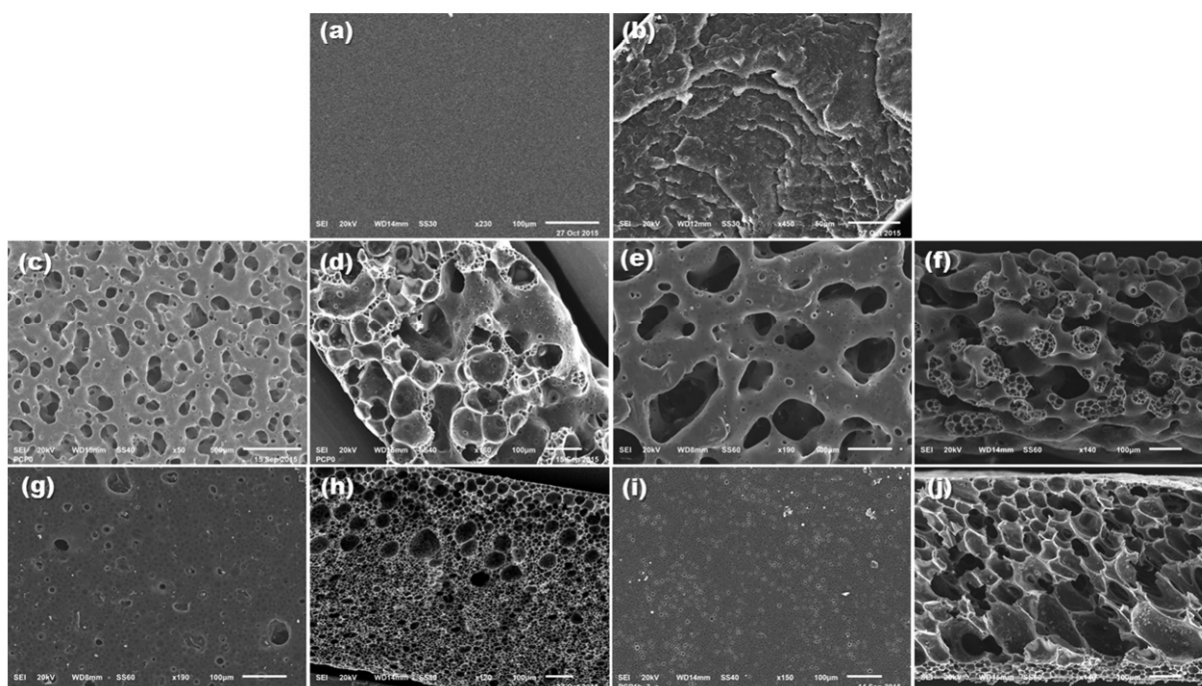


Fig. 6. Surface and cross-sectional SEM micrographs of: (a, b) MO, (c, d) MMM2, (e, f) MMM3, (g, h) MMM4, (i, j) MMM6.

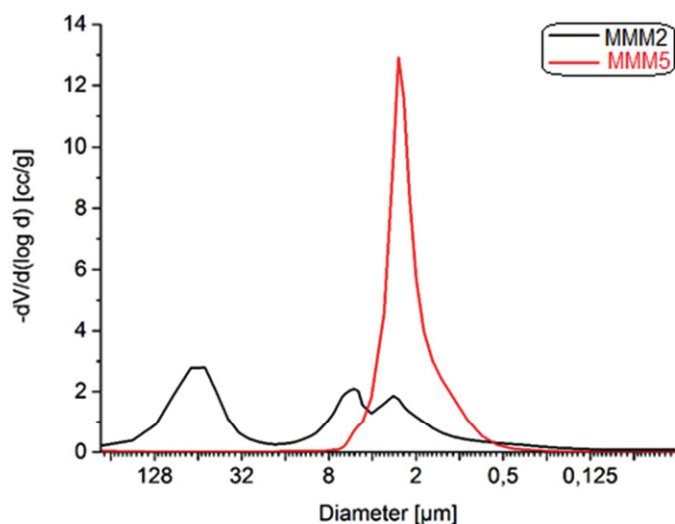


Fig. 7. Pore size distribution (PSD) curve which is calculated from the normalized volume curve by differentiation for MMM2 and MMM5 (representative examples of MMMs).

### 3.4.3. Porosity

The pore size distribution (PSD) plot for MMM2 and MMM5, as representative examples of MMMs is depicted in Fig. 7. As shown in this figure, MMM2 possess “channels and pores” where the surface shows many channel windows 10–100  $\mu\text{m}$ . Inside of the walls between channels, there are spherical pores with a hierarchical size distribution ranging from internal smaller pores with  $\sim 10 \mu\text{m}$  diameter to external larger pores of  $\sim 100 \mu\text{m}$  diameter. The MMM5 texture exhibited asymmetric pore distribution with large pores of 50–100  $\mu\text{m}$  in the center and small pores of 10–20  $\mu\text{m}$  to the outside of the membrane. Moreover, the surfaces of MMM2 and MMM5 show some pore windows 5–10  $\mu\text{m}$ , while, the untreated membrane (M0) shows slightly rough cross-section but no pores as revealed from its SEM micrograph (cf. Fig. 6).

## 3.5. Membranes performance

### 3.5.1. Water uptake (membrane swelling) and contact angle measurement

Water uptake, swelling ratio and contact angle values of new MMM surfaces were assessed to evaluate their hydrophilicity/hydrophobicity features. As revealed from Fig. 8a, the water uptake and swelling ratio values of **PILCSB**-blended MMMs were higher than those of the neat PSU membrane and CS-based PSU membranes because of the existence of poly-methoxypyridinium ethoxysalicylidene brushes on the active layer of membrane, as revealed from EDX (cf. Fig. S5, ESI<sup>†</sup>), which offer multiple active H-bonding sites for interaction with water. Noteworthy, water uptake performance was changed in a pH-dependence

Table 2

PWF ( $J_{w1}$ ) and BSA rejections of the membranes<sup>a</sup>.

Membrane ID	Composition	PWF (L/m <sup>2</sup> h)	BSA rejection (%)
M0	pure PSU	69	90
MMM1	PSU@CS	76	68
MMM2	PSU@CS@PEG	95	53
MMM3	PSU@CS@PEG@TNPs	99	52
MMM4	PSU@ <b>PILCSB</b>	129	43
MMM5	PSU@ <b>PILCSB</b> @PEG	144	37
MMM6	PSU@ <b>PILCSB</b> @PEG@TNPs	158	36

<sup>a</sup> PWF = pure water flux; BSA = Bovine serum albumin.

profile with maximum uptake under acidic conditions (pH = 4) due to protonation of the GlcNH<sub>2</sub> fragments of CS. At pH = 4, a maximum water uptake of 83.46% was achieved for PSU@**PILCSB**@PEG@TNPs (MMM6). Thus, water uptake in membranes depends on the content of hydrophilic TNPs. Noteworthy, the addition of TNPs didn't significantly change the hydrophilicity of the PSU membrane as revealed from water contact angle measurements depicted in Fig. 8b, however, **PILCSB** brushes coated TNPs was greatly enhanced the MMM6 hydrophilicity.

As shown in Fig. 8b, all woven membranes had water contact angles lower than 90°, indicating that the highly hydrophobic properties of the parent PSU (water contact angle = 93.48°) were decreased to be somewhat more hydrophilic as a result of its surface refinement with hydrophilic architectures (i.e., CS or **PILCSB**, PEG, TNPs). The membranes MMM4–6 modified with **PILCSB**, exhibit somewhat lower water contact angles compared to those modified with CS (MMM1–3) because the multiple hydrophilic fragments in the poly-methoxypyridinium ethoxysalicylidene brushes of **PILCSB** impart higher hydrophilicity than CS. Moreover, the entrapment of TNPs on the matrix of the membrane led to an enhancement of membrane hydrophilicity as revealed from the observed water contact angle (57.35°) for MMM6.

### 3.5.2. Permeation properties

The permeation performance of the pristine PSU membrane (M0) and the MMMs were determined by pure water (PWF) and BSA filtration experiments. From the PWF and BSA rejection data for the virgin PSU membrane and the MMMs presented in Table 2, it is noticeable that the virgin membrane M0 manifested an extremely low water flux of 60 L/m<sup>2</sup> h coupled with the elevated level of BSA rejection, 89.95%, under an operation pressure of 0.3 MPa, which is in accordance with its higher hydrophobicity. The water permeability of the PSU-based composite MMMs was distinctly enhanced by integration of the hydrophilic biopolymer CS or the amphiphilic copolymer (**PILCSB**), pore stabilizing agents (PEG) and TiO<sub>2</sub>-NPs into the matrix of the membrane. Particularly, the PWF of MMM6 is 158.10 L/m<sup>2</sup> h ( $\sim 2.7$  times higher

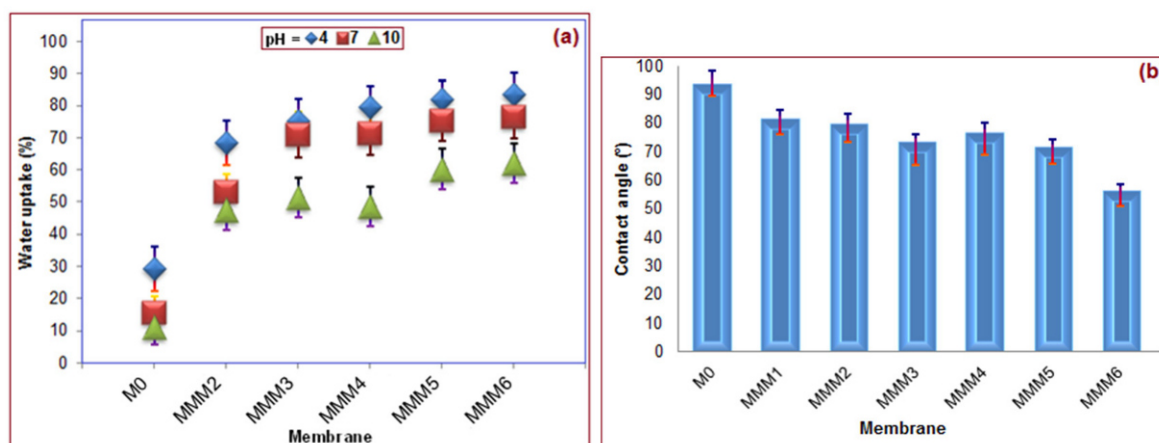
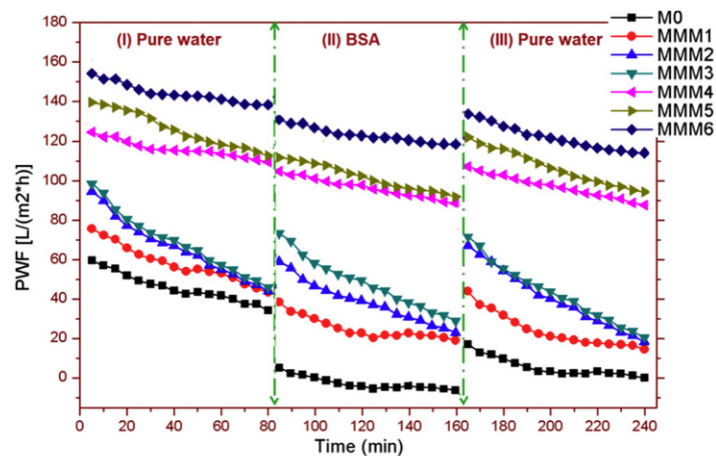


Fig. 8. (a) pH dependent water uptake of MMMs in comparison with neat PSU membrane M0. (b) Contact angle of MMMs compared to neat PSU membrane.



**Fig. 9.** Flux decline and recovery results for the as-fabricated MMMs. This permeation experiment contains three phases: (I) pure water permeation, Experimental conditions: Initially, a 5 cm<sup>2</sup> membrane was compacted at 0.10 MPa, a trans-membrane-pressure (TMP), for 30 min. Then, the time dependent pure water flux (PWF) was measured at 0.3 MPa. The permeate sample collection was started after 15 min of exposure to target TMP at 26 °C and the permeate was weighted every 10 min, and operation period of 90 min. (II) BSA solution (model foulant) filtration, and (III) pure water permeation after water flushing.

than that of the native PSU membrane), moreover, it has the maximum BSA rejection, 36%.

It is recognized that the water permeability of the membrane is governed by its physical (hydrophilicity/hydrophobicity), geometrical (porous network, pore size and roughness) and chemical (liquid-solid interactions) parameters [36]. In this context, enhancing the hydrophilicity of the surface of PSU membrane by blending it with a hydrophilic additive (CS or **PILCSB**) will reduce the membrane affinity for physisorption of organic contaminants (such BSA). A hydrophilic additive will also promote the hydrophilic pore-water interaction within the porous framework and, thus, improve the water mass transport. The BSA rejection was dramatically decreased as the hydrophilic additives (CS, **PILCSB**, PEG and TNPs) were incorporated into the PSU membrane as presented in Table 2. Specifically, MMM6 which exhibits promising performance because of it combines **PILCSB** with polar ionizable moieties that induce surface charges which promote wettability of the membrane while diminishing BSA-membrane interaction.

### 3.5.3. Antifouling properties of membranes

A consecutive water-BSA-water permeation experiment was used to assess the antifouling performance of the composite membranes (MMMs) in comparison with the virgin PSU membrane (MO). As shown in Fig. 9, the permeation flux for the MO dropped dramatically when the pure water permeation was followed with the fouling-inducing model BSA solution. This drop may be attributed to the hydrophobic surface which promotes membrane fouling via hydrophobic

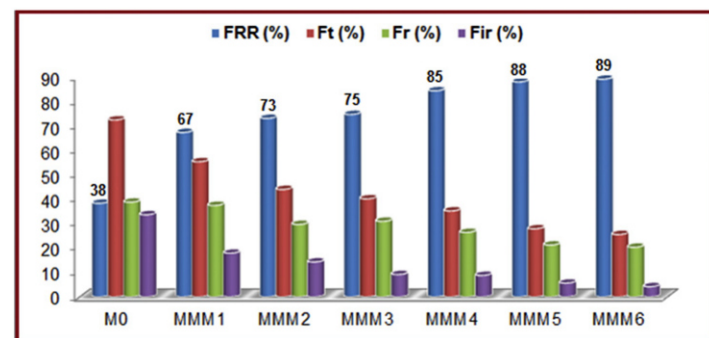


**Fig. 10.** A summary of total fouling ( $F_t$ ), reversible fouling ( $F_r$ ), irreversible fouling ( $F_{ir}$ ), and flux recovery ratio (FRR) for neat PSU (MO) and composite MMMs with CS, **PILCSB** and TNPs.

(MO-BSA) interaction. On the other hand, the MMMs exhibited lower flux decline than the neat PSU membrane MO suggesting that the composite membranes have lower fouling propensity than the pure PSU membrane. This could be assigned to an increase of the membrane surface hydrophilicity by blending with hydrophilic fillers which reduce its fouling propensity and diminish the flux declining degree, accordingly. Noteworthy, the composite membranes (MMMs) exhibited a higher relative fluxes recovery than MO after simple hydraulic cleaning as revealed from the water permeation following BSA filtration (section (III) in Fig. 9). These results suggest reversibility of the fouling for the MMMs which is in good agreement with their enhanced surface hydrophilicity.

Reversible fouling ( $F_r$ ): arises from reversible adsorption/deposition of a foulant protein (BSA) and can be easily removed by simple water flushing. Irreversible fouling ( $F_{ir}$ ) is due to the irreversible adsorption of a protein (BSA) and can only be eliminated by chemical treatment. Thereafter, quantitative assessment of the antifouling capacities of these membranes have been addressed based upon several ratios including flux recovery ratio (FRR), total fouling ( $F_t$ ), reversible and irreversible fouling ( $F_r$ ,  $F_{ir}$ ) as depicted in Fig. 10. It is clear from Fig. 10 that the FRR(%) values for the MMMs (67–89%) are much higher than those of nascent PSU (MO), confirming the lower fouling propensity of the MMMs [37]. This indicated that the MMMs could keep a higher water flux even after a BSA UF process [38]. Collected  $F_t$ ,  $F_r$  and  $F_{ir}$  values for the MMMs provide further evidence for their promotion of antifouling performance as revealed from Fig. 10, where these values are greatly reduced by blending of PSU with the antifoulants (**PILCSB** and TNPs) assignable to the increased hydrophilicity of MMMs.

Consequently, the hydrophilic fillers (**PILCSB** and TNPs) are believed to form a hydration barrier that diminished the fouling model (BSA) adsorption.

## 4. Conclusion

In our work, PSU UF-membrane was physically modified with chitosan (CS) and poly-ionic liquid-grafted chitosan Schiff base (**PILCSB**) and TNPs in presence of pore-stabilizing agent, PEG. The effect of these additives on the morphology, porosities features, water flux, protein rejections and antifouling performances of the modified membranes (MMMs) was investigated. The results revealed that incorporation of all additives into a mixed matrix membrane **MMM6** (PSU@**PILCSB**@PEG@TNPs) was significantly enhanced membrane texture and permeation performance with and improved pure water flux by 2.5 fold in comparison to the neat PSU membrane (MO). Moreover **MMM6** exhibited the highest resistance to biofouling for the UF applications.

## Acknowledgment

The authors gratefully acknowledge the financial support of the Federal German Ministry of Education and Research (BMBF) in the project Optimat under grant no. 03SF0492C

## Appendix A. Supplementary data

Supplementary data (experimental and spectral data) associated with this article are available with the article through the journal Web site. Supplementary data associated with this article can be found in the online version, at doi: <https://doi.org/10.1016/j.molliq.2018.06.100>

## References

- [1] Human Development Report, Chapter 4, United Nations Development Programme (UNDP), 2006.
- [2] Urban Urgency, Water Caucus Summary, World Water Council (WWC), Marseille, France, 2007.
- [3] M. Mulder, Basic Principles of Membrane Technology, Kluwer Academic Publishers, London, 1996.

- [4] (a) Y.H. Cho, H.W. Kim, S.Y. Nam, H.B. Park, Fouling-tolerant polysulfone–poly(ethylene oxide) random copolymer ultrafiltration membranes, *J. Membr. Sci.* 37 (2011) 296–306;
- (b) N. Nady, M.C.R. Franssen, H. Zuilhof, M.S.M. Eldin, R. Boom, K. Schroën, Modification methods for poly(arylsulfone) membranes: a mini-review focusing on surface modification, *Desalination* 275 (2011) 1–9.
- [5] K.J. Lee, J.Y. Jae, Y.S. Kang, J. Won, Y. Dai, G.P. Robertson, M.D. Guiver, Gas transport and dynamic mechanical behavior in modified polysulfones with trimethylsilyl groups: effect of degree of substitution, *J. Membr. Sci.* 223 (2003) 1–10.
- [6] Y. Liu, G. Wang Shuling Zhang, The preparation of antifouling ultrafiltration membrane by surface grafting zwitterionic polymer onto poly(arylene ether sulfone) containing hydroxyl groups membrane, *Desalination* 316 (2013) 127–136.
- [7] (a) J. Sikder, C. Pereira, S. Palchoudhury, K. Vohra, D. Basumatary, P. Pal, Synthesis and characterization of cellulose acetate–polysulfone blend microfiltration membrane for separation of microbial cells from lactic acid fermentation broth, *Desalination* 249 (2009) 802–808;
- (b) N.K. Saha, M. Balakrishnan, M. Ulbricht, Fouling control in sugarcane juice ultrafiltration with surface modified polysulfone and polyethersulfone membranes, *Desalination* 249 (2009) 1124–1131;
- (c) R. Kumar, A.M. Isloor, A.F. Ismail, S.A. Rashid, T. Matsuura, Polysulfone–Chitosan blend ultrafiltration membranes: preparation, characterization, permeation and antifouling properties, *RSC Adv.* 3 (2013) 7855–7861.
- [8] (a) Q. Shi, Y.L. Su, W. Zhao, C. Li, Y.H. Hu, Z.Y. Jiang, S.P. Zhu, Zwitterionic polyethersulfone ultrafiltration membrane with superior antifouling property, *J. Membr. Sci.* 319 (2008) 271–278;
- (b) D. Rana, T. Matsuura, Surface modifications for antifouling membranes, *Chem. Rev.* 110 (2010) 2448–2471;
- (c) J.A. Koehler, M. Ulbricht, G. Belfort, Intermolecular forces between a protein and a hydrophilic modified polysulfone film with relevance to filtration, *Langmuir* 16 (2000) 10419–10427.
- [9] (a) Q.F. Zhang, S.B. Zhang, L. Dai, X.S. Chen, Novel zwitterionic poly(arylene ether sulfone) s as antifouling membrane material, *J. Membr. Sci.* 349 (2010) 217–224;
- (b) Y.G. Dave, A.V.R. Reddy, Preparation, characterization, acid stability and organic fouling of poly(acrylonitrile-co-methacrylic acid) ultrafiltration membranes, *Desalination* 282 (2011) 9–18;
- (c) M.P. Sun, Y.L. Su, C.X. Mu, Z.Y. Jiang, Improved antifouling property of PES ultrafiltration membranes using additive of silica-PVP nanocomposite, *Ind. Eng. Chem. Res.* 49 (2010) 790–796.
- [10] (a) J. Jiang, L. Zhu, L. Zhu, H. Zhang, B. Zhu, Y. Xu, Antifouling and antimicrobial polymer membranes based on bioinspired polydopamine and strong hydrogen-bonded poly(*N*-vinyl pyrrolidone), *ACS Appl. Mater. Interfaces* 5 (2013) 12895–12904;
- (b) H. Susanto, M. Ulbricht, Characteristics, performance and stability of polyethersulfone ultrafiltration membranes prepared by phase separation method using different macromolecular additives, *J. Membr. Sci.* 327 (2009) 125–135;
- (c) H. Yu, Y. Cao, G. Kang, J. Liu, M. Li, Q. Yuan, Enhancing antifouling property of polysulfone ultrafiltration membrane by grafting zwitterionic copolymer via UV-initiated polymerization, *J. Membr. Sci.* 342 (2009) 6–13.
- [11] (a) H. Dong, Y. Xu, Z. Yi, J. Shi, Modification of polysulfone membranes via surface-initiated atom transfer radical polymerization, *Appl. Surf. Sci.* 255 (2009) 8860–8866;
- (b) D.S. Wavhal, E.R. Fisher, Hydrophilic modification of polyethersulfone membranes by low temperature plasma-induced graft polymerization, *J. Membr. Sci.* 209 (2002) 255–269.
- [12] (a) D. Liu, D. Li, D. Du, X. Zhao, A. Qin, X. Li, C. He, Antifouling PVDF membrane with hydrophilic surface of terry pile-like structure, *J. Membr. Sci.* 493 (2015) 243–251;
- (b) M.K. Sinha, M.K. Purkait, Preparation of fouling resistant PSF flat sheet UF membrane using amphiphilic polyurethane macromolecules, *Desalination* 355 (2015) 155–168;
- (c) Q. Shi, J. Meng, R. Xu, X. Du, Y. Zhang, Synthesis of hydrophilic polysulfone membranes having antifouling and boron adsorption properties via blending with an amphiphilic graft copolymer, *J. Membr. Sci.* 444 (2013) 50–59.
- [13] (a) F. Gao, G. Zhang, Q. Zhang, X. Zhan, F. Chen, Improved antifouling properties of poly(ether sulfone) membrane by incorporating the amphiphilic comb copolymer with mixed poly(ethylene glycol) and poly(dimethylsiloxane) brushes, *Ind. Eng. Chem. Res.* 54 (2015) 8789–8800;
- (b) Q. Liu, A.A. Patel, L. Liu, Superhydrophilic and underwater superoleophobic poly(sulfobetaine methacrylate)-Grafted glass fiber filters for oil–water separation, *ACS Appl. Mater. Interfaces* 6 (2014) 8996–9003;
- (c) A. Venault, M.R.B. Ballard, Y. Liu, P. Aimar, Y. Chang, Hemocompatibility of PVDF/PS-*b*-PEGMA membranes prepared by LIPS process, *J. Membr. Sci.* 477 (2015) 101–114.
- [14] (a) R.F.M. Elshaarawy, A.A. Refaee, E.A. El-Sawi, Pharmacological performance of novel poly-(ionic liquid)-grafted chitosan-*N*-salicylidene Schiff bases and their complexes, *Carbohydr. Polym.* 146 (2016) 376–387;
- (b) H.K. No, N.Y. Park, S.H. Lee, S.P. Meyers, Antibacterial activity of chitosans and chitosan oligomers with different molecular weights, *Int. J. Food Microbiol.* 74 (2002) 65–72;
- (c) J. Rhoades, S. Roller, Antimicrobial actions of degraded and native chitosan against spoilage organisms in laboratory media and foods, *Appl. Environ. Microbiol.* 66 (1) (2000) 80–86;
- (d) B.K. Choi, K.Y. Kim, Y.J. Yoo, S.J. Oh, J.H. Choi, C.Y. Kim, In vitro antimicrobial activity of a chitoooligosaccharide mixture against *Actinobacillus actinomycetemcomitans* and *Streptococcus mutans*, *Int. J. Antimicrob. Agents* 18 (6) (2001) 553–557.
- [15] (a) R.F.M. Elshaarawy, F.H.A. Mustafa, A. Herbst, A.E.M. Farag, C. Janiak, Surface functionalization of chitosan isolated from shrimp shells, using salicylaldehyde ionic liquids in exploration for novel economic and ecofriendly antibiofoulants, *RSC Adv.* 6 (2016) 20901–20915;
- (b) I.L. Roux, H.M. Krieg, C.A. Yeates, J.C. Breytenbach, *J. Membr. Sci.* 248 (2005) 127–136;
- (c) E. Bagheripour, A.R. Moghadassi, S.M. Hosseini, B. Van der Bruggen, F. Parvizian, Novel composite graphene oxide/chitosan nanoplates incorporated into PES based nanofiltration membrane: Chromium removal and antifouling enhancement, *J. Ind. Eng. Chem.* 62 (2018) 311–320.
- [16] A.M. Motawie, K.F. Mahmoud, A.A. El-Sawy, H.M. Kamal, H. Hefni, H.A. Ibrahim, Preparation of chitosan from the shrimp shells and its application for pre-concentration of uranium after cross-linking with epichlorohydrin, *Egypt. J. Pet.* 23 (2014) 221–228.
- [17] Y. Mansourpanah, H. Soltani, K. Alizadeh, M. Tabatabaei, Enhancing the performance and antifouling properties of nanoporous PES membranes using microwave-assisted grafting of chitosan, *Desalination* 322 (2013) 60–68.
- [18] (a) S. Zinadini, A.A. Zinatizadeh, M. Rahimi, V. Vatanpour, H. Zangeneh, M. Beygzadeh, Novel high flux antifouling nanofiltration membranes for dye removal containing carboxymethyl chitosan coated Fe<sub>3</sub>O<sub>4</sub> nanoparticles, *Desalination* 349 (2014) 145–154;
- (b) J. Miao, G. Chen, C. Gao, C. Lin, D. Wang, M. Sun, Preparation and characterization of *N*,*O*-carboxymethyl chitosan (NOCC)/polysulfone (PS) composite nanofiltration membranes, *J. Membr. Sci.* 280 (2006) 478–484;
- (c) J. Miao, G. Chen, C. Gao, S. Dong, Preparation and characterization of *N*,*O*-carboxymethyl chitosan/polysulfone composite nanofiltration membrane crosslinked with epichlorohydrin, *Desalination* 233 (2008) 147–156.
- [19] (a) R. Kumar, A.M. Isloor, A.F. Ismail, T. Matsuura, Synthesis and characterization of novel water soluble derivative of Chitosanas an additive for polysulfone ultrafiltration membrane, *J. Membr. Sci.* 440 (2013) 140–147;
- (b) Y. Chen, Y. Zhang, H. Zhang, J. Liu, C. Song, Biofouling control of halloysite nanotubes-decorated polyethersulfone ultrafiltration membrane modified with chitosan-silver nanoparticles, *Chem. Eng. J.* 228 (2013) 12–20;
- (c) M.K. Sinha, M.K. Purkait, Use of CS–PAA nanoparticles as an alternative to metal oxide nanoparticles and their effect on fouling mitigation of a PSF ultrafiltration membrane, *RSC Adv.* 5 (2015) 66109–66121.
- [20] B. Yu, F. Zhou, H.Y. Hu, C.W. Wang, W.M. Liu, Synthesis and properties of polymer brushes bearing ionic liquid moieties, *Electrochim. Acta* 53 (2007) 487–494.
- [21] Y. Ye, S. Sharick, Y.A. Elabd, Anion exchanged polymerized ionic liquids: high free volume single ion conductors, *Polymer* 52 (2011) 1309–1317.
- [22] W. Qian, J. Texter, F. Yan, *Chem. Soc. Rev.* 46 (2017) 1124–1159.
- [23] B.S. Lee, Y.S. Chi, J.K. Lee, Imidazolium ion terminated self-assembled monolayers on Au: effects of counter anions on surface wettability, *J. Am. Chem. Soc.* 126 (2004) 480–481.
- [24] Q. Ye, T. Gao, F. Wan, Grafting poly(ionic liquid) brushes for antibacterial and antibiofouling applications, *J. Mater. Chem.* 22 (2012) 13123–13131.
- [25] C. Du, X. Ma, C. Wu, Polymerizable ionic liquid copolymer P(MMA-co@BVIm@Br) and its effect on the surface wettability of PVDF blend membranes, *Chin. J. Polym. Sci.* 33 (2015) 857–868.
- [26] Y.-Y. Cheng, C.-H. Du, C.-J. Wu, K.-X. Sun, N.-P. Chi, Improving the hydrophilic and antifouling properties of poly(vinyl chloride) membranes by atom transfer radical polymerization grafting of poly(ionic liquid) brushes, *Polym. Adv. Technol.* 29 (2018) 623–631.
- [27] (a) A. Mollahosseini, A. Rahimpour, Interfacially polymerized thin film nanofiltration membranes on TiO<sub>2</sub> coated polysulfone substrate, *J. Ind. Eng. Chem.* 20 (5) (2014) 1261–1268;
- (b) S.H. Kim, S.-Y. Kwak, B.-H. Sohn, T.H. Park, Design of TiO<sub>2</sub> nanoparticle self-assembled aromatic polyamide thin-film-composite (TFC) membrane as an approach to solve biofouling problem, *J. Membr. Sci.* 211 (1) (2003) 157–165.
- [28] S. Pourjafar, A. Rahimpour, M. Jahanshahi, Synthesis and characterization of PVA/PES thin film composite nanofiltration membrane modified with TiO<sub>2</sub> nanoparticles for better performance and surface properties, *J. Ind. Eng. Chem.* 18 (4) (2012) 1398–1405.
- [29] (a) R.F.M. Elshaarawy, T.B. Mostafa, A.A. Refaee, E.A. El-Sawi, Ionic Sal-SG Schiff bases as new synergetic chemotherapeutic candidates: synthesis, metalation with Pd(II) and in vitro pharmacological evaluation, *RSC Adv.* 5 (2015) 68260–68269;
- (b) R.F.M. Elshaarawy, H.R.Z. Tadros, R.M. Abd El-Aal, F.H.A. Mustafa, Y.A. Soliman, M.A. Hamed, *J. Environ. Chem. Eng.* 4 (2016) 2754–2764;
- (c) L. Carson, P.K.W. Chau, M.J. Earle, M.A. Gilea, B.F. Gilmore, S.P. Gorman, M.T. McCann, K.R. Seddon, *Green Chem.* 11 (2009) 492–497;
- (d) R.F.M. Elshaarawy, I.M. Eldeen, E.M. Hassan, Efficient synthesis and evaluation of bis-pyridinium/bis-quinolinium metallosalophens as antibiotic and antitumor candidates, *J. Mol. Struct.* 1128 (2016) 162–173.
- [30] M. Padaki, A.M. Isloor, J. Fernandes, K.N. Prabhu, New polypropylene supported chitosan NF-membrane for desalination application, *Desalination* 280 (2011) 419–423.
- [31] O. Iguer, C. Poleunis, F. Mazéas, C. Compère, P. Bertrand, Antifouling properties of poly(methyl methacrylate) films grafted with poly(ethylene glycol) monoacrylate immersed in seawater, *Langmuir* 24 (21) (2008) 12272–12281.
- [32] L. Liu, D.Y.W. Di, H. Park, M. Son, H.-G. Hur, H. Choi, Improved antifouling performance of polyethersulfone (PES) membrane via surface modification by CNTs bound polyelectrolyte multilayers, *RSC Adv.* 5 (2015) 7340–7348.
- [33] Y.S. Zhou, L.J. Zhang, X.R. Zeng, J.J. Vital, X.Z. You, A new structurally characterized organotin/Schiff-base complex with approximately rectangular molecular boxes formed through hydrogen bonds, *J. Mol. Struct.* 553 (2000) 25–30.
- [34] J.G. Yu, J.J. Fan, K.L. Lv, Anatase TiO<sub>2</sub> nanosheets with exposed (001) facets: improved photoelectric conversion efficiency in dye-sensitized solar cells, *Nano* 2 (2010) 2144–2149.

- [35] I.M. Wienk, R.M. Boom, M.A.M. Beerlage, Recent advances in the formation of phase inversion membranes made from amorphous or semicrystalline polymers, *J. Membr. Sci.* 113 (1996) 361.
- [36] (a) R. Taylor, R. Krishna, *Multicomponent Mass Transfer* Vol. 597, Wiley, New York, 1993;
- (b) F. Zhang, W. Zhang, Y. Yu, B. Deng, J. Li, J. Jin, Sol-gel preparation of PAA-g-PVDF/TiO<sub>2</sub> nanocomposite hollow fiber membranes with extremely high water flux and improved antifouling property, *J. Membr. Sci.* 432 (2013) 25–32.
- [37] T. Wang, Y. Wang, Y. Su, Z. Jiang, Antifouling ultrafiltration membrane composed of polyethersulfone and sulfobetaine copolymer, *J. Membr. Sci.* 280 (2006) 343–350.
- [38] H. Yu, Y. Cao, G. Kang, J. Liu, M. Li, Tethering methoxy polyethylene glycols to improve the antifouling property of PSF/PAA-blended membranes, *J. Appl. Polym. Sci.* 124 (2012) E123–E133.

## 4 ERGEBNISSE UND DISKUSSION

---

### 4.1 Baylis-Hillman-Reaktion zur Synthese eines neuen Liganden

#### 4.1.1 Veresterung von para-Terephthalaldehydsäure

In einem ersten Schritt wurde para-Terephthalaldehydsäure (p-Ts) mit Methyljodid zu Methyl-4-formylbenzoat umgesetzt. Dazu wurden p-Ts mit Kaliumcarbonat in *N,N'*-Dimethylformamid (DMF) vorgelegt und nach 10-minütigem Rühren langsam Methyljodid hinzugegeben. Es wurde über Nacht gerührt und das Produkt anschließend über Extraktion mit darauffolgender Vakuumtrocknung aufgereinigt (Abbildung 25).

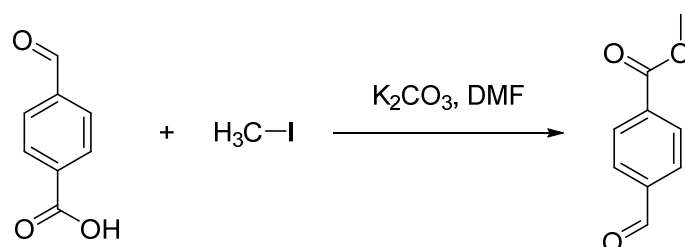


Abbildung 25. Veresterung von para-Terephthalaldehydsäure.

Im <sup>1</sup>H-NMR-Spektrum des erhaltenen Produktes konnte keine Verunreinigung durch Edukte festgestellt werden (Abbildung 26).



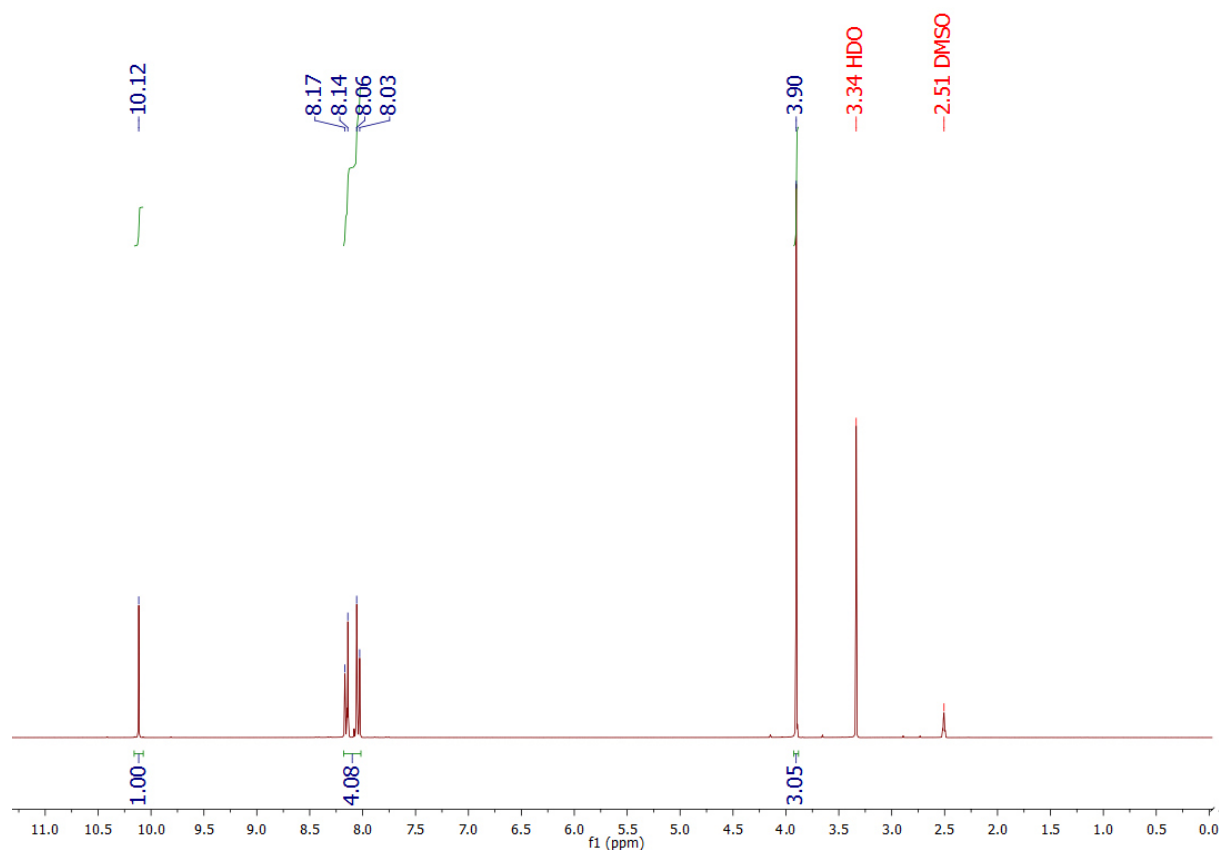


Abbildung 26.  $^1\text{H}$ -NMR-Spektrum von Methyl-4-formylbenzoat.

#### 4.1.2 Synthese von Methyl-4-(1-hydroxy-2-(methoxycarbonyl)allyl)benzoat

Die Baylis-Hillman-Reaktion ist eine C-C-bindungsknüpfende Reaktion, bei welcher ein durch eine elektronenziehende Gruppe aktiviertes Alken nukleophil von einem für gewöhnlich *in-situ* erzeugten Enolat angegriffen wird. Das Enolat wird dabei aus einem Aldehyd oder Keton sowie einer Base gebildet. In dieser Arbeit wurde als aktiviertes Alken Methylacrylat verwendet, als Keton das zuvor synthetisierte Methyl-4-formylbenzoat und als Base 1,4-Diazabicyclo[2.2.2]octan (DABCO) (Abbildung 27). Die Reaktion ist schematisch in Abbildung 27 dargestellt. Nach 3 Tagen Reaktionszeit in Dioxan bei Raumtemperatur konnten über Dünnschichtchromatographie (in Ethylacetat (EE)/Hexan 2:8 und Methanol/Toluol 3:7) nur die unreaktierten Edukte nachgewiesen werden.

In einem weiteren Versuch wurde die Reaktion unter veränderten Konzentrationen und verändertem Lösemittel (Methanol) durchgeführt. Nach chromatographischer

Aufreinigung mit EE/Hexan 2:8 als Laufmittel war das Produkt noch mit DABCO verunreinigt. Ein möglicher Grund für die schlechte Trennbarkeit besteht in einer Säure-Base-Reaktion zwischen der Alkoholgruppe des Produktes und DABCO, welche ebenfalls die schlechte Detektierbarkeit des Alkohol-Protons im  $^1\text{H-NMR}$ -Versuch erklären würde (5,08 ppm, Abbildung 28). Von einer weiteren Bearbeitung des Produktes wurde abgesehen, da andere Ligandensynthesen vielversprechender erschienen.

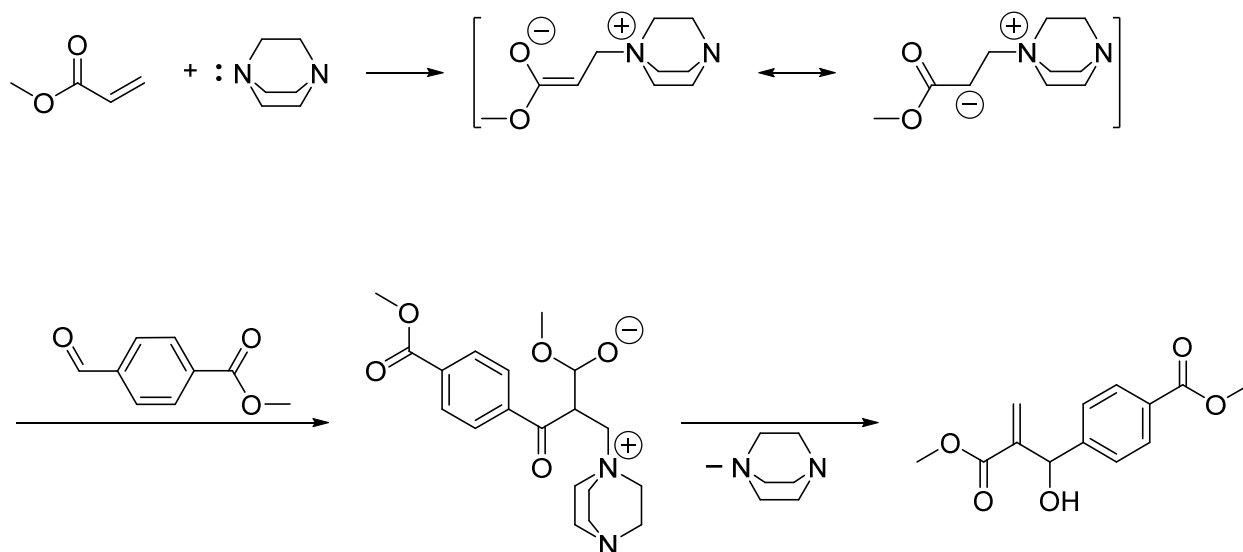


Abbildung 27. Schematische Darstellung der Baylis-Hillman-Reaktion zwischen Methyl-4-formylbenzoat und Methylacrylat in Anwesenheit von DABCO.

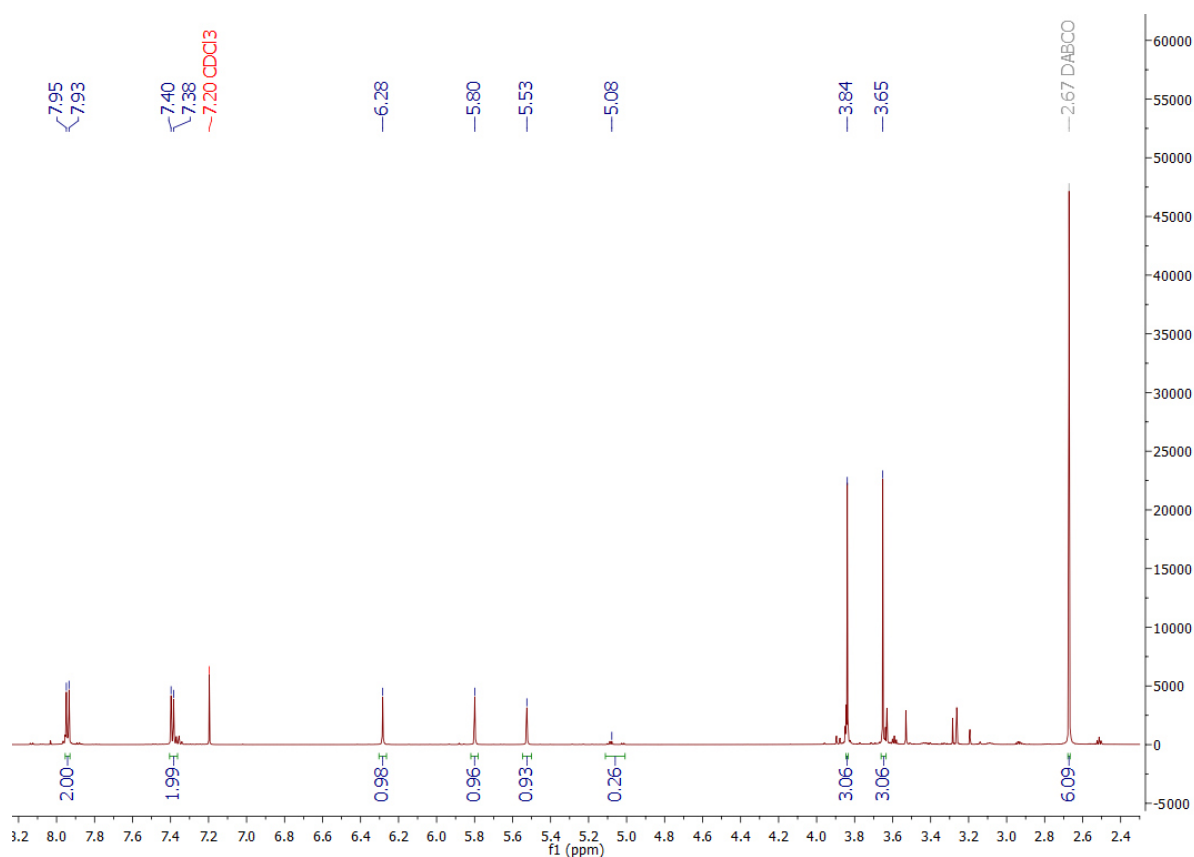


Abbildung 28. <sup>1</sup>H-NMR-Spektrum von Methyl-4-(1-Hydroxy-2-(methoxycarbonyl)allyl)benzoat, mit Verunreinigungen durch DABCO.

## 4.2 Synthese eines neuen Liganden basierend auf Melamin

### 4.2.1 Synthese von *N,N',N''*-(1,3,5-triazin-2,4,6-triyl)tris(4-methylbenzamid)

In einem ersten Versuch sollte para-Toluoylchlorid mit Melamin umgesetzt werden (Abbildung 29), um dann im nächsten Schritt die Methylgruppe zu oxidieren und so einen Carboxylat-Liganden mit mehreren Amidgruppen zu erhalten. Das <sup>1</sup>H-NMR-Spektrum deutete auf eine nur teilweise erfolgreiche Synthese hin. Das Rohprodukt war noch stark mit Melamin und Triethylammoniumchlorid, einem Nebenprodukt der Synthese, verunreinigt. Durch Waschen mit Chloroform konnte Triethylammoniumchlorid entfernt werden (Abbildung 30). Die Verunreinigung mit Melamin blieb jedoch, des Weiteren wurden Signale im Bereich über 10 ppm gefunden,



Veresterungs- und Verseifungschemie gewählt, um am Ende einer mehrstufigen Synthese das gewünschte Produkt zu erhalten (Abbildung 31).

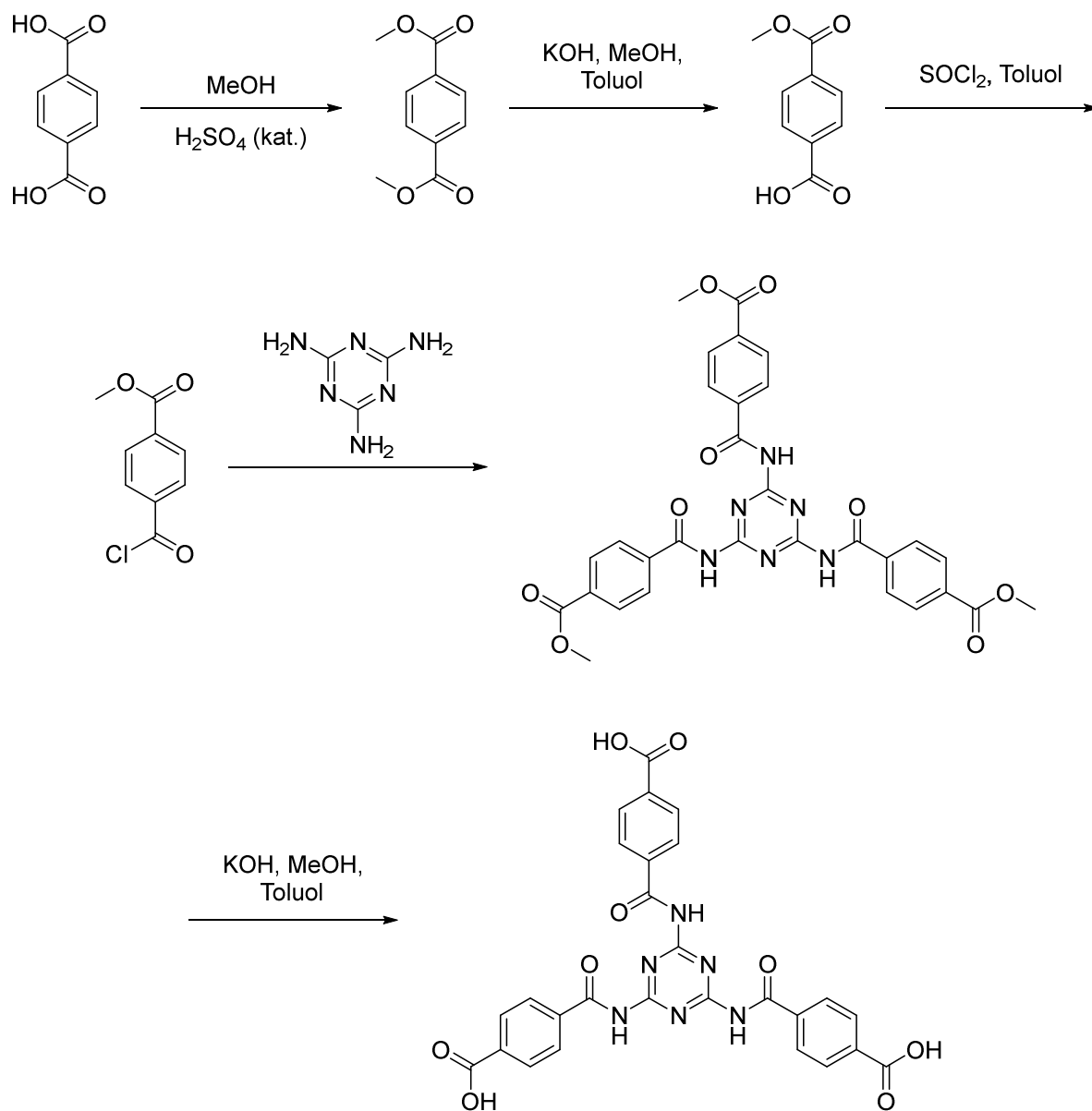


Abbildung 31. Geplante Syntheseroute zum Produkt 4,4',4''-(((1,3,5-triazin-2,4,6-triyl)tris(azanediyl))tris(carbonyl))tribenzoensäure.

Die Synthese des Säurechlorids ausgehend von Terephthalsäure verlief erfolgreich und in guten Ausbeuten. Für die folgende Umsetzung des Säurechlorids mit Melamin wurden mehrere Ansätze verfolgt. Es wurde in verschiedenen Lösemitteln gearbeitet, bei verschiedenen Temperaturen und mit verschiedenen Basen, oder auch als lösemittelfreie Reaktion direkt im aufgeschmolzenen Säurechlorid. Die schlechte Löslichkeit sowie die potentielle Gefahr der Hydrolyse des Säurechlorids verhinderten

insgesamt gesehen eine erfolgreiche Reaktion. Die besten Ergebnisse wurden in heißem DMF erzielt, mit Triethylamin ( $\text{NEt}_3$ ) als Base. Laut Massenspektrometrie konnte dabei bei im Verhältnis 3:1 eingesetztem Säurechlorid zu Melamin zumindest das einfach und zweifach substituierte Melamin erhalten werden, bei einem Verhältnis von 8:1 wurde sogar das sechsfach substituierte Melamin erhalten (siehe Abbildung 32).

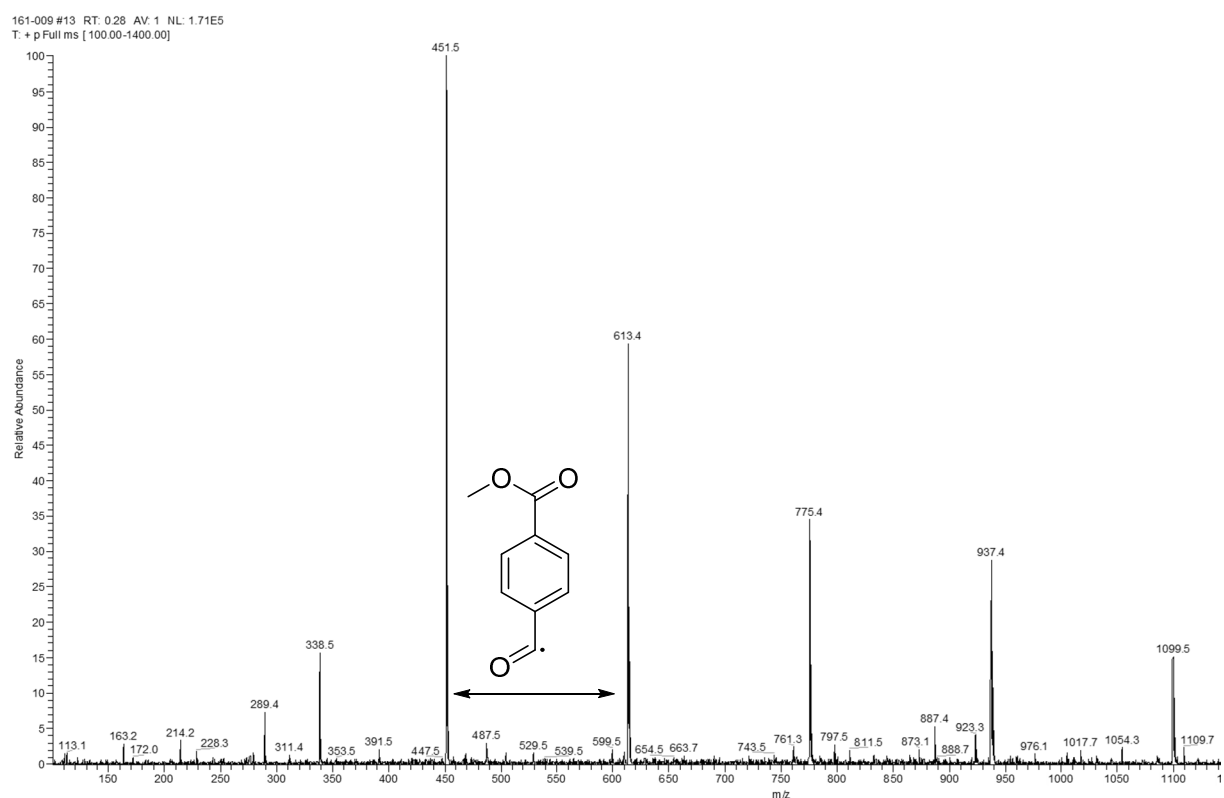


Abbildung 32. ESI-Massenspektrum der hergestellten Verbindung. Das Molekulargewicht der sechsfach substituierten Melaminverbindung beträgt 1099 g/mol, die Unterschiede zwischen den detektierten Signalen betragen ungefähr 162 g/mol und entsprechen damit dem über dem Doppelpfeil dargestellten Fragment.

Die chromatographische Aufreinigung des Moleküls gestaltete sich auf Grund stark polarer Gruppen sowie der enormen Größe mit den vorhandenen Mitteln unmöglich. Der weitere Einsatz des nicht aufgereinigten Moleküls wurde gar nicht erst erwogen, und die weiteren Reaktionen mit diesem potentiellen Liganden wurden nicht durchgeführt. Des Weiteren wurde die Synthese auch lösemittel- und basenfrei im aufgeschmolzenen Methyl-4-(chlorocarbonyl)benzoat (M4CCB) ausprobiert, unter Stickstoffstrom, welcher durch eine Natriumcarbonatlösung ausgeleitet wurde. Der Versuch verlief nicht erfolgreich.

Insgesamt lassen die Ergebnisse des ESI-MS darauf schließen, dass das Melamin bis hin zum Hexamethyl-4,4',4'',4''',4''''',4''''''-(((1,3,5-triazin-2,4,6-triyl)tris(azanetriyl))hexakis(carbonyl))hexabenzooat durchsubstituiert wurde.

#### 4.2.3 Synthese von 4,4',4''-(((1,3,5-triazin-2,4,6-triyl)tris(azanediy1))tris(carbonyl))tribenzoessäure

Um der Reaktivität des Säurechlorids zuvorzukommen wurde eine Reaktion zwischen dem einfach entschützten Terephthalsäureester und dem Melamin erwogen. In der klassischen Peptidsynthesechemie wird dazu häufig *N,N'*-Dicyclohexylcarbodiimide (DCC) verwendet, alternativ mit vorheriger Bildung eines Aktivesters aus der Carbonsäure und *N*-Hydroxysuccinimid (Abbildung 33). Aktivester werden, im Gegensatz zu normalen Estern, auch von schwachen Nukleophilen angegriffen (z. B. Aminogruppen). Diese Reaktionen verliefen allerdings ohne Ausbeute.

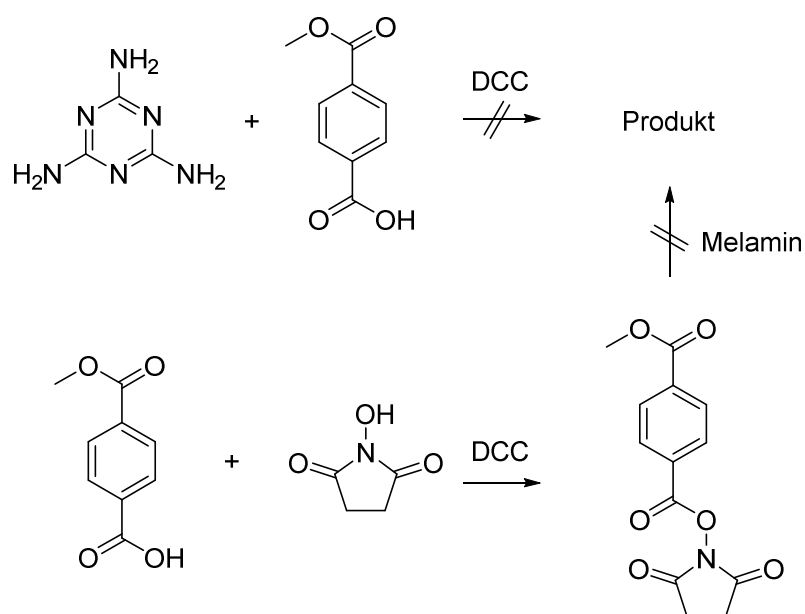


Abbildung 33. Geplante Synthese des mehrfach substituierten Liganden basierend auf Melamin. Die typische Kupplungsreaktion unter Verwendung von DCC (oben) verlief ebenso wenig erfolgreich wie die mit vorheriger *in-situ*-Bildung eines Aktivesters (unten).

#### 4.2.4 Synthese von Dimethyl-5-(chlorocarbonyl)isophthalat

Um den Zugang zu weiteren möglichen Liganden zu erhalten, wurde ausgehend von der Benzol-1,3,5-tricarbonsäure das Dimethyl-5-(chlorocarbonyl)isophthalat synthetisiert (Abbildung 34).

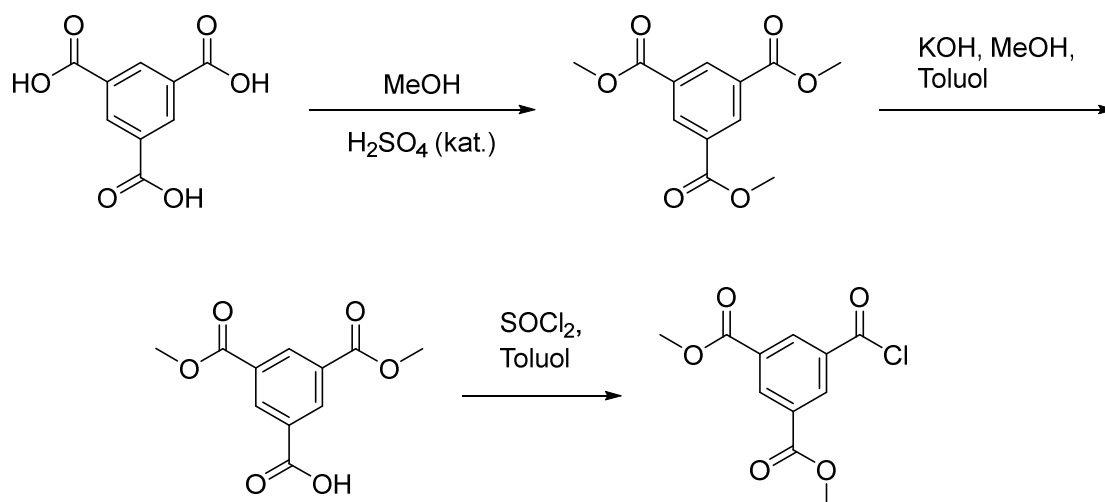
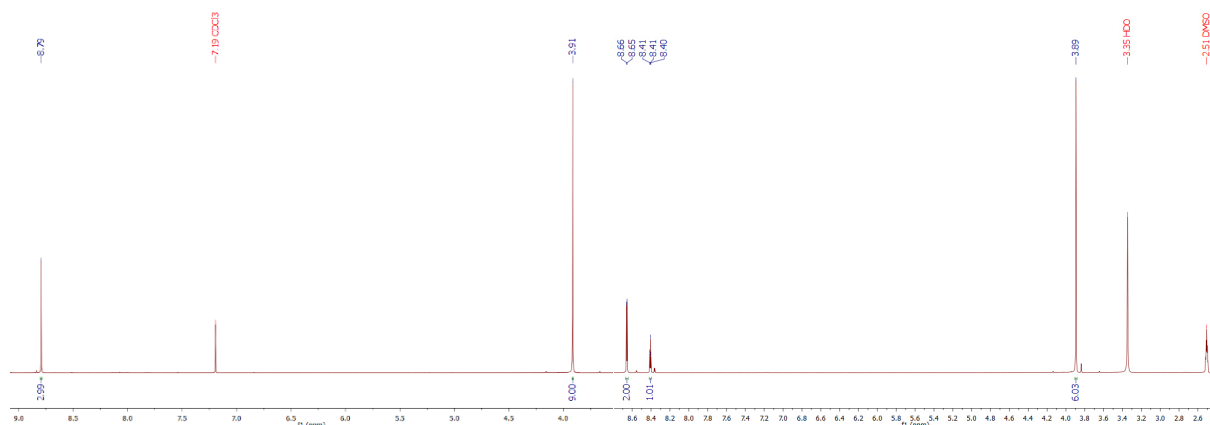


Abbildung 34. Schematischer Syntheseweg für Dimethyl-5-(chlorocarbonyl)isophthalat ausgehend von Benzol-1,3,5-tricarbonsäure.

Im ersten Schritt wurde dazu die Tricarbonsäure verestert, im nächsten dann stöchiometrisch zur einfachen Carbonsäure verseift und zuletzt zum Säurechlorid umgesetzt. Die Umsetzungen wurden mit  $^1\text{H}$ -NMR-Spektroskopie verfolgt (Abbildung 35).





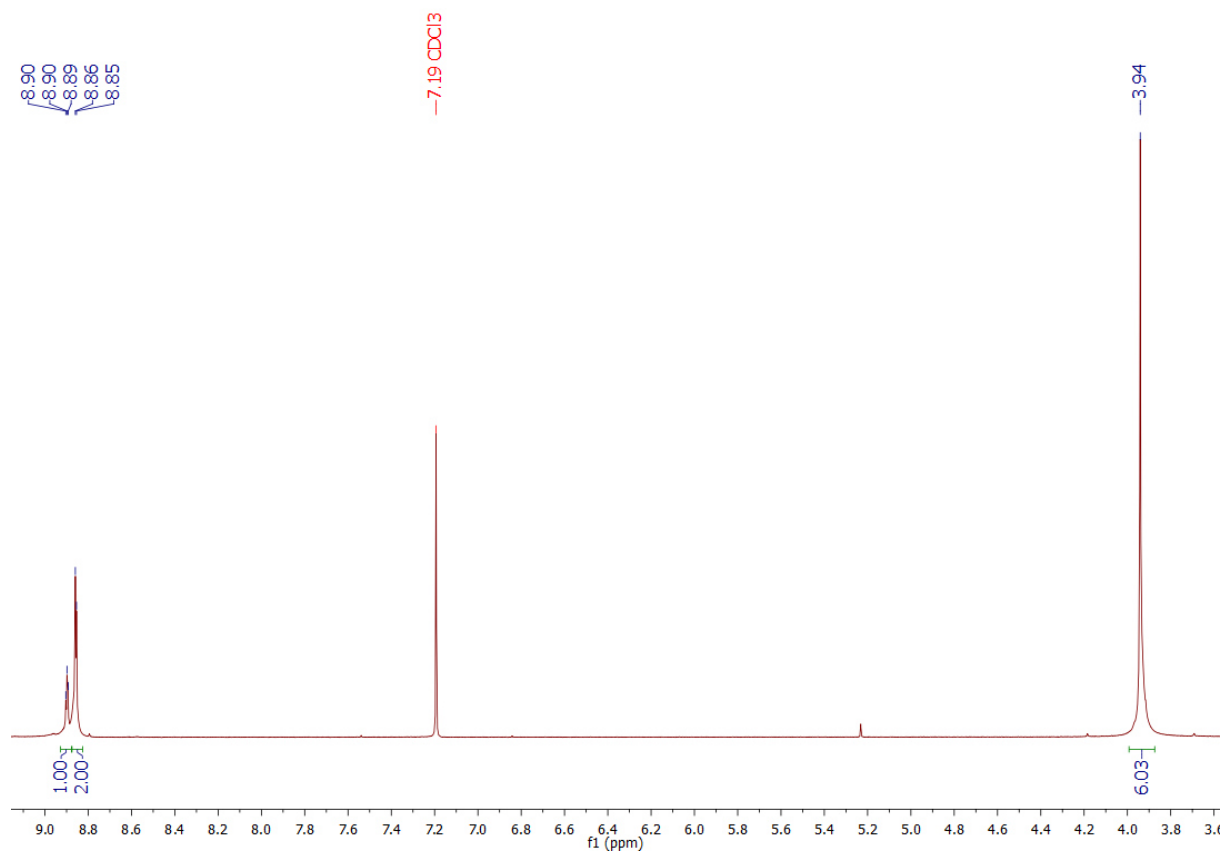


Abbildung 35.  $^1\text{H}$ -NMR-spektroskopische Verfolgung der Umsetzung von Benzol-1,3,5-tricarbonsäure zu Dimethyl-5-(chlorocarbonyl)isophthalat. Oben links:  $^1\text{H}$ -NMR-Spektrum von Trimethyl-1,3,5-benzoltricarboxylat. Oben rechts:  $^1\text{H}$ -NMR-Spektrum von 3,5-Bis(methoxycarbonyl)benzoesäure. Unten:  $^1\text{H}$ -NMR-Spektrum von Dimethyl-5-(chlorocarbonyl)isophthalat.

Des Weiteren wurde die erfolgreiche Synthese mittels IR- und Massenspektroskopie bestätigt.

#### 4.2.5 Syntheseveruche zu Hexamethyl-5,5',5''-(((1,3,5-Triazin-2,4,6-triyl)tris)azanediyl))tris(carbonyl)triisophthalat

Zur Synthese des gewünschten Melaminderivats wurde auch hier wieder die direkte Umsetzung des Säurechlorids mit Melamin in verschiedenen Lösemitteln unter Verwendung der Base Triethylamin getestet (Abbildung 36). Die erfolgreiche Umsetzung konnte unter Verwendung gängiger spektroskopischer Methoden nicht bestätigt werden.

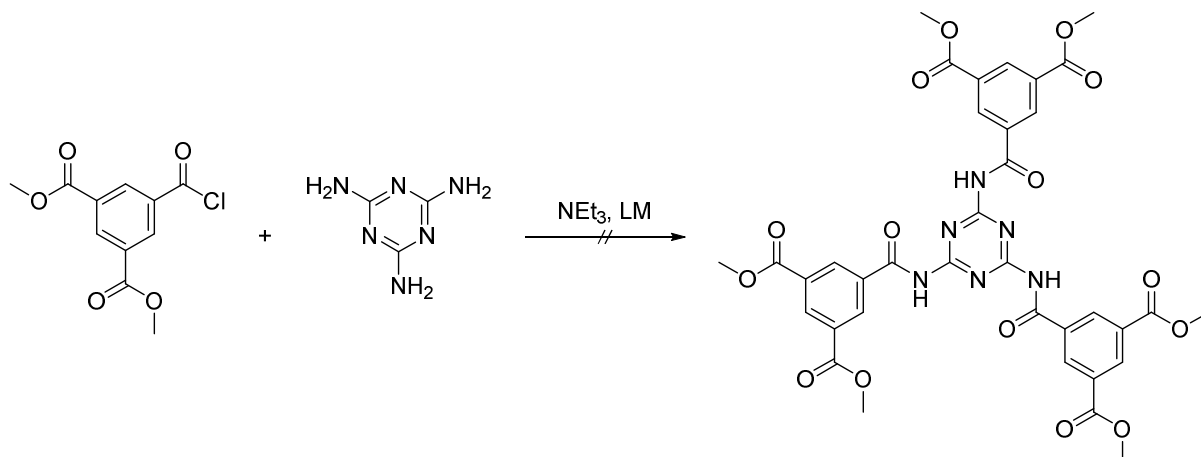


Abbildung 36. Geplante Synthese von Hexamethyl-5,5',5''-(((1,3,5-Triazin-2,4,6-triyl)tris(azanediyl))tris(carbonyl))triisophthalat.

Anders als in 4.2.2 konnte allerdings auch keine teilsubstituierte Substanz gefunden werden.

#### 4.2.6 Syntheseversuche zu 5,5',5''-(((1,3,5-Triazin-2,4,6-triyl)tris(azanediyl))tris(carbonyl))triisophthalsäure

Analog zu der in 4.2.3 durchgeführten Synthese sollte erneut eine Reaktion zwischen der 3,5-Bis(methoxycarbonyl)benzoesäure und Melamin unter Verwendung von DCC bewirkt werden (Abbildung 37).

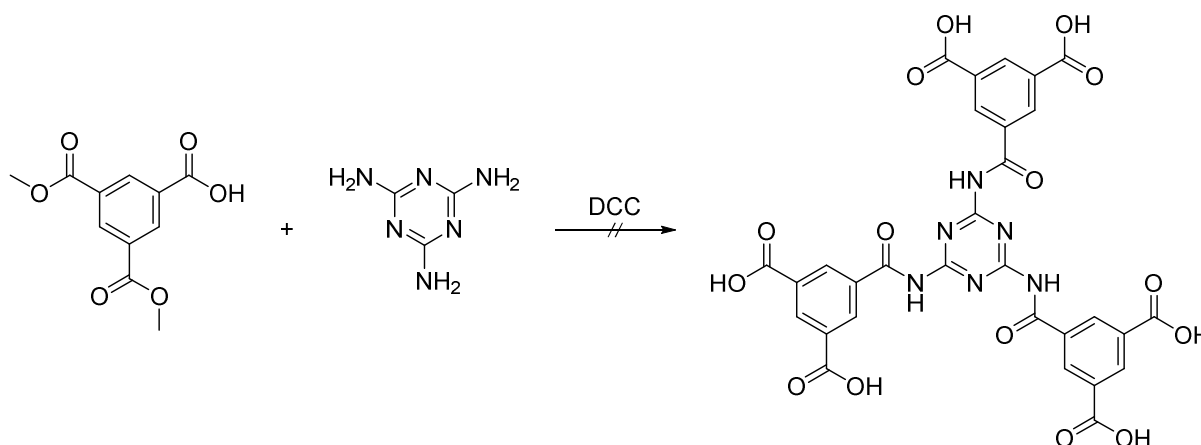


Abbildung 37. Geplante Synthese von 5,5',5''-(((1,3,5-Triazin-2,4,6-triyl)tris(azanediyl))tris(carbonyl))triisophthalsäure.

Wie auch zuvor konnte das Produkt dieser Synthese nicht identifiziert werden.

#### 4.2.7 Synthese von 2,2',2''-((1,3,5-Triazin-2,4,6-triyl)tris(piperazin-4,1-diyl))triessigsäure ausgehend von Cyanurchlorid

Als eine Alternative zu Melamin wurde das deutlich reaktivere Cyanurchlorid gewählt. Die Umsetzung sollte dabei mit primären oder sekundären Aminen erfolgen, um als Reaktionsprodukt ein Derivat des Melamins zu erhalten. In einer mehrstufigen Synthese konnte der mögliche Ligand 2,2',2''-((1,3,5-Triazin-2,4,6-triyl)tris(piperazin-4,1-diyl))triessigsäure erhalten werden (Abbildung 38).

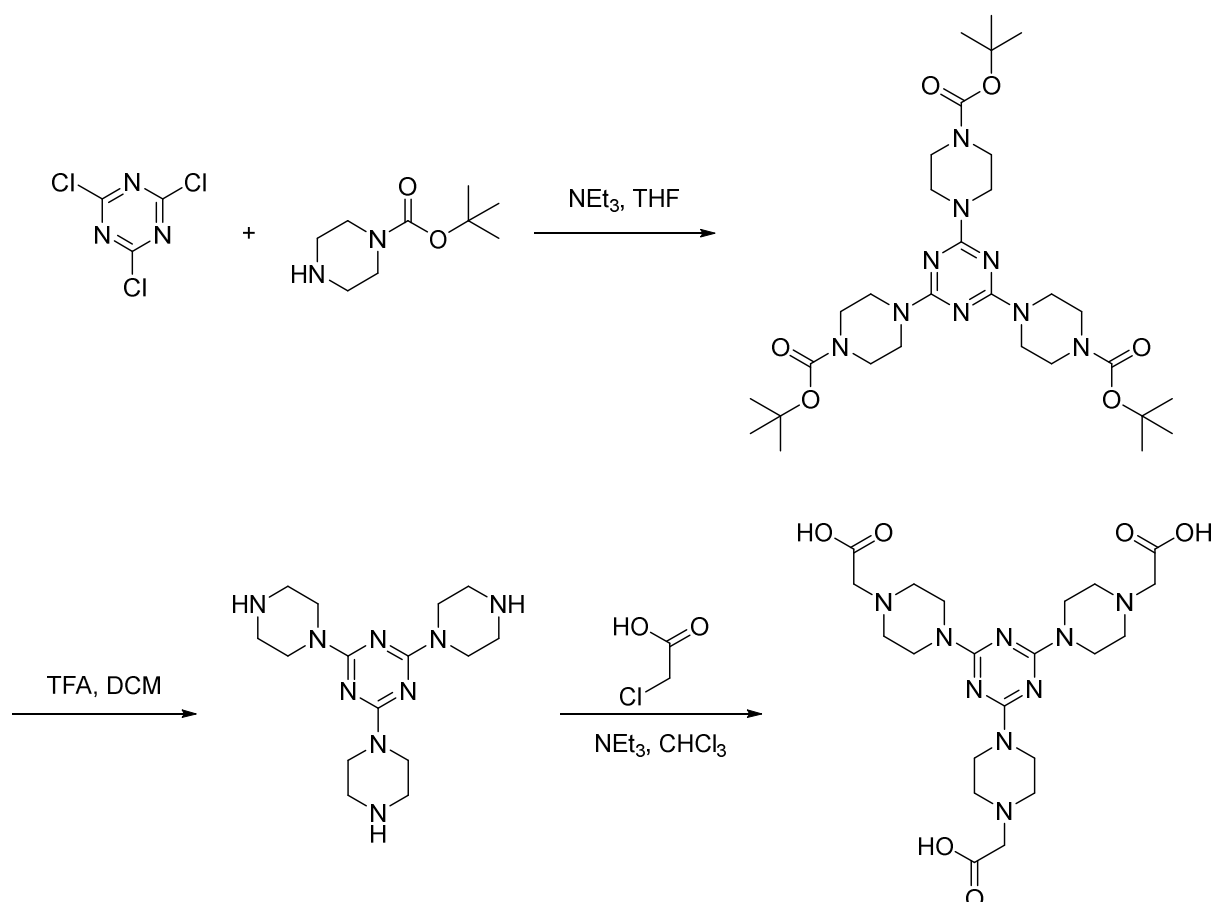


Abbildung 38. Synthese von 2,2',2''-((1,3,5-Triazin-2,4,6-triyl)tris(piperazin-4,1-diyl))triessigsäure ausgehend von Cyanurchlorid und 1-Boc-piperazin.

Alle Zwischenstufen wurden dabei mit gängigen Analysemethoden charakterisiert. Zur Verifizierung des Produktes des ersten Syntheseschrittes wurden dabei unter anderem <sup>1</sup>H-NMR-Spektren des Eduktes 1-Boc-piperazin mit denen des Produktes verglichen (Abbildung 39, oben links). Am Rasterelektronenmikroskop wurde ein Bild des Liganden angefertigt, als mögliche visuelle Referenz für Synthesen von metall-

organischen Koordinationsverbindungen basierend auf dem hier synthetisierten Liganden (Abbildung 40).

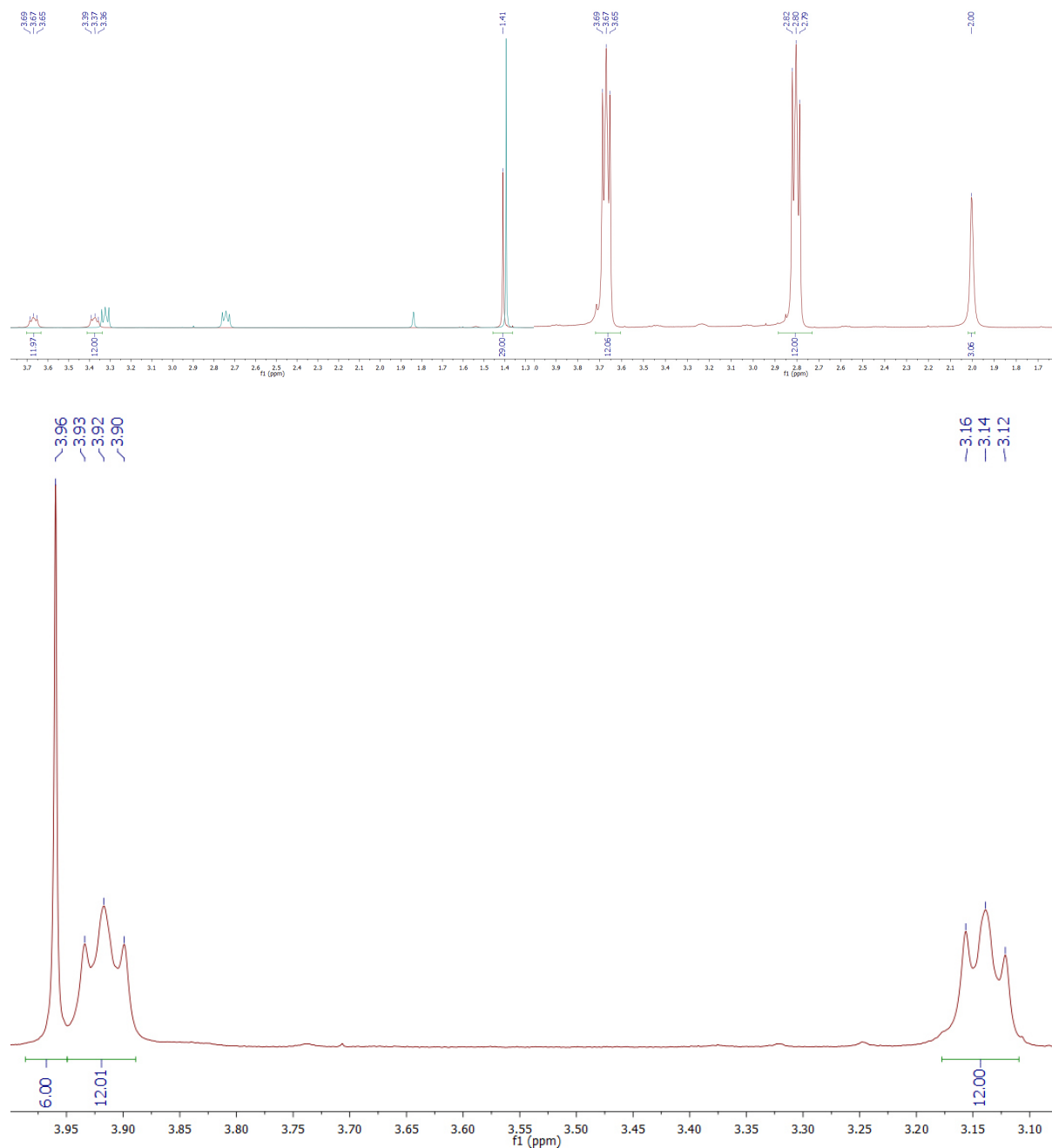


Abbildung 39. <sup>1</sup>H-NMR-Spektren der Zwischenprodukte und des Endproduktes der Synthese von 2,2',2''-((1,3,5-Triazin-2,4,6-triyl)tris(piperazin-4,1-diyl))triessigsäure. Oben links: <sup>1</sup>H-NMR-Spektrum von Tri-tert.-butyl-4,4',4''-(1,3,5-triazin-2,4,6-triyl)tris(piperazin-1-carboxylat). Oben rechts: <sup>1</sup>H-NMR-Spektrum von 2,4,6-Tri(piperazin-1-yl)-1,3,5-triazin. Unten: <sup>1</sup>H-NMR-Spektrum von 2,2',2''-((1,3,5-triazin-2,4,6-triyl)tris(piperazin-4,1-diyl))triessigsäure.

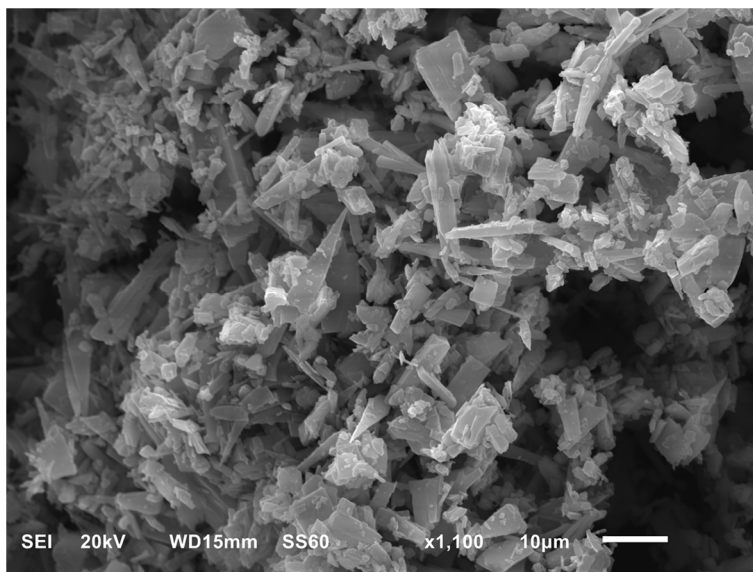


Abbildung 40. REM-Aufnahme von 2,2',2''-((1,3,5-Triazin-2,4,6-triyl)tris(piperazin-4,1-diyl))triessigsäure.

### 4.3 Synthese neuer Amidliganden ausgehend von Terephthaloylchlorid

#### 4.3.1 Synthese von *N,N'*-(4-Carboxyphenyl)terephthalamid

*N,N'*-(4-Carboxyphenyl)terephthalamid wurde nach der Vorschrift von Cronin et al. synthetisiert.<sup>50</sup> In der hier durchgeführten Variante wurde dabei allerdings 4-Aminobenzoesäure direkt eingesetzt, anstatt des dazugehörigen Esters, und THF wurde durch Wasser ersetzt (Abbildung 41). Trotz Zugabe von Kaliumcarbonat blieb dabei eine Hydrolyse des Säurechlorids aus. Die Entstehung des Produktes konnte über gängige Analysemethoden bestätigt werden (Abbildung 42). In den REM-Aufnahmen sieht man nadelförmige Kristalle (Abbildung 43). Der Eindruck der Kristallinität wurde durch ein Röntgenpulverdiffraktogramm bestätigt (Abbildung 44).

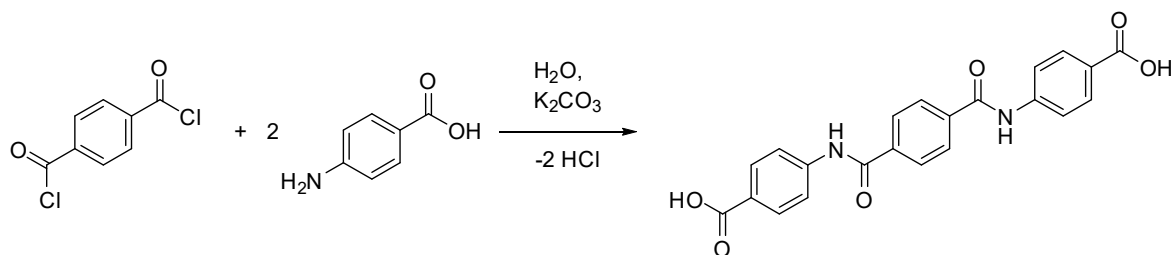


Abbildung 41. Synthese von *N,N'*-(4-Carboxyphenyl)terephthalamid.

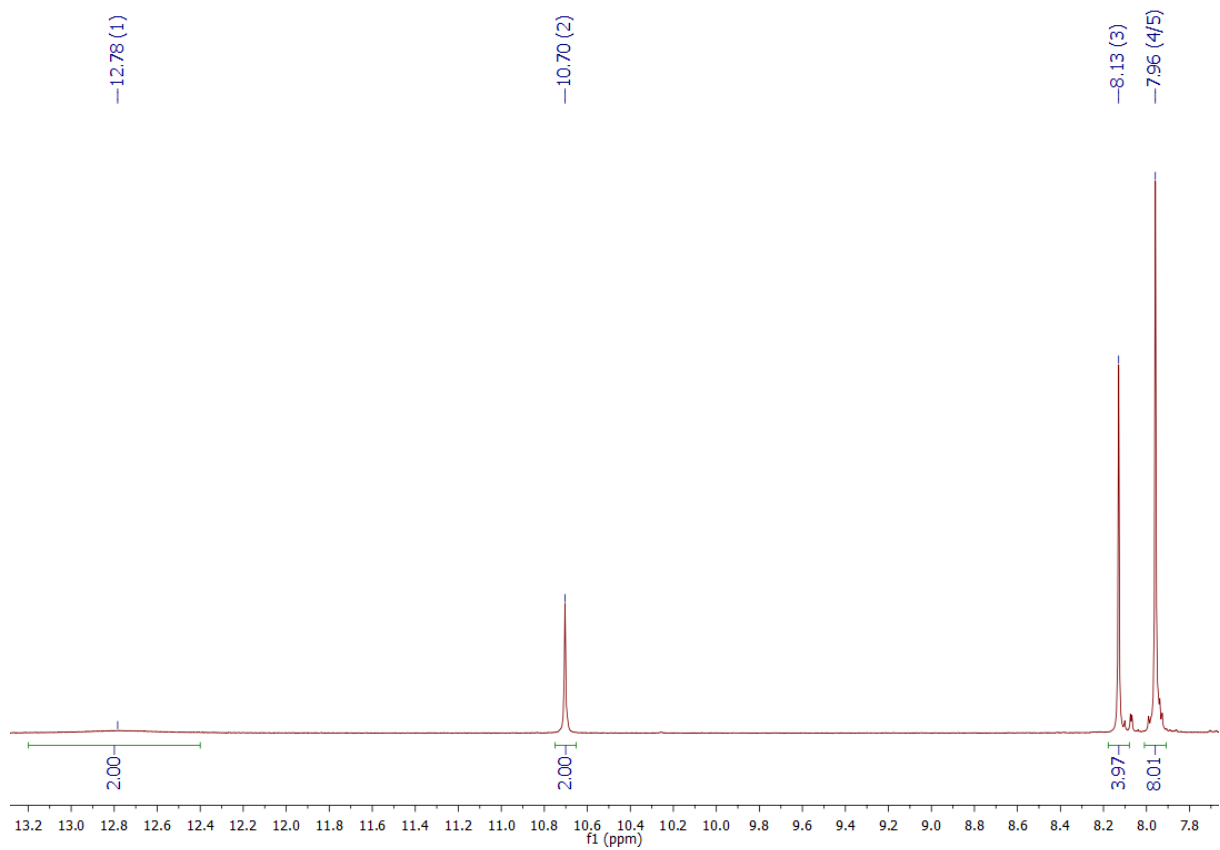


Abbildung 42. <sup>1</sup>H-NMR-Spektrum von *N,N'*-(4-Carboxyphenyl)terephthalamid.

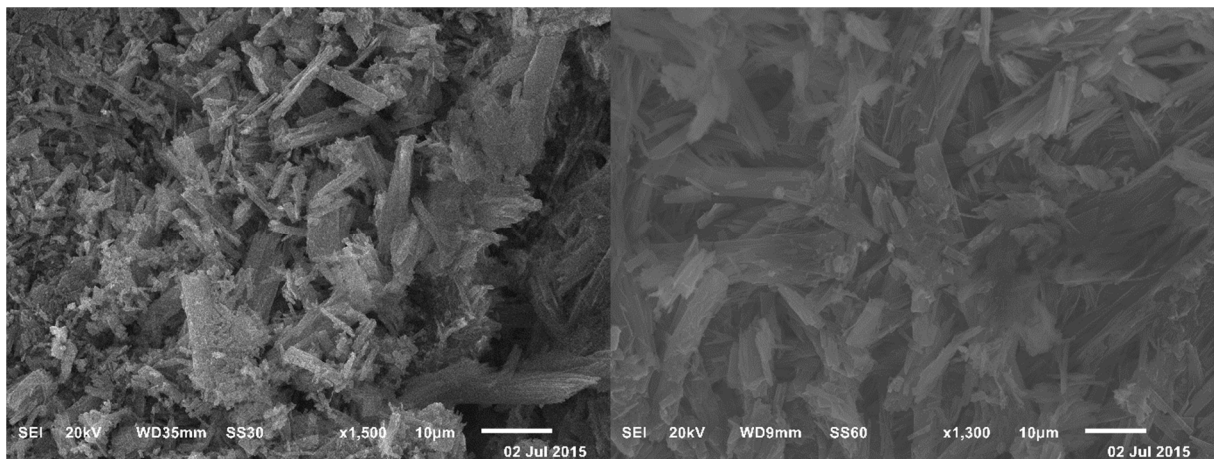


Abbildung 43. REM-Aufnahmen von *N,N'*-(4-Carboxyphenyl)terephthalamid.

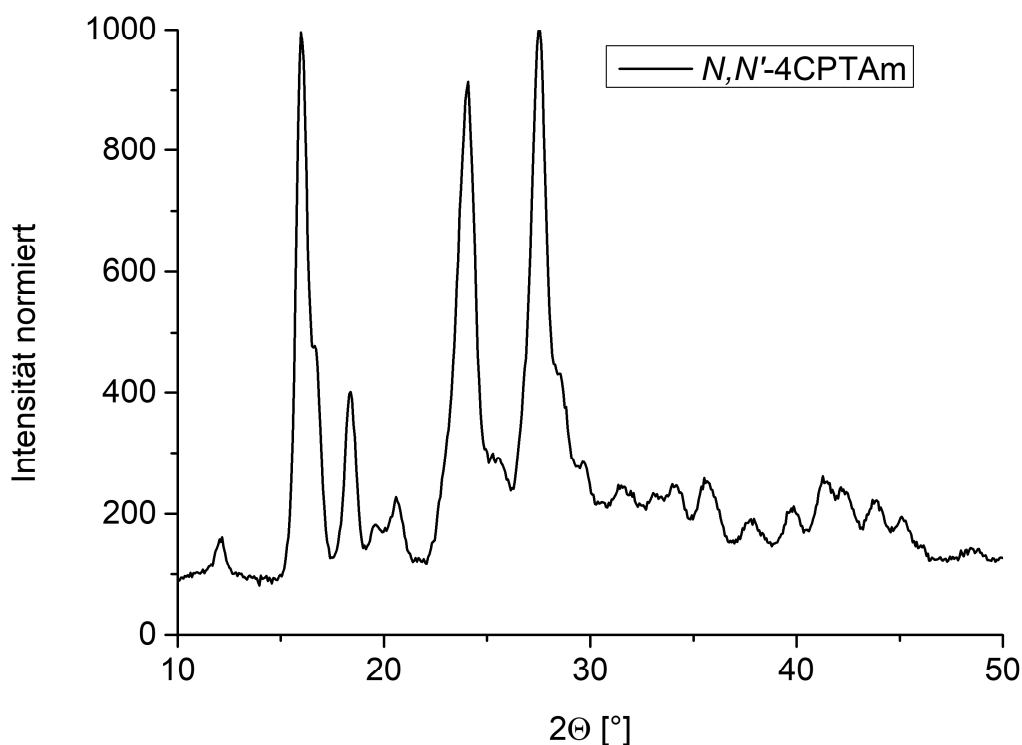


Abbildung 44. Röntgenpulverdiffraktogramm von *N,N'*-(4-Carboxyphenyl)terephthalamid.

#### 4.3.2 Synthese von *N,N'*-(3-Carboxyphenyl)terephthalamid

Auf demselben Wege wie in 4.3.1 wurde ebenfalls die Synthese von *N,N'*-(3-Carboxyphenyl)terephthalamid durchgeführt (Abbildung 45). Auch hier wurde wieder die Entstehung des Produktes über gängige Analysemethoden bestätigt und ein Röntgenpulverdiffraktogramm aufgenommen (Abbildung 46, Abbildung 47).

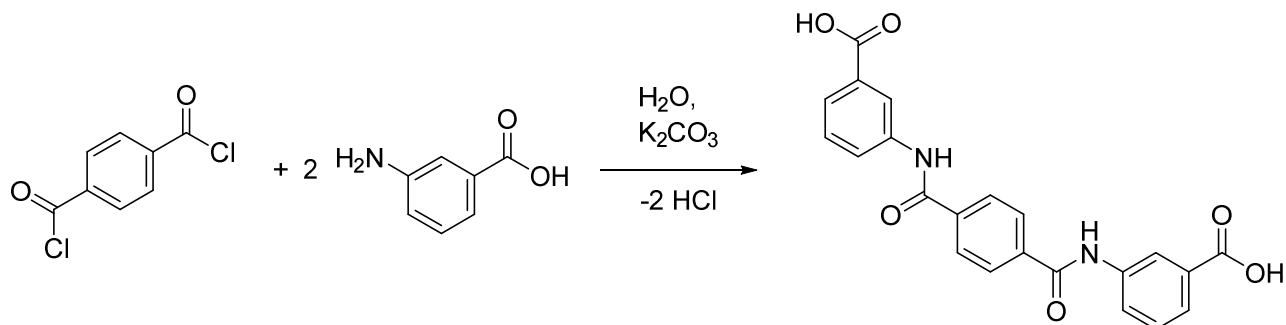


Abbildung 45. Synthese von *N,N'*-(3-Carboxyphenyl)terephthalamid.

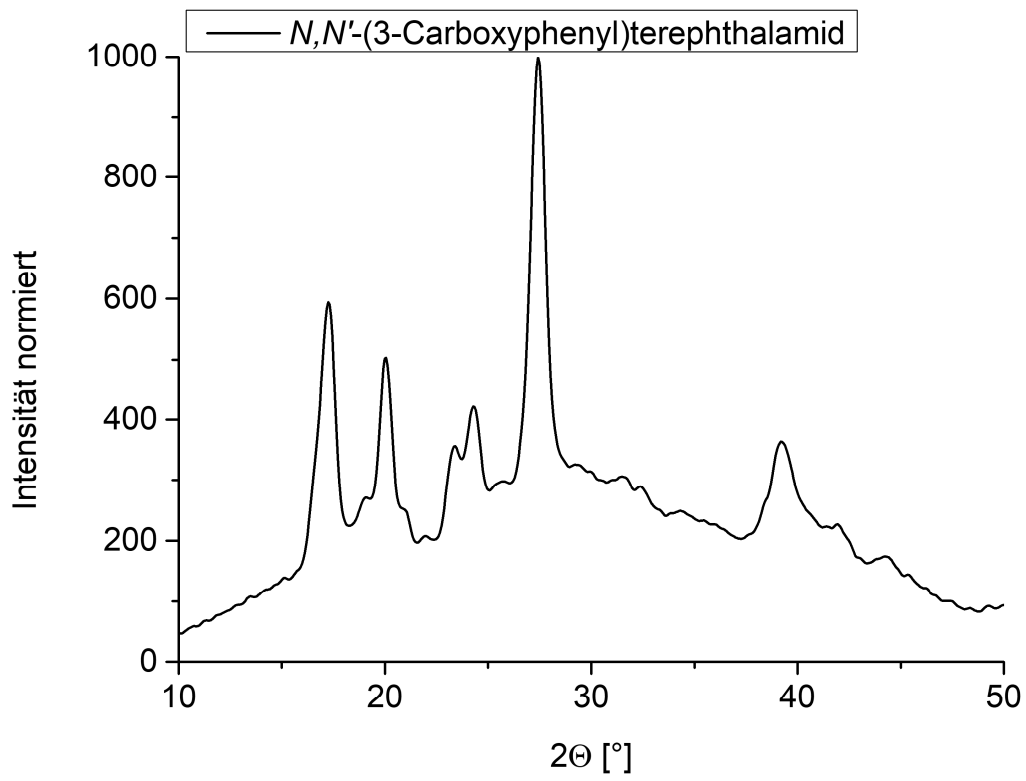


Abbildung 46. Röntgenpulverdiffraktogramm von *N,N'*-(3-Carboxyphenyl)-terephthalamid.



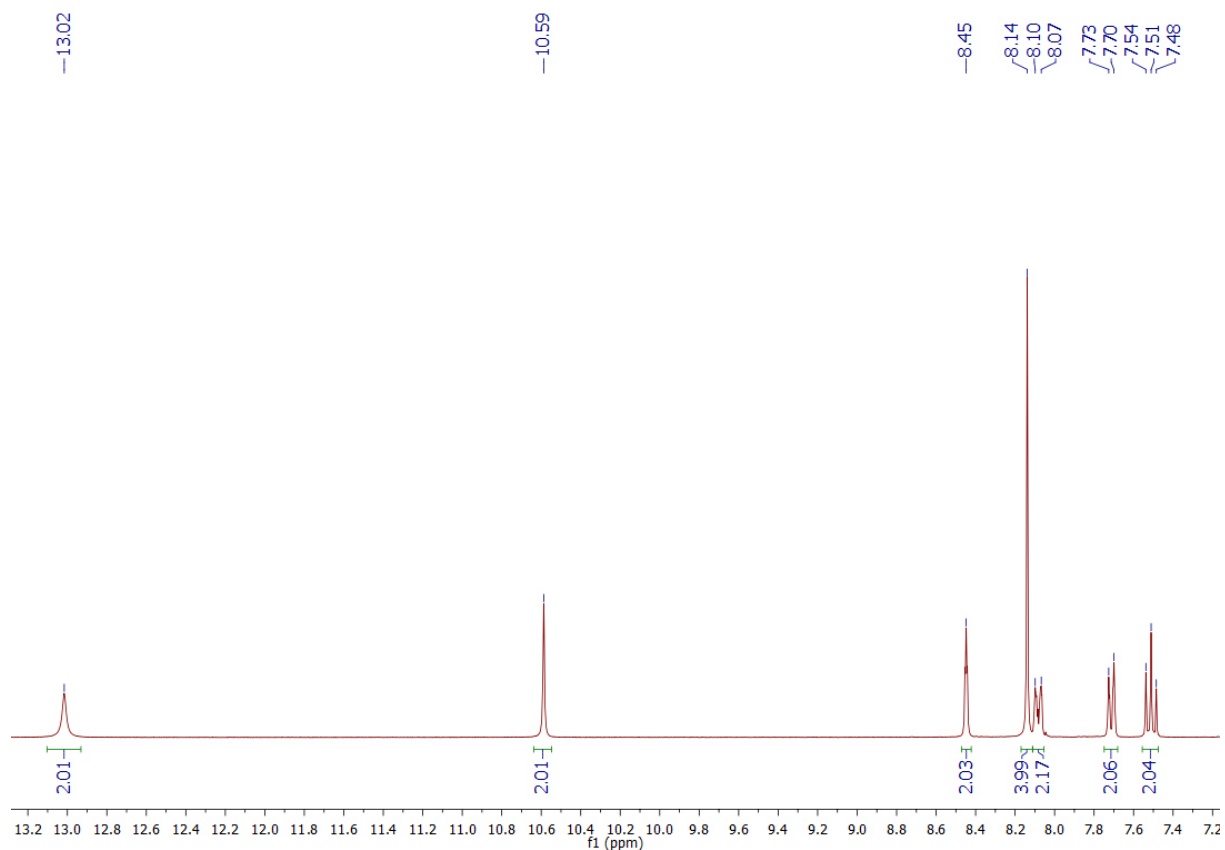


Abbildung 47.  $^1\text{H}$ -NMR-Spektrum von  $N,N'$ -(3-Carboxyphenyl)terephthalamid.

#### 4.3.3 Synthese dreier weiterer Derivate von $N,N'$ -(4-Carboxyphenyl)-terephthalamid.

Nach ähnlichen Bedingungen wie bei den vorangegangenen Synthesen wurden noch drei weitere Derivate des  $N,N'$ -(4-Carboxyphenyl)terephthalamids synthetisiert. Die 4-Aminobenzoesäure wurde hierbei durch 4-Amino-3-methylbenzoesäure, 4-Amino-2-methoxybenzoesäure oder 4-Amino-3-bromobenzoesäure ersetzt (Abbildung 48). Die Umsetzungen mit den ersten beiden Aminobenzoesäure-Derivaten zu den Produkten  $N,N'$ -(4-Carboxy,3-methylphenyl)terephthalamid ( $N,N'$ -4CMPTAm) und  $N,N'$ -(4-Carboxy,2-methoxyphenyl)terephthalamid ( $N,N'$ -4CMOPTAm) waren dabei erfolgreich, die Synthese von  $N,N'$ -(3-Bromo,4-carboxyphenyl)terephthalamid ( $N,N'$ -3Br-4CPTAm) verlief nicht erfolgreich. Die Farbe des Produktes war bei letzterem eher rot-braun, das  $^1\text{H}$ -NMR-Spektrum ließ sich weder den Edukten noch dem erwarteten Produkt zuordnen, die Bildung einer Amidgruppe ist jedoch sichtbar, was zumindest

auf eine Reaktion der Aminogruppe mit dem Säurechlorid schließen lässt (Abbildung 49).

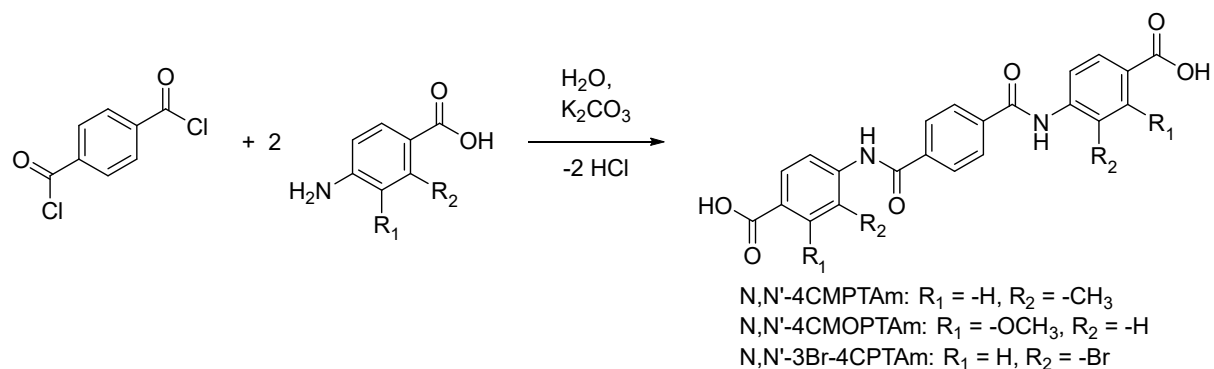


Abbildung 48. Synthese von *N,N'*-4CMPTAm, *N,N'*-4CMOPTAm und *N,N'*-3Br-4CPTAm.

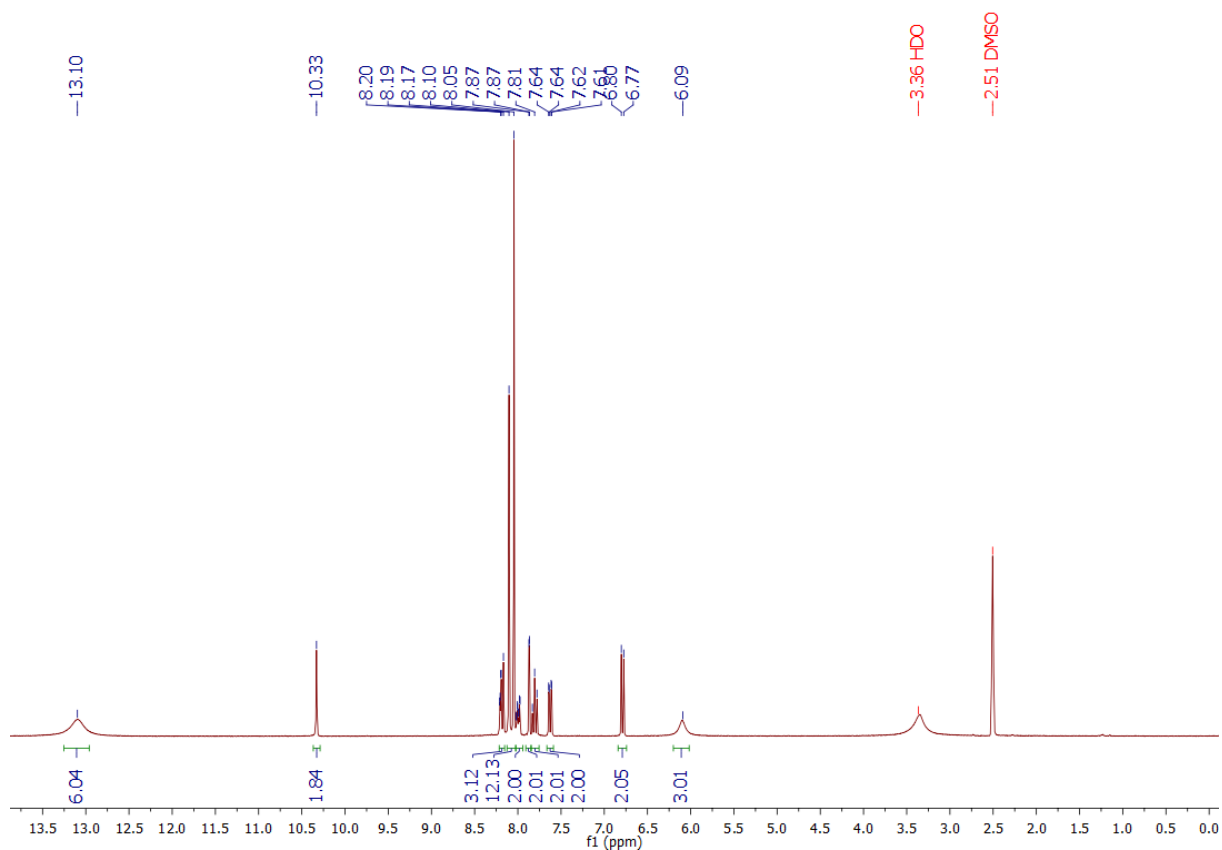


Abbildung 49.  $^1\text{H}$ -NMR-Spektrum der Reaktionsprodukte der versuchten Synthese von *N,N'*-3Br-4CPTAm.

Die Synthese von *N,N'*-4CMPTAm verlief zwar erfolgreich, wie im  $^1\text{H}$ -NMR-Spektrum an der Bildung der Amidgruppe zu sehen ist, allerdings ist das Produkt noch mit Edukt verunreinigt. Das Signal der Methylgruppe ist dabei kein sauberes Singulett, sondern

überlagert mit einem zweiten, kleineren Signal, und im aromatischen Bereich befinden sich zwei Protonensignale mehr als erwartet (Abbildung 50).

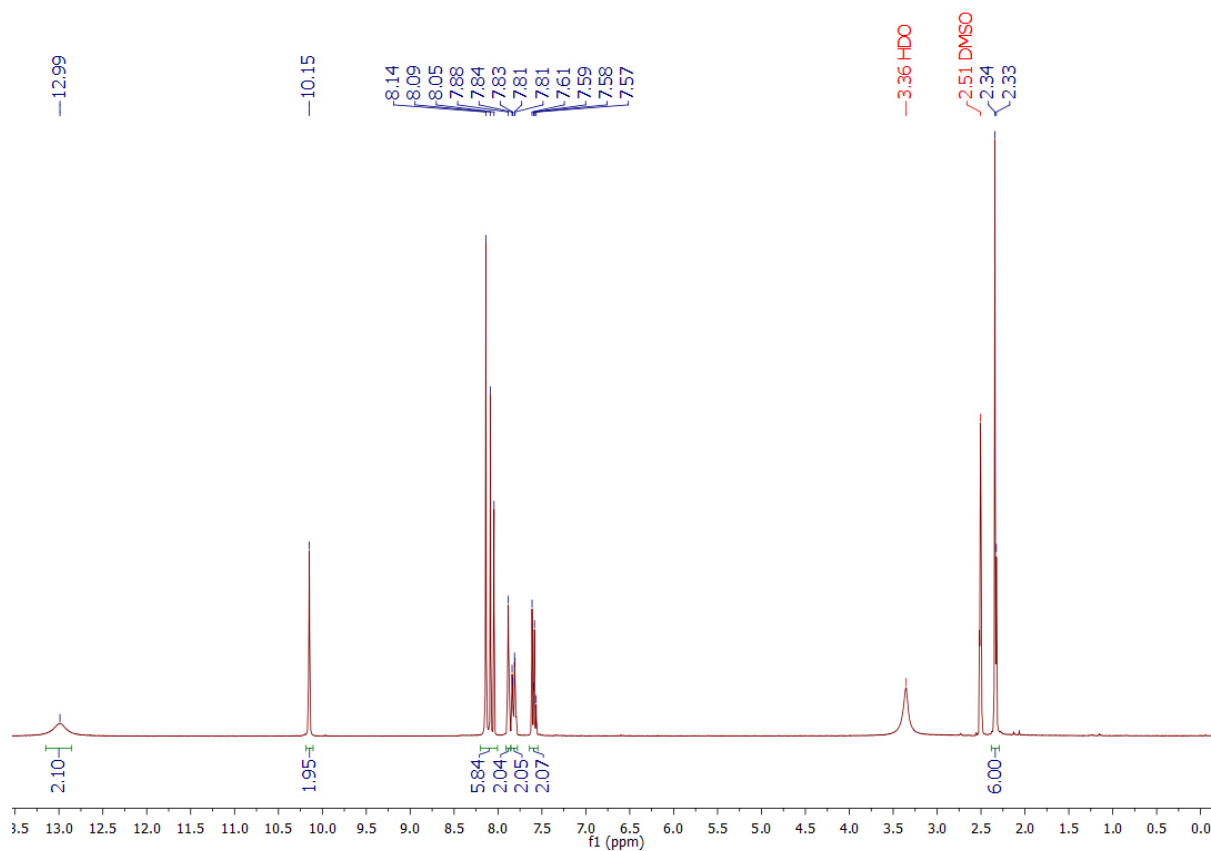


Abbildung 50.  $^1\text{H}$ -NMR-Spektrum von  $N,N'$ -4CMPTAm.

Bei der Synthese von  $N,N'$ -4CMOPTAm waren keine Auffälligkeiten zu beobachten. Das Produkt konnte mit nur sehr geringen Verunreinigungen erhalten werden; die Signale im  $^1\text{H}$ -NMR-Spektrum ließen sich eindeutig denen des gewünschten Produktes zuordnen.

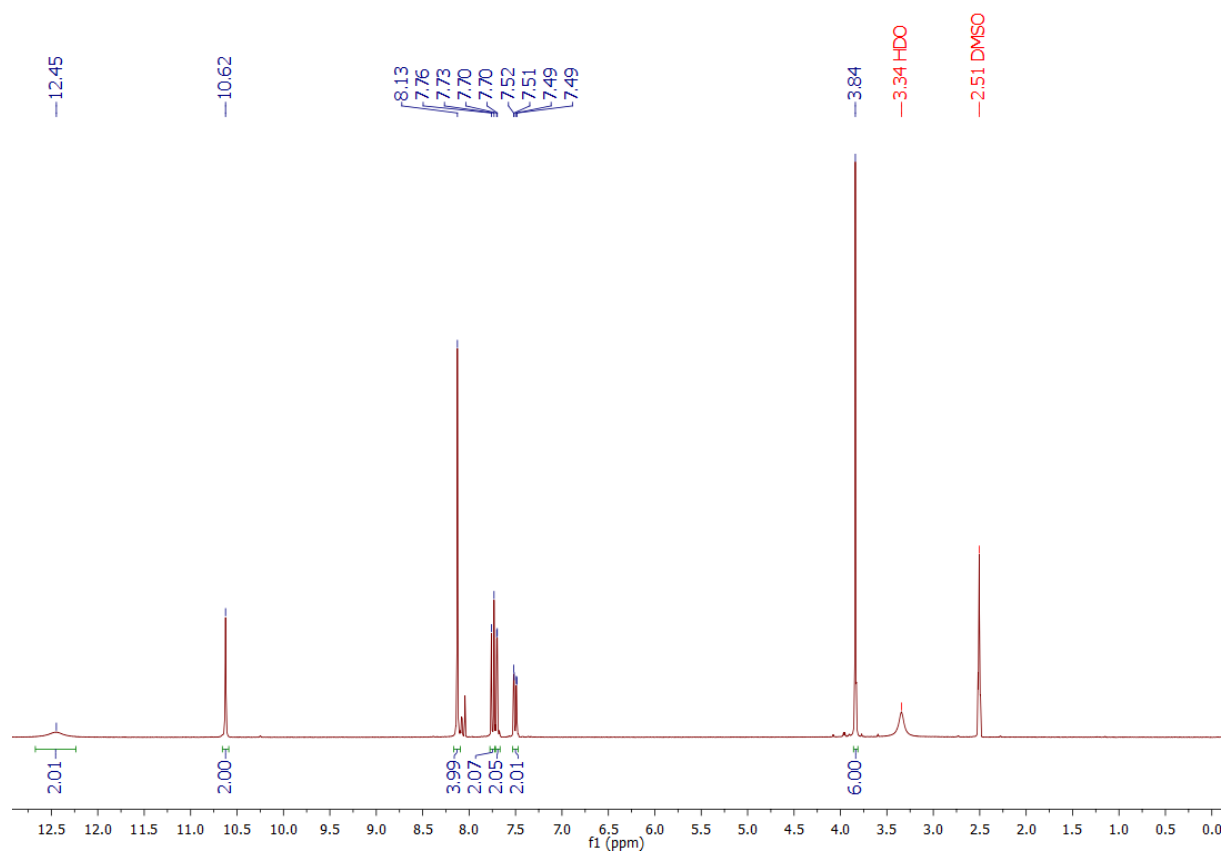


Abbildung 51. <sup>1</sup>H-NMR-Spektrum von *N,N'*-4CMOPTAm.

Alle drei Verbindungen lagen als kristalline Feststoffe vor und wurden mit dem Ausblick auf weitere Anwendungen in der Synthese von metall-organischen Gerüstverbindungen auch in einem Röntgenpulverdiffraktometer vermessen (Abbildung 52).

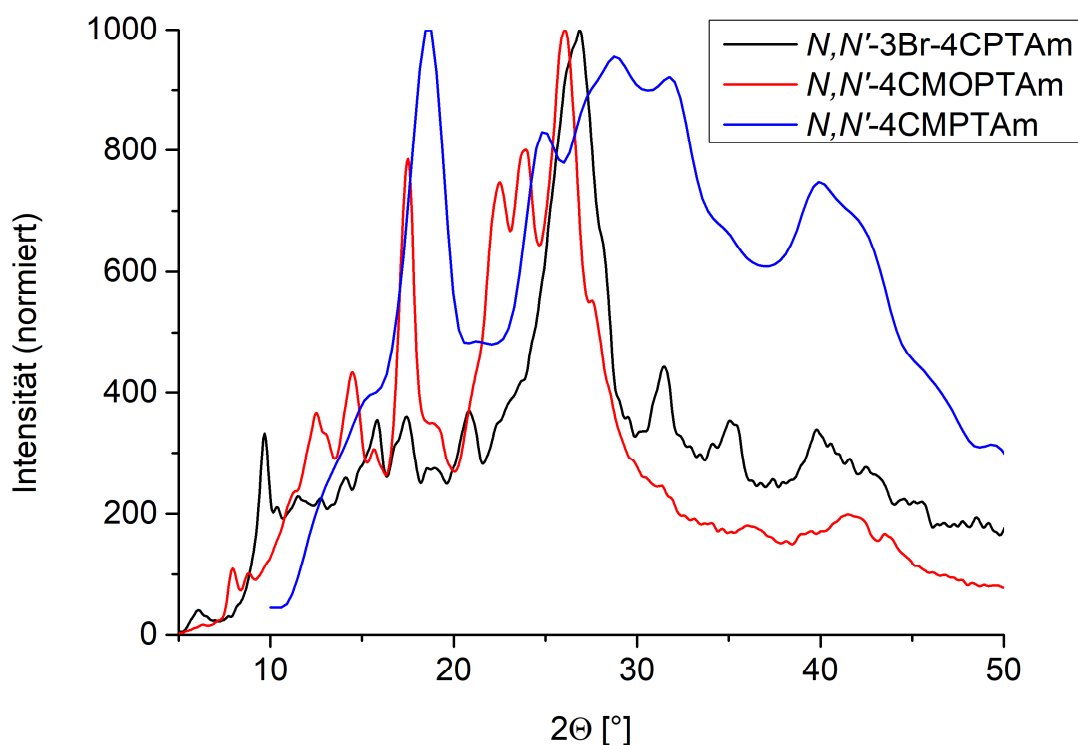


Abbildung 52. Röntgenpulverdiffraktogramme der Verbindungen  $N,N'$ -4CMPTAm,  $N,N'$ -4CMOPTAm und  $N,N'$ -3Br-4CPTAm.

#### 4.3.4 Synthese von $N,N'$ -(3,5-Dicarboxyphenyl)terephthalamid

Aus Zwecken der Vollständigkeit wurde außerdem noch die Synthese von  $N,N'$ -(3,5-Dicarboxyphenyl)terephthalamid ( $N,N'$ -3,5DiCPTAm) durchgeführt (Abbildung 53). In der Literatur ist diese Synthese bereits bekannt, des Weiteren wurden mit dem entstandenen Liganden auch schon metall-organische Gerüstverbindungen synthetisiert.<sup>51,52,53</sup> Der Vorteil der hier vorgestellten Synthese besteht darin, dass anstelle von  $N,N$ -Dimethylacetamid (DMAc) nur Wasser verwendet wird, einer einfachen anorganischen Base anstelle von 4-Dimethylaminopyridin (DMAP) und keine inerten Bedingungen herrschen müssen. Auch diese Synthese war erfolgreich, wie  $^1\text{H-NMR}$ -Spektren zeigten (Abbildung 54). Diese stimmen mit denen aus der Literatur überein. Für eine mögliche weitere Anwendung des Liganden wurde ebenfalls ein Röntgenpulverdiffraktogramm aufgenommen (Abbildung 55).

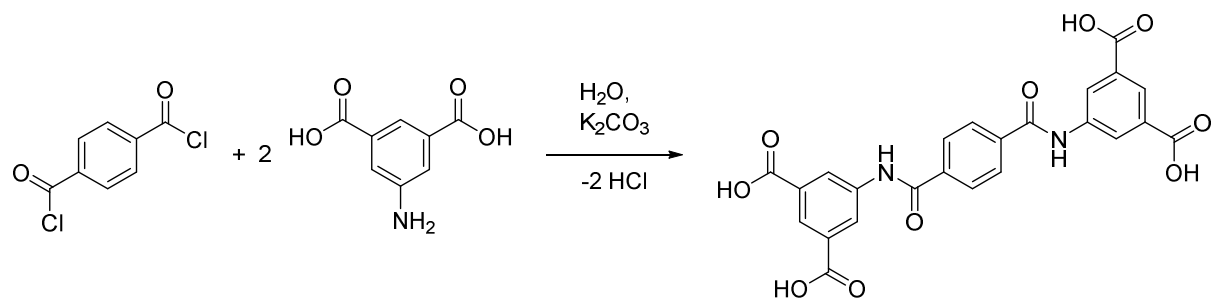


Abbildung 53. Synthese von *N,N'*-(3,5-Dicarboxyphenyl)terephthalamid.

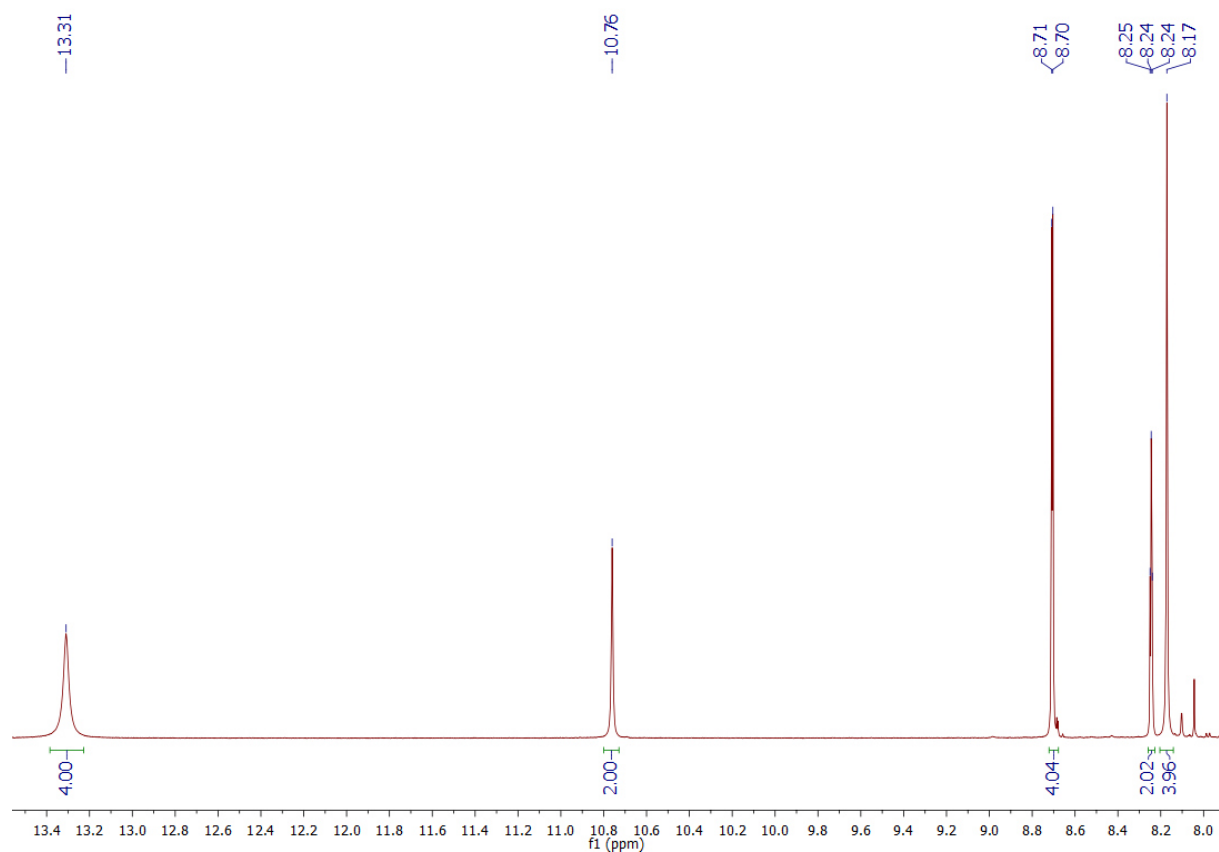


Abbildung 54.  $^1\text{H-NMR}$ -Spektrum von *N,N'*-(3,5-Dicarboxyphenyl)terephthalamid.

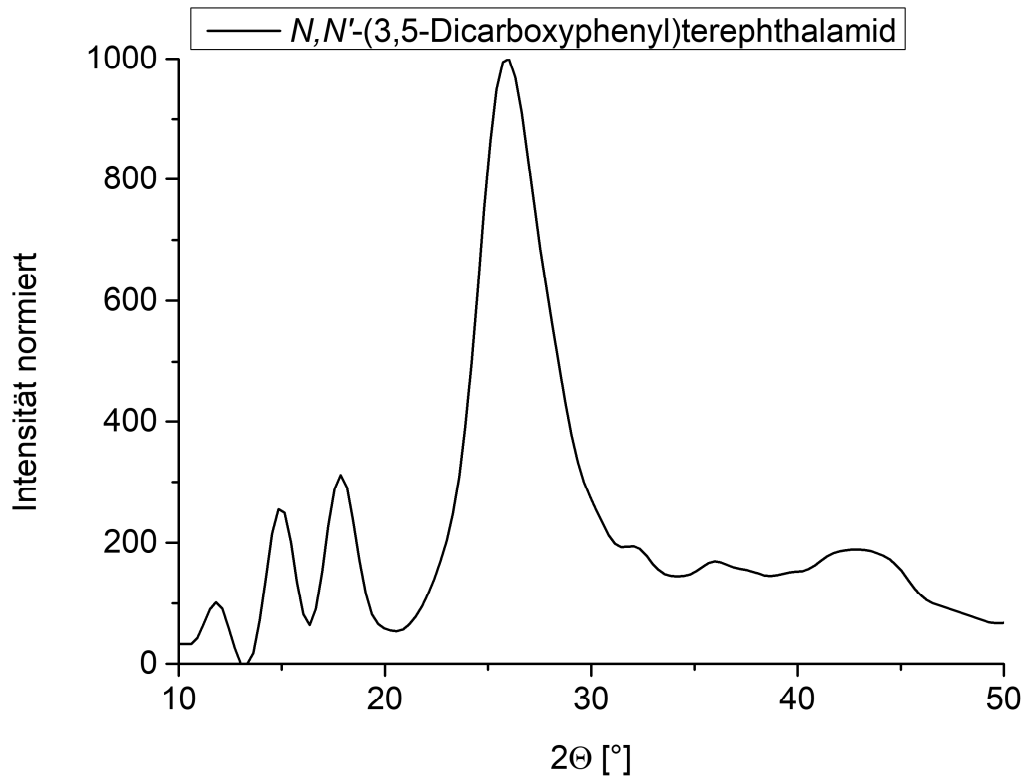


Abbildung 55. Röntgenpulverdiffraktogramm von *N,N'*-(3,5-Dicarboxyphenyl)terephthalamid.

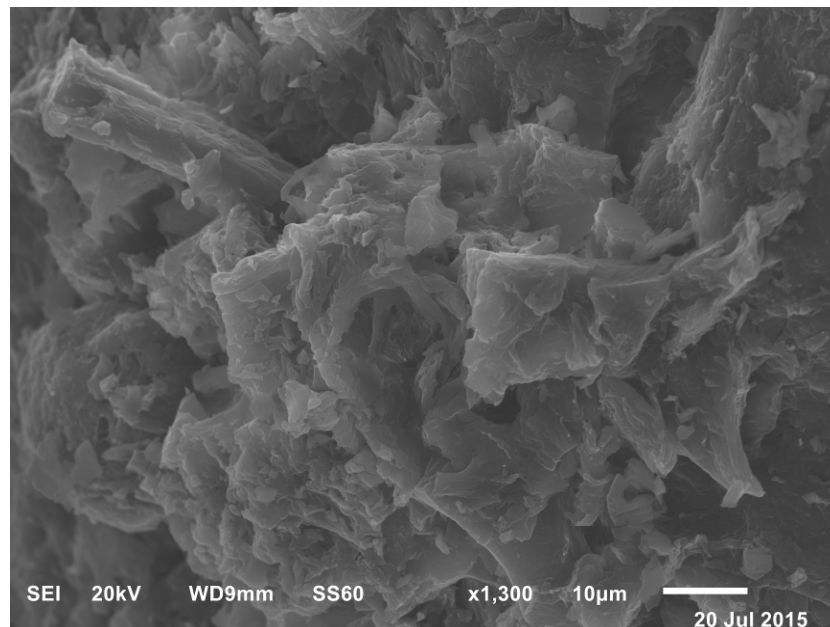


Abbildung 56. Rasterelektronenmikroskopaufnahme von *N,N'*-(3,5-Dicarboxyphenyl)terephthalamid.

## 4.4 Synthese neuer Amidliganden ausgehend von Phenylendiamin

Die in Kapitel 4.2 hergestellten Säurechloride, welche mit dem Triamin Melamin umgesetzt werden sollten, wurden außerdem noch für Reaktionen mit Phenylendiamin eingesetzt. Die bessere Löslichkeit und höhere Reaktivität Phenylendiamins verglichen mit Melamin sollten dabei die Reaktion ermöglichen.

### 4.4.1 Synthese von Dimethyl-4,4'-((1,4-phenylenbis(azanediyl))-bis(carbonyl))dibenzoat

Das unter 4.2.2 beschriebene Methyl-4-(chlorocarbonyl)benzoat wurde in einer Cronin et al. nachempfundenen Synthese mit Phenylendiamin umgesetzt.<sup>50</sup> Der entscheidende Unterschied in dieser Synthese liegt darin, dass anstatt der veresterten Aminobenzoesäure und Terephthaloylchlorid Phenylendiamin und ein verestertes Säurechlorid verwendet werden, sodass das Reaktionsprodukt im Vergleich zu dem in 4.2.3 hergestellten Produkt ein Konstitutionsisomer darstellt. Die Amidgruppen sind dabei in umgekehrter Reihenfolge im Molekül vorhanden (Abbildung 57). Des Weiteren wurde Chloroform statt Tetrahydrofuran als Lösungsmittel verwendet.

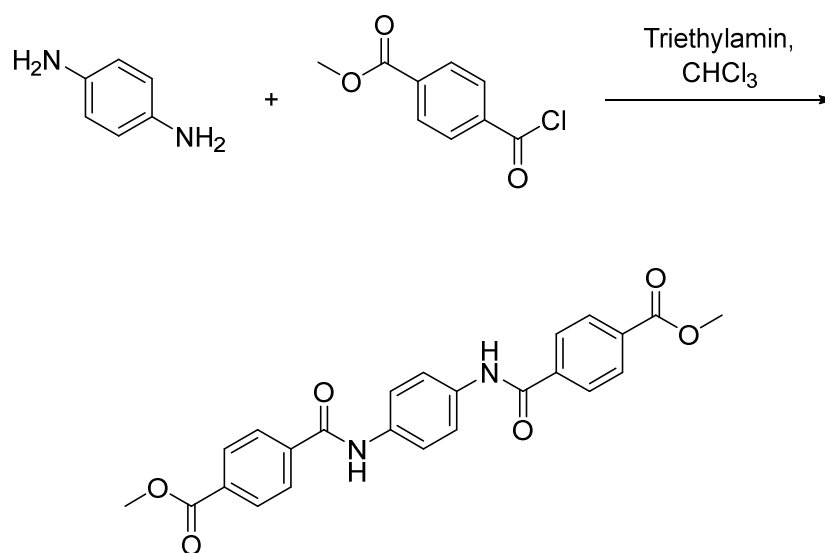


Abbildung 57. Reaktionsschema für die Synthese von Dimethyl-4,4'-((1,4-phenylenbis(azanediyl))-bis(carbonyl))dibenzoat.



Der geschützte Ligand konnte dabei in mittelmäßigen Ausbeuten erhalten und mit den gängigen Methoden charakterisiert werden. Das hauptsächliche Problem der Ausbeute ließe sich möglicherweise mit frischem Phenylendiamin beheben, da das verwendete Phenylendiamin bereits eine starke Braun- bzw. Schwarzfärbung durch Oxidation an der Luft zeigte.

#### 4.4.2 Synthese von Tetramethyl-5,5'-((1,4-phenylenbis(azanediyl))-bis(carbonyl))diisophthalat

Analog zu der in 4.4.1 beschriebenen Synthese wurde außerdem Tetramethyl-5,5'-((1,4-phenylenbis(azanediyl))bis(carbonyl))diisophthalat ausgehend von Phenylendiamin und Dimethyl-5-(chlorocarbonyl)isophthalat hergestellt. Als Lösemittel wurde hier Diethylether (Et<sub>2</sub>O) gewählt, in welchem sich letztendlich eine bessere Reaktivität feststellen ließ (Abbildung 58).

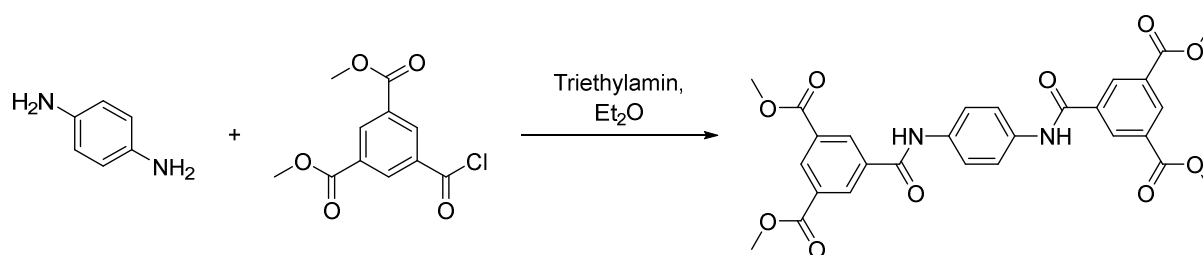


Abbildung 58. Reaktionsschema für die Synthese von Tetramethyl-5,5'-((1,4-phenylenbis(azanediyl))bis(carbonyl))diisophthalat.

Wie auch zuvor konnte das Produkt in guten Ausbeuten erhalten und mit den gängigen Methoden charakterisiert werden (Abbildung 59).

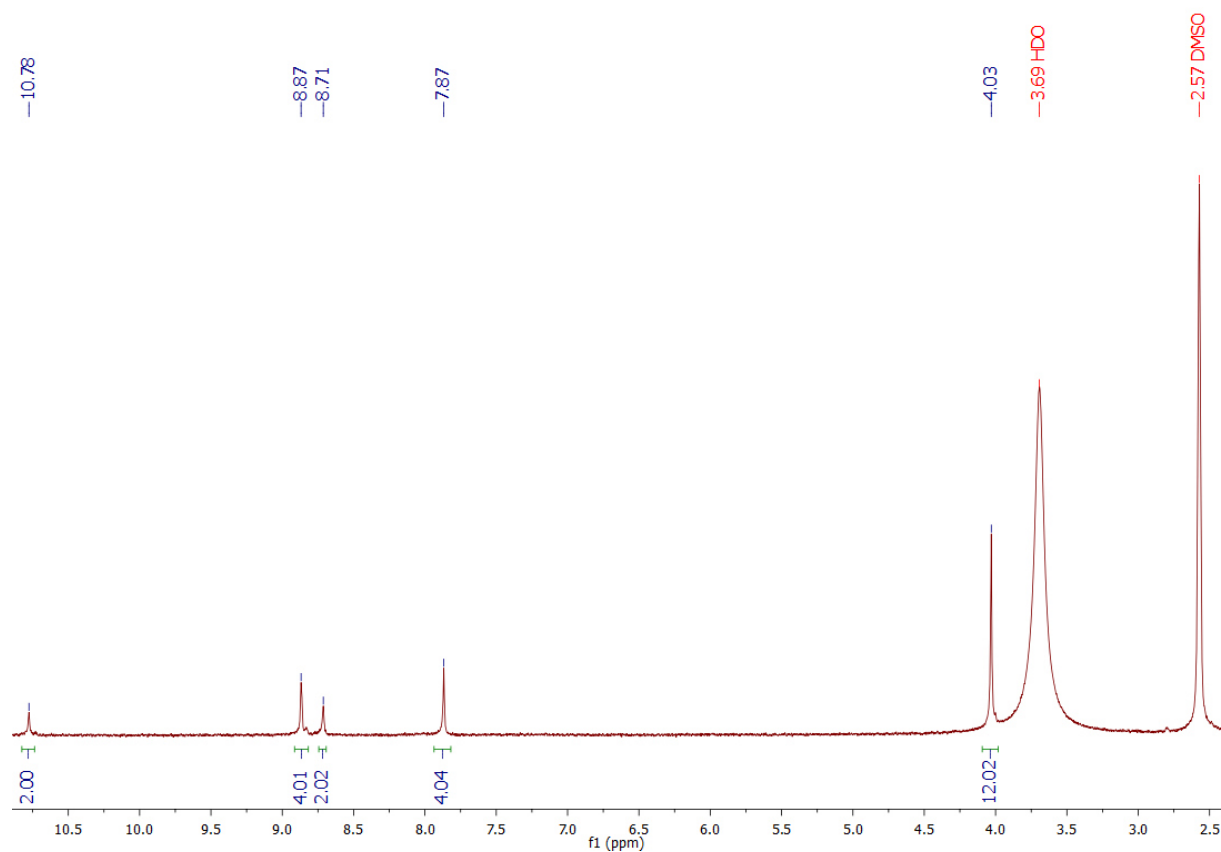


Abbildung 59.  $^1\text{H}$ -NMR-Spektrum von Tetramethyl-5,5'-((1,4-phenylenbis(azanediyl))bis(carbonyl))diisophthalat.

#### 4.4.3 Synthese von 5,5'-((1,4-Phenylenbis(azanediyl))bis(carbonyl))-diisophthalsäure

Im nächsten Schritt sollte Tetramethyl-5,5'-((1,4-phenylenbis(azanediyl))bis(carbonyl))diisophthalat zur 5,5'-((1,4-Phenylenbis(azanediyl))bis(carbonyl))diisophthalsäure verseift oder hydrolysiert werden. Dazu wurden zwei Reaktionen durchgeführt. In der ersten Reaktion wurde mit Kaliumhydroxid in Methanol gearbeitet, in der zweiten mit Schwefelsäure als Katalysator in Wasser (Abbildung 60).

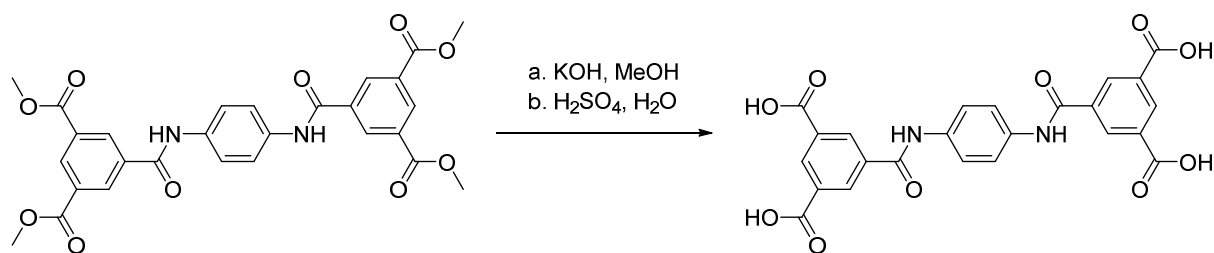


Abbildung 60. Reaktionsschema für die Synthese von 5,5'-((1,4-Phenylenbis(azanediyl))bis(carbonyl))diisophthalsäure über eine Verseifung (a.) und über Hydrolyse (b.).

Über  $^1\text{H-NMR}$ -Spektroskopie konnte dabei gezeigt werden, dass die Methylgruppen des Esters nach Beenden des Versuchs noch vorhanden sind. Des Weiteren ist bei der Verseifung ein neues Signal zu sehen, welches bei einer Verschiebung von 6,59 ppm dem von p-Phenyldiamin entspricht (Abbildung 61). Es kann also davon ausgegangen werden, dass die Amidgruppe zerstört wird, bevor der Ester verseift wird. Weitere Versuche wurden daher unterlassen.

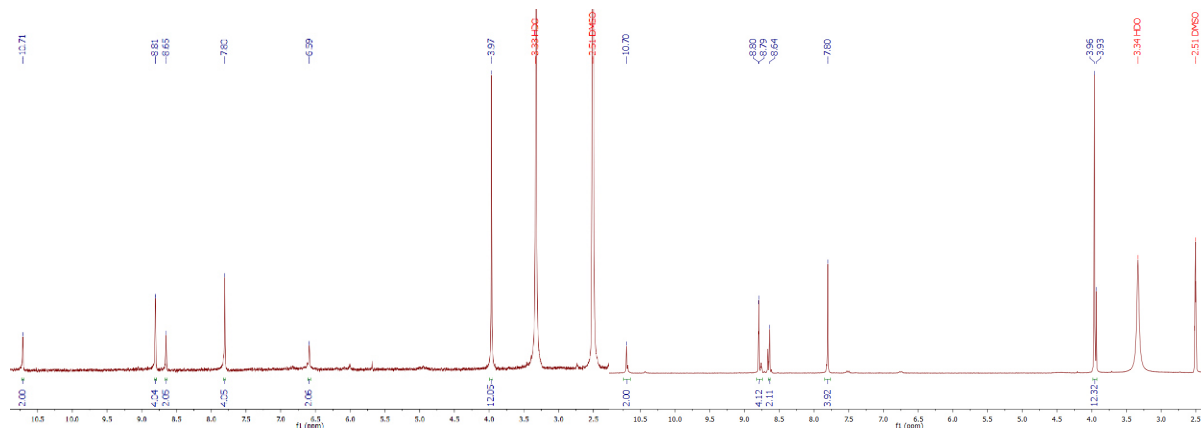


Abbildung 61.  $^1\text{H-NMR}$ -Spektren zur Verseifung (links) und Hydrolyse (rechts) von Tetramethyl-5,5'-((1,4-phenylenbis(azanediyl))bis(carbonyl))diisophthalat.

## 4.5 Sonstige Syntheseversuche neuer Amidliganden

### 4.5.1 Syntheseversuch von 5,5'-(Fumarylbis(azanediyl))diisophthalsäure

Ein weiterer neuer Ligand sollte aus der Reaktion zwischen Fumarylchlorid und 5-Aminoisophthalsäure entstehen. Das Fumarylchlorid sollte dabei *in-situ* erzeugt und direkt umgesetzt werden (Abbildung 62).

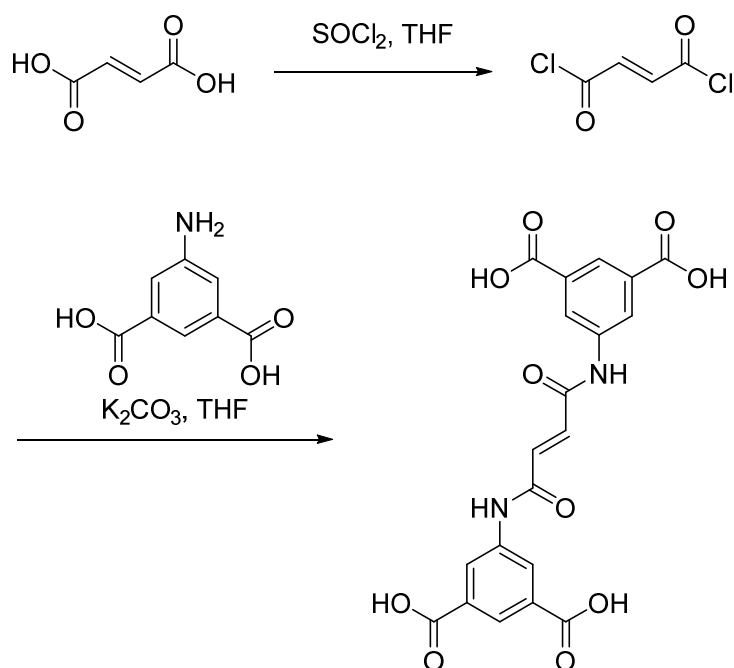


Abbildung 62. Synthese von 5,5'-(Fumarylbis(azanediyl))diisophthalsäure.

Im ersten Schritt wird dabei das Säurechlorid erzeugt und im zweiten Schritt mit einer Suspension aus Kaliumcarbonat und 5-Aminoisophthalsäure gequenchet. Die Reaktion zum gewünschten Produkt blieb dabei aus. Um sicherzustellen, dass sich Fumarylchlorid gebildet hat, wurde die Synthese erneut durchgeführt und nach dem ersten Schritt abgebrochen. Im <sup>1</sup>H-NMR-Spektrum ließ sich nur Fumarsäure feststellen. Es ist möglich, dass das Fumarylchlorid erst im deuterierten Lösemittel hydrolysiert ist; da die Reaktion zum Produkt allerdings nicht stattfand, wurde der Nachweis der Bildung des Fumarylchlorids als trivial eingestuft und die Reaktion nicht weiterverfolgt.

Des Weiteren wurde die Reaktion erneut und ebenfalls erfolglos in Toluol durchgeführt.

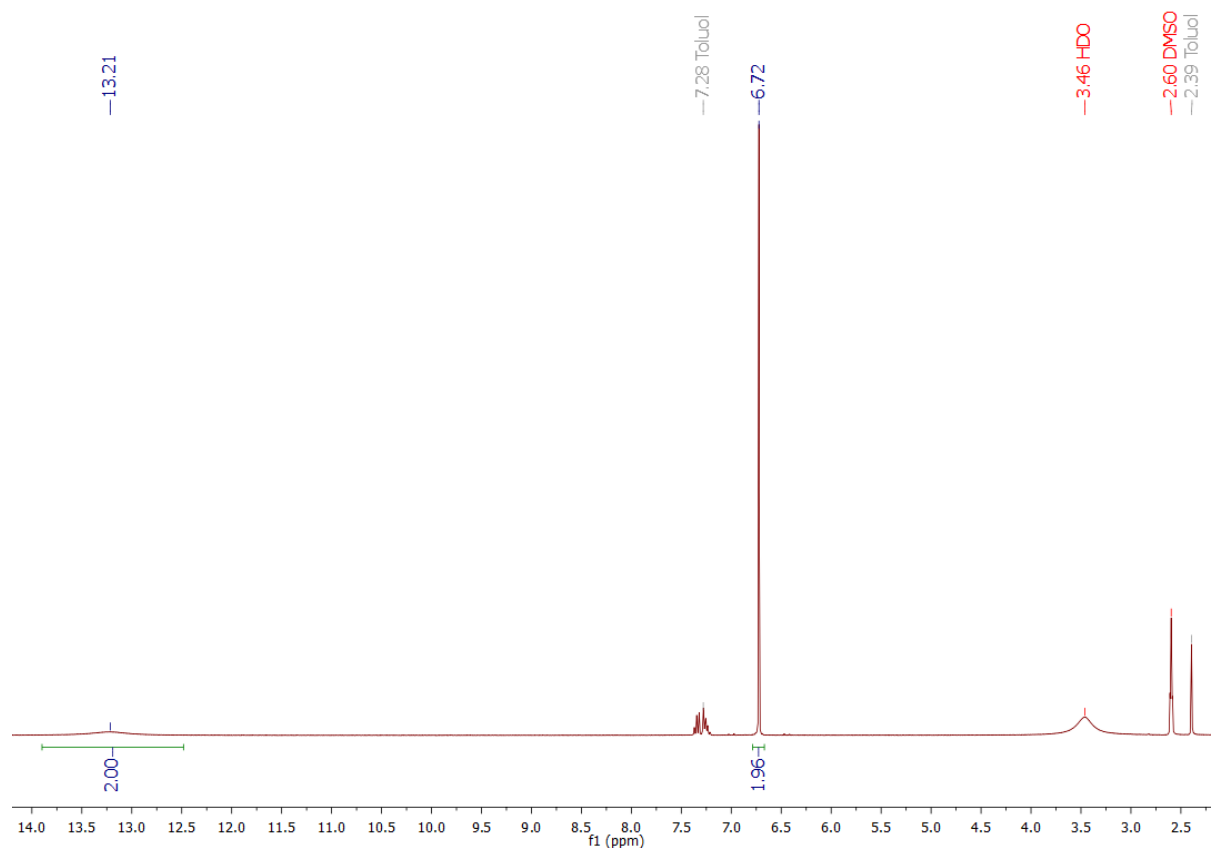


Abbildung 63. <sup>1</sup>H-NMR-Spektrum nach Abbruch der Synthese nach versuchter Erzeugung des Fumarylchlorids in Toluol. Es sind nur Signale der Fumarsäure zu sehen.

#### 4.5.2 Syntheseveruche von 3,3'-(Oxalylbis(azanediyl))dibenzoessäure und 4,4'-(Oxalylbis(azanediyl))dibenzoessäure

Die Reaktion von Oxalylchlorid mit 3- bzw. 4-Aminobenzoessäure sollte zwei weitere Liganden hervorbringen, welche für Koordinationsnetzwerke nutzbar sein sollten (Abbildung 64). Die in Toluol durchgeführte Reaktion verlief für beide Variationen allerdings ohne nennenswerte Ausbeute. Bei der Reaktion mit 3-Aminobenzoessäure ließ sich das Proton der Amidgruppe im <sup>1</sup>H-NMR-Spektrum noch nachweisen, das Produkt war allerdings stark verunreinigt, bei der Reaktion mit 4-Aminobenzoessäure waren nur die Edukte zu sehen (Abbildung 65, Abbildung 66). Das zweite Signal bei 9,93 ppm im Spektrum der Reaktion mit 3-Aminobenzoessäure lässt sich durch monosubstituiertes Oxalylchlorid erklären.

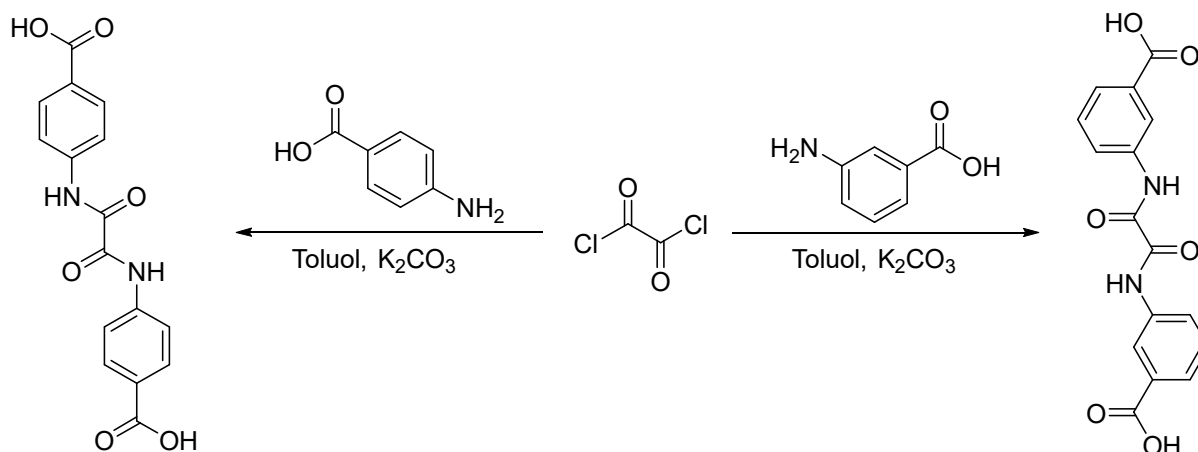


Abbildung 64. Reaktionsschema für die Synthesen von 3,3'-(Oxalylbis(azanediyl))dibenzoessäure und 4,4'-(Oxalylbis(azanediyl))dibenzoessäure aus Oxalylchlorid.

Die Protonen der Carbonsäure-Gruppen sind in keinem der beiden Spektren zu erkennen. Der hohe Anteil an Wasser im deuterierten DMSO, welches als Lösemittel für die NMR-Spektroskopie verwendet wurde, deprotoniert möglicherweise die Säuregruppen. Ein weiterer Hinweis darauf findet sich in der starken Verbreiterung der Wassersignale bei 3,3 ppm, was üblicherweise durch schnellen Protonenaustausch zwischen zwei chemisch unterschiedlichen Molekülen erklärt werden kann.<sup>54</sup>

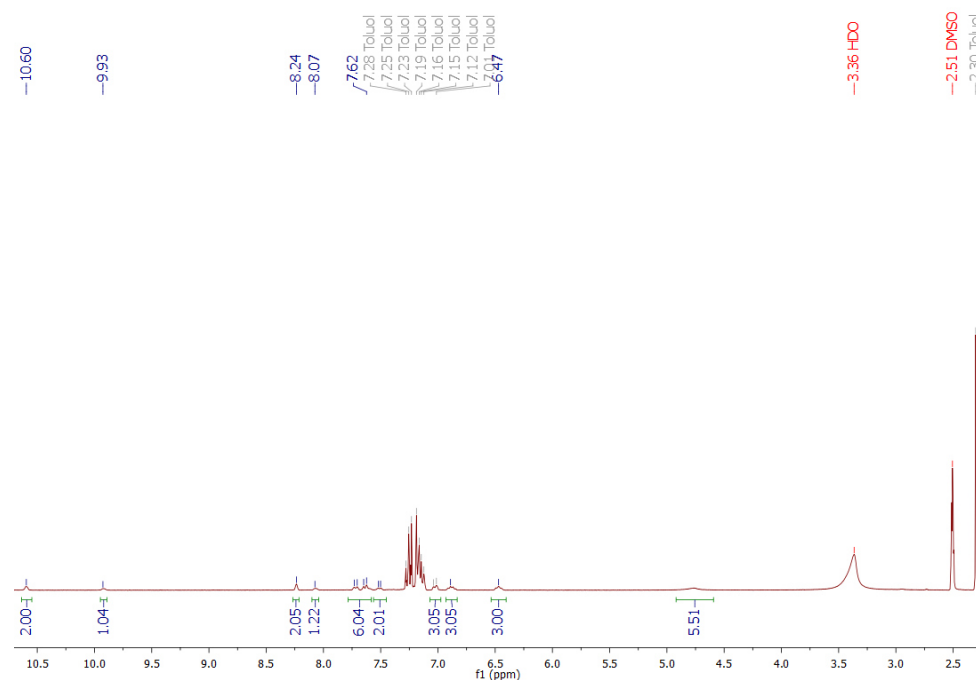


Abbildung 65. <sup>1</sup>H-NMR-Spektrum der Synthese von 3,3'-(Oxalylbis(azanediyl))dibenzoessäure. Bei 10,6 ppm ist das Signal der Amidprotonen

des Produktes zu sehen, bei 9,93 ppm das Amidproton des nur einfach mit 3-Aminobenzoessäure abreagierten Oxalylchlorids.

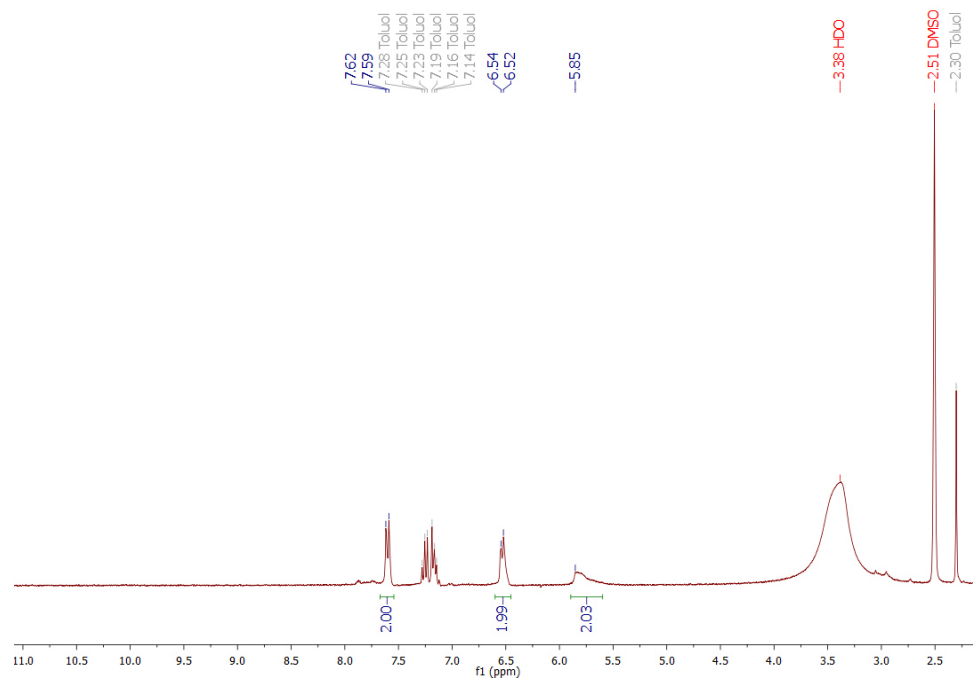


Abbildung 66.  $^1\text{H}$ -NMR-Spektrum der Synthese von 4,4'-(Oxalylbis(azanediyl))dibenzoessäure. Das Produkt liegt nicht vor.

## 4.6 Synthese neuer metall-organischer Gerüstverbindungen und Koordinationspolymere

### 4.6.1 Koordinationspolymere basierend auf 2,2',2''-((1,3,5-Triazin-2,4,6-triyl)tris(piperazin-4,1-diyl))triessigsäure.

Für die Synthese von Koordinationspolymeren basierend auf 2,2',2''-((1,3,5-Triazin-2,4,6-triyl)tris(piperazin-4,1-diyl))triessigsäure wurden verschiedene Ansätze unter variierenden Bedingungen verfolgt. Bei den Solvothermalsynthesen wurde für gewöhnlich Dimethylformamid als Lösemittel eingesetzt. Die Reaktionen wurden in Pyrex-Kulturröhrchen in niedrigen Konzentrationen durchgeführt, bei Temperaturen von 80–105 °C. Es wurden die Nitratsalze verschiedener Metalle verwendet, darunter Zn(II), Cu(II), Co(II), La(III), Fe(III) und Cr(III), und für mehrere Tage bei erhöhter Temperatur mit dem Liganden umgesetzt. Die Synthesen verliefen allesamt erfolglos. Bei vereinzelt Synthesen war das Ausfallen eines weißen Feststoffes zu beobachten,

welcher farblich allerdings nicht zu den erwarteten Koordinationsverbindungen passte und deshalb nicht weiter analysiert wurde.

Es wurden noch weitere Synthesen in einem Lösemittelgemisch aus Dimethylformamid und Wasser durchgeführt, welches schwach mit Salpetersäure angesäuert wurde, ebenfalls bei 80–105 °C. Hierbei wurden die Nitratsalze der Metalle Cu(II), Zn(II) und Cr(III) verwendet. Bei den Ansätzen mit Zn(II) konnte keine Kristall- oder Feststoffbildung beobachtet werden. Die Ansätze mit Cu(II) zeigten Niederschläge von rotem Kupfer(I)-oxid. Bei den Ansätzen mit Cr(III) fiel erneut der zuvor beobachtete weiße Feststoff aus.

Neben den solvothermalen Synthesen wurden auch noch Synthesen unter hydrothermalen Bedingungen durchgeführt. Diese wurden bei 130 °C im Autoklaven durchgeführt. Es wurden die Nitratsalze der Metalle Cu(II), Co(II), Cr(III) und Al(III) verwendet. Bei den Ansätzen mit Cr(III) war erneut ein weißer Feststoff zu beobachten.

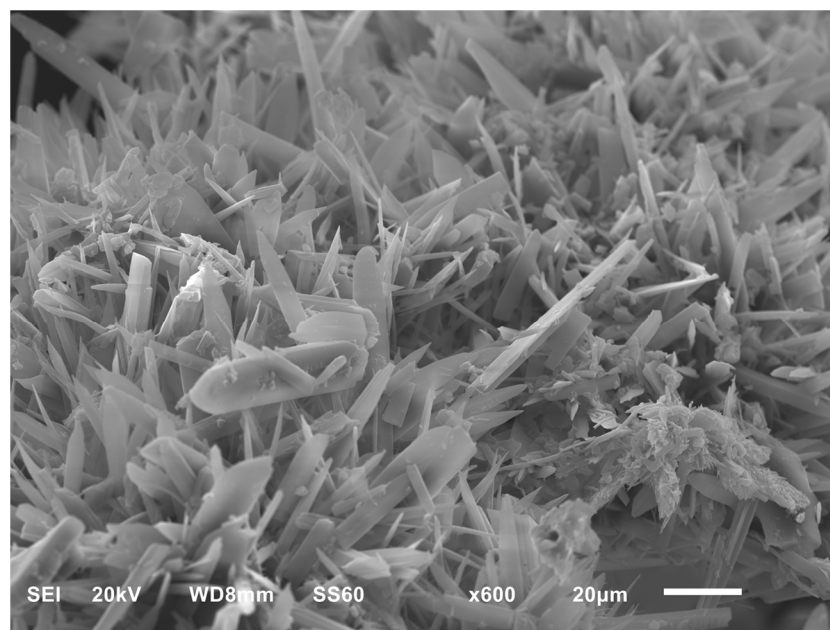


Abbildung 67. REM-Aufnahme des entstandenen Niederschlags der Synthese mit 2,2',2''-((1,3,5-Triazin-2,4,6-triyl)tris(piperazin-4,1-diyl))triessigsäure und Chrom(III)-nitrat.

Dieser wurde abzentrifugiert, der Überstand abdekantiert und der Feststoff erneut in Wasser suspendiert. Nach erneuter Zentrifugation und Abdekantieren des Wassers wurde der Feststoff getrocknet, um zu bestimmen, worum es sich bei dem Feststoff



handelt. Dazu wurden unter anderem Röntgenpulverdiffraktogramme sowie EDX-Analysen durchgeführt (

Abbildung 67, Tabelle 3).

Tabelle 3. EDX-Analyseergebnisse des entstandenen Niederschlags.

Element	Norm. At.% EDX-Analyse	Norm. At.% CNO aus EDX	Berechn. At.% Ligand	Berechn. At.% CNO (Ligand)
Kohlenstoff	66,64	67,89	49,70	53,18
Stickstoff	26,24	26,73	24,84	26,58
Sauerstoff	5,28	5,38	18,91	20,24
Gold	1,78			
Chrom	0,05			
Wasserstoff			6,55	

Die Ergebnisse der EDX-Analyse lassen darauf schließen, dass der Ligand decarboxyliert ist. Die gefundene Menge an Sauerstoff von nur 5,38 At.% liegt deutlich unter der erwarteten Menge von 20,24 At.%, während die Menge an Stickstoff trotz der relativ ungenauen Messmethode mit den berechneten Werten übereinstimmt. Die Menge an gefundenem Chrom in der Probe liegt im Bereich des Gerätefehlers. Die Eignung des Liganden für die Synthese von metall-organischen Koordinationsverbindungen, welche auf solvo- oder hydrothermale Wege hergestellt werden, könnte daher durch seine geringe Stabilität gegenüber der Zersetzung bei erhöhter Temperatur stark beeinträchtigt sein.

#### 4.6.2 Koordinationspolymere basierend auf *N,N'*-(4-Carboxyphenyl)-terephthalamid

Die Synthesen der MOFs mit *N,N'*-(4-Carboxyphenyl)terephthalamid als Liganden wurden unter ähnlichen Bedingungen durchgeführt wie die der bekannten IRMOF-Reihe, bei welcher ebenfalls lineare Carboxylatliganden eingesetzt werden.<sup>55</sup> Der Ligand wurde zusammen mit Zink(II)-nitrat in Dimethylformamid gelöst und auf 80 °C

temperiert, bis ein farbloser, kristalliner Niederschlag zu beobachten war. Der Niederschlag wurde noch in Mutterlauge im Röntgenpulverdiffraktometer vermessen (Abbildung 69). Das Diffraktogramm zweier verschiedener Ansätze stimmt dabei nicht dem des reinen Liganden überein. Da es die Möglichkeit gibt, dass der Ligand in Dimethylformamid nur umkristallisiert wird, benötigte es weiterer Analytik. Aus diesem Grund wurde die EDX-Analyse gewählt, um den Anteil an Zink im synthetisierten Material zu bestimmen (Tabelle 4). Die Werte für Zink in der EDX-Analyse entsprachen den Erwartungen. Es wurde demnach davon ausgegangen, dass erfolgreich ein kristallines Material synthetisiert wurde, welches Zink eingebaut hat. Bedingt durch die geringe Größe der Kristalle konnte keine Einkristallröntgenstrukturanalyse durchgeführt werden.

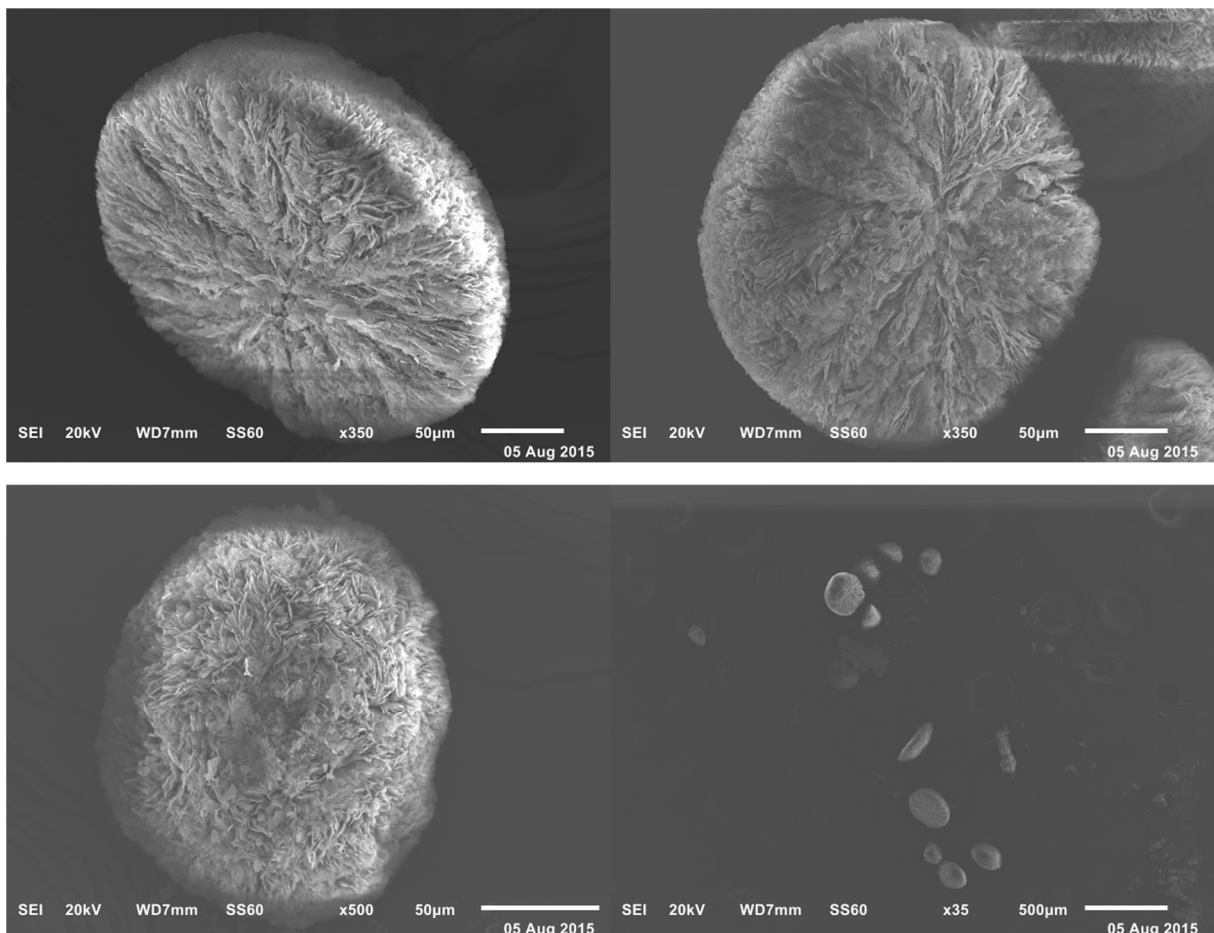


Abbildung 68. REM-Aufnahmen von Zn-*N,N'*-4CPTAm.

Es wurden verschiedene Methoden getestet, die Kristalle zu vergrößern, darunter Synthesen mit Modulatoren wie TMAOH oder Salpetersäure, sowie Änderungen der

Synthesemethode, z. B. über Konvektion, jedoch blieben eindeutige Verbesserungen aus. REM-Bilder lassen auf eine plättchenartige Struktur schließen, was die Schwierigkeiten bei der Synthese von für die Einkristallröntgenstrukturanalyse geeigneten Kristallen erklären könnte (Abbildung 68).

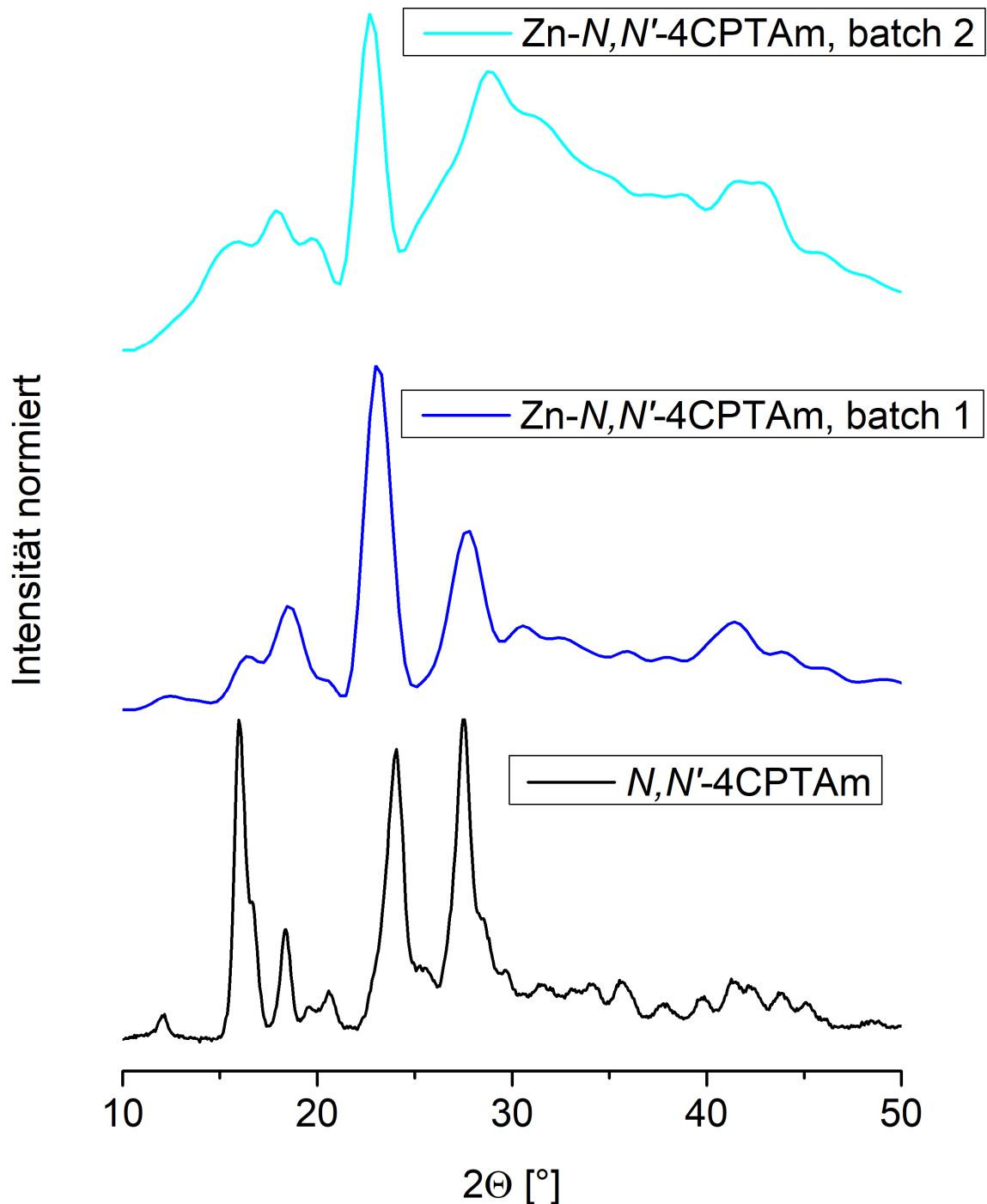


Abbildung 69. Röntgenpulverdiffraktogramme des Liganden  $N,N'$ -4CPTAm, sowie des Niederschlags zweier Synthesen mit dem Liganden und einem Zinksalz.

Tabelle 4. EDX-Analyseergebnisse von Zn-*N,N'*-4CPTAm.

Element	Normierte At.% aus EDX-Analyse	Berechnete At.% <sup>a</sup>
C	68,8	63,1
O	17,3	26,3
N	8,3	5,3
Zn	5,6	5,3

<sup>a</sup> Bei einem Metall:Ligand-Verhältnis von 2:1.

Ähnliche Ergebnisse konnten außerdem noch mit Kupfer erzielt werden. In der EDX-Analyse entsprachen die Ergebnisse erneut ungefähr den Erwartungen, in den Röntgenpulverdiffraktogrammen offenbarte sich ein kristalliner Feststoff, dessen Diffraktogramm sich von dem des Liganden unterscheidet (Tabelle 5, Abbildung 70). In den REM-Aufnahmen sieht man sphärische Partikel, welche teilweise als Hohlkörper erhalten werden (Abbildung 71).

Tabelle 5. EDX-Analyseergebnisse von Cu-*N,N'*-4CPTAm.

Element	Normierte At.% aus EDX-Analyse	Berechnete At.% <sup>a</sup>
C	76,5	63,1
O	12,0	26,3
N	6,9	5,3
Cu	4,6	5,3

<sup>a</sup> Bei einem Metall:Ligand-Verhältnis von 2:1.

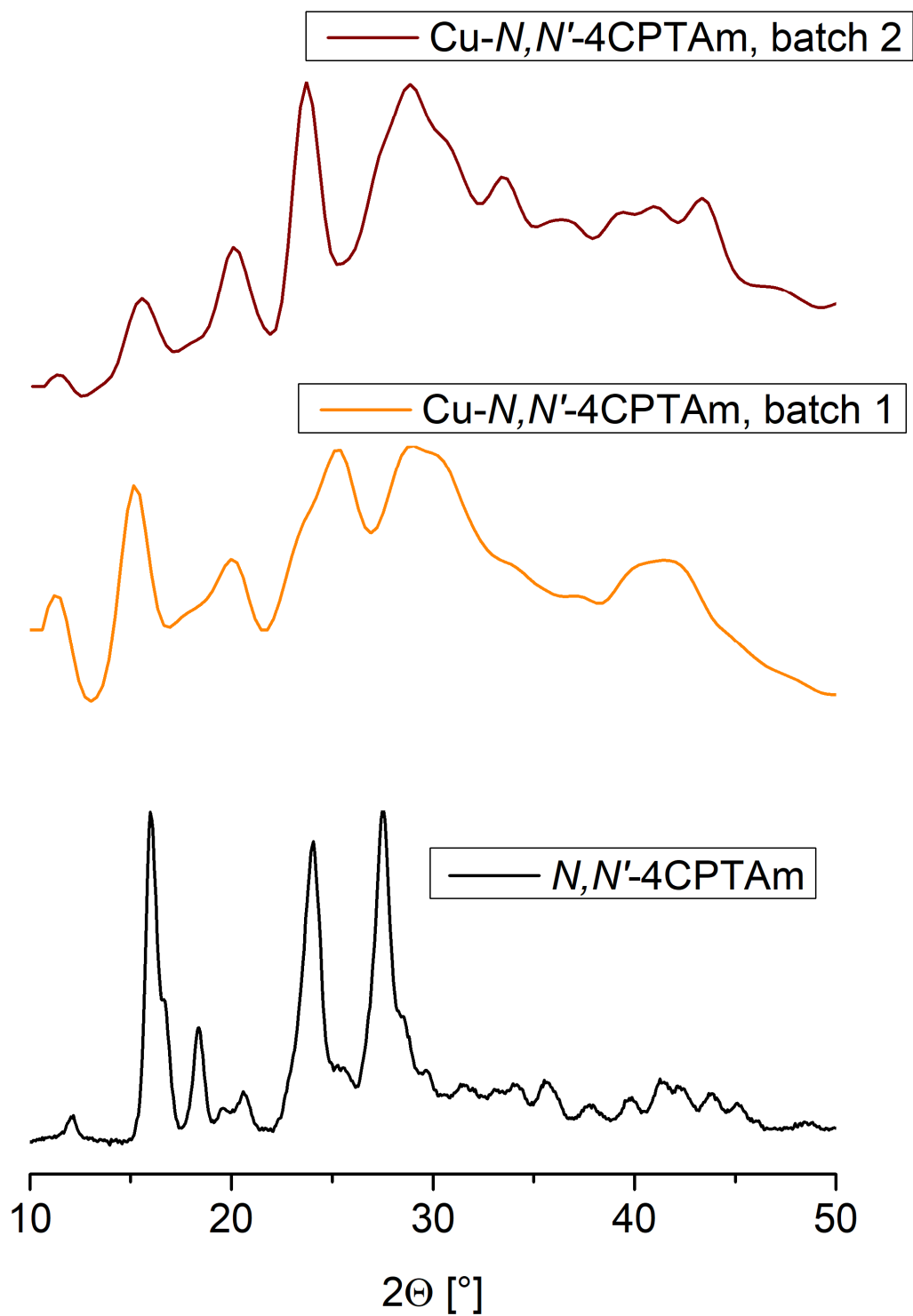
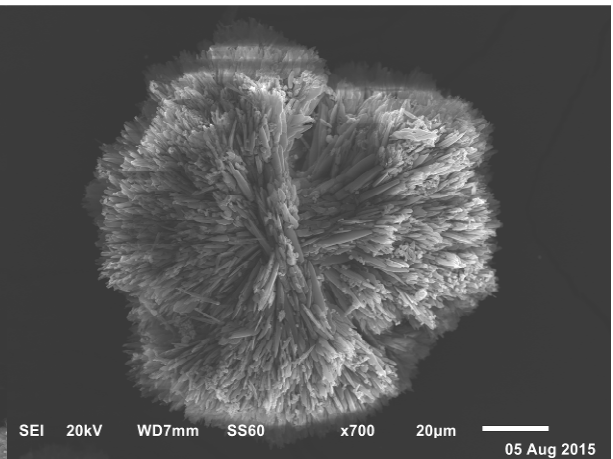
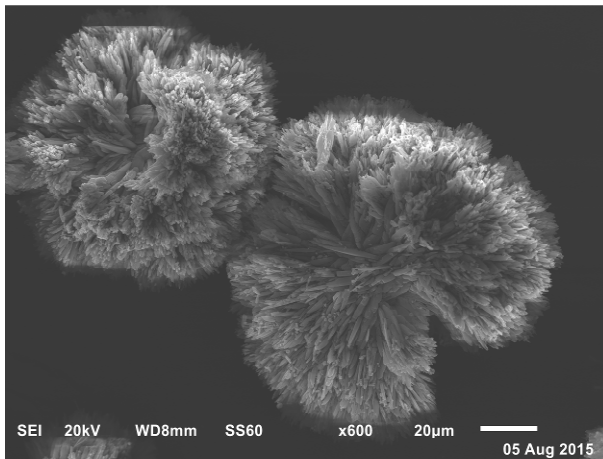
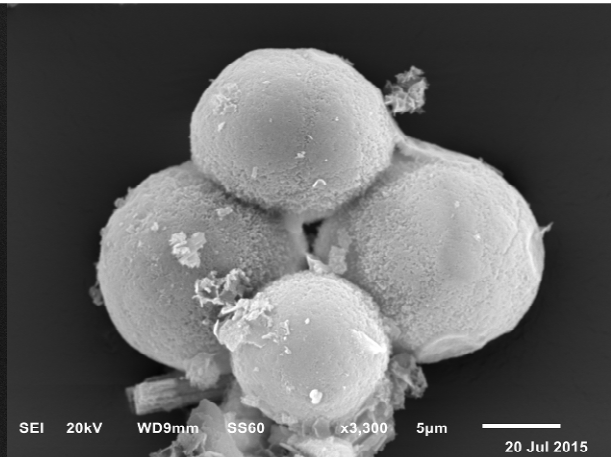
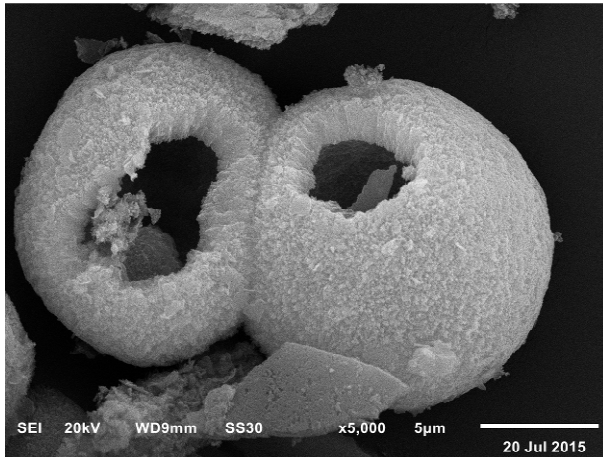
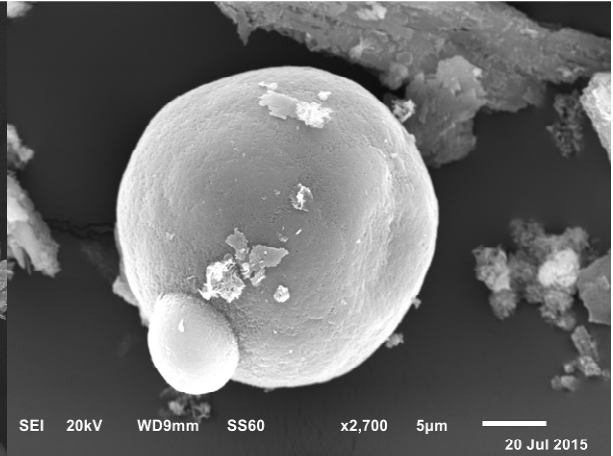
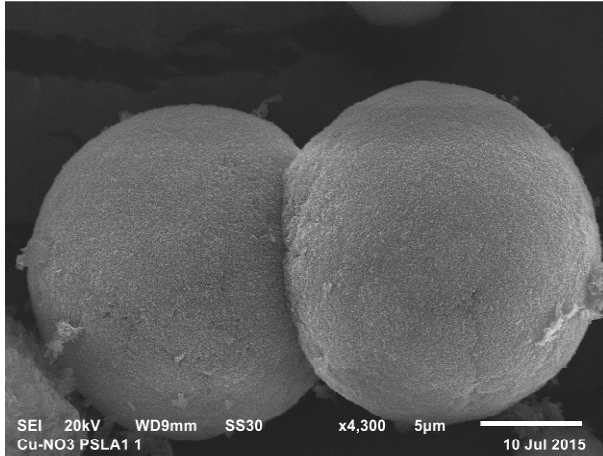


Abbildung 70. Röntgenpulverdiffraktogramme des Liganden *N,N'*-4CPTAm, sowie des Niederschlags zweier Synthesen mit dem Liganden und einem Kupfersalz.



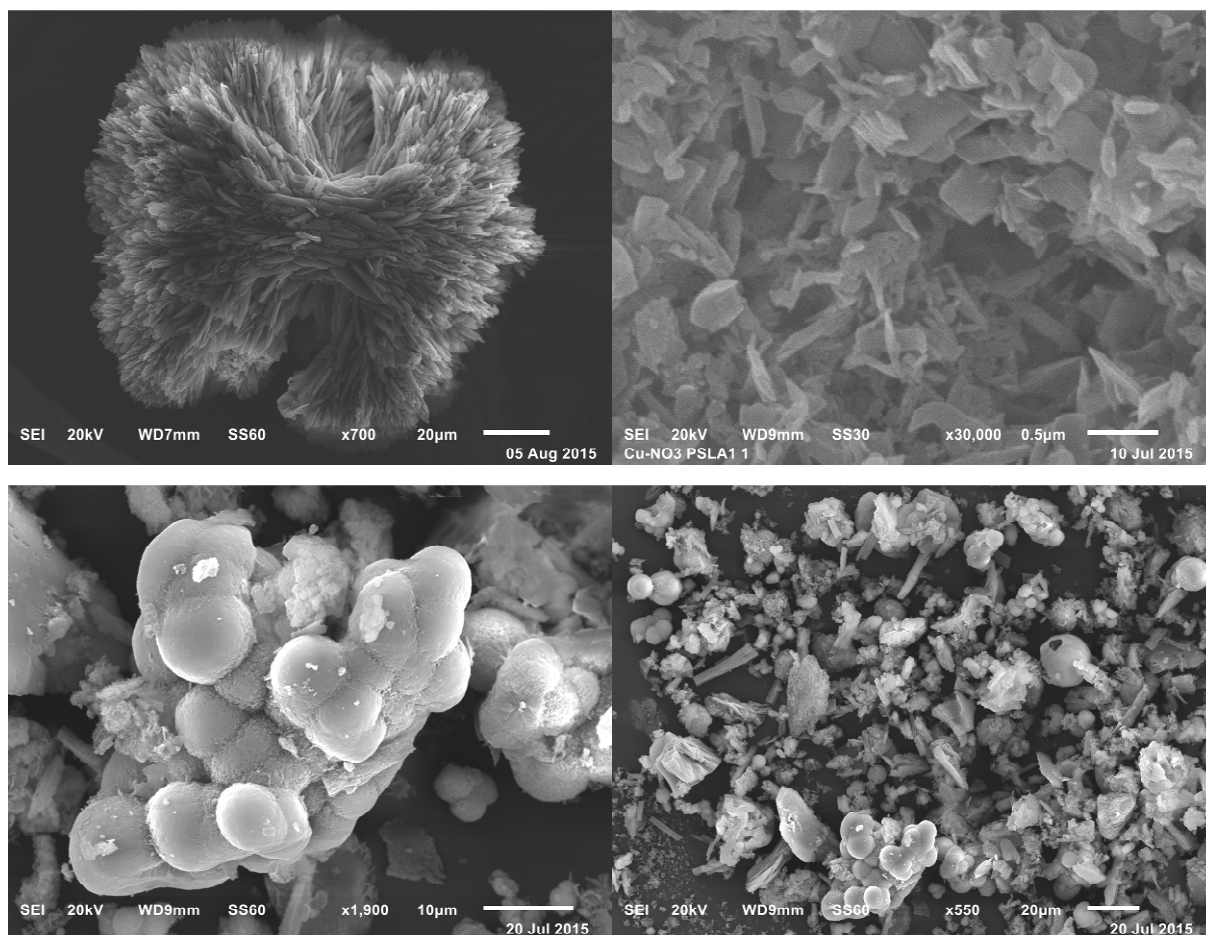


Abbildung 71. REM-Aufnahmen von Cu-*N,N'*-4CPTAm.

#### 4.6.3 Koordinationspolymere basierend auf *N,N'*-(3-Carboxyphenyl)terephthalamid

Analog zu den in 4.6.2 beschriebenen Koordinationspolymersynthesen wurden Synthesen mit dem Liganden *N,N'*-(3-Carboxyphenyl)terephthalamid durchgeführt. Auch bei diesen Synthesen waren kristalline Niederschläge zu beobachten, welche mittels Röntgenpulverdiffraktometrie und teilweise mit EDX-Analysen untersucht wurden.

In der Variante mit Zn(II) wurde dabei ein kristalliner, farbloser Feststoff erhalten. Im Röntgenpulverdiffraktogramm erkennt man ein von literaturbekannten Verbindungen sowie vom Liganden verschiedenes Diffraktogramm (Abbildung 72).

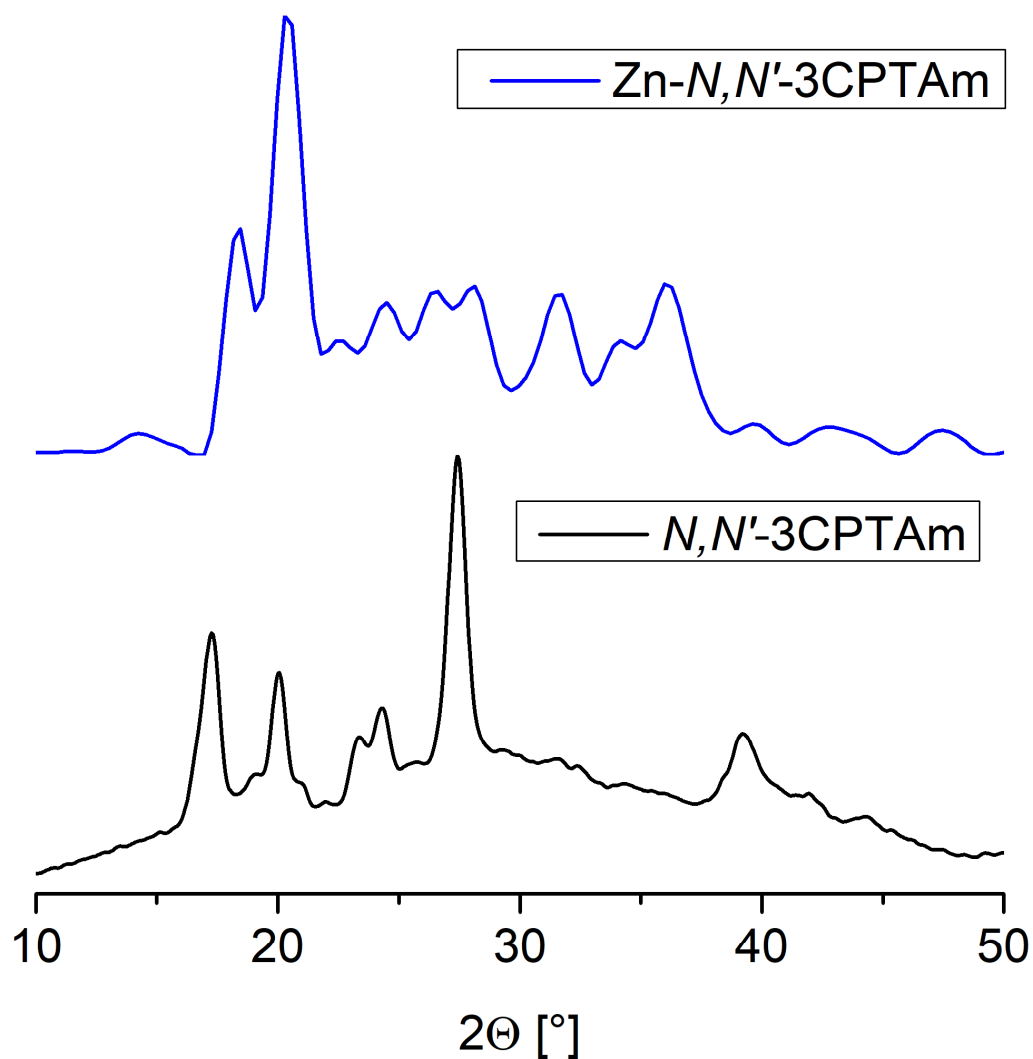


Abbildung 72. Röntgenpulverdiffraktogramme des Liganden *N,N'*-3CPTAm, sowie des Niederschlags einer Synthese mit dem Liganden und einem Zinksalz.

In einer Rasterelektronenmikroskopaufnahme erkennt man kleine, sphärische Partikel (Abbildung 73). Die dazugehörige EDX-Analyse wurde leider von meinem damaligen Bachelorstudenten verlegt.



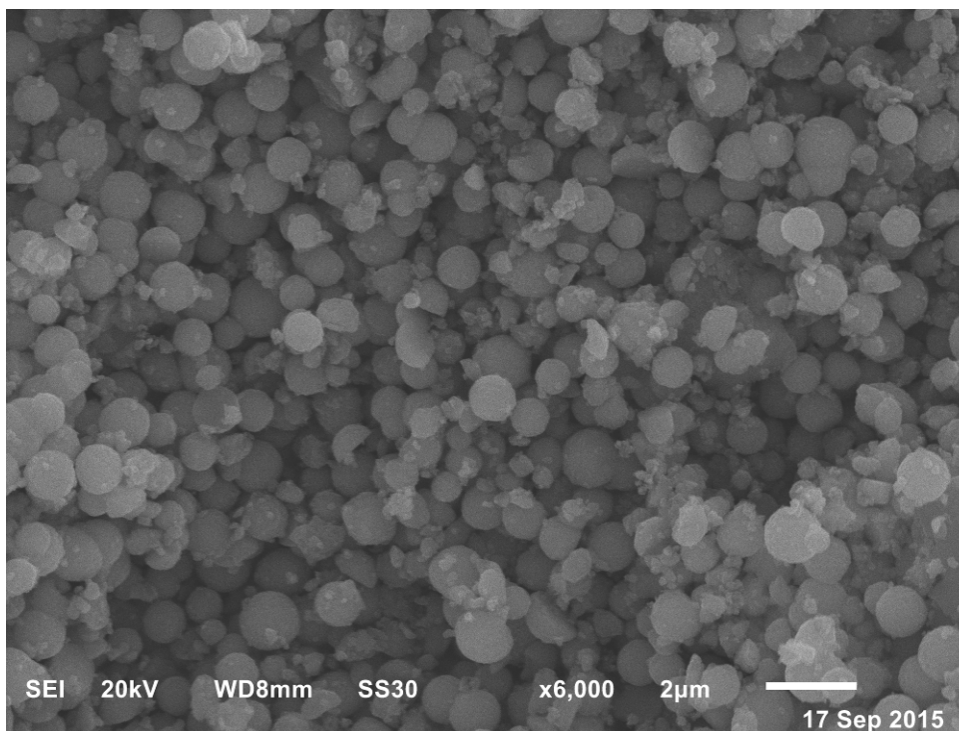


Abbildung 73. REM-Aufnahmen von Zn-*N,N'*-3CPTAm.

In der Variante mit Cu(II) wurde ein hellblauer Niederschlag erhalten. Die EDX-Analyse zeigte die Anwesenheit von Kupfer in den Erwartungen entsprechenden Mengen (Tabelle 6).

Tabelle 6. EDX-Analyseergebnisse von Cu-*N,N'*-3CPTAm.

Element	Normierte At.% aus EDX-Analyse (Ansatz 1; Ansatz 2; Ansatz 3)	Berechnete At.% <sup>a</sup>
C	78,0; 80,0; 71,2	63,1
O	11,7; 10,6; 17,4	26,3
N	5,0; 4,2; 5,9	5,3
Cu	5,3; 5,2; 5,5	5,3

<sup>a</sup> Bei einem Metall:Ligand-Verhältnis von 2:1.

Die Kristallinität wurde auch hier per Röntgenpulverdiffraktometrie erfasst und die entstandenen Spektren zeigten ein Material, welches von literaturbekannten Materialien sowie vom Liganden verschieden war (Abbildung 74).

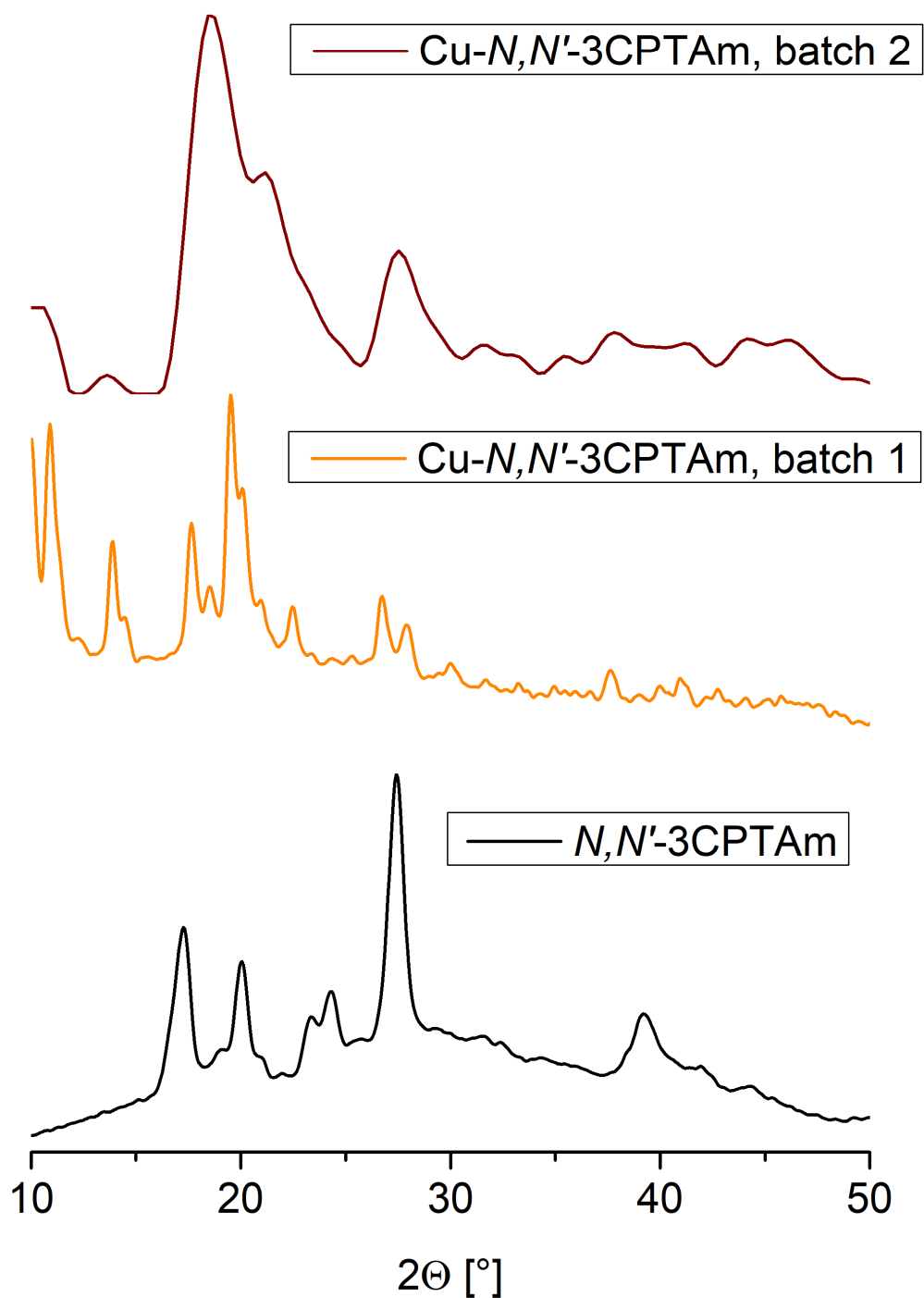


Abbildung 74. Röntgenpulverdiffraktogramme des Liganden  $N,N'$ -3CPTAm, sowie des Niederschlags einer Synthese mit dem Liganden und einem Kupfersalz.

In den Rasterelektronenmikroskopaufnahmen erkennt man größere, sphärische Partikel, welche aus Aggregationen kleiner Kristallite bestehen zu scheinen.

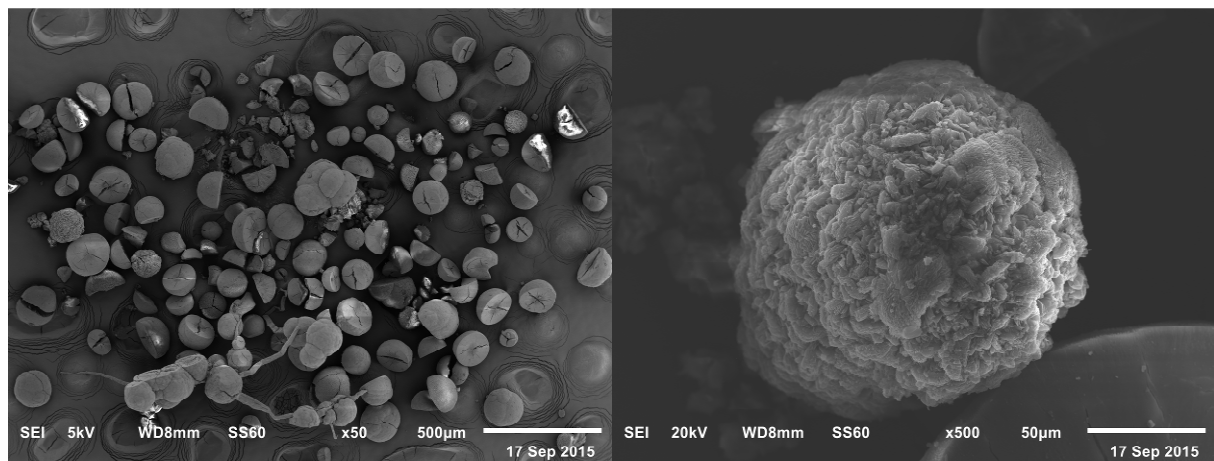


Abbildung 75. REM-Aufnahmen von Cu-*N,N'*-3CPTAm.

Die Versuche, größere Kristalle zu erhalten, um diese mittels Einkristallröntgenstrukturanalyse zu vermessen, schlugen sowohl für die Materialien mit Zn(II) sowie für die mit Cu(II) fehl.

## 5 ZUSAMMENFASSUNG UND AUSBLICK

---

Im Rahmen dieser Arbeit wurden neue Liganden zur Herstellung von metall-organischen Netzwerken und Gelen synthetisiert und charakterisiert. Diese neuen Liganden wurden im Anschluss zur Synthese neuer metall-organischer Koordinationsverbindungen und Hybridmaterialien verwendet. Die Koordinationsverbindungen und Hybridmaterialien durchliefen Untersuchungen, bei welchen, abhängig vom Material, die Porosität und Viskosität untersucht wurde.

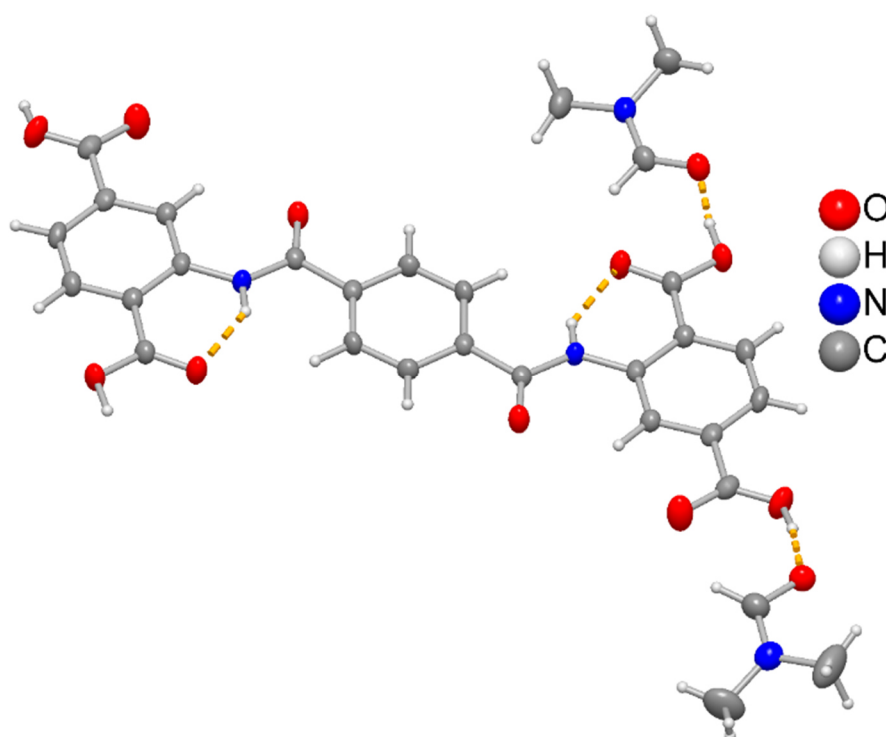


Abbildung 76. Struktur des Liganden  $H_4L1 \cdot 4DMF$ , mit zweien der vier wasserstoffverbrückten DMF-Moleküle (70% thermische Auslenkung, H-Atome mit arbiträren Radii). Die gelöste Fehlordnung der DMF-Moleküle ist nicht gezeigt. CCDC No. 1889949.

Vom Liganden  $N^1, N^4$ -(Diterephthalsäure)terephthalamid ( $H_4L1$ ,  $H_4Ditatam$ , Abbildung 76) wurden in Kombinationen mit Chrom(III), Eisen(III), Cobalt(III), Indium(III), Hg(II) und Al(III) neue metall-organische Gele (Metallogele) synthetisiert. Vom Cr-Metallogel konnten die abgeleiteten Aero- sowie Xerogele synthetisiert werden,

vom Al-Metallogel sowie von einem AlCr-Metallogel, welches beide Metallionen enthält, die Aerogele.



Abbildung 77. Links: Die Metallogele (v. l. n. r.) Cr-, AlCr-, Al-, Fe-, In-, Co-L1. Mitte: Cr-, AlCr-, Al-Aerogele, Cr-Xerogel. Rechts: Cr-, AlCr-, Al-Metallogel aus ihren Gefäßen entnommen. Die gute Formstabilität des Cr-Metallogels sorgt dafür, dass die zylindrische Form erhalten bleibt.

Im Metallogel-Zustand wurden die Rheologie des Cr-Metallogels sowie die Aufnahme verschiedener Farbstoffe der Cr- und AlCr-Metallogele untersucht. Der Speichermodul des Cr-Metallogels betrug dabei 1440 Pa, das Metallogel blieb elastisch bis zu 3 Hz und wurde bei Scherdeformationen über 0,3% zerstört. Die Farbstoffaufnahme war selektiv, und die Metallogele nahmen bevorzugt den krebserregenden Farbstoff Fuchsin auf. Die beiden anderen Farbstoffe, Calcein und Disulfinblau VN150, wurden ebenfalls aufgenommen, aber in geringerer Kapazität.

Von den Aero- und Xerogelen wurden Sorptionsisothermen bestimmt, um die Oberfläche und Porengrößenverteilung zu bestimmen (Abbildung 78). Die Ergebnisse sind in Tabelle 7 zusammengefasst.

Tabelle 7. BET-Oberflächen und Porenvolumina der Aero- und Xerogele aus Ar, N<sub>2</sub> und CO<sub>2</sub>-Sorptionsisothermen.

Verbindung	S <sub>BET</sub> , Ar at 87 K [m <sup>2</sup> g <sup>-1</sup> ] <sup>a</sup>	S <sub>BET</sub> , N <sub>2</sub> at 77 K [m <sup>2</sup> g <sup>-1</sup> ] <sup>b</sup>	V <sub>tot.</sub> (Ar) [cm <sup>3</sup> g <sup>-1</sup> ] <sup>c</sup>	V <sub>tot.</sub> (N <sub>2</sub> ) [cm <sup>3</sup> g <sup>-1</sup> ] <sup>d</sup>	V <sub>micro.</sub> (CO <sub>2</sub> ) [cm <sup>3</sup> g <sup>-1</sup> ] <sup>e</sup>
<b>Cr-L1</b> Aerogel	609	860	1.90	1.58	0.049
<b>Cr-L1</b> Xerogel	604	503	1.20	1.44	0.030

<b>AlCr-L1</b> Aerogel	441	480	0.69	1.21	0.036
<b>Al-L1</b> Aerogel	479	523	1.01	1.82	0.044

<sup>a</sup> BET-Oberflächen bestimmt bei  $0,08-0,25 p/p_0$ . <sup>b</sup> BET-Oberflächen bestimmt bei  $0,10-0,20 p/p_0$ . <sup>c,d</sup> Porenvolumen bei  $p/p_0 = 0,95$  für Poren  $\leq 20$  nm. <sup>e</sup> Porenvolumen für Poren  $\leq 1$  nm (10 Å) aus DFT-Rechnungen mit einem „CO<sub>2</sub> auf Kohle, Schlitzporen“-Modell bei 273 K.

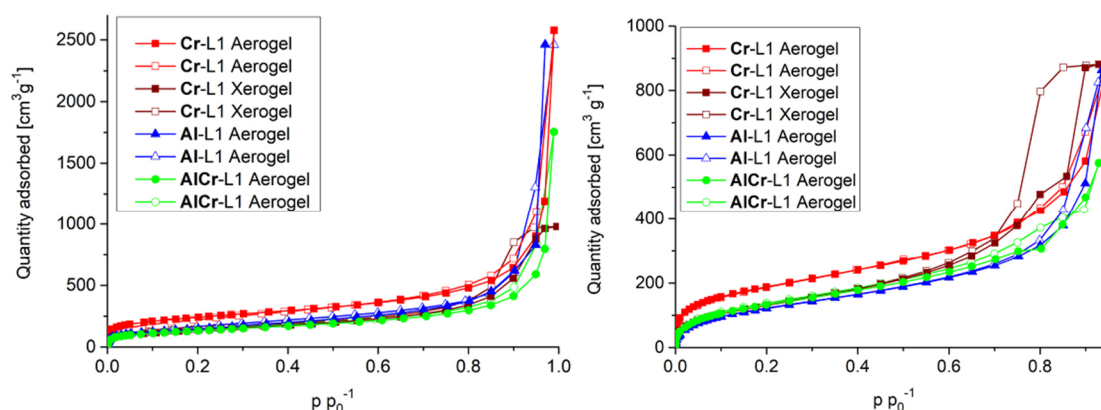


Abbildung 78. Adsorptions- (gefüllte Symbole) und Desorptionsisothermen (leere Symbole) der Aero- und Xerogele, links für Stickstoff bei 77 K, rechts für Argon bei 87 K.

Zusammen mit Daten aus Physisorptionsisothermen von CO<sub>2</sub>, SO<sub>2</sub> und H<sub>2</sub>O bei verschiedenen Temperaturen wurden Gleichgewichtsdaten errechnet, um anschließend die maximale Aufnahmekapazität von SO<sub>2</sub> und CO<sub>2</sub> bei erhöhter Temperatur zu bestimmen sowie Durchbruchkurven zu simulieren. Es konnte gezeigt werden, dass die hier synthetisierten Aero- und Xerogele die aktuellen Spitzenreiter für die SO<sub>2</sub>-Aufnahme unter den Aerogelen und vielversprechende Materialien für SO<sub>2</sub>-Gastrennung sind.

Mit dem Liganden H<sub>4</sub>L1 konnten außerdem noch kristalline Feststoffe mit den Metallen Zn(II), Ni(II), Cu(I) und Cu(II) erhalten werden, welche aber in ihrer Größe nicht ausreichend für die Einkristallstrukturanalyse waren.

Des Weiteren wurde als Teil dieser Arbeit die erste erfolgreiche Einbettung von lumineszenten, feuchtigkeitsempfindlichen metall-organischen Netzwerken (MOFs) in Polymeren dargestellt. Dabei wurde eine Kammer entwickelt, welche unter inerten Bedingungen die Möglichkeit zur Herstellung sowie Trocknung der Mixed-Matrix-Membranen ermöglicht und die Einbettung der MOFs in das Polymer mittels Rasterelektronenmikroskopie nachgewiesen. Weitere Experimente mit ähnlichen Materialien haben gezeigt, dass das Polymer das MOF gegenüber Hydrolyse schützt und somit die Lumineszenzhalbwertszeit verlängert, und dass die Zerstörung des MOFs durch Feuchtigkeit keinen Einfluss auf die Permeabilität der Mixed-Matrix-Membran hat. Die Defektfreiheit der Membranen wurde unter Zuhilfenahme des Maxwell-Modells ebenfalls bewiesen.

Anteilig an anderen Arbeiten wurden außerdem diverse Rasterelektronenmikroskopaufnahmen und EDX-Analysen angefertigt und ausgewertet, sowie die Digitalisierung einiger Messgeräte vorangetrieben.

Neben dem oben erwähnten Liganden H<sub>4</sub>L1 konnten noch weitere potenzielle Liganden synthetisiert werden. Dazu gehören einmal die Ligandenvorstufen, welche als Carbonsäuremethylester vorliegen und noch eine Verseifung oder Hydrolyse davon entfernt sind, um als tatsächliche Liganden eingesetzt zu werden (Abbildung 79), sowie die Liganden, welche bereits als Carbonsäuren vorliegen und auf die Möglichkeit der Bildung von metall-organischen Netzwerken untersucht wurden (Abbildung 80). Die Liganden, welche Amidgruppen enthalten, wurden dabei auf eine sehr kostensparsame Weise und zumeist ähnlich wie H<sub>4</sub>L1 synthetisiert. So konnte z. B. der literaturbekannte Ligand *N,N'*-(3,5-Dicarboxyphenyl)terephthalamid in Wasser mit Kaliumcarbonat als Base synthetisiert werden, im Gegensatz zu den in der Literatur verwendeten Lösungsmitteln *N,N*-Dimethylacetamid und 4-Dimethylaminopyridin.

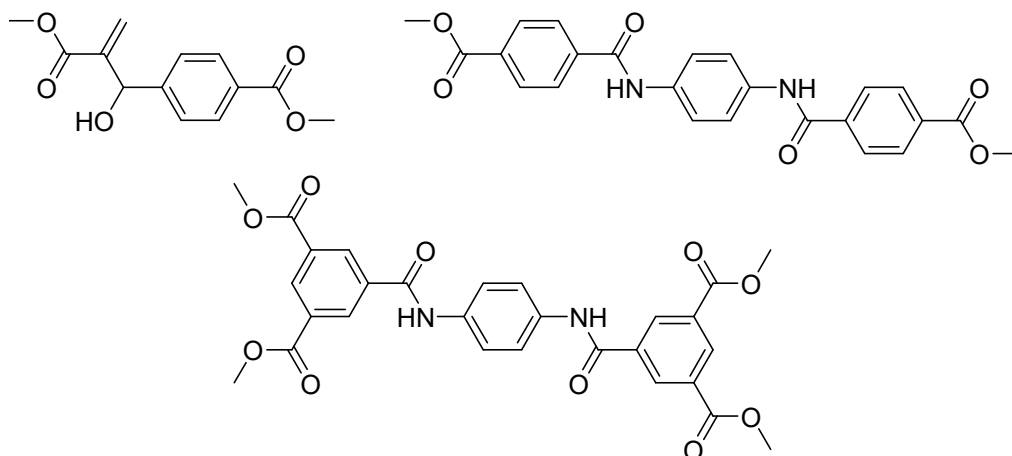


Abbildung 79. Mit Methylgruppen geschützte Ligandenvorstufen. Oben links: Methyl-4-(1-hydroxy-2-(methoxycarbonyl)allyl)benzoat. Oben rechts: Dimethyl-4,4'-((1,4-phenylenbis(azanediyl))bis(carbonyl))dibenzoat. Unten:  $N,N'$ -(3,5-Dicarboxyphenyl)terephthalamid.

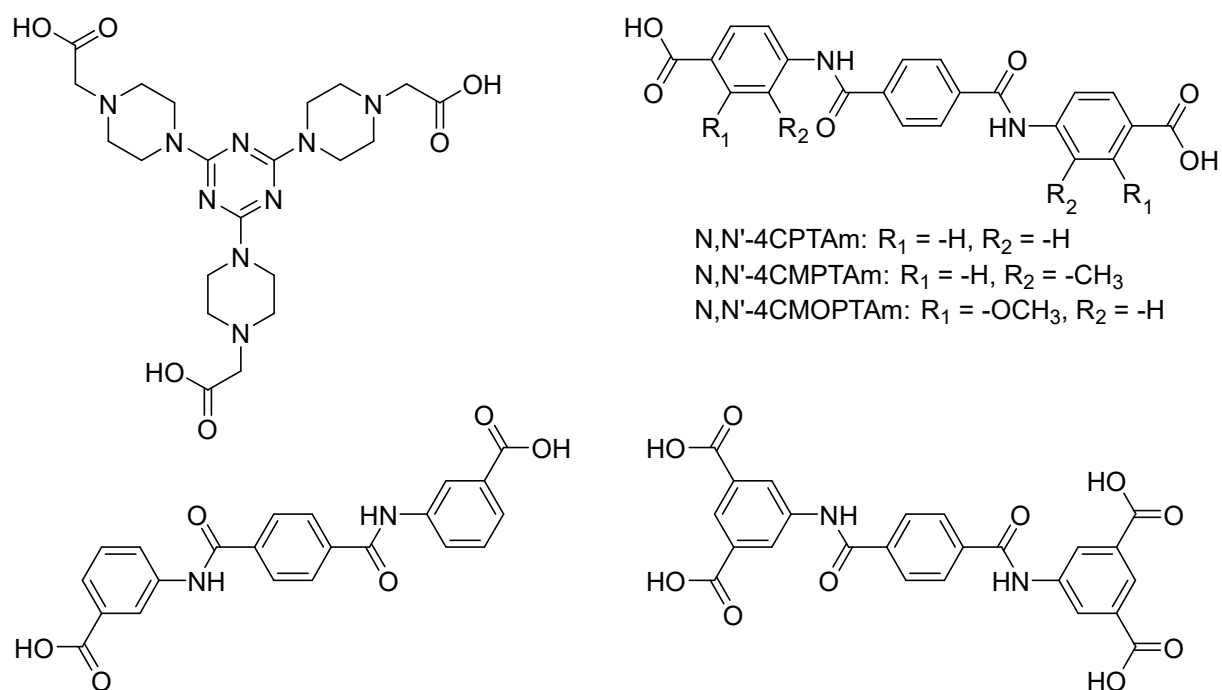


Abbildung 80. Synthetisierte, potenzielle Liganden. Oben links: 2,2',2''-(((1,3,5-Triazin-2,4,6-triyl)tris(piperazin-4,1-diyl))triessigsäure. Oben rechts:  $N,N'$ -(4-Carboxyphenyl)terephthalamid und zwei der erfolgreich synthetisierten Derivate. Unten links:  $N,N'$ -(3-Carboxyphenyl)terephthalamid. Unten rechts: Der literaturbekannte Ligand  $N,N'$ -(3,5-Dicarboxyphenyl)terephthalamid.



Die Liganden, welche als Carbonsäuren vorlagen, wurden zur Synthese neuer metallorganischer Gerüstverbindungen eingesetzt. Dabei zeigte sich, dass sich mit 2,2',2''-((1,3,5-Triazin-2,4,6-triyl)tris(piperazin-4,1-diyl))trissäure keine neuen Materialien herstellen lassen. Mit *N,N'*-(4-Carboxyphenyl)terephthalamid (*N,N'*-4CPTAm) ließen sich zwei neue Materialien mit Zn(II) und Cu(II) als Metallionen synthetisieren (Abbildung 81).

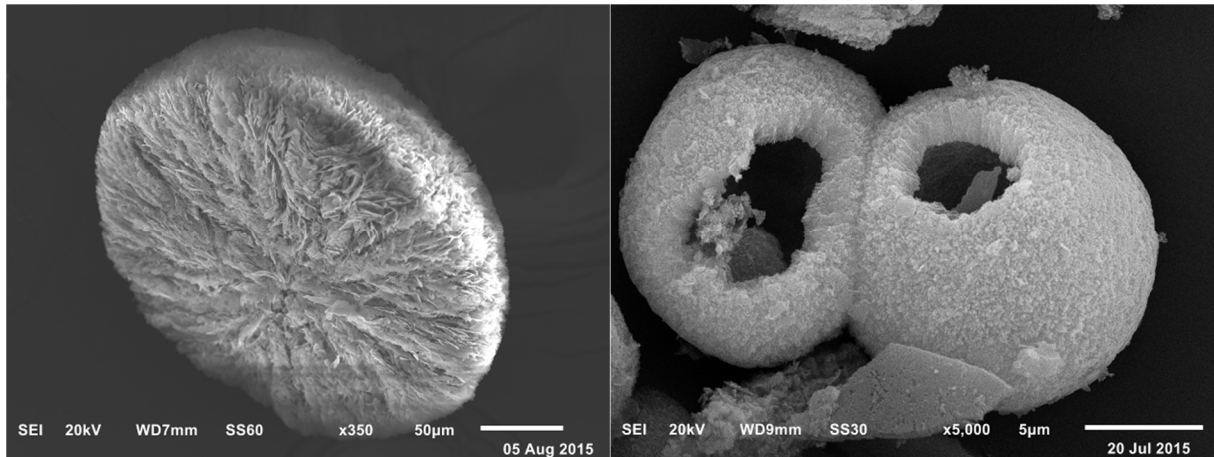


Abbildung 81. Rasterelektronenmikroskopaufnahmen von Zn-*N,N'*-4CPTAm (links) und Cu-*N,N'*-4CPTAm (rechts).

Mit *N,N'*-(3-Carboxyphenyl)terephthalamid (*N,N'*-3CPTAm) ließen sich ebenfalls zwei neue Materialien mit Zn(II) und Cu(II) als Metallionen synthetisieren (Abbildung 82).

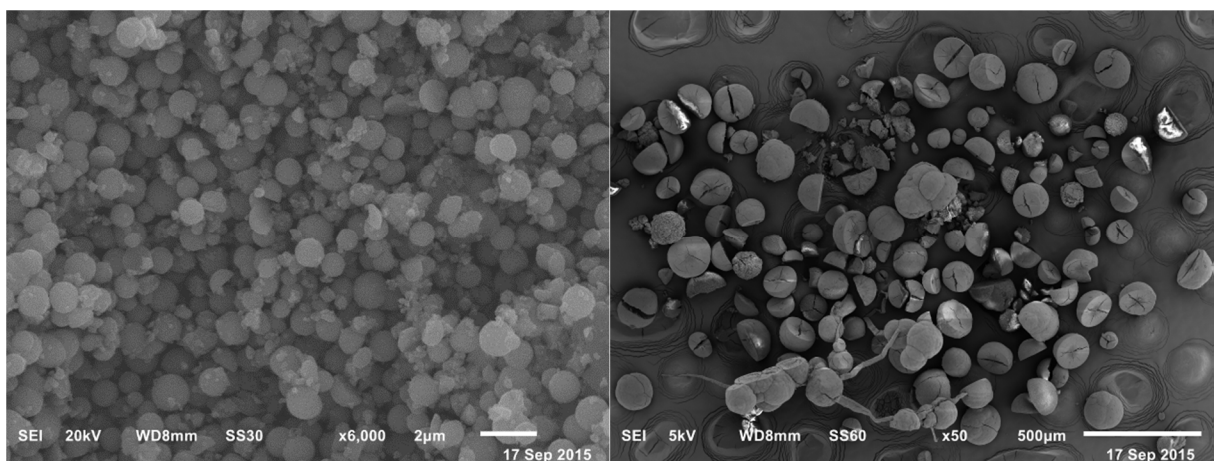


Abbildung 82. Rasterelektronenmikroskopaufnahmen von Zn-*N,N'*-3CPTAm (links) und Cu-*N,N'*-3CPTAm (rechts).

Da  $N,N'$ -(3,5-Dicarboxyphenyl)terephthalamid bereits in der Literatur bekannt ist, wurden hier keine Versuche zur Synthese von metall-organischen Gerüstverbindungen unternommen.

Da die Strukturaufklärung der Metallo-, Aero- und Xerogele sich als schwierig gestalten könnte, ließen sich in Zukunft nur noch die Synthesen der metall-organischen Gerüstverbindungen mit Co(III) und Zn(II) verbessern. Die möglicherweise daraus resultierenden Daten könnten anschließend zur Aufklärung der Gelstrukturen herangezogen werden. Allerdings lässt sich dazu sagen, dass bereits eine große Bandbreite an Bedingungen und Synthesemethoden durchprobiert wurde, weshalb es durchaus möglich ist, dass sich die Qualität und Größe der entstandenen kristallinen Verbindungen nicht weiter verbessern lässt.

Die Liganden  $N,N'$ -4CPTAm und  $N,N'$ -3CPTAm sollten noch weiter bearbeitet werden, da mit beiden Liganden vielversprechende Verbindungen mit Zn(II) und Cu(II) erhalten werden konnten. Die Probleme liegen hier in erster Linie in der Löslichkeit der Liganden in bestimmten Lösungsmitteln, welches die Zugänglichkeit zu einigen Synthesen erschwert.

Die Verseifung der noch geschützten Ligandenvorstufen ist ebenfalls noch eine Möglichkeit, neue Liganden für die Synthese von metall-organischen Gerüstverbindungen zu erhalten. Hierbei wären Synthesen unter milderer Bedingungen als den bereits getesteten zu empfehlen, da diese teilweise die Amidgruppen zerstört haben. Der Ligand Methyl-4-(1-hydroxy-2-(methoxycarbonyl)allyl)benzoat kann vernachlässigt werden, da sich die vorhandene terminale Doppelbindung höchstwahrscheinlich als zu reaktiv für die weitere Synthese erweisen wird. Auch ist die Stereochemie dieser Ligandenvorstufe ungeklärt und könnte die Synthese der metall-organischen Gerüstverbindungen erschweren. Bei einer erfolgreichen Synthese wiederum wären neue, stereoisomere MOFs vorstellbar.

## 6 EXPERIMENTELLER TEIL

---

### 6.1 Veresterung von para-Terephthalaldehydsäure

In einem 250 mL-Einhalskolben werden 5,1 g (34 mmol) p-Terephthalaldehydsäure (p-Ts) und 4,7 g (34 mmol) Kaliumcarbonat in 110 mL DMF vorgelegt. Der Kolben wird mit einem Septum verschlossen und es wird für 10 Minuten gerührt. Anschließend werden über eine Spritze 2,5 mL (40 mmol) Methyljodid langsam hinzugegossen. Nach 16–24 Stunden Rührzeit bei Raumtemperatur wird die Reaktionslösung in 250 mL Wasser gegeben. Es wird zwei Mal mit 200 mL EE extrahiert, die organischen Phasen werden gesammelt und über Natriumsulfat getrocknet. Das Natriumsulfat wird abfiltriert und das Filtrat am Rotationsverdampfer eingedunstet. Nach abschließender Hochvakuumtrocknung konnten 4,91 g (30,0 mmol) Methyl-4-formylbenzoat erhalten werden.

Ausbeute: 88% bezogen auf p-Ts.

$^1\text{H-NMR}$  (300 MHz,  $\text{DMSO-}d_6$ ):  $\delta = 10,41$  (s, -CHO), 8,15 (ddd,  $J = 1,71, 8,19, 2 = \text{CH-}$ ), 8,04 (ddd,  $J = 0,64, 1,27, 8,59, 2 = \text{CH-}$ ), 3,9 (s, 3 - $\text{CH}_3$ ).

Elementaranalyse berechnet: C 65,85, H 4,91; bestimmt: C 65,44, H 4,78 %.

### 6.2 Synthese von Methyl-4-(1-hydroxy-2-(methoxycarbonyl)-allyl)benzoat

In einem 100 mL-Einhalskolben werden 0,50 g (3,04 mmol) Methyl-4-formylbenzoat, 0,26 g (3,04 mmol) Methylacrylat und 0,34 g (3,04 mmol) DABCO in 50 mL Dioxan gelöst. Es wird für 3 d bei RT gerührt, anschließend eine DC in EE/Hexan 2:8 bzw. Methanol/Toluol 3:7 durchgeführt. Das Resultat der DC entspricht dem der Edukte.

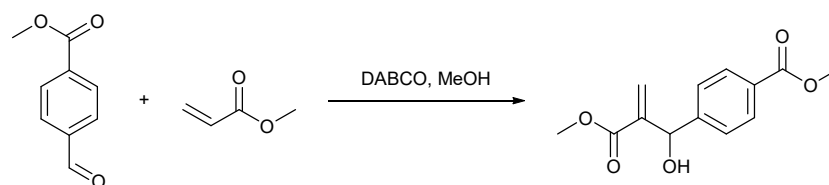


Abbildung 83. Baylis-Hillman-Reaktion zwischen Methyl-4-formylbenzoat und Methylacrylat.

Außerdem durchgeführt:

In einem 100 mL-Einhalskolben werden 1,0 g (6,1 mmol) Methyl-4-formylbenzoat, 1,58 g (18,4 mmol) Methylacrylat und 0,9 g (8,0 mmol) DABCO in 6 mL Methanol gelöst. Es wird für 24 h bei RT gerührt, die Lösung wird anschließend in 40 mL Chloroform gegeben und es werden 10 mL Wasser hinzugegeben. Über einen Scheidetrichter wird die organische Phase abgetrennt und die wässrige Phase noch zwei weitere Male mit jeweils 20 mL Chloroform extrahiert. Die vereinigten organischen Phasen werden über Magnesiumsulfat getrocknet, filtriert und das Lösemittel am Rotationsverdampfer entfernt. Anschließend wird das Rohprodukt chromatographisch aufgereinigt (Methanol/Toluol 3:7).

Ausbeute: 1,18 g (4,69 mmol), 76%.

<sup>1</sup>H-NMR (300 MHz, CDCl<sub>3</sub>): δ = 7,94 (ddd, *J* = 1,85, 8,42, 2 =CH-), 7,39 (ddd, *J* = 8,1, 2 =CH-), 6,28 (s, 1 =CH<sub>2</sub>), 5,8 (s, 1 =CH<sub>2</sub>), 5,53 (s, 1 -CHCCO), 5,08 (s, 1 -OH), 3,84 (s, 3 -CH<sub>3</sub>), 3,65 (s, 3 -CH<sub>3</sub>).

Elementaranalyse berechnet: C 62,39, H 5,64; bestimmt: C 62,90, H 6,70 %.

### 6.3 Syntheseveruche zu N,N',N''-(1,3,5-triazin-2,4,6-triyl)-tris(4-methylbenzamid)

In einem 250 mL-Einhalskolben mit Rückflusskühler werden 3,00 g (23,8 mmol) Melamin, 11,0 g (71,3 mmol) para-Toluoylchlorid und 7,21 g (71,3 mmol) Triethylamin in 150 mL Dioxan zum Rückfluss erhitzt. Nach 16 h Reaktionszeit wird filtriert, der weiße Rückstand mit wenig Dioxan gewaschen und anschließend in 150 mL Chloroform

suspendiert. Es wird erneut filtriert und der Rückstand mit wenig Chloroform gewaschen. Der Rückstand wird anschließend im Trockenschrank bei 80 °C getrocknet.

Ausbeute: 0,49 g, verunreinigt.

#### 6.4 Synthese von Dimethyl-1,4-benzoldicarboxylat (DMT)

In einem 250 mL-Zweihalskolben mit Rückflusskühler und Septum werden 21,28 g (128,1 mmol) Terephthalsäure in 150 mL Methanol vorgelegt. Über einen Zeitraum von 15 Minuten werden unter kräftigem Rühren 20 mL Schwefelsäure hinzugegeben. Anschließend wird über Nacht zum Rückfluss erhitzt. Nach dem Abkühlen wird die Reaktionsmischung absetzen gelassen, dann möglichst viel Methanol abdekantiert und die übrige Mischung in 150 mL Dichlormethan gegeben. Es wird drei Mal mit 150 mL Wasser extrahiert, bzw. solange, bis die wässrige Phase nicht mehr sauer abgeschieden wird. Die wässrige Phase kann verworfen werden, die organische Phase wird über Magnesiumsulfat getrocknet, filtriert und das Lösemittel am Rotationsverdampfer entfernt.

Ausbeute 24,6 g (99%).

$^1\text{H-NMR}$  (300 MHz,  $\text{CDCl}_3$ ):  $\delta = 8,03$  (s, 4 =CH-), 3,88 (s, 6 -CH<sub>3</sub>).

Elementaranalyse berechnet: C 61,85, H 5,19; bestimmt: C 62,04, H 5,25 %.

#### 6.5 Synthese von 4-(Methoxycarbonyl)benzoesäure (4-MCB)

In einem 250 mL-Zweihalskolben mit Rückflusskühler und Tropftrichter werden 10,0 g (51,5 mmol) DMT in 100 mL Toluol vorgelegt. Die Mischung wird auf 65 °C erhitzt und solange gerührt, bis sich das DMT vollständig gelöst hat. Es werden 2,06 g (51,5 mmol) Kaliumhydroxid (ggf. minimaler Unterschuss) in 16 mL Methanol gelöst und über einen Zeitraum von 45 Minuten langsam über den Tropftrichter hinzugegeben. Es wird für weitere 3 h bei 65 °C gerührt, anschließend wird auf RT abkühlen gelassen und über Nacht weiter gerührt. Die Suspension wird abfiltriert, mit wenig Toluol gewaschen, und anschließend erneut in 100 mL Toluol suspendiert und für 30 Minuten bei 65 °C gerührt. Es wird filtriert und der Rückstand getrocknet.

Ausbeute 9,27 g (99%).

$^1\text{H-NMR}$  (300 MHz,  $\text{DMSO-}d_6$ ):  $\delta = 7,89$  (d,  $J = 8,26$ , 2 =CH-), 7,83 (d,  $J = 8,26$ , 2 =CH-), 3,84 (s, 3 -CH<sub>3</sub>).

## 6.6 Synthese von Methyl-4-(chlorocarbonyl)benzoat (M4CCB)

In einem 100 mL-Dreihalskolben mit Septum und Rückflusskühler werden unter inerten Bedingungen werden 5,00 g (27,8 mmol) 4-(Methoxycarbonyl)benzoesäure in 40 mL Toluol vorgelegt. Über ein Septum werden unter Eisbadkühlung langsam 3,3 g (27,75 mmol) Thionylchlorid hinzugegeben und es wird über Nacht gerührt, während sich die Mischung auf Raumtemperatur erwärmt. Die Mischung wird filtriert, das Filtrat gesammelt und das Lösemittel unter Vakuum entfernt.

Ausbeute 5,45 g (99%).

$^1\text{H-NMR}$  (300 MHz,  $\text{DMSO-}d_6$ ):  $\delta = 8,08$  (d,  $J = 14,2$ , 4 =CH-), 3,89 (s, 3 -CH<sub>3</sub>).

Elementaranalyse berechnet: C 54,43, H 3,55; bestimmt: C 54,45, H 3,45 %.

## 6.7 Synthese von Trimethyl-4,4',4''-((benzol-1,3,5-triyltris(azanediyl))tris(carbonyl))tribenzoat

Alle Versuche wurden unter inerten Bedingungen durchgeführt.

In einem 100 mL Zweihalskolben mit Tropftrichter und Rückflusskühler werden 0,38 g (2,99 mmol) Melamin und 0,91 g (8,96 mmol) Triethylamin in 40 mL Dioxan vorgelegt. 1,78 g (8,96 mmol) M4CCB werden in möglichst wenig Dioxan gelöst und in den Tropftrichter gefüllt. Es wird zum Rückfluss erhitzt und anschließend langsam die Mischung aus dem Tropftrichter hinzu getropft. Es wird über Nacht zum Rückfluss erhitzt und anschließend 3 Tage bei Raumtemperatur weiter gerührt. Die Reaktionsmischung wird in einen Liter Wasser gegeben und abfiltriert.

In Variationen wurde mit einem Septum und Spritze statt eines Tropftrichters gearbeitet, oder im Stickstoffgegenstrom direkt pulverförmige Reagenzien hinzu gegeben. Im Folgenden sind verschiedene versuchte Ansätze tabellarisch aufgelistet.

Die Reihenfolge der Zugabe ist dabei gekennzeichnet mit „+“ für gleichzeitige Zugabe, „>“ für darauf folgende Zugabe, „M“ für Melamin, „CCB“ für M4CCB, „LM“ für Lösemittel, „B“ für Base.

Tabelle 8. Einwaagen, Reaktionsbedingungen und Zugabereihenfolge für die verschiedenen Synthesen.

Basenmenge [g, mmol]	Lösemittel	Lösemittelmenge [mL]	Temperatur [°C]	Dauer [h]	Reihenfolge
0,91, 8,99	DMSO	50	90, RT	24, 72	M+CCB+LM>B
1,21, 11,96	DMSO	50	90, RT	24, 72	M+CCB+LM>B
3,28, 23,73	Ethylacetat	150	RT	72	M+B+LM>CCB+ LM
0,30, 2,96 <sup>a</sup>	DMF <sup>a</sup>	50 <sup>a</sup>	100 <sup>a</sup>	72 <sup>a</sup>	M+B+LM>CCB <sup>a</sup>
0,48, 4,75 <sup>b</sup>	Acetonitril <sup>b</sup>	110 <sup>b</sup>	82, RT <sup>b</sup>	3, 21 <sup>b</sup>	M+CCB+LM>B+ LM <sup>b</sup>
0,55, 3,96	Wasser	50	RT	168	M+B+CCB+LM
0,88, 6,37	Wasser	30	RT	168	M+B+LM>CCB

Melamin [g, mmol]	M4CCB [g, mmol]	Base
0,38, 3,01	1,84	Triethylamin
0,38, 3,01	2,37, 11,93	Triethylamin
0,5, 3,96	3,15, 15,86	Kaliumcarbonat
0,13, 1,03 <sup>a</sup>	0,62, 3,12 <sup>a</sup>	Triethylamin <sup>a</sup>
0,2, 1,59 <sup>b</sup>	2,52, 12,69 <sup>b</sup>	Triethylamin <sup>b</sup>
0,1, 0,79	0,47, 2,74	Kaliumcarbonat
0,1, 0,7	0,79, 3,96	Kaliumcarbonat

<sup>a</sup> Versuch mit erfolgreicher ein- bis zweifacher Substitution des Melamins. <sup>b</sup> Versuch mit erfolgreicher ein- bis sechsfacher Substitution des Melamins.

Bedingt durch die Unübersichtlichkeit der NMR-Ergebnisse wurden diese omittiert.

<sup>b</sup>MS (ESI): m/z 1099,5, 937,4, 775,4, 613,4, 451,5, 289,4, (berechnet: 1099, 936,8, 774,7, 612,6, 450,4, 288,27).

Die Ergebnisse des ESI-MS lassen darauf schließen, dass Melamin bis hin zum Hexamethyl-4,4',4'',4''',4''''',4''''''-(((1,3,5-triazin-2,4,6-triyl)tris(azanetriyl))hexakis(carbonyl))hexabenzooat durchsubstituiert wurde.

Ausbeute 0 g (0%).

## 6.8 Synthese von 4,4',4''-(((1,3,5-triazin-2,4,6-triyl)tris(azanediy))tris(carbonyl))tribenzoesäure

Die Synthese wurde auf zwei verschiedene Arten getestet.

Bei der ersten Variante wurden 0,56 g (3,10 mmol) 4MCB, 0,13 g (1,00 mmol) Melamin zusammen mit 0,62 g (3,00 mmol) DCC und 5 mL DMF in einem Schlenkrohr für 7 Tage gerührt. In einem NMR-Experiment konnten dabei nur Edukte festgestellt werden.



Bei der zweiten Variante wurden in einem Zweihalskolben mit Rückflusskühler 0,43 g (2,38 mmol) 4MCB, 0,09 g (0,08 mmol) N-Hydroxysuccinimid und 0,49 g (2,38 mmol) DCC in 150 mL Acetonitril vorgelegt und zum Rückfluss erhitzt. Anschließend wurde das Melamin hinzugegeben und es wurde für 6 Tage zum Rückfluss erhitzt. In einem NMR-Experiment konnte auch hier nur Edukte festgestellt werden.

Ausbeute 0 g (0%).

## 6.9 Synthese von Trimethylbenzol-1,3,5-tricarboxylat

In einem 500 mL-Zweihalsrundkolben mit Septum und Rückflusskühler werden 10,0 g (47,6 mmol) 1,3,5-Benzoltricarbonsäure in 200 mL Methanol. Über eine Spritze werden 2,5 mL konzentrierte Schwefelsäure hinzugefügt. Die Mischung wird für 24 h zum Rückfluss erhitzt, anschließend in 1 L Wasser gegeben und mit Natriumhydrogencarbonat neutralisiert. Der Feststoff wird abfiltriert und mehrfach mit Wasser (4x50 mL) gewaschen. Der Feststoff wird über Nacht im Trockenschrank bei 50 °C getrocknet.

Ausbeute 10,9 g (91%).

$^1\text{H-NMR}$  (300 MHz,  $\text{CDCl}_3$ ):  $\delta = 8,86$  (s, 3  $-\text{CH}=\text{}$ ), 3,98 (s, 9  $-\text{CH}_3$ ).

IR (ATR)  $\nu(\text{cm}^{-1}) = 2957, 1726, 1612, 1446, 1431, 1341, 1239, 1140, 1101, 997, 927, 882, 872, 734, 720$ .

## 6.10 Synthese von 3,5-Bis(methoxycarbonyl)benzoesäure

In einem 250 mL-Zweihalskolben mit Rückflusskühler und Tropftrichter werden 9,84 g (39,05 mmol) Trimethylbenzol-1,3,5-tricarboxylat in 400 mL Toluol gelöst. Die Lösung wird zum Sieden erhitzt. Zur siedenden Lösung werden über den Tropftrichter 2,19 g (39,05 mmol) Kaliumhydroxid gelöst in 40 mL langsam hinzugegeben. Anschließend wird noch für weitere 24 h zum Rückfluss erhitzt. Das Produkt fällt als weißer Feststoff aus, wird abfiltriert und mit 3x100 mL Toluol gewaschen. Das Produkt wird bei 50 °C für 24 h im Trockenschrank getrocknet.

Ausbeute 5,24 g (94%).

$^1\text{H-NMR}$  (300 MHz,  $\text{DMSO-}d_6$ ):  $\delta = 8,65$  (s, 2  $-\text{CH}=\text{}$ ), 8,40 (s, 1  $-\text{CH}=\text{}$ ), 3,89 (s, 6  $-\text{CH}_3$ ).

IR (ATR)  $\nu(\text{cm}^{-1}) = 2957, 1724, 1631, 1588, 1563, 1443, 1430, 1308, 1243, 1153, 803, 743, 718$ .

## 6.11 Synthese von Dimethyl-5-(chlorocarbonyl)isophthalat

Die gesamte Synthese wird unter inerten Bedingungen durchgeführt.

In einem 250 mL-Zweihalskolben mit Septum und Rückflusskühler werden 3,00 g (12,6 mmol) 3,5-Bis(methoxycarbonyl)benzoesäure in 125 mL Dichlormethan vorgelegt. Unter Eiskühlung wird über eine Spritze ein molares Äquivalent (0,92 mL) an Thionylchlorid portionsweise hinzugegeben. Die Lösung wird unter Erwärmung auf Raumtemperatur über Nacht gerührt, anschließend wird unter vermindertem Druck das Lösemittel entfernt.

Ausbeute 2,97 g (92%).

$^1\text{H-NMR}$  (300 MHz,  $\text{CDCl}_3$ ):  $\delta = 9,87$  (s, 1  $-\text{CH}=\text{}$ ), 8,93 (s, 2  $-\text{CH}=\text{}$ ), 4,01 (s, 6  $-\text{CH}_3$ ).

IR (ATR)  $\nu(\text{cm}^{-1}) = 1802, 1725, 1607, 1447, 1432, 1324, 1243, 1203, 1175, 1122, 1055, 767, 732$ .

## 6.12 Syntheseveruche zu Hexamethylen-5,5',5''-(((1,3,5-triazin-2,4,6-triyl)tris(azanediyl))tris(carbonyl))isophthalat

Die Reaktion wird unter inerten Bedingungen durchgeführt.

In einem 100 mL-Zweihalskolben mit Tropftrichter werden 0,10 g (0,79 mmol) Melamin in 50 mL Dimethylformamid vorgelegt. Über den Tropftrichter werden 0,44 mL Triethylamin in 5 mL Dimethylformamid hinzugegeben. 0,61 g (2,37 mmol) Dimethyl-5-(chlorocarbonyl)isophthalat werden in 10 mL Dimethylformamid gelöst und unter Eisbadkühlung über den Tropftrichter innerhalb einer Stunde in die Reaktionsmischung

getropft. Es wird unter Erwärmung auf Raumtemperatur für drei Tage gerührt. Analytische Methoden zeigten ausschließlich die Edukte.

Ausbeute 0 g (0%).

In einem 250 mL-Zweihalskolben mit Tropftrichter und Rückflusskühler werden 1,00 g (0,79 mmol) Melamin mit 3,1 Äquivalenten (0,59 g, 2,46 mmol) 3,5-Bis(methoxycarbonyl)benzoesäure in 130 mL Dichlormethan vorgelegt. Unter Rühren wird langsam eine Lösung von 3,1 Äquivalenten (0,50 g, 2,46 mmol) *N,N'*-Dicyclohexylcarbodiimid in 20 mL Dichlormethan hinzugegeben. Es wird für 24 h zum Rückfluss erhitzt, anschließend noch fünf Tage bei Raumtemperatur gerührt. Die Reaktionskontrolle wurde über Dünnschichtchromatographie mit einer Mischung von Hexan/Ethylacetat 1:1 als Laufmittel durchgeführt, und es sollte die Umsetzung von DCC zu *N,N'*-Dicyclohexylurea (DCU) beobachtet werden. Es wurde jedoch keine Bildung von DCU beobachtet.

Ausbeute 0 g (0%).

### **6.13 Synthese von Tri-tert.-butyl-4,4',4''-(1,3,5-triazin-2,4,6-triyl)tris(piperazin-1-carboxylat)**

Die Reaktion wird unter inerten Bedingungen nach der Vorschrift von Chouai et al. durchgeführt.<sup>56</sup>

In einem 100 mL-Zweihalskolben werden 1,84 g (10,0 mmol) Cyanurchlorid und 3 Äquivalente (5,59 g, 30,0 mmol) 1-Boc-piperazin in 80 mL Tetrahydrofuran vorgelegt. Das Gemisch wird für eine Stunde bei Raumtemperatur gerührt, anschließend werden fünf Äquivalente Triethylamin (13,83 mL, 50,0 mmol) hinzu gegeben. Es wird eine weitere Stunde bei Raumtemperatur gerührt, bevor das Gemisch für 22 h zum Rückfluss erhitzt wird. Zur Reaktionskontrolle wird eine Dünnschichtchromatographie in Dichlormethan/Methanol 19:1 durchgeführt ( $R_f$ (Produkt): 0,7).<sup>56</sup> Nach Beenden der Reaktion wird das THF am Rotationsverdampfer entfernt. Der Rückstand wird in 100 mL Dichlormethan aufgenommen und drei Mal mit 100 mL Wasser und zwei Mal

mit 100 mL gesättigter Kochsalzlösung ausgeschüttelt. Die organische Phase wird mit Natriumsulfat getrocknet, das Natriumsulfat abfiltriert, das Dichlormethan am Rotationsverdampfer entfernt. Das weiße bis leicht gelbliche Produkt wird für 24 h bei 50 °C im Trockenschrank getrocknet.

Ausbeute 5,89 g (99%).

$^1\text{H-NMR}$  (300 MHz,  $\text{CDCl}_3$ ):  $\delta = 3,67$  (m, 12  $-\text{CH}_2-$ ),  $3,37$  (m, 12  $-\text{CH}_2-$ ),  $1,41$  (s, 27  $-\text{CH}_3$ ).

IR (ATR)  $\nu(\text{cm}^{-1}) = 2975, 2926, 2855, 1691, 1548, 1529, 1477, 1442, 1416, 1389, 1363, 1306, 1277, 1260, 1226, 1168, 1113, 1069, 999, 958, 866, 844, 831, 804, 767, 735$ .

MS (ESI):  $m/z$  634,7 (berechnet: 633,4).

## 6.14 Synthese von 2,4,6-Tri(piperazin-1-yl)-1,3,5-triazin

Die Reaktion wird unter inerten Bedingungen nach der Vorschrift von Chouai et al. durchgeführt.<sup>56</sup>

In einem 50 mL-Zweihalsrundkolben mit Septum und Rückflusskühler werden 1,50 g (2,37 mmol) Tri-tert.-butyl-4,4',4''-(1,3,5-triazin-2,4,6-triyl)tris(piperazin-1-carboxylat) in 24 mL Methanol vorgelegt und für 30 Minuten im Eisbad auf 0 °C heruntergekühlt. Anschließend werden mit Hilfe einer Spritze 8,30 mL 6N Salzsäure so langsam hinzu gegeben, dass die Temperatur nicht über 1 °C steigt. Nach Zugabe der Salzsäure lässt man die Reaktionsmischung auf Raumtemperatur erwärmen und erhitzt die Mischung für 22 h zum Rückfluss. Nach dem Abkühlen der Reaktionsmischung wird das Methanol am Rotationsverdampfer entfernt (inerte Bedingungen nicht mehr notwendig), die Mischung erneut auf 0 °C gekühlt und mit 10%-iger Natronlauge auf einen pH-Wert von 14 eingestellt. Die klare, gelbe Lösung wird drei Mal mit 60 mL Chloroform ausgeschüttelt, die gesammelten organischen Phasen über Natriumsulfid getrocknet, das Natriumsulfat abfiltriert und das Chloroform am Rotationsverdampfer entfernt. Das Produkt liegt als weißer Feststoff vor.

Ausbeute 0,14 g (18%).

$^1\text{H-NMR}$  (300 MHz,  $\text{CDCl}_3$ ):  $\delta = 3,67$  (m,  $J = 5,0$ , 12  $-\text{CH}_2-$ ),  $2,80$  (m,  $J = 5,0$ , 12  $-\text{CH}_2-$ ),  $2,00$  (s, 3  $-\text{NH}$ ).

IR (ATR)  $\nu(\text{cm}^{-1}) = 3316, 3269, 3005, 2941, 2909, 2847, 2824, 2744, 1520, 1478, 1429, 1364, 1338, 1315, 1297, 1239, 1191, 1172, 1137, 1124, 1092, 1052, 1006, 949, 899, 871, 704$ .

Bedingt durch die schlechte Ausbeute der Synthese wurde diese erneut unter anderen Bedingungen ausgeführt.

In einem 100 mL-Einhalskolben werden 4,00 g (6,31 mmol) Tri-tert.-butyl-4,4',4''-(1,3,5-triazin-2,4,6-triyl)tris(piperazin-1-carboxylat) in kleinen Portionen in eine Mischung aus 40 mL Dichlormethan und 9,72 mL (126 mmol) Trifluoressigsäure gegeben. Die Suspension wird für 3 h bei Raumtemperatur gerührt. Das Dichlormethan wird am Rotationsverdampfer entfernt, bis eine viskose, gelbe Flüssigkeit zurück bleibt. Die Flüssigkeit wird auf  $0\text{ }^\circ\text{C}$  abgekühlt und mit 5N Natronlauge auf einen pH-Wert von 14 eingestellt. Das Produkt wird drei Mal mit 60 mL Chloroform extrahiert, die organischen Phasen werden vereint und über Magnesiumsulfat getrocknet, welches anschließend abfiltriert wird. Das Chloroform wird am Rotationsverdampfer entfernt. Der dabei ausfallende weiß bis leicht gelbliche Feststoff wird im Trockenschrank für 24 h bei  $80\text{ }^\circ\text{C}$  getrocknet.

Ausbeute 1,64 g (78%).

$^1\text{H-NMR}$ - und IR-Spektrum identisch mit den vorherigen.

MS (ESI):  $m/z$  334,6 (berechnet: 334,4).

## **6.15 Synthese von 2,2',2''-((1,3,5-Triazin-2,4,6-triyl)-tris(piperazin-4,1-diyl))trifluoressigsäure**

Die Synthese wird unter inerten Bedingungen durchgeführt.

In einem 50 mL-Einhalsrundkolben werden 0,33 g (0,97 mmol) 2,4,6-Tri(piperazin-1-yl)-1,3,5-triazin in 15 mL Chloroform vorgelegt. Zu der Mischung werden 0,31 g (3,06

mmol) Triethylamin und 0,28 g (2,96 mmol) Chloressigsäure gegeben. Das Gemisch wird drei Tage bei Raumtemperatur gerührt. Der ausfallende Feststoff wird abfiltriert und drei Mal mit 60 mL Chloroform gewaschen. Der Feststoff wird für 24 h bei 50 °C im Trockenschrank getrocknet.

Ausbeute 0,39 g (73%).

$^1\text{H-NMR}$  (600 MHz,  $\text{D}_2\text{O}$ ):  $\delta = 3,96$  (s, 6  $-\text{CH}_2-$ ), 3,92 (m,  $J = 5,3$ , 12  $-\text{CH}_2-$ ), 3,14 (m,  $J = 5,3$ , 12  $-\text{CH}_2-$ ).

$^{13}\text{C-NMR}$  (300 MHz,  $\text{DMSO-}d_6$ ):  $\delta = 168,39$ , 164,45, 51,37, 42,06, 41,68.

Elementaranalyse berechnet: C 49,70, H 6,55, N 24,84; bestimmt: C 40,93, H 6,15, N 20,08 %.

MS (ESI):  $m/z$  508,5 (berechnet: 507,55).

Schmelzpunkt: Zersetzung ab ca. 215 °C.

## 6.16 Synthese von *N,N'*-(4-Carboxyphenyl)terephthalamid

Die Synthese wurde leicht abgewandelt zu der von Cronin et al. durchgeführt.<sup>50</sup>

In einem 100 mL-Rundkolben werden 0,71 g (5,18 mmol) 4-Aminobenzoesäure und 1,71 g (12,3 mmol) Kaliumcarbonat unter kräftigem Rühren in 70 mL vollentsalztem Wasser gelöst. Anschließend werden über einen Zeitraum von 10 Minuten 0,5 g (2,4 mmol) Terephthaloylchlorid hinzugegeben. Es wird für 3 Tage bei Raumtemperatur gerührt. Die entstandene Suspension wird in 300 mL 3N Salzsäure gegeben (vorsichtig, da Schaumbildung), anschließend wird der ausgefallene Feststoff abfiltriert und mit Wasser gewaschen, bis das Filtrat neutral abläuft. Nach dem Trocknen im Vakuumtrockenschrank wird ein weißer Feststoff erhalten.

Ausbeute 0,67 g (69%).

$^1\text{H-NMR}$  (300 MHz,  $\text{DMSO-}d_6$ ):  $\delta = 13,14$  (s, 2  $-\text{COOH}$ ), 10,68 (s, 2  $-\text{NH-}$ ), 8,12 (s, 4  $-\text{CH=}$ ), 7,94 (d,  $J = 2,8$ , 8  $-\text{CH=}$ ).

IR (ATR)  $\nu(\text{cm}^{-1}) = 3377$ , 1650, 1607, 1530, 1498, 1321, 1261, 771, 613.

## 6.17 Synthese von *N,N'*-(3-Carboxyphenyl)terephthalamid

Die Synthese wurde leicht abgewandelt zu der von Cronin et al. durchgeführt.<sup>50</sup>

In einem 100 mL-Rundkolben werden 0,368 g (5,18 mmol) 3-Aminobenzoesäure und 1,71 g (12,3 mmol) Kaliumcarbonat unter kräftigem Rühren in 70 mL vollentsalztem Wasser gelöst. Anschließend werden über einen Zeitraum von 10 Minuten 0,50 g (2,4 mmol) Terephthaloylchlorid hinzugegeben. Es wird für 3 Tage bei Raumtemperatur gerührt. Die entstandene Suspension wird in 300 mL 3N Salzsäure gegeben (vorsichtig, da Schaumbildung), anschließend wird der ausgefallene Feststoff abfiltriert und mit Wasser gewaschen, bis das Filtrat neutral abläuft. Nach dem Trocknen im Vakuumtrockenschrank wird ein weißer Feststoff erhalten.

Ausbeute 0,28 g (60%).

<sup>1</sup>H-NMR (300 MHz, DMSO-*d*<sub>6</sub>):  $\delta$  = 13,02 (s, 2 -COOH), 10,59 (s, 2 -NH-), 8,45 (t, *J* = 3,54, 1,76, 2 -CH=), 8,14 (s, 4 -CH=), 8,08 (ddd, 2 -CH=), 7,71 (dt, *J* = 7,9, 1,4, 2 -CH=), 7,51 (t, *J* = 7,9, 2 -CH=).

IR (ATR)  $\nu(\text{cm}^{-1})$  = 3290, 1686, 1607, 1498, 1582, 1323, 1288, 1196, 752, 613.

## 6.18 Synthese von *N,N'*-(4-Carboxy,2-methylphenyl)terephthalamid

Die Synthese wurde leicht abgewandelt zu der von Cronin et al. durchgeführt.<sup>50</sup>

In einem 100 mL-Rundkolben werden 0,113 g (0,740 mmol) 4-Amino-3-methylbenzoesäure und 0,272 g (1,960 mmol) Kaliumcarbonat unter kräftigem Rühren in 70 mL vollentsalztem Wasser gelöst. Anschließend werden über einen Zeitraum von 10 Minuten 0,076 g (0,370 mmol) Terephthaloylchlorid hinzugegeben. Es wird für 3 Tage bei Raumtemperatur gerührt. Die entstandene Suspension wird in 300 mL 3N Salzsäure gegeben (vorsichtig, da Schaumbildung), anschließend wird der ausgefallene Feststoff abfiltriert und mit Wasser gewaschen, bis das Filtrat neutral abläuft. Nach dem Trocknen im Vakuumtrockenschrank wird ein beiger Feststoff erhalten.

Ausbeute 0,044 g (27%).

$^1\text{H-NMR}$  (300 MHz,  $\text{DMSO-}d_6$ ):  $\delta = 12,99$  (s, 2  $-\text{COOH}$ ), 10,15 (s, 2  $-\text{NH-}$ ), 8,14-8,05 (m, 6  $-\text{CH=}$ ), 7,88 (m, 2  $-\text{CH=}$ ), 7,84-7,81 (m, 2  $-\text{CH=}$ ), 7,61-7,57 (m, 2  $-\text{CH=}$ ), 2,34 (s, 6  $-\text{CH}_3$ ).

IR (ATR)  $\nu(\text{cm}^{-1}) = 3286, 2928, 2574, 1678, 1607, 1582, 1498, 1315, 1302, 1277, 767, 677$ .

### **6.19 Synthese von $N,N'$ -(4-Carboxy,3-methoxyphenyl)-terephthalamid**

Die Synthese wurde leicht abgewandelt zu der von Cronin et al. durchgeführt.<sup>50</sup>

In einem 100 mL-Rundkolben werden 0,41 g (2,45 mmol) 4-Amino-3-methoxybenzoesäure und 0,75 g (5,43 mmol) Kaliumcarbonat unter kräftigem Rühren in 70 mL vollentsalztem Wasser gelöst. Anschließend werden über einen Zeitraum von 10 Minuten 0,25 g (1,23 mmol) Terephthaloylchlorid hinzugegeben. Es wird für 3 Tage bei Raumtemperatur gerührt. Die entstandene Suspension wird in 300 mL 3N Salzsäure gegeben (vorsichtig, da Schaumbildung), anschließend wird der ausgefallene Feststoff abfiltriert und mit Wasser gewaschen, bis das Filtrat neutral abläuft. Nach dem Trocknen im Vakuumtrockenschrank wird ein beiger Feststoff erhalten.

Ausbeute 0,45 g (78%).

$^1\text{H-NMR}$  (300 MHz,  $\text{DMSO-}d_6$ ):  $\delta = 12,45$  (s, 2  $-\text{COOH}$ ), 10,62 (s, 2  $-\text{NH-}$ ), 8,13 (s, 4  $-\text{CH=}$ ), 7,74 (d,  $J = 8,68$ , 2  $-\text{CH=}$ ), 7,70 (d,  $J = 1,76$ , 2  $-\text{CH=}$ ), 7,50 (dd,  $J = 8,49, 1,76$ , 2  $-\text{CH=}$ ), 3,84 (s, 6  $-\text{OCH}_3$ ).

IR (ATR)  $\nu(\text{cm}^{-1}) = 3294, 1710, 1590, 1523, 1506, 1325, 1286, 1019, 723, 676$ .

### **6.20 Versuchte Synthese von $N,N'$ -(3-Bromo,4-carboxyphenyl)-terephthalamid**

Die Synthese wurde leicht abgewandelt zu der von Cronin et al. durchgeführt.<sup>50</sup>

In einem 100 mL-Rundkolben werden 0,39 g (1,80 mmol) 4-Amino-3-bromobenzoesäure und 0,64 g (4,64 mmol) Kaliumcarbonat unter kräftigem Rühren in 70 mL



vollentsalztem Wasser gelöst. Anschließend werden über einen Zeitraum von 10 Minuten 0,18 g (0,90 mmol) Terephthaloylchlorid hinzugegeben. Es wird für drei Tage bei Raumtemperatur gerührt. Die entstandene Suspension wird in 300 mL 3N Salzsäure gegeben (vorsichtig, da Schaumbildung), anschließend wird der ausgefallene Feststoff abfiltriert und mit Wasser gewaschen, bis das Filtrat neutral abläuft. Nach dem Trocknen im Vakuumtrockenschrank wird ein rot-brauner Feststoff erhalten.

Rohausbeute 0,17 g (25%).

$^1\text{H-NMR}$  (300 MHz,  $\text{DMSO-}d_6$ ):  $\delta = 13,10$  (s, 6  $-\text{COOH}$ ), 10,33 (s, 2  $-\text{NH-}$ ), 8,20 (m, 2  $-\text{CH=}$ ), 8,17 (s, 1  $-\text{CH=}$ ), 8,07 (2s, 12  $-\text{CH=}$ ), 8,00 (m, 2  $-\text{CH=}$ ), 7,87 (d,  $J = 2,08$ , 2  $-\text{CH=}$ ), 7,81 (t,  $J = 8,27$ , 2  $-\text{CH=}$ ), 7,63 (dd,  $J = 8,49$ , 1,98, 2  $-\text{CH=}$ ), 6,78 (d,  $J = 8,64$ , 2  $-\text{CH=}$ ), 6,09 (s, 3  $-\text{NH}_2$ ).

## 6.21 Synthese von *N,N'*-(3,5-Dicarboxyphenyl)terephthalamid.

Die Synthese wurde leicht abgewandelt zu der von Cronin et al. durchgeführt.<sup>50</sup>

In einem 100 mL-Rundkolben werden 0,41 g (2,28 mmol) 5-Aminoisophthalsäure und 0,72 g (5,21 mmol) Kaliumcarbonat unter kräftigem Rühren in 70 mL vollentsalztem Wasser gelöst. Anschließend werden über einen Zeitraum von 10 Minuten 0,22 g (1,06 mmol) Terephthaloylchlorid hinzugegeben. Es wird für 3 Tage bei Raumtemperatur gerührt. Die entstandene Suspension wird in 300 mL 3N Salzsäure gegeben (vorsichtig, da Schaumbildung), anschließend wird der ausgefallene Feststoff abfiltriert und mit Wasser gewaschen, bis das Filtrat neutral abläuft. Nach dem Trocknen im Vakuumtrockenschrank wird ein beiger Feststoff erhalten.

Ausbeute 0,39 g (73%). Literatur 83%.

$^1\text{H-NMR}$  (300 MHz,  $\text{DMSO-}d_6$ ):  $\delta = 13,31$  (s, 4  $-\text{COOH}$ ), 10,76 (s, 2  $-\text{NH-}$ ), 8,70 (d,  $J = 1,54$ , 4  $-\text{CH=}$ ), 8,24 (t,  $J = 1,52$ , 2  $-\text{CH=}$ ), 8,17 (s, 4  $-\text{CH=}$ ).

Literatur  $^1\text{H-NMR}$  (300 MHz,  $\text{DMSO-}d_6$ ):  $\delta = 13,30$ , 10,81, 8,64, 8,23, 8,22.

IR (ATR)  $\nu(\text{cm}^{-1}) = 3480$ , 3093, 1710, 1590, 1542, 1509, 1281, 1250, 1190, 755, 660.

## 6.22 Synthese von Dimethyl-4,4'-((1,4-phenylenbis(azanediyl))-bis(carbonyl))dibenzoat

In einem 250 mL-Einhalsrundkolben werden 0,64 g (5,92 mmol) p-Phenylendiamin und 4 mL Triethylamin in 100 mL Chloroform vorgelegt. 2,35 g (11,84 mmol) Methyl-4-(chlorocarbonyl)benzoat werden portionsweise hinzugegeben. Es wird für zwei Tage an einem dunklen Ort gerührt. Die Mischung wird filtriert, der Rückstand zwei Mal mit 100 mL Chloroform gewaschen, anschließend in 50 mL DMF suspendiert und zum Sieden erhitzt. Nach Erreichen des Siedepunktes kühlt man die Mischung mit einem Eisbad ab und filtriert anschließend. Der Rückstand wird bei 80 °C im Vakuumtrockenschrank getrocknet.

Ausbeute 0,59 g (23%).

Elementaranalyse berechnet: C 66,66, H 4,66, N 6,48; bestimmt: C 65,92, H 4,81, N 6,64 %.

## 6.23 Synthese von Tetramethyl-5,5'-((1,4-phenylenbis(azanediyl))bis(carbonyl))diisophthalat

In einem 100 mL-Einhalsrundkolben werden 0,32 g (2,95 mmol) p-Phenylendiamin und 1,89 mL (14,6 mmol) Triethylamin in 50 mL Diethylether vorgelegt. Anschließend werden 1,50 g (5,84 mmol) Dimethyl-5-(chlorocarbonyl)isophthalat hinzugegeben. Die Lösung wird für vier Tage an einem dunklen Ort gerührt. Der ausfallende Feststoff wird abfiltriert, drei Mal mit 20 mL Diethylether gewaschen und bei 50 °C im Trockenschrank getrocknet. Anschließend wird der Feststoff in DMF suspendiert, zum Sieden erhitzt und mit einem Eisbad abgekühlt. Nach Abfiltrieren des Feststoffs wird dieser bei 80 °C im Vakuumtrockenschrank getrocknet.

Ausbeute 0,35 g (23%).

$^1\text{H-NMR}$  (300 MHz,  $\text{DMSO-}d_6$ ):  $\delta = 10,78$  (s, 2 -NH), 8,87 (s, 4 -CH=), 8,71 (s, 2 -CH=), 7,87 (s, 4 -CH=), 4,03 (s, 12 -CH<sub>3</sub>).

IR (ATR)  $\nu(\text{cm}^{-1}) = 3314, 2953, 1725, 1648, 1611, 1564, 1553, 1516, 1442, 1381, 1307, 1242, 1145, 999, 926, 735, 718.$

Elementaranalyse berechnet: C 61,31, H 4,41, N 5,11; bestimmt: C 60,58, H 4,61, N 5,69 %.

## **6.24 Syntheseversuch von 5,5'-(Fumarylbis(azanediyl))-diisophthalsäure**

In einem 100 mL-Dreihalsrundkolben mit Septum, Rückflusskühler und Tropftrichter werden 1,00 g (8,57 mmol) Fumarsäure in 25 mL THF oder Toluol vorgelegt. Die Suspension wird zum Siedepunkt erhitzt und es werden über eine Spritze 1,25 mL (2,05 g, 17,14 mmol) Thionylchlorid hinzugegeben. Es wird für weitere 4 h zum Rückfluss erhitzt und anschließend über Nacht bei Raumtemperatur gerührt. Über den Tropftrichter wird eine Suspension von 3,1 g (17,14 mmol) 5-Aminoisophthalsäure und 4,74 g (34,38 mmol) Kaliumcarbonat in 25 mL THF oder Toluol hinzutropft. Es wird für 3 Tage bei Raumtemperatur gerührt.

Ausbeute 0 g.

## **6.25 Syntheseversuch von 3,3'-(Oxalylbis(azanediyl))-dibenzoessäure**

In einem 50 mL-Einhalsrundkolben werden 0,46 g (3,65 mmol) Oxalylchlorid, 1 g (7,3 mmol) 3-Aminobenzoessäure und 1,51 g (10,9 mmol) Kaliumcarbonat in 25 mL Toluol gegeben. Die Mischung wird für 3 Tage bei Raumtemperatur an einem dunklen Ort gerührt. Die entstehende Suspension wird filtriert und der Rückstand bei 80 °C im Vakuumtrockenschrank getrocknet. Das Produkt liegt als stark verunreinigter, weißer Feststoff vor.

Ausbeute 0 g.

## 6.26 Syntheseversuch von 4,4'-(Oxalylbis(azanediyl))-dibenzoesäure

In einem 50 mL-Einhalsrundkolben werden 0,46 g (3,65 mmol) Oxalylchlorid, 1 g (7,3 mmol) 4-Aminobenzoesäure und 1,51 g (10,9 mmol) Kaliumcarbonat in 25 mL Toluol gegeben. Die Mischung wird für 3 Tage bei Raumtemperatur an einem dunklen Ort gerührt. Die entstehende Suspension wird filtriert und der Rückstand bei 80 °C im Vakuumtrockenschrank getrocknet. Mit spektroskopischen Methoden lässt sich keine erfolgreiche Umsetzung feststellen.

Ausbeute 0 g.

## 6.27 Syntheseversuch neuer Koordinationspolymere basierend auf 2,2',2''-((1,3,5-Triazin-2,4,6-triyl)tris(piperazin-4,1-diyl))triessigsäure

Für die Solvothermalsynthese mit Dimethylformamid als Lösungsmittel wird der Ligand 2,2',2''-((1,3,5-Triazin-2,4,6-triyl)tris(piperazin-4,1-diyl))triessigsäure zusammen mit einem Metallsalz in bestimmten molaren Verhältnissen zusammengemischt und in ein Pyrex-Kulturröhrchen überführt. Zur Mischung werden jeweils 5 mL Dimethylformamid gegeben. Die verschiedenen Ansätze werden für 7 Tage bei erhöhter Temperatur gehalten (Tabelle 9).

Tabelle 9. Einwaagen und Reaktionsbedingungen der Solvothermalsynthesen in 5 mL Dimethylformamid.

Metallsalz	Einwaage Metallsalz [mg]	Einwaage Ligand [mg]	Molares Verhältnis	Temperatur [°C]
Cr(NO <sub>3</sub> ) <sub>3</sub> ·9H <sub>2</sub> O	4,7	20,0	3:1	105
Fe(NO <sub>3</sub> ) <sub>3</sub> ·9H <sub>2</sub> O	4,8	20,0	3:1	105
Co(NO <sub>3</sub> ) <sub>3</sub> ·6H <sub>2</sub> O	8,6	10,0	3:2	80
Co(NO <sub>3</sub> ) <sub>3</sub> ·6H <sub>2</sub> O	11,4	10,0	2:1	80
Co(NO <sub>3</sub> ) <sub>3</sub> ·6H <sub>2</sub> O	22,9	10,0	4:1	80

$\text{Cu}(\text{NO}_3)_2 \cdot 3\text{H}_2\text{O}$	7,1	10,0	3:2	105
$\text{Cu}(\text{NO}_3)_2 \cdot 3\text{H}_2\text{O}$	9,5	10,0	2:1	105
$\text{Cu}(\text{NO}_3)_2 \cdot 3\text{H}_2\text{O}$	19,0	10,0	4:1	105
$\text{Zn}(\text{NO}_3)_2 \cdot 6\text{H}_2\text{O}$	8,8	10,0	3:2	80
$\text{Zn}(\text{NO}_3)_2 \cdot 6\text{H}_2\text{O}$	11,0	10,0	2:1	80
$\text{Zn}(\text{NO}_3)_2 \cdot 6\text{H}_2\text{O}$	23,0	10,0	4:1	80
$\text{La}(\text{NO}_3)_3 \text{ aq.}$	9,6	10,0	3:2	80
$\text{La}(\text{NO}_3)_3 \text{ aq.}$	12,8	10,0	2:1	80
$\text{La}(\text{NO}_3)_3 \text{ aq.}$	25,6	10,0	4:1	80

Für die Solvothermalsynthese mit einem Dimethylformamid-Wasser-Gemisch als Lösungsmittel werden 15 mL Dimethylformamid mit 15 mL Wasser gemischt und anschließend mit zwei Tropfen konzentrierter Salpetersäure angesäuert. Der Ligand 2,2',2''-((1,3,5-Triazin-2,4,6-triyl)tris(piperazin-4,1-diyl))triessigsäure wird zusammen mit dem Zink- oder Kupfermetallsalz in bestimmten molaren Verhältnissen zusammengemischt und in ein Pyrex-Kulturröhrchen überführt. Für die Synthese mit Chromnitrat werden das Metallsalz und der Ligand in einen Autoklaven gegeben. Zur Mischung in den Pyrex-Kulturröhrchen werden jeweils 5 mL Dimethylformamid-Wasser-Gemisch gegeben, zur Mischung im Autoklaven 20 mL. Die verschiedenen Ansätze werden für 7 Tage bei erhöhter Temperatur gehalten (Tabelle 10).

Tabelle 10. Einwaagen und Reaktionsbedingungen der Solvothermalsynthesen im Dimethylformamid-Wasser-Gemisch.

Metallsalz	Einwaage Metallsalz [mg]	Einwaage Ligand [mg]	Molares Verhältnis	Temperatur [°C]
$\text{Cr}(\text{NO}_3)_3 \cdot 9\text{H}_2\text{O}$	630,0	100,0	8:1	130
$\text{Cu}(\text{NO}_3)_2 \cdot 3\text{H}_2\text{O}$	38,0	10,0	8:1	80
$\text{Zn}(\text{NO}_3)_2 \cdot 6\text{H}_2\text{O}$	8:1	10,0	8:1	80

Bei den Ansätzen mit Cr(III) fällt ein weißer Niederschlag aus. Bei den Ansätzen mit Cu(II) fällt ein roter Niederschlag von Kupfer(I)oxid aus. Bei den Ansätzen mit Zn(II) wurden keine Niederschläge beobachtet.

Für die Hydrothermalsynthesen mit Wasser als Lösungsmittel wird der Ligand 2,2',2''-((1,3,5-Triazin-2,4,6-triyl)tris(piperazin-4,1-diyl))triessigsäure zusammen mit einem Metallsalz in bestimmten molaren Verhältnissen zusammengemischt und in einen Autoklaven überführt. Zur Mischung werden jeweils 20 mL Wasser gegeben. Die verschiedenen Ansätze werden in einen Ofen gegeben, welcher zunächst über 1,5 h auf 130 °C aufgeheizt, dann kontinuierlich für 48 h bei 130 °C gehalten und anschließend über einen Zeitraum von 8 h auf Raumtemperatur abgekühlt wird.

Tabelle 11. Einwaagen und Reaktionsbedingungen der Hydrothermalsynthesen.

Metallsalz	Einwaage Metallsalz [mg]	Einwaage Ligand [mg]	Molares Verhältnis
Cr(NO <sub>3</sub> ) <sub>3</sub> ·9H <sub>2</sub> O	315,0	100,0	4:1
Co(NO <sub>3</sub> ) <sub>3</sub> ·6H <sub>2</sub> O	229,0	100,0	4:1
Cu(NO <sub>3</sub> ) <sub>2</sub> ·3H <sub>2</sub> O	190,0	100,0	4:1
Al(NO <sub>3</sub> ) <sub>3</sub> ·9H <sub>2</sub> O	295,6	100,0	4:1

Bei den Synthesen mit Cr(III) fällt ein weißer Feststoff aus. Dieser wird abzentrifugiert, der Überstand abdekantiert und der Feststoff erneut in Wasser suspendiert. Nach erneuter Zentrifugation und Abdekantieren des Wassers wurde der Feststoff bei 80 °C im Vakuumtrockenschrank getrocknet.

## 6.28 Syntheserversuche neuer Koordinationspolymere basierend auf *N,N'*-(4-Carboxyphenyl)terephthalamid

In einem Pyrex-Kulturröhrchen werden der Ligand zusammen mit einem Metallsalz in 5 mL Dimethylformamid vorgelegt. Das Pyrex-Kulturröhrchen wird schräg (ca. 45°) in ein Sandbad, welches von unten beheizt wird, eingetaucht. Die Temperatur am unteren

Ende des Röhrchens wird gemessen und auf 85 °C eingestellt. Das Röhrchen wird nur so tief eingetaucht, dass die Temperatur am oberen Ende (d.h. in der Flüssigkeit, von oben vermessen) 45 °C beträgt. Das Röhrchen wird verschlossen. Durch Konvektion bewegt sich das Lösemittel durch das Röhrchen und es bilden sich Kristalle im kälteren Bereich (Abbildung 84). Der Versuch wird bis zur sichtbaren Bildung von Kristallen laufen gelassen.

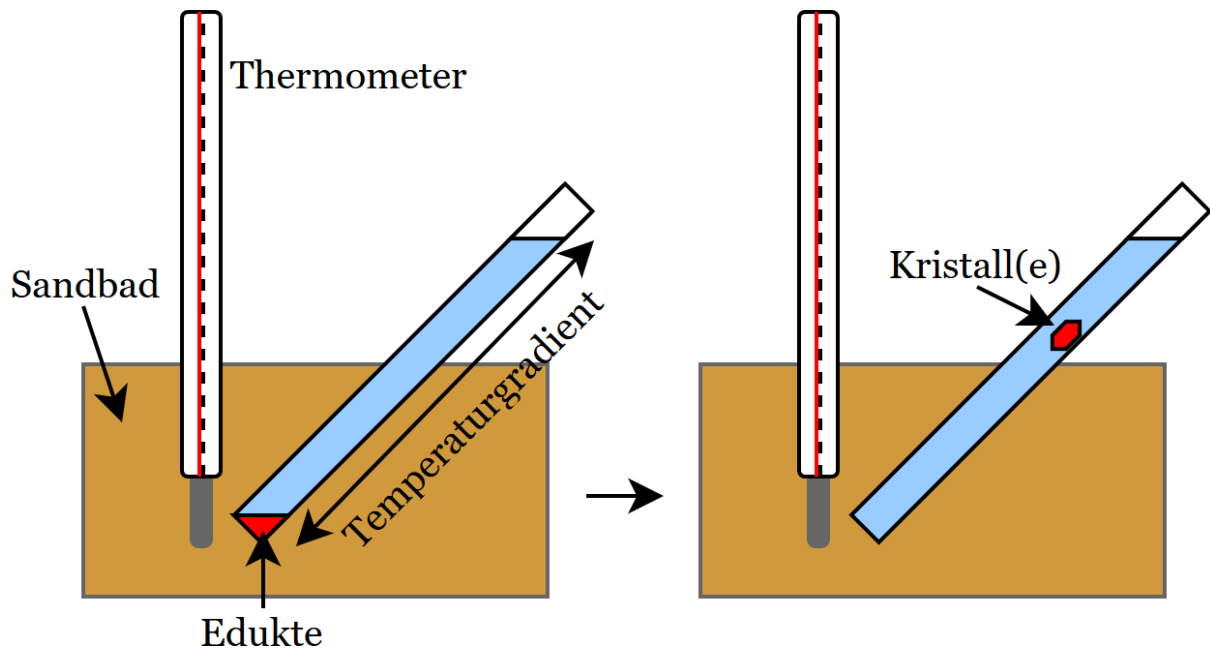


Abbildung 84. Aufbau und Prinzip der Konvektionssynthese im Sandbad.

Tabelle 12. Einwaagen der verschiedenen Kristallisationsansätze.

Metallsalz	Metallsalz [mg; mmol]	Ligand [mg; mmol]	Modulator	Temperaturgradient [°C]
Zn(NO <sub>3</sub> ) <sub>2</sub> ·6H <sub>2</sub> O	29,4; 0,1	10; 0,025		85-45
Zn(NO <sub>3</sub> ) <sub>2</sub> ·6H <sub>2</sub> O	29,4; 0,1	10; 0,025	TMAOH	85-45
Zn(NO <sub>3</sub> ) <sub>2</sub> ·6H <sub>2</sub> O	29,4; 0,1	10; 0,025	Salpetersäure	85-45
Zn(NO <sub>3</sub> ) <sub>2</sub> ·6H <sub>2</sub> O	29,4; 0,1	10; 0,025	Salzsäure	85-45
Zn(NO <sub>3</sub> ) <sub>2</sub> ·6H <sub>2</sub> O	29,4; 0,1	10; 0,025	Benzoessäure	85-45
Zn(NO <sub>3</sub> ) <sub>2</sub> ·6H <sub>2</sub> O	29,4; 0,1	10; 0,025		65-25
Zn(NO <sub>3</sub> ) <sub>2</sub> ·6H <sub>2</sub> O	58,8; 0,2	10; 0,025		85-45

Zn(NO <sub>3</sub> ) <sub>2</sub> ·6H <sub>2</sub> O	58,8; 0,2	10; 0,025	Salpetersäure	85-45
Zn(NO <sub>3</sub> ) <sub>2</sub> ·6H <sub>2</sub> O	58,8; 0,2	10; 0,025		95-65
Cu(NO <sub>3</sub> ) <sub>2</sub> ·3H <sub>2</sub> O	23,9; 0,1	10; 0,025		85-45
Cu(NO <sub>3</sub> ) <sub>2</sub> ·3H <sub>2</sub> O	23,9; 0,1	10; 0,025	TMAOH	85-45
Cu(NO <sub>3</sub> ) <sub>2</sub> ·3H <sub>2</sub> O	23,9; 0,1	10; 0,025	Salpetersäure	85-45
Cu(NO <sub>3</sub> ) <sub>2</sub> ·3H <sub>2</sub> O	23,9; 0,1	10; 0,025	Salzsäure	85-45
Cu(NO <sub>3</sub> ) <sub>2</sub> ·3H <sub>2</sub> O	23,9; 0,1	10; 0,025	Benzoessäure	85-45
Cu(NO <sub>3</sub> ) <sub>2</sub> ·3H <sub>2</sub> O	23,9; 0,1	10; 0,025		65-25
Cu(NO <sub>3</sub> ) <sub>2</sub> ·3H <sub>2</sub> O	47,8; 0,2	10; 0,025		85-45
Cu(NO <sub>3</sub> ) <sub>2</sub> ·3H <sub>2</sub> O	47,8; 0,2	10; 0,025	Salpetersäure	85-45
Cu(NO <sub>3</sub> ) <sub>2</sub> ·3H <sub>2</sub> O	47,8; 0,2	10; 0,025		95-65

Bei allen Ansätzen ist die Bildung eines Feststoffs zu beobachten. Die Suspensionen werden anschließend zentrifugiert, abdekantiert und mit 5 mL frischem DMF versetzt. Nach kräftigem Schütteln werden die Röhren auf 95 °C erhitzt und über Nacht bei dieser Temperatur gehalten. Es wird erneut zentrifugiert, abdekantiert und mit 5 mL Ethanol aufgefüllt. Die Röhren werden auf 70 °C temperiert und erneut über Nacht bei dieser Temperatur gehalten. Nach Zentrifugation und Abdekantieren des Lösemittels wird der entstandene Feststoff bei 80 °C im Vakuumtrockenschrank getrocknet.

## 6.29 Syntheseveruche neuer Koordinationspolymere basierend auf *N,N'*-(3-Carboxyphenyl)terephthalamid

In einem Pyrex-Kulturröhrchen werden der Ligand zusammen mit einem Metallsalz in 5 mL Dimethylformamid vorgelegt (Tabelle 13). Das Pyrex-Kulturröhrchen wird schräg (ca. 45°) in ein Sandbad, welches von unten beheizt wird, eingetaucht. Die Temperatur am unteren Ende des Röhrchens wird gemessen und auf 85 °C eingestellt. Das Röhrchen wird nur so tief eingetaucht, dass die Temperatur am oberen Ende (d.h. in der Flüssigkeit, von oben vermessen) 45 °C beträgt. Das Röhrchen wird verschlossen. Durch



Konvektion bewegt sich das Lösemittel durch das Röhrchen und es bilden sich Kristalle im kälteren Bereich (Abbildung 84). Der Versuch wird bis zur sichtbaren Bildung von Kristallen laufen gelassen.

Tabelle 13. Einwaagen der verschiedenen Kristallisationsansätze.

Metallsalz	Metallsalz [mg; mmol]	Ligand [mg; mmol]	Modulator	Temperaturgradient [°C]
Zn(NO <sub>3</sub> ) <sub>2</sub> ·6H <sub>2</sub> O	29,4; 0,1	10; 0,025		85-45
Zn(NO <sub>3</sub> ) <sub>2</sub> ·6H <sub>2</sub> O	29,4; 0,1	10; 0,025	TMAOH	85-45
Zn(NO <sub>3</sub> ) <sub>2</sub> ·6H <sub>2</sub> O	29,4; 0,1	10; 0,025	Salpetersäure	85-45
Zn(NO <sub>3</sub> ) <sub>2</sub> ·6H <sub>2</sub> O	29,4; 0,1	10; 0,025	Salzsäure	85-45
Zn(NO <sub>3</sub> ) <sub>2</sub> ·6H <sub>2</sub> O	29,4; 0,1	10; 0,025	Benzoessäure	85-45
Zn(NO <sub>3</sub> ) <sub>2</sub> ·6H <sub>2</sub> O	29,4; 0,1	10; 0,025		65-25
Zn(NO <sub>3</sub> ) <sub>2</sub> ·6H <sub>2</sub> O	58,8; 0,2	10; 0,025		85-45
Zn(NO <sub>3</sub> ) <sub>2</sub> ·6H <sub>2</sub> O	58,8; 0,2	10; 0,025	Salpetersäure	85-45
Zn(NO <sub>3</sub> ) <sub>2</sub> ·6H <sub>2</sub> O	58,8; 0,2	10; 0,025		95-65
Cu(NO <sub>3</sub> ) <sub>2</sub> ·3H <sub>2</sub> O	23,9; 0,1	10; 0,025		85-45
Cu(NO <sub>3</sub> ) <sub>2</sub> ·3H <sub>2</sub> O	23,9; 0,1	10; 0,025	TMAOH	85-45
Cu(NO <sub>3</sub> ) <sub>2</sub> ·3H <sub>2</sub> O	23,9; 0,1	10; 0,025	Salpetersäure	85-45
Cu(NO <sub>3</sub> ) <sub>2</sub> ·3H <sub>2</sub> O	23,9; 0,1	10; 0,025	Salzsäure	85-45
Cu(NO <sub>3</sub> ) <sub>2</sub> ·3H <sub>2</sub> O	23,9; 0,1	10; 0,025	Benzoessäure	85-45
Cu(NO <sub>3</sub> ) <sub>2</sub> ·3H <sub>2</sub> O	23,9; 0,1	10; 0,025		65-25
Cu(NO <sub>3</sub> ) <sub>2</sub> ·3H <sub>2</sub> O	47,8; 0,2	10; 0,025		85-45
Cu(NO <sub>3</sub> ) <sub>2</sub> ·3H <sub>2</sub> O	47,8; 0,2	10; 0,025	Salpetersäure	85-45
Cu(NO <sub>3</sub> ) <sub>2</sub> ·3H <sub>2</sub> O	47,8; 0,2	10; 0,025		95-65

Bei allen Ansätzen ist die Bildung eines Feststoffs zu beobachten. Die Suspensionen werden anschließend zentrifugiert, abdekantiert und mit 5 mL frischem DMF versetzt. Nach kräftigem Schütteln werden die Röhrchen auf 95 °C erhitzt und über Nacht bei dieser Temperatur gehalten. Es wird erneut zentrifugiert, abdekantiert und mit 5 mL

Ethanol aufgefüllt. Die Röhren werden auf 70 °C temperiert und erneut über Nacht bei dieser Temperatur gehalten. Nach Zentrifugation und Abdekantieren des Lösemittels wird der entstandene Feststoff bei 80 °C im Vakuumtrockenschrank getrocknet.

### 6.30 Reaktionen aus dem Appendix zu „Metal-Organic Framework Gels Based on a Bisamide Tetracarboxyl Ligand for Carbon Dioxide, Sulfur Dioxide and Selective Dye Uptake“

#### 6.30.1 Synthesen mit Co-Liganden

Bei allen Synthesen wurden die Bedingungen durchvariiert und verschiedenste Ansätze getestet. Tabelle 14 fasst die gewählten Bedingungen zusammen. Alle Synthesen wurden in einem Pyrex-Kulturröhrchen mit einem Volumen von ca. 5 mL durchgeführt. Die Edukte wurden zusammengegeben und im Ultraschallbad auf 80 °C temperiert.

Tabelle 14. Einwaagen, Synthesebedingungen und Co-Liganden der Synthesen.

Metallsalz	Einwaagen an Ligand [mg]	Molare Verhältnisse Ligand:Metall:Co-Ligand	Co-Liganden	Temperaturen [°C]	Lösemittel, Menge [mL]
Cr(NO <sub>3</sub> ) <sub>3</sub> ·9H <sub>2</sub> O	10, 20, 30, 60	1:2:0, 1:4:0, 1:2:2, 1:4:2, 1:4:4, 1:8:4	DABCO, 4,4'-Bipyridin, Pyrazin	80-130	DMF, DEF, 5 mL
Zn(NO <sub>3</sub> ) <sub>2</sub> ·6H <sub>2</sub> O	10, 20, 30, 60	1:2:2, 1:4:2, 1:4:4, 1:8:4	DABCO, 4,4'-Bipyridin, Pyrazin	80-130	DMF, DEF, 5 mL

$\text{Cu}(\text{NO}_3)_2 \cdot 3\text{H}_2\text{O}$	10, 20, 30, 60	1:2:2, 1:4:2, 1:4:4, 1:8:4	DABCO, 4,4'- Bipyridin, Pyrazin	80-130	DMF, DEF, 5 mL
$\text{Cd}(\text{NO}_3)_2 \cdot 4\text{H}_2\text{O}$	10, 20, 30, 60	1:2:2, 1:4:2, 1:4:4, 1:8:4	DABCO, 4,4'- Bipyridin, Pyrazin	80-130	DMF, DEF, 5 mL

### 6.30.2 Synthesen entsprechend Cr-L1, Al-L1 und AlCr-L1

Unter den gleichen Bedingungen wie in der Publikation für **Cr-**, **Al-** und **AlCr-L1** beschrieben wurden Synthesen mit den Salzen  $\text{Cr}(\text{NO}_3)_3 \cdot 9\text{H}_2\text{O}$ ,  $\text{Mn}(\text{NO}_3)_2 \cdot 6\text{H}_2\text{O}$ ,  $\text{Fe}(\text{NO}_3)_3 \cdot 9\text{H}_2\text{O}$ ,  $\text{Co}(\text{NO}_3)_2 \cdot 6\text{H}_2\text{O}$ ,  $\text{Ni}(\text{NO}_3)_2 \cdot 6\text{H}_2\text{O}$ ,  $\text{Cu}(\text{NO}_3)_2 \cdot 3\text{H}_2\text{O}$ ,  $\text{Zn}(\text{NO}_3)_2 \cdot 6\text{H}_2\text{O}$  und  $\text{Cd}(\text{NO}_3)_2 \cdot 4\text{H}_2\text{O}$  durchgeführt.

Am Ende der Synthesen entstandene Niederschläge werden abzentrifugiert und erneut in DMF suspendiert. Nach Erhitzen auf 80 °C für 24 h werden die Niederschläge abzentrifugiert und in Ethanol suspendiert. Nach Erhitzen auf 70 °C für 24 h werden die Niederschläge abzentrifugiert und für 24 h bei 80 °C im Vakuumtrockenschrank getrocknet.

### 6.30.3 Synthesen entsprechend Co-L1

Unter den gleichen Bedingungen wie in der Publikation für **Co-L1** beschrieben wurden Synthesen mit den Salzen  $\text{Cr}(\text{NO}_3)_3 \cdot 9\text{H}_2\text{O}$ ,  $\text{Co}(\text{NO}_3)_2 \cdot 6\text{H}_2\text{O}$ ,  $\text{Ni}(\text{NO}_3)_2 \cdot 6\text{H}_2\text{O}$ ,  $\text{Cu}(\text{NO}_3)_2 \cdot 3\text{H}_2\text{O}$ ,  $\text{CuCl}_2 \cdot 2\text{H}_2\text{O}$ ,  $\text{CuCl}$  und  $\text{AgNO}_3$  durchgeführt.

Die entstandenen Niederschläge werden in Mutterlauge im Röntgenpulverdiffraktogramm vermessen.

### 6.30.4 Raumtemperatursynthesen der Metallogele Cr-L1 und Al-L1

Die Ansatzgrößen werden in Bezug auf die molaren Verhältnisse identisch zu denen in der Publikation als **Cr-L1** und **Al-L1** beschriebenen Gelsynthesen gehalten. Als

Lösemittel werden anstatt reinem DMF Mischungen von je vier Teilen DMF und einem Teil EtOH, DMA, DMSO, NMP oder H<sub>2</sub>O eingesetzt.

Es werden Rollrandgläschen mit je 2 mL der Suspensionen gefüllt, anschließend werden diese in einem Exsikkator platziert. Ein weiteres Rollrandgläschen wird mit 2 mL Triethylamin gefüllt und ebenfalls im Exsikkator platziert. Der Exsikkator wird geschlossen und für 10 d nicht mehr geöffnet.

Abbildung 1. Schematische Darstellung über den Aufbau von Koordinationspolymeren. Oben sind mögliche Knotenpunkte gezeigt, unten mögliche Liganden. Nachdruck von Ref. 1 mit Genehmigung des Centre National de la Recherche Scientifique (CNRS) und der Royal Society of Chemistry. ....	1
Abbildung 2. Potentielle Anwendungsbereiche für MOFs außen; prototypische Liganden und schematische Darstellung von MOFs in der Mitte. Nachdruck von Ref. 1 mit Genehmigung des Centre National de la Recherche Scientifique (CNRS) und der Royal Society of Chemistry. <sup>1</sup> .....	2
Abbildung 3. Isothermentypen nach IUPAC-Klassifizierung. Nachdruck aus Ref. 10 mit Genehmigung von De Gruyter, IUPAC, ©2015. <sup>10</sup> .....	4
Abbildung 4. Hysteresetypen nach IUPAC-Empfehlung. Nachdruck aus Ref. 10 mit Genehmigung von De Gruyter, IUPAC, ©2015. <sup>10</sup> .....	5
Abbildung 5. (a) Schematische Darstellung des Quervernetzens des organischen Liganden in einem MOF (AzM) und anschließende Zerstörung des MOF-Netzwerkes, um ein polymeres Gel zu erhalten. (b) Molekülstrukturen des Liganden (AzTPDC) und der Quervernetzer. Nachdruck mit Genehmigung von Ref. . Copyright 2013 American Chemical Society.....	10
Abbildung 6. Mikroskopaufnahmen der MOFs (a) AzM-BP, (b) AzKUMOF, (c) AzUiOMOF, ihrer quervernetzten Zwischenprodukte und den daraus resultierenden polymeren Gelen. Nachdruck mit Genehmigung von Ref. 28. Copyright 2013 American Chemical Society.....	10
Abbildung 7. Schematische Darstellung der Synthese von kubischen Gelpartikeln. (a) Kristallisation, (b) Quervernetzungsreaktion, (c) Entfernen der koordinierten Metallionen. Nachdruck mit Genehmigung von Ref. . Copyright 2012 John Wiley and Sons. ....	11
Abbildung 8. Ergebnisse der Suche nach Publikationen bei SciFinder, nach Stichworten und Jahr sortiert.....	12
Abbildung 9. Bildung von metall-organischen Gelen über den Weg des gestörten Wachstums. Es bilden sich nano-MOF-Cluster, welche dann unregelmäßig miteinander	

vernetzen (rechte Hälfte der Abbildung). Nachdruck mit Genehmigung von Ref. . Copyright 2013 Springer Nature. ....	13
Abbildung 10. Schematische Darstellung der Permeation eines Gasgemisches durch eine dichte Membran. ....	14
Abbildung 11. Schematische Darstellung der Gastrennung an einer porösen Membran durch Knudsen-Diffusion. ....	15
Abbildung 12. Schematische Darstellung der Gastrennung an einer porösen Membran durch Oberflächendiffusion. ....	16
Abbildung 13. Schematische Darstellung der Gastrennung an einer porösen Molekularsiebmembran. ....	17
Abbildung 14. Schematische Darstellung der umgekehrten Korrelation zwischen Permeabilität und Selektivität, genannt <i>Robeson upper bounds</i> . Kommerziell relevante Materialien bewegen sich im Bereich dieser <i>upper bounds</i> oder übertreffen sie. Nachdruck von Ref. mit Genehmigung der Royal Society of Chemistry. ....	19
Abbildung 15. Schematische Darstellung einer Mixed-Matrix-Membran mit Füllstoffen verschiedener Größe und Form. ....	19
Abbildung 16. Ligand H <sub>4</sub> L1 und seine schematische Darstellung als „Brücke“ .....	103
Abbildung 17. H <sub>4</sub> L1 in verschiedenen geometrischen Aufbauten. Der Ligand ist gelb gefärbt, das Metallzentrum blau, neutrale Co-Liganden hellgrün. (a) H <sub>4</sub> L1 in einer „eindimensionalen“ Kettenstruktur. (b) Über einen neutralen Co-Liganden zweidimensional verknüpfte Ketten. (c) Dreidimensionales Koordinationsnetzwerk basierend auf H <sub>4</sub> L1 und einem neutralen Co-Liganden. ....	104
Abbildung 18. Rasterelektronenmikroskopaufnahmen von <b>Co-L1</b> , welches in Dimethylformamid synthetisiert wurde. ....	106
Abbildung 19. Rasterelektronenmikroskopaufnahmen von <b>Cu-L1</b> (oben links), <b>Fe-L1</b> (oben rechts), <b>Mn-L1</b> (unten links) und <b>Ni-L1</b> (unten rechts). ....	107
Abbildung 20. Rasterelektronenmikroskopaufnahmen von <b>Zn-L1</b> bei verschiedenen Vergrößerungen. ....	108
Abbildung 21. Röntgenpulverdiffraktogramme von H <sub>4</sub> L1 und der Verbindungen mit Zn(II). ....	109

Abbildung 22. <b>Co-L1</b> nachempfundene Ansätze mit verschiedenen Metallsalzen nach Abdampfen des Ammoniaks. Der Ansatz <b>Co-L1</b> ist hier ebenfalls zu sehen, über der Bildbeschriftung „Co(III) hexammine chloride“. Be den Ansätzen mit Ag(I) und Cr(III) konnten als einzige keine Niederschläge erhalten werden. Cr(NO <sub>3</sub> ) <sub>3</sub> ·9H <sub>2</sub> O erwies sich als unlöslich. ....	110
Abbildung 23. Röntgenpulverdiffraktogramme der <b>Co-L1</b> nachempfundene Ansätze mit verschiedenen anderen Metallionen. ....	111
Abbildung 24. In einer triethylaminhaltigen Atmosphäre und bei Raumtemperatur synthetisierte Cr- und Al-Metallogele unter Beimengung eines zweiten Lösemittels. Die grünen und braungrünen Gele enthalten Cr(III), die farblosen Gele Al(III). ....	113
Abbildung 25. Veresterung von para-Terephthalaldehydsäure.....	167
Abbildung 26. <sup>1</sup> H-NMR-Spektrum von Methyl-4-formylbenzoat.....	168
Abbildung 27. Schematische Darstellung der Baylis-Hillman-Reaktion zwischen Methyl-4-formylbenzoat und Methylacrylat in Anwesenheit von DABCO. ....	169
Abbildung 28. <sup>1</sup> H-NMR-Spektrum von Methyl-4-(1-Hydroxy-2-(methoxycarbonyl)allyl)benzoat, mit Verunreinigungen durch DABCO.....	170
Abbildung 29. Schematische Darstellung der Synthese von N,N',N''-(1,3,5-triazin-2,4,6-triyl)tris(4-methylbenzamid) aus Melamin und para-Toluoylchlorid.....	171
Abbildung 30. <sup>1</sup> H-NMR-Spektrum von N,N',N''-(1,3,5-triazin-2,4,6-triyl)tris(4-methylbenzamid) vor dem Waschen mit Chloroform (links) und danach (rechts)...	171
Abbildung 31. Geplante Syntheseroute zum Produkt 4,4',4''-(((1,3,5-triazin-2,4,6-triyl)tris(azanediyl))tris(carbonyl))tribenzoesäure. ....	172
Abbildung 32. ESI-Massenspektrum der hergestellten Verbindung. Das Molekulargewicht der sechsfach substituierten Melaminverbindung beträgt 1099 g/mol, die Unterschiede zwischen den detektierten Signalen betragen ungefähr 162 g/mol und entsprechen damit dem über dem Doppelpfeil dargestellten Fragment.....	173
Abbildung 33. Geplante Synthese des mehrfach substituierten Liganden basierend auf Melamin. Die typische Kupplungsreaktion unter Verwendung von DCC (oben) verlief ebenso wenig erfolgreich wie die mit vorheriger <i>in-situ</i> -Bildung eines Aktivesters (unten).....	174

Abbildung 34. Schematischer Syntheseweg für Dimethyl-5-(chlorocarbonyl)isophthalat ausgehend von Benzol-1,3,5-tricarbonsäure.....	175
Abbildung 35. <sup>1</sup> H-NMR-spektroskopische Verfolgung der Umsetzung von Benzol-1,3,5-tricarbonsäure zu Dimethyl-5-(chlorocarbonyl)isophthalat. Oben links: <sup>1</sup> H-NMR-Spektrum von Trimethyl-1,3,5-benzoltricarboxylat. Oben rechts: <sup>1</sup> H-NMR-Spektrum von 3,5-Bis(methoxycarbonyl)benzoesäure. Unten: <sup>1</sup> H-NMR-Spektrum von Dimethyl-5-(chlorocarbonyl)isophthalat. ....	176
Abbildung 36. Geplante Synthese von Hexamethyl-5,5',5''-(((1,3,5-Triazin-2,4,6-triyl)tris)azanediyl))tris(carbonyl)triisophthalat.....	177
Abbildung 37. Geplante Synthese von 5,5',5''-(((1,3,5-Triazin-2,4,6-triyl)tris-(azanediyl))tris(carbonyl))triisophthalsäure.....	177
Abbildung 38. Synthese von 2,2',2''-(((1,3,5-Triazin-2,4,6-triyl)tris(piperazin-4,1-diyl))triessigsäure ausgehend von Cyanurchlorid und 1-Boc-piperazin.....	178
Abbildung 39. <sup>1</sup> H-NMR-Spektren der Zwischenprodukte und des Endproduktes der Synthese von 2,2',2''-(((1,3,5-Triazin-2,4,6-triyl)tris(piperazin-4,1-diyl))triessigsäure. Oben links: <sup>1</sup> H-NMR-Spektrum von Tri-tert.-butyl-4,4',4''-(1,3,5-triazin-2,4,6-triyl)tris(piperazin-1-carboxylat). Oben rechts: <sup>1</sup> H-NMR-Spektrum von 2,4,6-Tri(piperazin-1-yl)-1,3,5-triazin. Unten: <sup>1</sup> H-NMR-Spektrum von 2,2',2''-(((1,3,5-triazin-2,4,6-triyl)tris(piperazin-4,1-diyl))triessigsäure.....	179
Abbildung 40. REM-Aufnahme von 2,2',2''-(((1,3,5-Triazin-2,4,6-triyl)tris(piperazin-4,1-diyl))triessigsäure. ....	180
Abbildung 41. Synthese von <i>N,N'</i> -(4-Carboxyphenyl)terephthalamid. ....	180
Abbildung 42. <sup>1</sup> H-NMR-Spektrum von <i>N,N'</i> -(4-Carboxyphenyl)terephthalamid. ....	181
Abbildung 43. REM-Aufnahmen von <i>N,N'</i> -(4-Carboxyphenyl)terephthalamid.....	181
Abbildung 44. Röntgenpulverdiffraktogramm von <i>N,N'</i> -(4-Carboxyphenyl)terephthalamid.....	182
Abbildung 45. Synthese von <i>N,N'</i> -(3-Carboxyphenyl)terephthalamid.....	182
Abbildung 46. Röntgenpulverdiffraktogramm von <i>N,N'</i> -(3-Carboxyphenyl)terephthalamid.....	183



Abbildung 47. $^1\text{H-NMR-Spektrum}$ von 3,3'-(Terephthaloylbis(azanediyl))dibenzoesäure. ....	184
Abbildung 48. Synthese von $N,N'$ -4CMPTAm, $N,N'$ -4CMOPTAm und $N,N'$ -3Br-4CPTAm. ....	185
Abbildung 49. $^1\text{H-NMR-Spektrum}$ der Reaktionsprodukte der versuchten Synthese von $N,N'$ -3Br-4CPTAm. ....	185
Abbildung 50. $^1\text{H-NMR-Spektrum}$ von $N,N'$ -4CMPTAm. ....	186
Abbildung 51. $^1\text{H-NMR-Spektrum}$ von $N,N'$ -4CMOPTAm. ....	187
Abbildung 52. Röntgenpulverdiffraktogramme der Verbindungen $N,N'$ -4CMPTAm, $N,N'$ -4CMOPTAm und $N,N'$ -3Br-4CPTAm. ....	188
Abbildung 53. Synthese von $N,N'$ -(3,5-Dicarboxyphenyl)terephthalamid. ....	189
Abbildung 54. $^1\text{H-NMR-Spektrum}$ von $N,N'$ -(3,5-Dicarboxyphenyl)terephthalamid. ....	189
Abbildung 55. Röntgenpulverdiffraktogramm von $N,N'$ -(3,5-Dicarboxyphenyl)terephthalamid. ....	190
Abbildung 56. Rasterelektronenmikroskopaufnahme von $N,N'$ -(3,5-Dicarboxyphenyl)terephthalamid. ....	190
Abbildung 57. Reaktionsschema für die Synthese von Dimethyl-4,4'-((1,4-phenylenbis(azanediyl))bis(carbonyl))dibenzoat. ....	191
Abbildung 58. Reaktionsschema für die Synthese von Tetramethyl-5,5'-((1,4-phenylenbis(azanediyl))bis(carbonyl))diisophthalat. ....	192
Abbildung 59. $^1\text{H-NMR-Spektrum}$ von Tetramethyl-5,5'-((1,4-phenylenbis(azanediyl))bis(carbonyl))diisophthalat. ....	193
Abbildung 60. Reaktionsschema für die Synthese von 5,5'-((1,4-Phenylenbis(azanediyl))bis(carbonyl))diisophthalsäure über eine Verseifung (a.) und über Hydrolyse (b.). ....	194
Abbildung 61. $^1\text{H-NMR-Spektren}$ zur Verseifung (links) und Hydrolyse (rechts) von Tetramethyl-5,5'-((1,4-phenylenbis(azanediyl))bis(carbonyl))diisophthalat. ....	194
Abbildung 62. Synthese von 5,5'-(Fumarylbis(azanediyl))diisophthalsäure. ....	195

Abbildung 63. $^1\text{H}$ -NMR-Spektrum nach Abbruch der Synthese nach versuchter Erzeugung des Fumarylchlorids in Toluol. Es sind nur Signale der Fumarsäure zu sehen. ....	196
Abbildung 64. Reaktionsschema für die Synthesen von 3,3'-(Oxalylbis(azanediyl))dibenzoessäure und 4,4'-(Oxalylbis(azanediyl))dibenzoessäure aus Oxalylchlorid. ....	197
Abbildung 65. $^1\text{H}$ -NMR-Spektrum der Synthese von 3,3'-(Oxalylbis(azanediyl))dibenzoessäure. Bei 10,6 ppm ist das Signal der Amidprotonen des Produktes zu sehen, bei 9,93 ppm das Amidproton des nur einfach mit 3-Aminobenzoessäure abreagiertem Oxalylchlorids. ....	197
Abbildung 66. $^1\text{H}$ -NMR-Spektrum der Synthese von 4,4'-(Oxalylbis(azanediyl))dibenzoessäure. Das Produkt liegt nicht vor. ....	198
Abbildung 67. REM-Aufnahme des entstandenen Niederschlags der Synthese mit 2,2',2''-((1,3,5-Triazin-2,4,6-triyl)tris(piperazin-4,1-diyl))triessigsäure und Chrom(III)-nitrat.....	199
Abbildung 68. REM-Aufnahmen von Zn- $N,N'$ -4CPTAm.....	201
Abbildung 69. Röntgenpulverdiffraktogramme des Liganden $N,N'$ -4CPTAm, sowie des Niederschlags zweier Synthesen mit dem Liganden und einem Zinksalz. ....	202
Abbildung 70. Röntgenpulverdiffraktogramme des Liganden $N,N'$ -4CPTAm, sowie des Niederschlags zweier Synthesen mit dem Liganden und einem Kupfersalz. ....	204
Abbildung 71. REM-Aufnahmen von Cu- $N,N'$ -4CPTAm. ....	206
Abbildung 72. Röntgenpulverdiffraktogramme des Liganden $N,N'$ -3CPTAm, sowie des Niederschlags einer Synthese mit dem Liganden und einem Zinksalz. ....	207
Abbildung 73. REM-Aufnahmen von Zn- $N,N'$ -3CPTAm.....	208
Abbildung 74. Röntgenpulverdiffraktogramme des Liganden $N,N'$ -3CPTAm, sowie des Niederschlags einer Synthese mit dem Liganden und einem Kupfersalz.....	209
Abbildung 75. REM-Aufnahmen von Zn- $N,N'$ -3CPTAm.....	210
Abbildung 76. Struktur des Liganden $\text{H}_4\text{L1}\cdot 4\text{DMF}$ , mit zweien der vier wasserstoffverbrückten DMF-Moleküle (70% thermische Auslenkung, H-Atome mit	

arbiträren Radii). Die gelöste Fehlordnung der DMF-Moleküle ist nicht gezeigt. CCDC No. 1889949. ....	211
Abbildung 77. Links: Die Metallogele (v. l. n. r.) Cr-, AlCr-, Al-, Fe-, In-, Co-L1. Mitte: Cr-, AlCr-, Al-Aerogele, Cr-Xerogel. Rechts: Cr-, AlCr-, Al-Metallogel aus ihren Gefäßen entnommen. Die gute Formstabilität des Cr-Metallogels sorgt dafür, dass die zylindrische Form erhalten bleibt. ....	212
Abbildung 78. Adsorptions- (gefüllte Symbole) und Desorptionsisothermen (leere Symbole) der Aero- und Xerogele, links für Stickstoff bei 77 K, rechts für Argon bei 87 K. ....	213
Abbildung 79. Mit Methylgruppen geschützte Ligandenvorstufen. Oben links: Methyl-4-(1-hydroxy-2-(methoxycarbonyl)allyl)benzoat. Oben rechts: Dimethyl-4,4'-((1,4-phenylenbis(azanediyl))bis(carbonyl))dibenzoat. Unten: <i>N,N'</i> -(3,5-Dicarboxyphenyl)terephthalamid. ....	215
Abbildung 80. Synthetisierte, potenzielle Liganden. Oben links: 2,2',2''-((1,3,5-Triazin-2,4,6-triyl)tris(piperazin-4,1-diyl))triessigsäure. Oben rechts: <i>N,N'</i> -(4-Carboxyphenyl)terephthalamid und zwei der erfolgreich synthetisierten Derivate. Unten links: <i>N,N'</i> -(3-Carboxyphenyl)terephthalamid. Unten rechts: Der literaturbekannte Ligand <i>N,N'</i> -(3,5-Dicarboxyphenyl)terephthalamid. ....	215
Abbildung 81. Rasterelektronenmikroskopaufnahmen von Zn- <i>N,N'</i> -4CPTAm (links) und Cu- <i>N,N'</i> -4CPTAm (rechts).....	216
Abbildung 82. Rasterelektronenmikroskopaufnahmen von Zn- <i>N,N'</i> -3CPTAm (links) und Cu- <i>N,N'</i> -3CPTAm (rechts).....	216
Abbildung 83. Baylis-Hillman-Reaktion zwischen Methyl-4-formylbenzoat und Methylacrylat.....	219
Abbildung 84. Aufbau und Prinzip der Konvektionssynthese im Sandbad. ....	238

<sup>1</sup> Janiak, C.; Vieth, J. K. MOFs, MILs and more: concepts, properties and applications for porous coordination networks (PCNs). *New J. Chem.* **2010**, *34* (11).

<sup>2</sup> Hoskins, B. F.; Robson, R. Infinite polymeric frameworks consisting of three dimensionally linked rod-like segments. *Journal of the American Chemical Society* **1989**, *111* (15), 5962-5964.

- 
- <sup>3</sup> Hoskins, B. F.; Robson, R. Design and construction of a new class of scaffolding-like materials comprising infinite polymeric frameworks of 3D-linked molecular rods. A reappraisal of the zinc cyanide and cadmium cyanide structures and the synthesis and structure of the diamond-related frameworks  $[N(CH_3)_4][CuIZnII(CN)_4]$  and  $CuI[4,4',4'',4''']$ -tetracyanotetraphenylmethane]BF<sub>4</sub>.x C<sub>6</sub>H<sub>5</sub>NO<sub>2</sub>. *Journal of the American Chemical Society* **1990**, *112* (4), 1546-1554.
- <sup>4</sup> Yaghi, O. M.; Li, H. Hydrothermal Synthesis of a Metal-Organic Framework Containing Large Rectangular Channels. *J. Am. Chem. Soc.* **1995**, *117* (41), 10401-10402.
- <sup>5</sup> Yaghi, O. M.; Li, G.; Li, H. Selective binding and removal of guests in a microporous metal-organic framework. *Nature* **1995**, *378* (6558), 703-706.
- <sup>6</sup> Puppe, L. Zeolithe - Eigenschaften und technische Anwendungen. *Chem. unserer Zeit* **1986**, *20* (4), 117-127.
- <sup>7</sup> Holderich, W.; Hesse, M.; Naumann, F. Zeolites - Catalysts for Organic Syntheses. *Angew. Chem. Int. Edit.* **1988**, *27* (2), 226-246.
- <sup>8</sup> Thomas, J. M.; Raja, R. Review: The Materials Chemistry of Inorganic Catalysts. *Aust. J. Chem.* **2002**, *54* (10), 551-560.
- <sup>9</sup> Dong, Y.-B.; Jin, G.-X.; Smith, M. D.; Huang, R.-Q.; Tang, B.; zur Loye, H.-C.  $[Ag_2(C_{33}H_{26}N_2O_2)(H_2O)_2(SO_3CF_3)_2] \cdot 0.5C_6H_6$ : A Luminescent Supramolecular Silver(I) Complex Based on Metal-Carbon and Metal-Heteroatom Interactions. *Inorg. Chem.* **2002**, *41* (19), 4909-4914.
- <sup>10</sup> Thommes, M.; Kaneko, K.; Neimark, A. V.; Olivier, J. P.; Rodriguez-Reinoso, F.; Rouquerol, J.; Sing, K. S. W. Physisorption of gases, with special reference to the evaluation of surface area and pore size distribution (IUPAC Technical Report). *Pure Appl. Chem.* **2015**, *87* (9-10).
- <sup>11</sup> Langmuir, I. The Adsorption of Gases on Plane Surfaces of Glass, Mica and Platinum. *J. Am. Chem. Soc.* **1918**, *40* (9).
- <sup>12</sup> Brunauer, S.; Emmett, P. H.; Teller, E. Adsorption of Gases in Multimolecular Layers. *J. Am. Chem. Soc.* **1938**, *60* (2).
- <sup>13</sup> Piepenbrock, M. O.; Lloyd, G. O.; Clarke, N.; Steed, J. W. Metal- and anion-binding supramolecular gels. *Chem. Rev.* **2010**, *110* (4), 1960-2004.
- <sup>14</sup> Terech, P.; Weiss, R. G. Low Molecular Mass Gelators of Organic Liquids and the Properties of Their Gels. *Chem. Rev.* **1997**, *97* (8), 3133-3160.
- <sup>15</sup> Flory, P. J. Introductory lecture. *Faraday Discuss. Chem. Soc.* **1974**, *57*.
- <sup>16</sup> Fages, F. Metal coordination to assist molecular gelation. *Angew Chem Int Ed Engl* **2006**, *45* (11).
- <sup>17</sup> Banerjee, S.; Adarsh, N. N.; Dastidar, P. A crystal engineering rationale in designing a CdII coordination polymer based metallogel derived from a C<sub>3</sub> symmetric tris-amide-tris-carboxylate ligand. *Soft Matter* **2012**, *8* (29), 7623.
- <sup>18</sup> Adarsh, N. N.; Sahoo, P.; Dastidar, P. Is a Crystal Engineering Approach Useful in Designing Metallogels? A Case Study. *Cryst. Growth Des.* **2010**, *10* (11).
- <sup>19</sup> Tam, A. Y.-Y.; Wong, K. M.-C.; Wang, G.; Yam, V. W.-W. Luminescent metallogels of platinum(ii) terpyridyl complexes: interplay of metal...metal,  $\pi$ - $\pi$  and hydrophobic-hydrophobic interactions on gel formation. *Chem. Commun.* **2007**, (20).
- <sup>20</sup> Piepenbrock, M.-O. M.; Clarke, N.; Steed, J. W. Metal Ion and Anion-Based "Tuning" of a Supramolecular Metallogel†. *Langmuir* **2009**, *25* (15).
- <sup>21</sup> Nath, K.; Husain, A.; Dastidar, P. Metallogels and Silver Nanoparticles Generated from a Series of Transition Metal-Based Coordination Polymers Derived from a New Bis-pyridyl-bis-amide Ligand and Various Carboxylates. *Cryst. Growth Des.* **2015**, *15* (9).
- <sup>22</sup> Tam, A. Y.; Yam, V. W. Recent advances in metallogels. *Chem Soc Rev* **2013**, *42* (4), 1540-1567.
- <sup>23</sup> Hirst, A. R.; Escuder, B.; Miravet, J. F.; Smith, D. K. High-tech applications of self-assembling supramolecular nanostructured gel-phase materials: from regenerative medicine to electronic devices. *Angew. Chem. Int. Ed. Engl.* **2008**, *47* (42).
- <sup>24</sup> Kistler, S. S. Coherent Expanded Aerogels and Jellies. *Nature* **1931**, *127* (3211), 741.
- <sup>25</sup> Barron, R. F.; Nellis, G. F. *Cryogenic Heat Transfer*, CRC Press: **1999**.
-

- 
- <sup>26</sup> Maleki, H.; Durães, L.; Portugal, A. An overview on silica aerogels synthesis and different mechanical reinforcing strategies. *J. Non-Cryst. Solids* **2014**, *385*, 55-74.
- <sup>27</sup> Marrero-Tellado, J. J.; Díaz, D. D. Transformation of rigid metal-organic frameworks into flexible gel networks and vice versa. *Cryst. Eng. Comm.* **2015**.
- <sup>28</sup> Ishiwata, T.; Furukawa, Y.; Sugikawa, K.; Kokado, K.; Sada, K. Transformation of metal-organic framework to polymer gel by cross-linking the organic ligands preorganized in metal-organic framework. *J. Am. Chem. Soc.* **2013**.
- <sup>29</sup> Furukawa, Y.; Ishiwata, T.; Sugikawa, K.; Kokado, K.; Sada, K. Nano- and micro-sized cubic gel particles from cyclodextrin metal-organic frameworks. *Angew. Chem. Int. Ed. Engl.* **2012**, *51* (42), 10566-10569.
- <sup>30</sup> Lohe, M. R.; Rose, M.; Kaskel, S. Metal-organic framework (MOF) aerogels with high micro- and macroporosity. *Chem. Commun. (Camb.)* **2009**, (40), 6056-6058.
- <sup>31</sup> <https://www.cas.org/>
- <sup>32</sup> Saraji, M.; Shahvar, A. Metal-organic aerogel as a coating for solid-phase microextraction. *Anal. Chim. Acta* **2017**, *973*, 51-58.
- <sup>33</sup> Albo, J.; Vallejo, D.; Beobide, G.; Castillo, O.; Castano, P.; Irabien, A. Copper-Based Metal-Organic Porous Materials for CO<sub>2</sub> Electrocatalytic Reduction to Alcohols. *Chem. Sus. Chem.* **2017**, *10* (6), 1100-1109.
- <sup>34</sup> Sutar, P.; Maji, T. K. Coordination polymer gels: soft metal-organic supramolecular materials and versatile applications. *Chem Commun (Camb)* **2016**, *52* (52), 8055-8074.
- <sup>35</sup> Kitagawa, S.; Kitaura, R.; Noro, S. Functional porous coordination polymers. *Angew. Chem. Int. Ed. Engl.* **2004**, *43* (18), 2334-2375.
- <sup>36</sup> Li, L.; Xiang, S.; Cao, S.; Zhang, J.; Ouyang, G.; Chen, L.; Su, C. Y. A synthetic route to ultralight hierarchically micro/mesoporous Al(III)-carboxylate metal-organic aerogels. *Nat Commun* **2013**, *4*, 1774.
- <sup>37</sup> Koros, W. J.; Mahajan, R. Pushing the limits on possibilities for large scale gas separation: which strategies? *J. Memb. Sci.* **2000**, *175* (2), 181-196.
- <sup>38</sup> He, X.; Hagg, M. B. Membranes for environmentally friendly energy processes. *Membranes (Basel)* **2012**, *2* (4), 706-726.
- <sup>39</sup> Ohlrogge, K.; Stürken, K. The Separation of Organic Vapors from Gas Streams by Means of Membranes. In *Wiley-VCH Verlag GmbH*; Pereira Nunes, S.; Peinemann, K.-V., Eds.; **2001**.
- <sup>40</sup> Chung, T.-S.; Jiang, L. Y.; Li, Y.; Kulprathipanja, S. Mixed matrix membranes (MMMs) comprising organic polymers with dispersed inorganic fillers for gas separation. *Prog. Polym. Sci.* **2007**, *32* (4), 483-507.
- <sup>41</sup> Baker, R. W. Future Directions of Membrane Gas Separation Technology. *Ind. Eng. Chem. Res.* **2002**, *41* (6), 1393-1411.
- <sup>42</sup> Robeson, L. M. Correlation of Separation Factor Versus Permeability for Polymeric Membranes. *J. Memb. Sci.* **1991**, *62* (2), 165-185.
- <sup>43</sup> Robeson, L. M. The upper bound revisited. *J. Memb. Sci.* **2008**, *320* (1-2), 390-400.
- <sup>44</sup> Qiu, S.; Ben, T. *Porous Polymers: Design, Synthesis and Applications*, Royal Society of Chemistry: **2015**.
- <sup>45</sup> Liu, J.; Yu, J. Chapter 1 - Toward Greener and Designed Synthesis of Zeolite Materials. In *Zeolites and Zeolite-Like Materials*; Sels, B. F.; Kustov, L. M., Eds.; Elsevier: Amsterdam, **2016**; pp 1-32.
- <sup>46</sup> Davis, M. E. Zeolites and molecular sieves: not just ordinary catalysts. *Ind. Eng. Chem. Res.* **1991**, *30* (8), 1675-1683.
- <sup>47</sup> Tanh Jeazet, H. B.; Staudt, C.; Janiak, C. Metal-organic frameworks in mixed-matrix membranes for gas separation. *Dalton Trans.* **2012**, *41* (46), 14003-27.
- <sup>48</sup> Merkel, T. C.; Freeman, B. D.; Spontak, R. J.; He, Z.; Pinnau, I.; Meakin, P.; Hill, A. J. Ultraporous, reverse-selective nanocomposite membranes. *Science* **2002**, *296* (5567), 519-22.
- <sup>49</sup> O'Keeffe, M.; Eddaoudi, M.; Li, H.; Reineke, T.; Yaghi, O. M. Frameworks for Extended Solids: Geometrical Design Principles. *J. Solid State Chem.* **2000**, *152* (1), 3-20.
-

- 
- <sup>50</sup> Kitson, P. J.; Marshall, R. J.; Long, D.; Forgan, R. S.; Cronin, L. 3D printed high-throughput hydrothermal reactionware for discovery, optimization, and scale-up. *Angew. Chem. Int. Ed. Engl.* **2014**, *53* (47), 12723-12738.
- <sup>51</sup> Hu, D.; Kluger, R. Functional cross-linked hemoglobin bis-tetramers: geometry and cooperativity. *Biochemistry* **2008**, *47* (47), 12551-12561.
- <sup>52</sup> Wang, F.; Wang, C.; Yu, Z.; He, Q.; Li, X.; Shang, C.; Zhao, Y. Two luminescent metal-organic frameworks with multifunctional properties for nitroaromatic compounds sensing and photocatalysis. *RSC Advances* **2015**, *5* (86), 70086-70093.
- <sup>53</sup> Wang, F.; Wang, C.; Yu, Z.; Xu, K.; Li, X.; Fu, Y. Two multifunctional Mn(II) metal-organic frameworks: Synthesis, structures and applications as photocatalysis and luminescent sensor. *Polyhedron* **2016**, *105*, 49-55.
- <sup>54</sup> Kaplan, J.; Echange Broadening in Nuclear Magnetic Resonance. *J. Chem. Phys.*, **1958**, *28*, 278-282.
- <sup>55</sup> Yaghi, O. M.; O'Keeffe, M.; Ockwig, N. W.; Chae, H. K.; Eddaoudi, M.; Kim, J. Reticular synthesis and the design of new materials. *Nature* **2003**, *423* (6941), 705-714.
- <sup>56</sup> Chouai, A.; Venditto, J.; Simanek, E. E.; Large Scale, Green Synthesis of a Generation-1 Melamine (Triazine) Dendrimer. *Org. Synth.* 2009, *86*, 141-150.